Search for supersymmetry with the ATLAS detector and development of the High Granularity Timing Detector

Christina Agapopoulou

université
PARIS-SACLAY

Research of Supersymmetry with the ATLAS detector and development of the High Granularity Timing Detector

Thèse de doctorat de l'Université Paris-Saclay

École doctorale n° 576, Particules, Hadrons, Energie, Noyau, Instrumentation, Imagerie, Cosmos et Simulation (PHENIICS)
Spécialité de doctorat: Physique des Particules
Unité de recherche: Université Paris-Saclay, CNRS, IJCLab, 91405, Orsay, France
Référent: : Faculté des sciences d'Orsay

Thèse présentée et soutenue à Orsay, le 25 Septembre 2020, par

Christina AGAPOPOULOU

Composition du jury:

Marie-Hélène Schune Directrice de recherche, IJCLab	Présidente
Didier Contardo Directeur de recherche, IP2I	Rapporteur
Isabelle Wingerter-Seez Directrice de recherche, CPPM	Rapporteuse
Ana Maria Henriques Correia Research Physicist, CERN	Examinatrice
Andreas Hoecker Research Physicist, CERN	Examinateur
Steven Lowette Professeur, Vrije Universiteit Brussel	Examinateur
Nikola Makovec Chargé de recherche, IJCLab	Directeur

Thèse de doctorat

NNT: 2020UPASP019

Acknowledgements

I would like to start by expressing my gratitude to Isabelle Wingerter-Seez, Didier Contardo, Marie-Helene Schune, Ana Maria Henriques Correia, Steven Lowette and Andreas Hoecker for honouring me with accepting to be in my jury. I would particularly like to thank the former two for taking the time to read this manuscript and provide extremely useful remarks and corrections.

Of course, I foremost thank Nikola Makovec, for partaking in this 3-year journey as my supervisor. I would like to thank you for providing me with the opportunity to work on two fascinating subjects, but also for your continued guidance, support and stress-management skills! It was a true pleasure to collaborate with you and learn from your immense knowledge while engaging in an incredible experience full of interesting people, ideas and places. During those three years, I knew your office to be always open for any question or concern that I had, while in parallel I felt sure of my independence. In summary, I could not have wished for a better supervisor!

I would like to continue by giving thanks to Laurent Serin, who, despite not being my supervisor, acted as an unofficial mentor, especially in my first steps in the world of detectors and hardware. Discussing with you has always been a pleasure, and I knew I could come to you for any questions without hesitation. Thank you for all the useful advice, countless recommendations and experience you gave me during those three years! And of course, thanks to you, me (and the whole lab), has managed to survive an entire year without a cafeteria, for which you deserve our wholehearted gratitude.

I would also like to equally thank all the members of the HGTD group. In particular, I would like to thank Sabrina Sacerdoti for being an amazing office-mate, providing me with mate, advice and company during long working hours. I would also like to express my gratitude to the rest of the HGTD testbeam team, and in particular Chiara Grieco and Lucia Castillo Garcia for creating a wonderful atmosphere in a challenging and tiring environment. Corentin Allaire, for his excellent work with the HGTD geometry, as well as his never-ending list of interesting topics for conversation during coffee breaks. I would like to also thank Dirk Zerwas for introducing me to the group as a master student, for his help whenever I had a simulation-related question, as well for reading and giving useful feedback in the theory chapter of this manuscript.

A few words of gratitude for my colleagues at OMEGA, for an amazing collaboration. I would like to especially thank Nathalie Seguin-Moreau for her patience at my ignorance of electronics and the countless hours spent trying to understand ALTIROC. I want to equally express my gratitude to Christophe de la Taille, for all his help, and in particular for his two very informative introductory lectures on electronics that I had the chance to attend.

Additionally, I wish to thank all the members of the 0-lepton group. A special thanks to Kenta Uno and Zuzana Rurikova, for their endless patience and team spirit during the long approval process, which, as I write these words, is almost complete. Finally, I would like to thank Laurent Duflot, for his aid in reading and correcting a large part of this thesis.

I would like to continue by giving thanks to the members of the ATLAS-LAL-IJCLab group for their welcoming and friendly spirit. I am particularly grateful to Lydia Fayard for always being a helpful and kind group leader, to which I could turn for any problem. A big thank you to the administrative personnel of IJCLab for their patience with me, and especially to

Geneviève Gilbert and Catherine Nizery, for always handling the increasing amount of paperwork and problems with a kind attitude and a smile.

I could not of course leave out my fellow doctoral students, with whom I shared the same boat for these three years. Thanks to Antoine Laudrain, whose everlasting knowledge and almost inhuman stamina was an inspiration, to Steven Kalvez for teaching me to always lock my laptop and to Antinea Guerguichon, for sharing her office and good humour with me in my first days as an intern. A big thank you to Mathieu Ehrhart, for always making a bad joke in difficult days (also for helping me eat half a kilo of fish). Anastasia Kotsokechagia, thank you for following me to the ends of the world and to the lab, and for helping me spread the Greek spirit in the corridors - and good luck with the writing. Finally, I would like to thank and congratulate my fellow third year students, Aishik Gosh and Konie Al Khoury and wish them all the best in their future steps, which I have no doubt will be successful. A special thanks to Laurent Basara - despite your non-student status - your sugar-seeking visits to my office were always a welcome distraction.

I would also like to thank the rest of my friends, here in Paris or in the rest of the world. I would like to especially thank Anastasia Loukrezi, Rabi Denguir, Sagar Pal, Gaurav Prabhudesai, Martin Novoa and Felipe Garcia, for always being here to listen to me complain over a glass of beer, for providing support and distractions through bizare conversations, fun activities or late night festivities. I could not have hoped for a better adopted family here in Paris.

Finally, I cannot begin to express my gratitude for my family and friends in Greece. I hope the rest of the readers will forgive me for switching to my mother tongue for this last part.

Σας ευχαριστώ που είστε πάντα δίπλα μου, σε κάθε δύσκολη στιγμή, παρόλο που μας χωρίζουν χιλιάδες χιλιόμετρα. Μου δίνετε απίστευτο κουράγιο και δύναμη κάθε μέρα, χωρίς το οποίο σίγουρα δεν θα τα είχα καταφέρει. Στους γονείς μου, θα ήθελα να τους πω ένα τεράστιο ευχαριστώ που με στηρίζουν σε κάθε μου βήμα και επιλογή, παρόλο που μπορεί να με κρατάει μακριά τους.

Contents

1. Introduction

With the discovery of the Brout-Englert-Higgs boson from the ATLAS and CMS experiments of LHC in 2012, particle physics has entered an unprecedented era; the Standard Model (SM) is complete, with many precise tests confirming its validity and predictive power. On the other hand, there are various experimental observations that indicate that there must be physics beyond the standard model. The existence of dark matter, needed to explain several astrophysical and cosmological observations, the generation of the masses of neutrinos, necessary for their observed oscillations and the strain between the SM predicted and experimentally observed muon anomalous magnetic moment are examples of such phenomena that cannot be explained in the framework of the SM. In addition, various theoretical problems that have risen within our current understanding of fundamental physics, such as the hierarchy problem and the unification of the gauge coupling constants, while not in direct contradiction with the SM, indicate the desirability of new physics.

Any candidate theory that attempts to resolve one or many of the aforementioned issues has to keep in mind the impressive vastness of the success of the SM and ensure that all of its experimentally validated predictions stand under the new theorized model. This can prove to be quite a challenge, and many models are constrained in this way. Out of the remaining valid extensions to the Standard Model, one stands out both for its elegance and relative simplicity but also for the fact that it can resolve simultaneously many of the shortcomings of the SM; this is no other than *supersymmetry*, a theory that proposes a symmetry between bosons and fermions. Initially formulated as a purely theoretical development, it was soon understood that supersymmetry (SUSY) could play a crucial role in shaping modern particle physics, since it predicts a new spectrum of super-particles, partners to the SM ones. This impression was reinforced with the discovery of the Higgs boson at a mass of $\sim$ 125 GeV, which gave rise to the hierarchy problem that can be removed in the supersymmetric frame. Furthermore, with the mounting experimental evidence for the existence of dark matter, supersymmetry was once again coming to the rescue, with the prediction of a viable dark matter particle candidate in the case of an additional supposed Z_2 symmetry, called R-parity. The extensive supersymmetry programs at collider experiments are therefore no surprise. Starting from LEP and Tevatron, SUSY searches reach their peak at the Large Hadron Collider (LHC), where the high energy and luminosity of proton-proton collisions greatly extend the experimental sensitivity to new physics up to the TeV scale. While the first run (Run 1) at the LHC was responsible for the discovery of the Higgs boson, no evidence of SUSY was found. The search efforts continued unwavering in the second run of the collider (Run 2) that took place between 2015-2018. With all LHC experiments collecting a record breaking amount of physics worthy data, the constraints on SUSY related physics are the most stringent so far.

The super-partners of quarks and gluons, named s-quarks and gluinos respectively, are a key to the search strategies of the LHC experiments. These particles, thanks to their coupling to the strong force, could be produced in abundance at proton-proton collisions. The first part of my work focuses on the search of squarks and gluinos with the ATLAS experiment in decays that are mediated once more by strong interactions, giving rise to many jets in the final state. The heavy initial SUSY particles decay through a cascade to the lightest supersymmetric particle (LSP), that under R-parity conservation, is stable and neutral. In order to be compatible with a dark matter candidate, the LSP interacts only weakly and therefore escapes detection, giving rise to large missing transverse momentum in the final state.

Precision measurements like the self-coupling of the Higgs boson and the search for rare process of Beyond the Standard Model (BSM) physics constitute a major part of the current experimental particle physics program. To achieve an even higher precision and statistical power, the LHC is planning to enter a high luminosity phase (HL-LHC) in 2026. In that phase, the instantaneous luminosity is expected to reach up to 7.5×10^{34} cm^{-2}s^{-1} corresponding to approximately a factor of 5 increase with respect to the typical luminosities of Run 2. Under these conditions, pile-up, defined as the p-p interactions occurring close to the one of interest, will be an important issue. With around 200 pile-up interactions happening at the same bunch-crossing interval, the ability of tracking detectors to correctly reconstruct the primary vertex and associate event objects to it becomes challenging. The situation becomes increasingly difficult at larger rapidity, where the particle density is the highest. In order to mitigate the undesirable effects of pile-up, the ATLAS experiment is proposing the addition of a picosecond precision timing detector of high granularity in the forward region, the High Granularity Timing Detector (HGTD). The timing information provided by this detector will be used to help disentangle objects that are merged in space but resolved in time. In order to assign time information for every Minimum Ionizing Particle (MIP), the HGTD, as the name suggests, will be a highly granular device. The chosen detection technology is silicon based Low Gain Avalanche Detectors (LGADs), providing a time resolution better than 50 ps per track. My involvement in the development of the HGTD was focused, on one hand on studies of the performance system and on the other hand, on the characterization of the prototype of the front-end electronics chip, ALTIROC.

Before diving into the details of this thesis, the reader is invited to go through an overview of the theoretical context and key phenomenological aspects of the Standard Model and Supersymmetry in Chapter 2. In addition, Chapter 3 provides a detailed description of the experimental apparatus used to perform the subsequent studies. This includes the LHC accelerator complex and the ATLAS experiment, starting from the detector components and the reconstruction procedure, all the way to the future HL-LHC upgrade.

After the presentation of the theoretical and experimental context on which this thesis is based, the first part of my work, the search of squarks and gluinos in hadronic states with the full Run-2 data of the ATLAS detector, will be detailed in Chapter 4. Starting from a description of the motivations and target signatures of the search, the analysis strategy will be outlined, with a particular focus on the novel Multi-bin fit approach, on which my work is focused. After going through key considerations on the selection of events of interest and the estimation/mitigation of the SM background, the statistical treatment of the analysis will be presented, which is a necessary step in order to obtain the final results. I have been heavily involved in this step of the search, evaluating various systematic uncertainties and maintaining the statistical inference tools. In addition, a detailed account of my work on the optimization of the multi-bin fit will be given, after which the results of the search will be presented. A stress will be given on the validation of the background estimation procedure and the interpretation of the results in simplified supersymmetric models, both of which were main subjects of my thesis.

Following the account of my involvement in the search for squarks and gluinos with the Run-2 data of ATLAS, my work on the High Granularity timing detector will be presented. The reader will be first re-directed to a general discussion of the main motivations, requirements and proposed design of the novel detector, in Chapter 5. An added weight will be given on the detector layout and proposed sensor and on-detector electronics technologies, both instrumental aspects for my work on this project. Finally, the expected improvements on the ATLAS performance and physics reach at the HL-LHC will be discussed as well.

The reader, now familiar with the HGTD upgrade, can continue to the two main subjects of my thesis within HGTD, which will be discussed in two separate chapters. In Chapter 6, my work on the optimization of the Data Transmission system and the geometry of the detector active area will be presented. After developing a framework that implements a realistic representation of the HGTD active area layout, I continued to evaluate important aspects of the detector design, such as the occupancy and the power dissipation, using simulation. Taking this a step further, I optimized the components necessary to perform the data transmission from the active area to the central ATLAS system. Finally, I developed a simplified fast simulation package, in order to perform quick performance comparison studies under different layout organizations.

Finally, a detailed account of my involvement in the characterization of a front-end ASIC prototype for precision time measurements with the HGTD will be given in Chapter 7. Two generations of the prototype chip, ALTIROC, were developed throughout this thesis, and after describing their main components, as well as the experimental setups used, results on their performance are presented. Studies with both calibration signals and highly energetic beam test particles have been performed, focusing on timing, efficiency and collected charge performance of the electronics, either alone or coupled to un-irradiated silicon LGAD sensors.

2. Theoretical Overview

In this chapter, starting from a brief description of the Standard Model (SM) and its particle content, the main motivations behind the conception of a theory based on supersymmetry will be discussed. The foundations of the theory will then be detailed, along with some popular models. An added focus will be given to the strongly interacting supersymmetric particles, squarks and gluinos, and in particular their expected phenomenology at the Large Hadron Collider (LHC). Finally, recent experimental results on direct searches for squarks and gluinos at the Large Hadron Collider (LHC) will be highlighted.

2.1 The Standard Model of particle physics

The Standard Model [1] is a theoretical formulation that embodies fundamental particles and describes their interactions. It was founded on the principles of Quantum Field Theory (QFT) [2] during the 20th century, in order to provide a coherent and unified explanation to the increasing amount of experimental discoveries in the field of particle physics. Since its conception, the SM has gained world-wide acclaim, both for consistently interpreting existing observations, but also for successfully predicting future experimental discoveries. The impressive ability of the SM to predict future discoveries spans to recent years, with the last missing part of the puzzle, the Higgs boson, being observed by the ATLAS [3] and CMS [4] experiments of LHC in 2012, roughly 60 years after its prediction.

The Standard Model is constructed on 3 major pillars, describing three out of the four fundamental interactions: the electromagnetic force, governing interactions between charged particles, the weak interaction, responsible for the weak decays of particles and weak neutral currents, and, finally, the strong interaction, acting on quarks and confining them to form nuclei. The last of the remaining forces, gravity, is currently understood in the domain of classical physics, through General Relativity. Its encapsulation in a QFT framework, such as the SM, has been a long standing theoretical problem, due to the non-renormalisability of its perturbative expression. Luckily, the effects of gravity can be considered negligible at the energies where the SM is tested experimentally.

2.1.1 Particle content in the Standard Model

Only fundamental particles, i.e. particles with no substructure, are considered in the SM. In QFT, fundamental particles arise as quantized excitation states of the underlying fields. They can be classified in two categories, depending on their spin: the fermions which have a half-integer spin, and the bosons with an integer-spin. Apart from the spin, particles are characterized by their mass and by various quantum numbers such as their electric, colour and hyper-charge as well as the lepton and baryon number. Each particle has an associated antiparticle with the same mass and spin but opposite electrical charge, as well as lepton and baryon number. A summary of the particle content in the SM can be seen in Figure 2.1.

Fermions are often considered as the building blocks of matter, as they are main ingredients in the formation of nuclei, and subsequently, atoms. They can be separated in two categories depending on whether they interact strongly. The first group of particles, referred to as leptons, do not act through the strong force and therefore have a null colour charge. On the other hand, quarks carry a colour charge and hence ”feel” the strong force. There exist in total 6 quark and 6 lepton types (or flavours), amounting to a total of 12 fundamental

fermions. They can be paired in three groups, or "generations". The first generation consists of the two lightest leptons and the two lightest quarks, which are stable and constitute "ordinary" matter. The remaining generations are copies of the first one but with particles of increasing mass. The structure of each generation in pairs of leptons and quarks (doublets) is related to the SU(2) nature of the weak interaction.

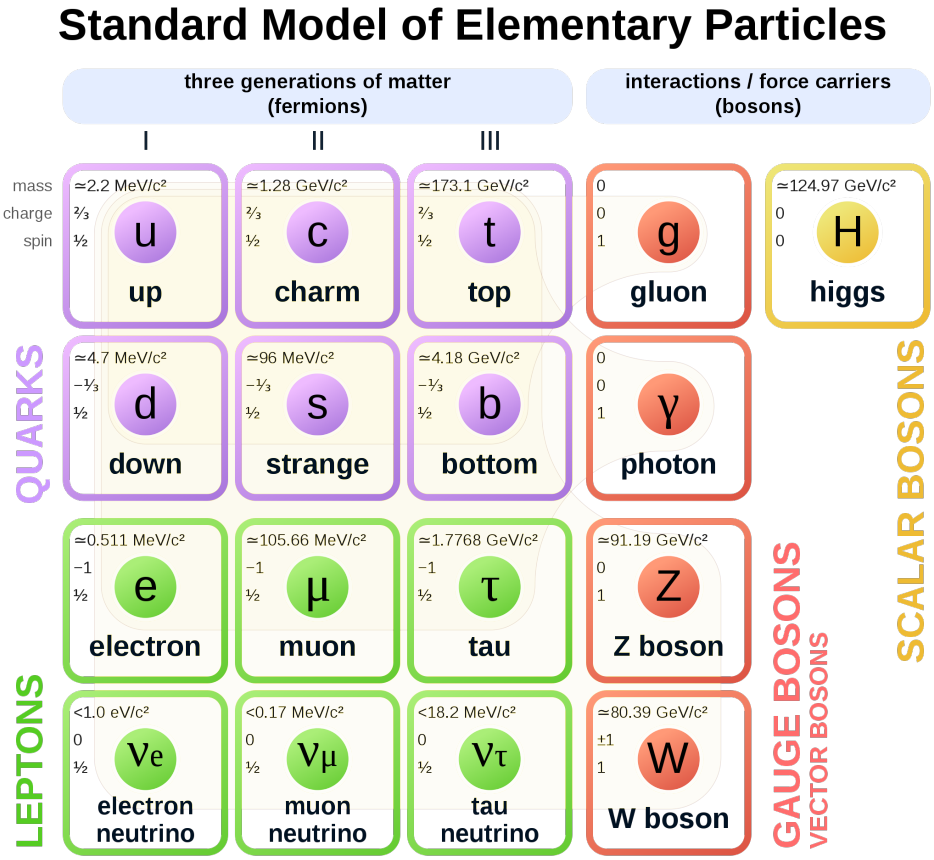

FIGURE 2.1: The particle content of the Standard Model.

Each lepton generation comprises a pair of particle with an electric charge of -1 and an associated neutral particle, the neutrino. For the first generation, this is the electron and the electron neutrino, while the second and third families are made of the muon - muonic neutrino and tau - tau neutrino particles. Since neutrinos are electrically neutral, they only interact via the weak force. Up to now, all experimental evidence points that the difference between the number of leptons and anti-leptons in an elementary interaction is a conserved number, independently for the three generations. This property has lead to the conception of three conserved quantum numbers, the lepton numbers (L_e, L_μ and L_τ). While the lepton numbers are conserved in particle interactions, they are violated in neutrino oscillations, which arise due to the mixing of the flavour eigenstates to form mass states. Neutrino oscillations have been experimentally observed by a multitude of experiments [5][6][7] and imply that neutrinos have an extremely small but non-null mass. The exact mechanism of the generation of neutrino masses is currently not resolved conclusively in the SM, while the reason for the large scale difference between neutrino masses and the rest of the SM spectrum is not understood.

Quarks are organized in a similar way to leptons, each generation comprising of a pair of particles with a $+\frac{2}{3}$ and $-\frac{1}{3}$ electric charge. The first generation consists of the up and down quarks, while the remaining flavours include the charm and strange quarks of the second

generation and the top and bottom quarks of the third generation. Quarks also interact via the strong force and carry a colour charge that can take 6 discrete values (red, green, blue and anti-red, -green and -blue). Due to confinement, quarks cannot be isolated in nature, but are always found in composite colourless states, the hadrons. Hadrons can be categorised in two classes, the mesons that consist of a quark-antiquark system, and the baryons, that are made of 3 quarks. A conservation of the number of baryons in particle interactions has also been experimentally observed, similarly to the leptons. Therefore, each quark carries also a baryon number, equal to (-) 1/3 for (anti-) quarks.

The second type of fundamental particles are the bosons, which have an integer spin. In the SM, the three fundamental interactions between particles result from the exchange of spin-1 bosons, also known as gauge bosons. Each force has its own corresponding boson; the electromagnetic force is carried by photons, the neutral and charged weak interactions are propagated by Z and $W^{\pm}$ bosons, respectively, and finally, the strong force is mediated by gluons. The last particle in the SM is the Higgs boson, which is a scalar. While not linked with a fundamental force, the Higgs field is responsible for the Brout-Englert-Higgs (BEH) mechanism for electroweak (EW) symmetry breaking, which is briefly discussed in 2.1.3.

2.1.2 The SM Lagrangian

The mathematical expression of the Standard Model is provided within the Lagrangian formalism of the particle fields. The Lagrangian controls the dynamics and kinematics of the theory with the help of symmetries, which are imposed transformations under which the system is left invariant. In the case of the SM, the Lagrangian is invariant under the local symmetries of the $SU(3)_C \times SU(2)_I \times U(1)_Y$ group, where the colour charge C, weak isospin I and hypercharge Y are conserved. The $SU(2)_I$ is often referred to as $SU(2)_L$, due to the chiral nature of the weak interaction.

A simple example to understand how fundamental interactions can arise as consequences of local symmetries is the conservation of the electric charge in the theory of Quantum Electrodynamics (QED). A freely propagating fermion of mass M will be described by a four component spinor Ψ of the fermion field, via the Lagrangian giving the Dirac equation:

$$\mathcal{L} = \bar{\Psi}(i\gamma^{\mu}\partial_{\mu} - M)\Psi \tag{2.1}$$

One can then consider a local U(1) transformation, corresponding to a rotation of the field phase by an angle $a(x)$:

$$\Psi(x) \rightarrow \Psi'(x) = e^{iqa(x)}\Psi(x), \tag{2.2}$$

under which the Dirac Lagrangian becomes:

$$\mathcal{L} = \bar{\Psi}(i\gamma^{\mu}\partial_{\mu} - M)\Psi - \bar{\Psi}\gamma^{\mu}\partial_{\mu}qa(x)\Psi \tag{2.3}$$

It can be seen that the Dirac Lagrangian is not invariant under the local U(1) phase transformation, unless we replace the derivative with the covariant derivative D_{μ}:

$$D_{\mu} = \partial_{\mu} - iqA_{\mu}, \tag{2.4}$$

where A_{μ} is a vector field being modified under local U(1) transformation in the following way:

$$A_{\mu} \rightarrow A'_{\mu} = A_{\mu} + \partial_{\mu}a \tag{2.5}$$

Under this modification, the Lagrangian becomes:

$$\mathcal{L}_{mod} = \bar{\Psi}(i\gamma^\mu D_\mu - M)\Psi = \bar{\Psi}(i\gamma^\mu \partial_\mu - M)\Psi + q\bar{\Psi}\gamma^\mu \Psi A_\mu \tag{2.6}$$

The first term of the modified Lagrangian is once again the Dirac equation for a freely propagating fermion particle, while the second term corresponds to the interaction of the fermion with a gauge field A_μ. In the context of QED, this field can be viewed as the photon, with which charged particles interact with a strength equal to the electromagnetic charge, $q = e$.

The concept of gauge theories can be generalised to encapsulate both the electromagnetic and weak force, in the so called Electroweak (EW) model [8], which respects the local $SU(2)_L \times U(1)_Y$ group symmetry. In this case, A_μ must be replaced by four fields: $W_\mu^{1,2,3}$ and B_μ. The covariant derivative is now:

$$D_\mu = \partial_\mu - ig\frac{\tau_a}{2}W_\mu^a - ig'\frac{Y}{2}B_\mu, \quad a = 1, 2, 3 \tag{2.7}$$

where g an g' are coupling constants of the $SU(2)_L$ an $U(1)_Y$ groups, respectively. The τ_a and Y are group generators of the $SU(2)_L$ an $U(1)_Y$, respectively, similarly to the electric charge for the QED example. The EW Lagrangian is:

$$\mathcal{L}_{EW} = i\bar{\Psi}\gamma^\mu D_\mu \Psi - \frac{1}{4}W_{\mu\nu}^a W_a^{\mu\nu} - \frac{1}{4}B_{\mu\nu}B^{\mu\nu} \tag{2.8}$$

The 4 electroweak fields mix in the following way:

$$\begin{aligned} W_\mu^\pm &= \frac{1}{\sqrt{2}}(W_\mu^1 \mp iW_\mu^2) \\ Z_\mu &= \frac{gW_\mu^3 - g'B_\mu}{\sqrt{g^2 + g'^2}} \\ A_\mu &= \frac{g'W_\mu^3 + gB_\mu}{\sqrt{g^2 + g'^2}} \end{aligned} \tag{2.9}$$

to form the $W^\pm$, Z and γ bosons. The rotation of the weak basis to the mass basis can be expressed through the weak mixing angle θ_w:

$$cos\theta_w = \frac{g}{\sqrt{g^2 + g'^2}}, \quad tan\theta_w = \frac{g'}{g} \tag{2.10}$$

The generation of the Z and γ bosons can then be expressed as:

$$\begin{pmatrix} Z_\mu \\ A_\mu \end{pmatrix} = \begin{pmatrix} cos\theta_w & -sin\theta_w \\ sin\theta_w & cos\theta_w \end{pmatrix} \begin{pmatrix} W_\mu^3 \\ B_\mu \end{pmatrix} \tag{2.11}$$

The EW theory is chiral, meaning that left- and right-handed particles do not interact in the same way. Due to the left-handed nature of SU(2), left-handed fermions are organized in doublets, while right-handed fermions are singlets A direct consequence of this is the violation of parity in weak interactions, a phenomenon that has been experimentally observed first in 1956 [9]. Parity violation in the charged EW sector is maximal, therefore the W boson does not interact with right-handed fermions. On the other hand, the Z boson being an admixture of both SU(2) and U(1) fields, it couples to both chiralities, but with a different strength.

Finally, the strong interactions are included in the SM through Quantum Chromodynamics (QCD), an SU(3) gauge group. The mediator of the force is the gluon field G_μ, carrying a colour charge. Since gluons lie in the adjoint representation SU(3), there can be 8 independent fields. Therefore, the covariant derivative can be expressed as:

$$D_\mu = \partial_\mu - ig_s \frac{\lambda_a}{2} G_\mu^a, \quad a = 1...8 \tag{2.12}$$

where λ_a are the 8 generator Gell-Mann matrices and g_s is the strong coupling constant. The QCD Lagrangian can be written in the following way:

$$\mathcal{L}_{QCD} = \bar{\Psi}(i\gamma^\mu D_\mu - m\delta_{ij})\Psi - \frac{1}{4} G_{\mu\nu}^a G_a^{\mu\nu} \tag{2.13}$$

where m is the mass of the quark corresponding to the field Ψ.

There are two main properties of QCD arising from the description of the theory in the SU(3) group. First, colour-charged particles cannot be isolated in nature due to the non-zero colour charge of the gluon, a phenomenon known as colour confinement. Another characteristic of QCD is asymptotic freedom, predicting that the strong interaction becomes asymptotically weaker as the energy scale increases. Therefore, at large energy scales, quarks and gluons interact weakly and can be treated as free particles.

2.1.3 EW symmetry breaking and the Higgs boson

The model which was presented in 2.1.2 describes the kinetic properties and interactions of the fundamental fields. However, it does not provide a way to generate particle masses - in fact, all aforementioned bosons and fermions were considered to be massless. Generating masses is not trivial for gauge bosons, as, simply adding a mass term, for example of the form $\frac{1}{2}m^2 Z^\mu Z_\mu$, would break the gauge invariance. While all experimental evidence points that gluons and photons are indeed massless, the discovery of the W and Z bosons with masses of 80.3 and 91.2 GeV [10][11], respectively, calls for a way to generate masses within the SM theory.

The problem of the gauge boson masses can be resolved with the Brout-Englert-Higgs mechanism [12][13], by adding a scalar field in the Lagrangian, here denoted as Higgs, of the form:

$$\mathcal{L}_{Higgs} = (D^\mu \phi)^\dagger (D_\mu \phi) - V(\phi), \quad with \quad V(\phi) = \mu^2 \phi^\dagger \phi + \lambda(\phi^\dagger \phi)^2 \tag{2.14}$$

where ϕ is a complex scalar doublet, $\lambda > 0$ and $\mu^2 < 0$. The first term of this Lagrangian corresponds to the kinetic term and the term describing the interaction of the scalar field with the gauge fields. The second term expresses the Higgs field potential, illustrated in Figure 2.2.

It can be seen that the Vacuum Expectation Value (VEV) of the potential is not at $\phi = 0$, but rather, at $v = \sqrt{-\mu^2/\lambda}$. Due to the shape of the potential, there are infinite degenerate states that have the minimum energy - choosing one breaks the EW symmetry spontaneously. One can arbitrarily choose:

$$\phi_0 = \frac{1}{\sqrt{2}} \begin{pmatrix} 0 \\ v \end{pmatrix}, \tag{2.15}$$

after which the potential can be expanded around the ground state to obtain the Higgs doublet:

$$\phi(x) = \frac{1}{\sqrt{2}} \begin{pmatrix} 0 \\ v + h(x) \end{pmatrix} \tag{2.16}$$

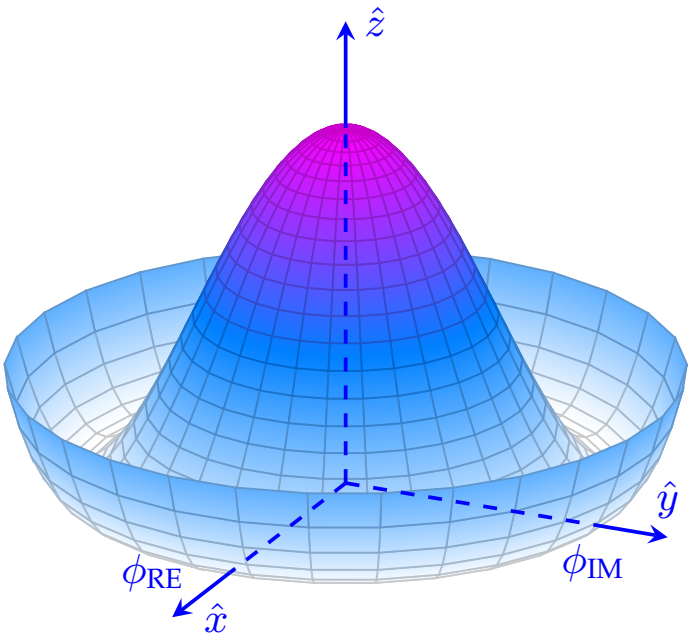

FIGURE 2.2: Illustration of the Higgs potential in the SM.

In order for the gauge bosons to acquire mass, a degree of freedom must be absorbed by the gauge field[1], corresponding to the gauge boson's longitudinal polarization. This additional degree of freedom is provided by the complex scalar Higgs field; after rearranging the degrees of freedom, the massive bosons emerge, along with a real scalar with 1 degree of freedom, the Higgs boson. The Higgs Lagrangian kinetic term now contains mass terms for the gauge bosons, while the potential term describes the Higgs boson self-interaction:

$$(D_\mu\phi)^\dagger(D_\mu\phi) = \frac{1}{2}(\partial_\mu h)(\partial^\mu h) + \frac{g^2}{4}(v+h)^2 W_\mu^+ W^{\mu-} + \frac{1}{8}(g^2+g'^2)(v+h)^2 Z_\mu Z^\mu \tag{2.17}$$

$$V(\phi) = \frac{\mu^2}{2}(v+h)^2 + \frac{\lambda}{4}(v+h)^4 \tag{2.18}$$

The masses of the W and Z bosons, as well as their interactions with the Higgs boson are directly derived from the second and third term of Equation 2.17, while the photon is massless, since it does not interact with the Higgs boson. The mass of the Higgs boson, along with its trilinear and quartic self-interaction couplings, are obtained by expanding the potential term. Finally, the masses of the EW gauge and the Higgs bosons can be summarized as follows:

$$\begin{aligned} M_W &= \frac{1}{2}gv \\ M_Z &= \frac{1}{2}(g^2+g'^2)v \\ M_A &= 0 \\ M_H &= \sqrt{2\lambda v^2} \end{aligned} \tag{2.19}$$

The Higgs field provides additionally a gauge-invariant way to generate fermion masses in the SM Lagrangian. Directly adding a fermion mass is forbidden in the $SU(2)_L \times U(1)_Y$ symmetry, since this would imply a mixing of the left- and right-handed components of the

[1]Massive gauge fields have three degrees of freedom, while massless fields have only two.

fermion fields, which transform differently under the EW gauge group. However, the Higgs doublet allows to express the fermion masses in a Yukawa Lagrangian:

$$\mathcal{L}_Y = -y_d \bar{Q_L} \phi d_R - y_u \bar{Q_L} \bar{\phi} u_R - y_l \bar{L_L} \phi l_R + h.c., \tag{2.20}$$

where $\bar{Q_L} = (\bar{u_L}, \bar{d_L})$ and $\bar{L_L} = (\bar{\nu_L}, \bar{l_L})$ are the quark and lepton left-handed doublets (for a single family) and u_R, d_R and l_R are the corresponding right-handed fermion singlets. The final term includes the equivalent expression with the hermitian conjugate scalar field. The masses of the fermions can then be expressed as:

$$m_f = y_f \frac{v}{\sqrt{2}} \tag{2.21}$$

It should be noted that the Yukawa couplings y_f are free parameters in the SM. Therefore, the masses of fermions cannot be predicted theoretically; instead, their estimation is an experimental endeavour. The origin of the vast difference between the masses of fermions belonging to different generations is not currently understood within the SM - it is one of the open questions in particle physics. The following section provides an overview of the currently known natural phenomena that are not engulfed in the SM.

2.1.4 Limitations of the Standard Model

Unification of the forces

The spontaneous electroweak symmetry breaking mechanism previously described is behind the inherent differences between the electromagnetic and weak force that are observed in nature. However, at higher energies these two forces are the same. One can imagine that, at a high enough energy scale, the three forces would be unified in a single Grand Unified Theory (GUT), that expresses all particle interactions with a single coupling and a minimum number of free parameters.

The coupling constants are in fact not constant, but depend on the energy scale. The evolution of the couplings with the scale, i.e. the running of the couplings, can be predicted by solving renormalization group equations. To achieve unification, there should be a value for which the three running coupling constants converge. However, as shown in Figure 2.4, when solving the renormalization equations in the SM for the three coupling constants, such a point does not exist. As will be discussed in 2.2.1, grand unification can be achieved by altering the coupling constants evolution with the introduction of an additional higher-energy (than the SM) theory, such as supersymmetry.

Dark matter

The history of Dark Matter (DM) begins in 1933, where the rotational speed of several galaxies was found to be inconsistent with the visible matter content in their outer radius. The physicist Fritz Zwicky then proposed an additional unseen mass called Dark Matter, that could explain the observations. Ever since, various astrophysical and cosmological measurements, as well as predictions from general relativity, call for the existence of a type of matter that does not interact electromagnetically and is responsible for roughly 26.8% of the energy in the universe.

The only SM candidate for dark matter are neutrinos. However, due to their extremely low mass, they cannot solely account for the currently estimated amount of dark matter in the universe. While the possibility of dark matter having a purely astronomical origin is accounted for in certain models [14][15], another popular hypothesis is that there exist additional neutral

particles, predicted in theories beyond the Standard Model. A few examples of such hypothetical particles are axions, heavy sterile neutrinos, or weakly interactive massive particles (WIMPs).

The hierarchy problem

The large difference (10^{24} orders of magnitude) between the strength of the weak and gravitational force is a puzzling phenomenon which is not understood in modern physics, and is often referred to as the hierarchy problem. If the existence of a more complete theory, such as the GUT, in a larger energy scale is assumed, the hierarchy problem has direct consequences on the mass of the Higgs boson. Any new particles that are predicted in the higher energy scale would couple to the Higgs boson, and inevitably increase its mass through quadratic radiative corrections. One can consider the example of a new Dirac fermion f of mass m_f, with which the Higgs field would couple through a Yukawa term $-y_f h\bar{f}f$. The mass of the Higgs boson is then defined by the bare mass m_0 and the radiative corrections that arise from loop diagrams such as the ones shown in Figure 2.3a:

$$m_h^2 = m_0^2 - \frac{|y_f|}{8\pi^2}\Lambda_{UV}^2 + ... \tag{2.22}$$

In this equation, y_f is the Yukawa coupling of the new fermion and Λ_{UV} is the ultraviolet momentum cut-off used to regulate the loop integral. Qualitatively, it can be viewed as the upper limit at which the theory can hold without the need to be modified by new physics. It has already been demonstrated in Equation 2.21 that the Yukawa coupling is directly proportional to the mass of the fermion. Therefore, if new physics exists at the order of the Planck or GUT scale, the Higgs boson would receive corrections that would increase its square mass by 30 orders of magnitude above the experimentally observed value at LHC ($m_h \sim 125$ GeV). This implies that an extreme fine-tuning would be necessary in the higher-scale theory, in order to introduce an exact cancellation between the bare mass and the quadratic correction.

It is clear that the hierarchy problem is not a problem of the Standard Model, but only arises when introducing a higher energy-scale theory. In fact, the formulation of the issue itself cannot be performed within the SM context, as the Higgs boson mass is a free parameter and not predicted by the theory. However, the attractiveness of a GUT-scale theory, in combination with the unnaturalness of fine-tuning has lead the theoretical community to search for ways to protect the Higgs boson from diverging corrections, such as supersymmetry.

Matter-antimatter asymmetry

Another physical observation that is not predicted by the Standard Model is the asymmetry between matter and anti-matter in the universe, also known as the baryon asymmetry problem. While, in the Big Bang, equal amounts of matter and anti-matter should have been produced, the universe today is believed to consist almost entirely of matter. According to the Sakharov conditions [16], a baryon-generating mechanism that produces the two matter states in different rates should violate the baryon number, the charge (C) and charge-parity (CP) symmetries, and additionally occur out of thermal equilibrium. While CP violation exists in the SM through the quark mixing, it is considered to be insufficient to account for the amount of matter-antimatter asymmetry observed [2]. Additionally, all existing experimental evidence point that baryon number is a conserved quantum number in fundamental particle interactions.

[2] CP-violation in the neutrino sector could provide an additional source of asymmetry. However, the neutrino CP-violating phase is not sufficiently constrained experimentally at the moment.

2.2 Beyond the standard model : Supersymmetry

The effort of the scientific community to find solutions to the limitations of the Standard Model is encapsulated in the field of Physics Beyond the Standard Model (BSM). In the effort to explain the remaining open questions of fundamental physics, the immense success of the SM should not be forgotten; all new theories, apart from formulating a mechanism to resolve one of the aforementioned problems, should also maintain intact all the properties and predictions of the Standard Model.

Supersymmetry (SUSY) [17] is a symmetry relating fermions and bosons, and vice versa. The generation of transformations under such a symmetry is done through an anti-commuting Weyl spinor, with:

$$Q|Boson\rangle = |Fermion\rangle, \qquad Q|Fermion\rangle = |Boson\rangle. \tag{2.23}$$

The irreducible representations of the supersymmetry algebra are the so called supermultiplets, each containing both fermion and boson states, commonly referred to as superpartners of each other. The Weyl spinors commute with the four-momentum generator of spacetime translations, as well as with the generators of gauge transformations. Therefore, particles in the same supermultiplet should have the same mass, electric charges, weak isospin and colour charges.

Evidently, the aforementioned expression of supersymmetry is in direct contradiction with experimental observations, as no superpartners to the SM particles have been found in particle searches. Supersymmetry must therefore be a broken symmetry. The class of theoretical models that include supersymmetry is often referred to as Supersymmetrical Models, or simply Supersymmetry.

2.2.1 Motivation

From a historical point of view, the conception of supersymmetry in the early 1970's was a purely theoretical development, rather than an effort to explain a puzzling experimental observation [18][19][20]. While initially a strictly intellectual achievement and an aesthetically appealing concept, supersymmetry has been since found to provide solutions to some of the major limitations of the Standard Model.

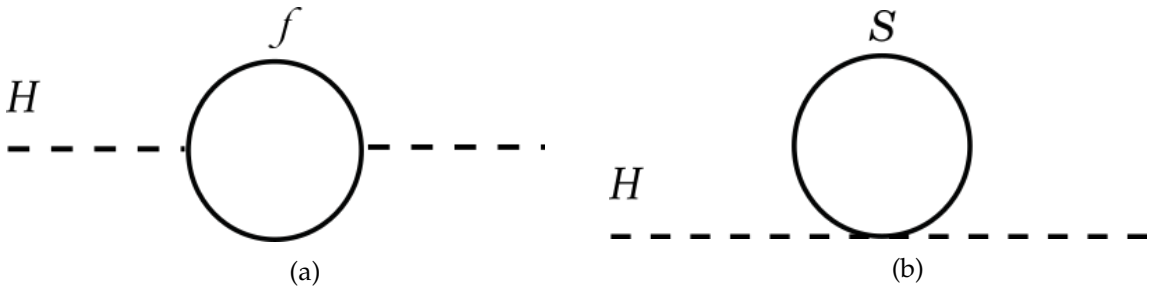

FIGURE 2.3: One-loop radiative corrections to the Higgs mass, due to (a) a Dirac fermion and (b) a scalar boson.

Due to the hierarchy problem, the mass of the Higgs boson is not safe against radiative corrections arising from within the SM or new physics. Example Feynman diagrams contributing to the Higgs mass are shown in Figure 2.3. The correction of the fermion diagram already being discussed in Equation 2.22, the equivalent expression for a scalar boson of mass

m_S is:

$$m_h^2 = m_0^2 + \frac{\lambda_S}{16\pi^2}\left[\Lambda_{UV}^2 - 2m_S^2 log(\Lambda_{UV}/m_S)\right] + ... \tag{2.24}$$

where λ_S is the coupling strength between the Higgs and the new scalar boson. Comparing equations 2.22 and 2.24, and in particular, the opposite sign of the quadratically diverging terms, it is clear that a cancellation can be achieved in a symmetry that relates fermions and bosons. This effect naturally arises when imposing supersymmetry. With the addition of superpartners with the exact same coupling to the Higgs as their SM counterpart, the cancellation of the quadratically divergent terms is exact. The remaining radiative corrections are only logarithmic. The mass of the Higgs boson with the remaining radiative corrections can be expressed as:

$$m_h^2 = m_0^2 - \frac{N_f|y_f|^2}{4\pi^2}\left[(m_S^2 - m_f^2)log(\Lambda_{UV}/m_S) + 3m_f^2 log(\Lambda_{UV}/m_f)\right] + ... \tag{2.25}$$

where m_S and m_f are the masses of the scalar boson and the fermion in the same supermultiplet. According to Equation 2.25, in order to obtain the observed Higgs boson mass without large fine-tuning, the mass difference $m_S - m_f$ should be small, of the order of TeV. In this case, one talks of *naturalness* of the Higgs mass. As experimental searches for supersymmetry at the LHC become increasingly sensitive, supersymmetric particle masses are excluded at increasingly higher mass scales, challenging the realisation of a fully natural Higgs boson mass.

Another limitation of the SM that is tackled by supersymmetry is the unification of the three forces. Figure 2.4 shows the running of the three coupling constants with the energy, as predicted by solving the renormalisation group equations in the SM or in the simplest supersymmetric theory, the Minimum Supersymmetric Standard Model (MSSM). The particle content of the MSSM makes the unification of the three couplings possible at the Grand Unification scale, $M_U \sim 1.5 \times 10^{16}$ GeV.

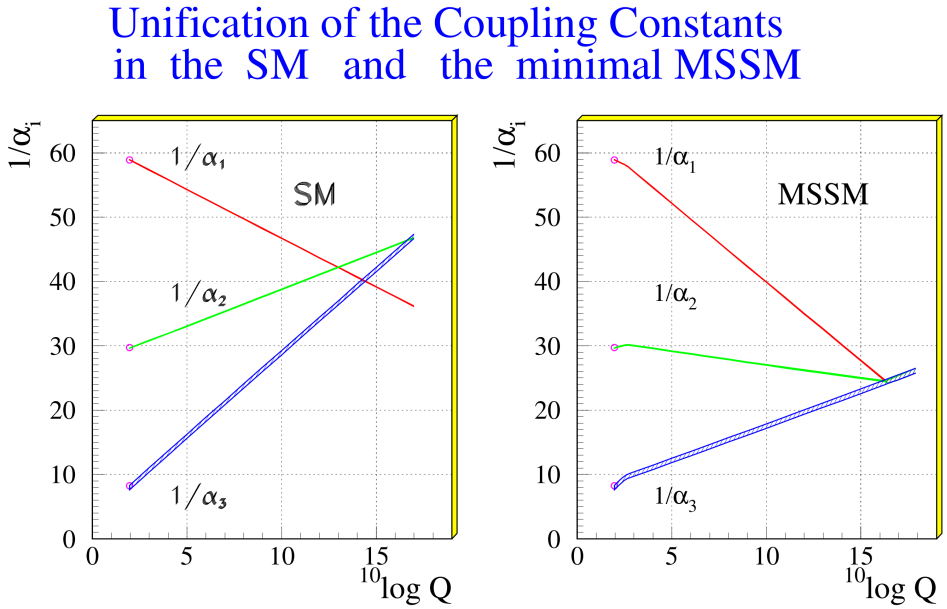

FIGURE 2.4: Evolution of the three coupling constants, α_1, α_2 and α_3, corresponding to the electrical, weak and strong force, respectively, as a function of the energy, as predicted by the Standard Model (left) or by the Minimal Supersymmetric Standard Model (MSSM) (right).

Finally, as will be discussed a bit later, the introduction of an additional symmetry, called R-parity, within a supersymmetric model, can provide a dark-matter particle candidate.

2.2.2 Supersymmetry breaking

If supersymmetry was introduced as an unbroken symmetry, the theoretical model would be classified as unrealistic, since no supersymmetric partners to the SM particles have been observed experimentally. The spontaneous breaking of a symmetry to a specific vacuum state has been successfully applied in the Electroweak theory with the introduction of the Higgs boson. An additional mechanism could be envisioned for SUSY, ensuring that the mass scale of the new particles is significantly higher than the SM. Many models predicting the exact mechanism SUSY breaking exist, however, in order to to parametrize the ignorance on the exact mechanism, one can consider the addition of a SUSY-breaking term "by hand" in the Lagrangian.

In order for broken SUSY to still provide a solution to the hierarchy problem, the cancellation of the dimensionless couplings that ensure the negation of quadratically divergent terms must be maintained. Therefore, the part of the Lagrangian that contains all the gauge and Yukawa couplings should remain unchanged. An additional term that leads to a "soft" supersymmetry breaking can be considered, including only mass terms and coupling parameters with positive mass dimension. The effective Lagrangian can then be written as:

$$\mathcal{L} = \mathcal{L}_{SUSY} + \mathcal{L}_{soft} \tag{2.26}$$

where the first part contains the invariant part of the theory, while $\mathcal{L}_{soft}$ introduces all the soft SUSY-breaking terms. The soft component of the Lagrangian is the origin between the mass difference between SM particles and their SUSY partners. Since soft mass terms are expected to contribute to the radiative corrections of the Higgs boson mass, the mass splittings between the known SM particles and their super-partners should not be too large, if one wants to preserve the solution to the hierarchy problem.

2.2.3 The MSSM

The simplest extension of the Standard Model that includes supersymmetry is the Minimum Supersymmetric Standard Model, or MSSM [21]. In the MSSM, SUSY is introduced as a softly broken symmetry. The predicted superpartners of the SM particles are commonly referred to as s-particles.

R-parity

While in the SM, lepton (L) and baryon (B) number conservation accidentally arises from gauge invariance, the particle content in the MSSM can violate L and B through gauge-invariant terms of the type: $\lambda^{ikj} L_i L_j \bar{e}_k$, $\lambda'^{ikj} L_i Q_j \bar{d}_k$ and $\lambda''^{ikj} \bar{u}_i \bar{d}_j \bar{d}_k$, where λ, λ' and λ'' are the corresponding couplings and i, j, k are quark and lepton generation indices. The terms $L_{i,j,k}$ and $Q_{i,j,k}$ denote the left-handed superfield doublets for leptons and quarks, while $\bar{e}$, $\bar{u}$ and $\bar{d}$ correspond to the right-handed lepton, up- an down-type quark superfield singlets. Such terms would lead to the decay of the proton, as seen in Figure 2.5. However, the proton lifetime has been measured experimentally to be larger than $\sim 10^{33}$ years [22]. One obvious way to resolve the contradiction would be to constrain the couplings to extremely small or zero values, but this approach suffers from a fine-tuning argument.

An elegant way to forbid lepton and baryon number violating terms in the MSSM is to introduce an additional discrete Z_2 symmetry, the R-parity [23]. A new quantum number is

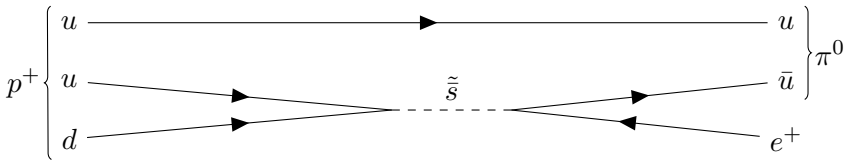

FIGURE 2.5: Example Feynman diagram for the decay of the proton in the case of R-parity violation.

then defined for each particle as:

$$R = (-1)^{3(B-L)+2s} \tag{2.27}$$

where s is the spin of the particle. Standard Model particles get assigned an R = +1, while s-particles have an R-parity of -1. If R-parity is exactly conserved, there can be no mixing between s-particles and their SM counterparts. Lepton and baryon number conservation is naturally reinstated, while the number of s-particles encountered in an interaction vertex should be even. The introduction of R-parity has direct phenomenological consequences:

- The lightest s-particle, commonly referred to as the "lightest supersymmetric particle", or LSP, cannot decay into lighter SM particles, and is therefore stable. Assuming additionally that the LSP is neutral and colourless, it can only interact weakly and is therefore an attractive dark matter candidate.
- All heavier s-particles than the LSP must decay, their decay containing an odd number of lighter s-particles.
- s-particles that are produced from SM interactions, for example in a collider experiment, must do so in even numbers (usually in pairs).

In the MSSM, R-parity is considered to be an exactly conserved symmetry. While this decision is well motivated from the proton decay constraints and the benefit of generating a dark matter candidate in the form of the LSP, it lacks a theoretical basis. In fact, the MSSM is perfectly self-consistent even in the absence of R-parity. A variety of extensions of the MSSM exist in which exact R-parity conservation is predicted on a theoretical level [24][25]. In parallel, R-parity violating SUSY models are also considered, with dedicated experimental searches being carried out to tackle the different phenomenologies. Such models usually predict the existence of only lepton or baryon number violating terms, since the proton decay occurs only with a simultaneous violation of B and L.

Particle content in the MSSM

The two simplest renormalisable supermultiplets are a chiral supermultiplet consisting of a 1/2-spin Weyl fermion and a complex scalar-spin, or a gauge supermultiplet containing a spin-1 vector boson together with a 1/2-splin Weyl fermion. Therefore, in the simplest supersymmetric extension, each known SM particle is in a supermultiplet with an s-particle of a spin differing by 1/2 unit. Table 2.1 lists the MSSM particle content, relating the SM particles to their corresponding s-particles. The spin-0 partners of the SM leptons and quarks are named after their partners, adding an "s" in the start (quark $\rightarrow$ squark). Since left- and right-handed fermions transform differently under the SM, they each get assigned their own SUSY scalar, which has the same gauge interactions. On the other hand, the SM gauge bosons are partnered with spin-1/2 fermions, their name reflecting their SM counterpart with an "ino" suffix (for example gluon $\rightarrow$ gluino). Similarly to the W and B bosons, the winos and

binos can mix after electroweak symmetry breaking to form the zino and photino. Finally, the Higgs boson being a scalar, it will partner with a Weyl fermion. In order to avoid triangle gauge anomalies in the electroweak sector [17], and to provide a mechanism for the generation of both up- and down-type quarks, two Higgs doublet complex scalar fields must be defined. The two fields are usually referred to as H_u and H_d, depending on whether they couple to up- or down-type fermions, respectively. The physical Standard Model Higgs boson then arises as a linear combination of the neutral components of H_u and H_d. The mixing of the two Higgs doublets yields additionally two more neutral and two charged states.

Names (SM, SUSY)	SM field	superpartner	SU(3)	SU(2)	U(1)
quarks, squarks	$(u_L\ d_L)$	$(\tilde{u}_L\ \tilde{d}_L)$	3	2	$\frac{1}{6}$
($\times$ 3 families)	$u_R^\dagger$	$\tilde{u}_R^*$	$\bar{3}$	1	-$\frac{2}{3}$
	$d_R^\dagger$	$\tilde{d}_R^*$	$\bar{3}$	1	-$\frac{1}{3}$
leptons, sleptons	$(\nu\ e_L)$	$(\tilde{\nu}\ \tilde{e}_L)$	1	2	-$\frac{1}{2}$
($\times$ 3 families)	$e_R^\dagger$	$\tilde{e}_R^*$	1	1	1
Higgs, higgsinos	$(H_u^+\ H_u^0)$	$(\tilde{H}_u^+\ \tilde{H}_u^0)$	1	2	$\frac{1}{2}$
	$(H_d^0\ H_d^-)$	$(\tilde{H}_d^0\ \tilde{H}_d^-)$	1	2	-$\frac{1}{2}$
gluons, gluinos	g	$\tilde{g}$	8	1	0
W boson, winos	$W^\pm, W^3$	$\tilde{W}^\pm, \tilde{W}^3$	1	3	0
B boson, bino	B^0	$\tilde{B}^0$	1	1	0

TABLE 2.1: Standard Model particles and their MSSM counterparts.

After electroweak and supersymmetry breaking, the supersymmetric particles can mix in the gauge representation to form different mass eigenstates. The mixing angles and masses of the new eigenstates heavily depend on assumptions made on the soft supersymmetry breaking. Similarly to the SM, the gluino cannot be included in the mixing, due to its colour charge. The charged higgsinos and winos combine to form two mass eigenstates, one of positive and one of negative electric charge, the charginos $\tilde{\chi}_1^\pm$ and $\tilde{\chi}_2^\pm$. In parallel, the neutral higgsinos and gauginos mix to four neutral mass eigenstates, the neutralinos $\tilde{\chi}_1^0$, $\tilde{\chi}_2^0$, $\tilde{\chi}_3^0$ and $\tilde{\chi}_4^0$. Squarks and sleptons can also mix seperately, provided they conserve R-parity, electric and colour charge. While a naive assumption would be that all generations combine in a similar manner, constraints from CP-violation and flavour-changing currents measurements [26] demand that the mixing between flavours is negligible. Mixing can still occur between the two scalars of the same flavour (like $\tilde{t}_L$ and $\tilde{t}_R$). Due to the substantially larger Yukawa coupling of the 3rd generation, only stops, sbottoms and staus have a substantial mixing to consider their combination into mass eigenstates; the lighter and heavier mass eigenstates are denoted with the subscript 1 and 2, respectively (for example $\tilde{t}_L, \tilde{t}_R \rightarrow \tilde{t}_1, \tilde{t}_2$). The other two generations remain in nearly degenerate unmixed states. A summary of the gauge and mass eigenstates of the MSSM particles can be found in Table 2.2.

2.2.4 Supersymmetric models

In total, the MSSM counts more than 100 free parameters, out of which, 32 are masses of undiscovered particles, while the rest are phases and mixing angles. Such a vast phase space

Names	Spin	R-parity	Gauge eigenstates	Mass eigenstates
Higgs bosons	0	+1	$H_u^0\ H_d^0\ H_u^+\ H_d^-$	$h^0\ H^0\ A^0\ H^\pm$
squarks	0	-1	$\tilde{u}_L\ \tilde{u}_R\ \tilde{d}_L\ \tilde{d}_R$	same
			$\tilde{c}_L\ \tilde{c}_R\ \tilde{s}_L\ \tilde{s}_R$	same
			$\tilde{t}_L\ \tilde{t}_R\ \tilde{b}_L\ \tilde{b}_R$	$\tilde{t}_1\ \tilde{t}_2\ \tilde{b}_1\ \tilde{b}_2$
sleptons	0	-1	$\tilde{e}_L\ \tilde{e}_R\ \tilde{\nu}_e$	same
			$\tilde{\mu}_L\ \tilde{\mu}_R\ \tilde{\nu}_\mu$	same
			$\tilde{\tau}_L\ \tilde{\tau}_R\ \tilde{\nu}_\tau$	$\tilde{\tau}_1\ \tilde{\tau}_2\ \tilde{\nu}_\tau$
neutralinos	1/2	-1	$\tilde{B}^0\ \tilde{W}^0\ \tilde{H}_u^0\ \tilde{H}_d^0$	$\tilde{\chi}_1^0\ \tilde{\chi}_2^0\ \tilde{\chi}_3^0\ \tilde{\chi}_4^0$
charginos	1/2	-1	$\tilde{W}^\pm\ \tilde{H}_u^+\ \tilde{H}_d^-$	$\tilde{\chi}_1^\pm\ \tilde{\chi}_2^\pm$
gluino	1/2	-1	$\tilde{g}$	same

TABLE 2.2: The particles in the Minimal Supersymmetric Standard Model both in the gauge and in the mass representation (with sfermion mixing for the first two families assumed to be negligible).

is extremely difficult to constrain experimentally. In reality, the largest amount of uncertainty in the MSSM originates from our ignorance on the exact mechanism of soft supersymmetry breaking. There exist various supersymmetric models introducing an exact mechanism to break supersymmetry, predicting the particle spectrum of the MSSM with far fewer parameters. Alternatively, some models reduce the phase space by imposing additional phenomenological constraints. A few popular examples of both model types are briefly described below.

mSUGRA/CMSSM

An example of a supersymmetric model with a specific mechanism to introduce $\mathcal{L}_{soft}$ is the minimal SUper GRAvity or Constrained Minimal Supersymmetric Standard Model (mSUGRA / CMSSM) [27], where the soft SUSY breaking is mediated by gravity. In the minimal expression of supergravity, two additional particles are included in the theory, the spin-2 boson mediator of gravity, or graviton, and its supersymmetric partner, the gravitino. Additional models with an entire gravitational hidden sector can also be considered. The gravitational interaction breaks supersymmetry, additionally giving mass to the gravitino. One of the merits of mSUGRA is the predictability of the theory, where the MSSM phase space is reduced to simply 5 parameters: a universal scalar mass (m_0), a universal gaugino mass $m_{1/2}$, a universal trilinear coupling A_0, the ratio of the vacuum expectation values of the two Higgs doublets $tan\beta$ and the sign of the higgsino mass parameter μ. Constraints from the SM, such as the mass of the Higgs boson greatly limit the realistic values of the aforementioned parameters, further simplifying the experimental searches. Additionally, mSUGRA-type models introduce a way to incorporate gravity in a quantum theory.

GMSB

Theories with gauge-mediated supersymmetry breaking (GMSB) [28] provide an interesting alternative to the scenario in which the soft terms are induced by gravity. In the GMSB scenario, the breaking of SUSY is mediated by the ordinary gauge interactions. Typically, these

models consist of an observable sector, containing the SM particles and their SUSY partners, together with an additional hidden sector which is responsible for breaking supersymmetry. The final piece of GMSB is the messenger sector, which communicates the SUSY breaking from the hidden to the observable sector through loop diagrams involving massive messenger fields. The messengers are new chiral supermultiplets, coupling both to the supersymmetry breaking VEV and the Standard Model particles. Similarly to gravitational models, GMSB models are highly predictive; additionally, they naturally suppress high Flavour Changing Neutral Currents (FCNCs) that would be in direct contradiction with experimental evidence.

pMSSM

The assumption of a specific SUSY breaking mechanism can have significant phenomenological consequences. A more general model that encapsulates the MSSM without explicitly defining the soft SUSY breaking mechanism can be envisioned. In order to decrease the number of free parameters, well motivated phenomenological constraints can be imposed. The most popular model of this type is the phenomenological Minimum Supersymmetric Standard Model, or pMSSM [29]. The phenomenological conditions aim to ensure that no additional CP violating or FCNC terms are introduced in the Lagrangian, while the universality of the two first families of squarks and sleptons is also assumed. Following these requirements, the number of free parameters are reduced to 19: the ratio of the vacuum expectation values of the two Higgs doublets, the mass of the pseudoscalar Higgs boson, the mass of the higgsino and of the three gauginos, 3 (2) mass parameters for the first and second generation squarks (sleptons) and 3 (2) mass parameters for the third generation squarks (sleptons). Finally, the three remaining parameters are the trilinear couplings for the third generation quarks and leptons, since their mixing is allowed. All the aforementioned parameters are expressed in the EW scale (in contrast to mSUGRA which is mostly defined at the GUT scale), making the pMSSM a low scale model.

Simplified models

The pMSSM offers one of the most general realistic representations of SUSY. However, scanning 19 parameters in an experimental search can be extremely challenging and time-consuming. Since experimental searches usually want to focus their efforts on a specific set of parameters, or s-particles, it is often very useful to consider an effective Lagrangian involving only the s-particles of interest and their interactions. Such descriptions are referred to as Simplified Models [30][31], and are usually driven by the experimental needs. This can be understood by the fact that they are usually parametrised directly to collider physics observables, such as particle masses, their production cross-sections and decay branching fractions. The latter are often assumed to be 100% to a specific experimental signature, further reducing the degrees of freedom in the model.

2.2.5 Phenomenology of squarks and gluinos at the LHC

During my thesis, I have been heavily involved in the searches for squarks and gluinos in hadronic signatures with the ATLAS detector at the LHC. Therefore, the remaining of this chapter will focus on phenomenological aspects in the production and hadronic decays of the strongly interacting supersymmetric particles in proton-proton colliders. The reader should note that R-parity is considered to be a conserved symmetry in all of the following discussion, meaning that s-particles are produced in pairs and decay (either directly or through cascades) to a stable LSP. Finally, a brief summary of experimental results from the ATLAS experiment regarding squarks and gluinos prior to the work of this thesis will be given.

Production

Squarks and gluinos are of particular interest to experimentalists in a hadron collider. Since these particles interact through the strong force in the exact same way as their SM partners, they're expected to be produced abundantly in proton-proton collisions, primarily through gluon-gluon and gluon-quark interactions [32][33]. The tree-level production modes of squarks and gluinos from the interaction of gluons and quarks are shown in Figure 2.6. Additionally, production of strongly interacting SUSY particles can arise through quark-quark scattering and quark-antiquark annhihilation, as presented in the tree-level s- and t-channels of Figure 2.7.

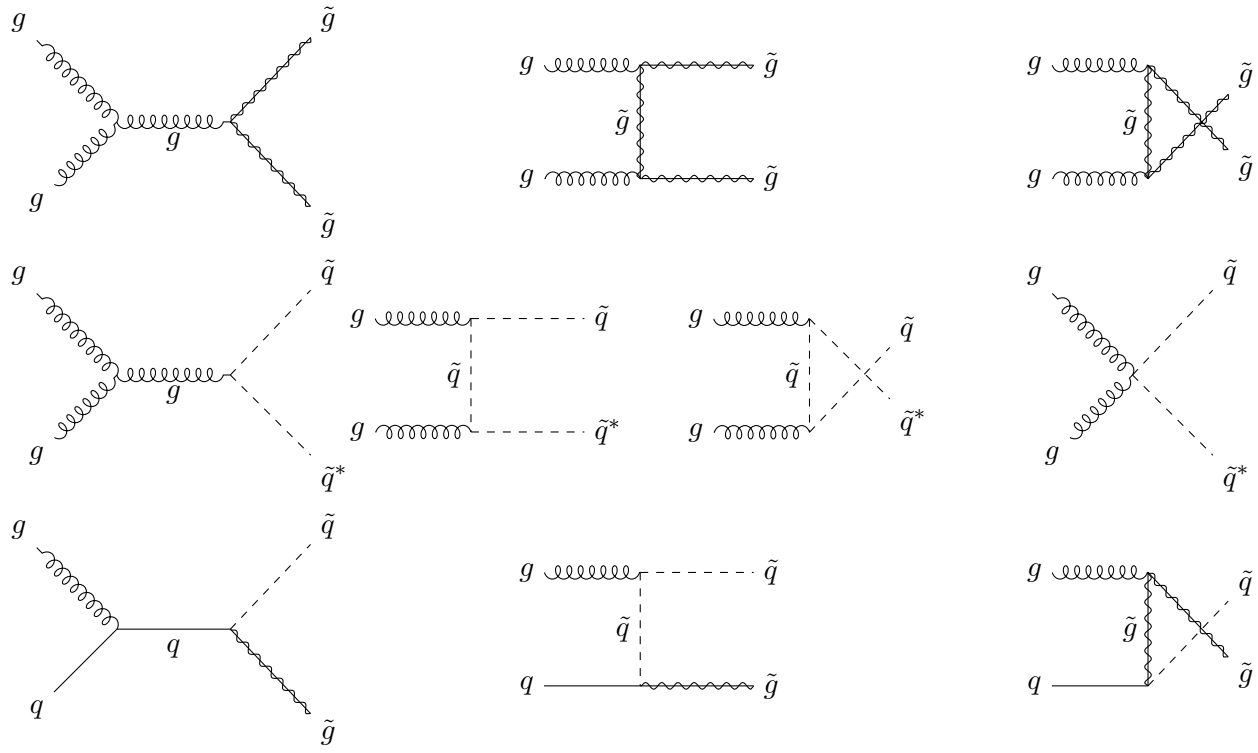

FIGURE 2.6: Feynman diagrams for gluino and squark production at hadron colliders from gluon- gluon and gluon-quark fusion [17].

Figure 2.8 [34][35] shows the expected production cross-section for particles of the MSSM as a function of their hypothesized mass at the LHC, when it is running at a center-of-mass energy of 13 TeV. Naturally, the probability of generating the new particles falls with the particle mass. Here, squarks of the first and second generations are considered separately from the stops and sbottoms. This classification is quite common in the MSSM, and is justified both from the different mixing behaviour of the third generation, and from the particular role that the stop and sbottom play in the hierarchy problem of the Higgs boson mass.[3] It is additionally motivated from the experimental aspect, since third generation quarks have particular final states that are targeted in dedicated searches. It can be seen that the first and second generation squarks and gluinos could be the most commonly produced s-particles at the LHC - for a given mass, their combined production cross-section is 3-4 larger than that of the electroweak SUSY sector and 2 orders of magnitude larger than that of the third generation. The latter is penalized due to the absence of t-channel stop production, since there are no top

[3]Since s-particles have the same Yukawa couplings as their SM partners, the third generation scalars dominate the radiative corrections to the Higgs mass.

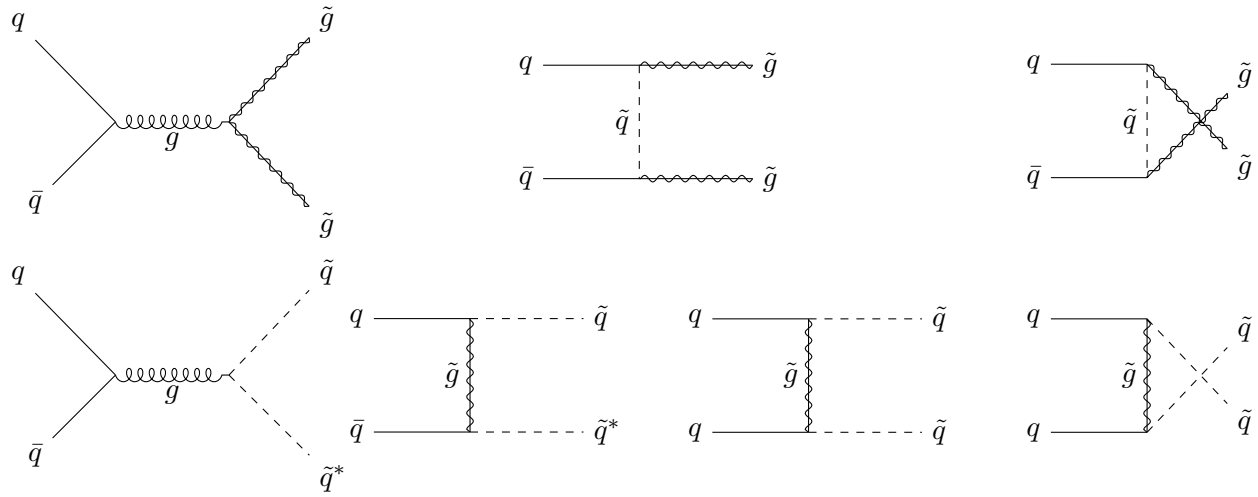

FIGURE 2.7: Feynman diagrams for gluino and squark production at hadron colliders from strong quark-antiquark annihilation and quark-quark scattering [17].

quarks in the proton. This makes first- and second-generation squarks and gluinos some of the most attractive candidates for SUSY searches at the LHC. As a comparison, the total production cross section of the SM Higgs boson at a center-of-mass energy of 13 TeV is around 50 pb [36].

Decays to hadronic signatures

The decay of the s-particles is the key to their detection in collider experiments. At the LHC, various decay channels are studied, including leptons, gauge bosons and/or quarks in the final state. Hadronic signatures are of particular interest, since they originate from strong interactions, and therefore have a large branching ratio. On the other hand, in hadron colliders, such signatures inevitably have larger background contributions from SM processes than their leptonic counterparts. An experimental handle on SUSY can arise from the conservation of R-parity, which imposes that the LSP is neutral and stable. From an experimental point of view, this translates to an escape of the LSP, similarly to the neutrino, giving rise to large missing transverse momentum ($E_{\mathrm{T}}^{\mathrm{miss}}$) in the detector. In addition, supersymmetric hadronic signatures include a large number of jets, arising from the hadronisation of quarks and gluons.

The mass hierarchy of the supersymmetric particles is an important factor when considering the possible decays of an s-particle, as decays to higher-mass states are automatically excluded. Squarks will dominantly decay via the QCD coupling to gluinos through $\tilde{q} \to q\tilde{g}$, if $\mathrm{m}(\tilde{q}) > \mathrm{m}(\tilde{g})$. Additional channels include decays to charginos and neutralinos, provided that they are kinematically allowed:

$$\tilde{q} \to q\tilde{\chi}_i^0, \quad i = 1, 2, 3, 4 \tag{2.28}$$

$$\tilde{q} \to q\tilde{\chi}_j^{\pm}, \quad j = 1, 2 \tag{2.29}$$

In models where the lightest neutralino is the LSP, the missing transverse momentum arises directly from decays like the ones of Equation 2.28. Squark decays can be direct to the LSP, or proceed through a cascade of lighter s-particles, depending on the SUSY mass spectrum. Example Feynman diagrams for both cases with a neutralino LSP are shown in Figure 2.9. Hadronic jets arise from the quark and gluon decay products, either directly from the squark decay vertices, or from the subsequent hadronic decays of EW gauge bosons.

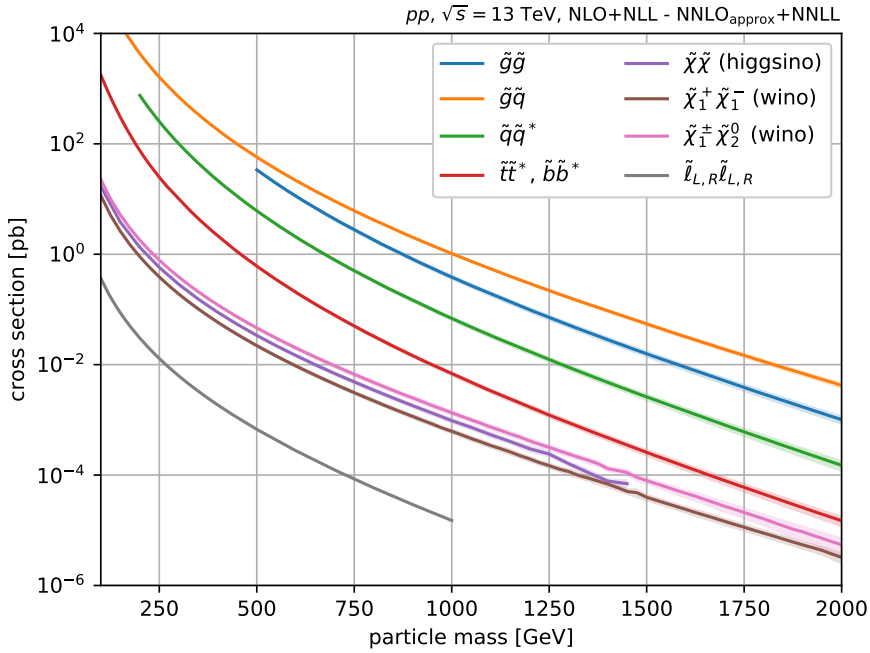

FIGURE 2.8: Production cross-sections of SUSY particles at the LHC with 13 TeV. The gluino (squark) is considered to be decoupled in squark (gluino) pair production calculations, while for squark-gluino associated production, the two s-particles are assumed to have equal masses [34].

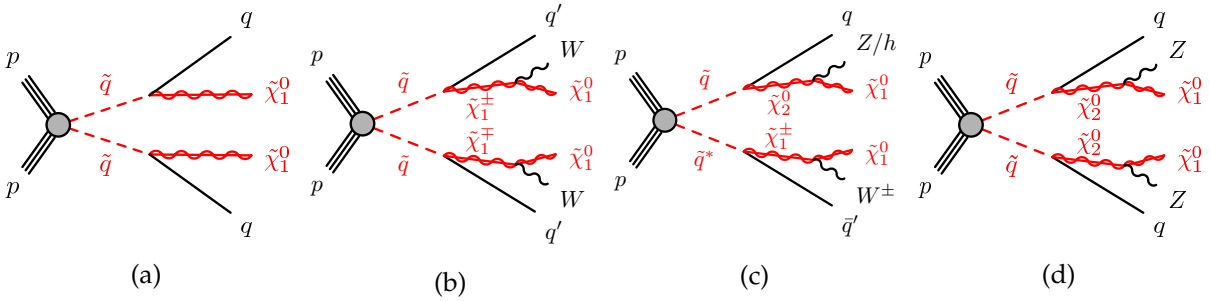

FIGURE 2.9: Example hadronic decay topologies of pair-produced squarks with direct or one-step decays to a neutralino LSP [37].

Gluinos, on the other hand, can only decay through a squark, either virtual or on-shell. When allowed, two-body decays to a squark and a quark, $\tilde{g} \to \tilde{q}q$ are the most common, once again due to the strong coupling. In case the mass of the squark is significantly larger than that of the gluino, three body decays through a virtual squark to two quarks and a chargino or a neutralino are favoured instead:

$$\tilde{g} \to q\bar{q}\tilde{\chi}_i^0, \quad i = 1, 2, 3, 4 \tag{2.30}$$

$$\tilde{g} \to qq\tilde{\chi}_j^{\pm}, \quad j = 1, 2 \tag{2.31}$$

Once again, depending on the mass difference between the gluino and the various charginos and neutralinos, some of the above decays might be forbidden. Heavier s-particle decay products will cascade through intermediate decays to SM particles and the LSP, producing jets and missing transverse momentum in the detectors. Figure 2.10 demonstrates example direct, one-step and two-step decay chains of pair produced gluinos, in cases where $m(\tilde{q}) > m(\tilde{g})$ and for a neutralino LSP.

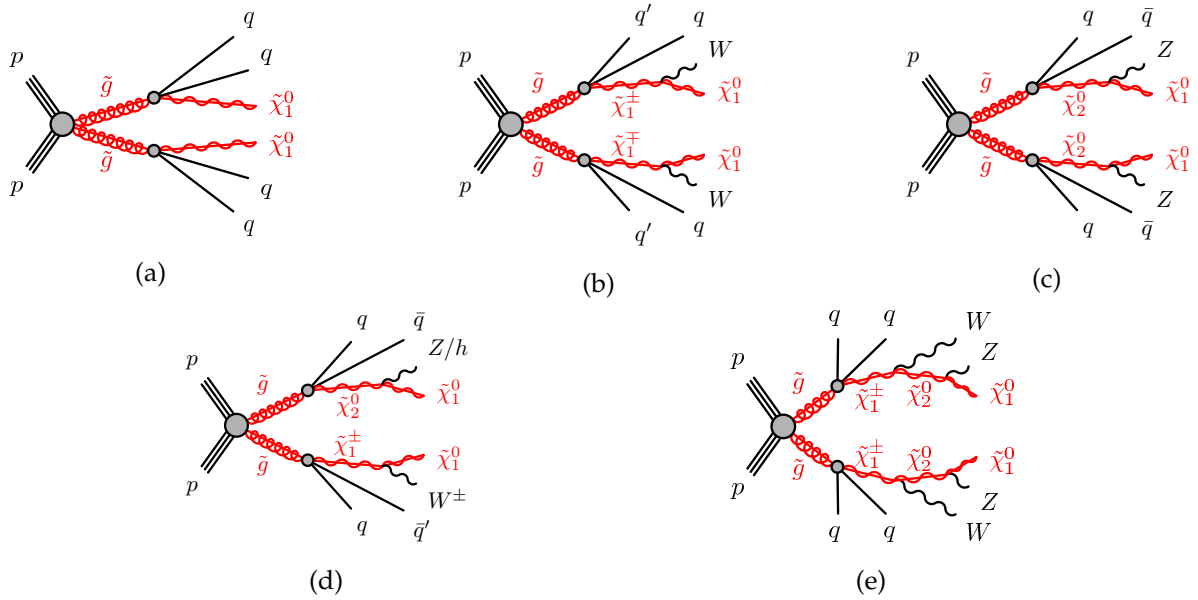

FIGURE 2.10: Example hadronic decay topologies of pair-produced gluinos with direct, one-step or two-step decays to a neutralino LSP [37] .

2.2.6 Recent experimental constraints on squarks and gluinos

Supersymmetry can be constrained experimentally either directly, through searches for heavy new resonances in colliders, or indirectly, from processes that are rare or forbidden in the Standard Model but can have contribution from loops involving s-particles. Such precision tests include among others the proton lifetime, electric dipole moments for the electron and neutron and neutral meson mixing. However, while indirect measurements can give valuable hints at BSM effects, direct detection without a doubt offers the most concrete way to verify a supersymmetric model, since the inference of the new particle properties is made available.

The leading force in direct searches for new particles which could be arising from a realisation of supersymmetry in nature is the LHC with its two general purpose experiments, ATLAS and CMS. As this thesis is being written, the LHC experiments have already been running for 10 years, and no signs of supersymmetry have yet been found. On the other hand, the exclusion of a significant fraction of the SUSY phase-space has been achieved, thanks to numerous analysis campaigns of the data in different kinematic regions and final states. A

small subset of results obtained from the ATLAS collaboration prior to my work, focusing on searches for squarks and gluinos in hadronic final states is presented hereafter.

Figure 2.11 shows limits for 1st and 2nd generation squarks and gluinos produced directly in simplified models where only the lightest neutralino is additionally considered. All other SUSY particles are assumed to be decoupled, including the squarks when considering gluino production (and vice versa). The lightest neutralino is the LSP and R-parity is conserved. In both cases, the s-particles decay with a 100% BR to quarks and the LSP, giving rise to jets and high $E_{\mathrm{T}}^{\mathrm{miss}}$ in the final state. Leptons are vetoed to avoid overlap with other analyses and to remove certain backgrounds. These results were obtained during the Run 2 of LHC, at a center-of-mass energy of 13 TeV, with a partial dataset amounting to 36.1 fb^{-1} [37]. The maximum excluded limit on the mass of the squarks, assuming a mass degeneracy between the two generations and the left- and right-handed components, is 1.55 TeV for a massless neutralino. Equivalently, gluinos are excluded up to 2.03 TeV. No exclusion is obtained for simplified models of squark (gluino) pair production with lightest neutralino masses above 630 GeV (970 GeV). These limits significantly extend the sensitivity of Run 1 results, which reached a maximum mass exclusion of $\sim$ 1 TeV for squarks and $\sim$ 1.5 TeV for gluinos.

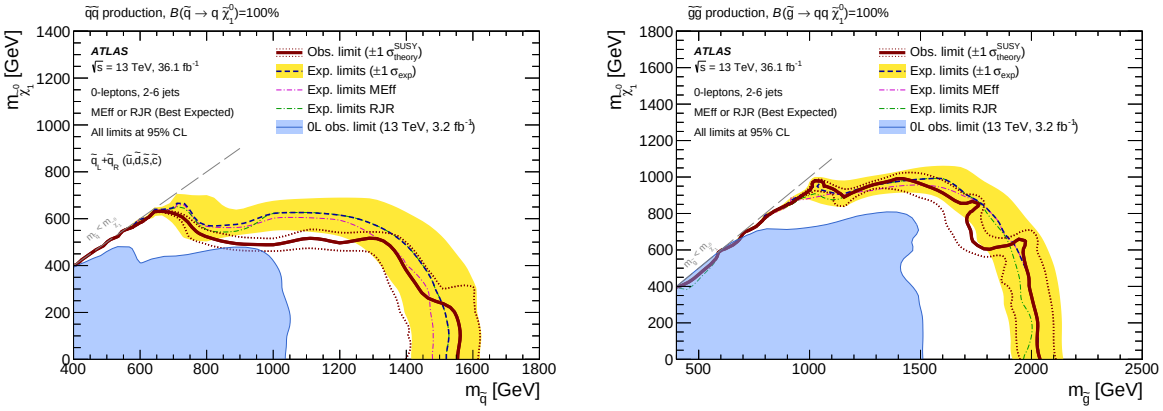

(a) (b)

FIGURE 2.11: Exclusion limits for direct production of (a) first- and second-generation squark pairs with decoupled gluinos and (b) gluino pairs with decoupled squarks. Gluinos (first- and second-generation squarks) are required to decay to two quarks (one quark) and a neutralino LSP. Results are compared with the observed limits obtained by the Run 1 ATLAS searches with jets, missing transverse momentum, and no leptons [37].

The validity of the interpretation of experimental results in simplified models is often questioned. Significant discrepancies between simplified interpretations and results obtained when deploying a complete supersymmetric model can arise, due to the large amount of assumptions (such as couplings, degeneracies and kinematics) in the former. In order to give a more realistic insight on the sensitivity of its searches, the ATLAS collaboration has performed a re-interpretation of some of its most constraining results in Run 1 in the 19-parameter pMSSM framework [29]. A total of 22 distinct ATLAS analyses are considered, spanning a wide range of different search strategies and final states. Out of those, seven searches specifically target gluinos and squarks of the first and second generations, in final states with jets, missing transverse momentum and in some cases, leptons. A few key results on the exclusion of squarks and gluinos are presented in Figure 2.12. In Figure 2.12a, the fraction of pMSSM points excluded by the combination of 8 TeV ATLAS searches in the $\tilde{q} - \tilde{\chi}_1^0$ mass plane is shown, superimposed to the interpretation of the most sensitive analysis, the 0-lepton + 2-6 jets + $E_{\mathrm{T}}^{\mathrm{miss}}$, in the simplified model. It can be seen that there is generally good agreement between the region excluded in the two different scenarios, demonstrating that the simplified

model is successfully capturing the main pMSSM phenomenology in this case. The equivalent result for the exclusion of squarks is presented in Figure 2.12b. In this case, the region within the solid simplified-model exclusion curve is only partially excluded within the pMSSM. This is primarily because the pMSSM-19 parameter space does not demand that the squarks be eight-fold degenerate, reducing the cross-section. There is a closer correspondence between the pMSSM sensitivity and that of an alternative simplified model (dashed line), in which the cross-section for direct (anti-)squark production has been reduced by a factor of four, to model the effect of only two of those eight squarks being mass degenerate.

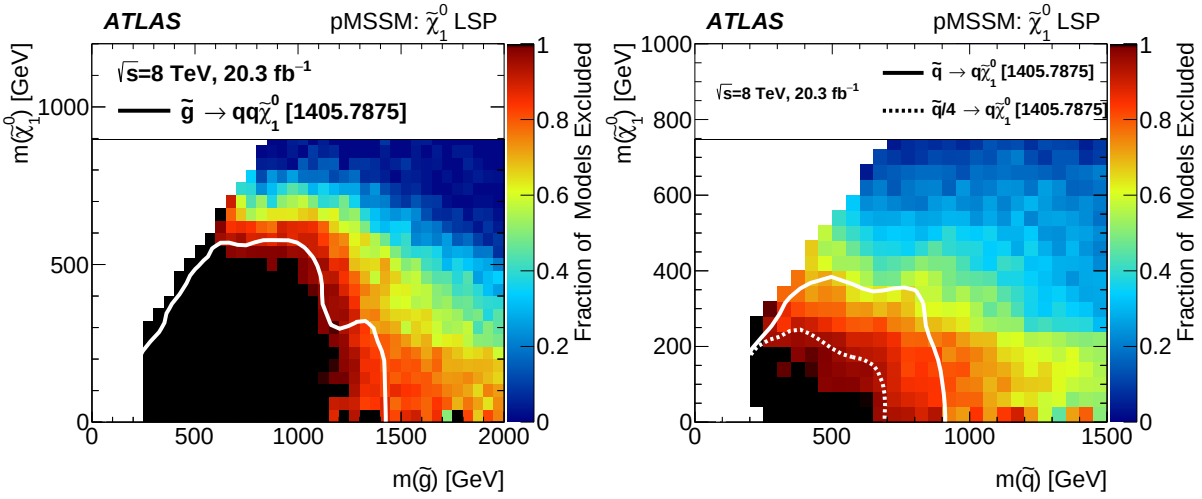

(a) (b)

FIGURE 2.12: Fraction of pMSSM points excluded by the combination of 8 TeV ATLAS searches in the (a) $\tilde{g} - \tilde{\chi}_1^0$ and (b) $\tilde{q} - \tilde{\chi}_1^0$ planes. In both cases, the solid white lines overlaid are observed simplified-model limits from the 0-lepton + 2-6 jets + $E_{\mathrm{T}}^{\mathrm{miss}}$ search of ATLAS with Run 1 data. In (b), the solid line corresponds to the case where all eight squarks from the first two generations are assumed to be degenerate. The dashed line has the squark production cross-section scaled down by a factor of four to emulate the effect of only two of those eight squarks being kinematically accessible [29].

3. The Large Hadron Collider and the ATLAS Detector

3.1 The Large Hadron Collider

The Large Hadron Collider (LHC) [38] is the world's largest particle accelerator. It is located at CERN, Geneva, at the existing 27 km tunnel where the Large Electron Positron (LEP) machine was previously operating. The LHC project was approved in 1994, while its construction started in 2000. The primary goal of the accelerator is to collide protons with a maximum center of mass energy of $\sqrt{s}$ = 14 TeV, in order to push the limits of our understanding of particle physics. Heavy ions such as lead (Pb) have also been collided with an energy of 2.5 TeV per nucleon, to study the particle interactions in conditions similar to those of the very early universe, such as quark-gluon plasma.

The machine has been operating since 2008, while the first physics run, referred to as Run 1, was completed between 2010 - 2012, with a center-of-mass energy gradually increasing from 7 to 8 TeV. One of the most important accomplishments of this period was the discovery of the Higgs boson, in 2012, by the ATLAS and CMS experiments [3, 4]. Moreover, Run 1 was instrumental in the consolidation of the SM through various precision measurements, but also a benchmark point for BSM searches.

In 2015, LHC entered it's second phase, Run 2, following a 2-year upgrade period. After gaining experience in the accelerator and detection instruments in Run 1, the capacity of the machine was almost fully exploited and data were collected at $\sqrt{s}$ = 13 TeV. In Run 2, which lasted from 2015 to 2018, a staggering number of collisions was delivered at the experiments, leading to impressively sized datasets. Following the discovery of the Higgs boson, measuring its properties became one of the main axes of the LHC physics program. In parallel, the higher amount of data and the increase in energy allowed to broaden the search for new physics and further test the consistency of the SM.

3.1.1 Accelerator complex and injection chain

In order to reach the design energy of the LHC, particles are gradually accelerated by a large fraction of the CERN accelerator complex, shown in Figure 3.1. Protons start their journey in the form of hydrogen atoms in a bottle. After being ionized, they enter the Linac 2, a 30 m long linear accelerator, where they reach an energy of 50 MeV and are squeezed into "bunches". At this point, they are guided to the first and smallest circular machine of the chain, the Proton Synchrotron Booster (PSB). The PSB consists of four superimposed synchrotron rings with a radius of 25 m, which bring the protons' energy up to 1.4 GeV. The higher energy provided by the booster allows for more protons to be injected in the next accelerator step, and therefore a higher final luminosity, compared to a configuration where the injection was done directly from Linac 2. Leaving the PSB, the protons enter the Proton Synchrotron (PS), the first ever synchrotron of CERN. Operational since 1959, this historic circular accelerator of 638 m circumference was briefly the world's highest energy particle accelerator. Since then, it has faithfully served a variety of experiments, handling many different types of particles. As part of the LHC injection chain, it increases the energy of the protons up to 25 GeV, before feeding them to the Super Proton Synchrotron (SPS). Originally a proton-antiproton collider, the SPS provided the collisions that lead to the discovery of the W and Z bosons by

the UA1 and UA2 experiments [10, 11]. Its primary use today is to serve as the final injector for the LHC, driving the proton energy up to 450 GeV. Additionally, the SPS provides particles for a variety of CERN based experiments, including NA62, AWAKE, SHINE, COMPASS, as well as the CERN testbeam areas, where research and design campaigns for future upgrades are being carried out.

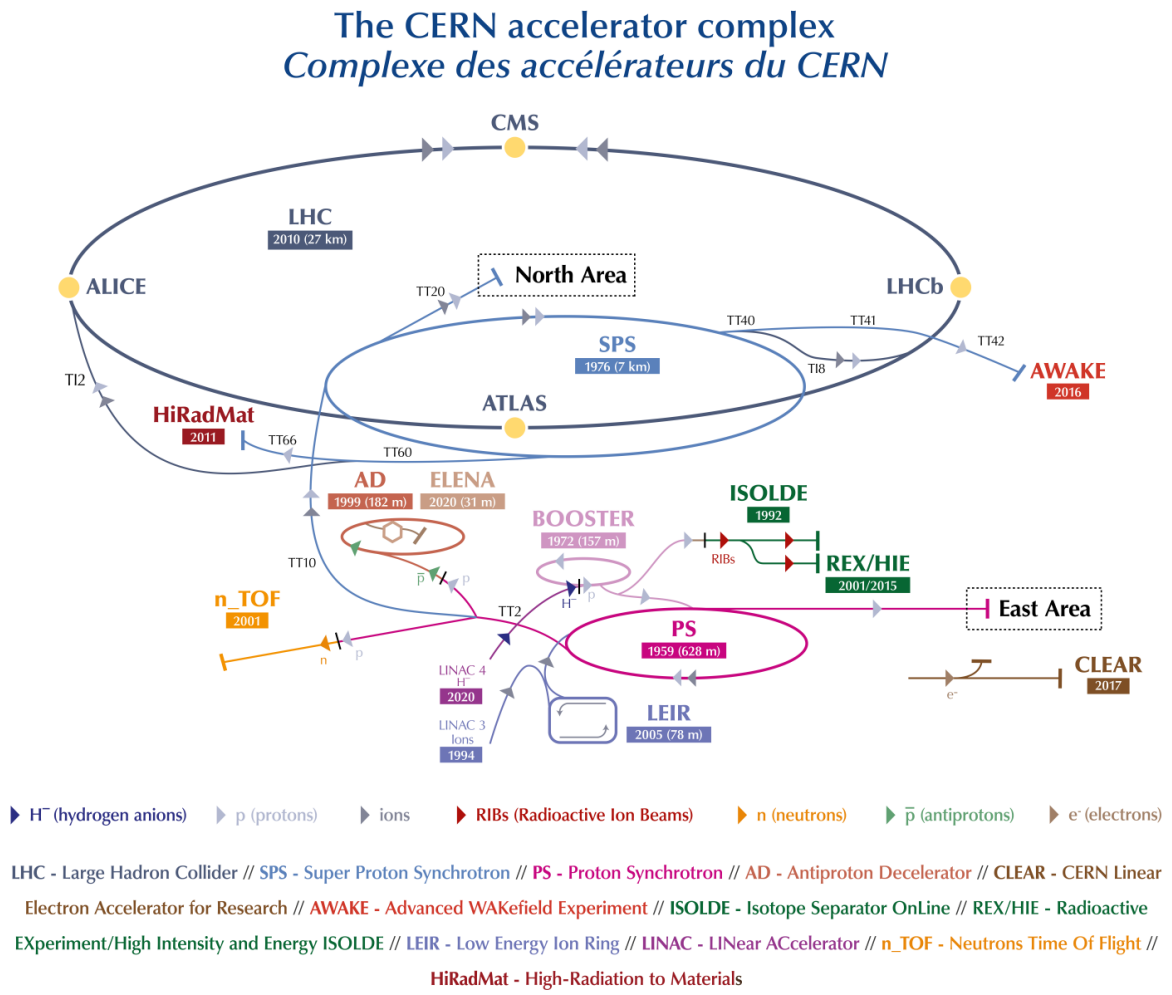

FIGURE 3.1: A representation of the CERN accelerator complex [39].

Lead ions are provided to the LHC in a similar fashion. First, the heavy ions are produced by an electron-cyclotron-resonance plasma source, after which they are accelerated up to 4.2 MeV by a dedicated linear machine, Linac 3. The ions then pass to the Low Energy Ion Ring (LEIR), where their long-pulse structure is transformed into short, dense bunches and their energy is increased to 72 MeV. The modified bunch structure and higher energy is suitable for injection to the Proton Synchrotron, after which, the ions follow the exact same path as the protons to reach the LHC.

3.1.2 The machine

Once reaching the maximum energy of 450 GeV, the SPS injects the protons to the LHC in the form of bunch trains, separated by 25 ns and each containing 1.15×10^{11} protons. One of the advantages of a circular accelerator is that in every round, the particles are further accelerated, and therefore the target energy can be gradually reached after many cycles. The LHC is

a particle-particle accelerator, meaning that, in contrast to a particle-antiparticle type, it needs two separate rings for the counter-rotating beams. Inside each ring, the particles are accelerated by an electric field while being kept focused in a curved trajectory by a magnetic field. When the beams have reached the desired energy, they are focused and brought to collisions in four interaction points (IPs) where the four experiments, ATLAS [40], CMS [41], ALICE [42] and LHCb [43] are stationed. ATLAS and CMS are general purpose experiments, oriented towards measuring the Higgs boson and its properties, the study of the SM and the discovery of new physics by generating heavy resonances. LHCb is a forward-based precision experiment dedicated to heavy-flavour physics, while ALICE is a heavy-ion detector, designed to study the limits of the energy density, where the quark-gluon plasma forms.

The acceleration is performed by a series of 16 Radio Frequency (RF) cavities (8 per beam), each providing a maximum field of 2 MV. The RF cavities are superconducting and are operated at a temperature of 4.5 K. The field in an RF cavity is made to oscillate at a given frequency, 400 MHz for the LHC. In this way, the beam is not only accelerated but also the bunch structure is reinforced, since particles with slightly different energies arriving earlier or later will be decelerated or accelerated so that they stay close to the desired energy.

In order to keep the particles in the circular trajectory, superconducting dipole magnets are used. There are 1232 main dipoles, each 15 metres long, providing a nominal field of 8.3 T. All main magnets are immersed in superfluid helium, operating at a temperature of 1.9 K. The superconducting technology has been revolutionary in achieving the required performance with a reasonably-sized accelerator. Apart from the main dipoles, additional magnet types are used in the LHC to focus the bunches. Quadrupole magnets are positioned in pairs in order to tighten the beam height and width, while additional focusing with the beam energy is achieved by sextupole magnets. Higher order multipoles (such as octapoles and decapoles) act to help in further tightening the beam and counteracting unwanted interactions from which the particles suffer. In total, more than 6000 superconducting corrector magnets exist in the LHC. Separate sets of dipole and quadrupole magnets are used to steer the beams at the IPs where the bunches collide.

3.1.3 Luminosity and pile-up

Besides the centre-of-mass energy of the colliding system, the number of interactions of interest is crucial in a collider. This is especially the case when studying rare processes, where the production cross-section is very small. The luminosity (L) is the quantity that measures the ability of a particle accelerator to produce the required number of interactions. It is defined by the following formula:

$$L = \frac{1}{\sigma}\frac{dN}{dt} \tag{3.1}$$

where σ corresponds to the interaction cross-section and N to the number of events that are recorded in a given time t. The unit of luminosity is therefore [length]$^{-2}$[time]$^{-1}$.

While this formula serves to understand the principle of the luminosity and its importance in a statistical analysis, in practice, the luminosity is an accelerator property and is directly linked to the beam structure. Assuming two colliding bunches, both having a transverse profile that is distributed according to a Gaussian, leads to the following expression:

$$L = \frac{N_1 N_2 f N_b}{4\pi\sigma_x\sigma_y} S \tag{3.2}$$

where N_1 and N_2 are the number of particles in the two colliding bunches, N_b is the number of bunches per beam, f is the revolution frequency of the bunches and σ_x and σ_y correspond

to the transverse beam size at the collision point. Finally, the factor S is a geometrical factor accounting for the reduction of the luminosity under a crossing-angle scheme.[1]

The accurate knowledge of the luminosity is essential for the performance of the experiments. This is especially the case in precision measurements of the cross section, where the luminosity is a major systematic. In order to accomplish this, the LHC experiments use dedicated detectors, called luminometers. The approach of ATLAS is to use multiple luminometers with different technologies [44], a scheme that offers redundancy and robustness against individual measurement biases. In Run 2, the primary bunch-by-bunch luminosity measurement in ATLAS is provided by the LUCID 2 Cherenkov detector [45], placed approximately at $\pm$ 17 m from the interaction point. The beam conditions monitor (BCM) [46] diamond detectors also measure luminosity at the bunch-crossing level, providing complementary information. In order to relate the measurements of the two detectors to the luminosity, an absolute calibration procedure is needed. This is performed during special LHC fills in each data-taking year, called van der Meer (vdM) scans [47]. In the vdM method, the overlap of the two beams in the transverse plane is scanned, and the relative interaction rates as a function of the transverse beam separation are measured. The two transverse planes (x and y) are scanned independently and, in this way, the size and shape of the interaction region is estimated. Additional sub-detector systems measure quantities that directly relate to the luminosity, and which, when combined off-line, help improve the overall accuracy. The evolution of the instantaneous luminosity over time during 2018 can be seen in Figure 3.2a. The LHC showed an excellent performance throughout its operation, reaching and greatly surpassing its design value of 10^{34} cm^{-2}s^{-1}.

Of particular importance for the physics potential of the experiments is the integrated luminosity, i.e. the total luminosity over the data-taking period. Figure 3.2b shows the evolution of the integrated luminosity over time in ATLAS for the Run 2 period. A total integrated luminosity of 156 fb^{-1} was delivered, almost 6 times more than in Run 1. The ATLAS detector registered 147 fb^{-1} of data, demonstrating an impressive efficiency of almost 95%. Of the recorded data, only a subset satisfying strict quality criteria is used in physics analyses, in order to ensure integrity against occasional hardware or software failures. In Run 2, 139 fb^{-1} of physics worthy data was registered. The search for squarks and gluinos which was performed in this thesis (presented in Chapter 4) makes use of the entire physics-worthy Run 2 ATLAS dataset.

It is clear that the increase in instantaneous luminosity is beneficial for the physics case of LHC, as more data can be accumulated in a shorter amount of time. However, this implies an increase of the number of interactions that occur in a given bunch crossing. That is an evident drawback, due to the fact that the LHC experiments are only interested in a single interaction of the bunch crossing, the one with the highest physics potential. This interaction is the so-called hard-scatter interaction, while all additional activity is referred to as pile-up. The presence of pile-up deteriorates the performance of the detectors, since, particles originating from pile-up interactions can contaminate hard-scatter events. Pile-up can be in-time, meaning that it originates from additional interactions in the same bunch crossing, or out-of-time, due to signals from previous bunch crossings. While the former contribution is the most challenging to mitigate, out-of-time pile-up can also introduce a non-negligible effect in cases where the detector signal-processing time is significantly larger than the time between crossings, like in the ATLAS Liquid Argon calorimeters. The number of pile-up interactions

[1] In the LHC, the two beams collide at a crossing angle of $\sim 300\,\mu\text{rad}$, in order to decrease the number of additional interactions.

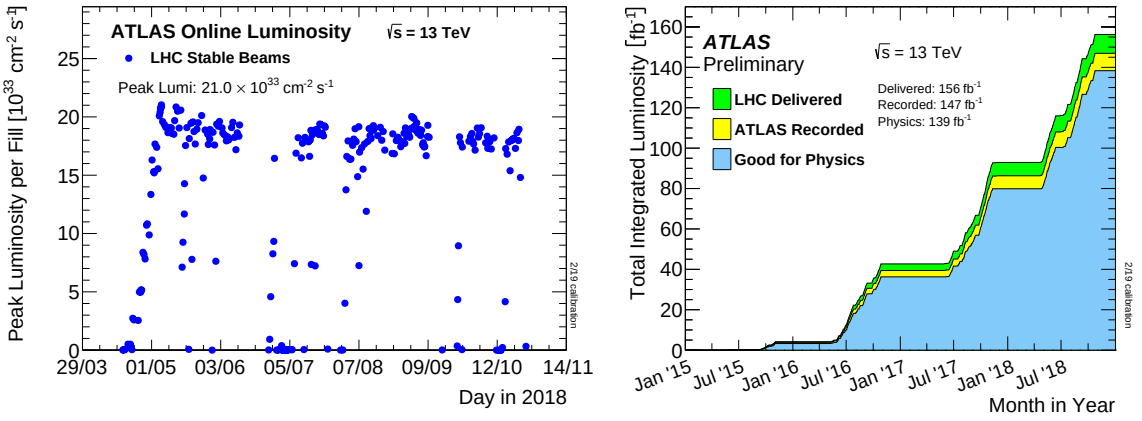

(a) (b)

FIGURE 3.2: (a) Peak instantaneous luminosity delivered to ATLAS as a function of time for the 2018 data-taking period. (b) Cumulative luminosity versus time delivered to ATLAS (green), recorded by ATLAS (yellow), and certified to be good quality data (blue) during stable beams for pp collisions at 13 TeV centre-of-mass energy in 2015-2018 [48].

per bunch-crossing, μ, can be expressed with the following formula:

$$\mu = \frac{L \times \sigma_{inel}}{N_b f} \tag{3.3}$$

where σ_{inel} is the proton-proton inelastic cross-section. Figure 3.3 shows the distribution of $< \mu >$ for each year of the Run 2 pp collisions. The average pile-up for the entire run was approximately 34 interactions / bunch crossing, compared to 21 in Run 1. These conditions provided an additional challenge in the calibration and performance of the detectors, and more sophisticated techniques were deployed to mitigate the undesired pile-up effects.

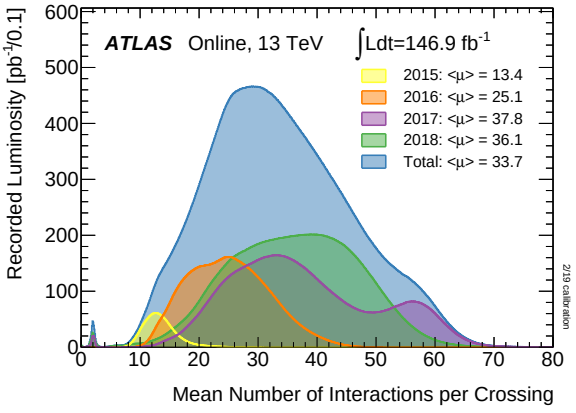

FIGURE 3.3: Distribution of the mean number of interactions per bunch-crossing for each year of the Run 2 pp collision data at 13 TeV centre-of-mass energy [48].

3.2 The ATLAS detector

The ATLAS detector [40] is one of two general-purpose detectors at the LHC. It investigates a wide range of physics, from the search for the Higgs boson to extra dimensions and particles that could make up dark matter. Beams of particles from the LHC collide at the center of the ATLAS detector making collision debris in the form of new particles, which fly out from the collision point in all directions. Different detecting subsystems arranged in layers

around the collision point record the paths, momentum, and energy of the particles, allowing them to be individually identified. Its main components are listed below:

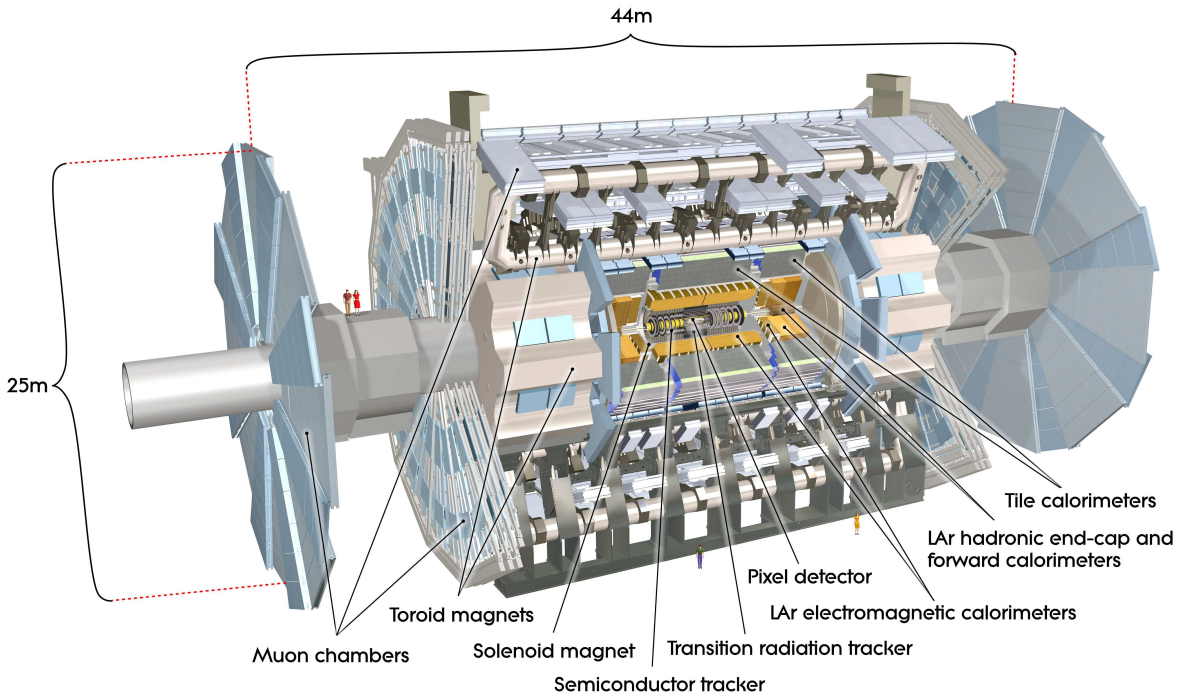

FIGURE 3.4: Schematic view of the ATLAS detector.

- The magnetic system bends charged particles, aiding in their separation, charge and momentum estimation. It comprises of two parts: a solenoid magnet providing a 2 T field to the inner detector, and a set of air-core toroid magnets in which the muon spectrometer is immersed. The particular shape of the latter is a trademark of the ATLAS experiment, and has largely driven the detector design.
- The Inner Detector, the innermost part of the apparatus. Composed of several high-granularity tracking layers, it infers the trajectories and momentum of charged particles using the magnetic field of the solenoid magnet. Additionally, it is used to reconstruct the interaction vertices of each bunch-crossing.
- The calorimeters that are situated outside the solenoidal magnet that surrounds the Inner Detector. Their purpose is to measure the energy from particles by absorbing them.
- The Muon Spectrometer is a tracking system of gaseous chambers. With the help of the toroid magnets, it complements the momentum measurement of muons, which first go through all the other elements of the detector without being absorbed.

The detector can be distinguished in two main areas; the central region (or barrel) and the two forward regions (or end-caps). ATLAS is a cylindrical detector, 44 m in length and 25 m in height.

3.2.1 The ATLAS coordinate system

The detector uses a right-handed coordinate system with its origin at the nominal interaction point. The z-axis is along the beam pipe, the x-axis points to the center of the LHC

ring and the y-axis points upward. Often, cylindrical coordinates (z, ϕ, θ) are used instead, ϕ being the azimuthal angle around the beam pipe and θ the polar angle. Usually, a range of $-\pi < \phi < \pi$ is chosen, while θ can be replaced by the distance r to the beam axis at a position z. A very useful variable is the pseudorapidity η, which is defined as:

$$\eta = -ln[tan(\theta/2)] \tag{3.4}$$

A pseudorapidity of η = 0 corresponds to the center of the detector, while $\eta \to \infty$ points to the beam axis. In hadron collider physics, the pseudorapidity is preferred over the polar angle θ because, assuming a particle speed very close to the speed of light, the outgoing particle rate is approximately constant in units of η. Additionally, measurements in η are not dependent on the longitudinal boost of the reference frame.

Distance measurements are often performed in the modified cylindrical coordinate system using η and ϕ as following:

$$\Delta R = \sqrt{\Delta\eta^2 + \Delta\phi^2} \tag{3.5}$$

Protons are composite particles, made of quarks and gluons that carry an unknown fraction of the proton energy. It is therefore impossible to know the momentum of the colliding partons. However, as the beams are travelling along the beam axis, the transverse momentum ($p_{\mathrm{T}} = p_x + p_y$) of the incident quarks and gluons is negligible. The total transverse momentum in the initial state is therefore close to zero, and so has to be the total transverse energy in the final state. This conservation is particularly important in the reconstruction of objects that do not leave a signature in the detector, such as neutrinos.

3.2.2 Inner detector

The inner detector (ID) [49] begins a few centimetres from the proton beam axis, extends to a radius of 1.2 metres, and is 6.2 metres in length along the beam pipe, covering up to $|\eta|$ = 2.5. Its basic function is to reconstruct the trajectory of charged particles by detecting their interaction with the material at discrete points, revealing detailed information about the types of particles and their momentum. It is surrounded by a thin superconducting solenoid magnet producing a 2T axial magnetic field, which is used to curve the charged particles and consequently measure their momentum and their charge. After the tracks have been identified, they are used to reconstruct the interaction vertices where the particles are produced.

One of the main goals of the ID is to measure the momentum of the charged particles. The momentum resolution is directly proportional to the curvature of the particles, meaning that the performance naturally deteriorates with increasing p_{T}. The expected resolution as a function of the particle p_{T} can be expressed as:

$$\frac{\sigma_{p_{\mathrm{T}}}}{p_{\mathrm{T}}} = a\, p_T[GeV] \oplus b \tag{3.6}$$

where a is the intrinsic resolution of the momentum measurement in a magnetic field and b is a term associated to multiple-scattering effects. For the ATLAS ID, the parametrization values have been derived to be a = 0.05% and b = 1.6% from cosmic ray muon data in 2009 [50].

Apart from reconstructing tracks, the ID is responsible of finding the primary vertex of the event. Vertices are reconstructed by extrapolating tracks to the beam axis and grouping the ones with overlapping extrapolated positions. The ID must therefore additionally provide a very good resolution of the track extrapolated position in the interaction plane. The compatibility of a track originating from a reference point can be quantified by the impact parameter,

which corresponds to the distance of the extrapolated track position from the reference point in a given plane. The ID must display an excellent performance in the estimation of both the longitudinal and transverse impact parameters, z_0 and d_0 respectively. The impact parameter resolution is intrinsically improved by measuring the track trajectory as close as possible to the interaction plane. However, material scattering effects can significantly deteriorate the performance, especially at low particle momenta, calling for extremely light detecting and supporting structures.

The ATLAS inner detector consists of four parts using different technologies, presented hereafter.

Insertable B-Layer

The ATLAS Insertable B-Layer (IBL) [51] is the innermost layer of silicon (Si) pixel detectors. Silicon sensors are semiconducting devices, characterised by the existence of a p-n junction. The principle of detection is the application of a reverse bias voltage that creates an electric field. When a particle crosses the sensor, it generates electron and hole pairs along its path, which drift towards the collection planes, the cathode and anode, respectively. The movement of both types of carriers produce an electric current which constitutes the signal.

The IBL belongs to the 2nd generation of subsystems, since it was not installed until 2014. It is located at a radius of 3.3 cm from the beam axis. This layer was put in place between the beam-pipe and the Pixel detector in order to ensure a high quality of the track and vertex reconstruction in view of the increase in instantaneous luminosity and radiation damages of the existing system. Its position in extreme proximity to the beam-pipe is particularly useful in the reconstruction of secondary vertices, that might point to events containing B-hadrons, which have a long lifetime. In order to be able to cope with high radiation and occupancy, the IBL uses Si sensors based on the hybrid planar and 3-D technologies, with a size of $50\,\mu\mathrm{m} \times 250\,\mu\mathrm{m}$ in r and z. With the addition of the IBL, the impact parameter resolution in both planes is improved by about 40% for tracks with p_T below 1 GeV, and reaches a maximum performance of $\sigma(d_0)$ ($\sigma(z_0)$) = $20\,\mu\mathrm{m}$ ($80\,\mu\mathrm{m}$) for tracks with $p_\mathrm{T} > 10$ GeV [52].

Pixel detector

Surrounding the IBL is the Pixel Detector, the second part of the ID. It consists of three concentric layers on the barrel of the detector and three disks on each end-cap. The three barrel layers are positioned in a distance of R = 50.5 mm, 88.5 mm and 122.5 mm from the beam pipe, respectively. The detecting material is silicon pixel modules that are segmented in r and z with an active size of $50\,\mu\mathrm{m} \times 400\,\mu\mathrm{m}$. The high granularity provides an excellent resolution of $14\,\mu\mathrm{m} \times 115\,\mu\mathrm{m}$. In total, the Pixel detector covers an area of 1.7 m^2 and counts roughly 80 million channels.

Semi-Conductor Tracker (SCT)

The SCT is the middle component of the ID. It is similar in concept and function to the Pixel Detector but with long, narrow strips rather than small pixels, making coverage of a larger area practical. It is also divided into a central part consisting of 4 cylindrical barrel layers and two forward parts, organized each in 9 planar end-cap disks. The strips are $80\,\mu\mathrm{m}$ long in r and 64 mm long in z, therefore providing an excellent resolution of $17\,\mu\mathrm{m}$ in r.

The Transition Radiation Tracker (TRT)

The TRT is the outermost component of the Inner Detector. It surrounds the rest of the ID and provides a coverage up to $|\eta| = 2$. It is a combination of a straw tracker and a transition radiation detector. In the barrel, there are around 50.000 straws with 144 cm length, while each endcap is equipped with 125.000 straws of 39 cm length. Each straw has a diameter of 4 mm and is filled with gas that becomes ionized when a charged particle passes through. The ionized particles in the gas are driven through a high electric field to an anode wire where they produce an electric signal.

The TRT has a significantly reduced position resolution of 0.17 mm. However, it has the additional functionality of being able to distinguish between particles. Between the straws, materials with widely varying refraction indices cause ultra-relativistic charged particles to produce transition radiation. The amount of transition radiation heavily depends on the mass of the crossing particles and therefore, the intensity of the radiated photons can be used for particle identification. The differentiating capabilities of the TRT aid particularly in the separation of electrons and pions.

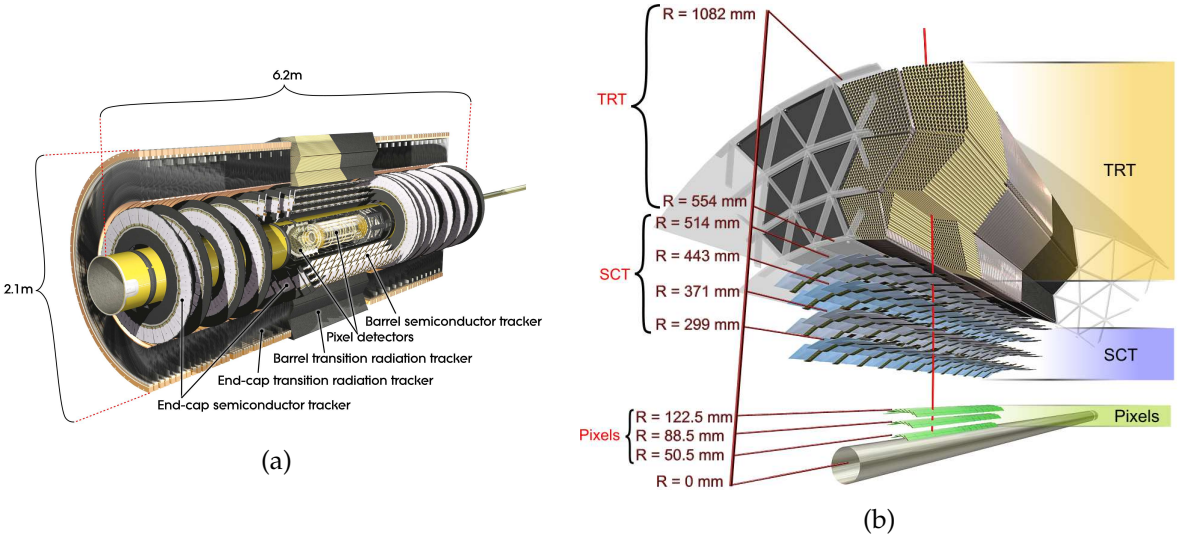

FIGURE 3.5: (a) Cut-away view of the ATLAS Inner Detector. (b) Drawing showing the sensors and structural elements traversed by a charged track in the barrel inner detector.

3.2.3 Calorimeters

The calorimeters of ATLAS are placed after the solenoid magnet that surrounds the ID. Their main purpose is to measure the energy of particles by absorbing them. Particles that cross the calorimeters initiate cascades of secondary particles called particle showers, through their interaction with a heavy material. The energy of the initial particle can be inferred by counting the number of particles constituting the shower. Therefore, the containment of the shower is an important goal of a calorimeter which primarily affects the depth and material choice. Calorimetry is an inherently destructive process, meaning that most of the particles deposit a large fraction of their energy in the shower and are stopped.

There exist two types of showers: electromagnetic ones, which are initiated by and contain only electrons and photons, and hadronic showers, which are initiated by hadrons and are propagated by strong interactions between the particles and the material. For electromagnetic showers, a useful quantity to quantify the shower depth is the radiation length, X_0, defined as the distance after which the incoming partilce retains 1/e of its original energy. A

similar quantity exists for hadronic showers, named interaction length, $\lambda_{int} = \frac{A}{N_A \sigma_{int}}$, where A is the atomic number, N_A is the avogadro constant and σ_{int} the cross section for nuclear interactions. Both radiation and interaction lengths are inherent material properties, which makes the material choice an important parameter to consider when designing a calorimeter.

The calorimetry system of ATLAS consists of three main components:

- The Electromagnetic Calorimeter (ECAL), which covers the area within $|\eta| < 3.2$ and whose main responsibility is the measurement of electromagnetic showers, initiated by electrons or photons.
- The Hadronic Calorimeter (HCAL), positioned at $|\eta| < 3.2$ aiming at stopping and measuring the energy of particles that produce hadronic showers.
- The Forward Calorimeter (FCAL), measures the energy of both electromagnetic and hadronic particles in the forward region, between $3.1 < |\eta| < 4.9$.

The coverage of the calorimeter extends up to $|\eta| = 4.9$. A schematic view of the system with the various components can be seen in Figure 3.6.

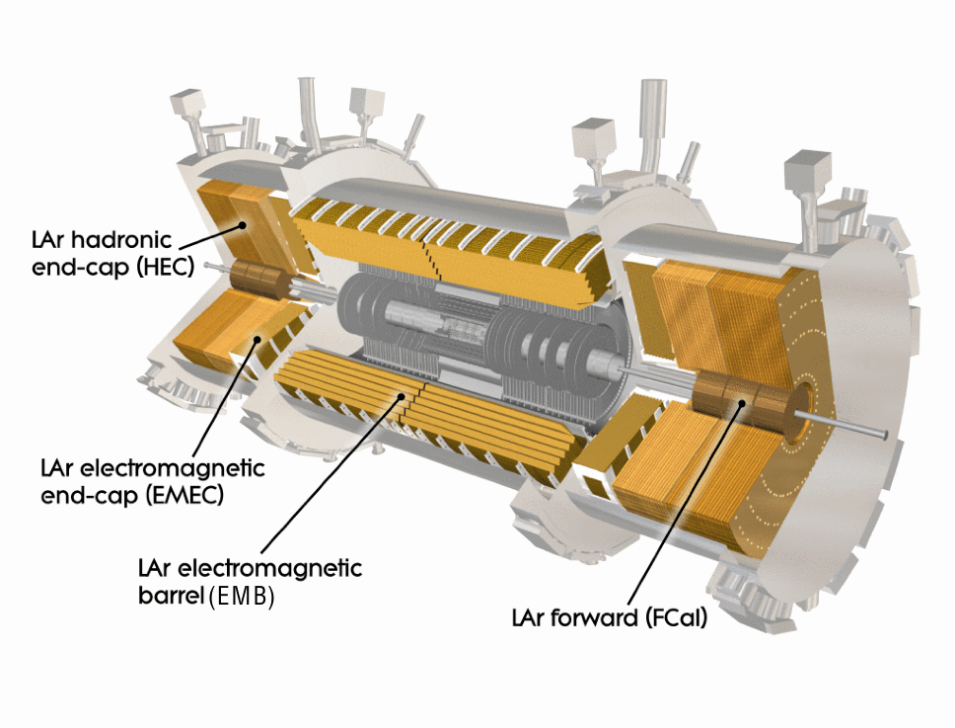

FIGURE 3.6: Cut-away view of the ATLAS calorimeter system.

The measurement strategy is another driving factor in the design of a calorimeter. In general, two main methods exist; the material that produces the particle shower (absorber) can be distinct from the material that measures the deposited energy (active material), in which case one refers to a sampling calorimeter. Alternatively, the entire area of the calorimeter can act as both the absorber and active material, in which case the calorimeter is referred to as homogeneous. All ATLAS calorimeter systems are sampling calorimeters, where absorber layers are alternated with layers of active material. This configuration presents the advantage that a fine segmentation can be achieved also in the longitudinal direction, allowing for a precise

reconstruction of the shower evolution in all dimensions. This is achieved at the cost of the energy resolution, as part of the energy is deposited in the absorber and never measured.

The intrinsic energy resolution of an ideal calorimeter, that is, a calorimeter with infinite size and no response deterioration due to instrumental effects, is mainly due to fluctuations of the shower development length. Since this length is proportional to the number of segments in the shower, and the shower development is a stochastic process, the intrinsic energy resolution increases with the original particle energy E, as $\sigma_E \propto \sqrt{E}$. In a real calorimeter, the energy resolution can be parametrized as follows:

$$\frac{\sigma_E}{E} = \frac{a}{\sqrt{E}} \oplus \frac{b}{E} \oplus c \tag{3.7}$$

where:

- a is the stochastic term, accounting for statistical fluctuations of the shower and the signal, along with inefficiencies of the energy deposition in the active material. An example of the latter contribution is the partial loss of shower information in a sampling calorimeter.
- b is the noise term, corresponding to the effects of electronics noise and pile-up.
- c is the constant term, which includes errors due to the non-uniformity of the energy response/collection, energy leakage caused by non fully contained showers and upstream energy losses. An excellent calibration procedure is required to minimize the constant term.

Electromagnetic calorimeter

The ATLAS electromagnetic calorimeter [53] is a sampling calorimeter. It consists of two parts, the barrel one covering a pseudorapidity range up to $|\eta|$ = 1.46 and the end-cap one ranging from $1.36 < |\eta| < 3.2$. The active material is Liquid Argon (LAr) maintained in a temperature around 89 K, while the absorber is lead (Pb). Each active layer is contained in a gap of 4.5 mm between two lead plates. The absorber thickness varies with pseudorapidity, so that the particles will cross the same amount of material in radiation lengths. Particles initiate electromagnetic showers in the absorber layers and, when the shower products cross the active layers, they cause ionization in the LAr. The resulting ionisation particles drift with the aid of an electric field towards an anode where they are collected.

The barrel ECAL consists of 3 layers with decreasing granularity and is around 24 X_0. In particular, the very fine granularity of the first layer offers the possibility to perform particle identification tasks, for instance by separating isolated photons from π_0 decay products. One of the most characteristic properties of the ATLAS barrel ECAL is its accordion shape, which enables for the full ϕ range to be covered without azimuthal cracks. A 3D view of a barrel ECAL module can be seen in Figure 3.7a. The resolution of the ATLAS LAr calorimeter is estimated to be:

$$\frac{\sigma_E}{E} = \frac{10\%}{\sqrt{E}} \oplus c \tag{3.8}$$

where the constant term c is less than 1% in the barrel and 1-2% in the end-caps [54]. The noise term, of the order of 270 MeV, has been omitted since it is negligible.

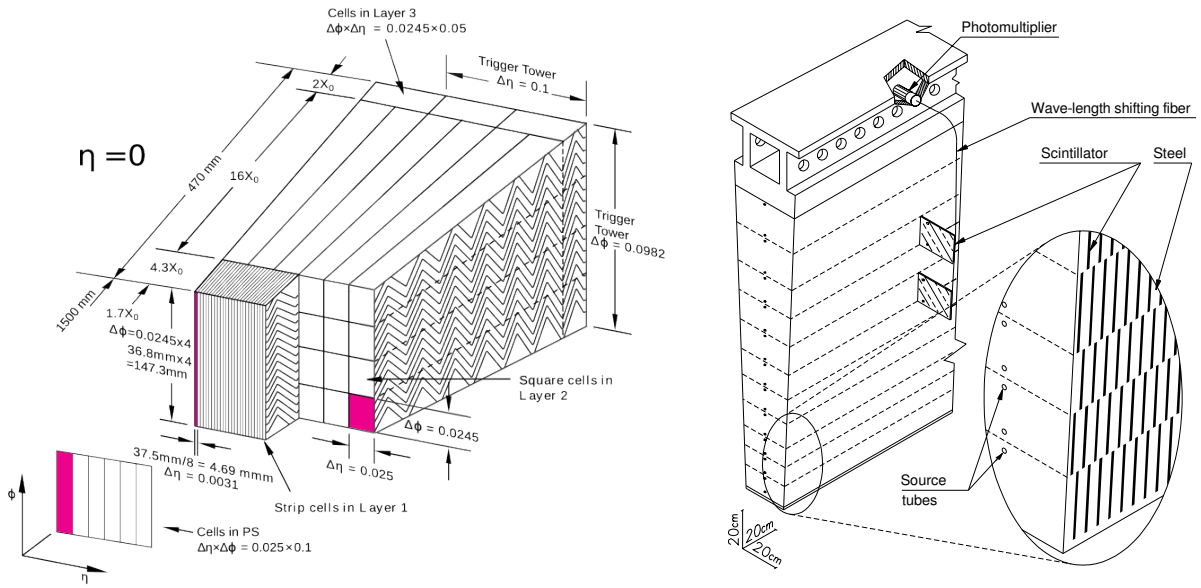

(a) (b)

FIGURE 3.7: (a) Sketch of a LAr barrel module, showing the three layers. (b) Schematic showing of a tile calorimeter module. The various components of the optical read-out, namely the tiles, the fibres and the photomultipliers, are shown.

Hadronic calorimeter

The hadronic calorimeter (HCAL) [55] surrounds the ECAL and its main target is to absorb energy from particles that pass through the EM calorimeter and interact via the strong force, primarily charged and neutral hadrons. It consists of two parts, the barrel covering the area with $|\eta| < 1.7$, and the end-cap part extending from $|\eta| = 1.7$ to $|\eta| = 3.2$. In the barrel, steel and scintillating tiles are used as the absorber and active material, respectively. When crossing the scintillator, particles ionise the polystyrene and induce an ultraviolet scintillation light. The light is transferred by wave-length shifting (WLS) fibres on both sides of the each tile to photo-multipliers (PMTs) in the outer radius, were it is read-out. The scintillating tiles are placed in the plane perpendicular to the colliding beams and are radially staggered in depth, as illustrated in Figure 3.7b. This particular orientation allows the WLS fibres to run straight to the outer radius, enabling a good calorimeter hermeticity. The calorimeter modules are segmented in three longitudinal layers. The total depth of HCAL is around 7.4 λ_{int} (for $\eta = 0$). In the end-cap part, a copper-LAr configuration is deployed instead, operating similarly to the end-cap electromagnetic calorimeter.

The HCAL is less precise, both in energy magnitude and in localization than the ECAL. The main reason for this discrepancy is that a significant part of the initial energy is diverted to low energy nuclear processes which proceed in a relatively large time-scale (like captured low energy neutrons) and are therefore not reconstructed. Another challenge in the HCAL is the fact that hadronic showers often contain an electromagnetic component (for example from $\pi^0 \rightarrow \gamma\gamma$ decays), which responds differently to the same material than the hadronic part. Both these effects add to the stochastic term leading to a decreased energy resolution, which can be expressed as follows [56]:

$$\frac{\sigma_E}{E} = \frac{52\%}{\sqrt{E}} \oplus 5.7\% \tag{3.9}$$

This result corresponds to the response of the Tile Calorimeter to hadrons, as extracted in test beam [56].

Forward calorimeter

The very forward region of ATLAS, between 3.1< $|\eta|$ < 4.9, is also instrumented by calorimeter components, constituting the Forward Calorimeter (FCAL) [57]. Due to the extremely high particle flux in the forward region, LAr is used as the active material in the FCAL, since it is intrinsically radiation hard. The FCAL is segmented into three layers; the first one uses copper as the absorber material, in order to achieve a good reconstruction of electromagnetic showers. The other two layers deploy tungsten absorbers, for a better performance in hadronic showers.

The main purpose of the FCAL is to extend the reach of the ATLAS detector in the forward region, and to cover the largest possible fraction of the total event energy. This is of particular importance in the calculation of the Missing Transverse Momentum, 3.3.5, from particles which do not interact with the detector, such as neutrinos or BSM particles.

3.2.4 Muon Spectrometer

Muons are particularly interesting particles regarding their interaction with the detector. Being Minimum Ionizing Particles (MIPs) for a large energy range, typically from O(100) MeV to the TeV scale, they cross the calorimeters without being absorbed, usually only losing a small fraction of their energy. While partial information on their momentum is already provided by the tracker, detecting their interaction outside of the calorimeter system is required to identify them and complement the measurement of their properties.

The Muon Spectrometer (MS) is an extremely large tracking system, dedicated to the identification of muons and the precise estimation of their transverse momentum. It is the outermost detector system in ATLAS, extending up to $|\eta| < 2.7$ and r = 11 m. It is immersed inside a toroid-magnet system providing a field of 0.5 in the endcaps and 1 T in the barrel. Figure 3.8 presents a schematic view of the ATLAS muon system. The MS functions similarly to the Inner Detector, with muons curving so that their momentum can be measured, albeit with a different magnetic field configuration, lower spatial precision, and a much larger volume. In order to efficiently cover the significantly larger area, the MS is a gaseous ionization detector. When a charged particle crosses the active area, it ionizes the gas. An applied electric field then guides the electrons and ions to be collected.

The MS system consists of 4 sub-detectors, 2 in the central barrel and the rest in the forward region. In each region, one detector system is dedicated for a precise trajectory measurement of the muons, while the other has a coarser resolution and is used to provide a trigger. The four MS sub-detectors are described below:

- The Monitored Drift Tubes (MDTs) perform the precision position measurement between -2.7 $< \eta <$ 2.7. The detector unit is a 30 mm diameter drift tube with a central collection wire. The tube is filled with gas and the wire is operated at high voltage, to maximize the collection efficiency. The tubes are organized in layers and stacked, forming chambers. In total, around 1.200 MDT chambers are used in ATLAS.
- The Cathode Strip Chambers (CSCs) perform the same task as the MDTs, but in the forward region, between $|\eta|$ = [2,2.7], where the counting rate is too high for the MDTs. The CSCs are multi-wire proportional chambers, where the higher applied voltage induces avalanches in the ionization gas when a particle crosses it. Instead of reading out

directly the anode wires, the precision coordinate is obtained by measuring the charge induced on the segmented cathode by the avalanche formed on the anode wires. In this way, a higher position resolution around $60\,\mu\mathrm{m}$ is achieved. Similarly to the MDTs, the CSCs are organized into layers that are stacked in a way that optimizes the resolution.

- The Resistive Plate Chambers (RPCs) are installed in the barrel and aim to provide a trigger for the Data Acquisition (DAQ) system. The basic RPC unit is a narrow gas gap formed by two parallel resistive plates. The primary ionization electrons are multiplied into avalanches by a high electric field. RPCs have a coarser granularity than their MDT counterparts, resulting in a reduced resolution of 1 cm, but can be read-out much faster, which motivates their use for the trigger.
- The Thin Gap Chambers (TGCs) serve the same purpose as the RPCs, but in the forward region. Due to the high event rates, TGCs are designed in a way similar to the CSC.

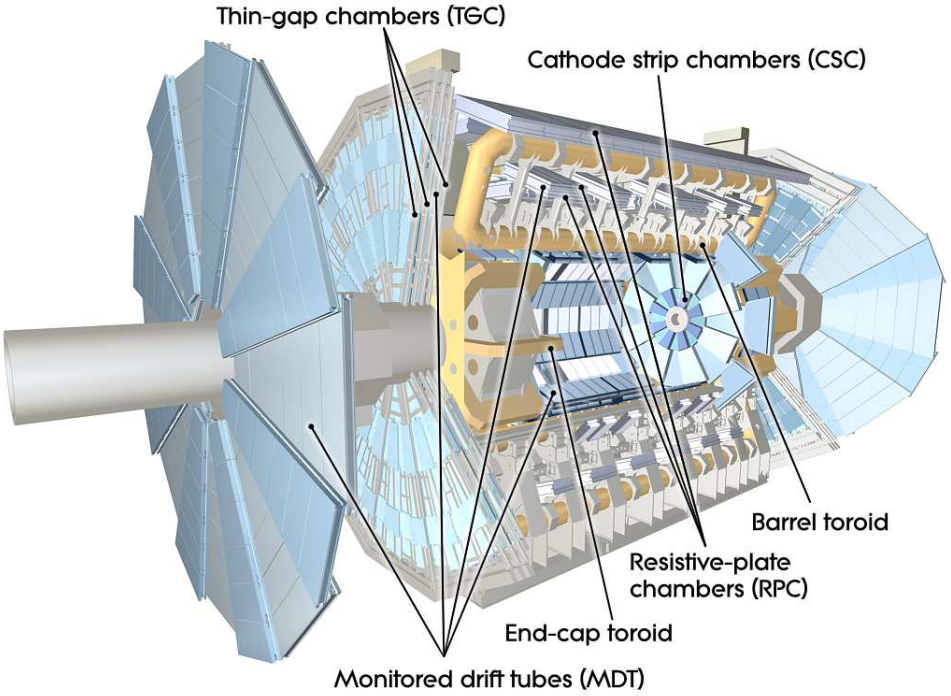

FIGURE 3.8: Cut-away view of the ATLAS muon system.

The MS can be used as a standalone detector for the identification and reconstruction of muons. A resolution of the order of 10% is achieved for muons of 1 TeV. The MS performance can be improved by using in addition the tracking information of the ID.

3.2.5 Trigger

Protons at the LHC collide at a frequency of around 40 MHz, i.e. every 25 ns. Taking into account the available information from all the ATLAS sub-detectors results in a staggering data rate of approximately 60 TB/s. However, out of all this information, only a few events are of interest for the physics searches of ATLAS. Because of the limited bandwidth and storage space available to record data, a selection must be performed in order to give priority to some signatures. The selection of the events of interest is the task of the trigger system. The layout of the ATLAS trigger [58] is shown in Figure 3.9. It consists of two independent levels, a hardware-based first level (L1) and a software-based high level trigger (HLT).

The L1 trigger is implemented in fast custom-made electronics and runs with a fixed latency of 2.5 µs. Only two sub-detector systems, the calorimeter and the muon spectrometer, provide signal inputs for the L1, independently to their off-line data stream. This data is treated by two autonomous sub-systems, the L1Calo and L1Muon, respectively, which search for Regions of Interest (RoIs). The L1Calo identifies regions with high transverse energy deposit in the electromagnetic calorimeter with a coarse granularity, while the L1Muon searches for a coincidence of hits across multiple layers of the MS trigger chambers, which are consistent with muons originating from the interaction point. The output of the L1 is a single-bit decision, which is transmitted across the detector systems to either read-out the full event or discard it. After the L1, the event rate is reduced from 40 MHz to 80 kHz.

The read-out of the accepted events is then passed to the HLT, which is a farm of CPU cores. At this point, more complex reconstruction algorithms can be executed within the L1 RoIs to build event objects such as tracks, electrons, muons and jets. The decision making process of the HLT is based on a list of pre-defined trigger selection criteria, the trigger menu. In the trigger menu, various interesting event topologies for physics but also for calibration and performance measurements are encapsulated. As an example, at the 2015 start-up trigger menu, there were four triggers requiring a single lepton with a minimum p_{T} above a certain threshold. The HLT typically provides a decision within 300 ms and further reduces the event rate to 1 kHz. Events that pass one (or more) of the trigger menu selections are recorded on disk, where physicists can further analyse them off-line.

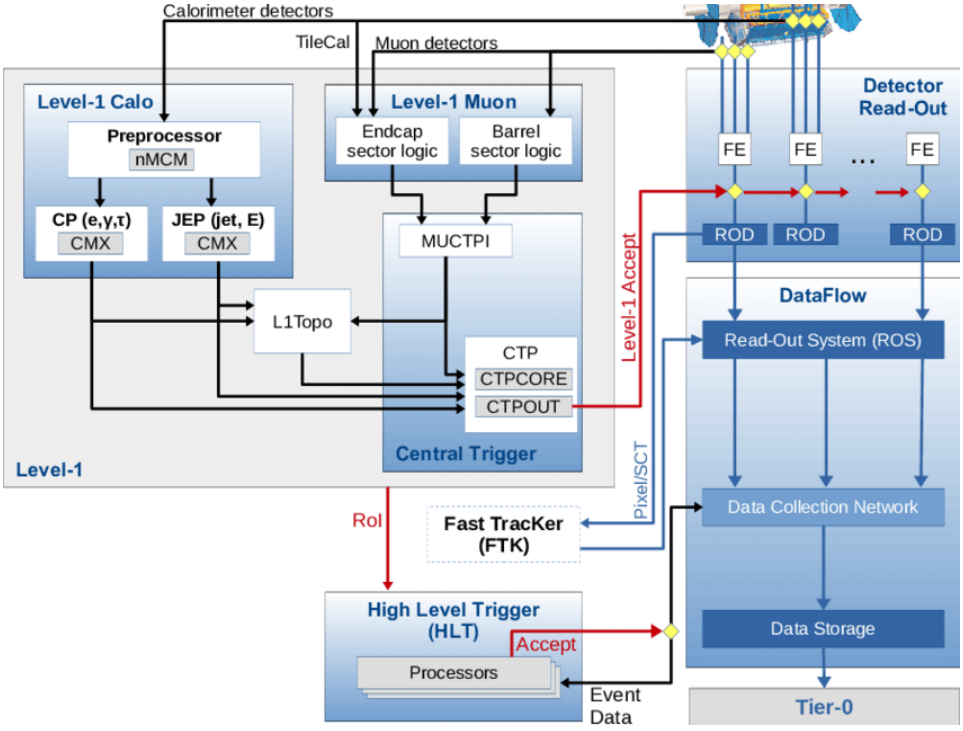

FIGURE 3.9: Schematic illustration of the ATLAS Run-2 Trigger and Data Acquisition system in 2017 [58].

3.3 Object reconstruction with the ATLAS detector

The conversion of the various detector signals of ATLAS to physics objects is a crucial step in all the physics analyses. As shown in Figure 3.10, different types of particles interact in particular ways with the various detector components, producing measurable signals. Following is a brief discussion of the reconstruction techniques employed by ATLAS for the

different physics objects. It should be noted that different objects are often reconstructed independently in ATLAS; ambiguities between the final candidate particles are resolved usually at the analysis level, depending on the final search signature and the main backgrounds.

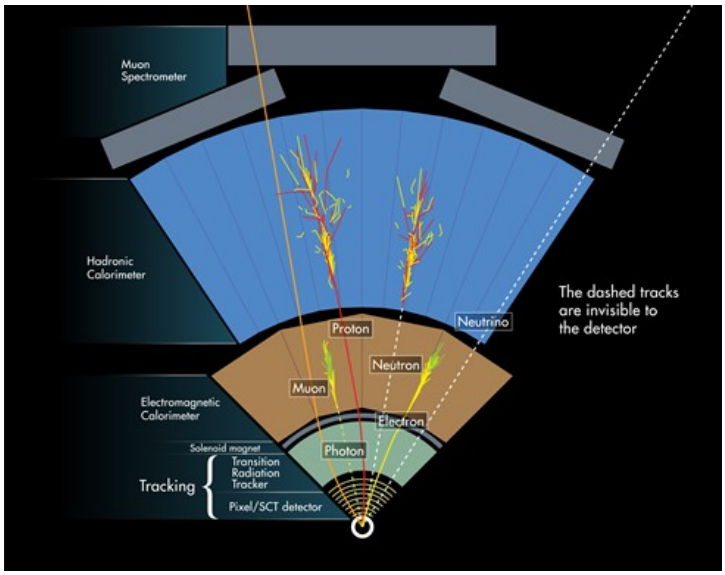

FIGURE 3.10: Transverse view of an ATLAS detector segment with a representation of the interaction of different types of particles in the different sub-detectors.

3.3.1 Tracks and vertices

A track corresponds to a trajectory of the charged particle inside the ID. Charged-particle reconstruction [59] begins by assembling clusters from raw measurements of the pixel and SCT detectors. These clusters are then converted into 3D "space-points", representing the interaction positions between the track and the ID active material. Track seeds are subsequently formed from sets of three space-points, at which moment a rough estimate of the track momentum and impact parameters can be performed. Selection criteria are applied on the seeds to enhance their purity. After selecting a seed, a combinatorial Kalman filter [60] is employed to build a track candidate, by using information from the remaining ID layers. Each track candidate is assigned a score, which measures the probability of it being a genuine track. The filter can create more than one track candidates per seed, in case more than one track-compatible cluster combination is found. Ambiguities arising from clusters being assigned to multiple track candidates are resolved by favourably weighting the track scores. Clusters can be shared by no more than two tracks and a track can have no more than two shared clusters. Finally, after resolving all ambiguities, a high-resolution fit is performed for the remaining good track candidates.

As already discussed in 3.1.3, multiple pp collisions occur in each bunch crossing. Physicists are interested in events with at least one interaction with high potential for interesting physics, the so called hard-scatter interaction, while the remaining ones constitute pile-up. It is therefore understandable that reconstructing the vertices of interest and correctly associating physics objects to them is crucial for the physics case of the experiment. The interaction(s) of interest, named primary (or hard-scatter) vertex(ices), PV (or HS), is reconstructed from a collection of tracks in two steps, the vertex finding and fitting [61]. In the former stage, collections of tracks with similar impact parameters are used to determine vertex seed positions. The tracks and the seed are then used as an input to the fitting step, where an iterative procedure is employed to estimate the best vertex position. In the iterative fit, each input track is assigned a weight, reflecting its compatibility with the vertex estimate, after which the vertex

position is recalculated taking into account the weighted tracks. Once the iterative fit is completed, tracks which are found to be highly incompatible with the vertex are removed from the vertex-associated list of tracks and can be used to find other vertices. The two-step process is repeated with the list of un-associated tracks, until no such tracks are left in the event or no additional vertex can be found in the remaining set of tracks.

3.3.2 Electrons and photons

Electrons [62] and photons [63] are particles that initiate electromagnetic showers, and therefore, their reconstruction is based on using information from the ECAL and the ID. In order to identify showers, localised energy deposits in the calorimeter are processed with a clustering algorithm to form cluster seeds.

To distinguish between electrons and photons, the different charge of these two particles is exploited; electrons, being charged particles are expected to leave a track in the ID. Electron track candidates are reconstructed with a similar procedure to 3.3.1, using an optimized algorithm to account for the significant energy losses due to Bremsstrahlung radiation. They are also required to be compatible with an origin from the PV. Electron candidates are then built by matching an electron-track candidate to a calorimeter seed cluster.

The reconstruction of photons proceeds in parallel to the electrons. Photons can interact with the detector subsystems in different ways, depending if the particle has undergone a conversion to an electron-positron pair, which, in ATLAS, occurs around 50% of the time. In case of a photon conversion before the calorimeter, two electron tracks originating from a displaced conversion vertex are expected to be detected in the ID. Tracks that are matched to the calorimeter cluster are used as input to a conversion vertex finding algorithm, to establish if a photon conversion has taken place. In case of more than one conversion vertex being found by the algorithm, a preference is given to the ones reconstructed from oppositely-charged track-pairs, compatible with electron signatures in the TRT.

As the photon and electron reconstructions run in parallel, an arbitration procedure is necessary to remove ambiguities. This process uses as input the properties of the tracks and conversion vertices matched to a given electromagnetic cluster. Clusters to which neither a conversion vertex candidate nor any track has been matched during the electron reconstruction are considered unconverted photon candidates. On the other hand, clusters that are matched to a conversion vertex candidate are considered converted photon candidates. Finally, in cases where converted photon candidates are also reconstructed as electrons, the electron-track candidate is evaluated against the conversion vertex tracks that are matched to the same cluster. Depending on the compatibility between the electron-track and the conversion vertex track candidates, the cluster is reconstructed as either an electron or a converted photon.

In order to identify the candidates as prompt particles and reject the background, they enter an identification procedure based on additional requirements on properties of their associated calorimeter clusters and tracks. Various sets of the cuts are defined, in order to select candidates with a different efficiency/purity. Prompt electrons are selected in three working points: tight, medium and loose, corresponding to an efficiency of 80%, 88% and 93%, respectively, for an electron with E_T = 40 GeV. Photons on the other hand have two defined reference sets of cuts, loose and tight.

3.3.3 Muons

Muons [64] are reconstructed using information from the MS and potentially other ATLAS sub-detectors. In the MS, tracks are reconstructed by searching for hit patterns in the different subsystems. Muon track candidates are then built by fitting together hits from segments in different layers with a global χ^2 fit. Additional constraints in the number and properties of the segments as well as the fit quality are imposed to ensure a good muon candidate.

Depending on additional signals from the rest of the detector, a combined muon reconstruction can be performed in four ways. Tracks from the ID can be matched to an MS candidate and a combined track can be formed after repeating the global fit with the additional ID hits. In case muons only leave hits in one layer of the MS (usually due to reduced acceptance regions or low p_{T}), tracks from the ID in combination with the local MS segment can be used to identify the muon. Muons in blind spots of the MS, where the instrumentation is greatly reduced, can be reconstructed with a reduced purity from ID tracks matched to calorimeter energy deposits that are compatible with a MIP. Finally, in case none of the above criteria are met, a stand-alone reconstruction of the muon track from the MS is performed, with an additional requirement for the track to originate from the PV. In this case, the muon is required to traverse at least two (three) MS layers in the central (forward) region.

Muon candidates are required to pass additional selection criteria to be identified as prompt particles. These include requirements on the compatibility between the individual momentum and charge measurements from the ID and MS, the number of hits in each individual sub-detector and the quality of the χ^2 fit. Similarly to electrons, three different efficiency working points are defined by tightening the selection criteria: the loose, medium and tight points correspond to an efficiency of 98.1%, 96.1% and 91.8% for muons with p_{T} = [20, 100] GeV. An additional working point exists to maximize the momentum resolution for muon tracks with p_{T} above 100 GeV.

3.3.4 Jets

A jet is a narrow cone of relativistic particles, mainly hadrons, that originate from particles carrying colour, i.e. quarks and gluons. Due to colour confinement, when those particles are released in a collision, they hadronise with other particles into colourless states, and finally form a jet. Jets are reconstructed by clustering topological energy deposits in both ECAL and HCAL in three dimensions [65]. The resulting clusters are then combined to form a jet by a clustering algorithm. Various clustering algorithms for the purpose of reconstructing jets exist; in ATLAS, a generalised use of the anti-kT algorithm [66] is employed.

The anti-kT is an iterative cone algorithm. It starts with the definition of two main distance variables between entities (in our case clusters) i and j and the beam (B):

$$d_{ij} = min(\frac{1}{k_{ti}^2}, \frac{1}{k_{tj}^2})\frac{\Delta_{ij}}{R^2}, \tag{3.10}$$

$$d_{iB} = \frac{1}{k_{ti}^2}, \tag{3.11}$$

where $\Delta_{ij}^2 = (\gamma_i - \gamma_j)^2 + (\phi_i - \phi_j)^2$ and k_{ti}, γ_i and ϕ_i are the transverse momentum, rapidity and azimuthal angle of the particle i, respectively. The parameter R defines the radius of the output jet. In each step, all distances are calculated and the smallest one is identified. If the smallest distance is d_{iB}, the single cluster is considered as a new jet and is removed from the

algorithm list. Otherwise, the two closest clusters are merged into a single larger cluster. The distances are recalculated and the procedure repeated until no clusters are left.

A cleaning procedure is applied on jet candidates, in order to remove calorimeter noise, cosmic muons and beam induced background. Jet candidates also pass through a pile-up mitigation procedure in order to ensure that they originate from a hard scatter interaction and not from pile-up. Already at the hardware level, the bipolar signal pulse shape of the LAr calorimeter naturally provides robustness against out-of-time pile-up. A first cleaning step is performed at the topological clustering level, where only calorimeter cells above a given noise threshold are considered. The cluster energy ratio between the electromagnetic and hadronic calorimeter, as well as tracking information from the ID can be further utilized to suppress pile-up. Remaining pile-up contributions to the measured energy are subtracted during the calibration procedure, described later on.

b-jet Tagging

A particularly interesting sub-category of jets are the ones originating from the hadronisation of a b-quark, commonly referred to as b-jets. The singularity of b-jets is in the relatively long lifetime of B hadrons - for an energy of about 50 GeV, the average flight length will be 3 mm before the decay. This means that B hadrons usually decay within the tracker. The identification of b-jets relies on reconstructing the secondary displaced vertex of the B hadron decay [67]. Additional kinematic properties of b-jets, such as the large mass and hard fragmentation of the B-hadron can be used to enhance the separation to c- or light-jets. In ATLAS, three complementary algorithms are used to take advantage of the aforementioned properties: the impact parameter based algorithms (IP2D,IP3D) exploit the large impact parameters of b-jets that originate from the long lifetime of the b-hadrons. Taking this a step further, the secondary vertex finding algorithm (SV) explicitly tries to reconstruct the secondary vertex. The third approach, the decay chain multi-vertex algorithm (JetFitter), attempts to reconstruct the full b-hadron decay chain by using the jet topological structure. The most probably decay of a b-quark is into a c-quark, and the algorithm explores the possibility of reconstructing both the b and c decay vertices. Inputs from these three algorithms are then combined in a single Boosted Decisions Tree (BDT) algorithm that uses the ROOT Toolkit for Multivariate Data Analysis (TMVA) [68], the MV2, to augment the b-jet discrimination performance. The output of this algorithm is a single variable, the BDT score, that ranges from -1 to 1, with 1 being more b-jet-like. Operating points are once again defined based on cuts on the output value, in order to select different b-jet selection / light- (or c-) jet rejection efficiencies. The typical working point is with a 77% b-tagging efficiency. The equivalent mis-tag rate, i.e. the rate of mistakenly assigning a different flavour jet as a b-jet, is 16% for c-jets and 0.77% for light-jets [69].

Calibration

The reconstruction procedure creates jets at the electromagnetic energy scale, which corresponds to the scale at which the response of the EM calorimeter to electrons and photons is close to unity. Detector effects such as pile-up, energy leakage and non-uniform response can significantly alter this scale from the true energy of the particles. In order to restore the jet energy to the particle scale, a multi-step calibration [70] is employed in ATLAS. The procedure heavily relies on simulation, utilizing Monte Carlo (MC) samples.

The main steps of the Jet Energy Scale (JES) calibration are shown in Figure 3.11. At first, the four-momentum of jets is recalculated to point to the hard-scatter primary vertex rather than the center of the detector, while keeping the jet energy constant. This step is referred

to as *origin correction* and improves the η resolution. Next, the excess energy due to in-time and out-of-time pile-up is removed at the *pile-up correction* stage. This is done in two steps; first, the median pile-up momentum density weighted to the jet area is subtracted from the p_{T} of each jet in each event. Due to the high pile-up conditions in Run 2, some residual contribution remains. Residual pile-up is corrected for as a function of the number of vertices in the event and the μ. After accounting for the effects of pile-up, the reconstructed jet four-momentum is brought to the particle level by comparing the energy of simulated jets between the truth and the reconstruction level. The *absolute MC-based correction* is parametrized both in the energy and η of the jets, in order to account for geometrical effects of the detector, such as dead material, lateral and longitudinal leakage of the showers, low energy deposits and non compensation. The calibration proceeds with the *global sequential correction*, which aims to remove residual dependencies of the JES on jet properties. A series of independent corrections on topological calorimeter and track information variables is derived, allowing to reduce the flavour dependence and energy leakage effects on the jet energy. The last step in the process is the *in-situ calibration*, where differences between the data and the MC simulation are accounted for. Such differences arise from the imperfect description of the detector response and detector material in MC simulation, as well as in the simulation of the hard scatter, underlying event, pile-up, jet formation, and electromagnetic and hadronic interactions with the detector.

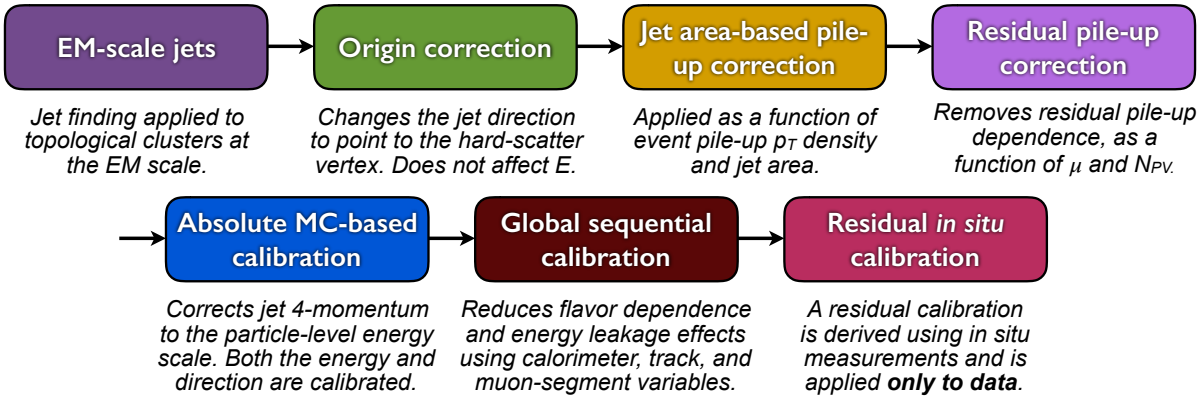

FIGURE 3.11: Calibration stages for EM-scale jets [70].

Particle flow

The jet reconstruction previously described relies only on calorimetric information. An alternative approach can be envisioned, where calorimeter deposits are combined to the tracking information provided by the ID. This approach, referred to as Particle Flow (pFlow), presents various advantages: the tracker momentum resolution is highly superior to the energy resolution of the HCAL, and in particular for low momentum particles. In addition, the ID provides enhanced angular resolution compared to the calorimeters, along with pile-up suppression capabilities. On the other hand, high-p_{T} and neutral particles are better/only reconstructed in calorimeters. This, along with the extended acceptance of the calorimeters in the forward region, offer an attractive complementarity of the two measurements.

In ATLAS, the Particle Flow algorithm [71] is based on matching good quality tracks to calorimeter clusters. Once clusters that match ID tracks have been identified, their energy is removed from the calculation. After this subtraction, jets are reconstructed by combining the selected tracks and the remaining clusters in the calorimeter. The anti-kT algorithm is used once again, and a similar calibration procedure to the one previously described is employed. The resulting jet energy and angular resolution is improved. As an example, for a true jet p_{T}

of 30 GeV, the resolution is enhanced from 17.5% for calorimeter jets to 14% for pFlow jets. Highly energetic tracks with $p_{\mathrm{T}} > 40$ GeV are excluded from the algorithm, since it was found difficult to accurately remove their associated calorimeter energy, while there was no gain from employing pFlow.

While in this thesis Particle Flow was not utilized, it is quickly becoming the default method for reconstructing and measuring the properties of jets in ATLAS.

3.3.5 Missing Transverse Momentum

As briefly discussed in 3.2.1, the transverse momentum in the event is a conserved property, meaning that the final state must count a total transverse momentum component compatible with zero. A significant deviation from a null value can indicate the presence of non-interacting particles, such as neutrinos or neutral, weakly-interacting particles not predicted by the SM. In order to establish the presence of such missing particles, one defines the missing transverse momentum, $\mathbf{E}_{\mathrm{T}}^{\mathrm{miss}}$, as the negative of the vectorial momentum sum of all reconstructed objects in the detector.

The reconstruction of $\mathbf{E}_{\mathrm{T}}^{\mathrm{miss}}$ [72] can be broken down in two contributions: the hard-event signals, which are objects fully reconstructed and calibrated as previously discussed in 3.3.1-3.3.4, and the soft-event signals. The latter correspond to reconstructed charged-particle tracks originating from the PV but not associated to any hard-scatter objects. The missing transverse momentum can be expressed by the following formula:

$$\mathbf{E}_{\mathbf{T}}^{\mathbf{miss}} = -\sum_{i\in\{hard\,objects\}} \mathbf{p_{T,i}} - \sum_{j\in\{soft\,objects\}} \mathbf{p_{T,j}} \tag{3.12}$$

In order to avoid multiple inclusions of the same energy deposit, only objects from mutually exclusive detector signals are added in the $\mathbf{E}_{\mathrm{T}}^{\mathrm{miss}}$ calculation, in a particular order. A priority is given to electrons, followed by photons and other leptons, while jets are rejected if they overlap with accepted higher-priority particles. The lowest priority is given to the tracks belonging to the soft term. The absolute value of the $\mathbf{E}_{\mathrm{T}}^{\mathrm{miss}}$ is often referred to as missing transverse energy, $E_{\mathrm{T}}^{\mathrm{miss}}$.

3.4 The High Luminosity LHC and the ATLAS upgrade

In order to increase the physics potential of the LHC an upgrade of the machine is planned. The key point of this upgrade is an increase of the instantaneous luminosity, which will enable researchers to collect ten times more data than in the LHC. In High-Luminosity LHC (HL-LHC) [73] instantaneous luminosity will be augmented, reaching a maximum value of 7.5 $\times$ 10^{34} cm^{-2}s^{-1}, a factor of 5 larger than the current one. Before the start of HL-LHC in 2027, a last 3-year LHC run, the Run 3, will be carried out, where the nominal instantaneous luminosity will be kept at the same level as at the end of Run 2. The integrated luminosity will increase to 350 fb^{-1} in Run 3 and could reach the final value of 4000 fb^{-1} at the end of the HL-LHC operation. The center of mass energy will initially remain the same, 13 TeV, with a possibility of increasing it to 13.5 or 14 TeV in Run 3, while in HL-LHC, the maximal design value of the accelerator, 14 TeV, is planned to be used.

Figure 3.12 presents the LHC schedule, including the HL-LHC upgrade plan. Already in the past, important work has taken place in the accelerator, in order to reach the ultimate performance. First, in Long Shutdown (LS) 1, a consolidation of the main dipole magnets was performed in order to be able to rump up the center-of-mass energy from 8 to 13 TeV. Currently we are traversing LS2, where the second upgrade phase of LHC is taking place,

including a renovation of the injector for higher brightness and various new/improved sub-detector systems of the experiments. The remaining work for the HL-LHC upgrade will be finalized in LS3, which will start in 2024 and last approximately 2-3 years. This last upgrade will focus, from the accelerator side, on installing novel magnet components in the interaction points, and from the side of the experiments, on finalizing all detector upgrades necessary to handle the increase in instantaneous luminosity. Following LS3, the first physics operation, Run 4, will consolidate the high luminosity phase up to 2030, while subsequent runs, alternated with shutdown periods are expected to last until around 2040.

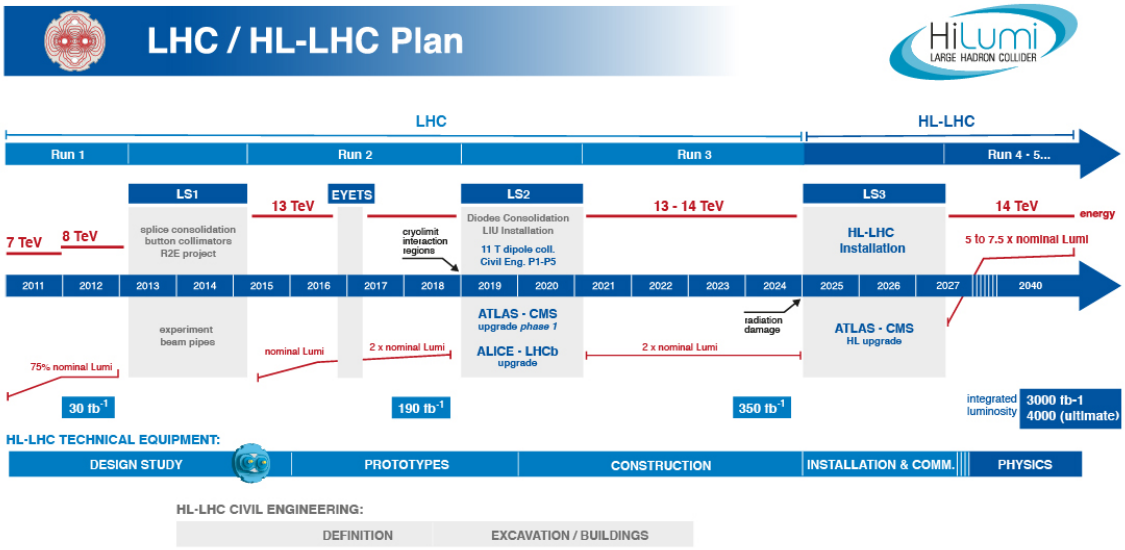

FIGURE 3.12: The LHC baseline programme including the HL-LHC run [74].

3.4.1 Accelerator upgrade and beam conditions

The main challenges of the high instantaneous luminosity regime at the HL-LHC are the radiation damages to the interaction region magnets and the peak pile-up in the experiments. In order to minimize these effects, the accelerator will be operated with a luminosity levelling regime. In this scheme, instead of allowing the natural decay of the luminosity in the fill, the luminosity is initially constrained to a lower level; by gradually loosening this constrain, the luminosity can be maintained constant for a larger period of time. The principle of luminosity levelling is displayed in Figure 3.13; it can be seen that, by optimizing the fill length and machine efficiency, the loss in average luminosity in the case of levelling is small compared to the no-levelling scenario, while the instantaneous luminosity can be maintained to reasonable values for long periods of time.

In order to reach the luminosity goals, an upgrade of the accelerator is foreseen. The main difference will be the increase of the number of protons in a bunch by a factor of 2, from 1.15×10^{11} to 2.2×10^{11} protons per bunch. Around 200 proton-proton interactions are expected to occur at each bunch crossing. At the same time, the emittance, i.e. the spread of the beam in space and momentum, will be maintained to the current low levels. To achieve this, a new generation of insertion magnets will be installed in the experiments. The insertion magnets are quadrupoles placed on either side of the interaction points, aiming at focusing the beams before and after the collisions take place. The new insertion magnets will be based on niobium-tin (Nb_3Sn) technology in a superconducting state. Their innovative design will allow to reach a magnetic field of up to 12 T, effectively reducing the transverse size of the bunch, which in turn increases the instantaneous luminosity. With the collision frequency

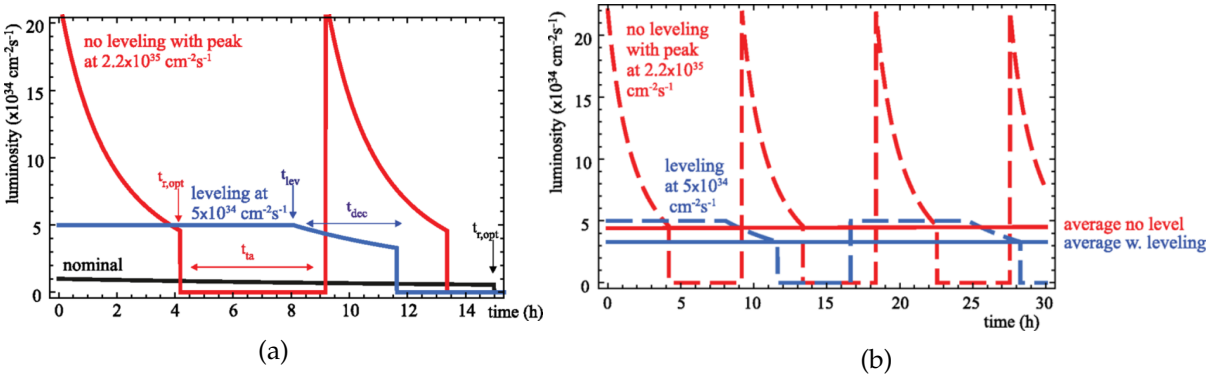

FIGURE 3.13: (a) Luminosity profile for a single long fill: starting at the LHC nominal peak luminosity (black line), with upgrade no levelling (red line), with levelling (blue line). (b) Luminosity profile with optimized run time, without and with levelling (blue and red dashed lines), and average luminosity in both cases (solid lines) [73].

being kept at the current levels, 40 MHz, the integrated luminosity goal of 4000 fb^{-1} will be reached after approximately 10 years of operation.

However, a disadvantage of reducing the transverse bunch size with quadrupole magnets is the implied increase of the crossing angle of the two bunches at the collision point. This causes a reduction of the luminosity due to the lower geometric overlap of the encountering bunches. An elegant solution to this problem is to introduce special superconducting RF cavities, capable of rotating the beams by generating transverse electric fields. These components are called Crab Cavities (CC) and are planned to be installed in both sides of ATLAS and CMS. With an appropriate rotation, the head-on collision of the two bunches can be achieved. The principle idea of operation with and without crab cavities is shown in Figure 3.14. Under the CC scenario, simulation studies show that in ATLAS, the vertex spread in z and time will be 4.5 cm and 150 ps, respectively.

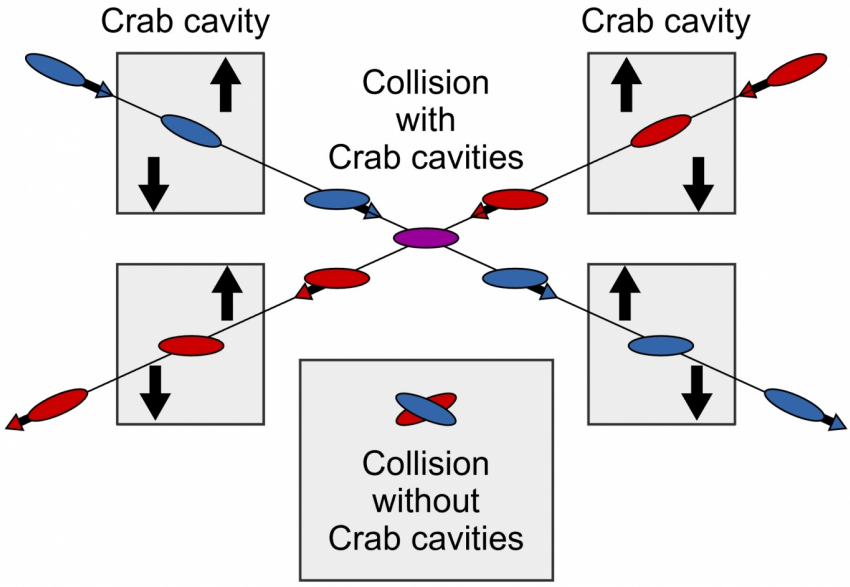

FIGURE 3.14: Schematic view of the effect of the crab cavities on the proton colliding bunches.

3.4.2 Physics at the HL-LHC

After Run 3, the statistical gain of running the accelerator with the same luminosity would be marginal. It is estimated that, with the present accelerator conditions, 10 years of operation would be needed to reduce the statistical uncertainties by half. It becomes clear that, in order to exploit the full LHC potential in a reasonable amount of time, an upgrade in the luminosity is needed [75].

One of the cornerstones of the physics programme at HL-LHC will be the measurements of the Higgs boson properties with a higher-than-ever precision. Dedicated studies of its production and decay modes are foreseen to estimate the Higgs boson couplings with extremely high accuracy [76], with any deviation from the SM prediction being an indicator for new physics. Along with improving the Higgs-sector precision measurement, rare processes involving the Higgs boson will become accessible thanks to the high luminosity. Such processes involve rare decays, like $H \rightarrow Z\gamma$ and decays to second generation fermions, or off-shell and high momentum Higgs production, which are particularly sensitive to new physics at the TEV scale. One rare channel of particular interest is the di-Higgs production, which gives access to the Higgs boson trilinear self-coupling. The latter being directly linked to the Higgs potential, this measurement provides a unique test of the Higgs sector in the SM. The extraordinary amount of data collected by the HL-LHC will allow physicists to start probing $H^* \rightarrow HH$ production modes, with an expected $\sim 3\sigma$ reach per experiment (ATLAS/CMS) [77].

Another pillar of the physics program at the HL-LHC will be precision measurements of various parameters in the SM. Such measurements include the improvement of our knowledge of the W boson and top quark masses, m_W and m_{top}, as well the precise estimation of EW multi-boson processes and couplings. Of particular interest will be the study of the weak mixing angle, currently constrained by a combination of data from LEP and SLD experiments that show a deviation from one another [78]. With its increased statistics, the HL-LHC will be able to improve systematics that significantly deteriorate the accuracy of the measurements , shining light into the source of the 3σ discrepancy currently observed by the two leading results [79]. Additionally, processes predicted by the SM but yet unobserved due to their rarity, might be accessible at the HL-LHC. One example is the simultaneous production of four top quarks, whose cross-section is particularly sensitive to enhancements from new physics phenomena, such as supersymmetry. While strong evidence of this process have already been observed by ATLAS in Run 2 [80], in the HL-LHC, the search of this production mode is expected to yield a significance well above 5σ, leading to a precise measurement with an uncertainty of 11% [81]. Another analysis of great interest for the HL-LHC physics program is the study of of $W^{pm}W^{pm}$ production via vector boson scattering (VBS) and in particular, the measurement of the longitudinally polarized component, which is particularly sensitive to new interactions in the electroweak breaking sector. The increase in integrated luminosity is expected to greatly benefit this analysis, reducing the total experimental uncertainty by more than a factor of 2 from the end of Run-3, and yielding a $\sim 3\sigma$ significance for observing the scattering of a pair of longitudinally polarized W bosons by ATLAS and CMS [82].

Finally, the HL-LHC will offer the possibility to continue the direct searches for new physics at high mass, with an unprecedent precision. New particles at a high mass scale are predicted by many BSM scenarios, aiming to resolve some of the long-standing problems of the SM, such as the Higgs boson naturalness, the origin of dark matter, the strong CP problem, the origin of the neutrino masses and baryogenesis. With the increase in collision energy being small to none, the primary advantage of the HL-LHC will be at the precision frontier, with rare processes expecting to gain significant ground in their discovery potential. Among the key models and theories in the BSM program of the general purpose experiments will be

the search of supersymmetry, dark matter, heavy resonances and long-lived particles.

3.5 ATLAS upgrades for the HL-LHC

Apart from the improvement of the accelerator, the upgrade of the detecting experiments is necessary. With the current number of average interactions per bunch crossing increasing from 30 to 200, the detectors demand advanced technologies to withstand the strain of the extra radiation and maintain their excellent performance, so as to achieve the desired sensitivity to new physics.

3.5.1 ITk

One of the major upgrades of ATLAS is the replacement of the entire ID by an all-silicon detector, the Inner Tracker (ITk). This upgrade is foreseen to augment the radiation hardness of the tracker but also to enhance its resolution under the severe pile-up conditions. A drawing of the foreseen detector is seen in Figure 3.15a; the detector will be composed of layers of silicon pixels in the inner radius and strips in the outer radius, shown in the red and blue hues of Figure 3.15b, respectively. This replacement is scheduled to take place during the LS3, before the start of HL-LHC.

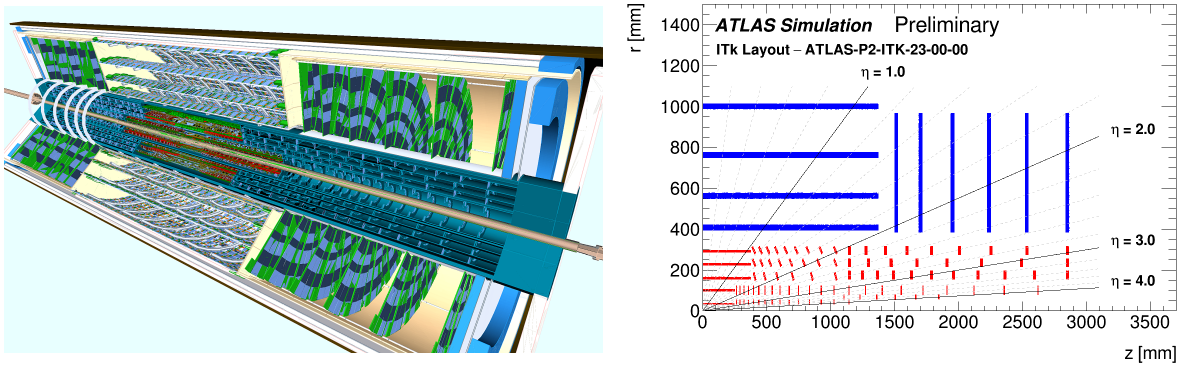

(a) (b)

FIGURE 3.15: (a) A visualisation of the ITk as implemented in the simulation framework. (b) Schematic depiction of the ITk Layout. Only one quadrant and only active detector elements are shown. The active elements of the strip detector are shown in blue, and those of the pixel detector are shown in red.

This upgrade will see an extension of the tracker coverage from $|\eta| < 2.5$ to $|\eta| < 4$. Therefore, the track reconstruction will be possible in the forward region, complementing a large fraction of the forward calorimetry and enabling a better reconstruction of forward objects, using algorithms like Particle Flow.

The innermost part of ITk [83] will be instrumented with high granularity silicon pixels up to $|\eta| = 4$. Two proposed pixel sizes are under consideration: $50\,\mu\text{m} \times 50\,\mu\text{m}$ or $25\,\mu\text{m} \times 100\,\mu\text{m}$. The pixel detector will be composed of 5 layers, organized in the so called "Inclined Layout". In this layout, pixels in the forward part of the barrel layers are tilted, in order to minimize the material traversed by particles at large η and to reduce the silicon surface required to cover the full η range.

Following the pixel layers will be the Strip detector [84], consisting of four layers in the barrel and 6 disks on each end-cap. This system will cover the $|\eta| < 2.7$ range and be instrumented with silicon-strip modules. In the innermost layers, short-strips with a length of 24.1

mm will be used, while in the outermost layers where the occupancy is lower, the strip length will be increased to 48.20 mm. The strips are placed radially in both sides of staves (petals) in the barrel (end-cap), thus providing a high resolution in the radial direction. A small rotation is introduced between strips on each side of the staves or petals, in order to increase the precision in the z-coordinate.

3.5.2 HGTD

While the finer granularity of ITk is a step towards the mitigation of pile-up, in the particularly challenging forward region the ATLAS experiment is planning to install a High Granularity Timing Detector (HGTD) [85], to complement the tracking with precise timing information. The HGTD will be installed between the ITk and the LAr forward calorimeter during LS3, covering an η range from 2.4 to 4. The timing information will be used to aid in the mitigation of pile-up by rejecting out-of-time tracks. An excellent timing resolution better than 50 ps for minimum ionizing particles is aimed for this novel detector. The utilized active material will be Si pads of 1.3 mm $\times$ 1.3 mm granularity, using the Low Gain Avalanche Detector (LGAD) technology for optimized timing performance. More details on the proposed detector design and its expected performance can be found in Chapter 5.

3.5.3 Calorimeter upgrade

Thanks to the intrinsic radiation hardness of Liquid Argon, the LAr calorimeters of ATLAS will continue functioning in the high-radiation environment of LHC. However, the current read-out does not provide sufficient buffering and bandwidth capabilities to accommodate the hardware trigger requirements of the HL-LHC. In addition, the expected total radiation doses are beyond the qualification range of the current front-end electronics. Therefore, a replacement of the LAr calorimeter electronics is scheduled, and will be carried out in two steps. In LS2, upgraded trigger electronics will be installed, in order to fully exploit the fine calorimeter 3-D segmentation [86]. This will allow for more complex trigger algorithms to be deployed, enhancing the physics reach of ATLAS. Additionally, it will be possible to employ more sophisticated filtering algorithms to minimize the pile-up contribution to the energy resolution noise term.

While the on-detector electronics are foreseen to withstand the radiation levels of Run 3, a complete replacement of the main read-out electronics and low-voltage powering system of the LAr calorimeter will need to take place before the HL-LHC [87]. The technological improvements since the construction of the original calorimeter will permit a more flexible read-out architecture, compatible with the upgraded trigger system.

3.5.4 Muon spectrometer upgrade

In order to maintain the excellent muon reconstruction performance, the ATLAS Muon Spectrometer will be upgraded in two periods. In order to cope with the increased trigger rates at higher luminosity without harming the physics capacity of the detector, part of the inner end-cap stations will be replaced by New Small Wheels (NSWs) [88], combining the small-strip Thin Gap Chamber and Micromegas technologies. The former are an improved version of the current TGCs, providing a better resolution, while the latter are gaseous detectors employing a high-field amplification gap, which is created by a micro-pattern mesh close to the read-out. The upgrade detectors will allow for an improvement of the online reconstruction performance and will reduce the trigger rate by rejecting fake muons. Given the estimates of the trigger rates' evolution with luminosity, this upgrade is already needed in Run 3 and is therefore being installed as this thesis is being written.

The Phase-II upgrade of the MS [89] will mainly focus on further improving the trigger system. To this end, the trigger electronics of the RPC and TGC will be completely replaced with newer technologies, allowing the full information of these chambers to be continuously read-out. In this way, more refined and flexible algorithms will be used. The MDT data will also be integrated in the first trigger, which calls out for a replacement of the MDT electronics as well. Part of the MDT and RPC chambers will be fully replaced in order to install new ones with increased rate capacities.

3.5.5 Trigger upgrade

Finally, the trigger and data acquisition system will be upgraded in LS3 to cope with the factor of 5 increase in instantaneous luminosity [90]. Currently, the main change under consideration is the replacement of the current L1 hardware trigger with a new single-level fully hardware trigger capable of providing a maximum rate of 1 MHz and a $10\,\mu s$ latency. This trigger, referred to as Level-0 (or L0), relies on information provided from the upgraded calorimeters and muon trigger stations of ATLAS. An alternative proposal of a two-level (Level-0 and Level-1) hardware-based trigger system, where the rate will be gradually decreased from 4 MHz with a $10\,\mu s$ latency to a 600 kHz with a $35\,\mu s$ latency, is also under consideration. In this scheme, information from the ITk could be used to perform online track reconstruction at the L1 level.[2] All systems are designed in a way that allows for an evolution from a single-level to a dual-level trigger architecture in case pile-up conditions are more challenging than expected or the hadronic triggers overflow the trigger rates.

[2]Currently, the option to deploy ITk information in the trigger is considered in the form of regional read-out.

4. Search for squarks and gluinos in final states with jets and missing transverse momentum

This chapter presents the search for squarks and gluinos in final states with jets, missing transverse momentum and no leptons, using the full Run2 dataset of ATLAS. The organization of the chapter is as follows: firstly, the motivation and strategy of the analysis are discussed in 4.1 and 4.2, followed by a detailed description of the dataset and simulation samples used, in 4.3. Next, the trigger and object reconstruction are presented in 4.4, after which the strategy for selecting events is discussed in 4.5. The main background components of the analysis and the methods of accurately estimating them are described in 4.6. My involvement in this analysis is heavily focused on the multi-bin fit, described in 4.5.3. In particular, I have worked on the design of the validation strategy of the background estimation procedure, with the design of validation regions in a fully hadronic environment, described in 4.6.2, as well as the optimization of the multi-bin configuration and background normalisation, detailed in 4.8. Additionally, I have carried out the statistical inference of the search, starting from the evaluation of various systematic uncertainties to the implementation of the fit strategy and work-flow, presented in 4.7. Finally, I have been responsible for the extraction of the results and their interpretation in simplified supersymmetric models, shown in 4.9 and 4.10, respectively.

4.1 Target models

The main target of this search are gluinos and first- and second-generation squarks. The large expected production cross-section of these particles in hadronic collisions for a fixed mass makes them an attractive target in the ATLAS search program. In this work, R-parity is considered to be an exact symmetry, and, therefore, the produced squarks and gluinos decay (either directly or with intermediate steps) to a neutralino ($\tilde{\chi}_1^0$) LSP, which is neutral, stable and escapes detection. In order to further increase the overall event rate, fully hadronic final states are chosen, giving rise to jets and missing transverse momentum from the escape of the neutralino. Electrons and muons are vetoed in the final state to avoid overlapping with other ATLAS searches and to reduce the background in final states where no leptons are expected (such as the ones shown in Figures 4.1a, 4.1c and 4.1e).

The targeted topologies are shown in Figure 4.1. Gluinos and squarks (including anti-squarks) are produced in pairs ($\tilde{g}\tilde{g}$, $\tilde{q}\tilde{q}$ and $\tilde{q}\tilde{g}$). Subsequently, they decay to SM particles and the LSP, either directly (Figures 4.1a, 4.1c and 4.1e), or through the intermediate production of an on-shell chargino $\tilde{\chi}_1^{\pm}$ (Figures 4.1b and 4.1d). The former decays are referred to as direct, while the latter as one-step. All supersymmetric interactions are described in terms of simplified models, where, for each target mode, only the involved SUSY particles are taken into account. The remaining SUSY spectrum is effectively decoupled by assigning masses beyond the reach of the LHC. In addition, the decay branching ratio to the final states shown in Figure 4.1 is considered to be 100% for each topology.

The interpretation of the results is performed in a two dimensional space of the s-particle masses. For the pair production of squarks and gluinos, the free mass parameters are chosen in a straight-forward manner to be the masses of the squark or gluino and of the LSP. For one-step decays, two discrete scenarios are considered; the free parameters are the m($\tilde{q}$) (or

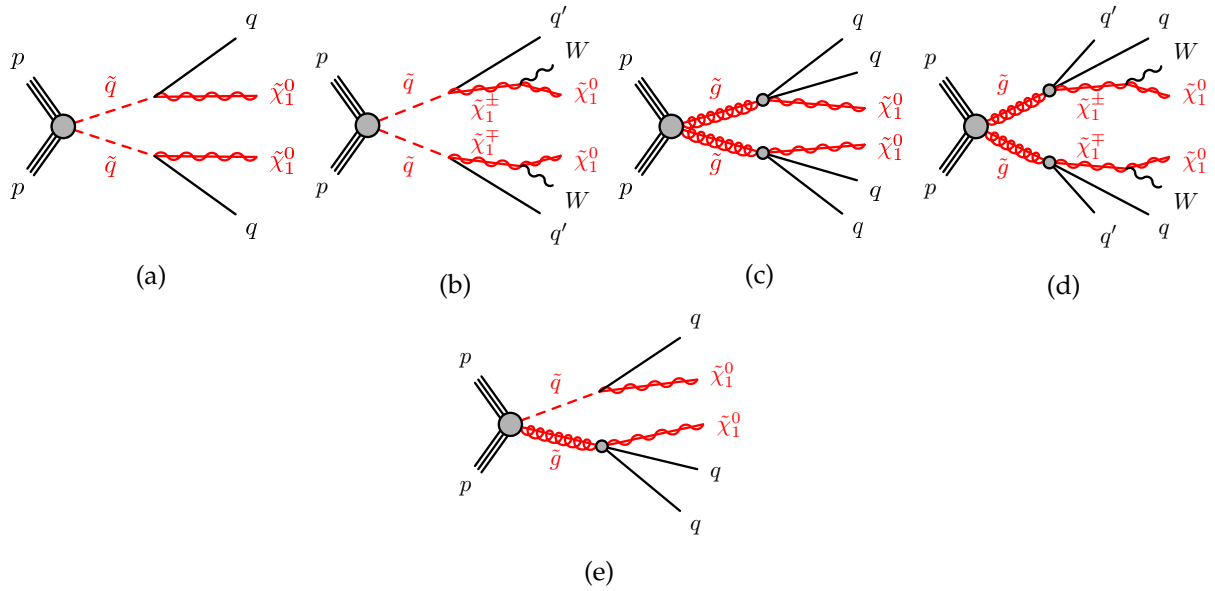

FIGURE 4.1: The decay topologies of (a, b) squark-pair production, (c, d) gluino-pair production and (e) squark-gluino production in simplified models with (a, c, e) direct decays of squarks and gluinos or (b, d) one-step decays of squarks and gluinos.

m($\tilde{g}$)) and, either the mass of the chargino m($\tilde{\chi}_1^{\pm}$) (with a fixed m($\tilde{\chi}_1^0$) = 60 GeV [1]), or the mass of the neutralino (with m($\tilde{\chi}_1^{\pm}$) = (m($\tilde{q}/\tilde{g}$) + m($\tilde{\chi}_1^0$))/2). For models with inclusive production of squarks and gluinos, the masses of both are varied independently and the mass of the neutralino is fixed to either 0, 995 or 1495 GeV. In the simplified model with direct squark decays, an eight-fold degeneracy of the first- and second-generation squarks is assumed, while an alternative case with a single non-degenerate squark is also considered. For one step decays involving squarks, chirality is maximally violated due to the involved W boson and therefore, the masses of the squarks are considered to be four-fold degenerate. In all models, only 4 flavours (u, d, c, s) are allowed in the quark decay products. The remaining two flavours are targeted by separate searches, since top and bottom quarks have special reconstructed signatures in the detector.

4.2 Analysis strategy

In order to select the aforementioned topologies, events with no leptons, large missing transverse momentum and with two to six jets are chosen. The search of this topology has been performed in the past and results have been presented with a partial 2015-2016 dataset and with the full Run 1 data [92, 37]. A complementary analysis that targets similar supersymmetric particles but in final states with larger jet multiplicities has been published in [93].

An effective discriminating variable to identify the events of interest is the effective mass, m_{eff}, defined as the scalar sum of the transverse momenta of jets in the event together with the $E_{\text{T}}^{\text{miss}}$:

$$m_{\text{eff}} = \sum_{j=1}^{n} |p_T^j| + |E_{\text{T}}^{\text{miss}}| \tag{4.1}$$

Only jets with $p_T > 50$ GeV are considered in the calculation, as well as to select events. The m_{eff} variable has been found to correlate well with the cross-section-weighted SUSY mass

[1] This is a value often chosen for the LSP, supported by dark-matter relic density measurements and might be favoured in Higgs-mediated dark-matter annihilation scenarios, where $m_{\tilde{\chi}_1^0} \sim m_h/2$ [91].

scale in cases where the LSP is massless [94]. It is therefore a powerful discriminant between the signal and most SM backgrounds, especially in the high SUSY mass phase-space that this search targets.

Based on cuts on m_{eff} and other key variables detailed in 4.5.1, search regions, called Signal Regions (SRs) are defined, where the sensitivity to new signals is expected to be high. In order to improve the power of this analysis over previous results, two novel and complementary approaches are deployed. Firstly, a 3-dimensional multi-bin (MB) fit, which exploits the shape of the signal over the background components to enhance their separation, is implemented, as discussed in 4.5.3. Secondly, a multivariate Boosted Decision Tree (BDT) technique is used to improve the sensitivity in complex final states with four or more jets, detailed in 4.5.4. This technique takes advantage of the correlations between various input variables to improve the separation power between signal and background events with similar topology. Both of these methods are optimized for possible signal signatures and are therefore model-dependent. While this strategy choice is justifiable by the lack of strong supersymmetric evidence in the partial Run 2 results, previous rounds of the analysis have demonstrated that similar search regions are also highly efficient for discoveries. Additionally, many SRs targeting different models and kinematic properties are included in the analysis, in an effort to reduce the overall model-dependence. The BDT search being constructed as a collection of cut&count SRs, it can be used to provide a model - independent estimate of the statistical significance. Due to the particularity of the multi-bin fit, it is not possible to do the same, and therefore, a separate single-bin (or cut&count) search is also designed, in order to provide a model - independent estimate of the statistical significance. The signal regions of this search, described in 4.5.5, rely on the inclusive versions of the multi-bin fit and, since they overlap, cannot be combined statistically. The single-bin SRs also aim to facilitate the re-interpretation of the results outside of the collaboration as well as to compare the results to the previous rounds of the analysis, where a similar approach was employed.

The analysis is divided in channels that aim to exploit the different event topologies and kinematic properties of the various production and decay modes. In general, there are 4 topology categories for which the analysis is optimized: direct squark pair production, gluino pair production with short or long decay cascades and a separate scenario where the mass spectrum of the SUSY particles is highly compressed, typically below 200 GeV. Long decay chains, especially when involving gluinos, typically result in a higher number of SM particles, and therefore, the jet multiplicity is a key variable for the separation of the first three channels. On the other hand, a compressed spectrum of the SUSY particles results in softer decay products and hence, lower missing transverse momentum originating from the escaping LSP. Events originating from such a mass-splitting regime could fail the $E_{\text{T}}^{\text{miss}}$ triggers of the search. For this reason, the presence of an initial state radiation (ISR) jet, against which the hard scatter system is boosted, is requested, in order to increase the $E_{\text{T}}^{\text{miss}}$ of the event and therefore enhance the sensitivity to this channel. While a separate category for squark-pair production with one-step decays has not been defined, the final state of this model greatly resembles the gluino models with direct decays, and is therefore targeted in the same way. The multi-bin fit and single-bin strategies implement signal regions designed to address all four of the mentioned channels. On the contrary, the BDT method is not applied on the direct squark scenarios, since it has been found to provide little gain on topologies with less than 4 jets.

The sensitivity of the search is limited by SM processes that give rise to similar final states as those of the target models. The main SM backgrounds of this analysis are, in decreasing order of their importance: Z+jets, W+jets, $t\bar{t}$ and single-t processes, di-boson and multi-jet QCD events. Simulation is used to determine the background contribution to the signal regions, except for the multi-jet background, which is derived from a data-driven method. A dedicated

procedure based on Control Regions (CRs) is used to accurately estimate each component. More details on the background estimation procedure are given in 4.6.

4.3 Data and simulation

4.3.1 Dataset

The data used in this analysis were produced in proton-proton collisions with a center-of-mass energy of 13 TeV and collected by the ATLAS detector in the full Run 2 period between 2015 and 2018. Three different periods can be distinguished, with different pileup conditions: in 2015-2016, the average number of pileup interactions was $<\mu>$ = 20, increasing to $<\mu>$ = 38 in 2017 and to $<\mu>$ = 37 in 2018. After applying beam, detector and data-quality criteria [95], the integrated luminosity over the full period is 139 fb^{-1}, with an uncertainty of 1.7% [96]. This is a significant increase, of almost a factor of 4, over the available statistics for the previous round of the analysis, which was 36.1 fb^{-1}.

4.3.2 Simulated samples

The simulation of events is essential to accurately estimate the underlying background, optimize the signal regions and assess the search sensitivity to potential signals. A common set of simulated Monte Carlo (MC) samples for the background and the SUSY signals is used in this analysis. The event generation proceeds by firstly determining all possible Feynman diagrams of the target process in a given order, from which the corresponding matrix elements are then calculated. Decay products are produced at the parton level and hadronized using dedicated algorithms. The underlying event from the remaining pp activity is simulated separately.

All SM backgrounds relevant to this analysis are simulated. Depending on the process, different matrix element generators, cross-section calculation orders, parton distribution functions (PDFs), parton shower and underlying event generators are used. A summary of all SM background processes together with their dedicated generation details is given in Table 4.1.

Physics process	Generator	Cross-section normalisation	PDF set	Parton shower	Tune
$W(\to \ell\nu)$ + jets	SHERPA 2.2.1 [97]	NNLO [98]	NNPDF3.0NNLO [99]	SHERPA [100]	SHERPA
$Z/\gamma^*(\to \ell\bar{\ell})$ + jets	SHERPA 2.2.1	NNLO	NNPDF3.0NNLO	SHERPA	SHERPA
γ + jets	SHERPA 2.2.2	NLO	NNPDF3.0NNLO	SHERPA	SHERPA
$t\bar{t}$	POWHEG-BOX v2 [101]	NNLO+NNLL [102, 103]	NNPDF2.3LO [104]	PYTHIA 8.230 [105]	A14 [106]
Single top (Wt-channel)	POWHEG-BOX v2	NNLO+NNLL [107, 108].	NNPDF2.3LO	PYTHIA 8.230	A14
Single top (s-channel)	POWHEG-BOX v2	NLO [109, 110]	NNPDF2.3LO	PYTHIA 8.230	A14
Single top (t-channel)	POWHEG-BOX v1	NLO	NNPDF2.3LO	PYTHIA 8.230	A14
$t\bar{t}+W/Z/H$	MG5_aMC@NLO 2.2.3 [111]	NLO [112, 113]	NNPDF2.3LO	PYTHIA 8.210	A14
$t\bar{t}+WW$	MG5_aMC@NLO 2.2.2	NLO	NNPDF2.3LO	PYTHIA 8.210	A14
$WW, WZ, ZZ, W\gamma, Z\gamma$	SHERPA 2.2.1	NLO	NNPDF3.0NNLO	SHERPA	SHERPA

TABLE 4.1: The SM background MC simulation samples used in this analysis. The generators, the order in α_s of cross-section calculations used for yield normalisation, PDF sets, parton showers and tunes used for the underlying event are shown.

Signal samples are generated in simplified models according to the scenarios shown in Figure 4.1. They are produced with up to two extra partons in the matrix element using the MG5_aMC@NLO 2.6.1 event generator (for signal samples describing squark- and gluino-pair production followed by the direct decay of squarks and gluinos) or MG5_aMC@NLO 2.6.2 [111] (for signal samples describing squark-gluino production and squark- and gluino-pair production followed by the one-step decay of squarks and gluinos) interfaced to PYTHIA 8.212

and PYTHIA 8.230 [105]. The A14 [114] set of tuned parameters (tune) was used for initial/final-state radiation (ISR/FSR) and underlying-event parameters together with the NNPDF2.3LO [104] parton distribution function (PDF) set. Signal cross-sections are calculated to approximate next-to-next-to-leading order in the strong coupling constant, adding the resummation of soft gluon emission at next-to-next-to-leading-logarithmic accuracy (approximate NNLO+NNLL) [115, 116, 117, 118, 119, 120, 121, 32]. The simulation is repeated for varying s-particle mass points, according to the free mass parameters in each topology, which was described in 4.1. The number of mass points and simulated events/point is chosen so as to ensure sufficient statistics and coverage of the mass phase-space.

For the SM processes, the detector response to the crossing particles is modelled with the full ATLAS detector simulation [122] based on GEANT4 [123]. Signal samples are prepared using a fast simulation based on a parametrization of the ATLAS electromagnetic and hadronic calorimeters' performance [124] and on GEANT4 for the rest of the sub-detectors.

All simulated events are overlaid with multiple pp collisions. The MC samples are generated with a variable number of additional pp interactions (pileup), and are reweighted to match the distribution of the mean number of interactions observed in data in 2015-2018. This process is referred to as pileup reweighting. The event simulation follows the same scheme as the data and three campaigns, denoted as mc16a for 2015-2016, mc16d for 2017 and mc16e for 2018 have been produced, in order to account for the different pileup, trigger, and detector conditions.

4.4 Trigger and object reconstruction

Events are registered for analysis according to three different types of triggers. Firstly, SR events are required to pass pure-$E_{\mathrm{T}}^{\mathrm{miss}}$ triggers. The same triggers are used to choose events for the estimation of the W+jets, top and multi-jet SM backgrounds. For the estimation of the major $Z(\rightarrow \nu\nu)$+jets background, two regions are constructed, one targeting a γ + jets topology, and the other $Z \rightarrow \ell\ell$ decays. A single-photon trigger is used for the former, while events for the latter are required to satisfy a single-lepton trigger. More details on the background estimation method for this analysis can be found in 4.6. The lowest possible unprescaled triggers are used in each data period, in order to increase as much as possible the statistics. The trigger for the W+jets and top backgrounds has been changed to a pure-$E_{\mathrm{T}}^{\mathrm{miss}}$ type from the previous round of the analysis, where a single-lepton one was used. This decision was taken in order to further augment the statistics by lowering the lepton-p_{T} requirements.[2]

The physics objects used for these studies are based on the definitions from the SUSY working group common package SUSYTools corresponding to AnalysisBase 21.2.68 release. For a more detailed look on the object reconstruction strategy of ATLAS, the reader is directed to 3.3. The primary vertex of the event is reconstructed as the vertex with the largest quadratic sum of p_{T} of associated tracks and is required to have at least two such tracks with $p_{\mathrm{T}} > 500$ MeV.

Jets are reconstructed from calorimeter cell clusters using the anti-k_t clustering algorithm with a jet-radius parameter of 0.4. Pileup and jet energy scale corrections are applied following the procedures described in 3.3.4. All corrected jets are required to satisfy $p_{\mathrm{T}} > 20$ GeV and $|\eta| < 2.8$. In order to identify and reconstruct jets containing a b-hadron (b-jets), an algorithm based on boosted decision trees, named *MV2c10* [125, 126] is deployed at a 77% efficiency

[2] On a pure-$E_{\mathrm{T}}^{\mathrm{miss}}$ trigger, this requirement can be dropped to 7 (6) GeV for electrons (muons), in contrast to a single-lepton trigger where the lepton p_{T} has to be at least 25 GeV to reach the efficiency plateau.

point (the rejection factor for gluons and light-flavour jets is 130 for this working point). These jets are also required to pass the $p_{\mathrm{T}} > 50$ GeV and $|\eta| < 2.5$ requirements.

When referring to leptons in this analysis, only electrons and muons are considered, and there is no additional effort to reconstruct or tag tau leptons. Leptons are vetoed in the signal regions, but are used in dedicated leptonic control regions to accurately estimate various background components. According to these two treatments, leptons are classified in two categories. Firstly, leptons that are found and rejected in the SRs are defined as *baseline*. The selections applied to identify baseline leptons are designed to maximize the efficiency with which W+jets and top quark backgrounds are mitigated. The residual backgrounds are estimated in leptonic control regions and leptons entering these regions are identified so as to maximize their purity. This second class is called *high-purity* and is a subset of the baseline leptons.

Muons are reconstructed by combining tracks from the Muon Spectrometer (MS) and the Inner Detector (ID) and are considered as baseline when they satisfy $p_{\mathrm{T}} > 6$ GeV and $|\eta| < 2.7$. They are tagged as high-purity candidates if, in addition, they pass isolation requirements described in [127] and are compatible with originating from the primary vertex both in the longitudinal and transverse plane. Similarly, baseline electrons are reconstructed from matching an isolated calorimetric energy deposit to a track in the ID. They are required to have $p_{\mathrm{T}} > 7$ GeV, $|\eta| < 2.47$ and to satisfy *Loose* likelihood- based identification criteria described in [128, 62]. A subset of them which additionally satisfies *TightLHH* quality criteria and isolation requirements of [128, 62] and is found to be compatible with the primary vertex is classified as high-purity electrons.

As already mentioned, photons are also used in the analysis to build a control region for the estimation of the $Z(\rightarrow \nu\nu)$+jets background, as well as in the calculation of the missing transverse momentum. Photon candidates are requested to have $p_{\mathrm{T}} > 25$ GeV and $|\eta| < 2.37$ (excluding the transition region $1.37 < |\eta| < 1.52$ between the barrel and endcap EM calorimeters), photon shower shape and electron rejection criteria, and to be isolated [128, 129, 130]. The reduced η range for photons is chosen to avoid a region of coarse granularity at high η where photon and π^0 separation worsens.

After the selections described above, ambiguities between electrons, muons, photons and jets are resolved to avoid double counting and/or remove non-isolated leptons/photons. The overlap removal process is described in detail in [131].

The missing transverse momentum is a key object of the analysis, since it indicates the escape of the neutralino LSPs. The missing transverse momentum vector $\mathbf{p}_{\mathrm{T}}^{\mathbf{miss}}$ is given by the negative vectorial sum of the momenta of all calibrated electron, muon, photon and jet candidates and of all the tracks that originate from the primary vertex and are not associated with the preceding objects [72, 132]. The absolute value of this quantity gives the missing transverse momentum $E_{\mathrm{T}}^{\mathrm{miss}}$.

4.5 Event selection

After identifying and reconstructing the objects of interest as mentioned above, events are categorized to signal regions based on criteria on powerful discriminating variables. Starting from the definition of this analysis' key variables, the selection procedure is described in detail.

4.5.1 Discriminating variables

Fundamental object and event properties, such as the p_{T} of the jets, the jet multiplicity and the $E_{\mathrm{T}}^{\mathrm{miss}}$ are used to select events of interest. They are also combined to build more complicated variables, that aim to take advantage of the full kinematic properties in each event. One such variable is the effective mass, which, as already stated in 4.2, relates to the mass of the primary SUSY particles produced. Additionally to the m_{eff}, the following variables are considered:

- H_T, defined as the scalar sum of the jets' p_{T}, represents the amount of jet activity in the event. All jets with $p_{\mathrm{T}} > 50$ GeV and $|\eta| < 2.8$ are considered in the calculation.
- missing transverse momentum significance $E_{\mathrm{T}}^{\mathrm{miss}} / \sqrt{H_{\mathrm{T}}}$, a variable which was originally introduced to reject QCD background with a large fake $E_{\mathrm{T}}^{\mathrm{miss}}$ component. It has been found to also be effective in the rejection of other backgrounds and in enhancing the search sensitivity, especially to models with quark-pair production.
- $E_{\mathrm{T}}^{\mathrm{miss}}/m_{\mathrm{eff}}(Nj)$, an alternative to the $E_{\mathrm{T}}^{\mathrm{miss}} / \sqrt{H_{\mathrm{T}}}$, particularly useful in topologies with 4 or more jets. It is used only in the BDT analysis.
- $\Delta\phi(j_i, \boldsymbol{p}_{\mathrm{T}}^{\mathrm{miss}})_{\text{ min}}$, an estimate of the alignment of the $E_{\mathrm{T}}^{\mathrm{miss}}$ and the jet p_{T}. This variable is a powerful discriminant against fake missing transverse momentum arising from mismeasurements or from the presence of neutrinos in the jets, which tends to be aligned with the jet direction.
- the aplanarity variable [133], defined as A = $3/2\lambda_3$, where λ_3 is the smallest eigenvalue of the normalised momentum tensor of the jets. This variable measures the amount of transverse momentum in the plane formed by the two leading jets and can be useful in separating planar from spherical events. Values close to 0 indicate highly planar events, less probable to originate from decays of gluino pairs.

4.5.2 Preselection

A common set of preselection criteria is applied in all the signal regions of the analysis. Table 4.2 lists the preselection cuts. Following the definition of the analysis as fully hadronic, all baseline electrons (muons) with $p_{\mathrm{T}} > 7$ (6) GeV are vetoed. In order to ensure a plateaued $E_{\mathrm{T}}^{\mathrm{miss}}$-trigger efficiency, only events with $E_{\mathrm{T}}^{\mathrm{miss}} > 300$ GeV are considered. Events are required to have at least 2 jets, with the leading (i.e. highest-momentum) one having a p_{T} above 200 GeV, while the subleading one is required to have $p_{\mathrm{T}} > 50$ GeV. The minimum azimuthal separation between the vector $\mathbf{p}_{\mathrm{T}}^{\mathbf{miss}}$ and the momenta of up to the first three leading jets, $\Delta\phi(j_{1,2,(3)}, \boldsymbol{p}_{\mathrm{T}}^{\mathrm{miss}})_{\text{ min}}$, is requested to be larger than 0.4 radians. This requirement is put in place in order to mitigate missing energy originating from jet energy mis-measurement. Finally, the effective mass of the event, as defined in equation 4.1, is required to be above 800 GeV. Distributions of the discriminating variables at the preselection level are shown in Figures 4.2 and 4.3.

Following the preselection procedure, the remaining events are further categorized into the three complementary approaches, where additional criteria are requested. The set of specific selection requirements constituting the multi-bin, BDT and single-bin signal regions are described below.

Lepton veto	No baseline electron (muon) with p_{T} >7 (6) GeV
$E_{\mathrm{T}}^{\mathrm{miss}}$ [GeV]	> 300
$p_{\mathrm{T}}(j_1)$ [GeV]	> 200
$p_{\mathrm{T}}(j_2)$ [GeV]	> 50
$\Delta\phi(j_{1,2,(3)}, \boldsymbol{p}_{\mathrm{T}}^{\mathrm{miss}})_{\mathrm{min}}$ [rad.]	> 0.4
m_{eff} [GeV]	> 800

TABLE 4.2: Summary of common preselection criteria used for all the searches of this analysis.

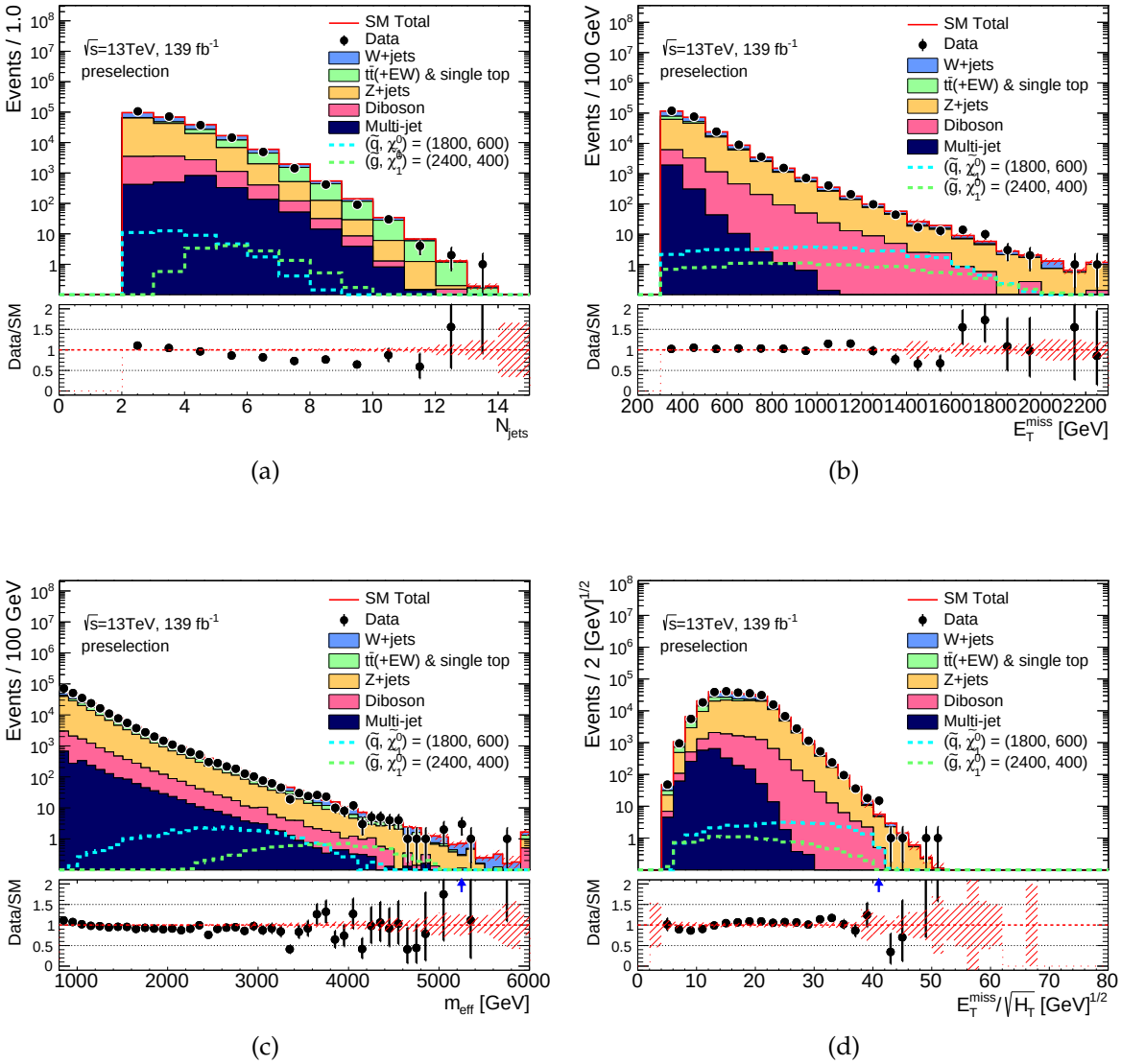

FIGURE 4.2: Observed (a) N_{j}, (b) $E_{\mathrm{T}}^{\mathrm{miss}}$, (c) m_{eff} and (d) $E_{\mathrm{T}}^{\mathrm{miss}}/\sqrt{H_{\mathrm{T}}}$ distributions in events satisfying the common signal region preselection of Table 4.2. The histogram denotes the MC background expectations, normalised to a luminosity of 139 fb^{-1}. Error bars show statistical uncertainty only. Expected distributions for benchmark signal model points, normalised using the approximate NNLO+NNLL cross-section times integrated luminosity, are also shown for comparison (masses in GeV). The last bin includes overflow events.

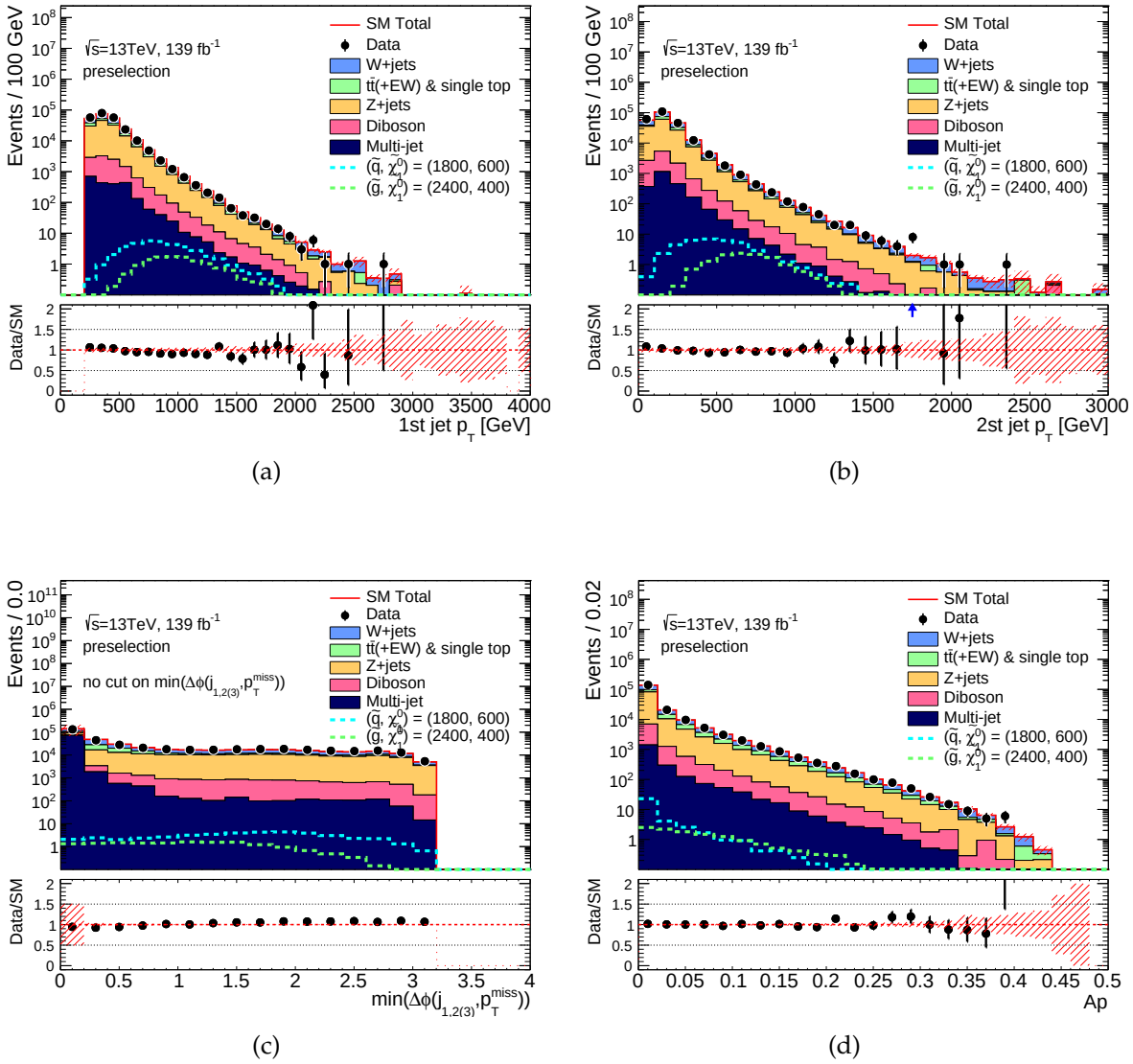

(a) (b)

(c) (d)

FIGURE 4.3: Observed (a) leading jet p_{T}, (b) sub-leading jet p_{T}, (c) $\Delta\phi(j_{1,2,(3)}, \boldsymbol{p}_{\mathrm{T}}^{\mathrm{miss}})_{\mathrm{min}}$ and (d) aplanarity distributions in events satisfying the common signal region preselection of Table 4.2. For Figure (c), the $\Delta\phi(j_{1,2,(3)}, \boldsymbol{p}_{\mathrm{T}}^{\mathrm{miss}})_{\mathrm{min}}$ preselection cut has been omitted. The histogram denotes the MC background expectations, normalised to a luminosity of 139 fb^{-1}. Error bars show statistical uncertainty only. Expected distributions for benchmark signal model points, normalised using the approximate NNLO+NNLL cross-section times integrated luminosity, are also shown for comparison (masses in GeV). The last bin includes overflow events.

4.5.3 Multi-bin search

In the multi-bin search, four sets of signal regions are defined in order to maximize the sensitivity to different SUSY scenarios: the direct decays of pairs of squarks and gluinos with large mass splittings to the neutralino are targeted with the MB-SSd and MB-GGd SRs respectively, while a dedicated search, MB-C, is in place for the compressed spectrum scenarios. One-step decays of gluinos result in a higher jet multiplicity and are therefore selected with a separate multi-bin set, the MB-GGo. Events are assigned to orthogonal bins according to their jet multiplicity, effective mass and missing transverse momentum significance $E_{\mathrm{T}}^{\mathrm{miss}}/\sqrt{H_{\mathrm{T}}}$. This variable was chosen as one of the three dimensions of the multi-bin fit, since it further suppresses high-$E_{\mathrm{T}}^{\mathrm{miss}}$ background arising from jet energy mis-measurements, and increases the search sensitivity.

Table 4.3 presents the common selection criteria that are applied inclusively in each of the multi-bin searches. The cuts are chosen so as to better discriminate against the background in each target topology. At least two jets with $|\eta| \leq 2.0$ are requested for the MB-SSd regions, with the p_{T} of the leading (subleading) jet(s) satisfying a 200 (100) GeV requirement. For the compressed region MB-C, a requirement of 600 GeV is requested on the leading jet p_{T}, in order to select events with a highly energetic ISR jet, that are expected to be boosted, and therefore yield a higher $E_{\mathrm{T}}^{\mathrm{miss}}$, above the trigger threshold. The $|\eta|$ cut is also relaxed to 2.8 in order to also include more forward events. In the MB-GGd regions, events with at least 4 jets with $|\eta| < 2.0$ are selected. In this case, the leading jet p_{T} must satisfy a 200 GeV requirement, while the remaining jets must have $p_{\mathrm{T}} \geq 100$ GeV. Finally, for the MB-GGo sets targeting one-step decays of gluinos, at least 6 jets with $p_{\mathrm{T}} \geq 75$ GeV are requested, with the leading jet having in addition $p_{\mathrm{T}} \geq 200$ GeV. Criteria on the azimuthal separation between jets and the vector of the missing transverse momentum are also applied to better discriminate against the background arising from jet-mis-measurements. The smallest azimuthal separation between the $\boldsymbol{p}_{\mathrm{T}}^{\mathrm{miss}}$ and the momenta of up to three leading jets, $\Delta\phi(j_{1,2,(3)}, \boldsymbol{p}_{\mathrm{T}}^{\mathrm{miss}})_{\mathrm{min}}$, and of the remaining jets in the event, $\Delta\phi(j_{i>3}, \boldsymbol{p}_{\mathrm{T}}^{\mathrm{miss}})_{\mathrm{min}}$, are required to be greater than 0.4 and 0.2, respectively, in all regions except in MB-SSd, where the tighter requirements of 0.8 and 0.4 are placed. In final states with high jet multiplicity, jets arising from signal processes are expected to be distributed isotropically. Therefore, a requirement on the aplanarity variable, A$\geq$ 0.04($\geq$ 0.08) is applied on the MB-GGd (MB-GGo) regions. All events are required to satisfy the $E_{\mathrm{T}}^{\mathrm{miss}}/\sqrt{H_{\mathrm{T}}} \geq 10$ GeV$^{1/2}$ and $m_{\mathrm{eff}} \geq$ 1000 GeV requirements, except from MB-C, where a tighter cut of $m_{\mathrm{eff}} \geq$ 1600 GeV is applied.

	MB-SSd	MB-GGd	MB-C	MB-GGo
N_{j}	≥ 2	≥ 4	≥ 2	6
$p_{\mathrm{T}}(j_1)$ [GeV]	≥ 200	≥ 200	≥ 600	≥ 200
$p_{\mathrm{T}}(j_{i=2,\ldots,N_{\mathrm{j}_{\mathrm{min}}}})$ [GeV]	≥ 100	≥ 100	≥ 50	≥ 75
$\lvert\eta(j_{i=1,\ldots,N_{\mathrm{j}_{\mathrm{min}}}})\rvert$	≤ 2.0	≤ 2.0	≤ 2.8	≤ 2.0
$\Delta\phi(j_{1,2,(3)}, \boldsymbol{p}_{\mathrm{T}}^{\mathrm{miss}})_{\mathrm{min}}$	≥ 0.8	≥ 0.4	≥ 0.4	≥ 0.4
$\Delta\phi(j_{i>3}, \boldsymbol{p}_{\mathrm{T}}^{\mathrm{miss}})_{\mathrm{min}}$	≥ 0.4	≥ 0.2	≥ 0.2	≥ 0.2
Aplanarity	-	≥ 0.04	-	≥ 0.08
$E_{\mathrm{T}}^{\mathrm{miss}}/\sqrt{H_{\mathrm{T}}}$ [GeV$^{1/2}$]	≥ 10	≥ 10	≥ 10	≥ 10
m_{eff}[GeV]	≥ 1000	≥ 1000	≥ 1600	≥ 1000

TABLE 4.3: Summary of selection criteria used inclusively for the multi-bin searches.

Following the aforementioned selection, events are categorized into orthogonal bins in jet multiplicity, m_{eff} and $E_{\mathrm{T}}^{\mathrm{miss}}/\sqrt{H_{\mathrm{T}}}$. These bins will be combined in the fit, as will be explained in 4.7, in order to take advantage of the signal over background shape and maximize the sensitivity to a variety of s-particle masses.

The binning scheme of the MB-SSd search is as follows:

- 2 bins in jet multiplicity, N_j=[2, 3] and N_j=[4, ∞)
- up to 6 bins in effective mass: [1.0, 1.6), [1.6, 2.2), [2.2, 2.8), [2.8, 3.4), [3.4, 4.0) and [4.0, ∞) TeV
- up to 4 bins in $E_T^{miss}/\sqrt{H_T}$: [10, 16), [16, 22), [22, 28) and [28, ∞) [GeV$^{1/2}$]

The bin definitions for MB-SSd are displayed in a tabular format in Table 4.4. Each table cell represents an orthogonal bin. Bins are often merged, either in m_{eff}, $E_T^{miss}/\sqrt{H_T}$ or N_j in order to increase statistics and reduce the total number of bins with a small loss of performance. For the jet multiplicity bins with N_j = [2,3] or [2,∞), tighter criteria are applied to the subleading jet $p_T \geq 250$ GeV. The last column of the tables is inclusive, except from the highest m_{eff}, $E_T^{miss}/\sqrt{H_T}$ bin of the N_j = [4, ∞), where an upper $m_{eff} < 3.4$ TeV cut is imposed to avoid an overlap with the highest four m_{eff}, $E_T^{miss}/\sqrt{H_T}$ bins of the N_j=[2, 3] table, which are inclusive in N_j. This design was imposed to ensure sufficient statistics in the high m_{eff}- $E_T^{miss}/\sqrt{H_T}$ phase-space, where the sensitivity to high squark (and low neutralino) masses is enhanced. In total, 24 bins are defined in the MB-SSd search.

N_j=[2, 3], $p_T(j_{i=1,2}) > 250$ GeV		m_{eff} [TeV]					
		[1.0, 1.6)	[1.6, 2.2)	[2.2, 2.8)	[2.8, 3.4)	[3.4, 4.0)	[4.0, ∞)
$E_T^{miss}/\sqrt{H_T}$ [GeV$^{1/2}$]	[10, 16)						
	[16, 22)						
	[22, 28)					N_j=[2.0,∞)	N_j=[2.0,∞)
	[28, ∞)					N_j=[2.0,∞)	N_j=[2.0,∞)

N_j=[4, ∞)		m_{eff} [TeV]			
		[1.0, 1.6)	[1.6, 2.2)	[2.2, 2.8)	[2.8, ∞)
$E_T^{miss}/\sqrt{H_T}$ [GeV$^{1/2}$]	[10, 16)				
	[16, 22)				
	[22, ∞)				m_{eff} =[2.8,3.4)

TABLE 4.4: Summary of the bin boundaries for the MB-SSd signal regions. For each jet multiplicity category (N_j=[2, 3] and N_j=[4, ∞)), the highest bins in respectively m_{eff} and $E_T^{miss}/\sqrt{H_T}$ are inclusive in that variable. In order to guarantee sufficient event yields in the highest four m_{eff} and $E_T^{miss}/\sqrt{H_T}$ bins of the upper (N_j=[2, 3]) table, no upper limits on N_j are imposed, as indicated in the relevant entries. As a result of this, in order to remove overlap with the highest m_{eff} and $E_T^{miss}/\sqrt{H_T}$ bin of the lower (N_j=[4, ∞)) table, a requirement that m_{eff} =[2.8,3.4) is imposed, as indicated in the relevant entry.

The MB-GGd bins are defined similarly, as shown in Table 4.5. Since this category targets direct gluino pair decays, only events with 4 or more jets are considered, and there is only one jet multiplicity bin. The m_{eff} and $E_T^{miss}/\sqrt{H_T}$ variables are segmented into 6 and 3 bins, starting from 1000 GeV and 10 GeV$^{1/2}$, respectively. In total, 18 bins are defined.

N_j= [4, ∞)		m_{eff} [TeV]					
		[1.0, 1.6)	[1.6, 2.2)	[2.2, 2.8)	[2.8, 3.4)	[3.4, 4.0)	[4.0, ∞)
$E_T^{miss}/\sqrt{H_T}$ [GeV$^{1/2}$]	[10, 16)						
	[16, 22)						
	[22, ∞)						

TABLE 4.5: Summary of the bin boundaries for the MB-GGd signal regions. The highest bin for each variable is inclusive in that variable.

The bin boundaries of the remaining multi-bin searches, MB-C and MB-GGo, are presented in Tables 4.6 and 4.7. For the MB-C search, the phase-space is separated into 3 jet multiplicity, 3 m_{eff} and 2 $E_{\text{T}}^{\text{miss}}/\sqrt{H_{\text{T}}}$ bins, making a total of 18 bins. As already mentioned, at least 6 jets are requested for the MB-GGo SRs. Events are further classified into 5 m_{eff} and up to 3 $E_{\text{T}}^{\text{miss}}/\sqrt{H_{\text{T}}}$ bins, constructing a grid of 14 bins.

N_{j}= [2, 3]; 4; [5, ∞)		m_{eff} [TeV]		
		[1.6, 2.2)	[2.2, 2.8)	[2.8, ∞)
$E_{\text{T}}^{\text{miss}}/\sqrt{H_{\text{T}}}$ [GeV$^{1/2}$]	[16, 22)			
	[22, ∞)			

TABLE 4.6: Summary of the bin boundaries for the MB-C signal regions. The highest bin for each variable is inclusive in that variable.

$N_{\text{j}} \geq 6$		m_{eff} [TeV]				
		[1.0, 1.6)	[1.6, 2.2)	[2.2, 2.8)	[2.8, 3.4)	[3.4, ∞)
$E_{\text{T}}^{\text{miss}}/\sqrt{H_{\text{T}}}$ [GeV$^{1/2}$]	[10, 16)					
	[16, 22)					
	[22, ∞)					

TABLE 4.7: Summary of the bin boundaries for the MB-GGo signal regions. The highest bin for each variable is inclusive in that variable.

This binning configuration has been decided based on results of an optimization study, discussed in 4.8.2.

4.5.4 BDT search

The BDT search targets gluino models, such as the ones illustrated in Figures 4.1c and 4.1d. Two groups of signal regions are designed. The first group, denoted as BDT-GGd, is optimized for the search of gluinos with direct decays, while the second set, BDT-GGo, targets one-step decays of gluinos. Each group comprises four signal regions that are optimized for a different mass splitting range between the gluino and the neutralino, $\Delta m(\tilde{g}, \tilde{\chi}_1^0)$.[3] In contrast to the multi-bin fit, the BDT SRs are not necessarily orthogonal and therefore cannot be combined statistically. A single-bin fit is deployed for each SR of the BDT search, as will be discussed in 4.7.

All BDT-GGd regions are required to have at least 4 jets, with $\Delta\phi(j_{1,2,(3)}, \boldsymbol{p}_{\text{T}}^{\text{miss}})_{\text{min}}$ and $\Delta\phi(j_{i>3}, \boldsymbol{p}_{\text{T}}^{\text{miss}})_{\text{min}} \geq 0.4$ to suppress the multi-jet background. In place of the transverse momentum significance, the ratio of the $E_{\text{T}}^{\text{miss}}$ to the effective mass is used in the BDT search, with a requirement of $E_{\text{T}}^{\text{miss}}/m_{\text{eff}}(Nj) \geq 0.2$. For large mass splittings between the $\tilde{g}$ and $\tilde{\chi}_1^0$ (MB-GGd1 and MB-GGd2) a tight cut of 1.4 TeV is applied on the m_{eff}. A looser 800 GeV cut is required to be satisfied for the low $\Delta m(\tilde{g}, \tilde{\chi}_1^0)$ regions (MB-GGd3 and MB-GGd4) to be more in accord with the expected soft topologies arising from decays in compressed spectra.

For the GGo category, at least 6 (GGo1 and GGo2) or 5 (GGo3 and GGo4) jets are requested. The azimuthal angle separation between the missing transverse momentum and either the three first of the remaining jets is required to be equal or larger than 0.4, except for the lowest mass splitting region (GGo4), where a looser cut of 0.2 is requested. The m_{eff} and $E_{\text{T}}^{\text{miss}}/m_{\text{eff}}(Nj)$ variables need to satisfy the same requirements as for the BDT-GGd regions.

[3] The mass splitting decreases with the increasing SR index.

Apart from the traditional kinematic cuts, a BDT discriminant is used to enhance the sensitivity of the search by exploiting correlations between input variables. The BDT algorithm learns to distinguish between signal and background by a method called *training*. In the training step, a mixture of both signal and background-like events is given to the algorithm, which is called to make a decision on the nature of each event (signal or background). The resulting classification is weighted according to its accuracy, and the process is repeated iteratively in order to maximize the BDT classification performance. In this analysis, the training is done with simulated signal samples. In order to ensure the robustness of the training, sufficient statistics must be used and to this goal, signal points with similar $\Delta m(\tilde{g}, \tilde{\chi}_1^0)$ are combined into a single sample, given that their event kinematics are similar. All background samples that are summarized in Table 4.1 are also included in the training. Up to 12 variables are selected among $E_{\mathrm{T}}^{\mathrm{miss}}$, m_{eff}, aplanarity, p_{T} and η of selected jets, and used as inputs in eight independent trainings for the eight signal regions.

After training the algorithm in a subset of the events, it can be applied to another sample to estimate the signal and background components in the form of a BDT score. However, this would imply a loss of statistics, since the training sample cannot be used as input for the score estimation, as that could induce over-training of the BDT score. In order to maintain the full statistics of the analysis, MC events and data are randomly separated in two groups and an independent training is performed in each of them. The BDT score that is calculated using the first event-set is then applied to the second event-set, and vice versa. The resulting BDT score has a [-1,1] range, from -1 being most background-like to 1 being most signal-like. While the aforementioned method already provides robustness against biases, dedicated studies have been carried out to ensure that no overtraining is present in the utilized samples. BDT score cuts that provide the maximal sensitivity for a benchmark signal model are then used to define the signal regions.

Table 4.8 summarizes the selection criteria that are applied in addition to the common preselection cuts to define the 8 BDT SRs. The last row in each table shows the $\Delta m(\tilde{g}, \tilde{\chi}_1^0)$ range for which each SR BDT is trained and optimized.

direct gluino decays				
	BDT-GGd1	BDT-GGd2	BDT-GGd3	BDT-GGd4
N_{j}	≥ 4			
$\Delta\phi(j_{1,2,(3)}, \boldsymbol{p}_{\mathrm{T}}^{\mathrm{miss}})_{\mathrm{min}}$	≥ 0.4			
$\Delta\phi(j_{i>3}, \boldsymbol{p}_{\mathrm{T}}^{\mathrm{miss}})_{\mathrm{min}}$	≥ 0.4			
$E_{\mathrm{T}}^{\mathrm{miss}}/m_{\mathrm{eff}}(Nj)$	≥ 0.2			
m_{eff} [GeV]	≥ 1400		≥ 800	
BDT score	≥ 0.97	≥ 0.94	≥ 0.94	≥ 0.87
$\Delta m(\tilde{g}, \tilde{\chi}_1^0)$ [GeV]	1600 – 1900	1000 – 1400	600 – 1000	200 – 600

one-step gluino decays				
	BDT-GGo1	BDT-GGo2	BDT-GGo3	BDT-GGo4
N_{j}	≥ 6		≥ 5	
$\Delta\phi(j_{1,2,(3)}, \boldsymbol{p}_{\mathrm{T}}^{\mathrm{miss}})_{\mathrm{min}}$	≥ 0.4			≥ 0.2
$\Delta\phi(j_{i>3}, \boldsymbol{p}_{\mathrm{T}}^{\mathrm{miss}})_{\mathrm{min}}$	≥ 0.4			≥ 0.2
$E_{\mathrm{T}}^{\mathrm{miss}}/m_{\mathrm{eff}}(Nj)$	≥ 0.2			
m_{eff} [GeV]	≥ 1400		≥ 800	
BDT score	≥ 0.96	≥ 0.87	≥ 0.92	≥ 0.84
$\Delta m(\tilde{g}, \tilde{\chi}_1^0)$ [GeV]	1400 – 2000	1200 – 1400	600 – 1000	200 – 400

TABLE 4.8: Signal region selections for the BDT search with the benchmark signal model parameters ($\Delta m(\tilde{g}, \tilde{\chi}_1^0)$) used in the optimisation.

4.5.5 Single-bin search

As already discussed, the analysis includes a third set of SRs for model-independent interpretation of the results in the MB kinematic phase-space. These regions are inclusive versions of multi-bin SRs. They are not orthogonal to each other and therefore are not combined statistically. After applying the preselection sequence of Table 4.2, 10 inclusive SRs are defined by increasing the jet multiplicity requirement. In order to acquire sensitivity into various mass splittings in the s-particle spectrum, regions with the same jet multiplicity, but with different m_{eff} and $E_{\text{T}}^{\text{miss}}/\sqrt{H_{\text{T}}}$ cuts are included. Tables 4.9 and 4.10 summarize the selection criteria for the single-bin search regions.

	SR2j-1600	SR2j-2200	SR2j-2800	SR4j-1000	SR4j-2200	SR4j-3400
N_{j}	≥ 2			≥ 4		
$p_{\text{T}}(j_1)$ [GeV]	> 250	> 600	> 250	> 200		
$p_{\text{T}}(j_{i=2,\ldots,N_{\text{j}_{\text{min}}}})$ [GeV]	> 250	> 50	> 250	> 100		
$\lvert\eta(j_{i=1,\ldots,N_{\text{j}_{\text{min}}}})\rvert$	< 2.0	< 2.8	< 1.2	< 2.0		
$\Delta\phi(j_{1,2,(3)}, \boldsymbol{p}_{\text{T}}^{\text{miss}})$ min	> 0.8	> 0.4	> 0.8	> 0.4		
$\Delta\phi(j_{i>3}, \boldsymbol{p}_{\text{T}}^{\text{miss}})$ min	> 0.4	> 0.2	> 0.4	> 0.4		
Aplanarity	-			> 0.04		
$E_{\text{T}}^{\text{miss}}/\sqrt{H_{\text{T}}}[\sqrt{\text{GeV}}]$	> 16					> 10
m_{eff}[GeV]	> 1600	> 2200	> 2800	> 1000	> 2200	> 3400

TABLE 4.9: Selection criteria used for single-bin search regions with minimum jet multiplicities up to four.

	SR5j-1600	SR6j-1000	SR6j-2200	SR6j-3400
N_{j}	≥ 5	≥ 6		
$p_{\text{T}}(j_1)$ [GeV]	> 600	> 200		
$p_{\text{T}}(j_{i=2,\ldots,N_{\text{j}_{\text{min}}}})$ [GeV]	> 50	> 75		
$\lvert\eta(j_i = 1, \ldots, N_{\text{j}_{\text{min}}})\rvert$	< 2.8	< 2.0		
$\Delta\phi(j_{1,2,(3)}, \boldsymbol{p}_{\text{T}}^{\text{miss}})$ min	> 0.4			
$\Delta\phi(j_{i>3}, \boldsymbol{p}_{\text{T}}^{\text{miss}})$ min	> 0.2			
Aplanarity	-	>0.08		
$E_{\text{T}}^{\text{miss}}/\sqrt{H_{\text{T}}}[\sqrt{\text{GeV}}]$	> 16			> 10
m_{eff}[GeV]	> 1600	> 1000	> 2200	> 3400

TABLE 4.10: Selection criteria used for single-bin search regionss with high jet multiplicities.

Table 4.11 summarizes the 0-lepton analysis SRs, along with the simplified models for which they have been optimized. It should be noted that SRs can have a high sensitivity to additional models apart from the one for which they have been optimized. One such example is the 4-jet SRs, which, while defined to target gluino-pair production with direct decays, are also sensitive to squark one-step models, thanks to the similar kinematics.

4.6 Background estimation

Standard model processes can give final states that resemble the expected signature from squarks and gluinos. While the selection criteria that were previously described aim to suppress these SM processes, a residual background that contaminates the signal regions remains, where a large amount of real or fake $E_{\text{T}}^{\text{miss}}$ is generated in association with many jets. The main SM processes that contribute to the residual background are (in decreasing order of magnitude):

Signal Regions	optimization signal model	diagram
MB-SSd, SR2j-1600, SR2j-2800	$\tilde{q}\tilde{q} \to qq\tilde{\chi}_1^0\tilde{\chi}_1^0$	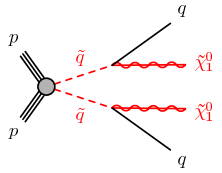
MB-GGd, GGd1-4, SR4j-1000, SR4j-2200, SR4j-3400	$\tilde{g}\tilde{g} \to qqqq\tilde{\chi}_1^0\tilde{\chi}_1^0$	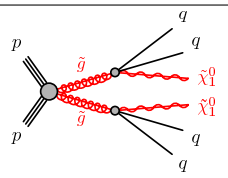
MB-GGo, GGo1-4, SR6j-1000, SR6j-2200, SR6j-3400	$\tilde{g}\tilde{g} \to qqWqqW\tilde{\chi}_1^0\tilde{\chi}_1^0$	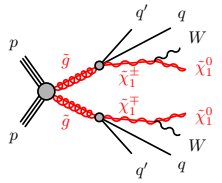
MB-C, SR5j-1600, SR2j-2200	$\tilde{q}\tilde{q} \to qq\tilde{\chi}_1^0\tilde{\chi}_1^0$ / $\tilde{g}\tilde{g} \to qqqq\tilde{\chi}_1^0\tilde{\chi}_1^0$ with compressed spectra	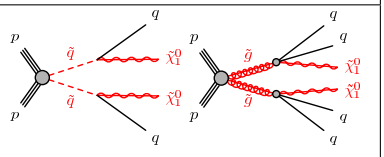

TABLE 4.11: Signal regions used in this analysis along with the simplified SUSY model for which they have been optimized.

- Z+jets, where the Z$\rightarrow \nu\nu$ decays give rise to large $E_{\mathrm{T}}^{\mathrm{miss}}$. This background is irreducible, i.e. cannot be distinguished from the signal.
- W+jets background, which mostly consists of W$\rightarrow \tau\nu$ events, in which the τ decays hadronically. Additional W$\rightarrow e\nu$ and W$\rightarrow \mu\nu$ decays can also contribute to this background, if the electron or muon is not reconstructed as baseline. In the former case, the $E_{\mathrm{T}}^{\mathrm{miss}}$ is generated from the escape of the neutrino, while in the latter scenario, the non-reconstructed electrons or muons can also contribute.
- Top quark processes followed by semi-leptonic decays also give rise to $E_{\mathrm{T}}^{\mathrm{miss}}$ and high N_{j} events that can satisfy the lepton-veto requirements, similarly to the W+jets background. Both $t\bar{t}$ or single-t contribute to this background, with the former being the dominant process, especially through the $t\bar{t} \rightarrow b\bar{b}\tau\nu qq'$.
- Diboson processes, ZZ, ZW and WW, which can generate the signal topologies in the same way as the Z(W)+jets backgrounds. This component, while partially irreducible, is a minor contribution in the overall background thanks to the small cross-section of diboson production.
- Multi-jet background from QCD processes, where the $E_{\mathrm{T}}^{\mathrm{miss}}$ can arise from mis-measurements of jet energies, jets not passing the selection criteria, as well as neutrinos from semi-leptonic decays of hadrons. While a priori this background component is one of the most important ones, dedicated selection criteria in the SRs reduce it to a negligible level.

4.6.1 Control regions

In order to interpret the result of the analysis in terms of significance of a potential signal over the background, a background estimation procedure based on Control Regions (CRs) is implemented. These regions are chosen to be orthogonal to the signal regions and are built to have a negligible contamination from SUSY signals, so as to provide independent data samples enriched in SM processes. They are also designed to have maximum purity and efficiency in the target background process (or an equivalent process), to allow for its estimation in a robust and accurate manner.

The background estimation procedure is common for the three analysis strategies. For each SR, four control regions are defined, one for each of the following components: Z+jets, W+jets, Top and Multi-jets. The remaining diboson background is estimated purely from MC simulation samples. Selection criteria that aim to enhance the target SM process, while maintaining sufficient statistics so as to ensure the accuracy of the estimation, are applied. In order to minimize the systematic uncertainty from the extrapolation of the background estimate in a CR to its corresponding SR, the same jet p_{T} thresholds and m_{eff} cuts are used. In the multi-bin analysis, each bin has its own set of CRs with identical m_{eff} and N_{j} boundaries. However, in order to increase the statistics, the multi-bin CRs are inclusive in $E_{\mathrm{T}}^{\mathrm{miss}}/\sqrt{H_{\mathrm{T}}}$. This means that SR bins which differ only in the $E_{\mathrm{T}}^{\mathrm{miss}}/\sqrt{H_{\mathrm{T}}}$ requirement share the same CR.

In the high energy regime of this analysis, far from the Z boson resonance, the Z and γ bosons display similar kinematic properties. The Z+jets background is therefore estimated from the γ+jets process in a photon-enriched control region, CRY. Events with jets and a photon with $p_{\mathrm{T}}^{\gamma} > 150$ GeV are selected and, then, the reconstructed photon is treated as a missing particle, thus contributing to the $E_{\mathrm{T}}^{\mathrm{miss}}$ calculation. CRY selections follow closely the SR requirements, except for the cut on the aplanarity variable, which is not applied. Additionally,

for BDT-GGo1 and BDT-GGo2 SRs, the $\Delta\phi(j, \boldsymbol{p}_{\mathrm{T}}^{\mathrm{miss}})_{\mathrm{min}}$ and $E_{\mathrm{T}}^{\mathrm{miss}}/m_{\mathrm{eff}}(N_j)$ selections are removed from the CR criteria in order to increase the γ+jets sample statistics.

A Z$\rightarrow \ell\ell$+jets sample (with $\ell = e, \mu$) was considered as an alternative to estimate the Z$\rightarrow \nu\nu$+jets background, but was rejected due to the small statistics - it is used as a validation region (VRZ) instead, as described in 4.6.2. In order to account for differences between the Z and γ boson samples, a correction factor κ is derived from the double ratio between data and MC events in CRY to the Z$\rightarrow \ell\ell$+jets VRZ region:

$$\kappa = \frac{N_{CRY}^{data}/N_{CRY}^{MC}}{N_{VRZ}^{data}/N_{VRZ}^{MC}} \tag{4.2}$$

This factor was estimated from the loosest CR bins of the MB-SSd multi-bin analysis ($1000 \leq m_{\mathrm{eff}} < 1600$, $E_{\mathrm{T}}^{\mathrm{miss}}/\sqrt{H_{\mathrm{T}}} \geq 10$) for the two jet multiplicity bins, N_{j}=[2,3] and N_{j}=[4,∞). In general, it was found that, while in VRZ the data to MC ratio is close to 1, in CRY, the simulation slightly overestimates the data[4]. The κ factor was found to be constant with respect to most key variables of the analysis, except from a slight dependence on the jet multiplicity. Two values were therefore extracted, $\kappa = 0.77 \pm 0.04$ for N_{j}=[2,3] and $\kappa = 0.85 \pm 0.05$ for N_{j}=[4,∞). The quoted uncertainty corresponds to the statistical contribution. Depending on the jet multiplicity requirement in each region, the appropriate value of κ is applied.

For the estimation of the W+jets and top quark backgrounds, two types of Control Regions, CRW and CRT, respectively, are used. Both of them are based on the selection of W$\rightarrow \ell\nu$+jets events (with $\ell = e, \mu$). For the CRT region, the presence of at least one b-jet is also required, to be consistent with the most probable decay of top quarks. A b-jet veto is applied in the CRW, in order to ensure the orthogonality of the two regions and the mitigation of top processes that contaminate the pure W+jets background. In both cases, the lepton is required to be high-purity and is treated as a jet with the same momentum. This approach is correct to model background events with a hadronically decaying τ-lepton or a non-reconstructed electron that leaves a calorimeter deposit. However, muons or electrons that escape the detector through cracks contribute to the missing energy, and therefore should be included in the $E_{\mathrm{T}}^{\mathrm{miss}}$ calculation instead. Since the contribution of the latter type of events to the total W$\rightarrow \ell\nu$ background was found to less than 20%, and additionally, the top processes are a small component of the overall background, a global treatment of all leptons as jets was implemented. As already mentioned in 4.4, a pure $E_{\mathrm{T}}^{\mathrm{miss}}$ trigger is used to select leptonic events to increase the available statistics. This allows to lower the cuts on the p_{T} of the leptons to 6 (7) GeV for muons (electrons), effectively bringing the CR phase-space closer to the SRs. In order to be consistent with the decay of a W boson, the transverse mass of the $E_{\mathrm{T}}^{\mathrm{miss}}$ and the selected lepton, $m_{\mathrm{T}} = \sqrt{2p_{\mathrm{T}}^{\ell}E_{\mathrm{T}}^{\mathrm{miss}}(1 - \cos[\Delta\phi(\ell,\ \boldsymbol{p}_{\mathrm{T}}^{\mathrm{miss}})])}$, is required to be between 30 GeV and 100 GeV. The $\Delta\phi(j, \boldsymbol{p}_{\mathrm{T}}^{\mathrm{miss}})_{\mathrm{min}}$ and aplanarity requirements of the SRs are omitted in all the CRW and CRT regions, so as to increase the statistics.

Finally, the multi-jet background is estimated using a data-driven technique, called Jet Smearing [134, 135]. In this method, a jet resolution function is applied to a sample enriched in good quality multi-jet events in order to measure the impact of jet energy mismeasurements and heavy-flavor semileptonic decays on $E_{\mathrm{T}}^{\mathrm{miss}}$ and other variables. The jet resolution function is initially estimated from the comparison of particle-level to reconstruction-level MC simulation, and is then calibrated to data in dedicated samples. A control region with high purity on multi-jet events is then constructed by reversing the SR cuts on $\Delta\phi(j, \boldsymbol{p}_{\mathrm{T}}^{\mathrm{miss}})_{\mathrm{min}}$

[4]This discrepancy could be due to the different order of the cross-section calculation for the two samples, NLO for γ+jets and NNLO for Z+jets.

and either $E_{\mathrm{T}}^{\mathrm{miss}}/\sqrt{H_{\mathrm{T}}}$ for the multi-bin and single-bin searches or $E_{\mathrm{T}}^{\mathrm{miss}}/m_{\mathrm{eff}}(N_j)$ for the BDT ones. For the $E_{\mathrm{T}}^{\mathrm{miss}}/\sqrt{H_{\mathrm{T}}}$ (or $E_{\mathrm{T}}^{\mathrm{miss}}/m_{\mathrm{eff}}(N_j)$) variable, a lower limit of 8 (0.14) is applied. The aplanarity cut is omitted in all CRQ regions, while for the signal regions targeting the lowest mass splittings in the BDT search, BDT-GGd4 and BDT-GGo4, the BDT score selections are slightly loosened from 0.87 to 0.70 and from 0.84 to 0.60, respectively.

The four control regions, along with their target background, used process and selection criteria are summarized in Table 4.12. Normalization factors are extracted from the comparison of simulation (or data driven estimate in the case of the multi-jet background) to data in each CR and are then applied to the pure MC estimate in the corresponding SR, as described in 4.7.

CR	SR background	CR process	CR selection
MB/BDT-CRγ	$Z(\rightarrow \nu\bar{\nu})$+jets	γ+jets	Isolated photon
MB/BDT-CRQ	Multi-jet	Multi-jet	reversed requirements on (i) $\Delta\phi(\mathrm{j}, \boldsymbol{p}_{\mathrm{T}}^{\mathrm{miss}})$ and (ii) $E_{\mathrm{T}}^{\mathrm{miss}}/m_{\mathrm{eff}}(N_{\mathrm{j}})$ or $E_{\mathrm{T}}^{\mathrm{miss}}/\sqrt{H_{\mathrm{T}}}$
MB/BDT-CRW	$W(\rightarrow \ell\nu)$+jets	$W(\rightarrow \ell\nu)$+jets	one lepton, 30 GeV$< m_{\mathrm{T}}(\ell, E_{\mathrm{T}}^{\mathrm{miss}}) <$ 100 GeV, b-veto
MB/BDT-CRT	$t\bar{t}$(+EW) and single top	$t\bar{t} \rightarrow b\bar{b}qq'\ell\nu$	one lepton, 30 GeV$< m_{\mathrm{T}}(\ell, E_{\mathrm{T}}^{\mathrm{miss}}) <$ 100 GeV, b-tag

TABLE 4.12: Control regions used in the analysis. Also listed are the main targeted background in the SR in each case, the process used to model the background, and the main CR requirement(s) used to select this process. The jet p_{T} thresholds and m_{eff} selections match those used in the corresponding SRs.

Example m_{eff} distributions in the four control regions based on the MB-GGd selection requirements are shown in Figure 4.4. The background components are normalised to the cross-section times integrated luminosity, except for the multi-jet background, which, since it is derived from a data-driven method, is normalised directly to the data. While a high purity in the target background is achieved in all CRs, contributions from the remaining backgrounds is accounted for in the normalization procedure, as detailed in 4.7.2. In general, a good agreement of the data with the SM prediction is observed in CRY and CRW, indicating a good modeling of the V+jets backgrounds. On the other hand, an overestimation of the data by the MC prediction is observed in the CRT with increasing m_{eff}. This effect arises from a mismodeling of top related backgrounds in simulation, due to the MC samples predicting in general harder kinematics [136].

Equivalent distributions on the other two binning variables, $E_{\mathrm{T}}^{\mathrm{miss}}/\sqrt{H_{\mathrm{T}}}$ and N_{j}, are presented in Figures 4.5 and 4.6, for the MB-C and MB-SSd searches, respectively. For the $E_{\mathrm{T}}^{\mathrm{miss}}/\sqrt{H_{\mathrm{T}}}$ variable, a good modelling is observed in all CRs but CRT, where again an overestimation of the data by the simulation is observed. For the CRQ distribution, the $E_{\mathrm{T}}^{\mathrm{miss}}/\sqrt{H_{\mathrm{T}}}$ cut has been omitted - the reader is reminded that the cut is inverted, in order to increase the region's purity in multi-jet events. A dependence of the data to MC ratio to the jet multiplicity is observed for all three major backgrounds, as demonstrated from the CRY, CRW and CRT distributions in Figure 4.6. It is imperative to account for this behaviour in the background normalisation procedure of the multi-bin searches, as will be discussed in 4.8.3. The remaining CR distributions of the four MB searches can be found in Appendix A.

4.6.2 Validation regions

A separate set of regions is implemented to validate the background estimation procedure described in 4.6.1. These regions, named validation regions (VRs), are designed to provide an

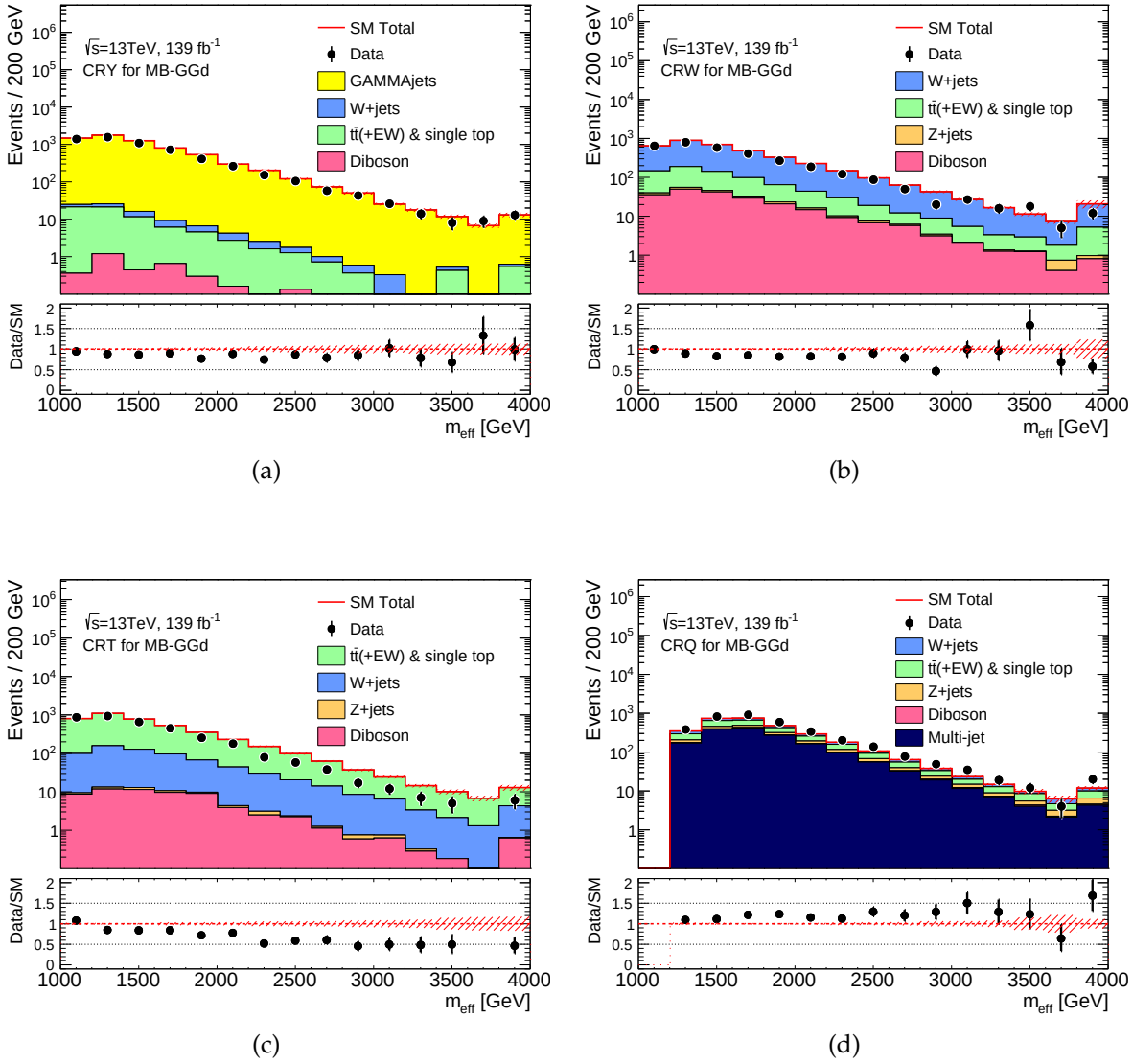

FIGURE 4.4: Observed m_{eff} distributions in control regions (a) MB-CRY, (b) MB-CRW, (c) MB-CRT and (d) MB-CRQ after applying the MB-GGd control region criteria and after requiring that events pass any of the equivalent CR bin cuts. The histograms show the MC background predictions normalised using cross-section times integrated luminosity, with the exception of multi-jet background which is normalised using data. In the case of the γ+jets background, a κ factor described in the text is applied. The hatched (red) error bands indicate the combined MC statistical, experimental and theoretical uncertainties. The latter two are calculated using the coarser binning of the MB analysis rather than the fine binning of the histogram. The last bin includes overflow events.

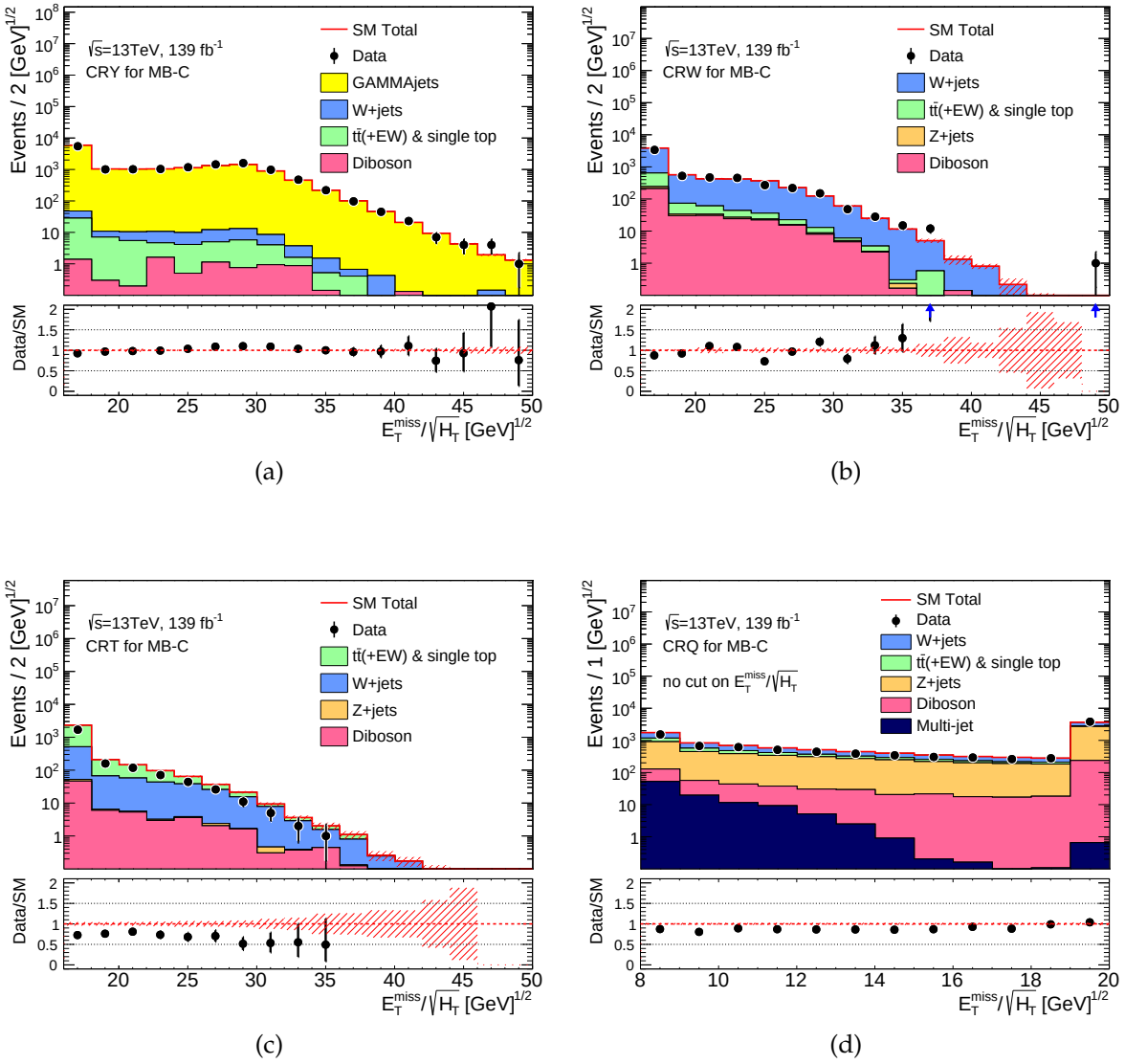

FIGURE 4.5: Observed $E_{\mathrm{T}}^{\mathrm{miss}}/\sqrt{H_{\mathrm{T}}}$ distributions in control regions (a) MB-CRY, (b) MB-CRW, (c) MB-CRT and (d) MB-CRQ after applying the MB-C control region criteria and after requiring that events pass any of the equivalent CR bin cuts. In (d) the inverted $E_{\mathrm{T}}^{\mathrm{miss}}/\sqrt{H_{\mathrm{T}}}$ cut has been omitted. The histograms show the MC background predictions normalised using cross-section times integrated luminosity, with the exception of multi-jet background which is normalised using data. In the case of the γ+jets background, a κ factor described in the text is applied. The hatched (red) error bands indicate the combined MC statistical, experimental and theoretical uncertainties. The latter two are calculated using the coarser binning of the MB analysis rather than the fine binning of the histogram. The last bin includes overflow events.

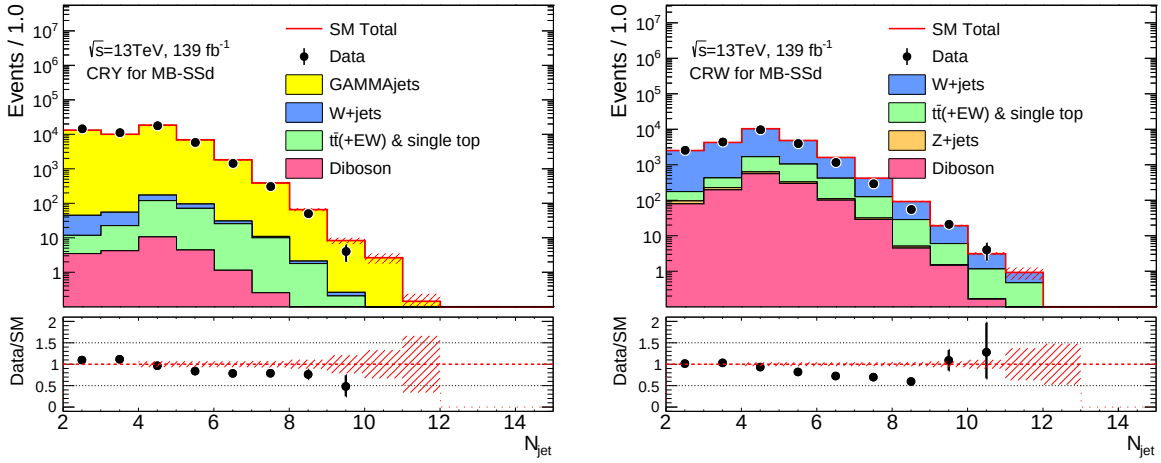

(a)

(b)

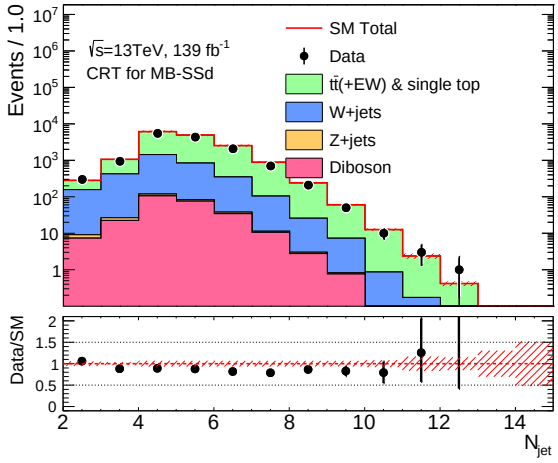

(c)

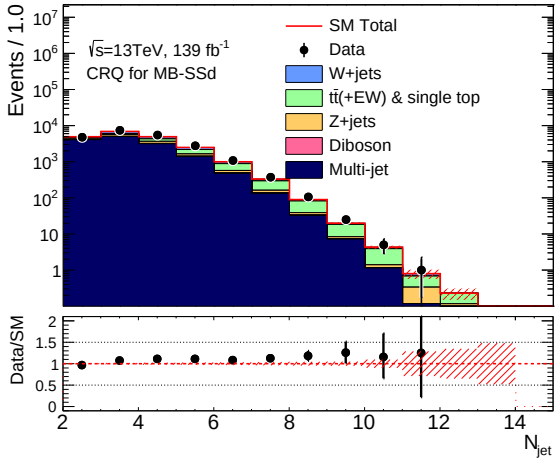

(d)

FIGURE 4.6: Observed N_j distributions in control regions (a) MB-CRY, (b) MB-CRW, (c) MB-CRT and (d) MB-CRQ after applying the MB-SSd control region criteria and after requiring that events pass any of the equivalent CR bin cuts. The histograms show the MC background predictions normalised using cross-section times integrated luminosity, with the exception of multi-jet background which is normalised using data. In the case of the γ+jets background, a κ factor described in the text is applied. The hatched (red) error bands indicate the combined MC statistical, experimental and theoretical uncertainties. The latter two are calculated using the coarser binning of the MB analysis rather than the fine binning of the histogram. The last bin includes overflow events.

independent handle on potential biases in the extrapolation from the CR to the SR. They are built in a phase-space as close as possible to the SR while maintaining a negligible contribution from signal. In general, validation regions are implemented to check either the consistency between different process types or the effect of relaxed/reversed selection cuts between CRs and SRs. Similarly to the CRs, validation regions are defined mostly in final states with leptons, allowing for high purity samples.

As already mentioned, the estimation of the Z($\rightarrow \nu\nu$)+jets background with the CRY regions (γ+jets) is validated with the VRZ regions, which are enriched in Z($\rightarrow \ell\ell$)+jets events, with $\ell = e, \mu$. Events are classified in this validation region if they contain a pair of same-flavour, opposite-charge and high purity leptons with an invariant mass lying within 25 GeV of the Z boson mass. A single-lepton trigger, as described in 4.4, is used to select events and the lepton-pairs are treated as contributing to the event $E_{\mathrm{T}}^{\mathrm{miss}}$. The generated sample, while closely resembling the background component, suffers from a lack of statistics. For this reason, the SR cuts on $\Delta\phi(j, \boldsymbol{p}_{\mathrm{T}}^{\mathrm{miss}})_{\mathrm{min}}$, aplanarity and $E_{\mathrm{T}}^{\mathrm{miss}}/\sqrt{H_{\mathrm{T}}}$ (or $E_{\mathrm{T}}^{\mathrm{miss}}/m_{\mathrm{eff}}(N_j)$ for the BDT SRs) are not applied. In order to ensure that no bias is introduced from the omission of the selection criteria, additional validation regions are designed where the cut on one of these variables is reinstated, constituting the MB/BDT-VRZdPhi, MB-VRZAp, MB-VRZmetSig regions for the $\Delta\phi(j, \boldsymbol{p}_{\mathrm{T}}^{\mathrm{miss}})_{\mathrm{min}}$, aplanarity and $E_{\mathrm{T}}^{\mathrm{miss}}/\sqrt{H_{\mathrm{T}}}$ cuts, respectively. In addition, for the BDT search regions, a validation region which requires the full SR kinematic requirements to be satisfied, BDT-VRZf, is implemented.

The extrapolation of the background estimation from the CRW and CRT regions is validated in the dedicated VRW and VRT regions, respectively. In these regions, the same process as in their corresponding CRs is targeted, but additional SR selection criteria that were omitted in the CR definition are now applied. The reinstatement of either the $\Delta\phi(j, \boldsymbol{p}_{\mathrm{T}}^{\mathrm{miss}})_{\mathrm{min}}$, aplanarity, $E_{\mathrm{T}}^{\mathrm{miss}}/\sqrt{H_{\mathrm{T}}}$ or all of the above define the MB/BDT-VRWdPhi, MB-VRWAp, MB-VRWmetSig and BDT-VRWf. The MB/BDT-VRTdPhi, MB-VRTAp, MB-VRTmetSig and BDT-VRTf are constructed similarly to the W+jets validation regions, but reversing the b-veto requirement and demanding at least one b-jet.

In order to validate the estimation of the multi-jet component as well as the extrapolation of the residual background estimates from a leptonic to a fully hadronic environment, I have implemented a separate set of regions, denoted as VR0L. These regions are built in the same $\Delta\phi(j, \boldsymbol{p}_{\mathrm{T}}^{\mathrm{miss}})_{\mathrm{min}}$ - $E_{\mathrm{T}}^{\mathrm{miss}}/\sqrt{H_{\mathrm{T}}}$ (or $E_{\mathrm{T}}^{\mathrm{miss}}/m_{\mathrm{eff}}(N_j)$) phase-space as their corresponding SR and CRQ. They are made orthogonal to both of them by reinstating one of the SR cuts that were reversed in the CRQ; MB/BDT-VR0LdPhi apply the $\Delta\phi(j, \boldsymbol{p}_{\mathrm{T}}^{\mathrm{miss}})_{\mathrm{min}}$ SR selection cut, while MB-VR0LmetSig and BDT-VR0Lmetmeff require the corresponding $E_{\mathrm{T}}^{\mathrm{miss}}/\sqrt{H_{\mathrm{T}}}$ or $E_{\mathrm{T}}^{\mathrm{miss}}/m_{\mathrm{eff}}(N_j)$ SR cut while maintaining a reversed $\Delta\phi(j, \boldsymbol{p}_{\mathrm{T}}^{\mathrm{miss}})_{\mathrm{min}}$ requirement. A schematic drawing of the CRQ, VR0L and SR regions in the 0-lepton phase-space for the multi-bin and BDT fit are shown in Figures 4.7a and 4.7b, respectively. For the multi-bin searches, the $E_{\mathrm{T}}^{\mathrm{miss}}/\sqrt{H_{\mathrm{T}}}$ extrapolation is validated in each bin, while the $\Delta\phi(j, \boldsymbol{p}_{\mathrm{T}}^{\mathrm{miss}})_{\mathrm{min}}$ validation is done inclusively for bins with the same $E_{\mathrm{T}}^{\mathrm{miss}}/\sqrt{H_{\mathrm{T}}}$ (following the same binning configuration as the CRs). In order to ensure a high purity in the multi-jet background, an upper cut on $\Delta\phi(j, \boldsymbol{p}_{\mathrm{T}}^{\mathrm{miss}})_{\mathrm{min}} < 0.4$ is applied in all CRQ regions. This is compatible with the lower cut on the corresponding SR in all regions except MB-SSd bins, where the tighter cut of 0.8 is applied in the SR, to further mitigate the residual QCD background. For the VR0LmetSig regions, a lower $\Delta\phi(j, \boldsymbol{p}_{\mathrm{T}}^{\mathrm{miss}})_{\mathrm{min}}$ cut which is equal to $0.5 \times cut_{\Delta\phi}^{SR}$ is applied, such that the regions are not completely dominated by the multi-jet background. This is done in order to be able to validate all the background components.

Figure 4.8 displays example m_{eff} distributions in the 0-lepton validation regions, based

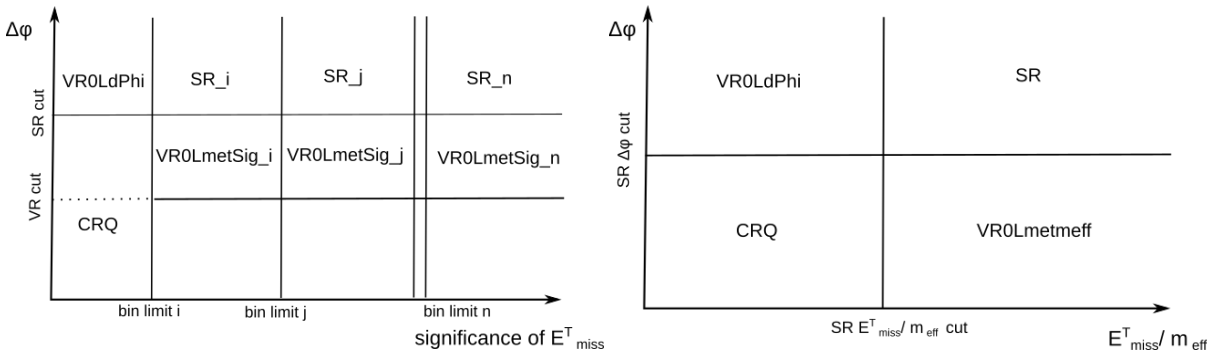

FIGURE 4.7: 0-lepton regions for (a) the multi-bin analysis in the $E_{\mathrm{T}}^{\mathrm{miss}}/\sqrt{H_{\mathrm{T}}}$ - $\Delta\phi(j, \boldsymbol{p}_{\mathrm{T}}^{\mathrm{miss}})_{\mathrm{min}}$ space or (b) the BDT analysis in the $E_{\mathrm{T}}^{\mathrm{miss}}/m_{\mathrm{eff}}(N_j)$ - $\Delta\phi(j, \boldsymbol{p}_{\mathrm{T}}^{\mathrm{miss}})_{\mathrm{min}}$ space. In order to ensure a high purity in the multi-jet background, an upper cut on $\Delta\phi(j, \boldsymbol{p}_{\mathrm{T}}^{\mathrm{miss}})_{\mathrm{min}} < 0.4$ is applied in all CRQ regions. Therefore, the CRQ regions neighbours their corresponding SRs except in the case of MB-SSd, where a tighter low $\Delta\phi(j, \boldsymbol{p}_{\mathrm{T}}^{\mathrm{miss}})_{\mathrm{min}}$ cut of 0.8 is applied in the SR bins. This separate configuration is distinguished by the dashed line of Figure (a). For the VR0LmetSig, a lower $\Delta\phi(j, \boldsymbol{p}_{\mathrm{T}}^{\mathrm{miss}})_{\mathrm{min}}$ cut which is equal to 0.5 $\times cut_{\Delta\phi}^{SR}$ is applied to enrich the regions in all background components.

on requirements of the MB-SSd search. In general, a good agreement of the MC expectation to the data is observed, even before the background normalisation procedure described in 4.7.3. The background composition is fairly similar to that of the 0-lepton SRs, allowing for the simultaneous validation of all the background components in the 0-lepton environment.

4.7 Statistical treatment

The statistical treatment encapsulates the procedure undertaken to transition from the experimental measurement to an interpretation of the collected data in a theoretical model. The interpretation is usually performed in terms of statistical tests, which aim to make a statement about how well the observed data stand in agreement with given predicted probabilities from a theory, i.e. a hypothesis.

4.7.1 Formalism of a statistical test

The hypotheses under consideration are modelled in terms of probability density functions (PDFs). The probability of observing n events, under an assumed model that predicts a fixed expected number ν, is given by the Poisson distribution:

$$P(n;\nu) = \frac{\nu^n}{n!}e^{-\nu} \tag{4.3}$$

In a simple cut and count experiment, the Poisson distribution corresponds to the PDF of a hypothesis that predicts ν events.

The compatibility of a theoretical model prediction to the data is often performed relatively, i.e. against an alternative hypothesis. The first hypothesis is referred to as the hypothesis under test H_1, while the alternative is the null hypothesis H_0. When searching for new phenomena, the null hypothesis describes the known processes, i.e. the SM background, while H_1 corresponds to the known processes plus a model describing the additional new signal. On the other hand, when setting limits in the absence of evidence for new physics, the

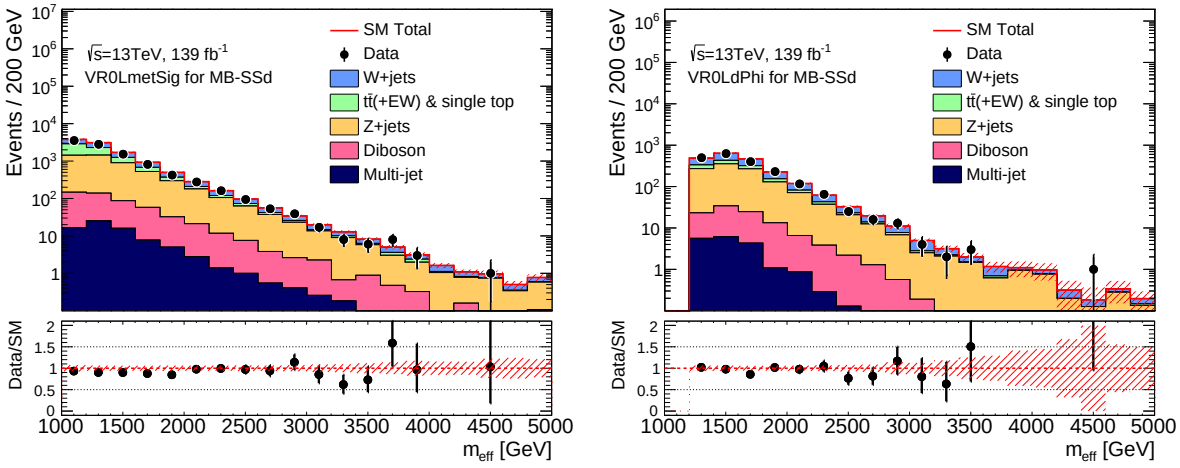

(a) (b)

FIGURE 4.8: Observed m_{eff} distributions (a) in the VR0LmetSig and (b) in VR0LdPhi, after applying the MB-SSd validation region criteria and after requiring that events pass any of the corresponding VR bin cuts. The histograms show the MC background predictions normalised using cross-section times integrated luminosity, with the exception of multi-jet background which is normalised using data. The hatched (red) error bands indicate the combined MC statistical, experimental and theoretical uncertainties. The latter two are calculated using the coarser binning of the MB analysis rather than the fine binning of the histogram. The last bin includes overflow events.

signal plus background hypothesis plays the role of H_0 and is tested against the background-only model, H_1.

In order to discriminate between the two alternatives, one constructs a function of the measured variables, called a test statistic. According to the Neyman-Pearson lemma [137], the test statistic with the maximum power for separating between two hypotheses is the likelihood ratio, given by the ratio of the PDFs of the two models: $t(x) = f(x|H_0)/f(x|H_1)$, where x is the set of observations. Since the measurements are all assumed to be independent, the probability for the observed dataset is then the product of the individual PDFs, which are Poisson distributions.

The definition of the PDFs often include a set of free unknown parameters ζ, $f(x;\zeta)$. The determination of the probability density functions' free parameters that best agree with the data is a crucial step in the statistical test and proceeds with the maximum likelihood method. The maximum likelihood (ML) [138] is a method of estimating parameter values of a model that best fit a finite sample of events. It is based on the maximization of the likelihood function:

$$L(\zeta) = \prod_{i=1}^{n} f(x_i;\zeta), \tag{4.4}$$

where $x_i...x_n$ is a set of independent measurements and $f(x_i;\zeta)$ the hypothesized PDF of the model under test. It stands to reason that, if the hypothesized density functions and parameter estimates are close to their true values, the probability for the data to be measured, and therefore, the likelihood, will also be high. With this motivation, the maximum of the likelihood function can be used as an estimator of the free parameters ζ_i (with i=1...m), the best-fit values of which can be derived by solving the $dL/d\zeta_i = 0$ equations.

The free parameters of the hypothesis under test typically fall in two categories, the parameters of interest (POI) and the nuissance parameters (NPs), denoted with the symbol θ. The first ones, as the name suggests, are parameters of the hypothesis that define the interpretation of the statistical test, such as the signal strength μ, an estimate of a particle mass etc. The second category includes parameters that are also needed to define the model, but are not used in the interpretation of the results. These are usually systematic uncertainties, and their estimate is constrained by additional probability function terms C_{syst}.

In order to test a hypothesized value of μ and in parallel infer the best-fit values of θ for the said value of μ, we consider the profile likelihood ratio:

$$\lambda(\mu) = \frac{L(\mu, \hat{\hat{\theta}})}{L(\hat{\mu}, \hat{\theta})} \tag{4.5}$$

where $\hat{\hat{\theta}}$ denotes the value of θ that maximizes L for the specified μ. Therefore, the nominator $L(\mu, \hat{\hat{\theta}})$ is the conditional ML estimator of θ as a function of μ. The denominator $L(\hat{\mu}, \hat{\theta})$ corresponds to the maximized (unconditional) likelihood function, i.e. $\hat{\mu}$ and $\hat{\theta}$ are their ML estimators. The presence of the nuisance parameters broadens the profile likelihood as a function of μ relative to what one would have if their values were fixed. This reflects the loss of information on μ due to the systematic uncertainties.

A convenient way to use the profile likelihood ratio to define a test statistic is by the following expression:

$$t_\mu = -2ln\lambda(\mu). \tag{4.6}$$

Higher values of t_μ thus correspond to increasing incompatibility between the data and hypothesis. In order to proceed with the statistical test, the distribution of the test statistic needs to be determined. Assuming a Gaussian regime, the test statistic can be approximated with an asymptotic formula [139, 140]. In this case, a convenient method for estimating the distribution spread is based on the construction of an artificial dataset, called Asimov dataset [141]. The Asimov dataset is defined in a way that, when used to evaluate the parameter estimators, the true parameter values are obtained. It can be understood that an Asimov sample is devoid of any statistical fluctuations, and is thus more suited in estimating the test statistic distribution with large-size samples, and only when the Gaussian regime is valid. A more accurate evaluation can be achieved with the use of pseudo-data samples, generated from the PDF. This method samples the true distribution of the test statistic, and is referred to as toy Monte Carlo sampling. While powerful in the lowest statistic limits, it is limited by the size of generated pseudo-data and is computationally expensive.

After deducing the form and free parameter estimates of the test statistic, the level of agreement between the observed data and a given hypothesis H can be quantified with the p-value, which gives the probability, under the assumption of H (either H_0 or H_1), of observing a result of equal or greater incompatibility with the predictions of H. Instead of the p-value, physicists often use the equivalent Gaussian significance, Z, which is defined as the quantile (inverse of the cumulative distribution) of $1 - p$:

$$Z = \Phi^{-1}(1 - p) \tag{4.7}$$

In this definition, a Gaussian distributed variable that is found to be Z standard deviations

above its mean has an upper-tail probability equal to p[5]. For the search of a new process, a signal is considered as discovered when a significance of at least $Z = 5$ (which corresponds to $p = 2.87 \times 10^{-7}$) is observed. When trying to exclude a hypothesis, usually in case of absence of strong evidence of new physics, upper limits on the number of events under this hypothesis are set with a fixed confidence level, $CL = 1 - p$. This level is usually pre-defined to 95%, corresponding to a $p(Z)$-value of 0.05 (1.64). In order to protect the interpretation from pathologies where a downward fluctuation of the background would give an unexpectedly strong exclusion power, the CL_s prescription [142] is used:

$$CL_s = \frac{CL_{s+b}}{1 - CL_b} \tag{4.8}$$

where CL_{s+b} is the confidence level computed under the signal plus background hypothesis and CL_b the one calculated under the background-only hypothesis.

4.7.2 Hypotheses under test

In this analysis, statistical tests are performed in each channel under three different assumptions, using the HistFitter package [143]. The first one, called *background-only* fit, is used to normalise the background processes to the data in their designated control regions. This fit aids in acquiring accurate background estimates and validating the normalisation procedure, but is not used to test the agreement of data and SM expectation in the SR. The SR is therefore excluded from the normalisation process and doesn't have an assigned free parameter. The normalisation factor of each background component is extracted from the comparison of data and simulation in the designated CR and is extrapolated in the SR according to the following equation:

$$\mathrm{N(SR, est, proc)} = \mathrm{N(CR, obs, proc)} \times \left[\frac{\mathrm{N(SR, raw, proc)}}{\mathrm{N(CR, raw, proc)}}\right] = \mu_{\mathrm{bkg}} \times \mathrm{N(SR, raw, proc)}, \tag{4.9}$$

where N(SR,est,proc) is the SR background estimate for the process, N(CR,obs,proc) is the observed number of data events in the CR for the process corrected for the contamination from other processes and N(SR,raw,proc) and N(CR,raw,proc) are estimates with raw cross-section times the integrated luminosity of the contributions from the process to the SR and CR respectively. The ratio appearing in the square brackets of the middle part of equation 4.9 is defined to be the transfer factor TF. Similar equations containing inter-CR TFs enable the background estimates to be normalised coherently across all the CRs. An advantage of using the TF approach is that some systematic uncertainties largely cancel in the ratio of the SR to CR count estimates. The ratio of the observed to the simulation-estimated data in the CR for each process, N(CR,obs,proc)/N(CR,raw,proc), defines the background normalisation of the process, μ_{bkg}. The normalisation factors for the 4 backgrounds which are assigned a control region are the main fit parameters in the background-only fit.

The second type of fit, called *discovery* or *model-independent*, attempts to quantify the level of agreement between the observation and the SM plus a generic non-SM process in the SR. It proceeds similarly to the background fit, where yields in the CRs are used to constrain the predictions of backgrounds in each SR. However, in this case, the SR yield is also used in the likelihood with an additional parameter describing potential signal contributions, the signal

[5] An alternative definition of Z also exists where the two-sided fluctuation of the Gaussian variable is considered. However, in the particle physics community, the one-sided Z definition is usually preferred, since it gives $Z = 0$ for $p = 0.5$.

strength μ_s. The discovery fit is used to compute the one-sided p-value of the background-only hypothesis, p_0, which quantifies the statistical significance of an excess. In the absence of strong evidence of signal excess compatible with a BSM signature, the results are interpreted in terms of upper limits on the number of BSM events or, when normalizing to the integrated luminosity of the data, on the visible cross-section of BSM physics. The upper limits are reported at a 95% Confidence Level (CL). The CL_s formalism, as described in 4.7.1 is used. Potential signal contributions in the CRs are neglected. The multi-bin searches are not used in the discovery fit, since, an assumption on the generic signal distribution among bins would need to be made, negating the interpretation's independence on a model.

Finally, the results are checked against predictions of the simplified SUSY models of Figure 4.1 with the *model-dependent* (or *exclusion*) fit. It proceeds in the same way as the model-independent fit, where, in place of the generic BSM signature, the yields from the SUSY signal samples are injected in the likelihood. Potential signal contributions in the CRs are also taken into account. The hypothesis under test includes both signal and background contributions, and, therefore, the upper limits on the visible SUSY cross-section at 95% CL are reported. Results from all the search channels (multi-bin, single-bin and BDT) are considered and, for each individual model, the one that obtains the best expected 95% CL exclusion limit is quoted.

4.7.3 The maximum likelihood function in the 0-lepton analysis

Following the previous definitions, the likelihood function in each of the 0-lepton analysis channels is the product of Poisson distributions of the SR and of the main control regions constraining the Z+jets (CRY), QCD jets (CRQ), W +jets (CRW) and $t\bar{t}$ + single-t (CRT) backgrounds, and of the PDFs constraining the systematic uncertainties C_{Syst}:

$$L(n|\mu, s, b, \theta) \quad = \quad P_{\text{SR}} \times P_{\text{CRW}} \times P_{\text{CRT}} \times P_{\text{CRY}} \times P_{\text{CRQ}} \times C_{\text{Syst}} \,. \tag{4.10}$$

Each Poisson function P_i is expressed in terms of the observed number of events in the region, n_i, and the expected number of events ν_i. In the case where the search channel is a multi-bin fit, the likelihood function includes the product of the PDFs of all SR and CR orthogonal bins. The expected number of events ν_i is given by the following contributions:

- the expected number of background events b from the various processes. In this analysis, the background components for each region used in the likelihood fit are QCD jets, W+jets, Z+jets, top and dibosons, and the corresponding expected events are referred to as $b_{i,j}$, where i refers to a region and j to a physics process respectively.
- the expected number of signal events s. In the case of the background-only hypothesis, $s = 0$.
- a set of free normalisation factors μ_j, where j refers to a SM background process or a signal. All μ_j have an initial (pre-fit) value of 1. Only SM processes with a dedicated control region (Z+jets, W+jets, multi-jets and top) have an associated normalisation factor. For the multi-bin searches, the normalisation factors are also binned, as is described in 4.8. The minor diboson background is considered as a fixed contribution to the various regions and its estimate is derived directly from Monte Carlo.
- nuisance parameters θ that parametrize the systematic uncertainties.

The expected number of events ν_i in a signal, control or validation region can then be expressed in terms of the previously defined contributions:

$$\nu_i(\mu, s_i, \mathbf{b}, \theta) \quad = \quad s_i(\theta) \cdot \mu_s + \sum_{j}^{W,Z,top,QCD} b_{i,j}(\theta) \cdot \mu_j + b_i^{VV}(\theta), \tag{4.11}$$

where i denotes the region and j the background process.

When performing hypothesis tests, the PDF of the profile likelihood function is determined in two ways: either by using the asymptotic formula and Asimov datasets, or by sampling with toy Monte Carlo pseudo-experiments. As already discussed in 4.7.1, the latter is more accurate in the case where statistics is lacking, and is therefore used in the discovery and exclusion fit, for SRs with $n_{obs} < 10$. For the rest of the SRs the asymptotic method is employed.

4.7.4 Systematic Uncertainties

Systematic uncertainties can arise from limitations in the modelling of the various processes with MC simulation, referred to as theory uncertainties, or from biases in the reconstruction of objects and measurement of their properties, the so called experimental uncertainties. Statistical fluctuations due to the limited number of data events used in the background estimation process, or the limited number of simulated events are additional sources of systematic uncertainties.

The systematic uncertainties are incorporated in the likelihood function through the probability density function $C_{Syst}(\theta^0, \theta)$where θ^0 are the nominal values around which θ can be varied when maximizing the likelihood. If ν_i is expressed in a way that places its dependence on θ only on the transfer factors, the term C_{syst} can be simplified by taking θ^0 = 0, after normalizing the individual PDFs appropriately. The nuisance parameters are considered to be independent, and therefore, C_{Syst} is given by the product of the individual PDFs $G(\theta_j^0, \theta_j)$:

$$C_{Syst}(\theta^0, \theta) = \prod_{j \in \mathrm{SU}} G(\theta_j^0, \theta_j)\,, \tag{4.12}$$

where SU is the set of systematic uncertainties considered. All the uncertainty PDFs are considered to be Gaussianly distributed. In the following, the main systematic uncertainties of the analysis and their evaluation techniques are described. I was particulary involved in the estimation of the theory uncertainties relating to the Top background and the experimental uncertainties.

Theory uncertainties

Uncertainties in the theoretical modelling of background or signal processes are estimated by comparing samples produced with different MC generators or by varying various parameters in the nominal generator. In order to be consistent with the transfer factor approach, theory uncertainties in the SR are normalised to the CR targeting the background to which they refer. In the case of multi-bin searches, the same binning as for the normalisation factors is used to calculate the relative uncertainties. All the theory uncertainties are treated as fully correlated across different regions (including bins in the multi-bin channels), but are considered to be independent per process.

The W/Z+jets modelling uncertainties are estimated by considering different merging (CKKW-L) and resummation (qsf) scales using alternative samples, PDF and strong coupling

constant (α_s) variations from the NNPDF3.0NNLO replicas [99], and variations of factorisation and renormalisation scales in the matrix element calculations. The last two are evaluated using 7 point variations, changing the renormalisation and factorisation scales by factors of 0.5 and 2, such that when one scale is increased the other is decreased, and vice-versa. The scale uncertainty is then calculated by the maximum shift of the envelope with respect to the nominal. Scale and PDF uncertainties are the dominant contributions and are typically of the order of 2-10%.

Uncertainties in the modelling of top quark pair production are estimated by comparing the nominal sample listed in Table 4.1 with alternative generators. The systematic uncertainty due to the hard-scattering process is evaluated using a comparison of the nominal sample with the sample generated with MG5_aMC@NLO interfaced to PYTHIA 8. Fragmentation and hadronization uncertainties are assessed using a comparison of the nominal sample with a sample generated with POWHEG-BOX interfaced to the HERWIG 7 package [144] package for parton showering. Initial- and final-state radiation uncertainties, as well as the variation of factorisation and renormalisation scales and the variable shower radiation uncertainty, are encapsulated in dedicated weights in the nominal sample.

Figure 4.9 shows the relative top theory uncertainties for the CRT and SR bins of the MB-C search. The uncertainties on the SRs have been normalised to the corresponding CRT ones, following the binning of μ_{Top}. It can be seen that all the uncertainty contributions are well contained within $\pm$ 1 of the nominal value. Interestingly, uncertainties related to the hard-scattering process show a dependence on the m_{eff} in CRT regions. This behaviour has been traced back to the different response of the alternative MadGraph generator, which predicts a more rapidly falling m_{eff} distribution. Given that the nominal generator overestimates the data at high m_{eff}, it is clear that the top theory uncertainties serve to partially cover the top background mismodelling.

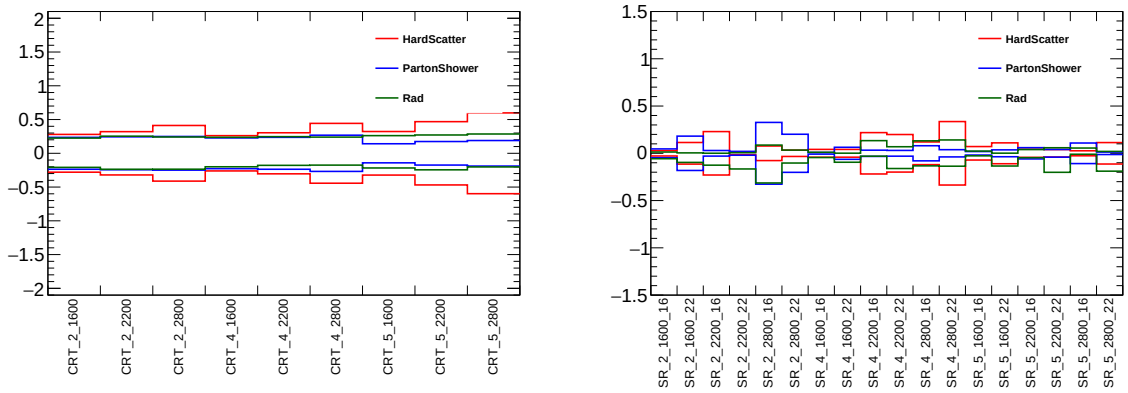

(a) (b)

FIGURE 4.9: Relative top theory uncertainties in (a) all CRT bins and (b) on the transfer factors for all SR bins of the MB-C search. Uncertainties related to the hard-scattering, fragmentation-hadronization or radiative processes are displayed in red, blue and green colour, respectively. The x-axis labels in both cases correspond to the bins of the MB search according to the folowing format: region _N_{j}^{low}_m_{eff}^{low}($E_{\text{T}}^{\text{miss}}/\sqrt{H_{\text{T}}}^{low}$). For example, SR_2_1600_16 in the MB-C search corresponds to the SR bin with N_{j}=[2,4), m_{eff}=[1600,2200), $E_{\text{T}}^{\text{miss}}/\sqrt{H_{\text{T}}}$=[16,22).

Uncertainties in diboson production due to PDF, strong coupling constant, and renormalisation and factorization scale uncertainties are estimated in a similar way as for the W/Z+jets modelling uncertainties. Renormalisation and factorisation scale uncertainties are once again

the dominant contribution, reaching typically 30%. A conservative 100% systematic is attributed to the negligible QCD background, in order to account for any uncertainties in the data driven multi-jet estimation method.

Finally, the uncertainty on the SUSY signal cross-section is calculated by varying the renormalisation and factorization scale, PDF and the strong coupling constant. The uncertainties in the generation of ISR and FSR in SUSY signal events are estimated by varying generator tunes in the simulation as well as scales used in the matrix-element generator as a function of the mass difference, Δm, between the gluino (or squark) and the $\tilde{\chi}_1^0$. For the latter contribution, since uncertainties on SUSY cross-sections already include these variations, only the impact on the distribution shape is considered (i.e. varied samples are normalised to the same yields).

Experimental uncertainties

The experimental systematics considered in this analysis include uncertainties in the Jet Energy Scale (JES) and Jet Energy Resolution (JER) [70, 145], as well as the uncertainties in the scale and resolution of the $E_{\mathrm{T}}^{\mathrm{miss}}$ (MET) [72]. All experimental systematics on physics objects are obtained via the official recommendations in the analysis software and the properties of the event are recalculated for all systematic variations that affects the kinematics. The JES uncertainties are calculated in the so-called Global reduction set with a parametrisation through 20 nuisance parameters. For the JER (MET) uncertainties the simple configuration with 8 (3) nuisance parameters is taken. Each uncertainty is calculated for each background/signal process and region (or bin) of the analysis.

Uncertainties related to the reconstruction of electrons and muons as well as the b-jet tagging/vetoing and the jet-vertex tagging (JVT) efficiency were found to have a negligible impact on the fit and where therefore not included.

Experimental systematics are treated as fully correlated across all regions (including the bins of the multi-bin channels) and all background (and signal) processes. A normalisation procedure similar to the theory uncertainties is applied; example contributions of each uncertainty of the MET and JER group on transfer factors of the MB-GGd search are shown in Figure 4.10. It can be seen that the JER uncertainties are well contained within 2-30% of the nominal value, while MET uncertainties have an even smaller contribution, usually less than 10%. In general, this behaviour is seen also for the other transfer factors and the rest of the MB searches, with an exception of a few tight-cut bins, where higher contributions are sometimes observed due to statistical fluctuations. JES uncertainties in most cases also amount to less than 30%.

Statistics-related uncertainties

The statistical limitations of the data samples in the control regions affect the background estimation process. Uncertainties due to the CR data statistics are incorporated in the uncertainty on the normalisation factor and are referred to as *CR statistics*. Uncertainties related to the data driven procedure applied to correct for the mismatch between CRY and VRZ, described in 4.6.1, are also included in this systematics category.

Uncertainties due to the limited statistics in the MC samples are also included in the fit and referred to as *MC statistics*. They are treated as fully uncorrelated across the different regions (or bins) and processes. Finally, the uncertainty on the integrated luminosity of the Run2, as estimated by the ATLAS collaboration, is included in each search as a constant.

Figure 4.11 shows a breakdown of the largest systematic uncertainty groups for the four

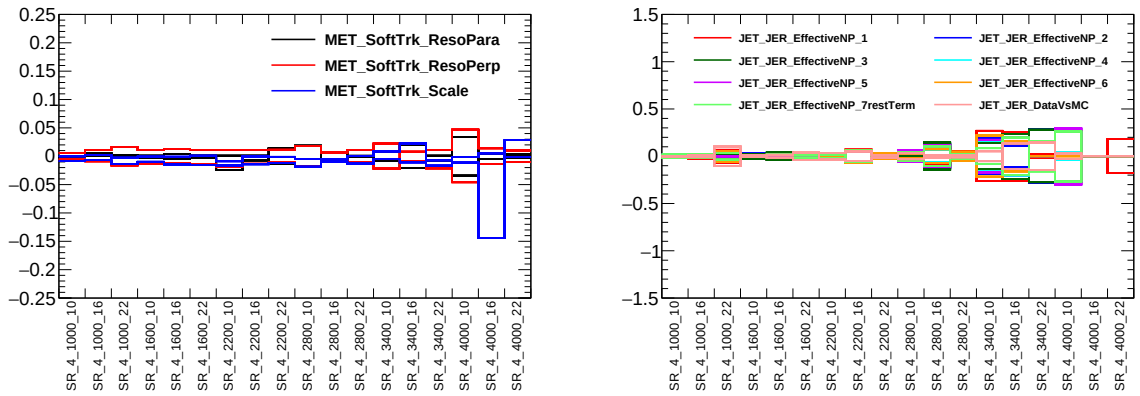

(a) (b)

FIGURE 4.10: Breakdown of the contributions of the (a) MET uncertainties on the Z+jets background transfer factor and (b) JER uncertainties on the W+jets transfer factor, for all SR bins of the MB-GGd search. The x-axis labels in both cases correspond to the bins of the MB search according to the folowing format: region _N_{j}^{low}_m_{eff}^{low}($E_{\mathrm{T}}^{\mathrm{miss}}/\sqrt{H_{\mathrm{T}}}^{low}$). For example, SR_4_1600_16 in the MB-GGd search corresponds to the SR bin with $N_{\mathrm{j}} \geq 4$, m_{eff}=[1600,2200), $E_{\mathrm{T}}^{\mathrm{miss}}/\sqrt{H_{\mathrm{T}}}$=[16,22).

multi-bin searches, evaluated after performing the background-only fit. The overall background uncertainties range from 5% in most of the MB-SSd regions to 60% in one of the tightest MB-GGd bins.

4.8 Multi-bin fit studies

This section presents my work on the optimization of the multi-bin fit. Starting from an estimation of the improvements brought on by the multi-bin strategy, I will be discussing studies on the optimization of the binning and the background normalisation process of the MB fit.

4.8.1 Multi-bin fit to single-bin comparison

The multi-bin fit is a technique used to improve the exclusion reach of the search. Therefore, the additional power it brings over a single-bin configuration can be established in the model-dependent fit [6]. The results of the model-dependent fit, are always presented in the 2-dimensional plane of the free mass parameters for each simplified model. The upper limit on the signal strength is determined by performing a scan. The value of μ_s for which the expected $\mathrm{CL_s}$ value is equal to 0.05 corresponds to the 95% expected upper limit. After the SR with the most powerful upper limit on μ_s has been selected, the $\mathrm{CL_s}$ corresponding to the nominal signal strength (μ_s = 1) is calculated for each mass point. An interpolation amongst points that have a limit at 95% $\mathrm{CL_s}$ is performed, in order to determine a 2-dimensional exclusion surface. Models with masses that are included in the exclusion surface are expected to be excluded at 95% confidence level.

Figure 4.12 demonstrates the model-dependent fit results in (a) the free $\tilde{q} - \tilde{\chi}_1^0$ mass plane of model 4.1a, (b) the free $\tilde{g} - \tilde{\chi}_1^0$ mass plane of model 4.1c and (c) the $\tilde{g} - \tilde{\chi}_1^0$ mass plane of models of the 4.1d type, with $m(\tilde{\chi}_1^{\pm})$ taken to be equal to $(m(\tilde{g}) + m(\tilde{\chi}_1^0))/2$. The multi-bin searches are compared against the single-bin SRs, which are constructed as inclusive versions of their MB counter-parts. For each signal point, the SR (or multi-bin search) with the most

[6] The CRs are un-blinded in this and the following studies.

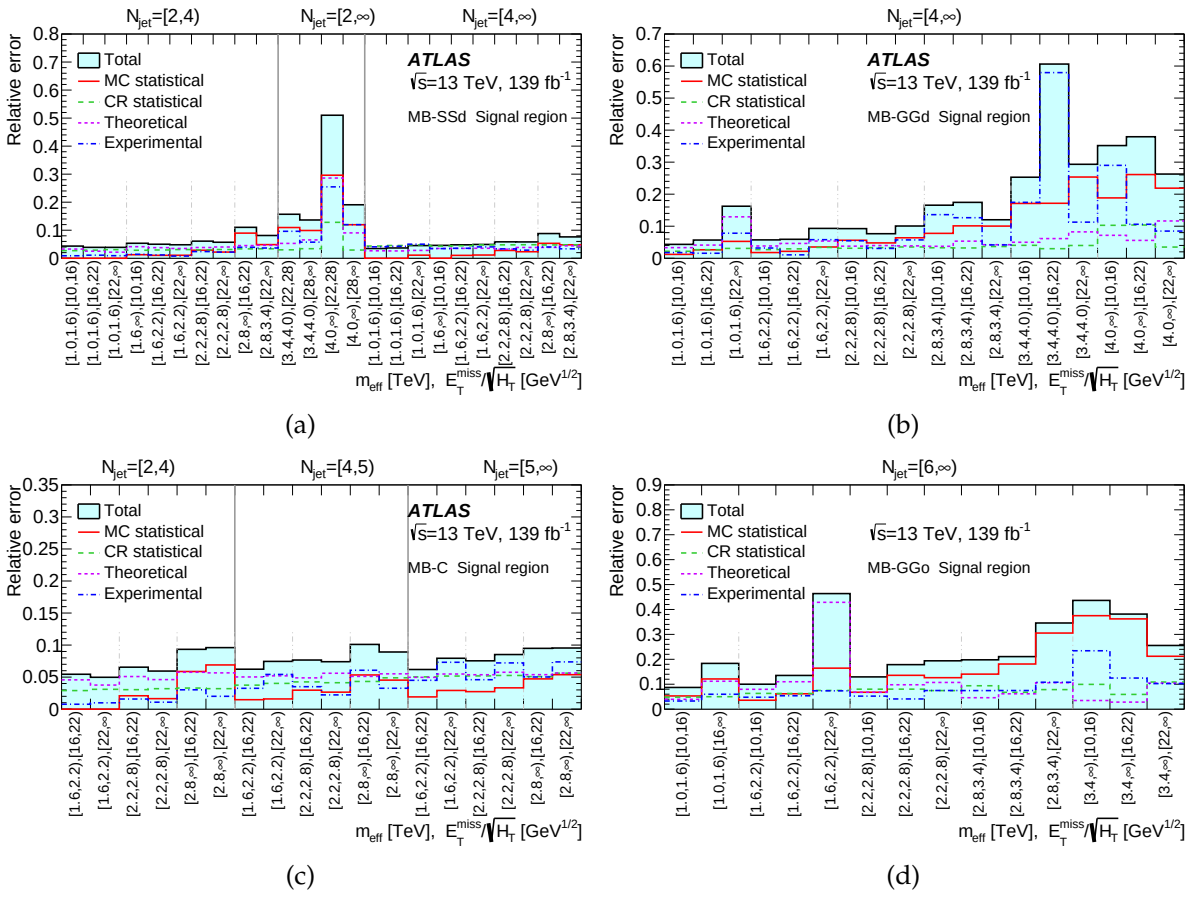

FIGURE 4.11: Breakdown of the largest systematic uncertainties in the background estimates for the (a) MB-SSd, (b) MB-GGd, (c) MB-C and (d) MB-GGo SRs from the multi-bin search. The individual uncertainties can be correlated, such that the total background uncertainty is not necessarily their sum in quadrature.

powerful expected upper limit on the signal strength is selected in both cases. The ratio of the signal strength upper limit between the two strategies is shown in the colour map. The benefit of using a multi-bin configuration is evident in the entire mass plane in both squark and the two gluino model types, where an improvement on the expected upper limit typically between 30% and 70% is observed. This enhancement translates directly to a reduction of the lower limit on the expected production cross-section of the involved primary SUSY particles.

Additionally, the exclusion range of the analysis assuming the nominal production cross-section is improved, as seen by comparing the solid (MB searches) to the dashed (single-bin SRs) lines. In particular, excluded squark masses are extended by up to 100 GeV, while in the case of gluinos, a ~ 50 GeV improvement is observed in both direct and one-step scenarios.

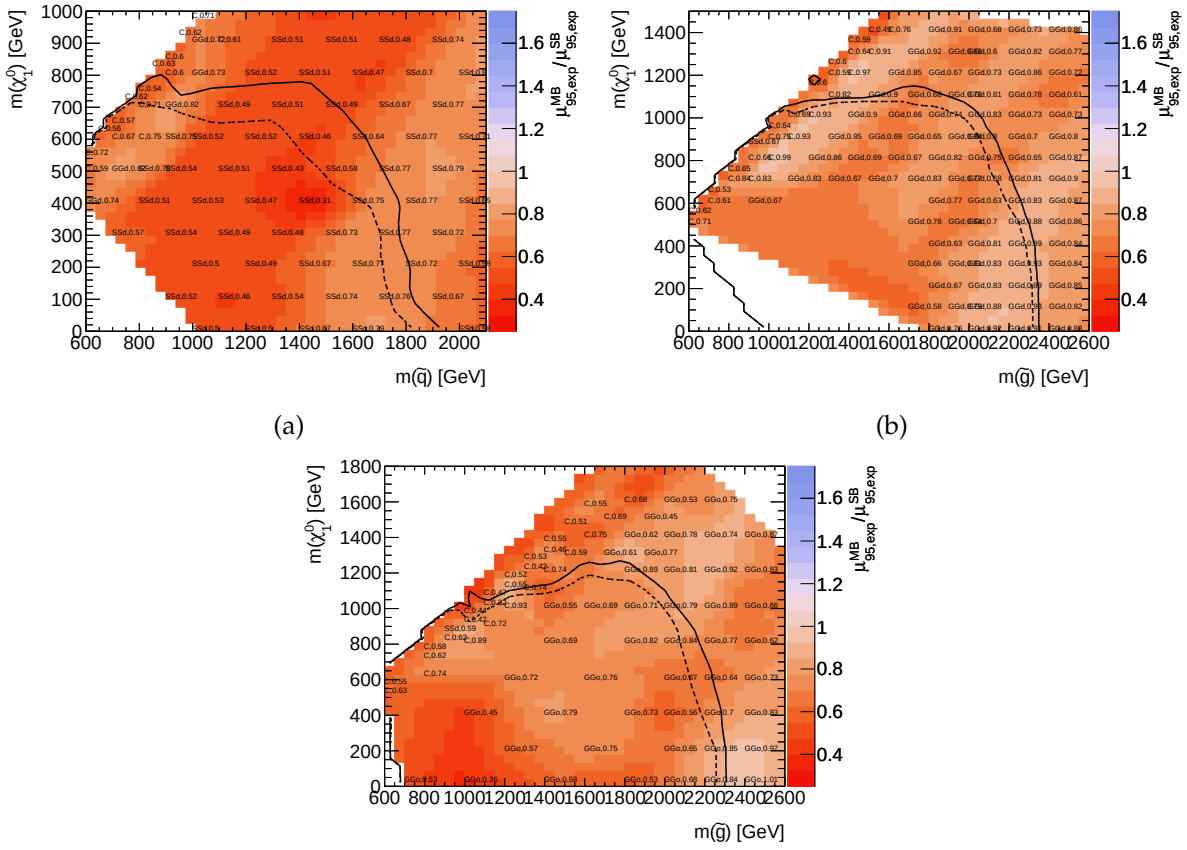

FIGURE 4.12: Ratio of expected upper limits on the signal strength between the multi-bin (MB) searches and the single-bin (SB) signal regions, ($\mu^{95,exp}_{MB}/\mu^{95,exp}_{SB}$) for models with (a) squark-pair production followed by direct decays to quarks and the LSP, and (b) gluino-pair decays with $\tilde{g} \to qq\tilde{\chi}^0_1$ and (c) gluino-pair one-step decays through $\tilde{g} \to \tilde{\chi}^\pm_1 qW \to qqq\tilde{\chi}^0_1$, with $m(\tilde{\chi}^\pm_1) = (m(\tilde{g}) + m(\tilde{\chi}^0_1))/2$. The full (dashed) line shows the expected limits on the s-particle masses assuming the nominal production cross-section for the multi-bin (single-bin) searches. For each signal point, the name of the best analysis is shown, along with the numerical value of the upper limit ratio.

4.8.2 Bin width optimization

In order to motivate the binning choice defined in 4.5.3, alternative configurations with a varied bin width were considered. The default m_{eff} binning of 600 GeV was tested against two settings, one with a bin width of 400 GeV and another with 800 GeV. The figure of merit to evaluate the comparison is once again the ratio of the 95% expected upper limit on the

signal strength between the nominal and alternative scenarios. The results are presented as a function of the $\tilde{q} - \tilde{\chi}_1^0$ masses for squark-pair production models with squark direct decays, or the $\tilde{g} - \tilde{\chi}_1^0$ masses for gluino-pair production models with gluino direct decays, as shown in Figure 4.13. For simplicity, experimental and theory uncertainties were assigned a flat contribution of 10% each.

As expected, the exclusion strength is degraded for larger binning and improved for lower binning, as the signal-over-background shape is more coarsely (finely) sampled. However, the relative gain when moving to a binning of 400 GeV is small, around 5%. On the other hand, the degradation of the performance for the 800 GeV setting is larger, reaching a 20% increase of the upper limit in a large fraction of the phase-space. The merits of moving to small bin size are evident. The nominal choice of 600 GeV has been chosen over smaller values, given the small relative improvement, the added complexity in the fit and the statistical limitations in the background estimation.

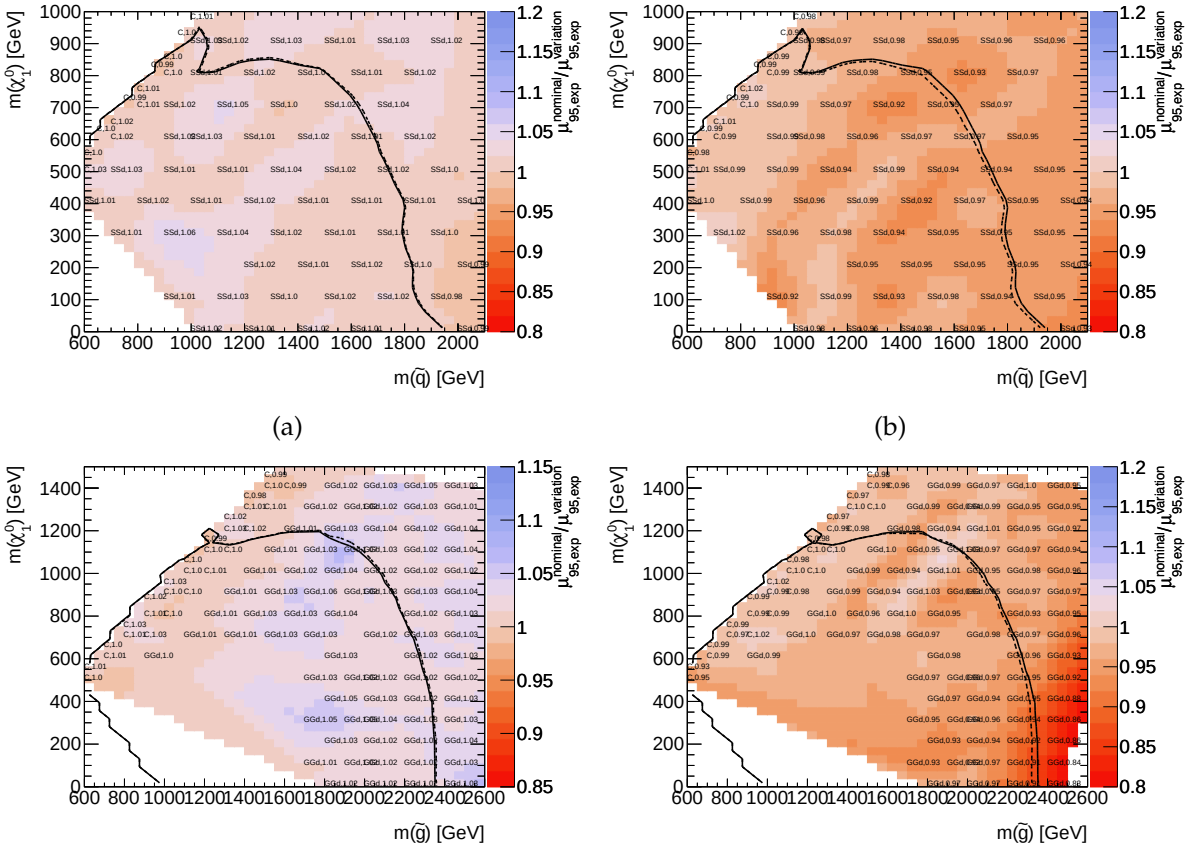

FIGURE 4.13: Ratio of expected upper limits on the signal strength for the squarks (a,b) and gluinos (c,d) pair production signal grids with direct decays to quarks and LSP as a function of the s-particle masses for m_{eff} bin width equal to 400 GeV (left) and 800 GeV (right). The full (dashed) line show the expected limits on the s-particle masses assuming the nominal production cross-section for the nominal (alternative) setting. For each signal point, the name of the best analysis is shown, along with the numerical value of the upper limit ratio.

4.8.3 Optimization of background normalisation

For the multi-bin channels, the normalisation strategy of the background prediction is not necessarily straightforward. The question whether to normalise the individual signal regions (or bins) separately or group them with the use of a single factor naturally arises. In the

following, I will be demonstrating my work on defining the best normalisation strategy for the multi-bin fit of the 0-lepton analysis with the use of a case study, the MB-SSd regions. The results of the following study have been extracted from the background-only fit.

Initially, each bin was normalised with a dedicated factor. Figure 4.14a shows the normalisation factors for the Z+jets, W+jets, Top and multi-jet processes that are extracted from the ML method for each SR bin of the MB-SSd search, in the background-only fit. For the V+jets backgrounds, the normalisation factors tend to be close to 1, indicating an accurate prediction of the data by the MC simulation. A similar trend is observed for the multi-jet background, where, since the estimation is done through a data-driven method, an arbitrary weight is applied prior to the fit to normalise the prediction to the data. For the top background, the normalisation factors progressively deviate from unity when moving to tighter m_{eff} cuts. The simulation can overestimate the measurements by more than 50% at the tightest region of the search phase-space. This behaviour is observed for the two jet multiplicity sets of regions, and is consistent with the mismodeling of the Top background, seen in Figure A.4c.

As a part of the validation procedure for the multi-bin fit, the deviation of the nominal value and error of the nuisance parameters from their original values, i.e. their pulling and profiling, have been checked, as shown in Figure 4.14b. As already mentioned, the definition of the nuisance parameters is simplified by setting the nominal value and its error to zero and ± 1, respectively. After the fit, all nuisance parameters largely agree with their original values, and no pulls are observed. Figure 4.14c presents the deviation of the VR estimated yields from the observation after the fit, in terms of significance. A good approximation for calculating the significance is given by the profile likelihood method [146]:

$$Z = \begin{cases} +\sqrt{2(n\ln\left[\frac{n(b^2+\sigma^2)}{b^2+n\sigma^2}\right] - \frac{b^2}{\sigma^2}\ln\left[1+\frac{\sigma^2(n-b)}{b(b+\sigma^2)}\right])} & \text{if n} \geq b \\ -\sqrt{2(n\ln\left[\frac{n(b^2+\sigma^2)}{b^2+n\sigma^2}\right] - \frac{b^2}{\sigma^2}\ln\left[1+\frac{\sigma^2(n-b)}{b(b+\sigma^2)}\right])} & \text{if n} < b \end{cases} \tag{4.13}$$

where Z is the significance for observing n events given a prediction of $b \pm \sigma$ events. In most regions, the significance is contained within $\pm 2.5\sigma$, indicating that the background estimation procedure is well established without residual mismodeling.

While the assignment of a separate normalisation factor for each bin results in a good prediction of the data and a stable fit, there are disadvantages from employing such a configuration. First, the introduction of this large number of normalisation factors can result in an over-constrained fit, which might not be entirely physical. Secondly, each normalisation factor is associated with an uncertainty arising from the statistical limitations of the region in which it is computed. The use of a fine binning for the definition of μ factors can result in large associated uncertainties, especially in the bins where tight selection criteria are applied. This can in tern reduce the exclusion strength of the multi-bin analysis.

In order to achieve a less conservative result, one can imagine the opposite extreme, where a single normalisation factor is used for each background process. Results from a background-only fit with this configuration are shown in Figure 4.15. In this case, validation regions, especially the ones related to W+jets and Top processes, show large pulls, reaching a 5σ significance. Additionally, the 0-lepton validation regions also display significant deviations of the observation from the prediction. This behaviour indicates a pathology of the background estimation, where simulation discrepancies from the data are not accounted for in the normalisation process. This is further confirmed by looking at the fitted nuisance parameters, presented in Figure 4.15a, where many display large pulls and profiling in an attempt to cover the mismodelling. In order to allow for more freedom in the fit, a more detailed parametrization

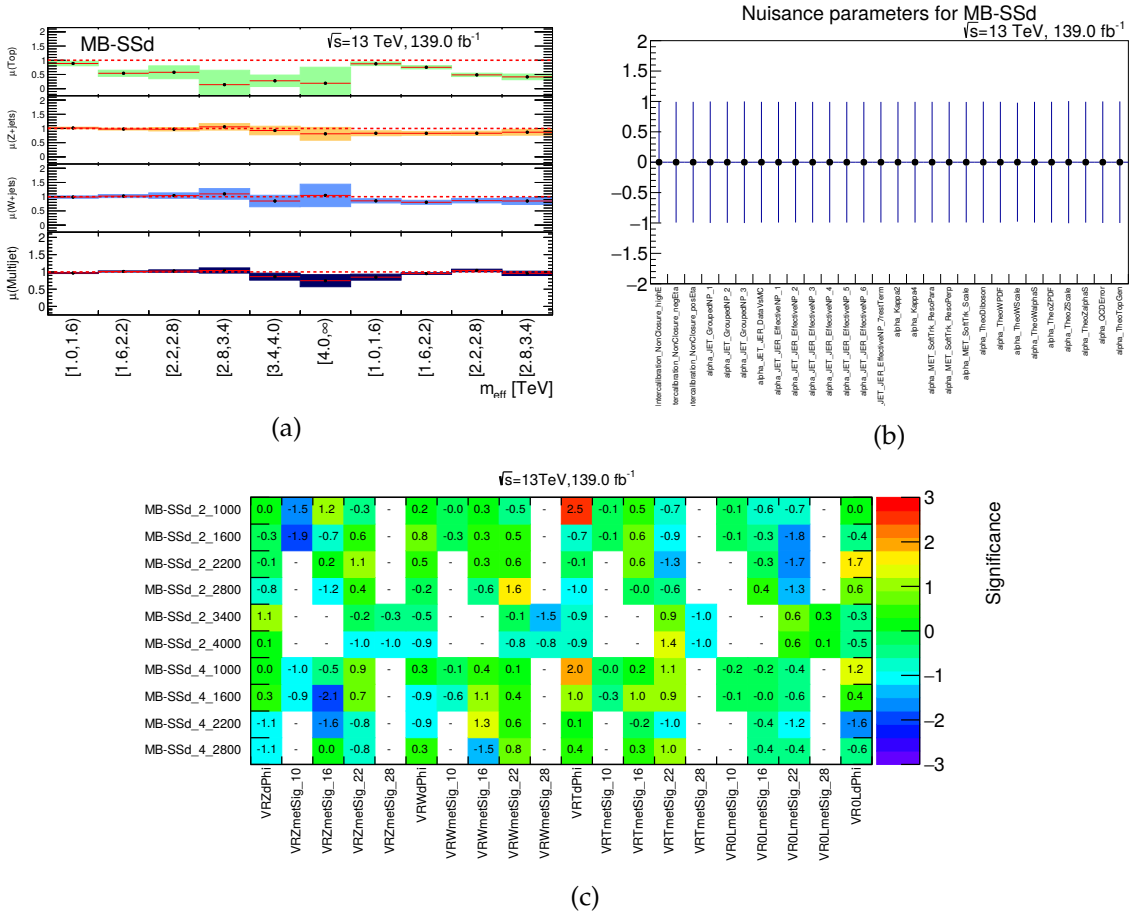

FIGURE 4.14: (a) Fitted normalisation factors per process as a function of the signal region considered in the MB-SSd search. The dashed horizontal lines at 1 correspond to pure MC estimates with the vertical size of the coloured regions corresponding to the total uncertainty in each background source. (b) The fitted nuisance parameters from the background-only fit for the MB-SSd search (c) Significance, as defined in Eq. 4.13, in the validation regions of the MB-SSd search. The y-axis labels in Figure (c) correspond to the bins of the MB search according to the folowing format: region _N_{j}^{low}_m_{eff}^{low}. For example, SR_2_1600 in the MB-SSs search corresponds to the SR bin with N_{j}=[2,4), m_{eff}=[1600,2200). One normalisation factor per CR bin is considered in the background-only fit.

of the JES/JER uncertainties (with 22 instead of 6 NPs) has been employed in this case.

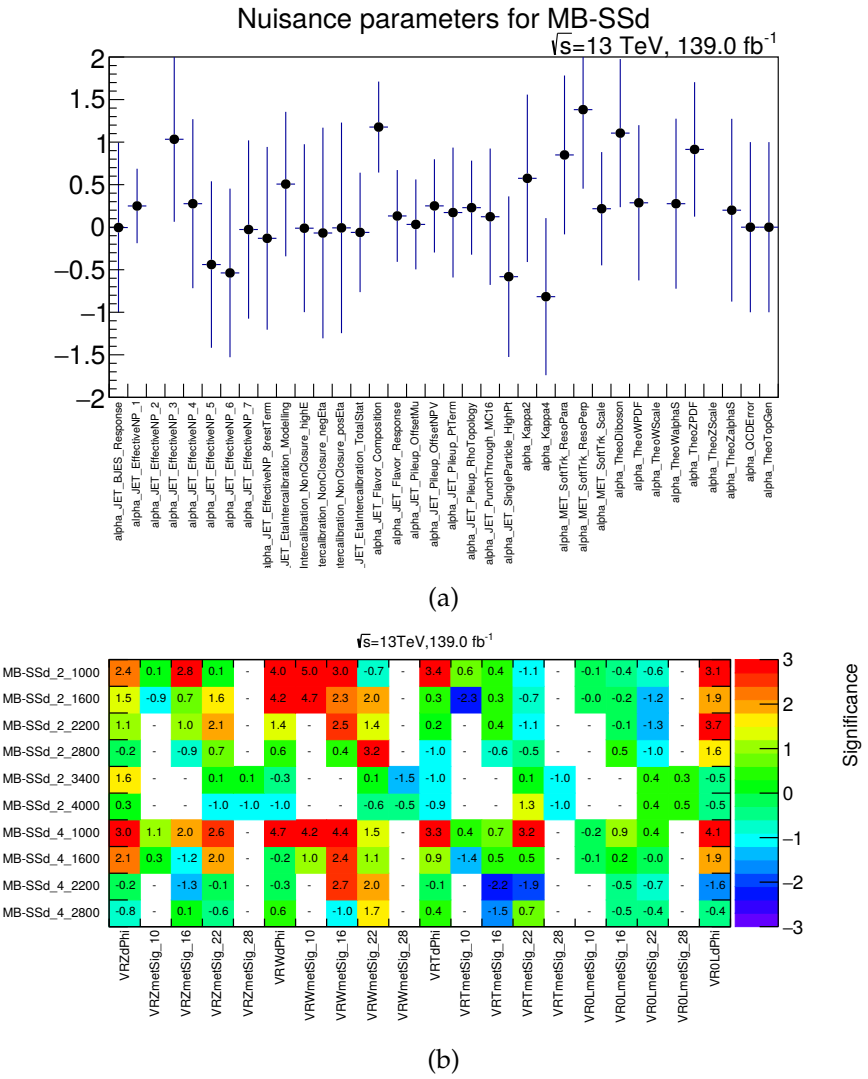

(a)

(b)

FIGURE 4.15: (a) The fitted nuisance parameters from the background-only fit for the MB-SSd search and (b) the significance, as defined in Eq. 4.13, in the validation regions of the MB-SSd search. The y-axis labels in Figure (b) correspond to the bins of the MB search according to the folowing format: region $\_N_{\mathrm{j}}^{low}\_m_{\mathrm{eff}}^{low}$. For example, SR_2_1600 in the MB-SSs search corresponds to the SR bin with N_{j}=[2,4), m_{eff}=[1600,2200). One normalisation factor per background process is considered in the background-only fit.

It is clear that there are significant discrepancies between the data and the MC prediction that cannot be corrected for with only one normalisation factor for each background process. An intermediate approach is tried next, with one μ for each set of bins with the same N_{j} requirements. This is well motivated by the discrepancies between data and MC seen in the pre-fit N_{j} distributions in CRY, CRW and CRT, shown in Figure 4.6. Figure 4.16 shows, on the top, the fitted nuisance parameters from the background-only fit and, on the bottom, the fitted significance in each validation region. Most nuisance parameters are now in good agreement with their original values, except the theory uncertainties relating to the radiative effects and hard-scattering process of the Top background, which are profiled and pulled to lower values. Additionally, most validation regions now exhibit a good agreement between data and MC, except for VRT regions, were in many cases, a large significance is observed. This behaviour seems to indicate that, while the minor mismodeling of the V+jets backgrounds is accounted

for in this normalisation scheme, a residual mismodeling of the Top background persists and cannot be corrected for with one μ per N_{j}.

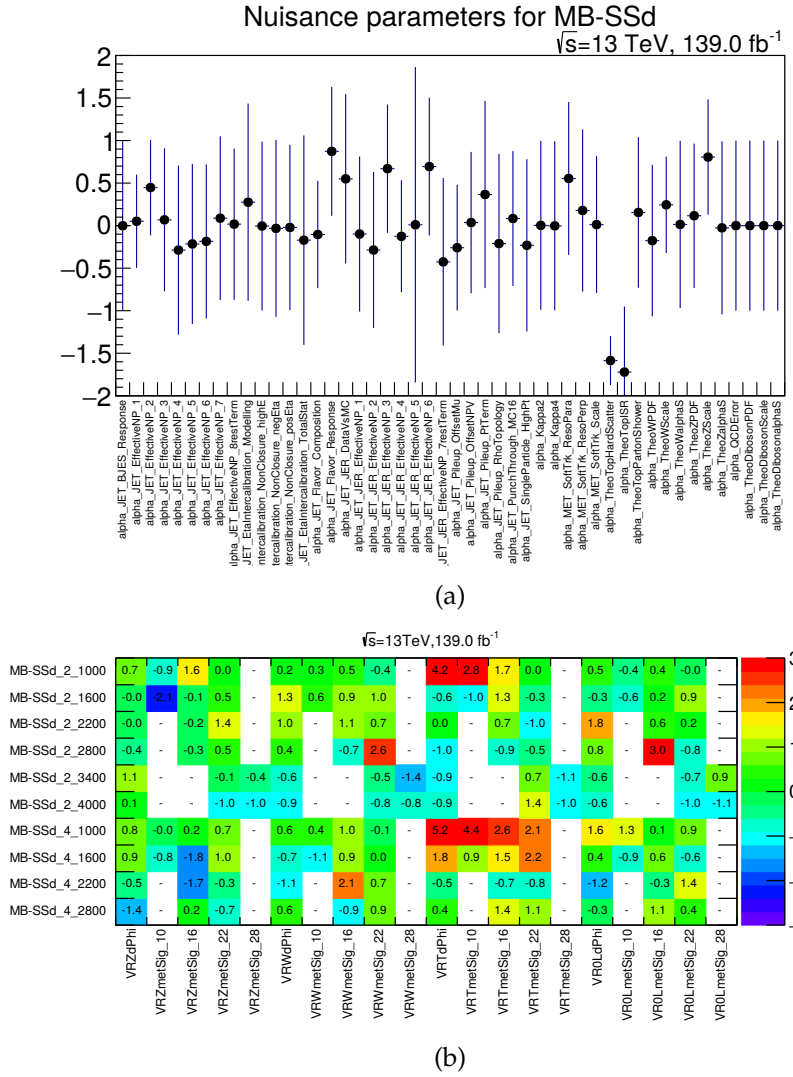

(a)

(b)

FIGURE 4.16: (a) The fitted nuisance parameters from the background-only fit for the MB-SSd search and (b) the significance, as defined in Eq. 4.13, in the validation regions of the MB-SSd search. The y-axis labels in Figure (b) correspond to the bins of the MB search according to the folowing format: region _N_{j}^{low}_m_{eff}^{low}. For example, SR_2_1600 in the MB-SSs search corresponds to the SR bin with N_{j}=[2,4), m_{eff}=[1600,2200). Bins with the same jet multiplicity requirements are normalised with the same factor in the background-only fit.

Taking into account the aforementioned results, the following strategy has been decided: for the major V+jets backgrounds, where a small discrepancy between data and simulation was observed with increasing jet multiplicity, the normalisation factors are only binned in jet multiplicity, $\mu_{V+jets,N_{\text{j}}}$. For the top backgrounds, where there is a significant mismodeling in the dedicated control regions, a normalisation factor is assigned to each CR bin, $\mu_{top,(N_{\text{j}},m_{\text{eff}})}$. Finally, the same strategy as for the Top background is applied to the QCD background, in order to account for any possible mismodeling of the data-driven method.

4.9 Results

In this section, the results that I have obtained from the statistical treatment of the data and simulation samples will be discussed. An added focus is given to the validation of the

background estimation procedure and the robustness of the fit, and in particular for the MB regions. Additionally, I have performed the model-independent interpretation of the analysis with the remaining two searches, the BDT and the single-bin, which will be also discussed.

4.9.1 Background-only Fit

As a first step, the background-only fit was performed for all the channels of the analysis, in order to gain confidence in the background estimation procedure.

Figure 4.17 shows the normalisation factors for the Z+jets, W+jets and Top processes that are extracted from the ML method for each search. The multi-jet normalisation factors are omitted in the plot but are also calculated and included in the fit. As already mentioned in 4.8.3, in the multi-bin searches, the normalisation factors for the Z/W+jets processes reflect the one-dimensional binning of the search in jet multiplicity, while the Top and multi-jet backgrounds follow the two-dimensional CR binning in N_{j} and m_{eff}. The former configuration was chosen to account for the light overestimation of those backgrounds by the simulation with increasing N_{j}. The fit adjusts these normalisation factors to account for the mismodeling. The largest discrepancy between data and MC estimate was observed for the Top related processes with increasing m_{eff}. In that case, the simulation can overestimate the measurements by more than 50% at the tightest region of the search phase-space, and for this reason, each CR has a dedicated normalisation factor.

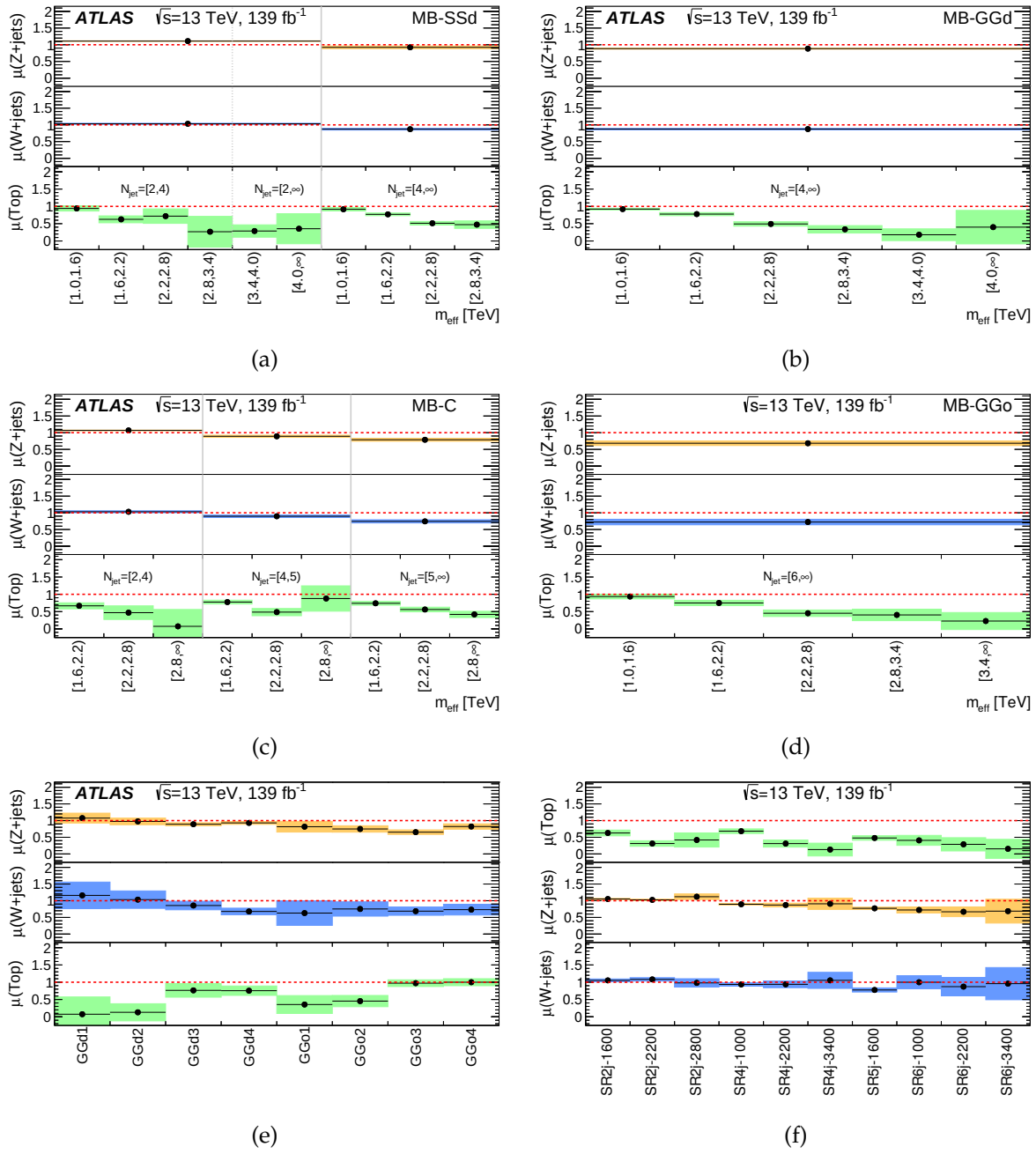

(a) (b) (c) (d) (e) (f)

FIGURE 4.17: Fitted normalisation factors per process as a function of the signal region considered in the (a) MB-SSd, (b) MB-GGd, (c) MB-C regions (d) MB-GGo regions from the multi-bin search, and regions from (e) the BDT (f) the single-bin search. The dashed horizontal lines at 1 correspond to pure MC estimates with the vertical size of the coloured regions corresponding to the total uncertainty in each background source.

Example inclusive distributions of the p_{T} of the leading jet, the $E_{\mathrm{T}}^{\mathrm{miss}}$ and the m_{eff} of the event for various control/validation regions of the multi-bin search can be seen in Figures 4.18 and 4.19. On the left-hand column of the plot, the MC raw yields before the fit are shown, normalised only to the total integrated luminosity times cross-section, while on the right hand side, the yields of SM backgrounds after the background-only fit are displayed, where the normalisation procedure has been applied. All systematic uncertainties are included. The merits of the normalisation procedure are evident when comparing the bottom pads between the pre-fit to the post-fit distributions that show the data to SM ratio; discrepancies between

the MC prediction and the data are corrected for and their ratio is in all cases consistent with unity. This beneficial effect is observed not only in the binning variables, but in other key variables of the analysis, such as the leading jet p_{T} and the $E_{\mathrm{T}}^{\mathrm{miss}}$. In addition, the distributions after the background-only fit remain smooth, indicating that the boundary regions between bins are well modelled.

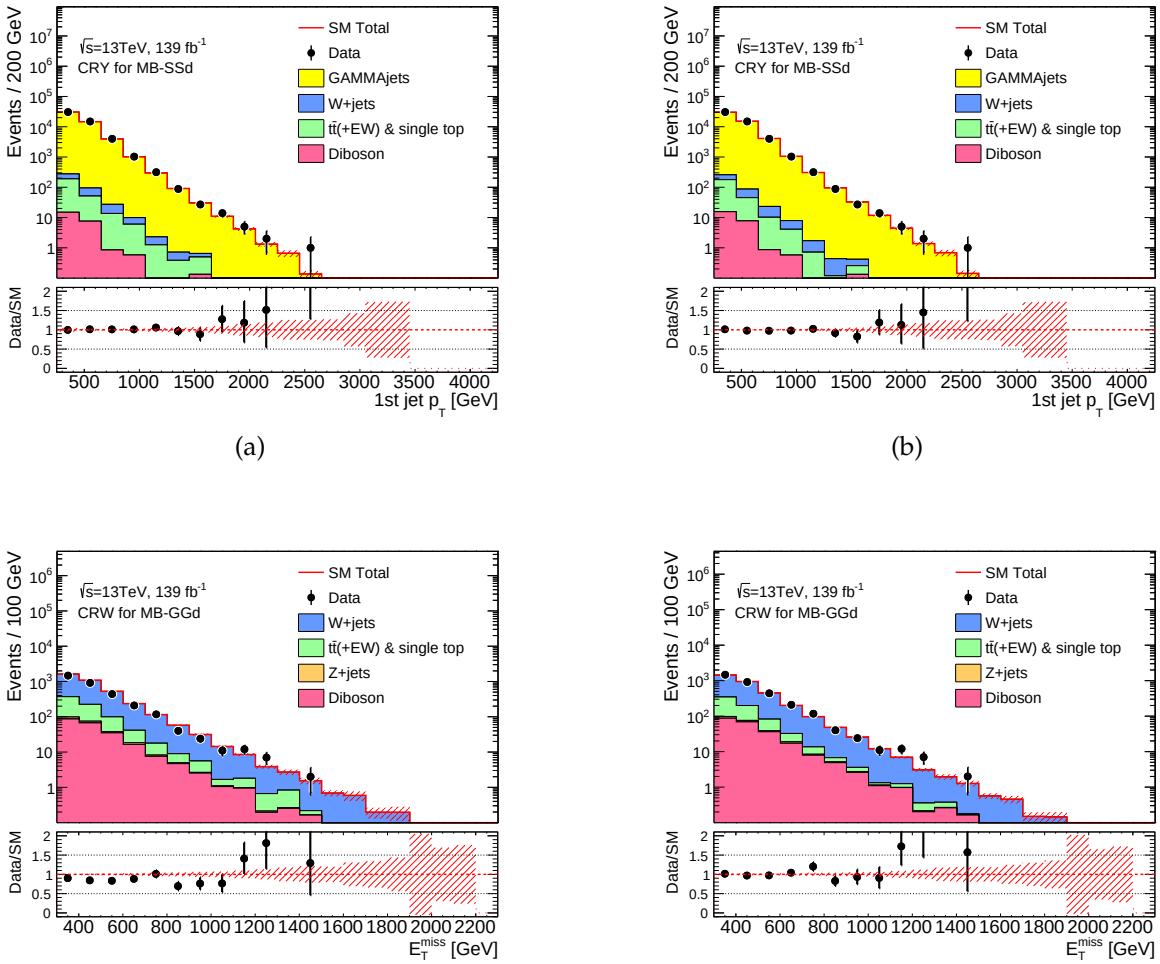

FIGURE 4.18: Observed distributions of (a,b) the leading jet p_{T} and (c,d) the $E_{\mathrm{T}}^{\mathrm{miss}}$, for events passing the selection criteria for any of the (a,b) CRY bins of MB-SSd or (c,d) CRW bins of MB-GGd. Plots on the left-hand side, (a,c), show the raw MC background predictions normalised to the cross-section times integrated luminosity, while, on the right-hand side, the histograms are normalised by the background-only fit. The hatched (red) error bands indicate combined experimental, theoretical and MC statistical uncertainties, with the experimental and theoretical uncertainties calculated using the coarser CR binning used in the fit rather than the finer binning used in the histograms. The last bin includes overflow events.

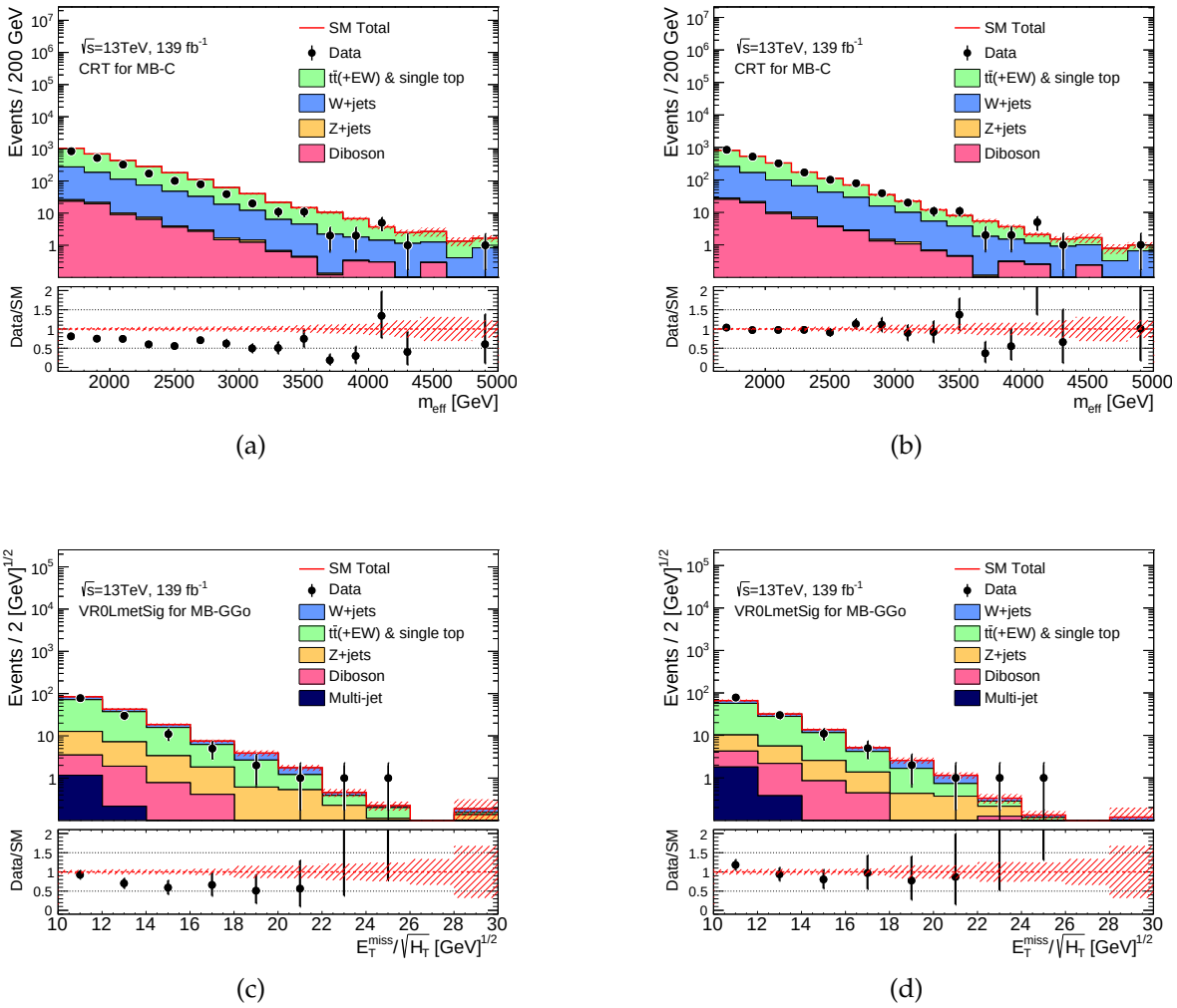

FIGURE 4.19: Observed distributions of (a,b) the m_{eff} and (c,d) the $E_{\text{T}}^{\text{miss}}/\sqrt{H_{\text{T}}}$, for events passing the selection criteria for any of the (a,b) CRT bins of MB-C or (c,d) VR0LmetSig bins of MB-GGo. Plots on the left-hand side, (a,c), show the raw MC background predictions normalised to the cross-section times integrated luminosity, while, on the right-hand side, the histograms are normalised by the background-only fit. The hatched (red) error bands indicate combined experimental, theoretical and MC statistical uncertainties, with the experimental and theoretical uncertainties calculated using the coarser CR binning used in the fit rather than the finer binning used in the histograms. The last bin includes overflow events.

As already described in 4.6.2, the integrity of the background estimation procedure is ensured in the validation regions. These regions do not have assigned free parameters in the fit and the individual background contributions are calculated in exactly the same way as in the signal regions, through the transfer factor approach. The compatibility between the fitted simulation yield and the observed data is quantified through the statistical significance. Figure 4.20 shows the significance, as computed in Eq. 4.13, for the validation regions of the four multi-bin searches. In all cases, it is centred at zero and is largely contained within 2.5σ, indicating a good quality of the background prediction. The significance distribution of the subcategory of validation regions in a 0-lepton environment (VR0LdPhi and VR0LmetSig) are superimposed for comparison and a similar trend is observed. It should be stressed that only the 0-lepton set of VRs are orthogonal to each other and to the CRs.

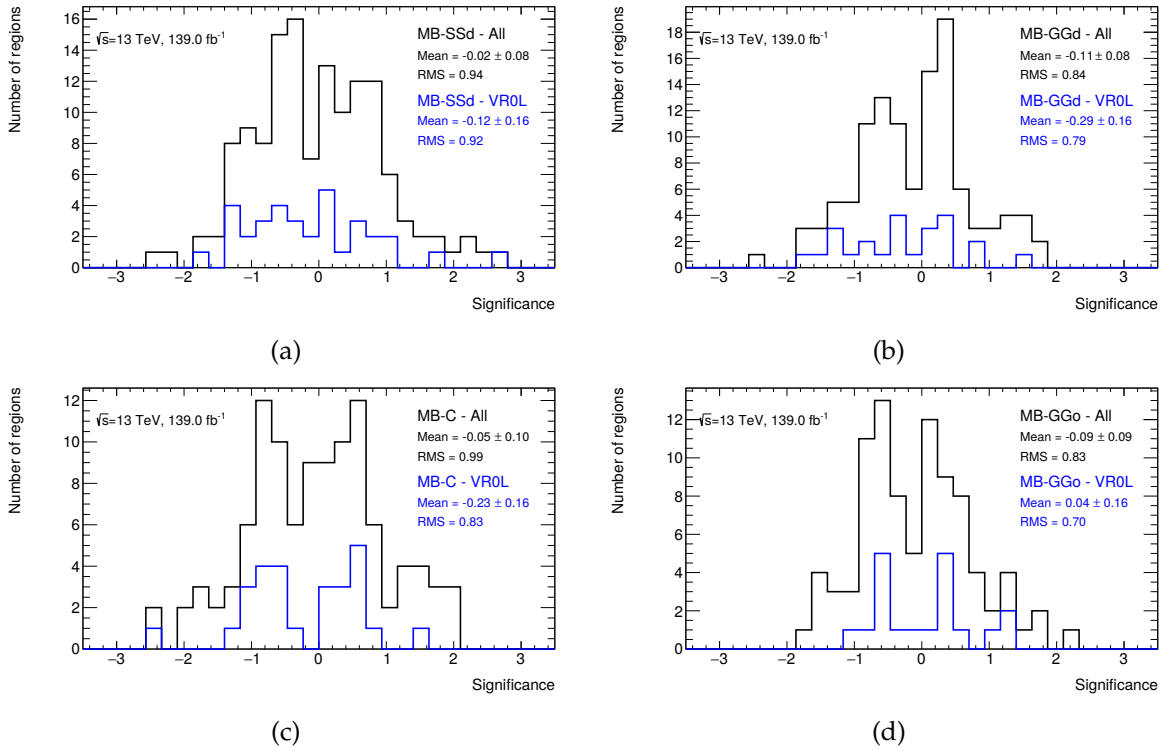

FIGURE 4.20: Distribution of the significance, as computed in Eq. 4.13, in the validation regions of (a) MB-SSd, (b) MB-GGd (c) MB-C and (d) MB-GGo channels. All validation regions are included in the distribution shown in black, while the distribution in blue includes only the subgroup of 0-lepton validation regions.

As a part of the validation procedure for the multi-bin fit, the profiling and pulling of the nuisance parameters has been checked. Figure 4.21 shows the fitted nuisance parameters for the four multi-bin channels. In general, the nuisance parameters after the fit are compatible with their pre-fit values, with only few cases of light profiling and pulling. The background theory uncertainties are of particular interest, since their small observed profiling corresponds to an attempt of the fit to account for a residual mismodeling of the equivalent backgrounds, that has not been corrected for with the normalisation factors.

Figure 4.22 shows the correlation matrix of the likelihood parameters after the fit has been performed for the MB-SSd. For simplicity, only parameter pairs with a high absolute correlation, above 0.3, are shown. Interestingly, a large correlation is observed between the normalisation factors of the various background procedures. While these factors are, a priori, largely independent, they correlate to each other through the experimental uncertainties, which are treated as fully correlated between regions and background processes.

Distributions of m_{eff} and $E_{\text{T}}^{\text{miss}}/\sqrt{H_{\text{T}}}$ for events passing the selection criteria for any of the bins in the (a) MB-SSd, (b) MB-GGd,(c) MB-C or (d) MB-GGo signal regions are shown in Figures 4.23 and 4.24, respectively. The MC samples are normalised using the background-only fit described in section 4.7. Example SUSY signals from simplified models are superimposed for comparison. In each search, a model in which the expected sensitivity is high is chosen. In general, a good agreement between data and background distributions is seen, within uncertainties.

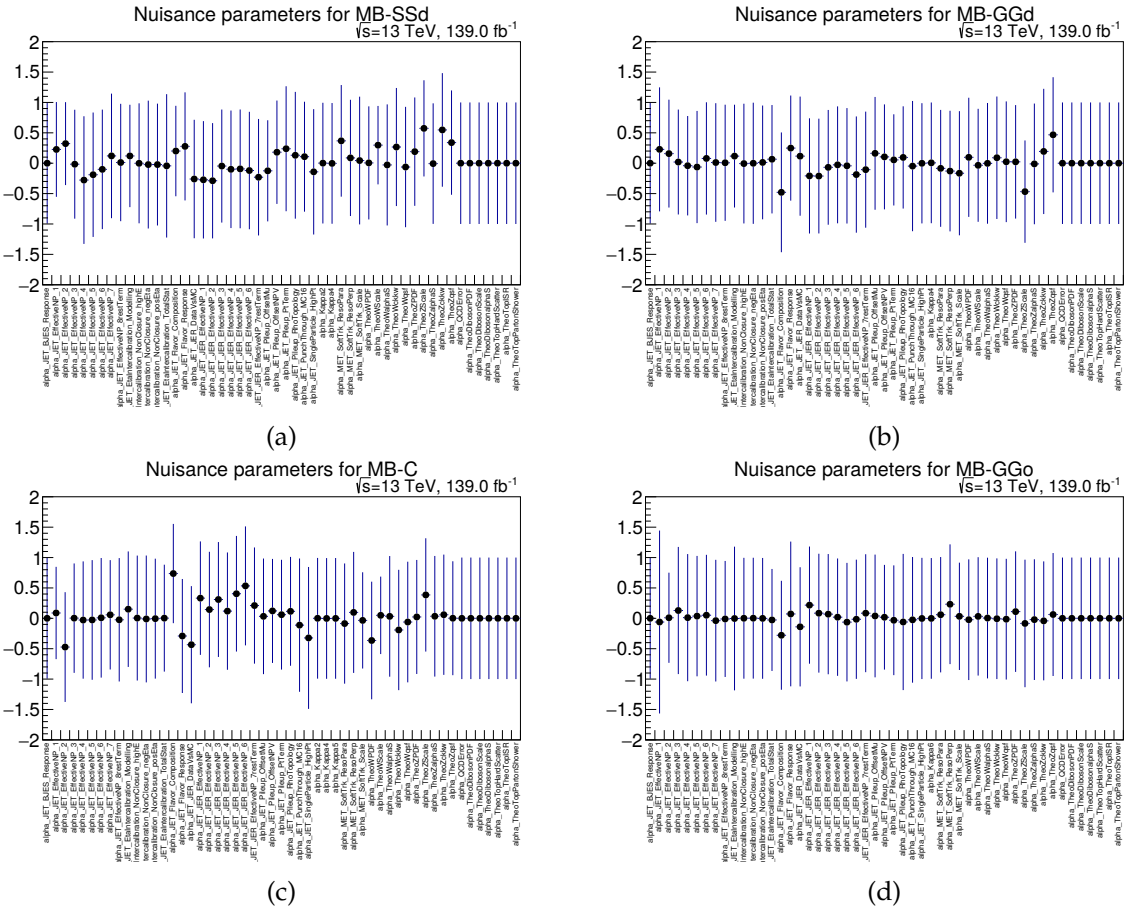

FIGURE 4.21: The fitted nuisance parameters from the background-only fit for the (a) MB-SSd, (b) MB-GGd, (c) MB-C regions (d) MB-GGo regions from the multi-bin search.

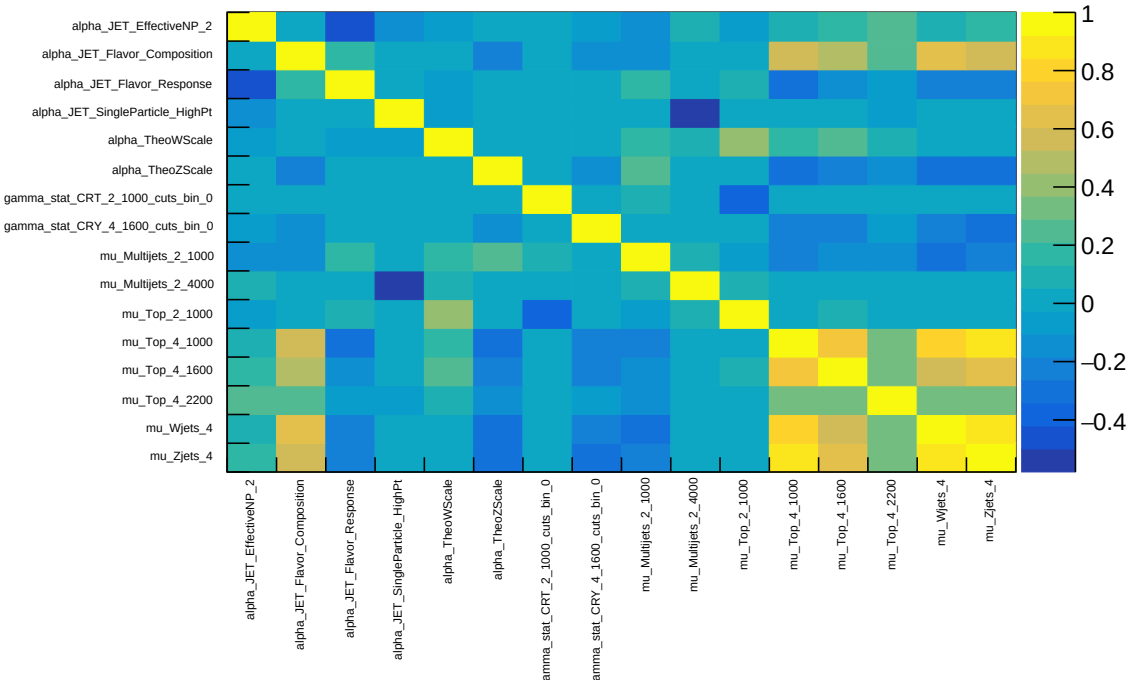

FIGURE 4.22: Fit parameter correlation matrix after fit for the MB-SSd analysis. Nuisance parameters for theoretical and experimental uncertainties are denoted a *alpha_uncertainty*, while parameters starting with *gamma* or *mu* are used to parametrize MC statistical or normalisation factor errors, respectively. Only parameter pairs with an absolute correlation above 0.3 are presented.

The data-to-MC comparison is summarized in Figure 4.25, where the observed and expected yields in each SR, along with the individual background component yields, are presented for all the searches of the analysis. The significance, estimated in the same way as in the VRs, is used to quantify the importance of any deviation from the prediction. In the majority of regions, it is found to be within $\pm$ 2σ. The largest value of 2.4σ is observed for a bin of the MB-GGd channel, but, given the absence of an excess in neighbouring bins as well as in the model independent region that covers the same phase-space, this deviation has been attributed to a statistical fluctuation. In summary, no significant excess over the SM prediction is observed, and therefore, the interpretation of the results proceeds in the form of limit-setting.

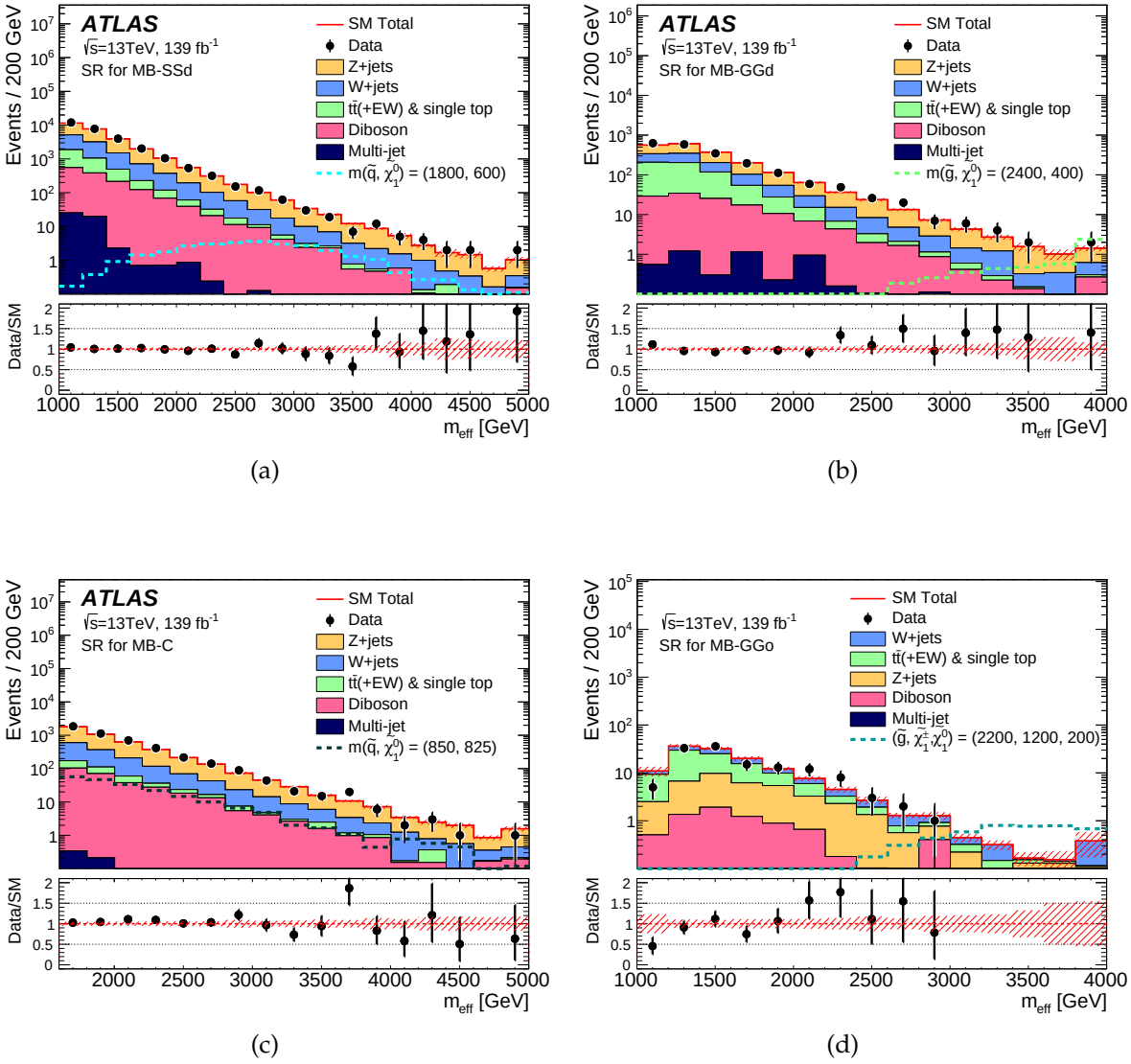

FIGURE 4.23: Observed m_{eff} distributions of events passing the selection criteria for any of the bins in the (a) MB-SSd, (b) MB-GGd, (c) MB-C or (d) MB-GGo signal regions. The histograms show the MC background predictions normalised by the background-only. The hatched (red) error bands indicate combined experimental, theoretical and MC statistical uncertainties, with the experimental and theoretical uncertainties calculated using the coarser SR binning used in the fit rather than the finer binning used in the histograms. Expected distributions for benchmark signal model points, normalised using the approximate NNLO+NNLL cross-section times integrated luminosity, are also shown for comparison (masses in GeV). The last bin includes overflow events.

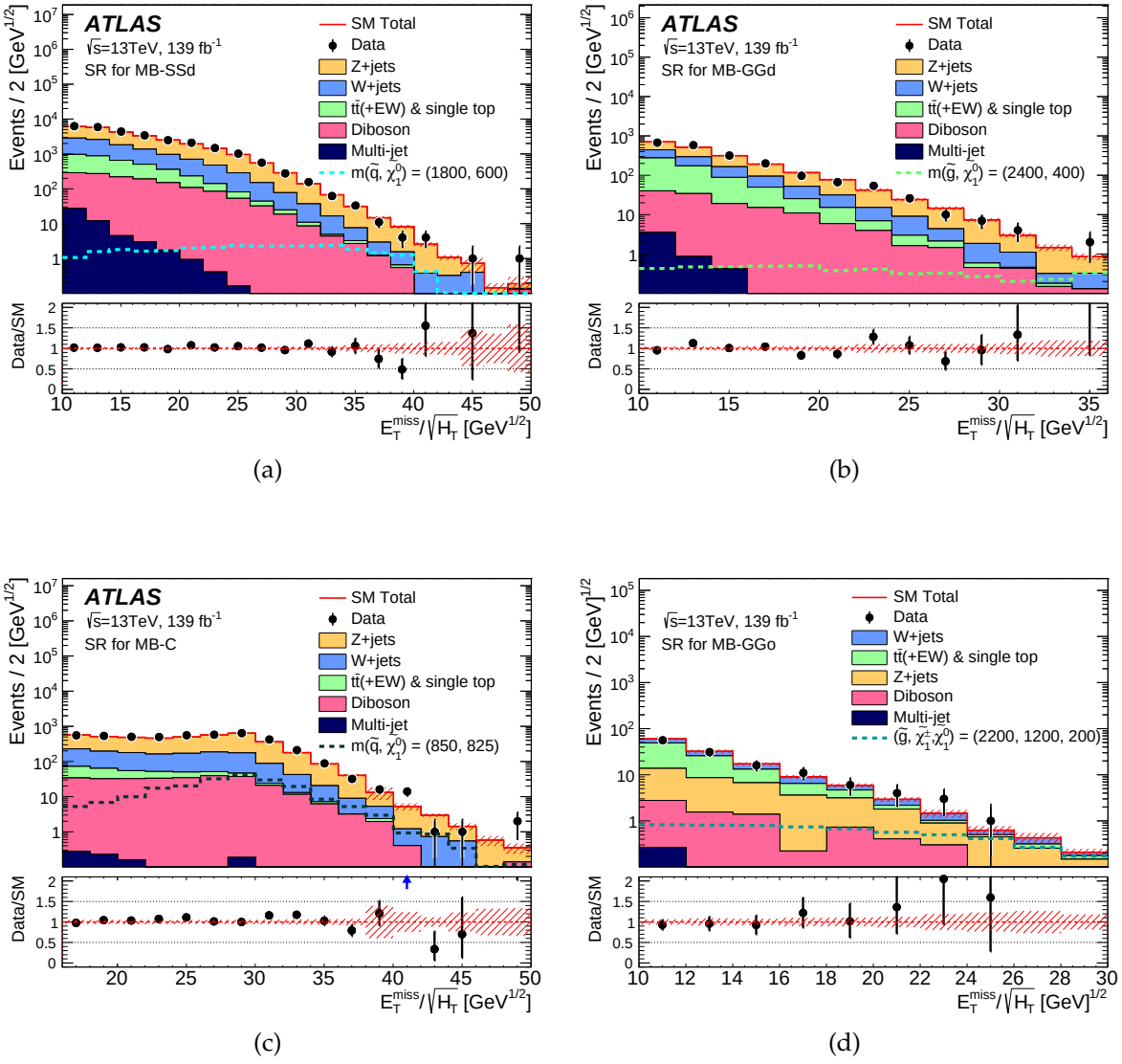

FIGURE 4.24: Observed $E_{\mathrm{T}}^{\mathrm{miss}}/\sqrt{H_{\mathrm{T}}}$ distributions of events passing the selection criteria for any of the bins in the (a) MB-SSd, (b) MB-GGd, (c) MB-C or (d) MB-GGo signal regions. The histograms show the MC background predictions normalised by the background-only fit. The hatched (red) error bands indicate combined experimental, theoretical and MC statistical uncertainties, with the experimental and theoretical uncertainties calculated using the coarser SR binning used in the fit rather than the finer binning used in the histograms. Expected distributions for benchmark signal model points, normalised using the approximate NNLO+NNLL cross-section times integrated luminosity, are also shown for comparison (masses in GeV). The last bin includes overflow events.

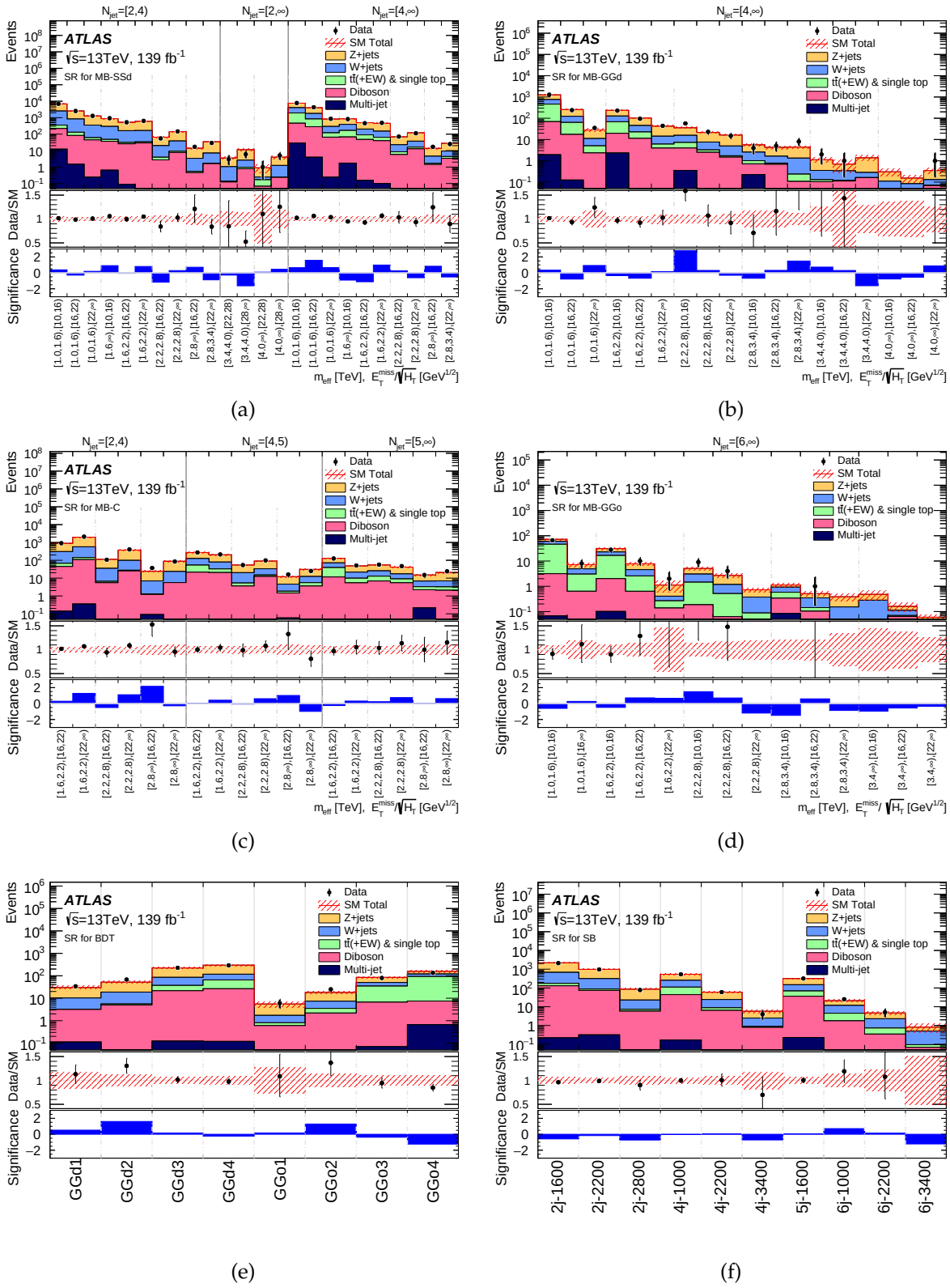

FIGURE 4.25: Comparison of the observed and expected event yields as a function of signal region in the (a) MB-SSd, (b) MB-GGd, (c) MB-C and (d) MB-GGo regions from the multi-bin fit and regions from the (e) BDT and (f) single-bin search. The background predictions are those obtained from the background-only fits, as discussed in the text. The bottom panel in each case shows the ratio of observed data yields to the total predicted background. The significance is computed following the profile likelihood method, Eq. 4.13. The hatched (red) error bands indicate the combined systematic uncertainties.

4.9.2 Model-independent interpretation

Given the lack of strong supersymmetric evidence in the SRs, already discussed in 4.9.1, a model-independent fit is performed to estimate the exclusion power of the analysis without assumptions on the expected BSM physics. A dummy signal with an associated strength parameter is injected in the fit. The multi-bin fit signal regions cannot be used in this case, since, a distribution of the signal in each bin would need to be assumed, which implies a dependence on a model of some sort. Therefore, the model-independent fit is performed only in the single-bin and BDT regions.

The number of observed and expected yields in the SRs of the single-bin and BDT search, as extracted from the background-only fit, are summarized in Tables 4.13 and 4.14, respectively. The results of the model-independent fit are reported for each SR in the bottom part of each table. In order to establish the PDF of the profile likelihood ratio, the asymptotic formula with Asimov datasets is used, except in SRs where the observed statistics are insufficient (less than 10). In that case, MC toy samples are generated to provide an accurate estimate of the PDF distribution. Very small differences are observed between the two approaches, except in the very tight SR6j-3400 SR, where the number of observed events is 0.

Expected and observed upper limits at 95% CL are then set, using the CL_s prescription, on the number of BSM events, S^{95}_{exp} and S^{95}_{obs}, respectively. These limits, when normalised by the integrated luminosity of the data sample, may be interpreted as upper limits on the visible cross-section of BSM physics, $\langle \epsilon\sigma \rangle^{95}_{obs}$, where the visible cross-section is defined as the product of production cross-section, acceptance and efficiency. Examples of upper limit scans on the signal strength for one single-bin and one BDT SR are shown in Figure 4.26.

Finally, the model-independent fit is also used to compute the one-sided p-value p_0 and significance Z of the background-only hypothesis. In case there is a deficit of observed events with respect to the expectation, the p_0 value is truncated at 0.5, to avoid a negative significance. The largest deviation from the background expectation is found to have a significance Z = 0.71 for SR-6j-1000 and Z = 1.28 for GGo2, further confirming the lack of strong evidence of a BSM signature.

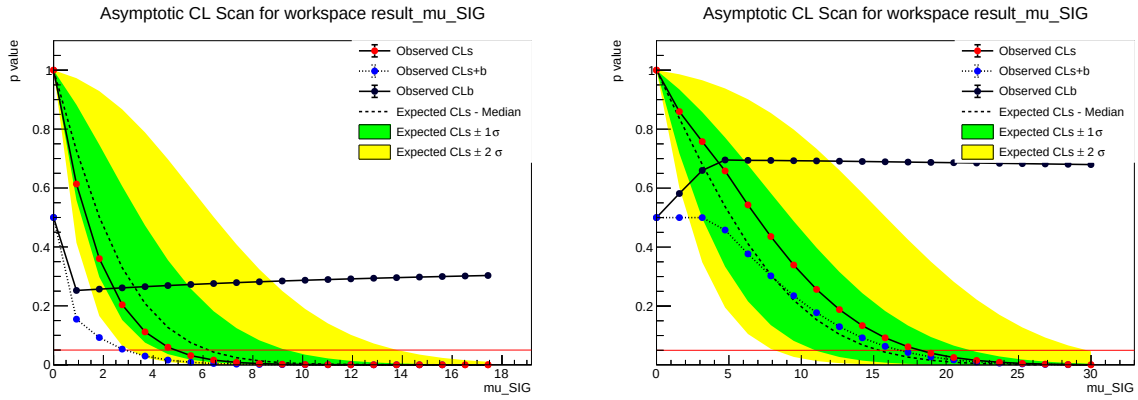

(a) (b)

FIGURE 4.26: Scans of the signal strength for a generic BSM signal in (a) SR4j-3400 of the single-bin search and (b) GGd1 of the BDT search. The observed p-values, as calculated in the signal+background, signal, and background-only hypotheses are shown as blue, red and black points, respectively. The dashed line corresponds to the expected p-value from the CL_s prescription, with the green and yellow bands denoting the $\pm 1\sigma$ and $\pm 2\sigma$ variations, accordingly. The value of μ_s for which the p-value from the expected CL_s is equal to 0.05 (horizontal red line) corresponds to the 95% expected upper limit.

	Model independent regions				
Signal Region	**SR-2j-1600**	**SR-2j-2200**	**SR-2j-2800**	**SR-4j-1000**	**SR-4j-2200**
	Fitted background events				
Diboson	130 ± 29	74 ± 17	5.8 ± 1.7	44 ± 12	6.3 ± 1.7
Z/γ^*+jets	1510 ± 120	670 ± 50	64 ± 7	281 ± 23	35 ± 4
W+jets	500 ± 50	225 ± 16	15.5 ± 2.4	144 ± 12	15.4 ± 1.9
$t\bar{t}$(+EW) + single top	44 ± 9	14 ± 5	1.4 ± 0.8	67 ± 14	2.4 ± 0.9
Multi-jet	0.2 ± 0.2	0.3 ± 0.3	–	0.2 ± 0.2	–
Total MC	2120	979	82	610	71
Total bkg	2190 ± 130	980 ± 50	87 ± 8	536 ± 32	60 ± 5
Observed	2111	971	78	535	60
$\langle\epsilon\sigma\rangle^{95}_{obs}$ [fb]	1.47	0.78	0.14	0.52	0.14
S^{95}_{obs}	204	108	19	72	19
S^{95}_{exp}	247^{+90}_{-67}	114^{+43}_{-31}	24^{+9}_{-7}	73^{+27}_{-20}	19^{+8}_{-5}
p_0 (Z)	0.50 (0.00)	0.50 (0.00)	0.50 (0.00)	0.50 (0.00)	0.48 (0.05)
Signal Region	**SR-4j-3400**	**SR-5j-1600**	**SR-6j-1000**	**SR-6j-2200**	**SR-6j-3400**
	Fitted background events				
Diboson	0.7 ± 0.2	36 ± 10	1.8 ± 0.6	$0.3^{+0.8}_{-0.3}$	–
Z/γ^*+jets	3.3 ± 0.8	170 ± 16	9.3 ± 1.8	2.4 ± 0.6	0.3 ± 0.2
W+jets	1.6 ± 0.4	80 ± 7	7.2 ± 1.6	1.5 ± 0.5	0.4 ± 0.3
$t\bar{t}$(+EW) + single top	$0.1^{+0.1}_{-0.1}$	33 ± 6	2.7 ± 1.5	0.4 ± 0.3	–
Multi-jet	$0.1^{+0.1}_{-0.1}$	0.2 ± 0.2	–	–	–
Total MC	7	427	29	7	1.1
Total bkg	5.7 ± 1.0	319 ± 20	21 ± 3	4.6 ± 1.0	0.8 ± 0.4
Observed	4	320	25	5	0
$\langle\epsilon\sigma\rangle^{95}_{obs}$ [fb]	0.04	0.37	0.11	0.04	0.02
S^{95}_{obs}	5.0	51	16	6.2	3.1
S^{95}_{exp}	$6.2^{+2.6}_{-1.7}$	51^{+20}_{-14}	12^{+5}_{-3}	$6.1^{+2.1}_{-1.4}$	$3.1^{+1.2}_{-0.1}$
p_0 (Z)	0.50 (0.00)	0.48 (0.06)	0.24 (0.71)	0.47 (0.06)	0.50 (0.00)

TABLE 4.13: Numbers of events observed in the signal regions used in the model-independent search, compared with background expectations obtained from the fits described in the text and from MC simulation. Empty cells (indicated by a '–') correspond to estimates lower than 0.01. The p-values (p_0) give the probabilities of the observations being consistent with the estimated backgrounds. For an observed number of events lower than expected, the p-value is truncated at 0.5. Between parentheses, p-values are also presented in terms of the number of equivalent

	BDT regions			
Signal Region	**GGd1**	**GGd2**	**GGd3**	**GGd4**
	Fitted background events			
Diboson	3.0 ± 0.9	4.9 ± 1.4	21 ± 5	26 ± 7
Z/γ^*+jets	20 ± 4	33 ± 5	139 ± 14	180 ± 18
W+jets	7.1 ± 2.6	13 ± 4	48 ± 8	52 ± 9
$t\bar{t}$(+EW) + single top	$0.1^{+0.3}_{-0.1}$	$0.6^{+0.8}_{-0.6}$	16 ± 5	39 ± 11
Multi-jet	$0.1^{+0.1}_{-0.1}$	–	$0.1^{+0.1}_{-0.1}$	$0.1^{+0.1}_{-0.1}$
Total MC	29	56	253	348
Total bkg	30 ± 5	52 ± 6	223 ± 17	298 ± 23
Observed	34	68	227	291
$\langle\epsilon\sigma\rangle^{95}_{obs}$ [fb]	0.13	0.24	0.33	0.36
S^{95}_{obs}	18	33	46	50
S^{95}_{exp}	15^{+6}_{-4}	20^{+8}_{-6}	44^{+17}_{-12}	54^{+21}_{-15}
p_0 (Z)	0.30 (0.51)	0.05 (1.60)	0.44 (0.15)	0.50 (0.00)
Signal Region	**GGo1**	**GGo2**	**GGo3**	**GGo4**
	Fitted background events			
Diboson	0.6 ± 0.2	2.2 ± 0.6	6.6 ± 2.2	6.8 ± 2.1
Z/γ^*+jets	3.8 ± 1.3	10.9 ± 1.9	35 ± 6	39 ± 7
W+jets	0.9 ± 0.5	3.9 ± 1.3	16 ± 4	27 ± 6
$t\bar{t}$(+EW) + single top	0.2 ± 0.2	1.3 ± 0.8	28 ± 6	85 ± 14
Multi-jet	–	–	$0.1^{+0.1}_{-0.1}$	$0.7^{+0.7}_{-0.7}$
Total MC	7	25	111	177
Total bkg	5.5 ± 1.5	18 ± 2.4	85 ± 9	159 ± 16
Observed	6	25	80	135
$\langle\epsilon\sigma\rangle^{95}_{obs}$ [fb]	0.05	0.12	0.16	0.18
S^{95}_{obs}	7.1	17	22	25
S^{95}_{exp}	$6.9^{+2.3}_{-1.6}$	11^{+5}_{-2}	25^{+10}_{-7}	37^{+14}_{-10}
p_0 (Z)	0.49 (0.01)	0.10 (1.28)	0.50 (0.00)	0.50 (0.00)

TABLE 4.14: Numbers of events observed in the signal regions used in the BDT search compared with background expectations obtained from the fits described in the text and from MC simulation. Empty cells (indicated by a '–') correspond to estimates lower than 0.01. The p-values (p_0) give the probabilities of the observations being consistent with the estimated backgrounds. For an observed number of events lower than expected, the p-value is truncated at 0.5. Between parentheses, p-values are also presented in terms of the number of equivalent Gaussian standard deviations (Z). Also shown are 95% CL upper limits on the visible cross-section ($\langle\epsilon\sigma\rangle^{95}_{obs}$), the visible number of signal events (S^{95}_{obs}) and the number of signal events (S^{95}_{exp}) given the expected number of background events (and $\pm 1\sigma$ excursions of the expectation).

4.10 Interpretation in simplified SUSY models

The exclusion power of the analysis for specific models is determined in the model-dependent fit, where all searches, including the multi-bin fits, are included.

The models under test are the ones described in 4.1. Each of them has two free parameters, the masses of two supersymmetric particles. In case more than two such particles are present, the remaining masses are fixed to a given value. The free parameters are scanned individually and a different model-dependent fit is performed for each mass point and search channel. Different channels cannot be combined statistically, since the various SRs are not

always orthogonal.

The results of the model-dependent fit are presented in Figures 4.27-4.31. Limits are obtained by using the expected best performing SR (or multi-bin fit) in each mass point. A detailed account of the best-performing SRs for the 9 simplified model types considered in this analysis can be found in Appendix B. The grey dashed lines show the expected limits at 95% CL, with the light yellow bands indicating the 1σ excursions due to experimental and theoretical uncertainties. Observed limits are indicated by dark maroon curves where the solid contour represents the nominal limit, and the dotted lines are obtained by varying the signal cross-section by the renormalisation and factorization scale and PDF uncertainties. Results are compared with the observed limits obtained by the previous ATLAS searches with jets, missing transverse momentum, and no leptons [147], which are shown in light blue shade. The expected limits from using only the multi-bin (MB), BDT or single-bin searches are also shown as dashed lines of magenta, light green or orange colour, respectively.

Figure 4.27a shows the exclusion limits in simplified models with squark-pair production and subsequent direct squark decays to a quark and the lightest neutralino, where first- and second-generation squarks are considered as fully degenerate. From the observed limits, neutralino masses below about 800 GeV can be excluded for squark masses of 1300 GeV, while for a massless neutralino, squark masses are excluded below 1850 GeV. The expected limits from using only the multi-bin (MB), BDT or single-bin searches are also shown as dashed lines, and it is clear, that the multi-bin search is the best performing analysis for the exclusion of this model. This is not surprising, since, the MB-C and MB-SSd regions have been optimized to target the direct decays of squarks in small and medium/large mass splittings, respectively. The improvement that the multi-bin strategy brings over the standard single-bin approach can be quantified by comparing the exclusion limit achieved by the MB search to the one of the equivalent single-bin signal regions. The sensitivity enhancement is most obvious for medium to large compression scale, where a 100-200 GeV increase in the upper limit of the excluded squark mass is expected. This result is consistent with the study presented in 4.8.1.

In Figure 4.27b, limits are shown both for a hypothesis of eight mass-degenerate light-flavour squarks and for the case of a single non-degenerate light-flavour squark. In the latter scenario, the obtained exclusion strength is significantly weakened due to the cross-section reduction, leading to a m($\tilde{q}$) limit of approximately 1.2 TeV for a massless neutralino.

The equivalent limits in simplified models with gluino-pair production, where each gluino decays directly to $\tilde{g} \rightarrow qq\tilde{\chi}_1^0$ are shown in Figure 4.28. For a fixed mass, the expected production cross-section of gluinos is higher than that of squarks and, consequently, higher mass limits are achieved than in the $\tilde{q}\tilde{q}$ model. For gluino masses up to about 1000 GeV, neutralino masses can be excluded up to 950 GeV close to the kinematic limit near the diagonal. These limits are achieved thanks to the optimized MB-C regions. For small neutralino masses the observed limit on the gluino mass is as large as 2300 GeV and is driven by the MB-GGd regions, while for medium gluino masses the multi-bin search competes in sensitivity with the dedicated BDT SRs. For gluino masses up to about 1700 GeV the best sensitivity is obtained with the optimized BDT regions, excluding the neutralino masses below about 1160 GeV.

The mass limits of models with squark-pair production, where the squarks proceed to one-step decays via an intermediate chargino into $qW\tilde{\chi}_1^0$, are presented in Figure 4.29. Since this type of model includes three s-particles, an assumption is made on the mass of one of them, and two distinct cases are considered. In Figure 4.29a, models in which the chargino mass is fixed at $m(\tilde{\chi}_1^{\pm}) = (m(\tilde{q})+m(\tilde{\chi}_1^0))/2$ are shown in the $(m(\tilde{q}), m(\tilde{\chi}_1^0))$ plane. In the region close to the kinematically forbidden limit, neutralino masses up to 600 GeV are excluded, driven once

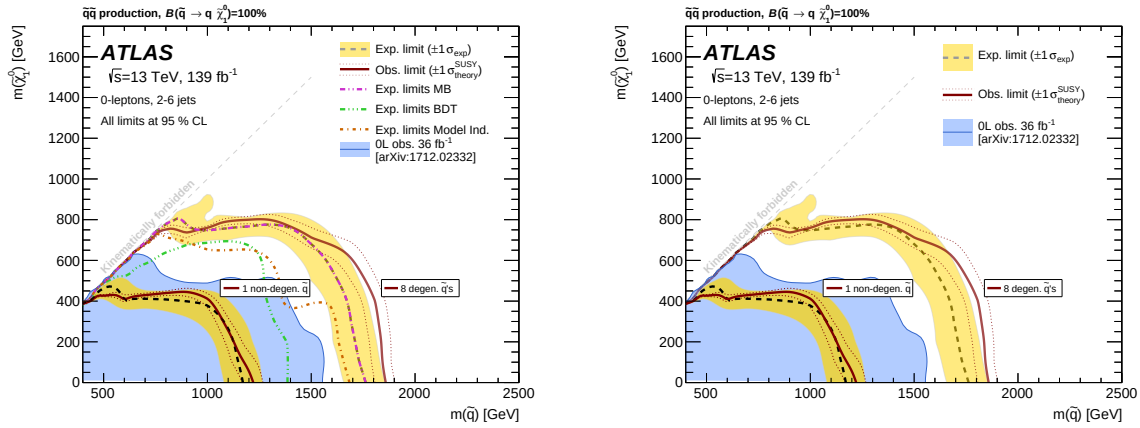

FIGURE 4.27: Exclusion limits in the mass plane of the lightest neutralino and first- and second-generation squarks, assuming squark-pair production and direct decays $\tilde{q} \to q\tilde{\chi}_1^0$. In Figure (a) models where squarks are considered as fully degenerate are considered, and expected limits from using only the multi-bin (MB), BDT or single-bin (SB) searches are also shown for comparison. The comparison between models where all squarks have the same mass (8 degenerate $\tilde{q}$s) and models with a single squark (non-degenerate $1\tilde{q}$) is shown in Figure (b). In both cases, nominal exclusion limits are obtained by using the signal region with the best expected sensitivity at each point. The best-SR map for each mass point can be found in Appendix B.

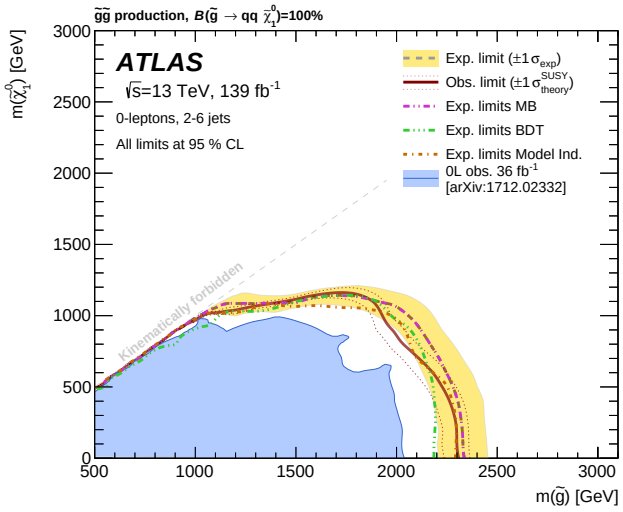

FIGURE 4.28: Exclusion limits in the mass plane of the lightest neutralino and the gluino, assuming gluino-pair production and direct decays $\tilde{g} \to qq\tilde{\chi}_1^0$. Exclusion limits are obtained by using the signal region with the best expected sensitivity at each point. The expected limits from using only the multi-bin (MB), BDT or single-bin (SB) searches are also shown for comparison. The best-SR map for each mass point can be found in Appendix B.

more by the sensitivity of the MB-C search in compressed scenarios. For a massless neutralino, squark masses are excluded below 1310 GeV, thanks to the MB-GGd search. This search, while optimized for gluino-pair production, performs well in the one-step squark models, thanks to the additional jets that originate from the W-boson decays. Similarly to Figure 4.28, the BDT search often dominates for intermediate squark masses.

Figure 4.29b shows the exclusion limits for the alternative type of models, in which the neutralino mass is fixed at 60 GeV, for $\chi = \Delta m(\tilde{\chi}_1^{\pm}, \tilde{\chi}_1^0)/\Delta m(\tilde{q}, \tilde{\chi}_1^0)$ as a function of the squark mass. The multi-bin searches offer the best sensitivity in the entirety of the scanned mass range. In cases where the squark and chargino masses are comparable ($\chi \sim 1$), close to the kinematic limit, squark masses are excluded up to 1350 GeV. In this region, the large mass splitting between the chargino and the neutralino results in highly boosted W-bosons that subsequently decay hadronically into merged (unresolvable) jets. The best performing search in this case is MB-SSd, thanks to the lower jet multiplicity and high jet p_T requirements of the N_j = [2,4) bins. For a lower mass difference between the chargino and the neutralino, the jets from the W-boson decay are distinguishable, and therefore, the MB-GGd regions drive the limit for intermediate χ values. A drop in sensitivity is observed around $\chi \sim 0.1$, due to the particular mass splitting between the chargino and the neutralino, which is close to the mass of the W boson. In these models, the chargino decay products are produced at rest in the chargino rest frame, leading to reduced signal acceptance. When moving to even lower χ, the W boson decay products are soft, leading to an increased sensitivity of lower jet multiplicity regions such as the MB-C and the MB-SSd, and in cases of extremely low χ, an increase in acceptance due to leptonic W-boson decays passing the lepton veto.

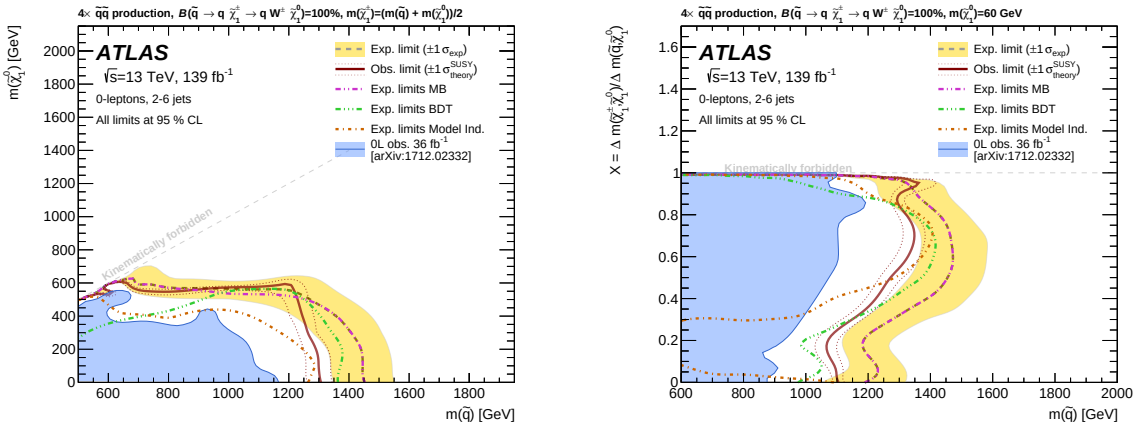

(a) (b)

FIGURE 4.29: Exclusion limits for squark-pair production with a one-step decay via an intermediate chargino into $qW\tilde{\chi}_1^0$. Figure (a) shows the limits in the $(m(\tilde{q}), m(\tilde{\chi}_1^0))$ plane for a chargino mass fixed at $m(\tilde{\chi}_1^{\pm}) = (m(\tilde{q}) + m(\tilde{\chi}_1^0))/2$. Alternatively in Figure (b), the neutralino mass is fixed at 60 GeV and exclusion limits are given for $\chi = \Delta m(\tilde{\chi}_1^{\pm}, \tilde{\chi}_1^0)/\Delta m(\tilde{q}, \tilde{\chi}_1^0)$ as a function of the squark mass. Exclusion limits are obtained by using the signal region with the best expected sensitivity at each point. The expected limits from using only the multi-bin (MB), BDT or single-bin (SB) searches are also shown for comparison. The best-SR map for each mass point can be found in Appendix B.

Mass limits for gluino-pair production with one-step decays via an intermediate chargino into $qqW\tilde{\chi}_1^0$ are shown in Figure 4.30. Similarly to the one-step decays of squarks, two types of models are defined. Figure 4.30a presents limits in the $(m(\tilde{g}), m(\tilde{\chi}_1^0))$ plane for a chargino mass fixed at the intermediate point between the masses of the gluino and the neutralino. This model is characterised by a high jet multiplicity, typically above 4 jets. In the region close to the

kinematic limit near the diagonal, neutralino and gluino masses up to 900 GeV are excluded, driven by the multi-bin search dedicated to models with small mass differences. For massless neutralinos, gluino masses are excluded below 2360 GeV, thanks to the performance of the MB-GGo search. Intermediate gluino masses are best excluded from the dedicated BDT signal regions with high jet multiplicity, GGo1-4. Figure 4.30b shows limits on the variable χ, in this case defined as $\chi = \Delta m(\tilde{\chi}_1^{\pm}, \tilde{\chi}_1^0)/\Delta m(\tilde{g}, \tilde{\chi}_1^0)$, for a neutralino mass of 60 GeV. The mass limit close to the kinematically forbidden region is driven once more from the MB-SSd regions, due to their sensitivity to merged jets originating from unresolved decay products of boosted W-bosons. Gluino masses are excluded up to 2350 GeV for small and intermediate values of χ, thanks to the MB-GGo search. Finally, for low χ values, the same drop in sensitivity as in the equivalent squark-onestep grid is observed, and has the same origin, i.e. a reduced acceptance due to the chargino decay products being produced at rest. For very low values of χ, below 0.8, 4-jet SRs, such as the MB-GGd or the single-bin SR4j-3400 dominate [7].

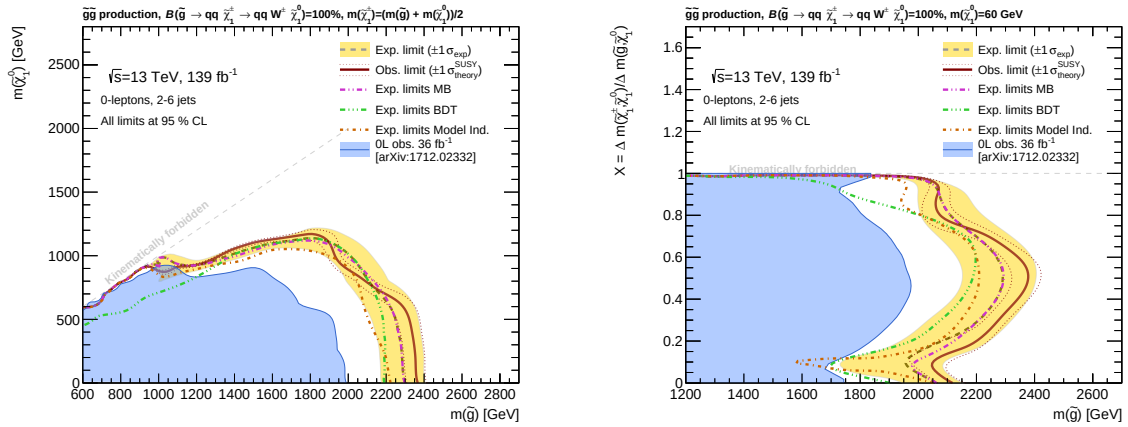

(a) (b)

FIGURE 4.30: Exclusion limits for gluino-pair production with a one-step decay via an intermediate chargino into $qqW\tilde{\chi}_1^0$. Figure (a) shows the limits in the $(m(\tilde{g}), m(\tilde{\chi}_1^0))$ plane for a chargino mass fixed at $m(\tilde{\chi}_1^{\pm}) = (m(\tilde{g}) + m(\tilde{\chi}_1^0))/2$. Alternatively in Figure (b), the neutralino mass is fixed at 60 GeV and exclusion limits are given for $\chi = \Delta m(\tilde{\chi}_1^{\pm}, \tilde{\chi}_1^0)/\Delta m(\tilde{g}, \tilde{\chi}_1^0)$ as a function of the gluino mass. Exclusion limits are obtained by using the signal region with the best expected sensitivity at each point.The expected limits from using only the multi-bin (MB), BDT or single-bin (SB) searches are also shown for comparison. The best-SR map for each mass point can be found in Appendix B.

Finally, Figure 4.31 shows the exclusion limits in the $(m(\tilde{g}),m(\tilde{q}))$ for a combined production of squark, gluino and squark-gluino pairs. The interpretation is performed for three assumed neutralino masses: 0, 995 and 1495 GeV. When the mass hierarchy allows, the $\tilde{g} \to \tilde{q}q$ and $\tilde{q} \to \tilde{g}q$ decays are included in the decay chain. The decay topology in these inclusive models highly depends on the mass difference between the gluino and the squark, since different production modes will be enhanced. For example, for m($\tilde{q}$) = 2500 GeV and m($\tilde{g}$) = 6250 GeV, the squark-pair production cross-section is roughly 4 orders of magnitude larger than the gluino-pair production. The squark production cross section which is, in the considered models, strongly dominated via t- and u-channel diagrams, decreases with increasing gluino mass, leading to weaker limits in the mass plane where gluino masses are high. In regions where gluino mass becomes higher than 8 TeV, the kinematics is expected to stay the same, and the change of the production cross section is expected to provide a smooth transition of the exclusion limits between a gluino mass of 8.5 TeV and the decoupled gluino scenario. In

[7] The SR4j-3400 was found to be better than the MB-GGd counterpart in some very low-χ mass points, due to a non-negligible signal contamination in CRW and CRT.

scenarios with m($\tilde{\chi}_1^0$) = 995 GeV, the search becomes less sensitive to models with very small mass difference between the particles, as seen in models with gluino masses around 6 TeV and squark masses around 1 TeV. In similar compressed regions, with squark (gluino) mass close to the mass of the LSP and the gluino (squark) mass reaching up to 4 TeV, the search still has sensitivity to such models due to $\tilde{q}\tilde{g}$ production processes that provide sufficient acceptance.

For all three neutralino masses considered, the multi-bin searches provide the best expected exclusion in the majority of mass points. For high gluino masses, squark-pair production modes are more frequent and therefore, MB-SSd regions perform the best. On the other hand, for high squark masses, the situation is reversed, and MB-GGd regions dominate, since they target the higher jet-multiplicity final states of gluino decays. Finally, for high neutralino masses, 995 or 1495 GeV, there exist mass points with $\Delta m(\tilde{\chi}_1^0, \tilde{q}/\tilde{g}) < 100$ GeV, in which case the compressed MB-C regions give the highest sensitivity.

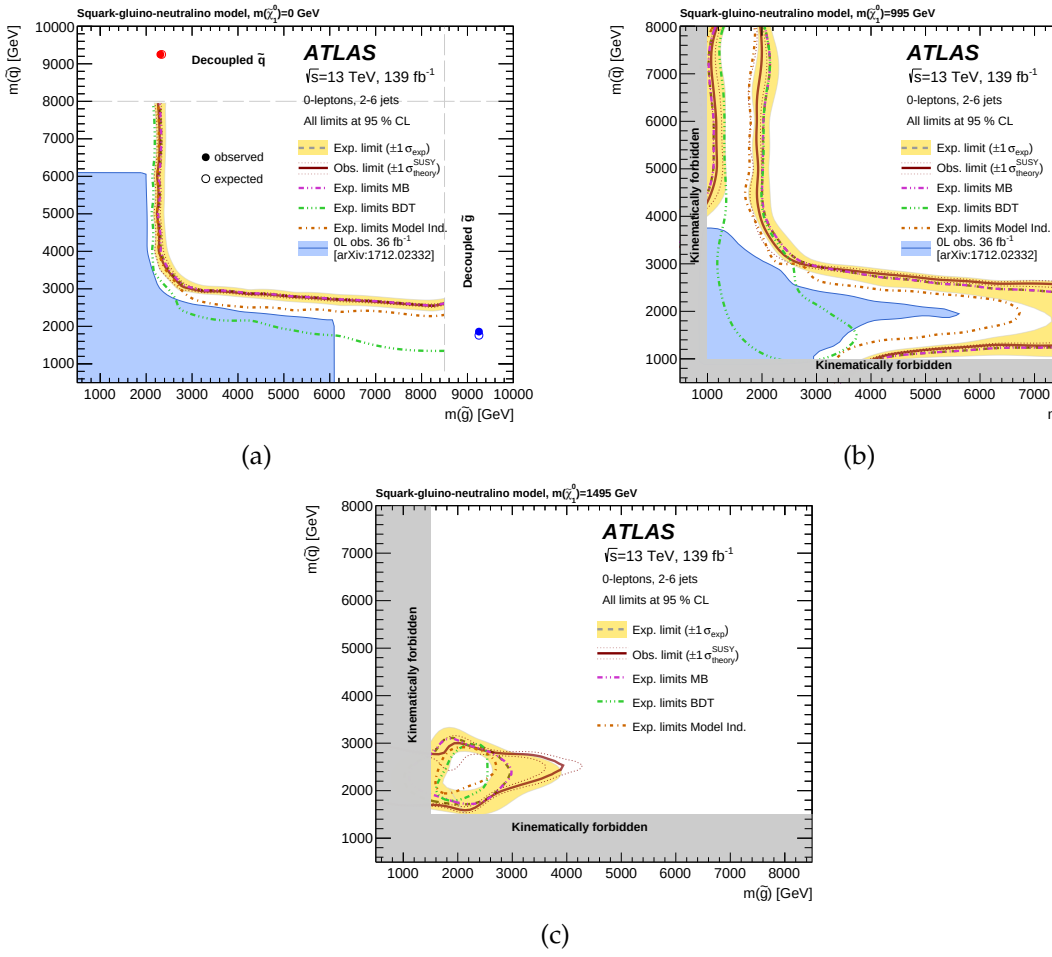

FIGURE 4.31: Exclusion limits for the model with combined production of squark pairs, gluino pairs, and of squark-gluino pairs, for different assumptions on the neutralino mass: (a) $m(\tilde{\chi}_1^0) = 0$ GeV, (b) $m(\tilde{\chi}_1^0) = 995$ GeV and (c) $m(\tilde{\chi}_1^0) = 1495$ GeV varying values of $m(\tilde{g})$ and $m(\tilde{q})$. Exclusion limits are obtained by using the signal region with the best expected sensitivity at each point. The expected limits from using only the multi-bin (MB), BDT or single-bin (SB) searches are also shown for comparison. In Figure (a), observed and expected limits on squark (gluino) masses are also shown, assuming gluino (squark) masses are decoupled as in simplified models presented in Figure 4.27 (4.28). The best-SR map for each mass point can be found in Appendix B.

4.11 Conclusions and prospects of the analysis

The results of the search of squarks and gluinos in final states with 2 or more high-p_{T} jets, large missing transverse energy but no electrons or muons, with the full Run 2 data of the ATLAS detector, have been presented. No significant excess over the SM expected background has been observed.

Results are then interpreted in terms of simplified supersymmetric models with only first- and second-generation squarks, or/and gluinos, together with a neutralino LSP. The masses of all other SUSY particles are set such that the particles are effectively decoupled. Gluino masses below 2.35 TeV are excluded at 95% confidence level in simplified models where the gluino decays directly and the neutralino is massless. For a simplified model involving the strong production of squarks of the first and second generations, with direct decays to a massless lightest neutralino, squark masses below 1.85 TeV are excluded, assuming mass-degenerate squarks of the first two generations. The equivalent limit for the case where all but the lightest squark are decoupled is reduced to 1.2 TeV. In simplified models with pair produced squarks or gluinos that decay via an intermediate chargino to a $\tilde{\chi}_1^0$ and one or two quarks, respectively, squark masses below 1.31 TeV and gluino masses below 2.34 TeV are excluded in the case where the $\tilde{\chi}_1^0$ is massless. For models with a mixed production of squarks and gluinos, a lower limit of 3 TeV is found in the case where the squark and gluino masses are equal and the neutralino is massless. These limits greatly improve the exclusion range of searches for squarks and gluinos obtained with partial Run 2 datasets.

4.11.1 The 0-lepton results in the LHC SUSY phase-space

Figure 4.32a shows the exclusion limits in simplified models with squark-pair production and subsequent direct or cascade decays of squarks to the lightest neutralino, obtained by the ATLAS collaboration [148]. The observed limits of the most sensitive searches are presented individually - the 0-lepton analysis with 2-6 jets displays a high sensitivity, excluding squark masses up to 1.93 TeV for a massless neutralino. It should be noted that this is the only of the displayed analyses performed with full Run2 dataset and is therefore favoured by the higher luminosity. The next most powerful result is obtained with a combination of the 0 and 1 lepton squark searches with one-step decays through a W boson, performed with a partial Run2 dataset (36.1 fb^{-1}). The remaining limits correspond to searches with two-step decays of squarks with Run1 data (integrated luminosity ranging from 20.1 to 20.3 fb^{-1}). The most sensitive ATLAS limits for simplified models with gluino-pair production followed by direct $\tilde{g} \to qq\tilde{\chi}_1^0$ decays are shown in Figure 4.32b. The 0-lepton with 2-6 jets analysis is once again giving one of the most powerful limits, especially at low neutralino mass. Comparable results are obtained by searches for gluinos decaying directly to b- and top-quark pairs with the same luminosity. Again, limits for models with one- and two- step gluino decays, obtained with Run-2 datasets with reduced statistics (36.1 fb^{-1}), are shown for comparison. The complementarity of ATLAS searches targeting different SUSY decay topologies is evident and is extremely important in constraining a more complete supersymmetric spectrum.

The CMS collaboration has performed two searches for squarks and gluinos in R-parity conserving scenarios decaying to fully hadronic states with the entire Run2 dataset [149, 150]. The former employs a similar approach as the analysis of this thesis, while the latter uses the kinematic variable M_{T2} [151]. Both analyses use a multi-bin fit; the mass limits in simplified models with squarks and gluinos decaying directly to quarks and the lightest neutralino are in both cases comparable to the results presented in this thesis.

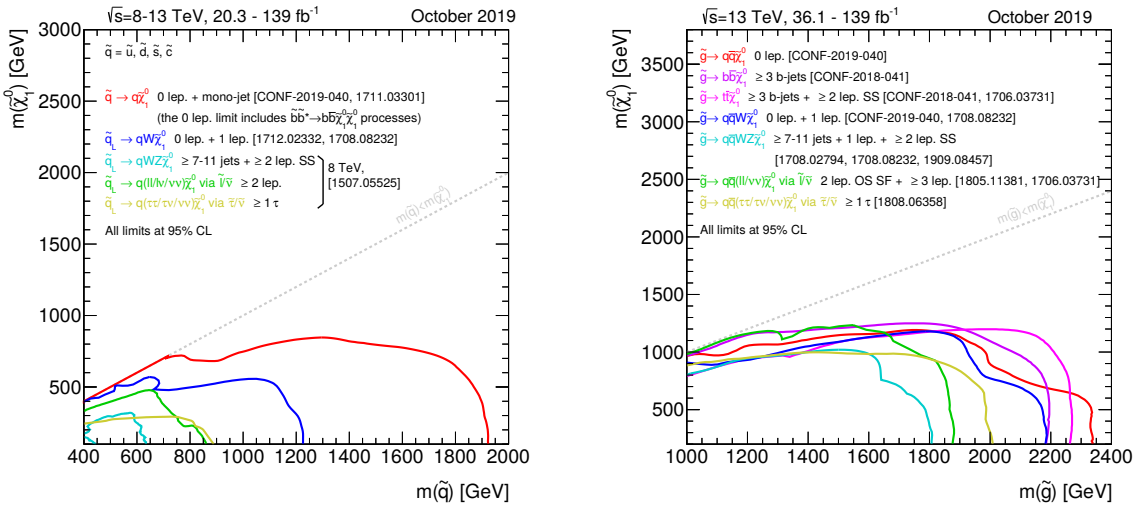

(a) (b)

FIGURE 4.32: Summary of the mass exclusion limits obtained with the most sensitive ATLAS searches at 95% CL based on 13 TeV data in a simplified model with (a) squark-pair production, followed by direct decays to a quark and a neutralino, displayed in the (squark, lightest neutralino) plane and (b) gluino-pair production with $\tilde{g} \rightarrow qq\tilde{\chi}_1^0$ direct decays, shown in the mass plane of the (gluino, lightest neutralino) [148].

4.11.2 Re-interpretation potentials

The search for squarks and gluinos in fully hadronic final states with large missing transverse momentum has proven to be a very promising channel, providing with some of the most strict limits on simplified strong SUSY models. The search strategy has been designed in a way that maximizes the sensitivity in the target scenarios but maintains a flexibility for possible re-interpretations in other models.

An evident case where the 0-lepton analysis can be used is in the interpretation in SUSY models deploying the MSSM spectrum, instead of a simplified approach. It should not be forgotten that simplified models, while being a powerful tool to quickly interpret a result, are only rough approximations of the SUSY phenomenology. By including the MSSM particle content, a more realistic interpretation can be achieved, since the mass spectrum of the additional s-particles can have a significant impact on the results. Additionally, dropping the assumption of a 100% BR to a desired signature, the simplified limits can be greatly altered. A significant effort has been put in the ATLAS collaboration to re-interpret Run-1 search results in the context of the R-parity conserving 19-parameter pMSSM, in which the lightest supersymmetric particle is a neutralino [29]. The Run-1 0-lepton analysis was shown to be one of the most sensitive searches in a vast range of parameters, excluding the largest fraction of scanned models. An equivalent re-interpretation campaign is being prepared with the Run-2 set of ATLAS analyses, in which the 0-lepton search is expected to give a significant contribution.

Another case in which the 0-lepton analysis naturally offers sensitivity is the search for leptoquarks, decaying into quarks and neutrinos. Leptoquarks are hypothetical heavy exotic particles that carry both lepton and baryon number, and can therefore decay to leptons and quarks, as shown in Figure 4.33. The jets in the final state arise from the hadronisation of the quarks, while the missing transverse energy is due to the escape of the neutrinos.

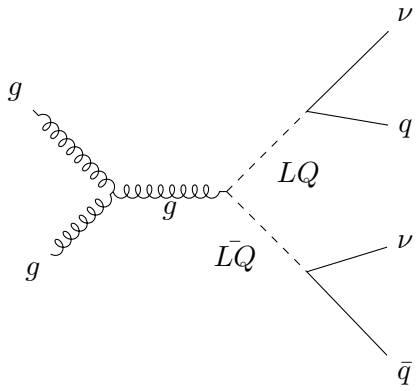

FIGURE 4.33: Feynman diagram of leptoquark pair-production through gluon-gluon interactions, followed by the decay of each leptoquark to a neutrino and a quark.

Thanks to the adaptation of the analysis in the RECAST framework [152, 153], re-interpretations of the results in other BSM physics scenarios with similar expected signatures will be possible using the full power of the multi-bin and BDT searches.

5. HGTD: Detector Overview

This chapter presents a detailed description of the High Granularity Timing Detector. Starting from the main motivations behind the conception of this novel detector in 5.1, an overview of the key detector requirements and design are given in 5.2 and 5.3. The chapter proceeds to describe the principle ideas and activities on the design and optimization of the active area of the detector in 5.4 and 5.5. Finally, the expected impact of the detector on the physics and performance of ATLAS in the HL-LHC era is presented in 5.7.

5.1 Physics motivation

With the average number of simultaneous interactions ($< \mu >$) increasing to 200, pile-up defined as the additional interactions that occur nearby the vertex of interest, will be one of the main challenges of the HL-LHC. Figure 5.1a shows the density of pile-up vertices under two different $< \mu >$ scenarios; $< \mu >$ = 30, corresponding to approximately the Run 2 conditions, and $< \mu >$ = 200, the estimated value at HL-LHC. It can be seen that not only the average density is expected to increase from 0.2 to 1.4 vertices/mm, but there will be events with up to a density of 4 vertices/mm. Under such high-density conditions, identifying the primary vertex and correctly associating physics objects to it is no longer trivial for the ATLAS experiment. The upgrade of the ATLAS inner tracker, ITk, is foreseen to maintain an excellent track reconstruction and vertex association performance. The acceptance will also be extended up to $|\eta|$ = 4. With the new pile-up conditions, the tracking becomes increasingly challenging in the forward region, where the density of produced particles reaches its maximum. This issue is illustrated in Figure 5.1b, where the resolution of the determination of the track longitudinal impact parameter by the ITk, σ_{z_0}, is shown for single muons with a momentum of either 1 or 10 GeV as a function of the particle η. For a good vertex separation to be achieved, σ_{z_0} should be significantly smaller than the inverse of the average pile-up density, i.e. 700 µm for the HL-LHC conditions. While this criteria is met in the central region, it is clear that in the forward region, tracks coming from different collisions will not always be correctly paired to their corresponding vertices, especially when they have low momentum.

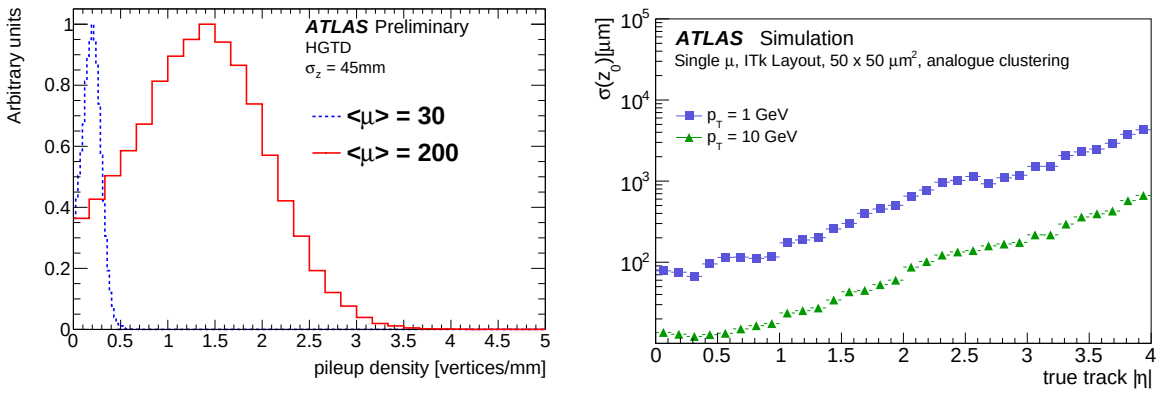

(a) (b)

FIGURE 5.1: (a) Local pile-up vertex density for different values of $< \mu >$. (b) Resolution of the longitudinal track impact parameter, z_0 , as a function of η for muons of p_T = 1 GeV and p_T = 10 GeV. [154]

The undesirable effects of pile-up can be mitigated if an accurate time measurement is combined with the existing spatial information, since these two attributes are orthogonal to each other. This idea is visualised in Figure 5.2, where it can be seen that objects originating from vertices that are close in space but separated in time can be disentangled using the latter.

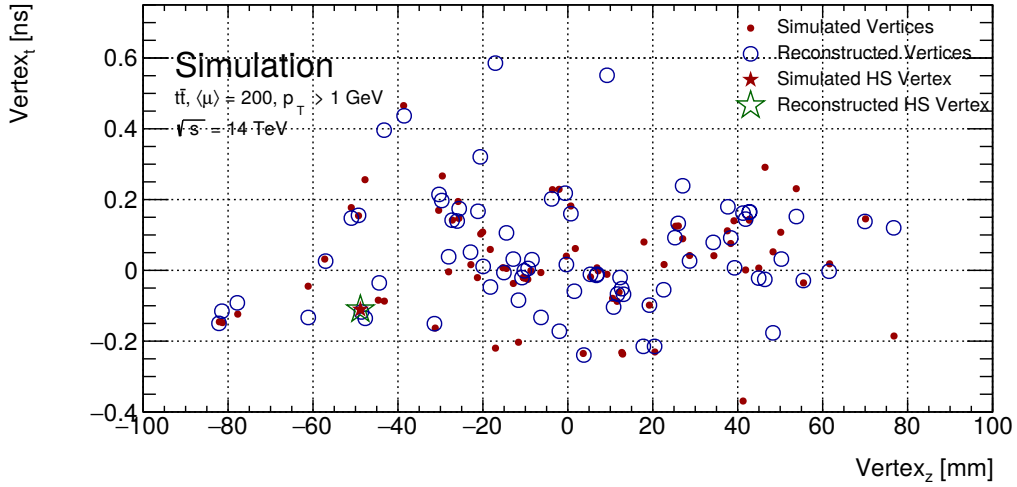

FIGURE 5.2: Visualisation of the primary vertices in an event in the $z - t$ plane, showing the simulated Hard Scatter (HS) with pile-up interactions superimposed for $< \mu >$ = 200. The reconstructed vertices (blue circles) are overlaid along with the reconstructed HS vertex (green star). [154]

Another challenge of the HL-LHC is the accurate estimate of the luminosity, which is essential for precision measurements of the cross-section of a physics process. The designated luminosity detectors will have to cope with the increasing particle density and harsh irradiation conditions, while maintaining a luminosity uncertainty below 2% (more details in 5.7.3. In addition, if bunch-by-bunch luminosity information is to be achieved, the detectors will have to be read-out at the very challenging rate of 40 MHz. The luminosity technologies already in use in the Run 2 of ATLAS, such as the Cherenkov counters coupled to PMTs [45] cannot alone satisfy these requirements. Ideally, for the HL-LHC, luminosity information will be provided by at least 3 independent detector systems, in order to correct for calibration biases and long-term instabilities. The HGTD, being robust against radiation and pile-up, could provide an unbiased luminosity measurement of high precision by counting the number of particles produced in the collisions and within its acceptance. It is therefore an excellent candidate for one of the individual luminometers for ATLAS at HL-LHC.

5.2 Detector requirements and overview

The ATLAS experiment is planning to implement this pile-up mitigation concept by the addition of a forward timing detector made of Low Gain Avalanche Detectors (LGADs) [155], called High Granularity Timing Detector (HGTD) [154]. This new detector will be able to provide a time measurement with a high accuracy for tracks in the forward region between 2.4 $< |\eta| <$4.0 (equivalent to a radial range in the x-y plane of 120 - 640 mm). This excellent timing performance will be achieved by the combination of timing information in different layers; a 25 ps resolution per track is expected at the beginning of the detector lifetime, deteriorating to 50 ps after 4000 fb^{-1}. An additional use of the detector as a luminometer and a minimum bias trigger is foreseen. As seen in Figure 5.3, it will be located in the gap region between the barrel and the end-cap calorimeters, at a distance in the beam-axis of approximately $\pm$ 3.5 m from the nominal interaction point. Two identical vessels will be placed symmetrically

in the two end-cap regions of ATLAS, in the space currently occupied by the Minimum Bias Trigger System (MBTS) and part of the moderator which protects the ID from the neutron flux originating from the calorimeter.

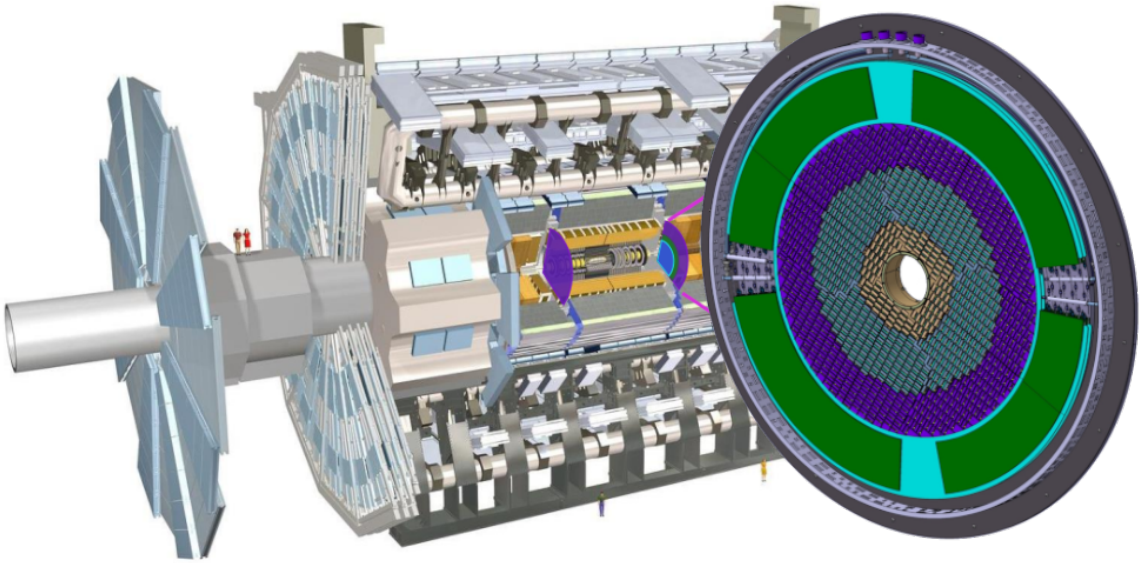

FIGURE 5.3: Position of the HGTD within the ATLAS Detector. The HGTD acceptance is defined as the surface covered by the HGTD between a radius of 120 mm and 640 mm at a position of z = $\pm$ 3.5 m along the beamline, on both sides of the detector. [154]

The design of such a detector is challenging from many aspects. Constraints on the available space in the forward region of ATLAS dictate that the detector must be compact, especially in the z-direction. For this reason, a silicon-based technology has been chosen based on LGADs, a recently developed sensor that can provide the required time resolution in harsh irradiation conditions. The timing information should be provided at the level of Minimum Ionizing Particles (MIPs), and therefore, the envisioned design should have a high granularity. A pad size of 1.3×1.3 mm^2 ensures an occupancy below 10% at the largest particle-density region. This size, along with the chosen sensor thickness of $50\,\mu\mathrm{m}$, guarantee additionally a low sensor capacitance, which, as will be described in section 5.5, is important for the time resolution. The sensors will be operated at $-30\,^{\circ}\mathrm{C}$, so as to mitigate the irradiation-induced increase of the leakage current, further described in section 5.4. The cooling will be provided by an evaporative CO_2 system shared with ITk.

The signal from the LGAD sensors will be processed and read-out by dedicated Application Specific Integrated Circuits (ASICs), on which the sensors will be directly bump-bonded. Such a circuit should provide a time measurement at the bunch crossing rate of the HL-LHC (40 MHz), while maintaining the excellent signal properties of LGADs in the same harsh irradiation conditions. In addition, the circuit should be able to count and transmit information on the number of registered hits, in order to allow for an unbiased luminosity measurement at the bunch-crossing level. An ASIC meeting the above requirements, named ALTIROC, is currently under development. Current estimates on the performance have shown that the ASIC should be able to process an injected charge down to 4 fC with a high efficiency, above 95%. This limitation is directly linked to the LGAD performance under irradiation, guiding the design of the sensor and the replacement scheme of the HGTD, which will be discussed in the following.

The information that is acquired from the ASIC will be transferred to the periphery of the detector using flex cables. Dedicated electronic boards at the periphery will be responsible of the grouping and further transmission of the data to the central ATLAS DAQ system. In parallel, they will be able to provide powering and conditions monitoring functionalities.

HGTD should be able to maintain its outstanding performance in the extremely harsh irradiation conditions of the forward region for the entirety of the HL-LHC lifetime. In particular, as the LGAD gain is reduced with irradiation, the sensors should be able to provide a charge larger than 4 fC, in order for the ASIC to provide a correct time measurement. As shown in Figure 5.4a, at the end of the HL-LHC (4000 fb^{-1}), the nominal neutron-equivalent fluence at the lowest radius of HGTD (120 mm), should reach 8.3 $\times$ 10^{15} $n_{eq}/cm^2$and the total ionising dose (TID) will be about 7.5 MGy, (including safety factors) [1], values that exceed the resilience of LGADs. In order to ensure the functionality of HGTD for the full HL-LHC period, the innermost part (r $<$ 230 mm) of the sensors and electronics should be replaced after each 1000 fb^{-1}, i.e. three times. Taking into account the evolution of the irradiation as a function of the radius suggests that also the middle part of the active material, between 230 mm $<$ r $<$ 470 mm should be replaced once at 2000 fb^{-1}. Under this replacement scheme, the received neutron-equivalent fluence will not exceed 2.5 $\times$ 10^{15} n_{eq}/cm^2, as demonstrated in Figure 5.4b, under which conditions the LGAD sensors will still be able to provide the minimum charge of 4 fC required by the electronics. Additionally, the TID will remain below 2 MGy for the entire lifetime of the detector.

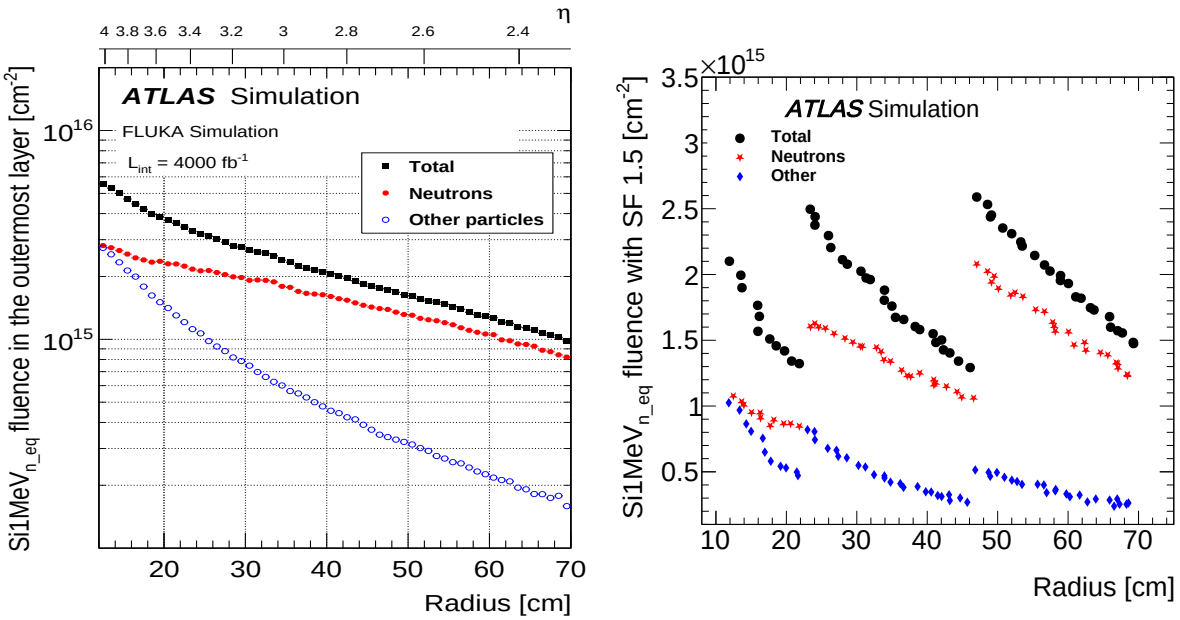

FIGURE 5.4: Expected nominal $Si1MeV_{neq}$ fluence in the HGTD, using FLUKA [156, 157] simulations, as functions of the radius after 4000 fb^{-1} (a) without a replacement scheme and without applying any safety factors and (b) considering a replacement of the inner ring every 1000 fb^{-1} and of the middle ring once at 2000 fb^{-1}, and after applying a 1.5 safety factor. For the radiation levels, the particle type is included and the contribution from charged hadrons is included in 'Others'. [154]

[1] A 1.5 safety factor is applied to the sensor irradiation requirements in order to consider the fluence simulation uncertainty, while for the electronics, influenced mostly by the TID, a larger factor of 2.25 is used to account additionally for uncertainties in the electronics behaviour under irradiation.

5.3 Detector Design

In order to meet the constraints and requirements previously described, the HGTD will be a disk-like planar detector, placed in front of each of the two end-cap calorimeters. A breakdown schematic view of one side of the HGTD can be seen in Figure 5.5. The active area of the detector, consisting of the sensors and front-end electronics (in deep blue), along with the peripheral electronics (in green) are organised in two cooling plates (cyan). The envelop of the detector has a radial range (in the x-y plane) between 110 mm and 1000 mm, while the active area is situated between r=[120, 640] mm. The two plates are placed inside a hermetic vessel. There are two moderators to minimise the neutron flux originating from the calorimeter and protect the HGTD and ITk; one is positioned inside and one outside the hermetic vessel. This separation was chosen to facilitate the installation of the HGTD before the LAr end-cap.

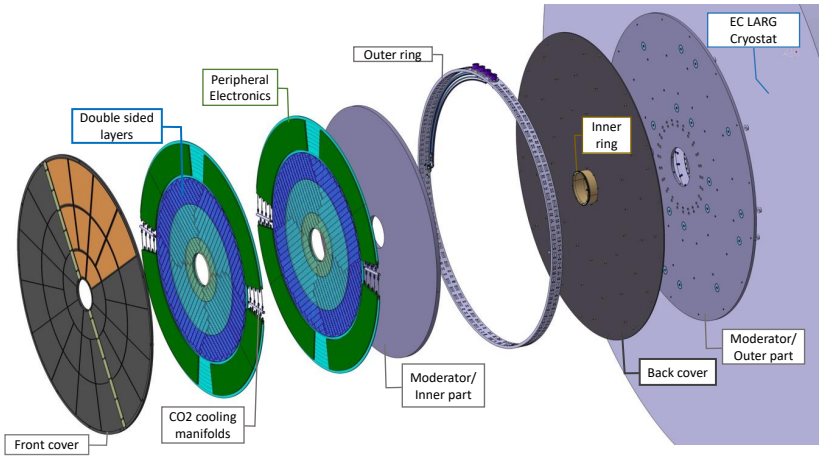

FIGURE 5.5: Global view of the HGTD to be installed on each of two end-cap calorimeters. The various components are shown: hermetic vessel (front and rear covers, inner and outer rings), two instrumented double-sided layers (mounted in two cooling disks), two moderator pieces placed inside and outside the hermetic vessel. [154]

The active area is made out of 4×2 cm^2 modules, where a module consists of a 30×15 pad sensor bump-bonded to two ASICs. Each module is glued to a small flex cable PCB, which in turn is connected to a long flex cable tail. A schematic view of an HGTD module, equipped with its read-out flex cable PCB and tail is shown in 5.6a. Each cooling plate is two-sided, i.e. instrumented on both of its sides. The modules are positioned on each side in such a way as to introduce an overlap, in order to increase the number of hits per track and minimise the dead area. The spacing and overlap between modules are optimised to maintain a constant timing performance as a function of η. Since the performance decreases with irradiation, a phenomenon which is highly dependent on the radius, the modules are placed more densely at low r, where also the track extrapolation is more challenging. As already mentioned in section 5.1, the active area of the detector will be partially replaced in two radial regions, one in r = [120, 230] mm and the second in r = [230,470] mm, to cope with the received dose. For simplicity, the spacing and overlap is kept constant in each of these radial regions. An overlap of 20% for the outer radial ring at r>470 mm, 54% for the middle region at $230 < r < 470$ mm and 70% at r< 230 mm has been decided, as illustrated in the schematic of Figure 5.6b.

Under this overlap configuration, each track will register between 2 and 3 hits (sensor pads with energy deposition above a given threshold, constituting a measurable signal), depending on its η. The time resolution of the track will be given by the hit resolution, divided by the

square root of the number of its associated hits. Therefore, in order to maintain the 50 ps requirement, the resolution of the module should not exceed 70 ps.

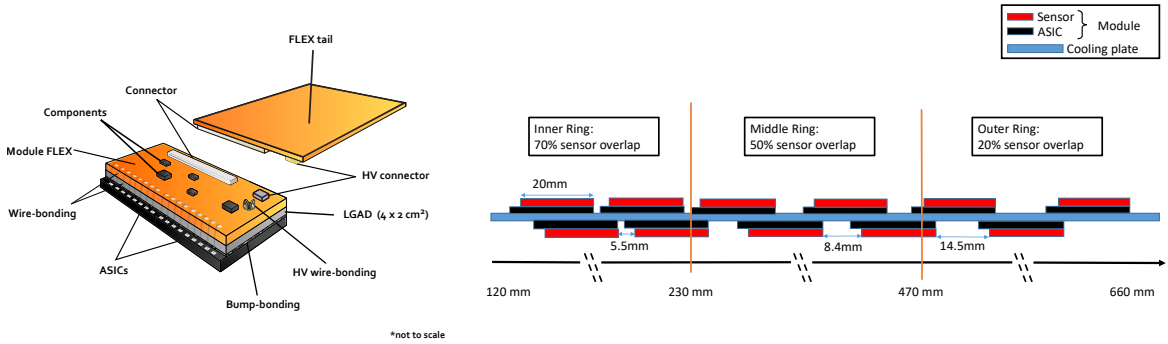

(a) (b)

FIGURE 5.6: (a) View of an HGTD hybrid module equipped with its read-out flex cable tail. The bare module, glued on the flex module PCB, is made of a 4×2 cm^2 sensor with two bump bonded ASICs. (b) Schematic drawing showing the overlap between the modules on the front and back of the cooling disk. There is a sensor overlap of 20% for r> 470 mm, 54% for 230 mm < r < 470 mm and 70% for r > 470 mm. [154]

The modules are organised in rows, on the direction of which the flex cables travel to reach the peripheral electronics, as shown in Figure 5.7. This particular row geometry has been chosen to achieve an even distribution of modules to the peripheral electronic boards (PEBs) while not exceeding the maximum possible length of flex cable circuits. The instrumented zone of the second cooling plate is identical to the first, but the second disk is rotated by 180° along the transverse Y axis, creating a mirror symmetry between the active layers of the fist and second disk. Furthermore, the two disks are rotated in opposite directions by 10°. This rotation, along with the mirror symmetry, ensure that the dead zones between active layers are not overlapping, and that there is sufficient space for the placing of the cooling manifolds between the peripheral electronics. The geometry scheme presented is the result of optimization studies that are described in more detail in chapter 6.

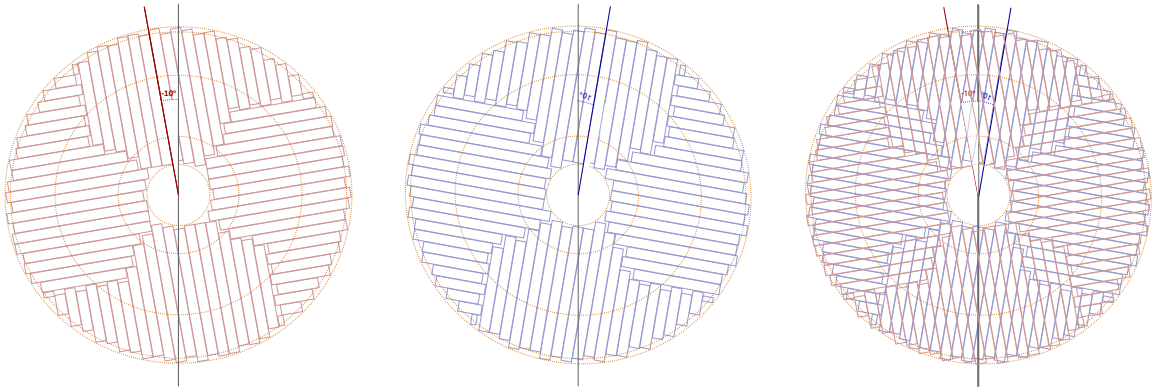

(a) First layer (b) Last layer (c) Overlay

FIGURE 5.7: The rotation of the readout rows for the front active layer of the first disk and front active layer of the second disk, separately and with the overlay of both. Each layer is rotated in alternating directions by 10°, while the second disk is rotated by 180° on the Y axis. The dashed lines correspond to the limits of the concentric radial rings where the overlap between modules of the two disk sides is constant: 20% overlap for r> 470 mm, 54% for 230 mm < r < 470 mm and 70% for r > 470 mm.

5.4 Sensors

As already explained, silicon is the chosen detection material for the HGTD. A new sensor technology, named Low Gain Avalanche Detector (LGAD) has been developed to meet the excellent timing performance and radiation tolerance requested by the new generation of collider experiments - it is the baseline choice for HGTD.

5.4.1 Low Gain Avalanche Detectors

The LGAD technology is based on the principle of an n-on-p diode. The p-n junction is inversely polarised by an externally applied bias voltage (V_{bias}), thus creating a large depletion region, otherwise referred to as bulk. When a charged particle crosses the sensor, it creates electron-hole pairs, that, due to the applied electric field, drift in opposite directions, towards the cathode and anode respectively. The particularity of an LGAD sensor is the addition of a highly doped p^+ layer below the cathode. This layer induces a large increase of the electric field over a thin multiplication zone, as displayed in Figure 5.8a. When the carriers reach this zone, they experience the amplified field, and start copiously producing additional e-h pairs, creating an avalanche. The total generated current is a sum of the currents induced by the movement of both primary and avalanche holes and electrons. Its evolution in time, along with that of the individual current components, is shown in Figure 5.8b.

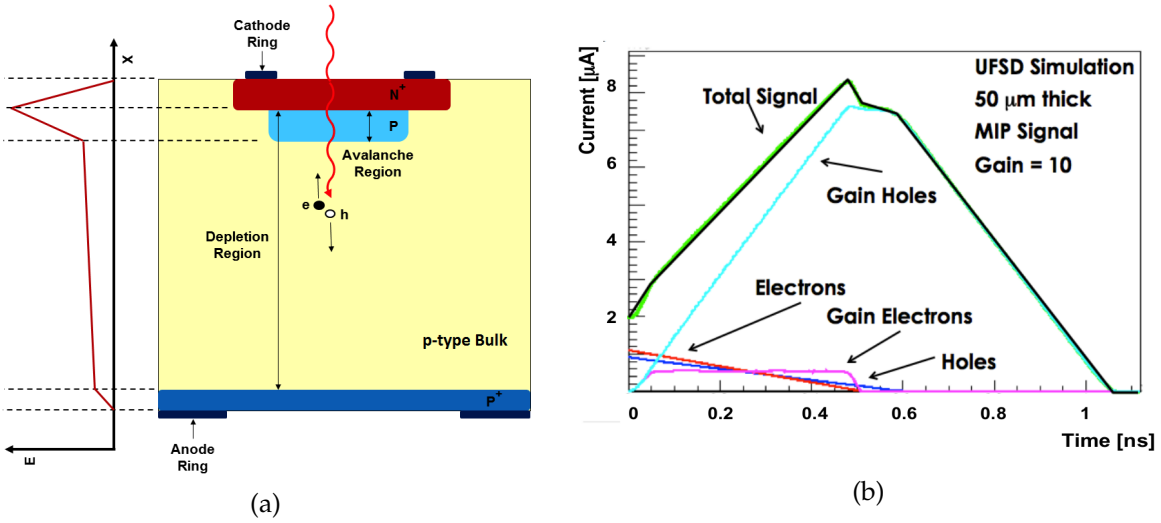

FIGURE 5.8: (a) Schematic of the LGAD principle. (b) Simulated total current signal (in green), along with the combined currents from primary or gain electrons (in blue shades) and holes (in red shades) [155].

The gain, defined as the ratio between the signal amplitude of the sensor under study and a common diode without an amplification layer, is crucial to the performance of the detector. While in single-photon detection devices, like SiPMs, the gain is usually of the order of O(10^3-10^4), the larger induced current of charged particles allows for a lower gain to be used for LGADs. This has the advantages of lower power consumption, easier segmentation and robustness under irradiation. Dedicated studies have shown that a gain of ~ 20 is the optimum choice for LGAD operation. This corresponds to a MIP-deposited charge of ~ 10 fC.

The timing performance of the detector is highly dependent on the slope of the sensor signal. Thanks to the amplification scheme of LGADs, the maximum amplitude of their current depends solely on the gain, while the drift time is proportional to the sensor thickness. Therefore, the desired steepness of an LGAD signal is achieved by making the sensors thin. However, a caveat is present in this logic; while thin sensors create faster signals, they also

give rise to higher capacitance values, a limiting factor for the performance of the electronics, as discussed in 5.5. In addition, the total collected charge is highly dependent on the number of produced carriers, and is thus not favoured by very thin sensors. Consequently, the sensors should not be too thin. A favourable value of $50\,\mu\mathrm{m}$ has been chosen for the HGTD.

5.4.2 Time resolution

The time resolution of a detector based on LGADs can be expressed as the quadratic sum of three terms:

$$\sigma_t^2 = \sigma_{Sensor}^2 + \sigma_{Electronics}^2 + \sigma_{Clock}^2 \tag{5.1}$$

The sensor contribution to the time resolution, σ_{Sensor}, arises mainly from the intrinsic non-uniformity of the energy deposited by a charged particle in silicon. This phenomenon, that is due to variations in the local density of e-h pairs along the particle's path, creates irregularities in the signal that follow the Landau distribution and are often referred to as Landau noise [155]. The contribution of the electronics ($\sigma_{Electronics}$) and of the reference clock (σ_{Clock}) to the time resolution are further explained in 5.5.

5.4.3 Production

LGAD sensors have been produced in the past years by several manufacturers: Hamamatsu Photonics (HPK), Japan; CNM, Spain; Fondazione Bruno Kessler (FBK), Italy; Micron, UK; Brookhaven National Lab (BNL), USA; and Novel Device Laboratory (NDL), China. Different production campaigns sought out to establish the basic parameters of the sensors such as size and depth and doping concentration. For the baseline production, Boron has been used as the default dopant while specialised manufacturing runs have also been undertaken to test radiation tolerance of alternative dopants, such as Gallium or additional carbon implantations. In general, devices from different productions perform similarly before irradiation, while post-irradiation, some discrepancies are observed.

Module assembly

The interconnection of the sensor to the front-end chip is a critical procedure of the device assembly process. Each sensor channel is DC-coupled to the corresponding read-out channel on the ASIC through a small electrically conductive bump ball, that is put in place through an hybridisation process called *bump-bonding*.

Solder bump-bonding consists of three steps. First under-bump metallization (UBM) is deposited on both sensor and ASIC pads. Then, SnAg solder bumps are deposited on the ASIC, and finally, the sensor and ASIC channels are interconnected. The hybridisation process is done on single tiles, ie, both sensor and ASIC are already diced before UBM.

The $90\,\mu\mathrm{m}$ wide aluminium pads of the sensor and read-out chip are covered with 4 to $6\,\mu\mathrm{m}$ of NiAu through an auto-catalytic chemical technique. The substrates are inspected and excess of UBM on the edges, if present, is removed. SnAg solder bumps of $80\,\mu\mathrm{m}$ diameter are then deposited on the ASICs with a bump deposition machine. The solder bumps are further reflowed in a dedicated machine in order to improve the placement and the shape uniformity of the bump balls. Flip-chip is performed with a bonder machine that allows to align, heat and press together the two substrates. After flip-chip, the assemblies are reflowed once again with formic acid.

Inspection of the devices is then carried out using x-rays in order to verify the good connectivity of all the bump bonds. In assembled prototypes, the topology of the bumps was found to be mostly cylindrical, with a diameter of about $90\,\mu\mathrm{m}$ and a height of $50\,\mu\mathrm{m}$ approximately.

An alternative process using Au bumps has also been developed. With Au bumps, UBM is not needed since the ball bumps can be deposited directly on the aluminium of the front-end pads. An alignment and thermo-compression cycle is used to interconnect the channels of the sensor and ASIC. Studies determined that the bump topology resembled a conical frustum with a base of about $140\,\mu\mathrm{m}$ and a height of $15\,\mu\mathrm{m}$. The Au bump-bonding process was performed only for R&D purposes - it is not planned to be used for the final production of HGTD modules.

5.4.4 LGAD performance

An extensive experimental program has been put in place to test the performance of the LGAD sensors. This was done both in laboratories, using beta-sources or laser setups, and in beam test campaigns, were the sensors were exposed to highly relativistic particles, more in line with the conditions at the ATLAS experiment. In order to estimate the LGAD radiation hardness, devices were exposed to radiation, either by protons or neutrons. Although results from either types of particles are expressed in the neutron-equivalent unit, protons are known to be more destructive due to the additional charged interactions with the sensor material.

The effect of irradiation

In the very forward position of the HGTD, the resilience of the sensors under irradiation becomes crucial for the performance of the detector. There are three main effects of irradiation that degrade the performance of LGADs [158]; the reduction of the charge collection efficiency due to trapping defects in the bulk of the sensor, the reduction of the gain due to the removal of active dopants from the amplification layer and the increase of the leakage current, defined as the intrinsic current that flows between the anode and cathode in the absence of crossing particles, due to the presence of defects. The former two have a negative impact on the produced charge, which can be seen in simulation, as demonstrated in Figure 5.9a. The introduction of some effective acceptors in the bulk of the sensor due to irradiation, partially mitigates the reduction of the gain, since they contribute to the charge multiplication in the bulk [159]. The generated signal is also faster in irradiated sensors, which partially improves the timing performance. In addition, the increase of the bias voltage can further augment the collected charge. The recovery of the gain with the bias voltage has been verified with beta-source measurements as shown in Figure 5.9b.

The leakage current affects the generated noise of the sensor. Since its generation is exponentially dependent on the temperature, its increase can be partially mitigated by decreasing the temperature. With the choice to run the HGTD at $-35\,^{\circ}\mathrm{C}$, a reduction of the leakage current by a factor of $\sim$130 is anticipated.

Figure 5.10a shows the time resolution of an HPK-type sensor as a function of the applied absolute bias voltage for various irradiation levels. Both proton and neutron irradiated sensors have been tested in a beta source laboratory setup. The time resolution degrades with the fluence, indicating a need to operate the sensors at a higher V_{bias} in order to recover its performance. However, the increase of the bias voltage is upper bound by the breakdown voltage, at which the leakage current becomes so large that it destroys the p-n junction, and consequently, the sensor. Therefore, it is important to establish an operating voltage, V_{op}, at which the performance in terms of charge and time resolution is acceptable and at which the

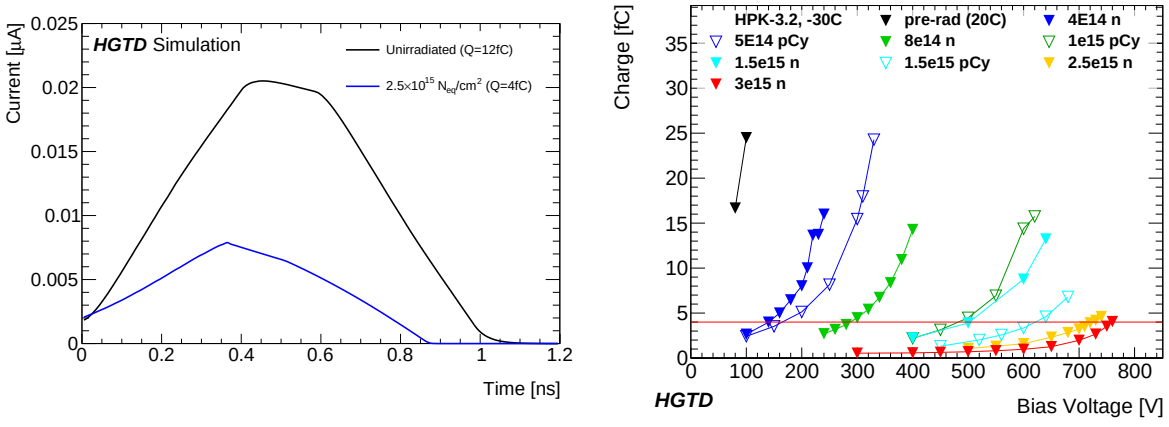

(a) (b)

FIGURE 5.9: (a) Simulated signal current in LGADs at the start and after the full integrated neutron fluence received at the HGTD end-of-life. (b) Collected charge as a function of bias voltage for different fluences for HPK-3.2. The horizontal lines indicate the HGTD lower charge limit of 4 fC at all fluences. Solid (open) markers indicate neutron (proton) irradiation. Measurements were performed at $-30\,^{\circ}\mathrm{C}$. [154]

sensor can be safely operated for prolonged periods of time. It can be seen in Figure 5.10b, that by choosing for each irradiation level such an appropriate operating point, the timing performance can be maintained within the HGTD requirements, displayed in the green band, for fluences up to $3\times\ 10^{15}\ \mathrm{n_{eq}/cm^2}$.

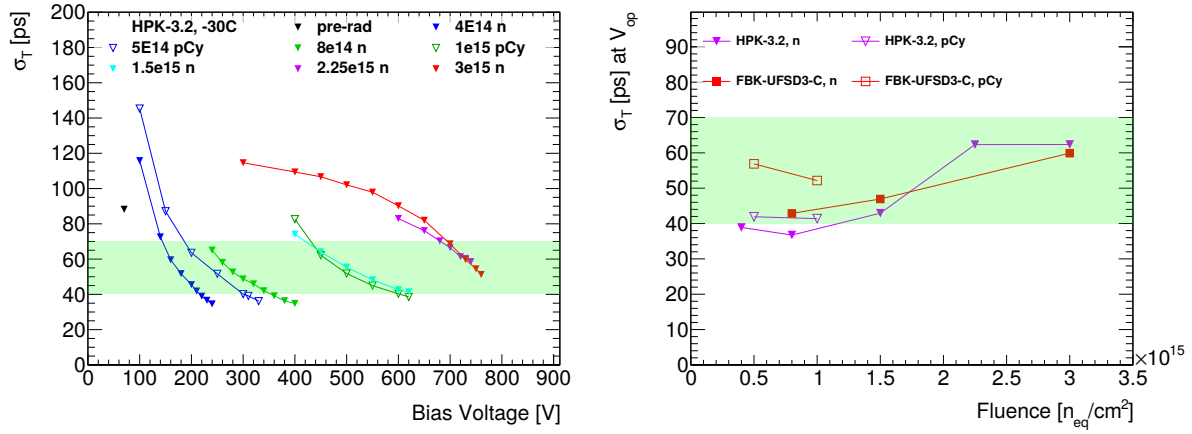

(a) (b)

FIGURE 5.10: (a) Time resolution as a function of bias voltage for different fluences for HPK-3.2. (b) The time resolution at V_{op} as a function of fluence. The green band represents the interval of time resolution in the lifetime of HGTD. Solid markers indicate n irradiation, open markers p irradiation. [154]

5.5 Front-end Electronics

The performance of any silicon detector is strongly linked to the design of the initial electronic circuit, usually referred to as front-end. A common front-end configuration consists of the sensor, followed by a preamplifier that amplifies the sensor signal. The now amplified signal of the preamplifier is translated into an analogue time measurement using a discriminator circuit. The last step in the front-end chain is the digitization of the time information using

a Time-to-Digital Converter (TDC). The digitised output can be further stored and trigger-matched before transmission to the outside of the detector.

5.5.1 Electronics contribution to the time resolution

The electronics contribution to the time resolution, $\sigma_{Electronics}$ can be viewed as the quadratic sum of 3 individual components:

$$\sigma^2_{Electronics} = \sigma^2_{Jitter} + \sigma^2_{TimeWalk} + \sigma^2_{TDC} \tag{5.2}$$

The jitter term represents the uncertainty in the time measurement due to the presence of noise in the signal, as is schematically displayed in the right-hand side of Figure 5.11. It is directly proportional to the noise (N) and inversely proportional to the slope of the signal (dV/dt), as shown on the middle part of equation 5.3; assuming that the latter is constant, the jitter can be modelled as the ratio of the rise time (t_{rise}) to the signal amplitude-over-noise (A/N) ratio:

$$\sigma_{\text{jitter}} = \frac{N}{dV/dt} \sim \frac{N}{A/t_{rise}} \tag{5.3}$$

where t_{rise} is the time from the beginning to the maximum point of the pulse.

Time walk is an error in the time measurement of the pulse using a constant threshold due to the fact that larger signals cross this threshold faster than smaller ones. This effect, shown graphically on the left-hand side of Figure 5.11, produces a dependence of the measurement on the amplitude of the signal. Assuming that the signal crosses the threshold at a time t_{cross}, the time walk is defined as the RMS of t_{cross}. Supposing once more that the signal slope is constant results in the following expression:

$$\sigma_{\text{TimeWalk}} = [t_{cross}]_{RMS} = [\frac{t_{rise}V_{th}}{A}]_{RMS} \tag{5.4}$$

Thankfully, the time walk effect can be corrected by the additional measurement of a quantity that is proportional to the signal amplitude. The measurement of the width of the pulse above the constant threshold, referred to as the Time-Over-Threshold (TOT), is known to be well correlated with the pulse amplitude. The baseline HGTD choice for the time walk correction method is a TOT measurement with a constant threshold discriminator. With a residual error after correction less than 10 ps, which is the current HGTD requirement, the effect of the time walk can be considered negligible. An alternative method to mitigate time walk, based on a Constant Fraction Discriminator (CFD) method, has been considered by the HGTD community. In this method, the time walk is minimised by defining the time of arrival as the time when the signal crosses a constant fraction of the maximum amplitude. A CFD method cannot be realistically implemented in a read-out circuit, since the maximum amplitude is reached after the threshold is crossed. Instead, the realization of this idea in a circuit is done with a Zero-Crossing Discriminator (ZCD). In the ZCD, the signal is copied, and the copy is delayed by a delay factor d_{ZCD} and attenuated by an attenuation factor f_{ZCD}. The zero-crossing time of the difference of the original signal and the attenuated copy is by construction independent of the signal amplitude, under the assumption that the pulse shape remains identical.

Finally, the digitization of the time measurement introduces an error due to the binning of the TDC circuit. Assuming an ideal TDC with bins of equal size, this contribution is equal to $\Delta T/\sqrt{12}$, where ΔT is the bin size. In order to minimise this term, HGTD is designing a novel TDC of fine binning ($\sim$ 20 ps), described in detail in 5.5.5.

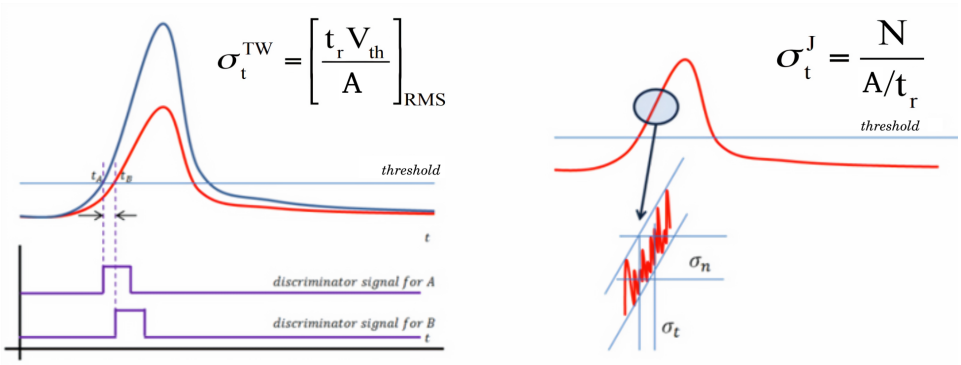

FIGURE 5.11: Effect of (right) the time walk and (left) the jitter in the time measurement using a constant threshold discriminator.

5.5.2 Preamplifier choice

A silicon sensor from the viewpoint of the electronics is equivalent to a current source I_d in parallel with a detector capacitance C_d. A key aspect in the optimization of the electronics design is the choice of the preamplifier architecture. Charge sensitive preamplifiers have been a common choice in particle physics detectors, thanks to their low noise and stability. This type of preamplifiers is typically characterised by a small bandwidth and therefore integrates the signal to a certain degree. However, with recent developments on sensor technologies, the sensor capacitance is being pushed to continuously lower limits. A new type of preamplifier, where the integration of the signal is performed directly on the detector capacitance without a critical reduction of its amplitude, can now be envisioned. This type of preamplifier is usually referred to as broadband (or current sensitive) and is characterised by large bandwidths that can take full advantage of fast signals. Broadband preamplifiers are also better suited for high acquisition rates, since they produce a fast and steep output. Given the fast LGAD signals and the need for operation at the high-rate environment of the LHC, a current sensitive configuration has been chosen.

The preamplifier design can be further optimised by the choice of the input impedance value Z_s. A small Z_s (typically O(10) Ohm), usually referred to as a transimpedance (TZ) configuration, results in an input that is sensitive to the input current. A simplified schematic view of such a configuration is shown in Figure 5.12a. The output of TZ preamplifiers are typically short-duration steep signals of small amplitude. The detector capacitance, in combination with Z_f and the wire induction create an RLC circuit. TZ configurations are therefore prone to oscillations. On the contrary, if a large value of Z_s (of the order of $O(10^3)$) is used, the input becomes more sensitive to the input voltage V_{in} and the resulting output signals tend to be longer and more amplified. This preamplifier, named voltage sensitive (VPA), can be seen in Figure 5.12b. Voltage sensitive configurations are more stable than their TZ counterparts. Another drawback of the TZ configuration is that their parallel noise is larger.

When dealing with LGAD sensors, the preamplifier speed becomes less crucial, because of the duration of their current (not negligible with respect to the preamplifier rise-time) and the capacitive impedance of the sensor. Taking additionally into account the stability benefits of voltage sensitive preamplifiers has led to them being the baseline choice for the HGTD ASIC. I have performed detailed study of the two preamplifier type's performance that supports this choice, as discussed in 7.2.2.

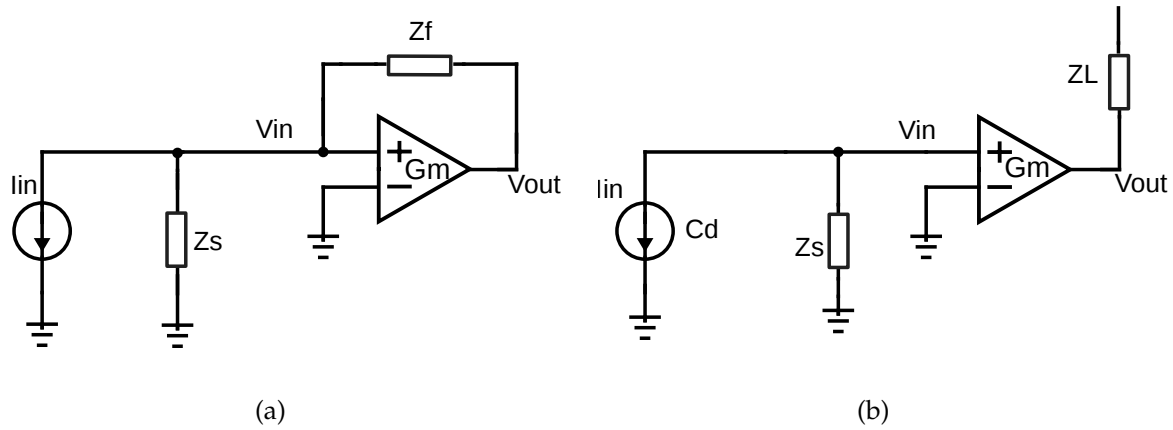

(a) (b)

FIGURE 5.12: Simplified configuration of (a) a transimpedance and (b) a voltage sensitive preamplifier

5.5.3 Jitter optimization in a voltage-preamplifier configuration

In a voltage configuration the jitter can be easily calculated assuming that the detector is a constant current source I_{in} with a duration time of t_{dur}. The corresponding input charge Q_{inj} is then equal to $I_{in} \times t_{dur}$. I_{in} is converted into an input voltage (V_{in}) through the overall input impedance Z_s, which is given by the sensor input impedance $1/j\omega C_d$ in parallel with the input resistance of the preamplifier. At high frequency and for $C_d \sim$ 1-10 pF, the input impedance is dominated by the detector capacitance, and therefore, the signal is integrated in C_d. Given that, at this high speed domain, the maximum voltage is reached before the preamplifier feedback network reacts and drains out the charge from the input capacitance, the input voltage is given by:

$$V_{in} = \int I_{in}(t)/C_d dt = Q_{in}/C_d. \tag{5.5}$$

The preamplifier output voltage is:

$$V_{out}^{pa} = g_m Z_L V_{in}, \tag{5.6}$$

where g_m represents the trans-conductance of the transistor and Z_L the preamplifier load impedance.

The output pulse would reach its maximum in the input pulse drift duration time (t_{dur}) if the preamplifier was infinitely fast. With a real preamplifier, where the output signal is the convolution of the input current and the preamplifier response, a convenient approximation to take into account its speed is given by the quadratic sum of the t_{dur} and the preamplifier rise-time ($t_{r_{pa}}$): $\sqrt{t_{dur}^2 + t_{r_{pa}}^2}$. If, instead of a constant current, the LGAD's triangular signal is considered, the result is quite similar, but the Full Width at Half Maximum (FWHM) of the detector current pulse, t_{FWHM} is used instead of t_{dur} .

The voltage RMS (V_n) at the preamplifier output and the signal slope (dV/dt) are then given by:

$$V_n = G_{pa} \times e_n \sqrt{\pi * BW/2} \sim \frac{G_{pa} \times e_n}{\sqrt{2 t_{r_{pa}}}} \text{ and } \frac{dV}{dt} = \frac{G_{pa} Q_{in}}{C_d \sqrt{t_{r_{pa}}^2 + t_d^2}} \tag{5.7}$$

where G_{pa} is the gain of the preamplifier, BW the preamplifier bandwidth, e_n the noise spectral density and t_d is either the t_{dur} in the case of a constant current source or the t_{FWHM} in the case of an LGAD pulse. Combining all the terms results in the following formula for the jitter :

$$\sigma_{jitter} = \frac{e_n C_d}{Q_{in}} \sqrt{\frac{t_{r_{pa}}^2 + t_d^2}{2t_{r_{pa}}}} \tag{5.8}$$

It can be seen that the condition to minimise the jitter is to match the preamplifier rise time to the t_d : $t_{r_{pa}} = t_d$, thus reducing the jitter formula to :

$$\sigma_{jitter} = \frac{e_n C_d}{Q_{in}} \sqrt{t_d}. \tag{5.9}$$

However, the dependence of the jitter on this matching condition is not very strong. For instance, simulations show that for a sensor drift-time of 600 ps, if the preamplifier rise time is reduced or increased by a factor of 2 with respect of the optimal matching value, the jitter would deteriorate by just about 12%. Given these considerations, in order to minimise the jitter, the sensor should have a small capacitance, a short pulse duration and be capable of providing a large charge.

5.5.4 ASIC architecture

ALTIROC, the designated front-end ASIC of HGTD, will be a 20 mm $\times$ 22 mm chip, integrating 225 channels arranged in a 15 $\times$ 15 channel matrix. It will be designed using TSMC[2] CMOS 130 nm. The design of the ALTIROC is optimised to ensure its radiation hardness up to 4 MGy. Table 5.1 summarises the performance requirements that the ALTIROC ASIC must satisfy to be successfully used in the HGTD.

Maximum leakage current	5 µA
Single-pad noise	$<$ 0.5 fC
Cross-talk	$<$ 5%
Threshold dispersion after tuning	$<$ 10%
Maximum jitter	25 ps at 10 fC
TDC contribution	$<$ 10 ps
Time Walk contribution	$<$ 10 ps
Minimum threshold	2 fC
Dynamic range	4 fC - 50 fC
TDC conversion time	$<$ 25 ns
Trigger rate	1 MHz L0 or 0.8 MHz L1
Trigger latency	10 µs L0 or 35 µs L1
Clock phase adjustment	100 ps

TABLE 5.1: Performance requirements for the HGTD ASIC. The values given for the noise, minimum threshold and jitter have been specified considering a detector capacitance C_d = 4 pF.

The main structures of the ASIC are: the single-channel electronics (repeated 225 times), which include the preamplifier, discriminators and TDCs as well as a local storage unit; the end-of-column logic (EOC), responsible of reading out the data along each of the 15 columns and transferring them to further processing units; and finally, the common digital part which prepares the received data for transmission to the peripheral electronics that are described in 5.6.3.

[2]Taiwan Semiconductor Manufacturing Company

There exist two prototype versions of ALTIROC at the moment: ALTIROC0, a first 4×4 channel prototype that includes the preamplifier and discriminator components of the single-cell electronics and ALTIROC1, a 5×5 chip that includes in addition the TDCs and a simplified memory logic. A large part of this thesis has been dedicated in the characterization of the two prototypes and results of this work are presented in Chapter 7.

5.5.5 Single-channel readout electronics

Figure 5.13 is a schematic representation of the read-out electronics for one of the 225 channels of the ALTIROC ASIC. The channel architecture can be broken down in two parts; the analog front-end, that contains the preamplifier, discriminator and TDC stages of the read-out, and the digital block, which is responsible of identifying and storing the hits. The digital part includes also a separate block for processing the luminosity information.

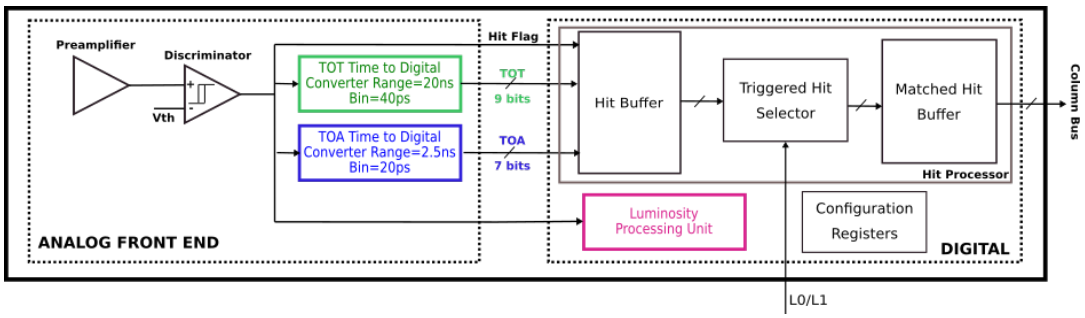

FIGURE 5.13: Schematic of the single-channel read-out electronics. Two main blocks are identified, the analogue and the digital part. The input pulse from the sensor enters the preamplifier on the left. The TOA and TOT data are read out by the column bus on the right. [154]

Preamplifier design

The ALTIROC baseline preamplifier, shown in Figure 5.14a, is a voltage preamplifier built around a cascoded common source configuration (M1) followed by a voltage follower (M2). The R_2 resistor corresponds to the resistive component of Z_S of Figure 5.12b and is connected as a feedback to ensure the biasing of the preamplifier input. Its value can be modified to adjust the fall time of the preamplifier output. The R_1 resistor corresponds to the load resistance R_L.

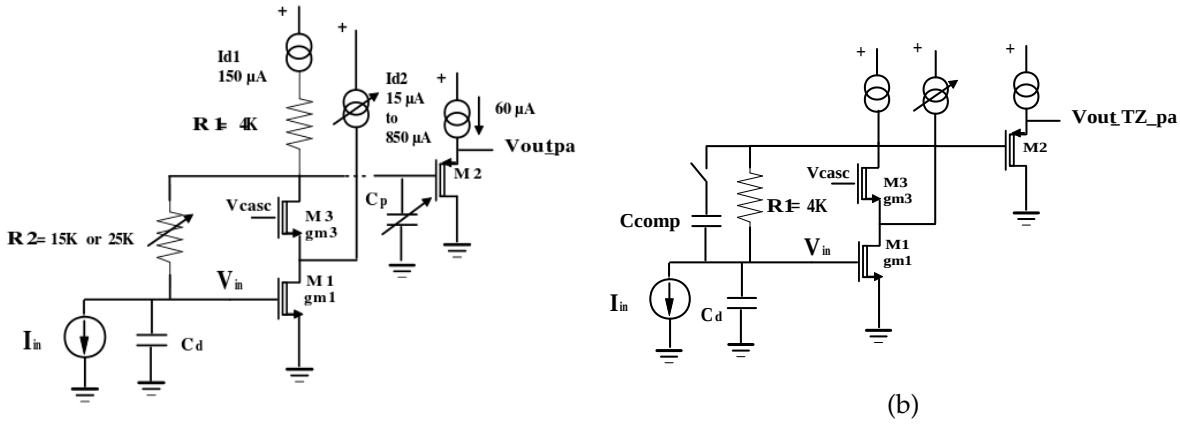

FIGURE 5.14: Schematic for the preamplifier implemented in the latest ASIC design, ALTIROC1 for (a) the baseline voltage configuration (b) the alternative pseudo-transimpendance configuration.

Given that the preamplifier is voltage sensitive, the detector capacitance is a key ingredient to calculate the input voltage for a given input charge. An input charge Q_{in} gives an input voltage V_{in} equal to Q_{in}/C_d. The voltage output of the preamplifier is given by the following expression:

$$V_{out}^{pa} = G_{pa} \times V_{in} = G_{pa} \times Q_{in}/C_d \tag{5.10}$$

The gain of the preamplifier G_{pa} is, to first order, given by $g_{m1} \times R_1$ where g_{m1} is the transconductance of the input transistor. In weak inversion, the transconductance is given by

$$g_{m1} = q \times I_d/2kT \tag{5.11}$$

(where q=1.6 10^{-19} C) i.e. approximately $20 \times I_d$ at room temperature. The spectral density of the input transistor is equal to

$$e_n = \sqrt{2kT/g_{m1}}. \tag{5.12}$$

As both gain and noise depend on the current that flows in the input transistor, the drain current I_d is made of two current sources : I_{d1} is a fixed current source of 150 µA while I_{d2} can be tuned. Simulations have shown that increasing I_{d2} beyond 600 µA adds little gain as the transistor is no more in weak inversion mode.

To compensate for the rise time of the LGAD sensor becoming smaller when irradiated, the rise time of the preamplifier is tunable. This is done through the pole capacitance C_p that can be adjusted through slow control (from 0 to 175 fF) allowing to set a preamplifier rise time between 300 ps and 1 ns (bandwidth between 350 MHz to 1 GHz).

The input impedance R_{in} is given by the R_2 resistance divided by the open loop gain of the preamplifier. The value of the R_{in} depends therefore also on the drain current I_d. For I_d= 300 µA and R_2=25kΩ, the input impedance is around 1.6kΩ. The fall time of the preamplifier depends on the time constant of the RC circuit, which is given by R_{in} multiplied by the total capacitance seen on the input of the preamplifier (sum of the sensor capacitance (C_d) and any parasitic capacitance). With 3-4 pF capacitance, this fall time is within the bunch-crossing interval of the HL-HLC. However, the width of the discriminator pulse, which is used to correct for the time walk effect, can be slightly longer than the time between two consecutive bunch crossings at the HL-LHC, provided a large injected charge and a low threshold. This could disturb the measurements and, therefore, on the second version of the ASIC prototype (ALTIROC1), the values of R_2 and I_{d2} are tunable through slow control. The resistance R_2 is also used to absorb the leakage current I_{leak} of the sensor. This leakage current would induce a drift of the output DC voltage of the preamplifier by an amount of the order $R_2 \times I_{leak}$. The threshold of the discriminator needs to be corrected accordingly to this shift.

A pseudo-transimpedance configuration (TZ), shown in Figure 5.14b, has also been integrated in some channels of the two ALTIROC prototypes, in order to choose the best-performing preamplifier version. The configuration is very similar to the voltage one except that the R_1 resistor is now in the feedback of the amplifier and it corresponds to the resistive component of Z_f in Figure 5.12a. At high frequency, the gain of the pseudo-TZ preamplifier is not given as in a usual TZ preamplifier by $R_1 I_{in}$, but by $g_m R_1 V_{in}$. That's why this architecture is named pseudo transimpedance. The input impedance is about 10 times smaller than the one obtained with the voltage configuration. The fall time of the TZ preamplifier is therefore around 10 times shorter than the fall time of the VPA. This can present some challenges in the time walk correction, since the fall time is very strongly dependent on the amplitude of the signal, meaning that the TOT measurement needs to be determined with a very high accuracy.

Discriminator

The time measurement is performed by two discriminators that follow the preamplifier. One is dedicated for the measurement of the Time Of Arrival (TOA) of the crossing particles and the second for the Time Of End (TOE), i.e. the falling edge. The combination of these two measurements provides the TOT, which is then used off-line to correct for the time walk effect. A constant fraction discriminator (CFD) was also included as an alternative in some channels of a first version of the chip, but a residual time walk was observed. Finally, the residual dependence of the TOA to the signal amplitude was larger than the one observed with a constant threshold discriminator and a TOT-based time walk correction. The shape of the remaining time walk was not investigated further and this alternative was removed from the design of the current prototype, as it has no advantage while it adds to the chip complexity and power consumption.

To ensure a jitter smaller than 10 ps at large signals, the discriminator is built around a high speed leading edge architecture with hysteresis to avoid re-triggering effects. Two differential stages with small input transistors are used to ensure a large gain and a large bandwidth (around 0.7 GHz). The discriminator threshold (V_{th}) is set by an external 10-bit DAC common to all channels. An additional 7-bit DAC (not present in the first prototype, ALTIROC0) allows to make small V_{th} corrections individually for each channel in order to compensate for differences among them or for different values of leakage current.

Time-to-Digital Converter

The time measurements provided by the discriminators are digitised from two Time-to-Digital Converters, one dedicated for the TOA and the other for the TOT information. The TOA TDC can convert the time information in a window of 2.5 ns centred at the bunch crossing. The position of the window is tunable through slow control parameters to account for any time drifts. A bin size of 20 ps is used in order to minimise the contribution of the digitization to the time resolution. For the TOT TDC, the measurement is performed in a much larger range of 20 ns. A reduced accuracy of 120 ps is used in this case, in order to minimise the conversion time and power dissipation.

Since the target bin size is smaller than the gate-propagation delay in the 130 nm technology, a Vernier delay configuration is used. This configuration consists of two lines, each composed by a series of delay cells, whose common delay value is controlled by a voltage level V_{ctrl}. The working principle of this type of TDC is as follows: the delays of the two lines are set differently, one to a smaller value (FAST) and one to a larger value (SLOW). The output of the discriminator (START signal) enters the SLOW delay line first, while the end-of-measurement window (STOP signal) enters the FAST line with some delay. While at the beginning the START signal precedes the STOP, since it is in the SLOW line, it is more delayed at each cell and therefore comes closer to the STOP with every step. The number of cells that are needed for the STOP signal to surpass the START constitute the result of the digitization, whose resolution is equal to the difference of the two delay values.

The working principle of the TOA TDC is shown graphically in Figure 5.15. In order to achieve the 20 ps requirement, the delay values are set to 120 ps for the FAST and 140 ps for the SLOW. A cyclic structure is employed to minimise the space occupied by the TDC. The reverse START-STOP scheme, with which the digitization process starts only upon the detection of a signal, is also used to reduce power consumption.

The design of the TOT TDC has significantly evolved as this thesis is being written. Initially, the TOT digitization was performed in two steps. First, a coarse single delay line of

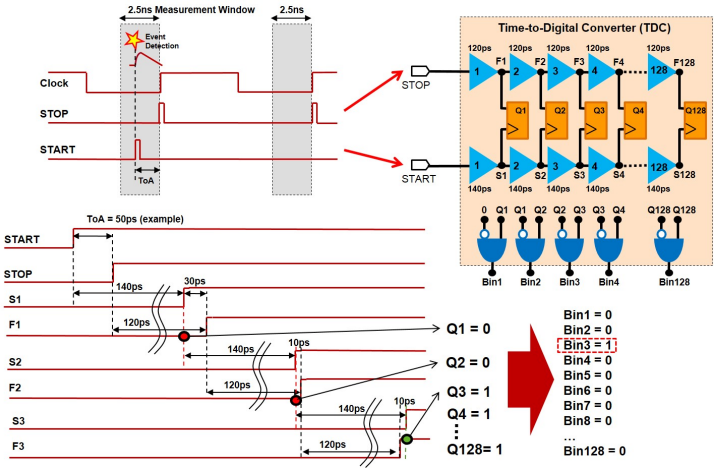

FIGURE 5.15: Graphic representation of the working principle of the TOA TDC. The drawing on the top left shows how the START and STOP signals are generated, the first with the discriminator output upon event detection, the second corresponding to the next clock edge. The grey area indicates the 2.5 ns detection window. On the top right, the schema represents the TDC, with the SLOW delay line (140 ps cells) that propagates the START signal, and the FAST delay line (120 ps cells) in which the STOP signal is propagated. The difference between delays defines the bin. After each cell the signals are compared, and the bin number provides the converted measurement.

160 ps bin size was used to extend the measurement range up to 20 ns. When the coarse measurement is complete, the signal entered a Vernier line identical to the one used for the TOA TDC which provided the better resolution of 40 ps. The aforementioned scheme on the TOT digitization was the default at the time of the ALTIROC1 design. However, recently, the requirements on the TOT accuracy have been re-evaluated and found to be less strict. In order to reduce the complexity of the TOT TDC and reduce the bits needed to encode the TOT information, a coarser design based on a single delay line with 120 ps bin size is envisioned for the final design of the chip.

Calibration

In order to be able to perform accurate calibration measurements of the common time reference used throughout the detector, an internal pulser, common to all channels, is integrated in the ASIC. The pulser consists of a programmable DC current (tunable with an internal 6-bit DAC) that flows continuously in a 50 kOhm resistor until it is interrupted by a command pulse that shorts the resistor to ground. An internal 200 pF calibration capacitor[3], which can be selected through slow control, is present at the preamplifier input of each pixel. The pulser generates a fast voltage step which is sent through the selected pixel calibration capacitor, inducing a short square pulse at the input of the preamplifier. The dynamic range of the pulser goes from 0 to 250 mV or equivalently from 0 fC up to $\sim$ 50 fC.

Luminosity

In order to determine the instantaneous luminosity, the number of detected hits in the ASIC matrix is measured at the bunch-crossing rate of 40 MHz (every 25 ns). The measurement is performed in two adjustable time windows; a 3.125 ns one, centred around the bunch-crossing, will be counting the number of hits at the expected arrival time of the particles from collision. A second window of adjustable position and width in steps of 3.125 ns will

[3]The value of the calibration capacitor was 100 pF in the first prototype, ALTIROC0

provide side-band information that can be useful in the control of background arising from single-beam activity, instrumental noise, and afterglow effects. While all ASICs are planned to be equipped with luminosity blocks, in order to reduce the required bandwidth for the transmission of the luminosity information, only ASICs at R>430 mm will be performing the aforementioned measurements.

5.6 DAQ system

The digitised information provided by the front-end ASICs needs to be transmitted to the central ATLAS data acquisition system; this is done in multiple steps, which constitute the HGTD Data Acquisition (DAQ) system. The path that the data undertake to exit the detector is graphically shown in Figure 5.16; starting from the common digital part of the ASIC, the data is transmitted through flex cables to the peripheral electronic boards, that are positioned at the outermost part of each cooling plate, on both of its sides. There, the data are serialised and adapted for high-speed optical transmission to the ATLAS back-end DAQ. The read-out of the timing and luminosity information is handled separately in all the aforementioned steps.

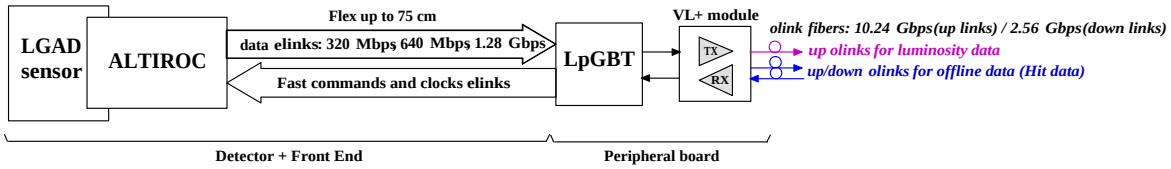

FIGURE 5.16: Upstream and downstream data flow. Flex cables containing e-links transmit data, fast commands and clocks between the ALTIROC ASIC and the lpGBT [160]. VL+ is the Versatile Link+ VTRX+ module [161].

5.6.1 Data format

The readout of the ASIC information is handled by dedicated timing and luminosity modules in the common digital part of the ASIC. As already described in 5.5.5, the TOA (TOT) TDC will measure time in a 2.5 (20) ns window with a 20 (40) ps [4] bin size. Therefore, 7 bits are needed for the TOA and 9 for the TOT to encode all possible digitised time values. The position of the hit pad needs to also be stored, which requires additionally 8 bits. In order to reduce the bandwidth and power consumption, a zero suppression logic is implemented, meaning that only information from hit cells is maintained. Finally, the total event size of each ASIC for one bunch crossing, including possible headers amounts to:

$$event\_size = 24 \times n_{hits} + (header) \tag{5.13}$$

where n_{hits} is the number of hit cells in the ASIC and the current estimate for the header is 24 bits. The data is stored until an L0/L1 trigger is received. The estimated L0/L1 trigger rate of ATLAS at the HL-LHC is approximately 1 MHz.

Contrary to the timing measurement, the luminosity information will be encoded in a constant event-size of 16 bits. It will be read-out at the bunch-crossing rate of 40 MHz and therefore always transmitted by 640 Mbps e-links.

[4] The older TOT resolution has been used in this thesis, as the decision to increase the TOT TDC binning to 120 ps was taken after the studies of Chapter 6.

5.6.2 Flex cables

The flex cables connect the signals from the modules to the peripheral electronics and vice versa. Each module, consisting of two ASICs, is glued to a small flex module PCB. The latter is connected to a long flex tail cable, which travels along the row to reach the designated PEB. Since flex tails from modules in the same row are stacked, it is imperative that they can be produced as thin as possible. A thickness less than $250\,\mu\mathrm{m}$ is currently placed as a requirement. In addition, the maximum manufacturable flex length is 750 mm, which creates a constraint on the row geometry.

The upstream part of the flex cables includes data differential e-links that transmit the timing and luminosity information. As already discussed, the average data rate is highly radius-dependent. In order to accommodate for the bandwidth variation with the radius, the transmission is performed through e-links of three different speeds. Modules in the innermost part of the detector, where the particle rate is the highest, are read-out with 1.28 Gbps links, while lower speed links of 640 and 320 Mbps are used for intermediate and outer parts of the active area of the detector, respectively. These three speeds are not arbitrary; they are defined as a functionality of the lpGBT ASIC, discussed in detail in 5.6.3. Flex cables have two additional e-links for the transmission of the luminosity information at a 640 Mbps speed.

Apart from the data read-out signals, flex cables also include HV, powering, slow control, ground and various monitoring lines. They are also responsible of distributing the clock and fast control commands to the front-end ASICs.

5.6.3 Peripheral Electronics Boards

The data that is collected from the modules is received in custom on-detector electronics at the periphery of HGTD, which handle its transmission to further centralised ATLAS systems. The PEBs play also a crucial role in the power distribution and monitoring of the active area. A key component of these boards is the low-power Gigabit Transceivers (lpGBTs), an ASIC that is developed by CERN, and is responsible of the serialization of up-stream data and down-stream transmission of ASIC control parameters.

Given the extremely limited available space at the periphery of HGTD, the PEB design becomes quite challenging. In order to optimise the distribution of the modules to the PEBs, each PEB will be serving multiple rows. In addition to the active area, the PEBs also require cooling, and are therefore mounted on the cooling plate. Consequently, the active area of each side of the cooling plate is serviced by their dedicated group of PEBs, a configuration that places even more stringent constraints on the PEB size. Fitting all the necessary components in such a small space becomes a non trivial issue and an optimization of the module distribution is needed. Chapter 6 describes studies on the optimization of the module geometry that have been undertaken to account for this issue.

low-power Gigabit Transceivers

In Figure 5.17, a simplified scheme of the lpGBT ASIC [160] is presented. This ASIC has the possibility to receive and serialise data from multiple ASICs as well as to transmit clock and fast control information. In addition, it contains 8 ADCs that can be used to monitor the low voltage power supply. A separate control block provides I2C ports that are currently planned to be used for the slow control transmission and possibly for reception of monitoring parameters such as temperature. For the upstream e-link ports, the organization of the entries is done in 7 groups. Each group is programmable independently and can have a different reception speed. The number of up-link entries depends on the speed chosen. There are

various speed combinations possible, while for the HGTD the current decision is to use the 7/14/28 entries at 1280/640/320 Mbps speeds protocol.

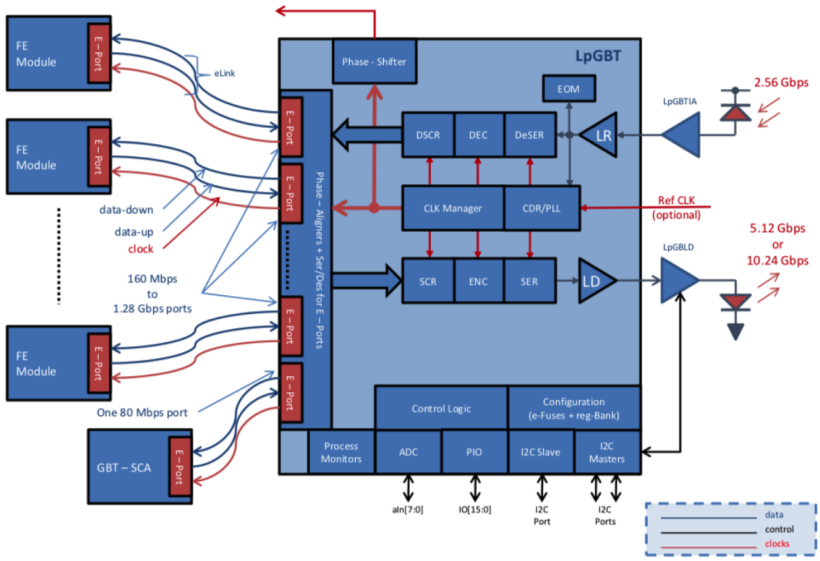

FIGURE 5.17: Block diagram of the lpGBT ASIC. The ASIC contains 7 independently programmable groups of e-ports that can be used at different speeds. A different block that uses I2C protocol is dedicated for the transmission of slow control parameters. Data from/to the lpGBT are transmitted/received through optical links at a 10.24 Gbps rate.

Optical links

The transmission of the serialised data to the off-detector systems and the control of the lpGBTs is handled by optical links. Two fibres, one up and one down type, are needed for each lpGBT that handles timing readout, while for the ones that only transmit luminosity information, only an up-link is necessary. In those LpGBTs the slow and fast control parameters are received from timing lpGBTs, which act as master units. The data is adapted for optical transmission by Versatile Link+ VTRX+ modules, a CERN-based technology [161]. The fibres send out and receive data at a rate of 10.24 and 2.56 Gbps, respectively.

5.6.4 Calibration of T_0

It is imperative for the timing performance of the HGTD that a common reference time is established throughout the detector. This time, referred to as T_0 (not to be confused with the primary vertex t_0 in section 5.7), is provided to each of the $\sim$ 3.6 million channels of the detector through the lpGBTs. The resolution of the T_0 is limited by the irreducible jitter of the lpGBT clock and additional jitter contributions of the flex and the ASIC. The combined non deterministic contribution to the T_0 resolution is estimated to be approximately 15 ps. However, an additional contribution can arise when the channels are not perfectly aligned to the bunch crossing clock. This misalignment can be due to time-static effects (different flex cable length, systematic difference between channels in one ASIC due the imperfect clock tree distribution, geometrical time of flight etc.) or time drifts over large regions and long periods (day/night effect on the LHC clock, temperature effects etc). Of the two, the first category is the most crucial, given that the HGTD physics case heavily relies on the relative comparison of the time of different channels within an event.

In order to correct for time-static effects, regular sets of inter-calibration runs between LHC

fills are foreseen, using a calibration pulser in each channel of the ASIC. Time-dependent effects will be estimated by measuring the average time of each channel in various time windows during normal data taking. The information from many calibration windows will be combined off-line to achieve the final correction.

5.7 HGTD Physics and Performance

After giving a thorough overview of the HGTD, the reader is invited to follow some of the latest studies on the impact of this foreseen detector on the overall performance and physics capabilities of ATLAS at the HL-LHC. As a first step, the performance of the HGTD relating to the reconstruction of tracks, primary vertices and other physics objects is discussed in 5.7.1, after which, potential impacts of the HGTD in future physics analyses are described in 5.7.2. Lastly, the performance of the HGTD as a luminometer is presented in 5.7.3.

5.7.1 Reconstruction and detector performance

As already discussed, the HGTD is a MIP detector whose primary aim is to assign a precise time information to the reconstructed tracks from the ITk. In order to associate hits in the HGTD active layers to tracks, a progressive algorithm is deployed. This algorithm starts from the last track measurement in the ITk, and, using a progressive Kalman filter, extrapolates the track to the HGTD layers, looking for nearby spatially-compatible hits. The hit with the lowest χ^2 and satisfying a minimum χ^2 requirement is chosen and the track parameters are updated to include it, after which the extrapolation moves on to the next HGTD layer where the procedure is repeated. A time-of-flight (TOF) correction is applied to the hit times, and the track time is computed as the arithmetic mean of the individual associated hit times.

The overall efficiency of the track-time association as a function of the pseudorapidity is shown in Figure 5.18 for single-muon events with p_T = 45 GeV and no pile-up. The plot also demonstrates a bin-by-bin breakdown of how often a fraction of the track-associated HGTD hits is caused by the correct primary particle (green shades, with different shades indicating the fraction, as noted in the legend) and when the track-time is determined using hits only caused by other particles (red/magenta), denoted as "misassignment" or "confusion".[5] The efficiency of assigning a correct time measurement to tracks with the HGTD is above 95% for $2.4 < \eta < 3.8$, while the misassignment ratio is negligible. Pions exhibit a lower efficiency of correct time matching, between 70-90%, due to the larger impact of upstream material. The performance is significantly different when the full pile-up potential of the HL-LHC is considered, as shown in Figure 5.19a for VBF Higgs $\rightarrow$ invisible events with $< \mu >$ = 200. In order to address the challenge of misassignment in that case, a hit cleaning procedure exploiting the number and position of the hits is applied. The procedure improves the purity of the track to time association, at the expense of a slight reduction of the efficiency, as demonstrated in Figure 5.19b. It was estimated that, after applying the cleaning procedure, the overall efficiency to correctly assign a time to a reconstructed track is around 50% at 1 GeV and plateaus at 60% for $p_{\mathrm{T}} > 4$ GeV, with a misassignment rate of approximately 10%. Intensive work is ongoing within the collaboration to improve the track-to-hit association performance.

The determination of the time of the primary vertex is one of the main reconstruction goals of the HGTD, as it offers a new way to remove pile-up tracks that contaminate the hard-scatter objects. This process is not trivial for the HGTD. Firstly, the limited pseudorapidity coverage

[5] In both cases, the timing information of the track is calculated from incorrectly assigned hits. The two categories are distinguished by whether the track has no true hits (misassignment) or at least one true unassigned hit (confusion) in the HGTD.

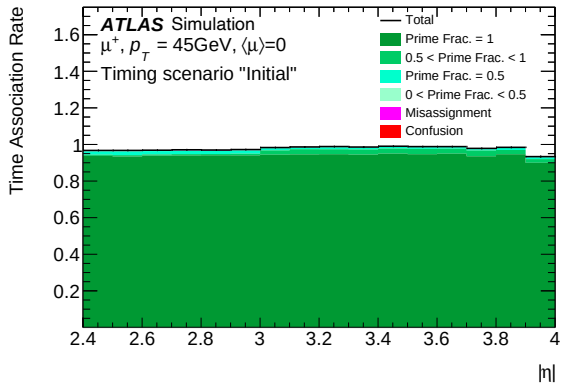

FIGURE 5.18: Rate of correctly assigned and misassigned times as a function of η for single-muon events without pile-up. A bin-by-bin breakdown of correct (green shades) and incorrect (red/magenta) hit associations is also shown. [154]

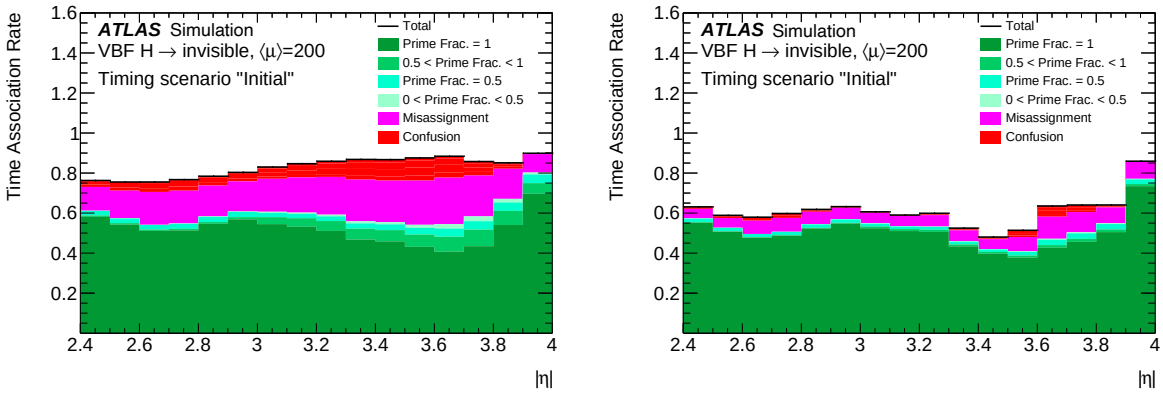

(a) (b)

FIGURE 5.19: Rate of correctly assigned and misassigned times as a function of η for (VBF Higgs→ invisible events with a pile-up of $< \mu > \sim 200$ (a) before and (b) after applying the hit cleaning procedure described in the text. A bin-by-bin breakdown of correct (green shades) and incorrect (red/magenta) hit associations is also shown. [154]

requires that enough high-p_T hard-scatter tracks are produced in $|\eta| > 2.4$. In addition, inefficiencies on the correct track to time association, especially for hadrons, further reduce the amount of good tracks for the calculation of t_0. The algorithm for the t_0 calculation proceeds as follows. Tracks that are within a window in z around the selected vertex and are also close in time are selected and clustered with an iterative time-clustering algorithm. The window is defined based on a parametrization of the track longitudinal impact parameter resolution on the track η and p_T. The resulting clusters are then inserted into a Boosted Decision Tree (BDT) algorithm, which is trained to identify the most likely hard-scatter cluster. After a time-compatible track cluster is chosen, the vertex t_0 is defined as the weighted average time of all the tracks belonging to the cluster. The efficiency of this technique to assign a global vertex time was estimated to be approximately 65% for events in a VBF Higgs $\rightarrow$ invisible sample with pile-up. Figure 5.20 shows the distribution of the difference between the reconstructed and truth t_0, depending on the track composition of the vertex. Signal (hard-scatter-like) clusters are defined as those clusters containing more than or equal to 50% of hard-scatter tracks in them, while those with less than 50% hard scatter tracks are classified as background (pile-up-like). The RMS of the calculated t_0 is found to be 22 ps for hard-scatter vertices, while pile-up vertices with a smaller than 50% fraction of HS tracks or only pile-up tracks have spreads of 70 ps and approximately 200 ps, respectively.

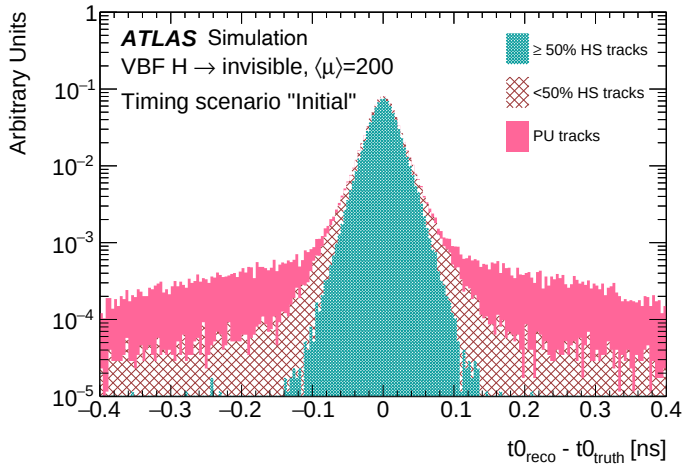

FIGURE 5.20: Vertex t_0 resolution separately for various track compositions in the vertex. [154]

Following the description of the time association to tracks and vertices, the strategy to improve the performance of physics objects with the timing information is discussed. The first and most intuitive way to use time to suppress pile-up is to check the compatibility of tracks against the global t_0. However, as previously explained, the association of a global time reference is not possible for all the events. For this reason, a second approach, called self-tagging, that does not require the knowledge of the hard-scatter time, is also deployed. The principal idea of this approach is to check the time consistency of tracks associated to the same object among themselves. Of course, this method is only effective for objects that consist of a cluster of tracks, such as jets, and can only be used to mitigate stochastic pile-up contributions.

The rejection of the pile-up component in jets is based on a key variable, R_{p_T}, which is defined as the scalar sum of the p_T of all tracks that are inside the jet cone and originate from the hard scatter vertex, divided by the fully calibrated jet p_T. Small values of this variable tend to be an indicator of pile-up jets, while large values usually correspond to hard-scatter jets. The performance R_{p_T} can be improved by the use of timing in the forward region. In the case that a global t_0 is available, the variable can be recomputed after rejecting out-of-time

tracks in the jet. Even in the absence of a hard-scatter time, the self-tagging method can be applied in order to find jet sub-clusters from time compatible tracks. In that case, the R_{p_T} variable is calculated for each sub-cluster and the maximum one is then taken as the correct one. These two approaches are not exclusive; in case sufficient information is available, they can be combined to provide a better performance. Figure 5.21a shows the rejection efficiency, i.e. the inverse of the mistag rate, of pile-up jets as a function of the selection of hard-scatter jets in the HGTD acceptance for VBF Higgs invisible events with $< \mu >$ = 200. The performance is shown for the cases where the reconstruction is done with only the ITk or with the ITk in combination with the HGTD. The improvement of the pile-up rejection can reach up to a factor of 1.5 when timing information is included, at a signal efficiency of 85%.

Another use of the HGTD timing information is the improvement of the lepton isolation under high pile-up conditions. The efficiency of the lepton isolation, defined as the probability that no additional tracks are reconstructed within the isolation cone of the lepton candidate, can be severely impacted by pile-up in the forward region. Timing information can be used to reject out-of-time pile-up tracks within the isolation cone. The isolation efficiency as a function of the pile-up density is shown in Figure 5.21b, for electrons originating from Z boson decays. As expected, the efficiency decreases quickly with the pile-up vertex density. However, the addition of the HGTD counters the reduction of the isolation performance, and an efficiency above 85% is maintained even at high pile-up density.

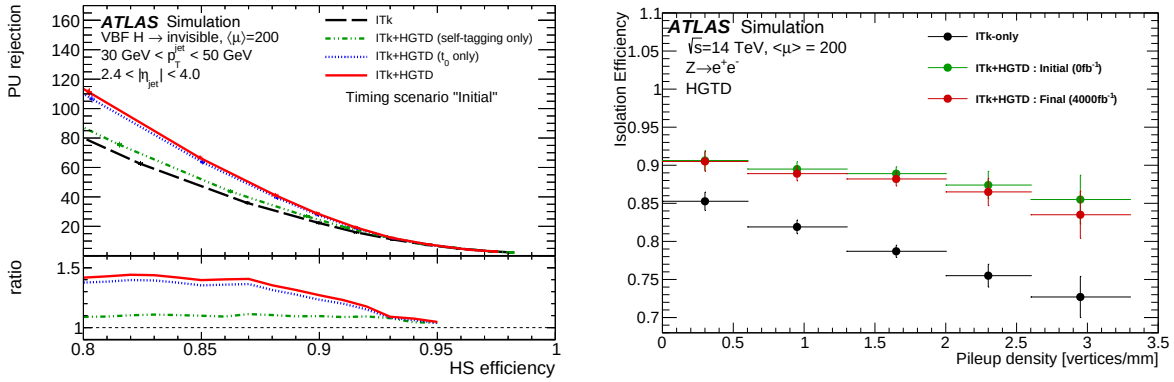

(a) (b)

FIGURE 5.21: (a) Pileup jet rejection as a function of hard-scatter jet efficiency in the $2.4 < |\eta| < 4.0$ region for jets with 30 GeV $< p_T <$ 50 GeV. (b) The efficiency for electrons to pass track-isolation criteria as function of the local vertex density. The performances with ITk and ITk + HGTD reconstruction, both with the "initial" time resolution of the detector as well as the "final" time resolution at the end of lifetime are shown for comparison [154].

The use of timing information in the improvement of the object performance is not limited to the previously mentioned examples. Its application to various other cases is foreseen, in order to mitigate the undesired effects of pile-up. Such cases, not further discussed in this thesis, include the improvement of b-jet tagging, pile-up suppression in the calculation of $E_{\mathrm{T}}^{\mathrm{miss}}$ and improvement of particle flow algorithms.

5.7.2 Physics analyses prospects

Taking an additional step from the object performance, the impact of the HGTD on future physics analyses can be estimated. Three main ways in which the HGTD can enhance the physics sensitivity of ATLAS have been identified so far:

- the forward object reconstruction improvement, as previously discussed, is intuitively

expected to improve the performance of analyses with forward topologies such as VBF and VBS.

- time, being a completely new and orthogonal dimension to all the other ones already used, can provide novel ways of handling and triggering on data.
- all precision measurements are expected to benefit from the improvement of the luminosity uncertainty, which the HGTD will provide in its luminometer functionality, as discussed in 5.7.3.

The physics impact of HGTD in the described categories has been investigated more quantitatively in the following example analyses. It should be noted that precision timing information is a novel dimension at hadron colliders, which physicists only recently started to explore. The search methods discussed below are but a subset of the potential applications of the new dimension, and undoubtedly, as the community matures, additional ways to fully exploit it will be uncovered.

An important part of the HL-LHC program is concentrating on the analysis of the Higgs boson produced by Vector Boson Fusion (VBF). The Feynman diagram of this production process is shown in Figure 5.22a. In order to estimate the potential gain in Higgs searches with VBF production, the VBF Higgs $\rightarrow$ invisible channel was chosen as a representative analysis. One of the main challenges in this decay channel is the absence of high - p_T handles apart from the VBF jets. It is therefore an ideal indicator of the HGTD power for pile-up mitigation in jets, since a large fraction of its topology is concentrated in the forward region. The improvement of the sensitivity in this case is expressed as the ratio of the signal to the background, where the major contribution to the latter are QCD Z+1 jet events. The improved pile-up rejection provided by the HGTD results in a signal-over-background increase of 10% or more.

The impact of the improvement of lepton isolation in physics was explored with SM measurements of a VBS WZ process, where the produced bosons decay fully leptonically, as demonstrated in Figure 5.22b. A precision measurement of the weak mixing angle $\sin^2\theta_{eff}$ was also used in order to quantify the influence of HGTD on the broader class of precision measurements with forward leptons. In HL-LHC, the weak mixing angle is estimated from the asymmetry in the angular distribution of positively and negatively charged leptons produced in Z boson decays. The best sensitivity is achieved at high rapidity of the Z boson, where at least one lepton is produced in the forward region. The improvement on the lepton isolation is the most significant contribution of the HGTD in this measurement, and results in a 13% increase of the $\sin^2\theta_{eff}$ sensitivity in one of the event categories.

The extension of the sensitivity of the ATLAS detector in monopole models through alternative triggering possibilities with the HGTD was also investigated. Magnetic monopoles are hypothetical particles predicted by various BSM models [162, 163, 164, 165]. The ATLAS experiment has a long precedent of searches for magnetic monopoles [166, 167, 168] that are expected to be extended in the HL-LHC era. The HGTD could enhance the monopole discovery capability of ATLAS in HL-LHC by providing an online trigger to highly ionising particles. Simulation show that single HGTD hits from monopoles are far more energetic than the deposits from MIPs and can be clearly separated. Signals from such particles would cause a saturation of the TOT measurement, a unique signatures that can be easily flagged and exploited with an online trigger.

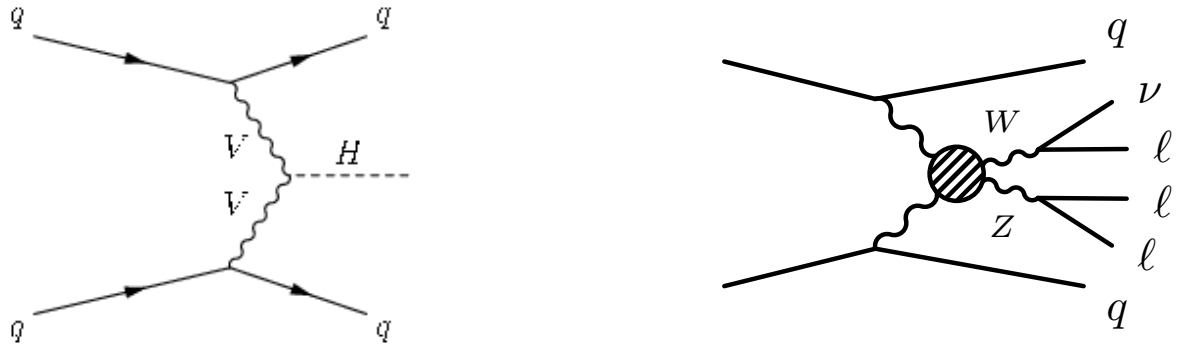

FIGURE 5.22: Feynman diagram describing (a) the VBF Higgs production (b) the VBS WZ production with fully leptonic decays.

5.7.3 Luminosity

In order to carry out a successful precision program, the accurate measurement of the luminosity is necessary for the HL-LHC. The importance of a precise luminosity estimate can be grasped when looking at the largest uncertainty contributions for important Higgs boson cross-section measurements; gluon-gluon fusion (ggF) with decay of the Higgs boson either to a photon or a Z-boson pair and combined ggF and VBF Higgs production with decay to $\tau\tau$. For all these channels, the largest uncertainties (excluding the luminosity) amount to less than 2%. It is clear that the error on the luminosity needs to be constrained better than 2% in order to not dominate the precision measurement of Higgs production cross-section [76]. Such an accuracy cannot be accomplished with a single luminometer, but only with the combination of independent measurements from different detector systems.

An important target of the HGTD is to provide one of those measurements. In order to accomplish this, the timing detector proposes a measurement of the number of hits in the ASICs of the outer ring of the detector at a rate of 40 MHz. Thanks to its fine granularity and forward position, it is expected that this measurement will be directly proportional to the instantaneous luminosity in ATLAS. The fast (order of a few ns) processing speed of signals is an essential advantage of HGTD, since it allows for both offline and online (i.e. bunch-by-bunch) measurements of the luminosity. The latter can be extremely useful to monitor the accelerator performance and apply on the fly corrections on calorimeter data, trigger menus and algorithms.

Figure 5.23a shows the average number of hits registered in the first double-sided HGTD layer (both sides of the innermost cooling plate) during one bunch crossing as a function of the number of simultaneous inelastic pp interactions. The black points correspond to fully simulated MC minimum bias events with $< \mu >$ = 200, while the green ones show toy MC events with μ=1, that have been superimposed to create samples of variable number of interactions. A linear fit on the green points is applied and extrapolated to the HL-LHC pile-up multiplicity region, where its prediction is compared to the full simulation. A small discrepancy of 0.5% is observed, which is believed to originate from pads with multiple hits. After correcting for this known effect, a residual of 0.1% is seen.

The statistical precision of the luminosity measurement of HGTD has also been investigated. The size of this uncertainty has been studied as a function of μ, using toy samples to simulate the average number of hits per bunch crossing. The simulation process is repeated

11000 times to emulate the number of turns of the LHC beams in one second and the number of hits is averaged. The relative uncertainty arising from statistical fluctuation as a function of $< \mu >$ is shown in Figure 5.23b. The uncertainty is smaller for a large number of pile-up interactions, thanks to the increased number of produced particles, and, therefore, hits. For $< \mu >$ = 1 it is found to be 1.4%. A larger averaging time can be used to improve the precision at low-μ operation modes, such as van der Meer scans.

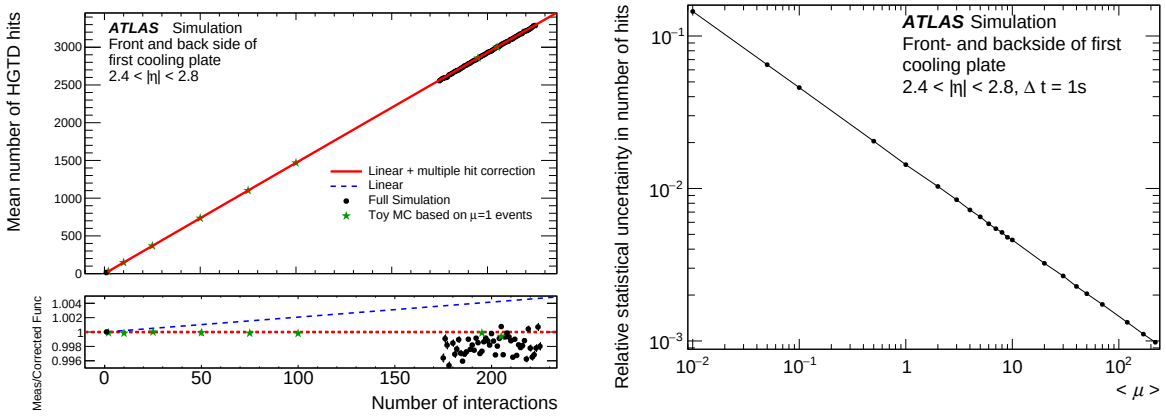

(a) (b)

FIGURE 5.23: (a) Mean number of HGTD hits per bunch crossing as a function of the number of pile-up interaction μ. (b) Pileup dependence of the statistical uncertainty per BCID, for an integration time of 1s. [154]

The ultra-fast electronics of HGTD offer a unique opportunity for the luminosity determination. As already described in 5.5.5, the occupancy measurement will be performed in two time windows, a central 3.125 ns wide one, and a sideband programmable window of 6.25 ns. The sideband window will provide an in-situ estimate on the afterglow and noise effects, thus constraining the luminosity systematic uncertainties to the percent level or better.

6. Geometry and Data Transmission System optimization

This chapter describes my work on various aspects of the HGTD detector layout and performance. At first, an overview of the evolution of the HGTD geometry is given in 6.1, after which the simulation used to realize the following studies is presented in 6.2. Section 6.3 shows studies that I have performed on the occupancy of the detector using the HGTD full simulation, while in 6.4, a review of optimization investigations on the Data Transmission system is presented. Finally, section 6.5 describes my work on the optimization of the detector geometry using a simplified simulation package.

6.1 A historical overview of the HGTD geometry

Most detector systems traverse a long and complicated path from their conception to their final design. An often simplified initial picture of a potential detector goes through many steps of refinement in order to reach its final version, where a vast number of parameters and constraints have been thoroughly studied and taken into account. The HGTD has been no exception to this trend; Figure 6.1 illustrates, on the left, a schematic of an HGTD layer at the conception phase, while on the right, the module layout of one disk, as currently implemented in simulation, is shown.

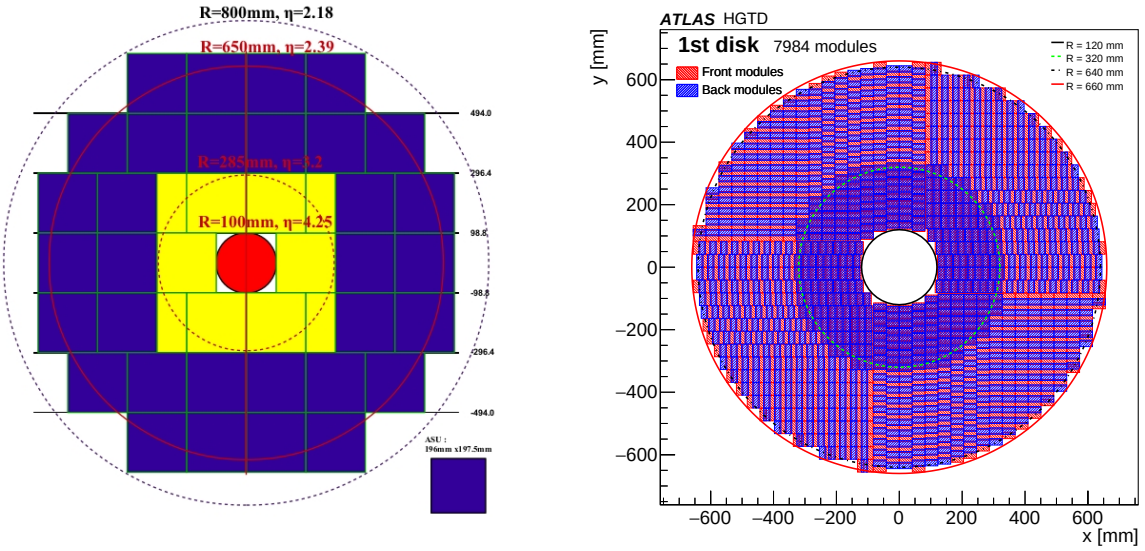

(a) (b)

FIGURE 6.1: (a) Initial cross-section of a potential HGTD layer design. The yellow (dark) area corresponds to the active area covered by 1×1 (3×3) mm^2 sensors, while the red circle illustrates the beam pipe. (b) Schematic of the module layout for one disk of the HGTD as implemented in the most recent simulation version. Both sides of the disk are instrumented - red modules are in the front side and blue in the back.

The initial design of the detector, as shown in Figure 6.1, was based on large-area square Active Sensor Units (ASU), which were composed of four 97 mm × 97 mm silicon sensors glued on a 195.5 mm × 195.5 mm PCB. A geometry with two different granularities was considered at the time, in order to minimize the number of active channels while ensuring an

occupancy below 10% in the entire active area. ASUs at low radius (shown in yellow) would have been equipped with pads of 1 mm $\times$ 1 mm, while at large radius, 3 mm $\times$ 3 mm pads were used. The active areas were organized into four identical layers on each side of ATLAS, fully covering a radial range from 142 mm to 640 mm, while an extended range from 100 mm to 800 mm was partially covered.

As the conception of the detector evolved, it became clear that the square-based design was suboptimal, since it did not provide the necessary space for the readout services that transport the data from the active area to the peripheral electronics. The design of the ASU was also problematic, since its large size was not optimized to fully cover a disk-like space; the resulting layouts included either gaps in the outer radius or a large number of unused sensors. In order to solve these problems, a row-based organization was chosen that is the baseline today. In this version, the active area is segmented in modules of 20.5 mm $\times$ 40 mm, that are placed in rows. Each module is communicating with the outside world through a flex cable which will be stacked on top of the ones serving modules of the same row. In addition, thanks to the smaller module size, it is easier to optimize the instrumentation at the radial limits of the detector. The size of the sensor pad was also fixed to an intermediate value of 1.3 mm $\times$ 1.3 mm for the entire detector. The option to vary the granularity with the radius was rejected, because a larger pad size would increase the detector capacitance, and therefore the jitter contribution to the time resolution, beyond the set limit of HGTD. An additional motivation for rejecting a layout with more than one pad size was the added complexity in the production and assembly of such a configuration.

Various row layouts have been implemented and tested with simulation, in order to find an optimal solution. In all cases, the length of each row must not exceed the maximum constructable length of a flex, which is about 750 mm. Additionally, the number of modules in each row must be kept low enough as to ensure that the maximum thickness of the stacked flex tails does not exceed the space between two layers of the HGTD, which is around 10 mm. With the minimum flex thickness currently estimated to be 220 μm, the number of stacked flex tails per layer should not exceed $\sim$ 20, in order to leave a $\sim$1 mm gap between the two disks. Finally, the number of modules should be distributed fairly uniformly in the azimuthal plane, to ensure that they can all be accommodated in the peripheral boards. These requirements have been at the core of the design of the different row layouts.

The number of disks on each side of HGTD was reduced from 4 to 2, in order to satisfy spatial and price constraints. While this change brought on a reduction of the number of hits per track, the degradation of the performance was partially mitigated by instrumenting each disk on both sides and introducing an overlap between them. Another important aspect in the design of the layout is the un-instrumented zones. With the choice of the row layout, it became evident that a space between modules in each row is needed to be left available for the connection of the ASICs to the sensor. The overlap between modules on the two sides of the cooling disk was also beneficial in the reduction of dead zones in the space between modules. Section 6.5.1 gives a detailed description of the two main overlap schemes of HGTD. Mechanical constraints dictated also that a small distance needs to be kept between the rows. A simple and elegant solution to reduce the inactive areas between rows was to rotate the two disks with respect to one another - a 20° relevant rotation is currently foreseen. Additionally, a 180° rotation of the back disk was introduced, effectively creating a mirror symmetry between the front (back) and back (front) side of the first and second disk. With this process, the dead zones are more randomly distributed in the X-Y plane, ensuring a higher detector efficiency. The combination of these two rotations has the additional advantage of creating an opening in the peripheral boards, necessary for the feed-through of cooling pipes.

6.2 HGTD Simulation

Simulation is an invaluable tool in the optimization of a detector design. This section gives an overview of the simulation packages that have been developed for the HGTD and on which the subsequent performance and optimization studies are based.

6.2.1 Geant4 Simulation

Based on the two designs of Figure 6.1, two main geometry versions are currently implemented in the Geant4 simulation toolkit and integrated in the ATLAS simulation framework. The first one (referred to as Technical Proposal (TP) [85] simulation from now on), was developed in a flexible way in order to perform a variety of R&D studies and reach a decision on fundamental aspects of the HGTD geometry. The second version, implemented a more definitive version of the HGTD geometry that was inspired from the outcomes of the optimization process performed with the TP simulation. In addition, a more recent layout of the ITk was implemented in the newer simulation, leading to an update of the material budget prior to the HGTD. This simulation version is the most recent in simulation as this thesis is being written, and is referred to as the post-TP simulation.

In the TP simulation, four HGTD active layers are included on each endcap of the ATLAS detector. All volumes are implemented as concentric disks, starting at a radius of 50 mm and reaching a maximum radius of 600 mm. The different volumes are stacked onto each other, resulting in a thickness of 43 mm, as shown in Figure 6.2. The active material is silicon and is distributed uniformly in the disks, without any dead zones. The hit information of tracks in the HGTD is stored in LArHits.[1] This object was chosen for its capability to easily combine hits in the same pad and store the deposited energy and time of the particle. The stored time is given by the interaction time of the particle with the active material. A 0.5×0.5 mm^2 granularity is used for the LAr hits, so as to be small enough to allow for optimization studies of the sensor pad size.

The post-TP framework follows closely an optimized geometry, shown in Figure 6.1b, that was decided after intensive studies with the TP simulation. The presented row and module layout is slightly different from the final detector design, for reasons that will be discussed in 6.5. In this version, 2 cooling plates are implemented on each side of ATLAS. They are instrumented on both sides by a silicon active area that is organized in modules of 22 mm $\times$ 40 mm with sensors of size 20.5 mm $\times$ 40 mm. The active area extends to approximately a radius of 640 mm. Dead material from mechanical space between modules is taken into account. Inactive sensor areas, like a 0.5 mm wide guard ring and the inter-pad distance (estimated to be $\sim 50\,\mu$m from testbeam measurements) are also included in the simulation, as illustrated in Figure 6.3. The two disks are rotated by 15 degrees in opposite directions.[2] LArHits are again used to store the hit information, but in this case, a 1.3×1.3 mm^2 granularity is used, reflecting the current choice of the HGTD community for the final detector. A pad size of 1 mm $\times$ 1 mm is also included in the simulation, as an alternative. Figure 6.4 shows an event display of a simulated QCD dijet event in one of the two forward regions of ATLAS. The HGTD, as implemented in the post-TP simulation, is shown in grey, along with the deposited hits of traversing tracks.

[1] LArHit is an object initially introduced to study the LAr calorimeter performance in simulation.

[2] A $\pm$ 10 degrees rotation was decided after the simulation implementation, due to updated constraints in the cooling feed-through requirements.

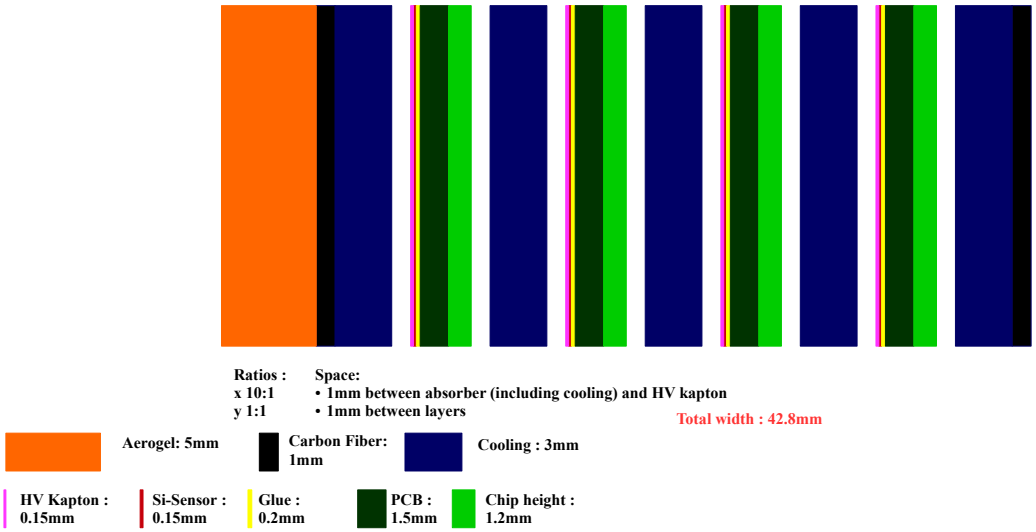

FIGURE 6.2: Schematic view of the HGTD volumes in the z-direction, as implemented in the TP simulation. The individual volumes are different colors and are in scale. The material used in simulation is listed in the legend.

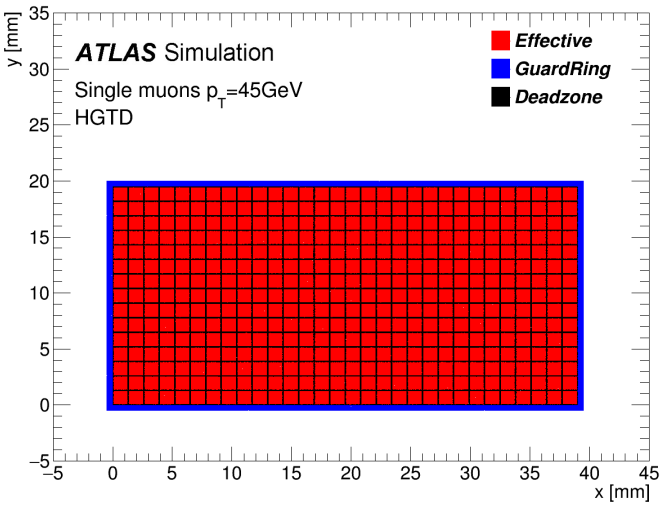

FIGURE 6.3: Positions of simulated energy deposits in active detector regions (red), inter-pad dead zones (black) and the guard ring surrounding the edges of a sensor (blue). This Figure is made through drawing points for individual Geant4 energy depositions from single-particles in the post-TP simulation.

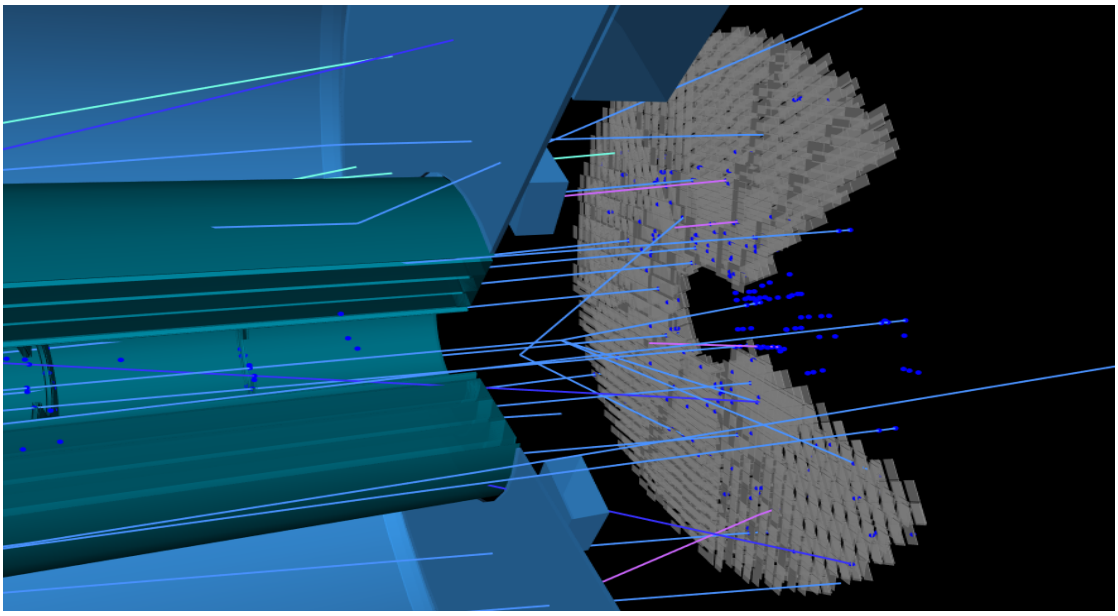

FIGURE 6.4: Visualization of a simulated QCD dijet event showing the trajectories of charged particles and the resulting hits in the HGTD. The post-TP simulation has been used for the geometry implementation. A wedge in ϕ and volumes representing services and support structures have been removed to expose the individual detector modules of the HGTD. No pile-up interactions were overlaid in this simulated event.

6.2.2 MC samples

As will be discussed in 6.3, my work has been heavily focused on the study of the detector occupancy. To this purpose, single neutrino samples, overlayed with $< \mu >$ = 200 pile-up interactions, were used. Given the fact that neutrinos do not interact with the detector, this type of sample is ideal to study the occupancy in minimum bias conditions. Additionally, a physics sample with VBF Higgs events, where the Higgs decays to invisible particles, was used in order to ensure the robustness of the minimum bias results in the presence of forward hard scatter jets.

6.3 Occupancy studies

The occupancy, defined as the fraction of read-out units that are activated per event, is a crucial aspect in the detector design. For a MIP detector like the HGTD, the occupancy should be as low as possible, to ensure that each particle-track can be reconstructed individually. As already discussed in 5.2, a 10% requirement has been set on the occupancy for the HGTD.

6.3.1 Occupancy in the TP simulation

As already mentioned, the TP simulation models the active area as a homogeneous silicon layer, which is clearly an oversimplified approach. As part of my work, I developed a framework that, starting from the LArHits of the TP simulation, constructed a more realistic detector geometry, including module and row readout structures. Inter-module dead regions and overlaps between different layers were also included. The presented results before the implementation of the post-TP simulation were obtained with this framework, after tuning it to a geometry very similar to the one shown in Figure 6.1b.

Figure 6.5a shows the deposited energy from particles within the HGTD acceptance in the LArHit granularity. The most probable value, equivalent to the deposited energy of a MIP, is

found to be 44 keV. The distribution of the time of the hits with respect to the time of the bunch crossing is presented in Figure 6.5b. The time of the LArHit is offseted by the average time of flight from the nominal interaction point to the middle of the HGTD.[3] In the simulation, only hits with a time smaller than 2.6 ns get a reconstructed time, while for larger times, an overflow value is assigned. The distribution is fitted with a Gaussian function, from which the σ_t is extracted to be 266 ps, compatible with the convolution of the beam-spot spread in space and time, discussed in 3.4.1.

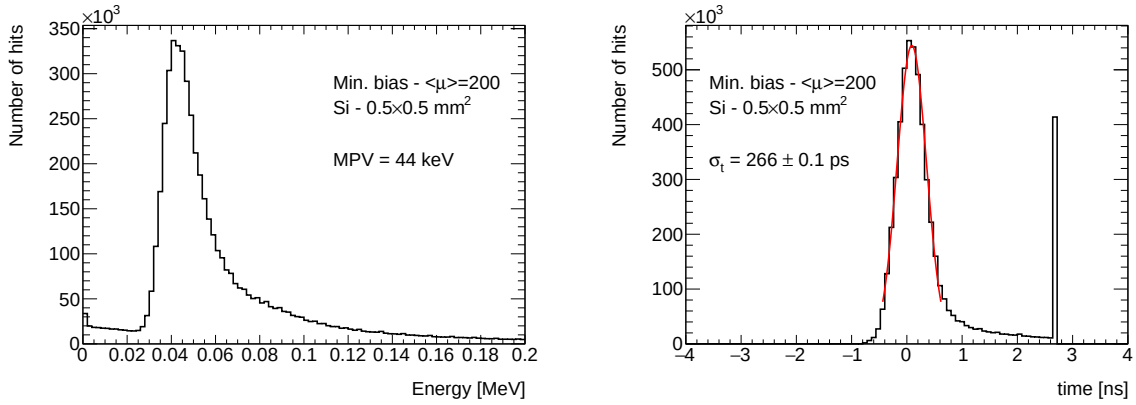

(a) (b)

FIGURE 6.5: Distribution of (a) the deposited energy and (b) the time of LArHits with respect to the time of the bunch crossing in the HGTD. The time distribution (b) is fitted with a Gaussian function, shown in red, to extract the RMS of the hits' time.

The versatility of the TP simulation framework allows the detector performance to be studied in various configurations. In particular, thanks to the fine 0.5×0.5 mm^2 LArHit granularity, the detector pad size can be investigated. Figure 6.6a shows the occupancy of the first and last layer of the HGTD as a function of the radius for 1×1, 2×2 and 1.3×1.3 mm^2 pads. For the two first sizes, the occupancy is calculated by simply integrating over either 4 or 16 LArHits. This method cannot be applied for 1.3×1.3 mm^2 pads, since they are not exactly divisible by the LArHit granularity. In order to extract a bias-free occupancy for this pad size, hits in between two pads are attributed to only one of them with a probability equal to the fraction of the pad-LArHit common area. The energy of the resulting pad is calculated as the sum of energies in each enveloped LArHit, while the time is taken to be equal to the time of the first hit. A 20 keV ($\sim$ 50% of a MIP) lower threshold is applied in the deposited pad energy, in order to mitigate the noise, whose average simulated value is 0.7 keV. Additionally, only hits within 4 ns are considered in the calculation of the occupancy, in order to discard overflow information. This value was chosen at a time when the range of the TOA TDC was not fully defined.

Evidently, the occupancy is highly dependent on the radius - in the outer part of the detector it is 20 times smaller than the innermost part. Showering and multiple scattering effects also contribute to the particle content in the HGTD, resulting in an occupancy that is slightly higher at larger depth. The maximum average occupancy for the last layer is found to be around 7, 11, 20 % for 1×1, 1.3×1.3 and 2×2 mm^2 pads, respectively, rapidly falling below 5% for R $>$ 180 mm, 230 mm and 330 mm, respectively. A compatible result is obtained when using a VBF Higgs $\rightarrow$ invisible sample, superimposed with pile-up interactions with $<\mu>$ = 200. This is expected, as the contribution of hits from the hard-scatter jets is small compared to the pile-up at HL-LHC conditions. It is clear that the occupancy requirements of the HGTD cannot be fulfilled for a pad size greater than 1.3×1.3 mm^2 and were therefore excluded from

[3] This is done to obtain the smallest numerical values to minimize the needed storing memory.

further deliberations on the geometry. While the 1.3×1.3 mm^2 pad size is marginally above the requirement for the first bin, it should be noted that the inter-pad fill factor and guard ring dead areas are not included in the simulation - together they contribute to $\sim$ 20% of the module area. Taking into account this result, the 1.3×1.3 mm^2 pad size was chosen over smaller values as the default for HGTD, in order to reduce the number of readout units and to provide a large enough space for the single-channel front-end electronics. The choice of the larger 1.3×1.3 mm^2 pad size over smaller values was also motivated by the smaller inter-pad fill factor.

The coincidence of more than one particle in the same HGTD pad is an undesirable effect that can bias the time measurement. Two cases can be distinguished; the particles can either be inseparable in time or they can be arriving with a discernable time difference. In the former scenario, the TOA remains unchanged and only the charge, and therefore the TOT, are affected. However, when the two incident particles are distinguishable in time, the TOA is given by the time of the first particle. In case the first particle is originating from a pile-up vertex, the resulting inferred time would be highly biased. It is clear that this category of multi-hit events is the most harmful one for the physics performance of the HGTD. The magnitude of this class of events was studied with simulation, using 1×1 mm^2 pads for simplicity. Figure 6.6b shows the fraction of hit pads that have 2 or more incident hits for the last layer of HGTD. Around 10% of the pads with signal have at least two incident hits at the inner radius, while this percentage drops rapidly to $\sim$ 5% at R = 600 mm. Out of the hit pads, only 3% have a maximum time difference between those hits larger than 20 ps at R = 120 mm. The fraction is highly dependent on the radius and reaches a negligible 0.1% at large radius. This study demonstrates that multi-particle coincidence effects are small in the chosen granularity of HGTD and can therefore be safely neglected.

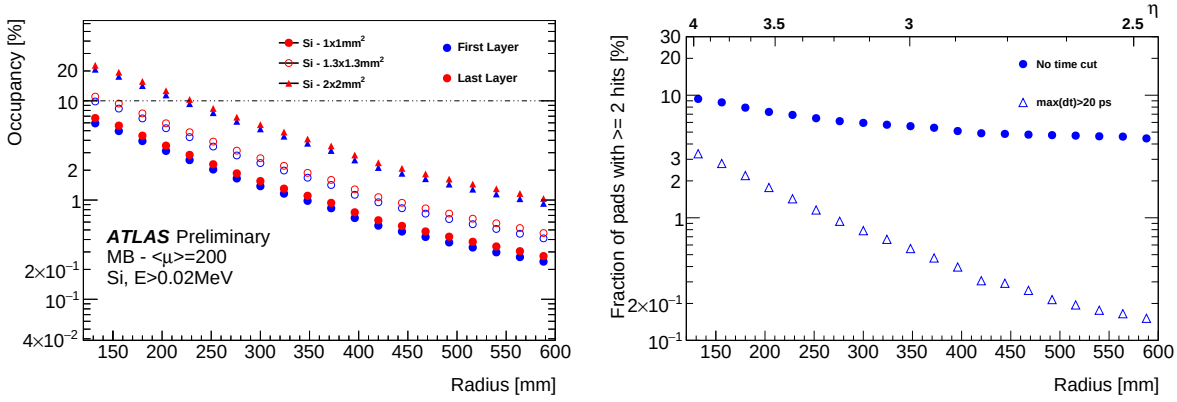

(a) (b)

FIGURE 6.6: (a) Occupancy (in %) in the first and last layer of the HGTD as a function of the pad size for 1×1, 2×2 and 1.3×1.3 mm^2 pad sizes. (b) Fraction (in %) of hit pads with at least 2 hits in the last layer of HGTD as a function of the radius. The fraction of hit pads where the maximum time separation between two hits is larger than 20 ps is also shown for comparison. Both results have been extracted using minimum bias samples with $< \mu >$ = 200.

6.3.2 Occupancy in the post-TP simulation

The post-TP simulation incorporates a more accurate description of the detector. The readout row and module structures, with all inter-module and inter-sensor dead areas are already included at the simulation level. The granularity of the LArHits is now 1.3 × 1.3 mm^2. Figure 6.7 shows the occupancy as a function of the radius for the first (blue markers) and last

(red markers) layer of the HGTD. As expected, the occupancy is smaller than the result obtained for the same granularity with the TP simulation (Figure 6.6a) due to the introduction of the inter-sensor dead zones. The maximum occupancy is now 7.4% at R$\sim$ 160 mm. The dependency of the occupancy on the radius is less steep than in the TP simulation due to the evolution of the ITk simulation. In particular, the distribution of the material budget of the future tracker was re-evaluated and found to be smaller (larger) in small (large) R. The interaction length prior to the HGTD, and, in consequence the occupancy, was altered accordingly. In addition, the un-instrumented space at the beginning of each row has been increased in the post-TP simulation version, to satisfy additional mechanical constraints. This result in a drop of the occupancy in the first radial bin.

The occupancy, calculated only for hits that are within 2.56 ns of the nominal interaction time, is also shown for comparison. This time window corresponds to the expected range of the TOA TDC in which the time measurement is valid. Currently, the front-end ASIC is designed to transmit an overflow TOA value in case the hit is outside this window. The option to discard overflow hits within the ASIC was rejected, given the small gain in occupancy compared to the complexity of implementing a suppression circuit.

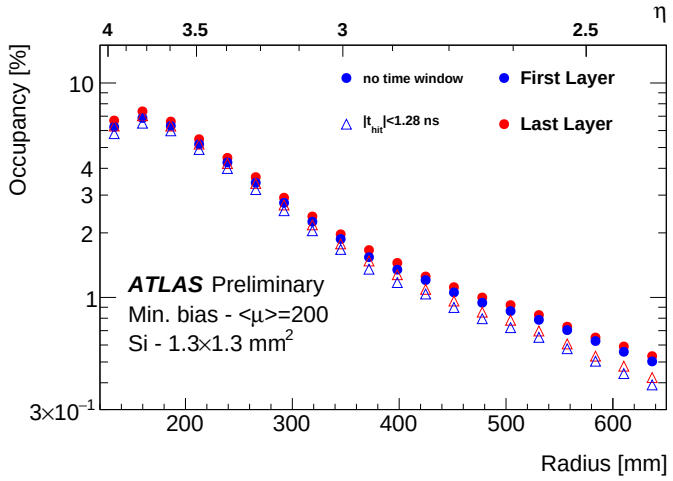

FIGURE 6.7: Occupancy as a function of the radius for a pad size of 1.3×1.3 mm^2 at a pile-up of $< \mu >$ = 200. Solid circles correspond to the occupancy without a time window applied on the hit, while the open triangles show the occupancy in a 2.56 ns time window around the average time of arrival. This window corresponds to the expected range of the TOA TDC, in which the time measurement is valid.

6.4 Data transmission optimization

Starting from the occupancy results previously presented, this section discusses performed studies on the on-detector data transmission system requirements and optimization.

6.4.1 Bandwidth and power consumption

The bandwidth, defined as the transmission capacity of the detector is a crucial parameter for the design of its acquisition system. In the HGTD, the bandwidth is given as the product of the event size in the ASIC and the acquisition frequency. As described in equation 5.13, the event size, and, as an extent, the bandwidth of the timing readout chain is directly proportional to the number of hit pads in the ASIC. Figure 6.8 presents, on the left, the average and on the right the maximum number of hits in each ASIC of a quadrant in the 3rd active layer of HGTD, calculated in the post-TP simulation. Each square is an ASIC, while the row geometry is illustrated with a solid black line. Following the occupancy, the average number of hits per

ASIC rapidly drops with the radius, from 17 to less than 1 hits. A uniform distribution in ϕ is observed, as expected. On the other hand, the map of the maximum number of hits can reach up to 50-60 hits in an ASIC of the inner radius. In addition, the distribution in this case is no longer uniform, due to statistical fluctuations.

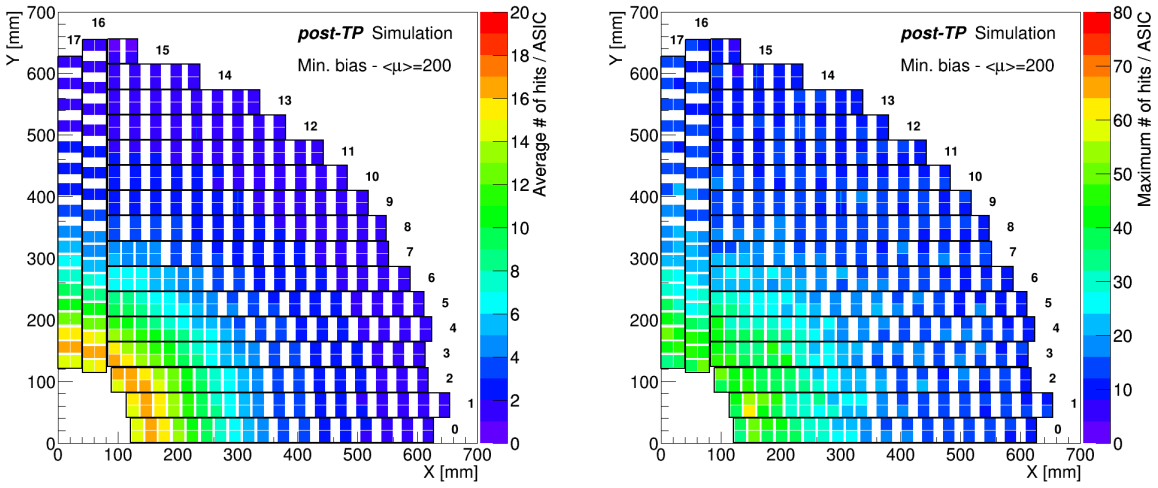

(a) (b)

FIGURE 6.8: 2-D map of the (a) average and (b) maximum number of hit pads in each ASIC of a quadrant of the 3rd active layer of the HGTD. A minimum bias simulation sample with an average pile-up of $< \mu >$ = 200 has been used.

A more quantitative image is shown in Figure 6.9a, where the distribution of the number of hit pads in three different ASICs is displayed. Around 16-17 hits/ASIC are observed in the innermost part of the detector. This number, following the occupancy, decreases quickly with the radius. However, there are large tails in the distributions corresponding to events with a significantly larger number of hits than the average. Figure 6.9b demonstrates the cumulative integral fraction for the same ASICs. It can be seen that 99% of the events have less than 28/11/5 hit pads for small/middle/large radius, respectively. Performed simulation studies ensure that the common memory depth and read-out rate are sufficient to accommodate such events at the L0/L1 trigger rate.

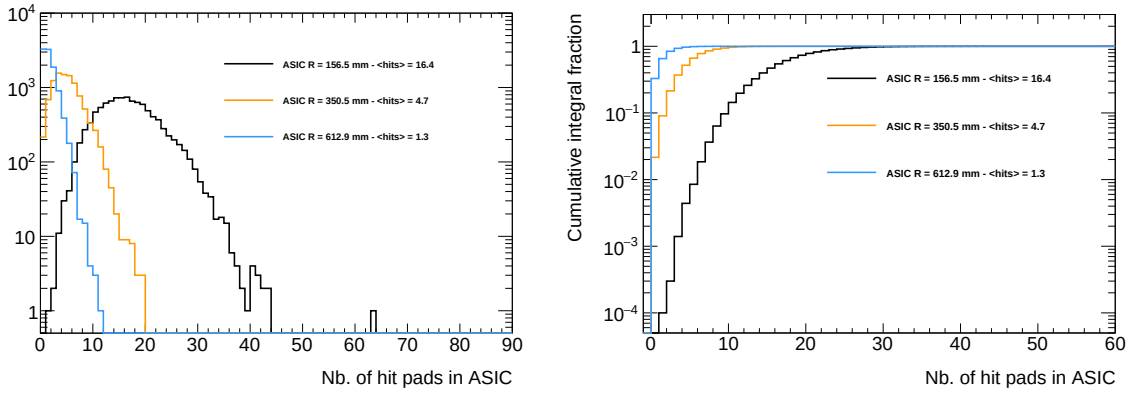

(a) (b)

FIGURE 6.9: Distributions of (a) the number of hit pads and (b) cumulative integral fraction in 3 ASICs positioned in the innermost (black), middle (yellow) and outer (cyan) part of the detector.

Using the extracted results on the number of hits/ASIC in equation 5.13, the average required bandwidth for the transmission of the timing data from each ASIC can be extracted. The readout of the timing information is done upon reception of an L0 trigger which is 1 MHz in the current baseline specifications of the ATLAS trigger system upgrade.[4] Figure 6.10a shows the average bandwidth in each ASIC for a quadrant of the 3rd active layer. The average bandwidth never exceeds 600 Mbps, a result that, as will be discussed in 6.4.2, is crucial for the design and optimization of the transmission system.

The cooling system is a key ingredient in the successful operation of the HGTD. A temperature of -35 °C must be maintained within the HGTD vessel, especially close to the modules, with a maximum variation of a few degrees Celsius from the nominal value. The low operating temperature ensures the performant use of the sensors after irradiation, as it mitigates the increase of the leakage current. In addition, as shown in equations 5.11 and 5.12, it benefits the ASIC performance in terms of signal amplitude and noise. The design of the system that provides the required cooling of the HGTD depends heavily on the power dissipation of the detector components. The largest contribution originates from the ASIC itself and can be separated in two terms; one arising from the common digital part of the ASIC and one from the pixel matrix. In order to decrease the later, the TDC and pixel memory have been designed in a way that saves power in the absence of hit information. Summarizing, the ASIC power consumption can be expressed as follows:

$$P = a_{pixel} \times 225 + b_{pixel} \times (1 - N_{hits}) + c_{pixel} \times N_{hits} + c_{common} \tag{6.1}$$

- Constant pixel term a_{pixel}. This term consists of the power dissipation of the preamplifier and discriminator (1.57 mW) that are continuously active.
- No-hit pixel term b_{pixel}, corresponding to the minimum consumption of the TDCs (0.4 mW) and pixel memory (1.38 mW) in case of no hits.
- Hit pixel term c_{pixel} arising from the larger power consumption of the TDCs and pixel memory in the presence of hits. The individual contributions of the blocks were extracted from simulation and were found to be 3.5 (3.9) mW for the TOA (TOT) TDC and 0.02 mW for the pixel memory.
- Constant common term c_{common}. This term accounts for the power consumption of the digital block of the ASIC and is currently estimated to be around 300 mW.

Many of the ASIC components are currently in the design phase, and, therefore, the individual contributions to the power consumption are estimates that could evolve in the future.

The average power dissipation of the ASIC as a function of the radius is shown in Figure 6.10b. An average power dissipation of 1.2 W / ASIC has been set as the maximally acceptable value for the HGTD; the result never exceeds 1.17 W, leaving a 3% margin. The dependence of the power dissipation on the radius is not as steep as the occupancy, due to the contribution of the constant terms; at high radius, the power consumption is around 1.05 W. Taking into account the radial dependence of the ASIC dissipation results in an average power consumption of 17.7 kW for the entirety of the HGTD. Regular calibration runs of the detector are also foreseen, where calibration pulses will be injected in the ASIC to monitor various parameters, like the TOA and TOT. For the purposes of this mode of operation, a 10% occupancy will be

[4] In the alternative two-level trigger scheme, the HGTD read-out will be performed upon reception of an L1 trigger at 0.8 MHz.

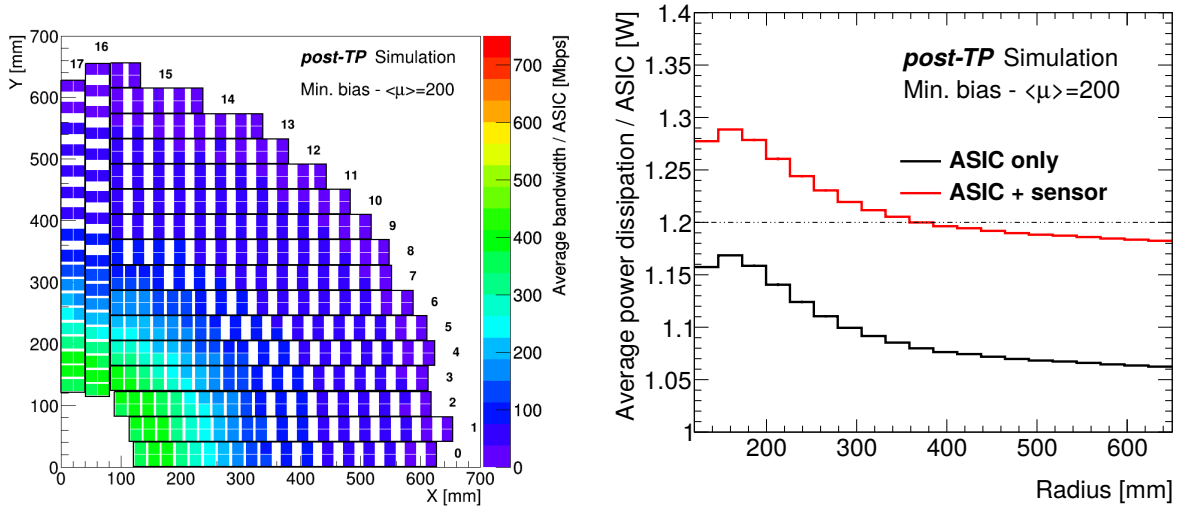

(a) (b)

FIGURE 6.10: (a) 2-D map of the average bandwidth in each ASIC of a quadrant of the 3rd active layer of the HGTD. (b) Average power consumption in the ASIC as a function of the radius. A minimum bias simulation sample with an average pile-up of $< \mu >$ = 200 has been used.

used in the entirety of the detector so as to not exceed the maximal specifications of the ASIC. The power consumption of the HGTD during the calibration runs is estimated to be 19.8 kW.

Since the sensor is a current source, it also dissipates power. The power dissipation of the sensor is the product of the total current and the applied bias voltage. As already discussed in 5.4.4, the bias voltage will be progressively increased through the lifetime of the HGTD in order to mitigate the loss of the sensor gain due to irradiation. This increase will not be uniform; sensors at low radius will be operated at higher V_{bias}, following the radial dependence of the received radiation doses. However, for LGAD sensors, the total current is dominated by the gain current that flows in the multiplication layer and which decreases with irradiation. It turns out that, due to the counterbalance of the two aforementioned effects, the dependence of the power dissipation to the radius is not very steep. An average value equal to 30 mW/cm^2 has been used in these calculations, equivalent to a fluence of around 1.5×10^{15} n_{eq}/cm^2. The total power consumption of the ASIC + sensor (half module) system is also displayed as a red line of Figure 6.10b - it reaches a maximum value of 1.3 W.

6.4.2 Optimization of readout components

As previously mentioned, the read-out system of the HGTD consists of two parts, the timing and luminosity data streams. The former can be optimized to reflect the strong dependence of the timing information bandwidth on the radius. In the following, an optimization work based on the TP simulation is presented.

e-links

Since the available space in the flex print is quite constrained, it is desirable to minimize the amount of links needed for each ASIC. This is achieved by matching the speed of the links with the bandwidth of each ASIC. Additionally, the number of lpGBTs should be kept as low as possible in order to fit in the very limited space of the PEBs. One of the main functionalities of the lpGBT, already discussed in 5.6.3, is the existence of seven independent groups with different speeds (1280/640/320 Mbps), where the number of entries in a group depends on

the chosen speed (7,14 or 28 entries respectively). Since the largest number of entries is made available for the lowest chosen transmission speed, it is clear that the upstream e-link speed should be as small as possible.

As shown in Figure 6.10a, the average bandwidth reaches a maximum of $\sim$ 600 Mbps in the inner radius. In order to accommodate this data rate with a safety margin, 1.28 Gbps e-links will be used for ASICs below R = 220 mm. At larger radius, the bandwidth reduces, and consequently, the e-link speed can be reduced to 640 Mbps for R$>$ 220 mm and to 320 Mbps for R$>$ 405 mm. These rates are chosen in order to minimise the numbers of lpGBTs while maintaining a 20% margin between the average ASIC bandwidth and the link speed.

For transmitting clock and fast control to the ASICs, the lpGBT ASIC has four transmission lines, each of the lines having the possibility to "fan-out" to a subsequent four outputs. Since our speed requirement for the clock and control is the same for all of the ASICs, all final 16 down-link outputs of each lpGBT can be used at the same rate; a speed of 320 Mbps has been found to be sufficient for the downstream information.

Contrary to the timing information, the luminosity data has a constant bandwidth of 640 Mbps/ASIC (16 bits at 40 MHz), therefore, 640 Mbps e-links are used for the transfer of the luminosity information. No downstream system is foreseen for the luminosity read-out. The clock, trigger and fast commands will be sent out to the ASIC by the dedicated timing lpGBT, while operation and control parameters for the luminosity lpGBTs themselves will also be transmitted from dedicated DAQ master lpGBTs through the I2C bus.

The data flow scheme for both timing and luminosity information, as well as the downstream and powering components can be viewed in Figure 6.11.

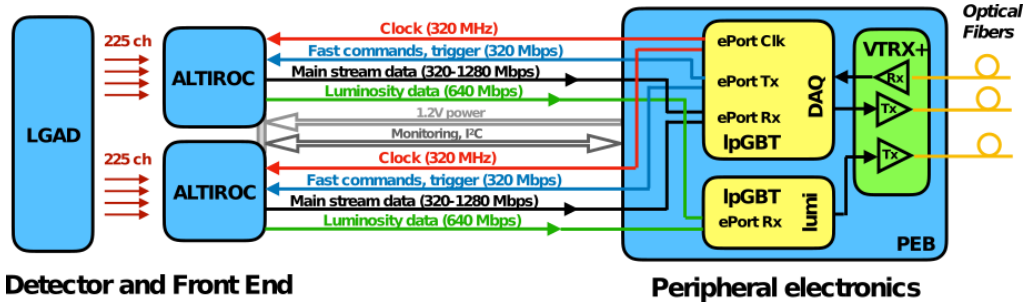

FIGURE 6.11: Upstream and downstream data flow from a module to the Peripheral Electronics Board (PEB).

lpGTBs - optical links

The minimization of the readout components in the peripheral boards is crucial, since the available space is very limited. Based on simulation estimates on the bandwidth of each module, an optimization of the number of lpGBTs was performed in the TP simulation. At the time of this work, the design of the PEBs was in a very preliminary stage, with many undefined parameters and unknown constraints. Therefore, this study was instrumental in estimating the DAQ requirements under various scenarios.

Initially, a simplified approach was considered, in which each peripheral board was serving a single readout row. In this approach, referred to as **TP baseline**, the lpGBT was using a single rate for receiving data, which is clearly an unoptimized approach. For simplicity of board connectivity and also to better control any problems with the clock transmission, the

up and down links of each module were required to be connected to the same lpGBT. A direct consequence of this is a constraint on the number of up e-links that can be connected to each lpGBT, since there has to be both a match to the number of down links and a grouping of the two ASICs in each module. The number of up e-links that can be connected to a lpGBT becomes 6, 14 or 16 for a rate of 1280, 640 or 320 Mbps, accordingly. Timing and luminosity information is handled by different lpGBTs. Finally, it was assumed that grouping of modules between the two sides of the cooling plate in the same PEB is not possible. This requirement was set because the peripheral boards need to be mounted on the cooling disk, in order to not overheat during operation. It was found that, in this scenario, 88 timing and 68 luminosity lpGBTs were needed per quadrant of the detector. This translates to 1408(timing)+1088(luminosity)=2496 lpGBTs for the full detector.

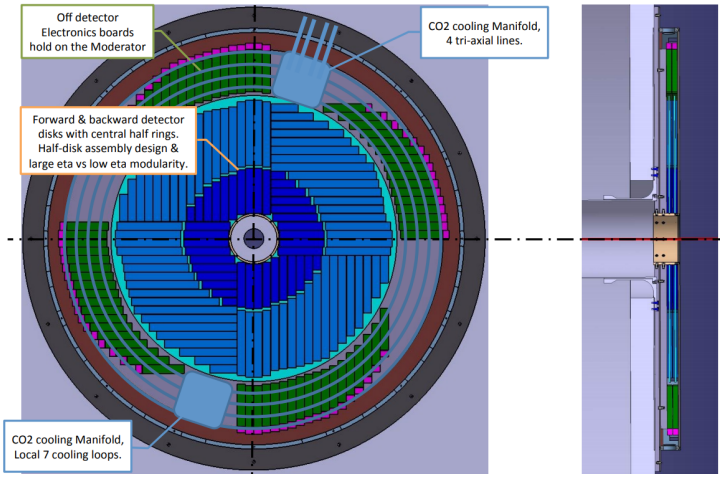

FIGURE 6.12: Schematic drawing of the front view of one side of the HGTD in the TP baseline scenario (cross-section on the left, transverse on the right). The modules are organized in rows on both sides of the cooling plate. Identical rows from the two sides of the cooling plate are readout by a dedicated peripheral board (green) that is not mounted on the cooling plate.

Some of the assumptions previously made were not originating from strict constraints on the physics or the used technologies and were revisited in an attempt to reduce the number of lpGBTs. Various alternative scenarios were considered in which one or more of the initial constraints were lifted. The different assumptions made in the various scenarios are summarized in Table 6.1.

- **Alternative 1:** in this scenario, the seven different speed groups of the lpGBT can now be used. Each group can host either one port at 1.28Gbps, or two ports at 640 Mbps or four ports at 320 Mbps. All other assumptions made on the TP baseline scenario are upheld.
- **Alternative 2:** building on alternative 1, in this case, control is transmitted downstream by separate lpGBTs than the upstream data. In this organization scheme, the upstream lpGBT can now have up to 28 entries at the lowest speed of 320 Mbps. The downstream lpGBTs on the other hand can have up to 16 entries (4×4) at 320 Mbps.
- **Grouping rows in the same peripheral boards:** a larger peripheral board unit that can connect to multiple rows can also be imagined in order to decrease the number of readout components. Due to constraints on the length and curvature of the flex cables, only rows that are close to each other can be read out by the same board. In addition, given that each half cooling disk will be assembled independently, it is not possible to group rows from different half-disks. A possible scheme could be the following: for each side

of a quarter rows 0+1, 2+3, 4+5, 6+7, 8-10, 11-15 and 16+17 (row numbering as in Figure 6.10a) are read out together. In this configuration, the amount of ASICs to be readout per board is fairly uniform. The possibility to mix speeds in each lpGBT is assumed. Both the cases where the up and down e-links are grouped or treated by separate lpGBTs can be considered:

- **Alternative 3:** in this case, the up and down e-links of each ASIC must be handled by the same lpGBT
- **Alternative 4:** alternatively, the downstream information is handled by dedicated "down"-lpGBTs.
- **Alternative 5:** in the case where we require that up and down e-links from each ASIC are not hosted in the same lpGBT (alternative 4), the luminosity lpGBTs can also be used for the treatment of the down e-links, since the luminosity information only flows upstream.

Assumptions	TP Baseline	Alt # 1	Alt # 2	Alt # 3	Alt # 4	Alt # 5
1 board per row	yes	yes	yes	no	no	no
speed mix in lpGBT groups	no	yes	yes	yes	yes	yes
match of up/down e-links	yes	yes	no	yes	no	no
match of down/lumi e-links	no	no	no	no	no	yes

TABLE 6.1: Summary of assumptions made for the calculation of lpGBTs/optical links needed for the readout of the HGTD in various scenarios. These assumptions are: if ASICs from different sides of the cooling plate can be hosted in the same peripheral board, if ASICs from different rows can be hosted in the same peripheral board, if groups of different rates are used in each lpGBT and if there is a matching of up, down and luminosity e-links from each ASIC to the same lpGBT.

The number of timing and luminosity lpGBTs needed to readout the entire detector is calculated for each of the aforementioned scenarios. In the calculation, the speed of the timing e-links of each ASIC is the minimum one allowing for the readout of the average event size as derived from full simulation, with a 20% margin. Only ASICs at the 20% overlap ring of the TP layout (R> 320 mm) transmit luminosity information at a constant speed of 640 Mbps. Data streams from the various ASICs are grouped to lpGBT entries following the imposed assumptions of each scenario, and all possible combinations are iterated to find the choice that minimizes the number of required lpGBTs. In case more than one such choice exists, the one that allows for a larger margin between the event size of the ASICs and the speed of the e-links is considered. The number of optical links can be directly derived from the number of lpGBTs, taking into account that each timing lpGBT is connected to two optical links (one up- and one down-type), while each luminosity (or down-type) lpGBT requires only an up-type optical link, except in case it is used also for downwards transmission.

Table 6.2 presents the resulting numbers of lpGBTs and optical links necessary to accommodate the complete detector readout under the TP baseline and the alternative scenarios. A 4% reduction of the number of lpGBTs can be achieved by using the seven programmable groups of the lpGBTs at different speeds. The improvement in the grouping is limited by the small number of ASICs that enter in the minimization algorithm, since only one row per PEB is considered. In assumption 2, the up- and down- e-links are handled by separate components in the PEBs, in order to exploit the most optimum grouping of the timing streams. The number of timing lpGBTs needed indeed decreases by 33%, but the number of lpGBTs

dedicated to the transmission of downstream information increases. The combined effect on the number of lpGBTs leads to a 30% increase of the total count. However, a more optimum distribution of the data to optical links is achieved, since all lpGBTs now require one optical link.

The clear advantage from using a PEB unit to handle ASICs from multiple rows is demonstrated in the calculations from alternative 3, where the number of necessary components is reduced by 20%, compared to the baseline. In alternative 4, a reduction of the number of optical links by 30% w.r.t. the baseline is achieved by additionally separating the timing and downwards streams, with the drawback of increasing the number of lpGBTs, similarly to alternative 2. The increase of down-lpGBTs can be mitigated by employing the unused down-ports of the luminosity lpGBTs to transmit downstream information, as in alternative 5. As it turns out, roughly 75% of ASICs can be controlled by luminosity lpGBTs, resulting in a 23% and 30% reduction of the lpGBTs and optical links (compared to the baseline), respectively.

Options	Timing lpGBTs	Luminosity lpGBTs	Total	$\frac{N^i_{lpGBT}}{N^{TP}_{lpGBT}}$	o-links
TP Baseline	1408	1088	2496	1	3904
Alt. # 1	1312	1088	2400	0.96	3712
Alt. # 2	880 (up)+1312 (down) = 2192	1088	3280	1.3	3280
Alt. # 3	1104	880	1984	0.79	3088
Alt. # 4	768 (up)+1088(down)=1856	880	2736	1.09	2736
Alt. # 5	768 (up)+272(down)=1040	880 (+down)	1920	0.77	2800

TABLE 6.2: Timing, luminosity and total number of lpGBTs and optical links to readout the full HGTD. The fraction of the total number of lpGBTs in each alternative scenario the TP baseline is presented in the next-to-last column. A description of the different scenarios used for the calculation is presented in Table 6.1.

This optimization study has been very important in converging towards a defined data transmission strategy. Taking into account the large reduction of necessary read-out units in alternatives 3-5, the choice has been made to group modules from different read-out rows in five large PEB structures. A schematic drawing of the most recent PEB configuration is shown in Figure 6.14. The grouping scheme is different from the one discussed in the optimization study, reflecting the change in row geometry and module layout that will be discussed in 6.5. It has been chosen in order to achieve a uniform distribution of the modules to the PEBs. The alternative to separate the timing stream to the clock and fast commands in the PEB has been rejected, given the increased number of lpGBTs and concerns on clock synchronization. Therefore, the alternative 3 has been chosen as the baseline for the HGTD. Separate lpGBTs with 14 e-link entries each will be used for the luminosity stream. In order to further decrease the number of the dedicated read-out components in the PEBs, only ASICs at R>430 mm will send-out luminosity information. This number results from using all available e-links of the minimum number of lpGBTs that allows all modules in the outer ring of the most-up to date geometry (again discussed in 6.5) to be included.

6.5 New geometry optimization

Since the definition of the post-TP geometry, new detector requirements have come to light, some of which are not satisfied with the implemented design. Starting from the description of the new conditions that make the post-TP geometry obsolete, I will be discussing my work on the path towards an adapted module layout for the HGTD Technical Design Report (TDR) [154].

6.5.1 New requirements

Figure 6.13a shows the row layout scheme for the 1st disk of HGTD with the post-TP geometry. In this layout, there are two defined radial rings, distinguished by the different overlap. In the inner ring, which extends to R = 320 mm, the modules are placed with an 80% overlap between the two sides of the cooling plate, and were planned to be replaced once at the half-life of HGTD. The rest of the modules are placed in the outer ring, between R = [320,640] mm, with a 20% overlap. At the time of the conception of the post-TP geometry, no replacement was foreseen for the outer modules.

Recently, the design of the peripheral electronics boards has significantly matured, thanks to a coordinated effort of the HGTD community. The amount and dimensions of the necessary components for the PEB functionalities are now established. The connection process between the flex cables and PEBs is also better understood. Taking into account all the newly acquired information, it has become clear that the post-TP readout-row layout needs to be re-optimized in order to distribute the modules more uniformly to their dedicated PEBs. In parallel, updates on the material distribution of the ITk have brought on a change in the expected irradiation dose in the HGTD. In addition, beam test and beta source results with irradiated sensors have provided us with a deeper knowledge of the LGAD lifetime in the HL-LHC conditions, calling for a change in the module layout and replacement plan.

A modified module layout and replacement scheme have been conceived in order to better accommodate the aforementioned requirements, while maintaining the performance, as shown in Figure 6.13b. The new geometry is referred to as TDR layout. The modules are now organized in three radial rings, an inner one, extending from R = 120 mm to R = 230 mm, a middle one in the R = [230, 470] mm and an outer one for R $>$ 470 mm. With this layout and under the replacement scheme already described in 5.2, the total received radiation dose of the modules will remain below 2 MGy or 2.5 $\times$ 10^{15} n_{eq}/cm^2 for the TID or neutron-equivalent fluence, respectively. In addition, the orientation of most of the readout rows alternates between parallel and perpendicular to the x-axis. This ensures that the modules are more uniformly distributed to the peripheral boards.

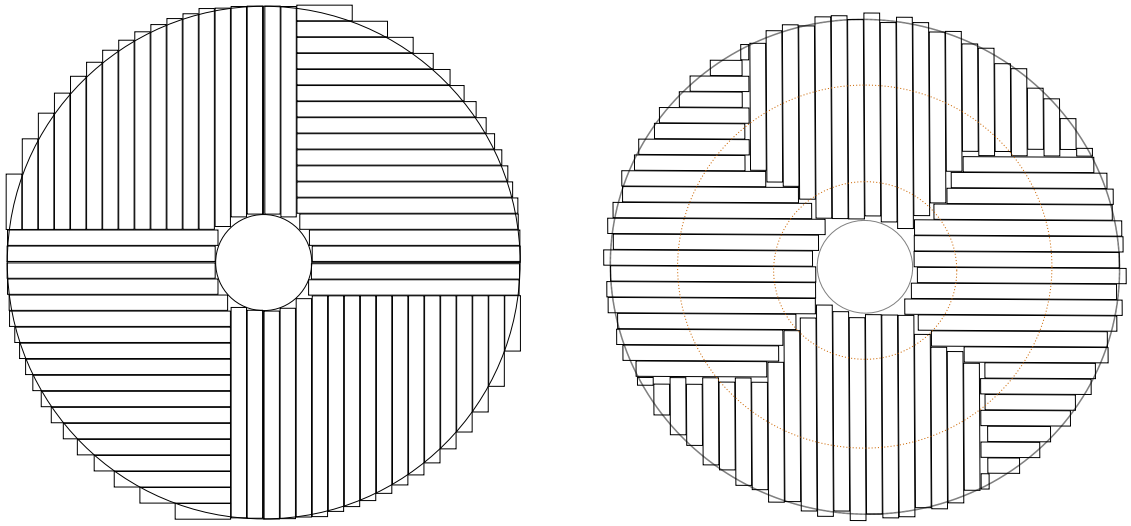

(a) (b)

FIGURE 6.13: Row layout scheme of the first HGTD disk in (a) the post-TP layout and (b) the TDR layout. The rotation of the disk is not displayed.

The second disk is a copy of the first one, but rotated by 180° along the Y axis, so that its front (back) side is a mirror of the back (front) side of the first cooling plate. The cooling plates are rotated by +/-10° along the XY plane, effectively creating a 20° relative angle between the active layers. This effective mirror symmetry, combined with the rotation of the two cooling plates, is crucial for the design of the cooling system, since, as shown in Figure 6.14, it provides the necessary space to allow the connection of the cooling pipes to the disks. In addition, since the two disks are essentially identical, the number of different PEB units (and therefore the production cost) is minimized.

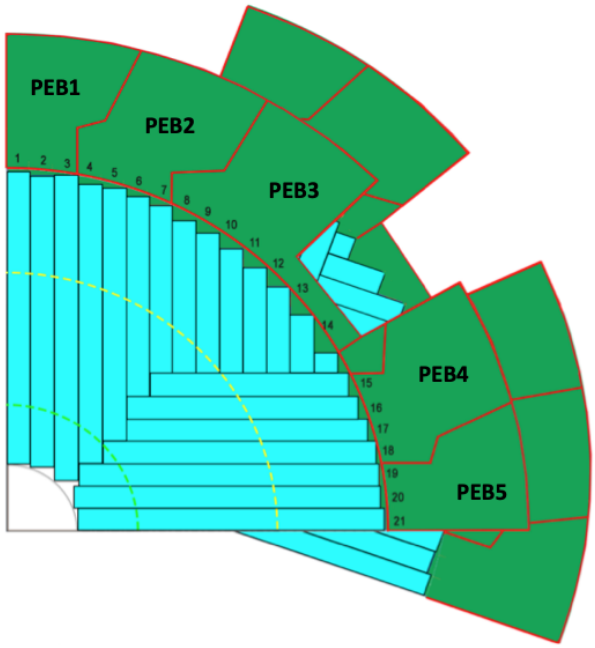

FIGURE 6.14: One quadrant of the HGTD front and back disk is shown. The PEBs (in green) are attached to the readout rows (numbered from 1 to 21).

6.5.2 Simplified geometry framework

Physics simulation with a detailed detector description is a very time consuming process. In order to be able to quickly study the performance of HGTD in alternative geometry scenarios before implementing them in full simulation, I have developed a simplified optimization framework that builds the HGTD geometry and propagates a straight-line track through it. In this framework, the HGTD is stand-alone, meaning that there are no other simulated detectors. Material effects within the HGTD and the magnetic field of ATLAS are also not taken into account. The beam spot is simulated as a Gaussian along the beam axis (z) with σ = 45 mm - the spread along the other two dimensions (x,y) is taken to be 0. Single track events are produced uniformly in θ and ϕ, in order to increase the statistics in the outer part of the detector. All dead regions between modules are reconstructed in the framework. The guard ring is also included. For simplicity, the fill factor dead regions are not simulated. Their effect is taken into account by introducing a hit probability factor of the track, equal to the relative inter-pad dead area.

This framework is by no means a replacement of full simulation. However, it is very useful in providing quickly a rough estimate of the potential effects of geometry modifications in the performance of HGTD. An implementation of the most recent module geometry is currently being implemented in Geant4 in order to perform more detailed performance studies. The following sections present results on various aspects of the detector geometry and performance

that have been obtained with the simplified framework.

6.5.3 Comparison with the full simulation

As a first step, results from the implementation of the post-TP geometry in the simplified framework were compared against the full simulation. Figure 6.15 shows the hit multiplicity per track as a function of the radius using full simulation or the simplified framework. In the simplified framework, the hit multiplicity is overestimated by 7% in the full radial range. As already stated, this framework is an overly simplified one. Effects from the magnetic field, the efficiency of the clustering algorithms and the material, such as scattering, showering, energy loss and insufficient energy deposition can reduce the number of hits deposited by a track in the HGTD.

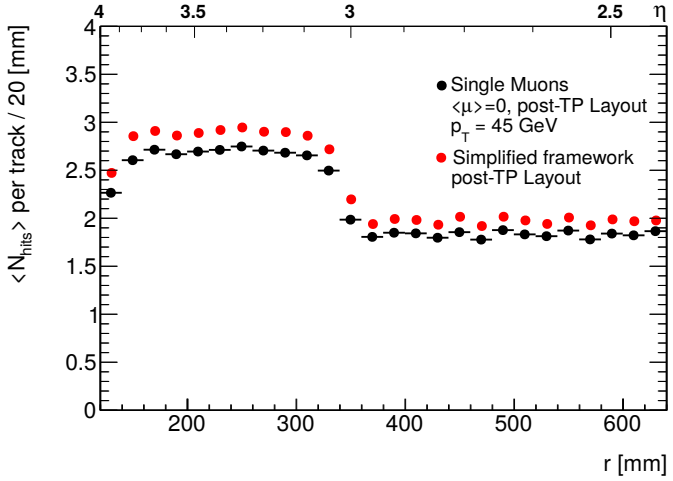

FIGURE 6.15: Average hit multiplicity of the tracks as a function of the radius in the post-TP module layout obtained using the simplified framework (in red). The equivalent result from the full simulation is shown in black. In the simplified framework, magnetic field, material and efficiency effects are not taken into account, and, as a result, the average hit multiplicity is slightly overestimated.

6.5.4 Overlap optimization

The recent updates on the material budget prior to the HGTD result in fluences that are more moderate in the inner and more severe in the middle of the detector w.r.t. the post-TP expectations. The overlap scheme between modules must reflect this change, in order to maintain a satisfying number of associated hits per track even under high irradiation doses. Therefore, a re-optimization of the module placement is needed. For simplicity of the assembly and replacement processes, the overlap between modules will be constant in each radial ring. Starting from the TDR row geometry, two alternative overlap configurations were conceived and tested with the simplified framework: in the first one, the same overlap is used in the inner and middle ring, in order to achieve a more uniform performance, while in the alternative scenario, a progressive decrease of the overlap in the three rings is envisioned. The total number of modules in the HGTD must remain very close to the one in the post-TP geometry, 7984. Taking into account this constraint, the overlap in the first scenario has been set to 60% in the inner-middle and 20% in the outer ring, resulting in exactly 7984 modules. In the alternative configuration, the overlap in the inner ring is set to 70%, while it is reduced to 54% in the middle and 20% in the outer ring, giving in total the same number of modules. The modules in a quadrant of the first HGTD disk are shown in the two alternative overlap schemes in Figure 6.16.

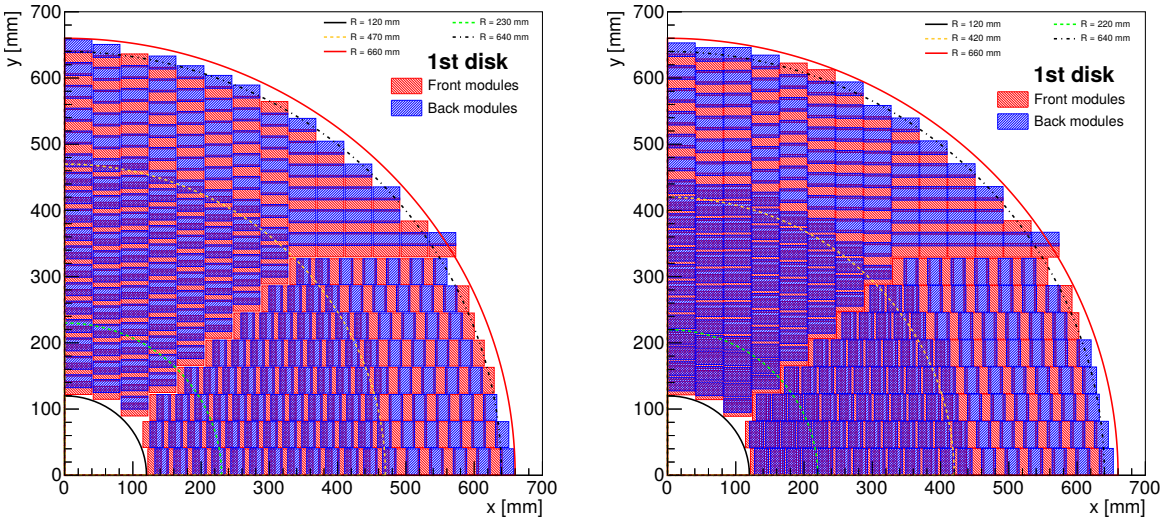

(a) (b)

FIGURE 6.16: Module placement scheme in a quadrant of the first HGTD disk in the TDR layout with (a) a 60%/ 60% / 20% overlap in the inner / middle / outer ring (b) a 70%/ 54% / 20% overlap in the inner / middle / outer ring. Modules on the front side of the cooling plate are shown in red and back ones in blue. The dashed lines illustrate the radial ring limits. The rotation of the disk is not displayed.

The average hit multiplicity as a function of the track radius with the TDR module layout is shown in Figure 6.17a, for the two overlap configurations. In both cases, a correction factor of 0.93 is applied on the average hit multiplicity, in order to account for the observed differences between the simplified framework and full simulation, shown in Figure 6.15. In the case of the progressive reduction of the overlap, three radial regions can be distinguished. In the inner part, where the overlap is the highest, there is an average of 2.5 hits per track. This number decreases to 2.3 hits/track in the middle and 1.8 hits/track in the outer ring of the detector. In the alternative case, the performance in the middle ring is only marginally improved, while in the bulk of the inner ring, the average number of hits per track is reduced to 2.3.

Figure 6.17b demonstrates the fraction of tracks as a function of the number of their associated hits, separated in the three radial rings. The uniform (decreasing) overlap configuration is shown with the solid (dashed) line. In both cases, there are less than 5% of the tracks with no hits in all of the rings, indicating a good coverage of the HGTD acceptance with active area. In the middle and outer ring, the two alternatives perform similarly, with at least 80% of the tracks having 2 or more hits. A large discrepancy is observed in the inner ring, where the difference in overlap is between the two scenarios is the highest. While the fraction of tracks with 2 or more hits is in both configurations around 85%, in the case where a 70% overlap is used, the fraction of tracks is shifted to higher values. Furthermore, the number of tracks with only one hit are decreased by $\sim 30\%$. It is clear that the best performance is achieved by choosing a progressively decreasing overlap, with a large overlap in the inner ring. The scheme with 70% - 54% - 20% overlap in the inner-middle-outer ring has been chosen as the baseline for the HGTD, and all of the following studies are performed in this configuration. This decision is of course subject to the evolution of the detector studies of both ITk and HGTD.

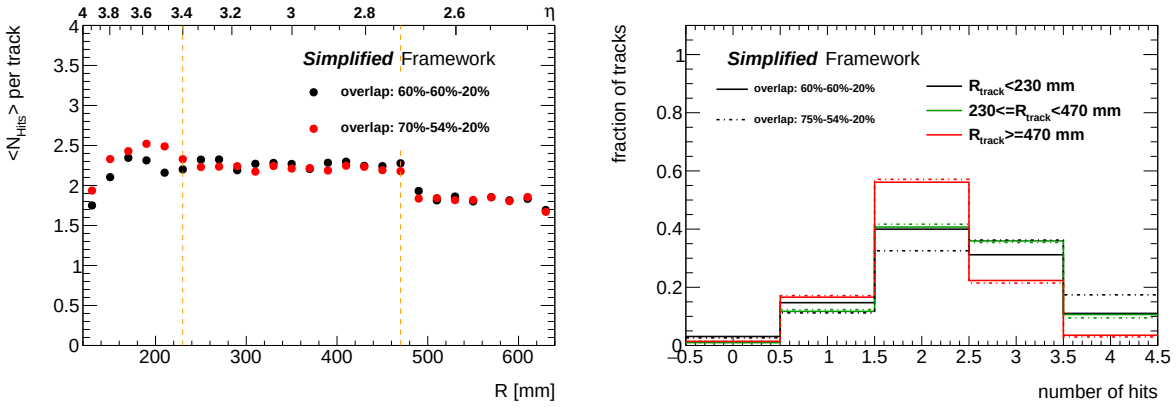

(a) (b)

FIGURE 6.17: (a) Average hit multiplicity of tracks in the HGTD as a function of the radius in the simplified framework. The TDR row layout scheme is used and the two alternative overlap scenarios are superimposed: the configuration with 60%/ 60% / 20% overlap in the inner / middle / outer ring is shown in black, while the one with 70%/ 54% / 20% overlap in the equivalent rings is shown in red. In both cases, a correction factor is applied to the average hit multiplicity in order to account for differences between the simplified framework and the full simulation. (b) Fraction of tracks as a function of their associated hits, separated in the three radial rings. The two overlap scenarios are superimposed for comparison.

6.5.5 Hit multiplicity and performance

Figure 6.18 shows hit maps extracted from the simplified framework in the 4 active layers of HGTD. The mirror symmetry and rotation between the two disks is applied. The TDR module layout, as described in 6.5.1, is implemented. The overlap has been chosen to be 70% for the inner, 54% for the middle and 20% for the outer ring, in order to maximize the number of hits per track while maintaining the same amount of modules.

Figure 6.19a shows the hit multiplicity as a function of the track incident position in X and Y at the first layer of HGTD. The three overlap regions are distinguishable and a good uniformity of the number of hits in ϕ is observed. In Figure 6.19b, the fraction of tracks that are within the HGTD acceptance but have no hits is shown as a function of the position in X and Y in the first layer. In the bulk of the detector, this fraction is usually smaller than 5%. Furthermore, thanks to the rotation strategy, they are uniformly distributed and no evident structures appear. Only near the edges of the detector, this fraction increases due to the lack of overlap between layers.

As the time resolution of the track is inversely proportional to the square root of the number of associated hits, a better performance is expected at low R at the beginning of the HGTD operation. However, this dependence will change during the lifetime of the detector, since the inner part will receive a higher irradiation damage. The estimate of the time resolution per track as a function of the radius in various stages of the HL-LHC program is shown in Figure 6.20. This result was calculated from a convolution of the per-hit time resolution extracted from full simulation with 0.1 - 5 GeV pions and the average number of hits/track from the simplified framework. In this way, an accurate estimate of the track performance in the TDR module and row layout is obtained prior to its implementation in the full simulation. The jumps of improvement in the resolution at 1001 and 2001 fb^{-1} correspond to the performance of the detector after a ring replacement. Thanks to this replacement scheme, the resolution is better than 50 ps for the entirety of the HL-LHC program.

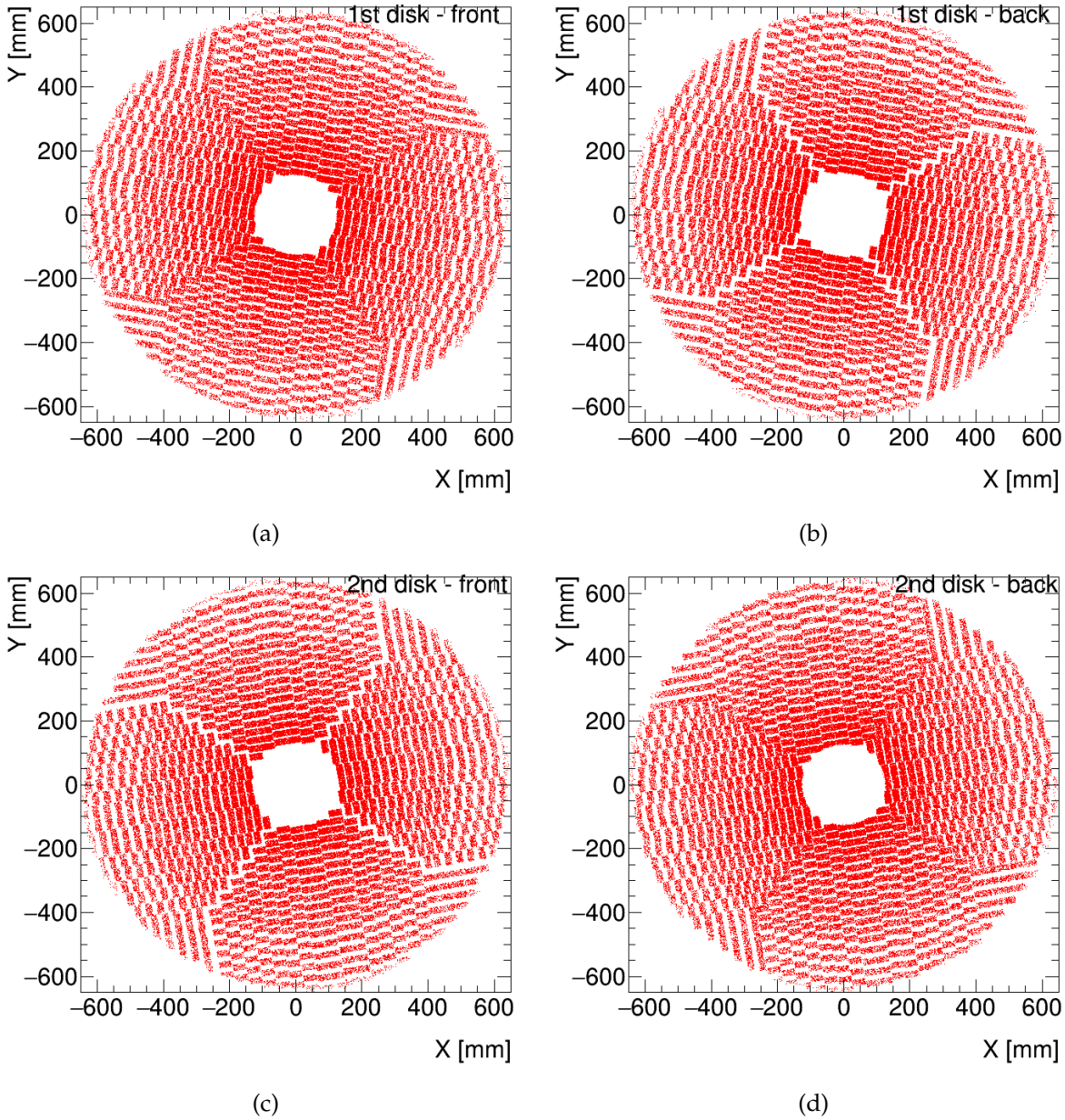

(a) (b)

(c) (d)

FIGURE 6.18: Distribution of hits in the X and Y of (a)-(b) the front and back side of the 1st cooling plate and (c)-(d) the front and back side of the 2nd cooling plate.

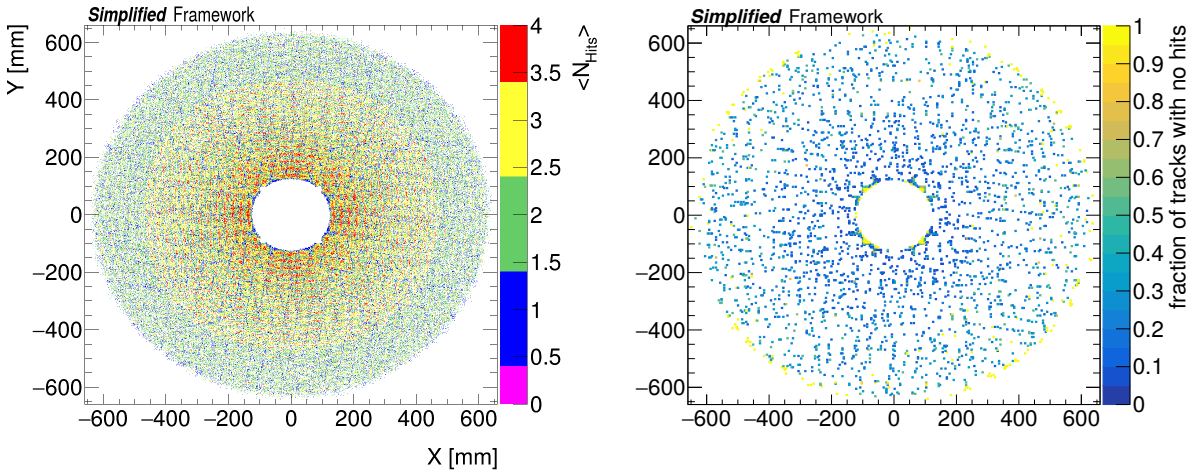

(a) (b)

FIGURE 6.19: (a) Average hit multiplicity as a function of the X and Y in the first active layer of HGTD. (b) Fraction of tracks within the HGTD acceptance without a hit as a function of the X and Y in the first active layer.

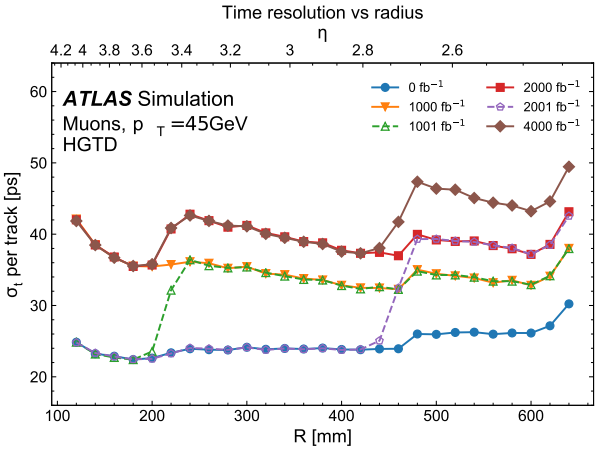

FIGURE 6.20: Time resolution per track within HGTD acceptance as a function of the radius. The time resolution is shown for various integrated luminosities. The time resolution is improved at higher luminosities corresponding to the replacements of the inner-most and middle rings during the lifetime of the detector.

6.5.6 Rotation optimization

The effect of the rotation angle between the two disks was also investigated with the simplified framework. Figure 6.21 shows the hit multiplicity per track as a function of the angle ϕ for three different relative rotation angles: 13° (± 6.5°) , 20° (± 10°) and 30° (± 15°). The average multiplicity, shown with the black points, is not affected by the relative rotation between the two disks. However, the full distribution displays non-uniformities at a small angle, as seen in Figure 6.21a. The azimuthal symmetry is restored for larger rotations. A value of 20° has been chosen as the default for the TDR geometry over higher rotations, since it creates a larger space for the entrance of the cooling system.

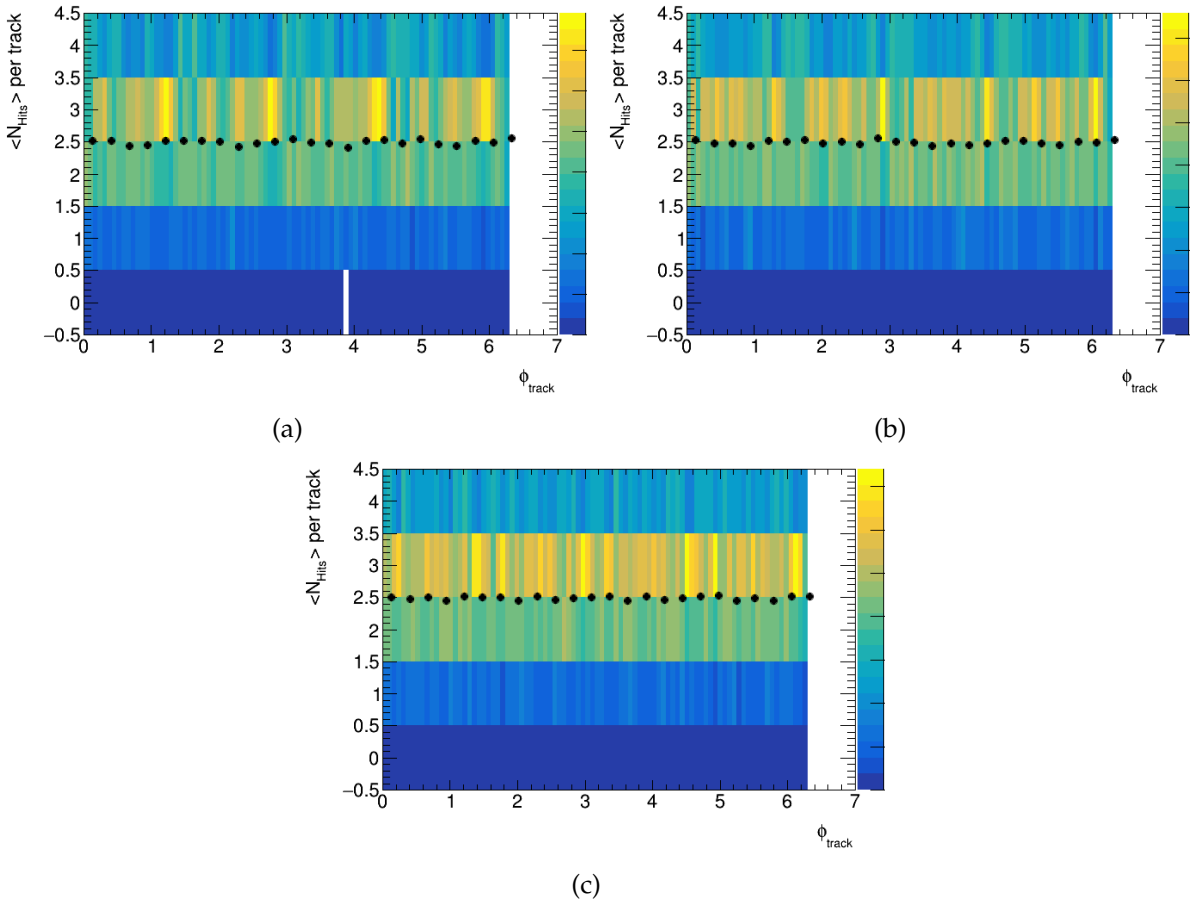

FIGURE 6.21: Hit multiplicity per track as a function of the azimuthal angle ϕ for a (a) 13° (b) 20° and (c) 30° relative rotation angle between the two disks. The black points show the average number of hits per track, corrected for differences between the simplified framework and the full simulation.

7. ALTIROC: a front-end prototype ASIC for the HGTD

In this chapter, my work on the characterization of the front-end prototype ASIC for the HGTD, ALTIROC, will be presented. Two prototype versions, ALTIROC0 and ALTIROC1 have been developed so far, the performance of which I have studied extensively. The first chip, ALTIROC0, integrates only the preamplifier and discriminator stages of the analogue read-out chain, while in ALTIROC1, the TDC and channel memory blocks are also included. The chapter is organized as follows: the design of the two prototypes and the available devices are described, in 7.1 and 7.4, respectively. Results with ALTIROC0, in laboratory and test-beam are presented in 7.2 and 7.3, respectively, while equivalent measurements with ALTIROC1 are shown in 7.5 and 7.6.

7.1 ALTIROC0

A first analogue prototype with eight channels has been designed in CMOS 130 nm by the OMEGA microelectronics center. It integrates four voltage sensitive preamplifier channels and 4 pseudo transimpedance, allowing for a direct comparison of the two designs' performance. Each channel is made of a preamplifier followed by a discriminator. The design of the chip includes bump bonding pads on each input and also on ground pads. The size of the chip is 3.4 $\times$3.4 mm^2 to accommodate the bump bonding to a 2$\times$2 sensor array with 1.1 $\times$ 1.1 mm^2 pad size. The main purpose of this prototype is a first characterization of the analogue performance to prove its feasibility to reach the timing requirements of the HGTD. The reader is reminded of Table 5.1, summarizing the main target requirements for the HGTD ASIC.

In order to inject an accurate calibration charge, a calibration capacitor (C_{test}=100 fF), which can be selected by slow control, is also integrated in each channel. With a fast voltage step of 100 mV, a short square pulse with a 10 fC charge can be delivered at the input of the preamplifier. Such an input signal allows the characterisation of the front end read-out but does not reproduce the jitter performance when having an LGAD signal as input, as its signal shape and time duration can not be neglected. Figure 7.1 demonstrates a comparison between the preamplifier output of an LGAD and a Dirac (infinitely short) pulse, as extracted from simulation, for the same input charge. On the left-hand side, the evolution of the voltage as a function of the time is presented, where it can be seen, that while the maximum reached amplitude is similar for a Dirac and an LGAD pulse, the rise-time of the latter is larger. This is further quantified from the right-hand side of the figure, where the derivative of the pulse as a function of the amplitude is shown. Positive derivative values correspond to the rise-time; the maximum derivative is reached for intermediate amplitude values, and is a factor of 1.65 smaller for LGAD signals. This directly translates to a deterioration of the LGAD jitter by the same factor compared to a Dirac pulse, when measured at the same constant threshold. On the other hand, the fall time, exhibited in the negative range of the derivative, displays similar behaviour between the two types of pulses. This is expected, since the falling time is modelled by the discharge of the RC circuit created by the preamplifier input impedance and detector capacitance, 5.5.5.

The pulser circuit, previously described in 5.5.5, is not integrated in this first version of the ALTIROC chip. Calibration pulses are instead provided by an external generator, as discussed in 7.2. The current I_{d2} can be tuned by an external resistor, allowing for I_d to be modified. As a

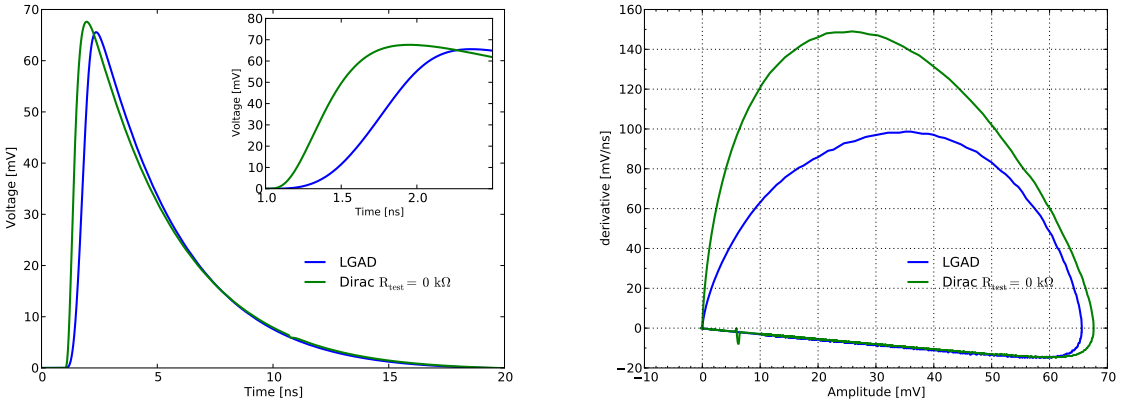

(a) (b)

FIGURE 7.1: Preamplifier output (a) amplitude as a function of the time and (b) derivative as a function of the amplitude, for an input LGAD signal (in blue) or a Dirac pulse (in Green), as extracted from simulation.

result, the input impedance, the preamplifier transconductance g_{m1} and the preamplifier fall time can be adjusted.

Dedicated read-out boards were produced on which the ASIC was wire-bonded, either alone, or bump-bonded to an LGAD sensor. In the latter case, the ASIC + sensor system is referred to as a bare module. A picture of the custom board used to characterise the ALTIROC0 ASIC is shown in Figure 7.2a. The board is equipped with a standard Field Programmable Gate Array (FPGA) used to load the slow control parameters. The four discriminator outputs can be read-out on SubMiniature version A (SMA) connectors. A dedicated probe is available on an SMA connector to read the output of the preamplifier after a second stage amplifier/shaper. The channel(s) to be read-out is selected through slow control. Finally, an additional SMA connector is used to inject the calibration pulse.

External capacitors can be soldered on the board to mimic the LGAD (C_d) at the preamplifier input when a sensor is not bump-bonded to the ASIC. In case the bare module is mounted, the preamplifier input is directly connected to the sensor, and therefore, the addition of an external capacitance does not affect the C_d.

Two versions of the custom read-out boards were produced to investigate the time-over-threshold issue observed when an LGAD sensor is connected to the input of the ASIC, that is discussed in section 7.2.3. The second version, as seen in Figure 7.2c, has an L-shaped High Voltage (HV) pad that allows for multiple HV wire bonds to be connected far from each other, minimising any possible inductance to the HV decoupling capacitor.

Table 7.1 lists the Devices Under Test (DUTs) that where available for the measurements performed in this thesis. The DUT in this case consists of an ALTIROC0 ASIC, wire bonded to a custom readout board, while an LGAD sensor might also be bump-bonded to the ASIC. Tests of the performance of the ASIC without the presence of a sensor were performed with DUT A3. A board with a modified L-shaped HV pad was equipped with a 2×2 LGAD sensor array, using SnAg bumps with under-bump metallization (UBM) for the bump-bonding, and characterised with the calibration setup (DUT A4). This device was not available for the October 2018 testbeam campaign.

For the October testbeam campaign, the results of which are presented in section 7.3, two

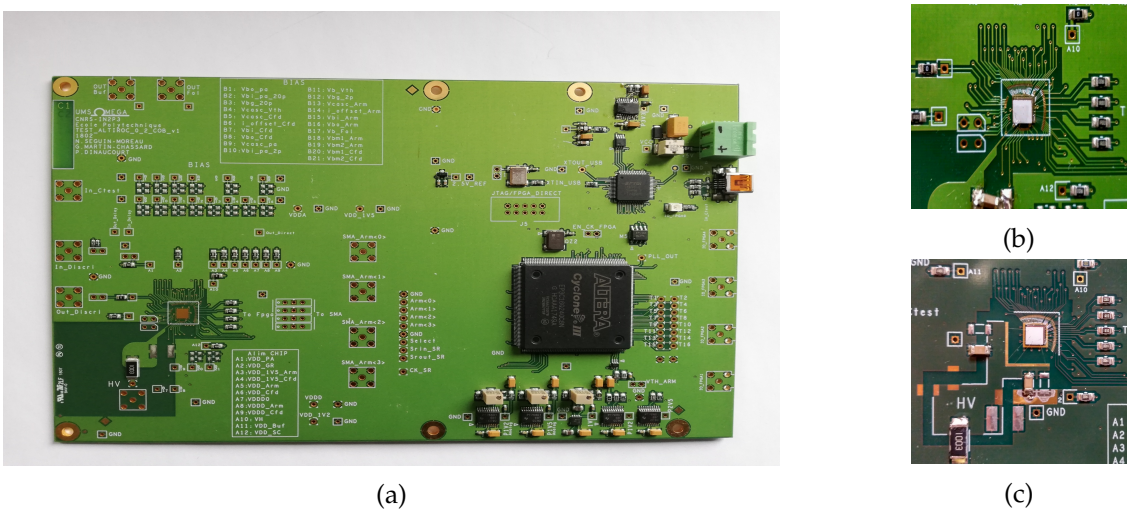

(a) (b) (c)

FIGURE 7.2: (a) Photograph of a standard ALTIROC0 board. (b) Zoom of Figure (a) on the flip-chip consisting of an ALTIROC0 ASIC bump bonded to a 2×2 LGAD sensor array. (c) Zoom on the flip-chip area of a modified L-shape HV pad board.

ALTIROC0 standard boards were available. Both were equipped with a 2×2 unirradiated sensor array that was bump bonded on the ASIC. Both sensor arrays were CNM LGAD with a 50 µm active thickness and 1.1 ×1.1 mm pixel size. The two boards and ASICs were identical. The bump and wire bonding of the two boards were performed in different laboratories; one of them, labelled DUT A1, was assembled in IFAE using SnAg bumps with UBM for the bump-bonding. The second one, labelled DUT A2, was assembled in BNL, while Au bumps without UBM were used for the bump-bonding. In A2, channel 1 was discovered before the testbeam to be disconnected, probably due to a faulty contact of the bump.

TABLE 7.1: List of available DUTs, consisting of an ALTIROC0 ASIC wire bonded to a readout board.

DUT name	active channels	with an LGAD sensor	HV pad shape	testbench/testbeam
A1	4	yes (SnAg + UBM)	standard	both
A2	3	yes (Au)	standard	testbeam
A3	4	no	standard	calibration
A4	4	yes (SnAg + UBM)	L-shape	calibration

7.2 Testbench measurements with ALTIROC0

7.2.1 Calibration setup

A generator with a picosecond level precision is used to generate a step pulse of a well defined voltage with a 70 ps rise-time. This signal is injected through the internal capacitor, thus producing a very short square pulse with a precise charge at the preamplifier input. A high frequency splitter is used to duplicate the injected signal to be also used as time reference for the time resolution measurement. The time resolution of the generator has been measured from the time difference of the two copies' time of arrival to be about 6 ps. The generator provides also the trigger of the acquisition, done with a Lecroy oscilloscope having

a 20 GSamples/s sampling rate and 2.5 GHz bandwidth. The full waveforms are registered for each trigger and analysed off-line.

7.2.2 Performance of ASIC alone

As a first step, the performance of the ASIC alone was evaluated with a calibration injection setup in which the ASIC was wire-bonded directly on a dedicated read-out board. Most of the measurements were done with an additional external soldered capacitor (C_{sold}) of 2 pF to emulate the sensor capacitance. This value was chosen to match the jitter from calibration measurements of boards with a mounted module (ASIC+sensor) that are presented in section 7.2.3. The soldered capacitance in combination with the parasitic capacitance of the board mimics the capacitance of the full module, in which a 1.3 mm $\times$ 1.3 mm LGAD sensor with a thickness of $50\,\mu m$ is expected to contribute around 4 pF. Charge scans were performed from 5 to 50 fC as the typical charge deposited. As explained previously, the current I_{d2} can be modified by an external resistor and for most measurements, a value of I_{d2}= $600\,\mu A$ was used, corresponding to I_d= $800\,\mu A$.

Pulse properties

Figure 7.3a shows the average discriminator response for different injected charges from 5 to 40 fC: the larger the input charge, the larger is the pulse width and the earlier the pulse time. The average pulse shape of the preamplifier probe is shown in Figure 7.3b for various values of soldered capacitance. As expected, the amplitude of the pulse decreases with the capacitance, while the falling time also becomes longer.

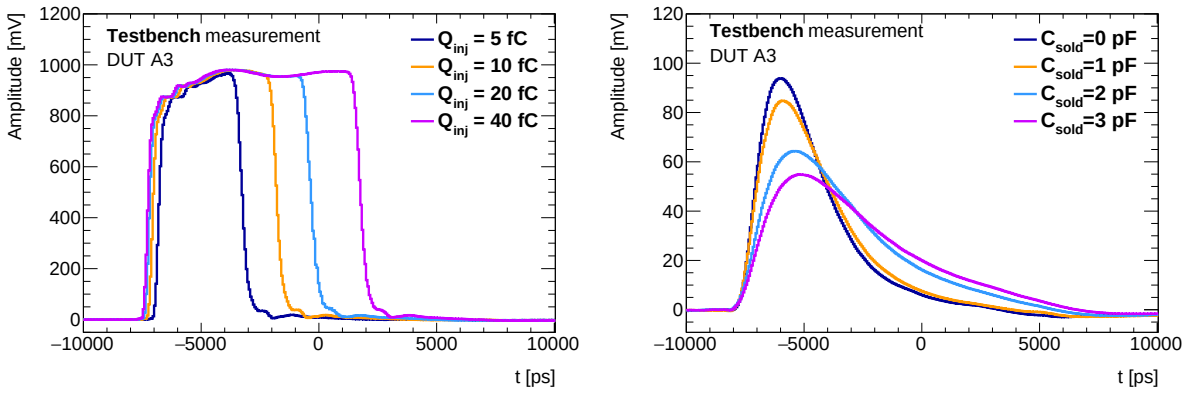

(a) (b)

FIGURE 7.3: (a) Average discriminator pulse shape for Q_{inj}=5-40 fC and C_{sold}=2 pF. (b) Average probe pulse for C_{sold}=0-3 pF and for Q_{inj}=10 fC

Parasitic capacitance

Apart from the capacitance of the sensor (or the soldered capacitance in the case of an ASIC alone), there are two additional contributions to the total capacitance to be considered; the parasitic capacitance of the ASIC itself, and the parasitic capacitance of the custom board.

As shown in Eq. 5.10, the total detector capacitance is inversely proportional to the amplitude of the preamplifier output. Under the assumption that $C_d = C_{sensor} + C_{par}$, where C_{par} is the parasitic capacitance, Eq. 5.10 can be modified as follows:

$$\frac{1}{V_{out}^{pa}} = \frac{C_{sensor}}{G_{pa} * Q_{in}} + \frac{C_{par}}{G_{pa} * Q_{in}} \tag{7.1}$$

The measurement was performed with the ASIC wire-bonded to the board directly, while an externally soldered capacitance was acting in place of the sensor. The value of the soldered capacitance was modified individually for all channels in a range of 0 - 4 pF and the probe amplitude was used as an estimator of the preamplifier output. As shown in Figure 7.4, a linear dependence of the inverse of the probe amplitude to the soldered capacitance was observed, in agreement with Eq. 7.1. The total parasitic capacitance of each channel was extracted from the fit to the measurements and was found to be between 3.8 and 4.3 pF.

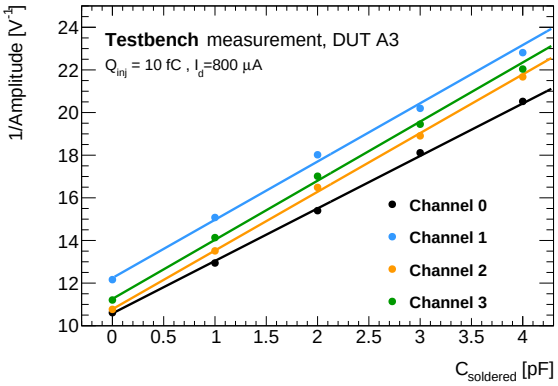

FIGURE 7.4: $1/V_{out}^{probe}$ as a function of the soldered capacitance for channels 0-3 of an ALTIROC0 ASIC wire-bonded to a custom board. The solid lines correspond to the linear fits used to extract the parasitic capacitance of each channel.

The contribution of the ASIC to the C_{par} was estimated from a channel whose input had been disconnected from the board, using again the probe amplitude as an estimate of V_{out}^{pa}. It was measured to be 0.8 pF, a value that is expected from simulation. Of the two contributions, only the parasitic capacitance of the ASIC is relevant to the module performance, since, when the ASIC is bump-bonded to the sensor, the preamplifier input is directly connected to the sensor.

Jitter

The jitter was calculated from a Gaussian fit to the difference between the discriminator output time and the trigger input signal. For both discriminator and trigger input, the time was measured at the 50% of the maximum amplitude. Figure 7.5a demonstrates that the time distribution for a 10 fC input charge is well modelled by a Gaussian with a 13 ps resolution. Figure 7.5b shows the jitter as a function of the injected charge for a 2 pF soldered capacitance and a discriminator threshold of 2.5 fC, after having subtracted quadratically the reference time resolution of 6 ps. The red line corresponds to a fit which follows the theoretical prediction of Eq. 5.8. The resolution reaches a plateau of 4 ps at high charges.

The variation of the jitter is also shown in Figure 7.6 for a 10 fC input charge (most probable MIP charge in HGTD pre-irradiation) as function of the soldered capacitance: as expected a linear dependence is observed, thus justifying the choice of small area pad sensors with an active thickness of $50\,\mu\mathrm{m}$ for the final detector.

Time walk correction

The TOT of the discriminator will be used as an estimate of the input charge to correct for the time walk effect. Figure 7.7a shows the TOT distribution for 12 fC input charge. As seen previously for the TOA, the distribution is well modelled by a Gaussian fit of 120 ps width, shown with the red superimposed line. The correlation of the TOT and the probe amplitude

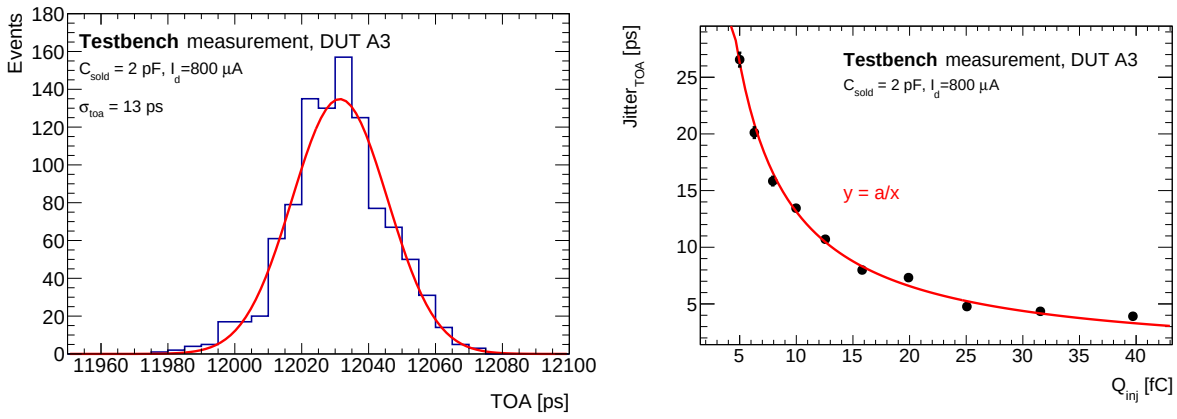

(a) (b)

FIGURE 7.5: (a) TOA distribution for Q_{inj} = 10fC. The RMS of the distribution, i.e. the jitter, is found to be 13 ps. The red line corresponds to a Gaussian fit. (b) Jitter as a function of the injected charge. The fit (red line) follows the theoretical prediction of Eq. 5.8. Both measurements have been done with a C_{sold} = 2 pF and a 2.5 fC discriminator threshold.

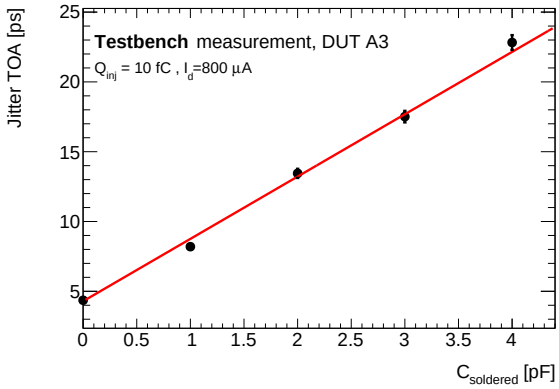

FIGURE 7.6: Jitter as a function of the soldered capacitance for an injected charge of 10fC. The solid line corresponds to a linear fit.

with the input charge is shown in Figure 7.7b, where it can be seen that the behaviour of the probe is linear while the TOT displays a reduction of the slope with the charge. For very high charge, both the TOT and the probe amplitude display some saturation, which probably originates from the preamplifier itself.

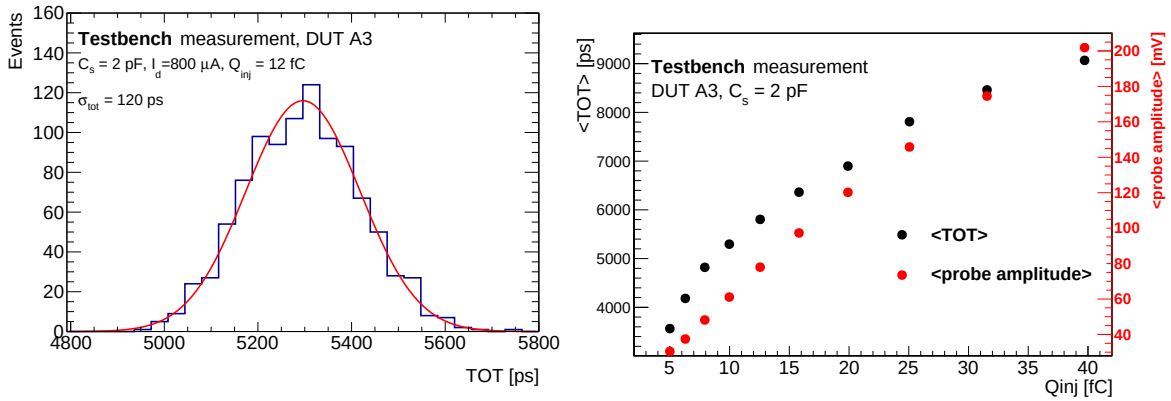

(a) (b)

FIGURE 7.7: (a) distribution of the discriminator TOT for Q_{inj} = 12 fC. (b) Average TOT (in black) and probe amplitude (in red) as a function of the injected charge.

The average time of arrival (TOA) as a function of the TOT or the probe amplitude is shown in Figures 7.8a and 7.8b respectively, for a soldered capacitance of 2 pF and an injected charge ranging from 5-40 fC. The red line in both figures corresponds to a polynomial fit used to apply the time walk correction. A time walk of about 500 ps is observed, corresponding to a total bandwidth of 700 MHz [1] for the preamplifier and discriminator. The bottom pad of 7.8a shows the residuals of the TOA after correcting for the time walk using the TOT. They are calculated to be in a peak-to-peak range of 45 ps, while a better performance of 20 ps is achieved using the amplitude of the probe, presented in the bottom pad of Figure 7.8b. In both cases, assuming a pessimistic uniform distribution of the peak-to-peak residual, the achieved residual RMS is $\sim$ 10 ps. This value is consistent with requirements of the time-walk correction performance for the HGTD, see Table 5.1.

VPA vs TZ preamplifier

The performance of the two implemented preamplifiers, VPA and TZ, has been compared in DUT A3. No additional capacitance has been soldered for these measurements. The pulse shapes of the discriminator and probe for the two preamplifier types can be seen in Figure 7.9. As expected, the output of the VPA has a larger amplitude and is longer, resulting in a wider discriminator pulse.

Figure 7.10a shows the average TOA as a function of the TOT, for the two preamplifier types and an injected charge ranging from 8 to 80 fC. A time walk of $\sim$ 500 ps is observed for the voltage preamplifier, while for the TZ, a smaller value of 300 ps is seen. As expected, the pseudo-transimpedance preamplifier pulse has a much shorter fall time, and as a result, the TOT varies by only 600 ps in the aforementioned scan range. The equivalent range of the VPA TOT is almost 5 ns. A polynomial fit is applied in both cases, displayed as a solid line of the same colour, from which the time walk correction is applied. The residual after this correction is shown in the bottom pad of Figure 7.10a; a peak-to-peak value of 50 (40) ps is observed for the VPA (TZ) preamplifier. For the VPA preamplifier, a 5 ps difference in the residual after the

[1] In electronics, the bandwidth can be approximated by $0.35/t_{90\%-10\%}$, where t is the time interval between the 10% and 90% of the pulse maximum amplitude.

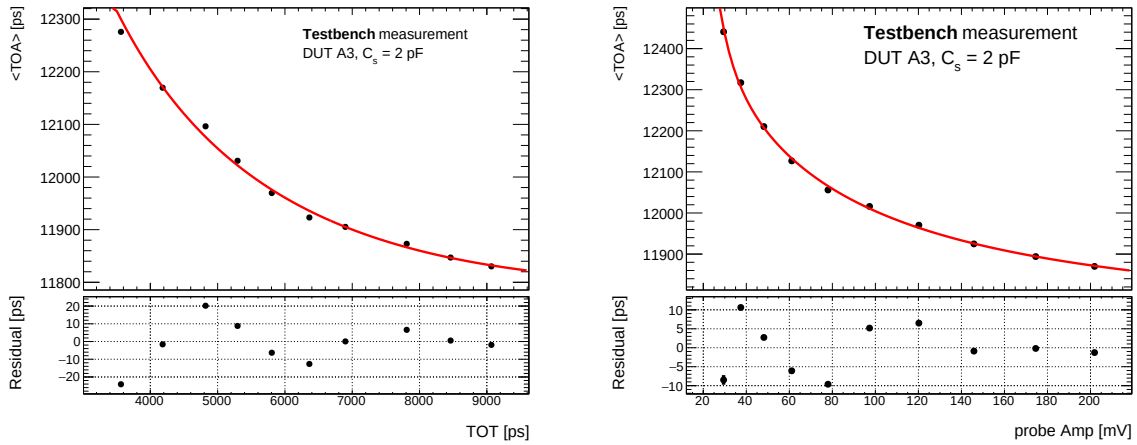

(a) (b)

FIGURE 7.8: Average time of arrival as a function of (a) the average time over threshold and (b) the probe average amplitude for various injected charges for various injected charges. The fit used for the time walk correction is superimposed (red line) in both cases while the bottom plots in both figures show the residual of the average after the time walk correction. A 2 pF soldered capacitance was used to emulate the sensor capacitance. Error bars on both TOA and TOT (or probe amplitude) values are included but are not visible in the upper pad plots, since they amount to less than 1% in all cases.

time walk correction is observed between this measurement and the one of Figure 7.8a, most probably due to measurement fluctuations.

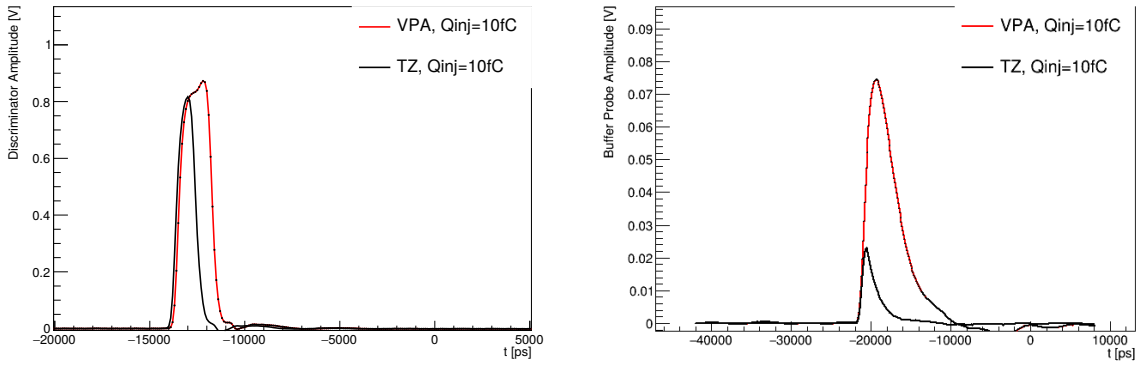

(a) (b)

FIGURE 7.9: Average (a) discriminator and (b) preamplifier probe pulse shape for a VPA or a TZ preamplifier, for Q_{inj} = 10 fC.

The jitter as a function of the injected charge for the two preamplifier types is shown in Figure 7.10b. The same threshold has been used in both sets of measurements. It is clear that the voltage type performs slightly better in terms of jitter in the full charge range. For 10 fC, a 9 ps jitter is observed, compared to 11 ps in the case of the TZ channel. A plateau of 4 ps is reached for high charges in the case of the VPA, contrary to 7 ps for the TZ. Given this result, the voltage preamplifier has been confirmed as the default for the ALTIROC chip and all following studies are performed with VPA channels. Channels with TZ preamplifiers have been implemented in the second prototype of the chip, ALTIROC1, where it has been confirmed that this difference in performance is observed also at the TDC level. Therefore, using a TZ preamplifier has been rejected as an alternative option to the nominal VPA.

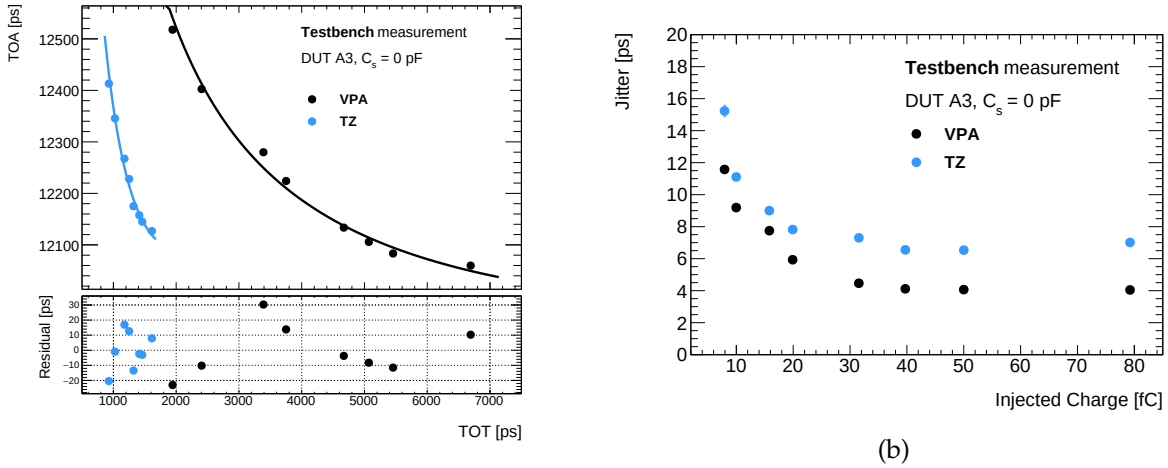

(a) (b)

FIGURE 7.10: (a) Average time of arrival as a function of the average time over threshold for various injected charges, for a channel containing a VPA (in black) or a TZ (in blue) preamplifier. The fit used for the time walk correction is superimposed in both cases while the bottom plot shows the residual of the average after the time walk correction. (b) Jitter as a function of the injected charge for a channel containing a VPA (in black) or a TZ (in blue) preamplifier. Both sets of measurements have been performed without any additional soldered capacitance.

7.2.3 Performance of bare module

The sequence of measurements shown in 7.2.2 have been repeated with the ASIC bump bonded to the sensor, seen as a capacitance C_d. The tested sensors were always operated at a bias voltage of V_{bias} = -90 V. This operating point was chosen to ensure their full depletion. The leakage current of the modules at this bias voltage was measured to be of the order of 10^{-2} µA, a value that has a negligible impact on the overall performance of the devices.

Jitter

The TOA jitter as a function of the injected charge is shown in Figure 7.11 for two configurations; one with the preamplifier probe turned off and the other with the probe activated. The latter configuration allows for a direct comparison to testbeam data, where the probe was continuously active, in order to perform the time walk correction. In both cases, a constant threshold equivalent to 2.5 fC is used. When the probe is not activated, it is found that, for 5 fC, the measured jitter is 25 ps, while for 10 fC it is approximately 13 ps. These results are consistent with the ones presented in section 7.2.2 where the ASIC was without a sensor and with a soldered capacitance of 2 pF. The activation of the probe naturally degrades the performance of the discriminator mainly due to an increase of the preamplifier rise time. The probe contribution to the time resolution σ_{probe}, defined as the quadratic difference of the TOA jitter between having or not the probe active can be extracted from calibration, as seen in the bottom pad of Figure 7.11; this contribution shows a strong dependence on the injected charge. It is dominant at low charge, while it is found to be 8 ps for Q_{inj} = 10 fC and reaches a negligible value of 4 ps for $Q_{inj} > 15$ fC.

Measurements at cold temperature

Within the HGTD, the ASIC is expected to operate down to $-35\,^{\circ}\mathrm{C}$ in order to mitigate the increase of the sensor leakage current with irradiation. For this reason, the performance of ALTIROC0 was studied using a climate chamber, constantly supplied with dry air to avoid

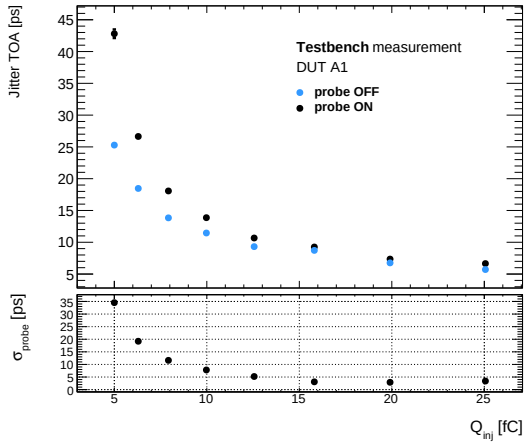

FIGURE 7.11: (a) (up) Discriminator jitter as a function of the injected charge, after subtraction of the generator time resolution. The two sets of measurements correspond to a configuration where the preamplifier probe is either active or inactive. (down) Probe contribution to the time resolution, defined as the quadratic difference of the TOA jitter between having the probe active or inactive. The activation of the preamplifier probe naturally degrades the performance.

condensation. The results are shown in Figure 7.12. The signal amplitude over noise ratio at the output of the preamplifier can be estimated from the probe output. As shown in Figure 7.12b, there is a 7% increase in the A/N ratio between 20 and $-30\,^{\circ}\mathrm{C}$. In parallel, the rise time of the probe, defined as the difference between the time when the pulse is at the 10% and 90% of its maximum amplitude, decreases with the temperature by the same order of magnitude as the increase in A/N. This behaviour of the rise time is not predicted in simulation and could originate from the probe shaper and not the preamplifier itself.

Figure 7.12a, shows the jitter of the discriminator TOA as a function of the injected charge. As expected, the jitter improves when moving to lower temperatures. The effect of the temperature on the jitter arises from the temperature dependence of the noise and of the transistor transconductance g_{m1}, the latter of which is directly proportional to the output amplitude of the preamplifier. Indeed, by combining equations 5.11 and 5.12, it follows that the N/A, and therefore, the jitter, is proportional to the square of the temperature. This effect is more prominent for low values of the injected charge while for values above 10 fC, it becomes less pronounced due to the saturation of the preamplifier. An overall reduction of the jitter of the order of 6% is observed for a Q_{inj} = 10 fC at the lowest temperature point. While this reduction follows the expected trend, it is less pronounced than the combined effect expected from the simultaneous increase (decrease) of the preamplifier signal amplitude over noise (rise time) with temperature for the same injected charge, which is of the order of 14%. Assuming that the rise time dependence on the temperature is arising from the probe shaper and not the preamplifier, the 6% increase is compatible with the noise reduction due to the temperature. Detailed investigations will continue with ALTIROC1 in the future, to ensure that the temperature effects are fully understood.

Time walk correction

For the modules which include an LGAD sensor, a different way to apply the time walk correction was developed. The problem that led to this new approach along with the performance of the modified method of the time walk correction are presented below.

It was observed that the TOT of the discriminator output does not scale proportionally

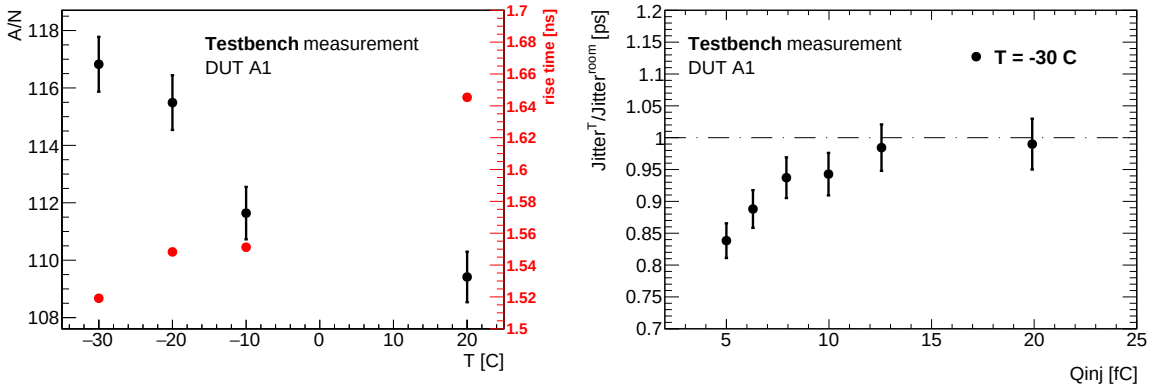

(a) (b)

FIGURE 7.12: (a) Signal over noise ratio (in black) and rise time (in red) as a function of the temperature for an injected charge of 10 fC. (b) Ratio of the TOA jitter at T = $-30\,^{\circ}\mathrm{C}$ to the jitter at room temperature as a function of the injected charge.

with the amplitude of the probe when a sensor is bump bonded to the ASIC. Moreover, re-triggering was seen on the discriminator falling edge, as demonstrated in Figure 7.13. The number of additional triggers was found to be fluctuating, depending on the injected charge and the discriminator threshold, however the re-triggering frequency was found to be constant and around 500 MHz. This suggests that a high-frequency coupling is behind the issue.

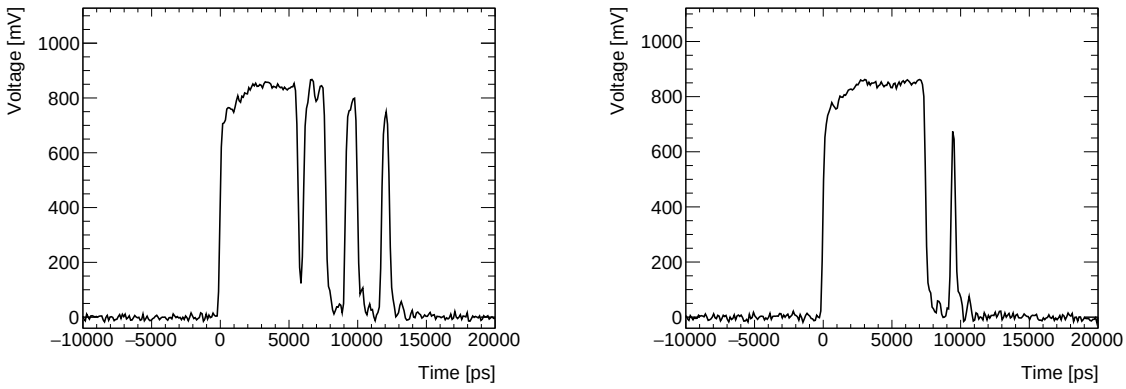

FIGURE 7.13: Example discriminator pulses of DUT A1, where the re-tiggering effect on the discriminator falling edge can be observed.

The retriggering behaviour itself is not as concerning for the time walk correction as the discreteness of the first falling time. Figure 7.14a shows how, when using a calibration pulse with a charge ranging from 5-20 fC, the time of end (TOE) of the pulse (measured at the first discriminator pulse in case of re-triggering) presents a discrete behaviour with respect to the probe amplitude, while the relation should be continuous. Two possible reasons for this problem have been theorised; an inductance caused by the length of the pad-sensor HV connection or a coupling of the direct discriminator output to the PCB.

In order to investigate the former, a new board with a larger L-shaped HV connection pad was manufactured. This particular shape of the HV pad allows for many wire bonds to be attached far from each other in order to reduce any possible inductance. It can be seen in Figure 7.14b, that the issue is still present in the modified board for $Q_{inj} < 10$ fC. However, it is clearly reduced for higher charges. Figure 7.15a shows the distribution of the TOA in the reduced charge range between 12 - 20 fC (corresponding to a probe amplitude 60 - 140 mV)

, before and after applying a time walk correction using the TOT. The time walk correction results in a 40% improvement of the TOA RMS, which is found to be 14 ps after subtracting the generator resolution.

For the second version of the ALTIROC, ALTIROC1, an L-shaped pad has been implemented as the default. Additionally, in this version, there is no direct discriminator output; instead, the pulses are digitized in the TDC.

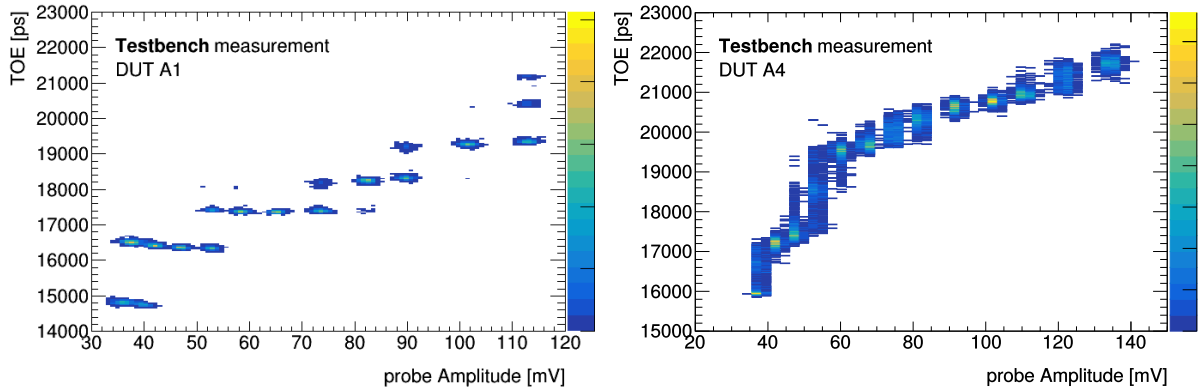

(a) (b)

FIGURE 7.14: TOE as a function of the probe amplitude for various injected charges for (a) standard HV-connection board (b) L-shaped HV pad board. Both boards are equipped with an ASIC bump-bonded to an unirradiated 2x2 sensor array.

Due to the discreteness problem in the falling time mentioned previously, the time-over-threshold of the discriminator was not chosen as the default method for the time walk correction in ALTIROC0 boards with the standard HV pads. Instead, the time walk was corrected using the probe amplitude. As shown in Figure 7.15b, the correction in a charge range of 5 to 20 fC results in a residual with a peak-to-peak variation of 12 ps, compatible with measurements of the ASIC alone and within the requirements of the HGTD. The time walk correction using the amplitude of the probe was used for the testbeam measurements, since only boards with the standard HV pads were available at that time.

7.3 Testbeam results with ALTIROC0

While calibration measurements can provide a detailed account of the ASIC performance in a highly controlled environment, a more realistic estimate of the ASIC+sensor performance is achieved in tests with real particles. For this reason, two ALTIROC0 modules were exposed to 120 GeV charged pions at the H6B beam line at the CERN-SPS North Area during one week in October 2018. This section presents the results collected during this data taking period.

7.3.1 Testbeam setup

A picture of the testbeam setup is shown in Figure 7.16 .The pulses of 2×2 LGAD sensor arrays mounted on up to 2 ALTIROC0 boards were sampled by two Agilent Infiniium DSA91204A oscilloscopes with a 40 GSample/s sampling rate and a bandwidth of 12 GHz. For an accurate timing reference, two fast Cherenkov trigger counters were used. Each one consists of a Cherenkov-light emitting Quartz bar of 3×3 mm^2 area transverse to the beam and 10 mm length along the beam, coupled to a Silicon Photomultiplier (SiPM). The time resolution of these devices was measured to be about 40ps.

A EUDET-type beam telescope [169] based on MIMOSA 16 pixel planes with a track

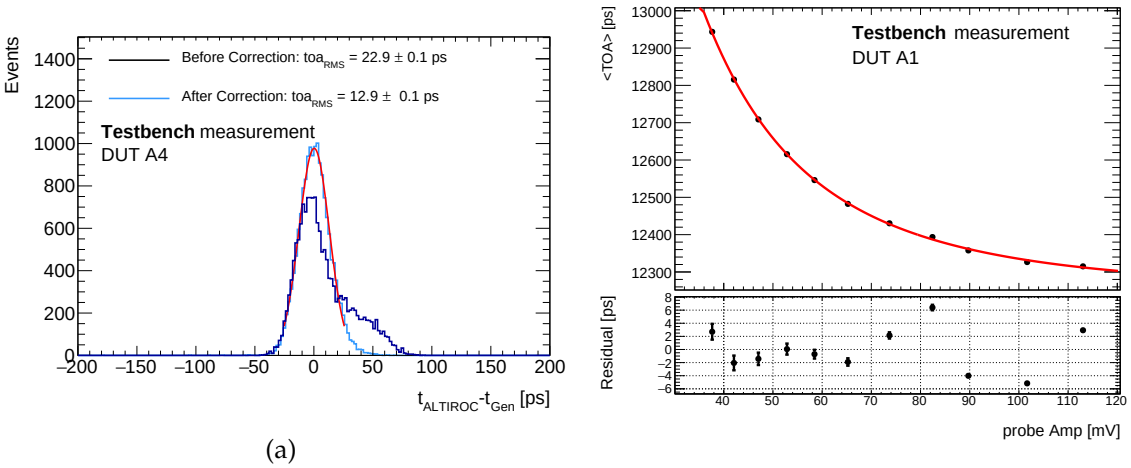

(a) (b)

FIGURE 7.15: (a) TOA distribution for a charge between 12 and 20 fC before and after time walk correction for an L-shaped HV pad board equipped with an ASIC bump-bonded to an unirradiated 2x2 sensor array. The time walk has been corrected using the discriminator TOT. A Gaussian fit (red line) is applied to the corrected distribution. (b) (up) Average time of arrival as a function of the average probe amplitude. The fit used for the time walk correction is superimposed (red line)., Error bars on both TOA and probe amplitude values are included but are not visible in the plots, since they amount to less than 1% in all cases. (down) Residual of the average after the time walk correction. Both measurements were performed on a board with a sensor bump-bonded to the ASIC.

position precision of few micrometers was also included in the data taking, allowing for position-dependent measurements. Each MIMOSA 26 sensor consists of pixels sized $18.4\,\mu\text{m} \times 18.4\,\mu\text{m}$, covering an active area of about 10.6 mm $\times$ 21.1 mm. In total, 6 MIMOSA planes were used to reconstruct tracks, three in the up-stream and three in the down-stream region, with respect to the ALTIROC DUTs. The trigger was provided by the coincidence of signals on a scintillator coupled to a photo multiplier tube (PMT) and a special 3D FE-I4 plane [170]. This plane, consisting of a 3D CNM Silicon sensor connected to the FE-I4 readout chip is a pixel detector with pixel size of 50 and $250\,\mu\text{m}$ in the x (horizontal) and y (vertical) direction, respectively, and using a 25 ns clock. It served two purposes. Firstly, it provided a so-called hitOr trigger that fires when at least one of the pixels selected in a user-defined mask has a hit. Hence, it was used as a region-of-interest (ROI) trigger to only accept tracks traversing the small area of the LGAD sensors. Secondly, with its 25 ns time binning of the hits it has a very short integration time, compared to the telescope planes that integrate hits over $112.5\,\mu\text{s}$ and hence usually provides multiple tracks within this period at the typical SPS particle rates. Therefore, by matching the unique hit of the FE-I4 plane to one of the several tracks provided by the telescope, the track that fired the trigger can be selected. The trigger signals were combined in the Trigger Logic Unit (TLU) , whose output was used by the telescope and connected to the oscilloscopes, to ensure a perfect correspondence between the events recorded by the oscilloscopes and by the telescope. The two data acquisition chains were separate and the information from both systems was combined off-line. The data from the ALTIROC DUTs and the Cherenkov trigger counter was collected by the oscilloscope, while the beam telescope and FE-I4 data was saved in a National Instrument (NI) PXIe crate. The synchronicity of the two data streams was constantly monitored and failed rarely under normal beam conditions.

Custom-made support structures provided mechanical stability of the ALTIROC and SiPM

boards. The ALTIROC DUTs were mounted on a base plate integrated in the EUDET telescope. A separate base plate was used for the positioning of the SiPM devices, while a styrofoam box ensured their light-tightness. Both ALTIROC and SiPM DUTs were operated at room temperature. Remotely controllable stage motors enabled movement in the horizontal and vertical directions perpendicular to the beam direction with micrometer precision of both base plates. This allowed for a precise positioning of the sensors at the centre of the beam and alignment of the DUTs to the SiPMs.

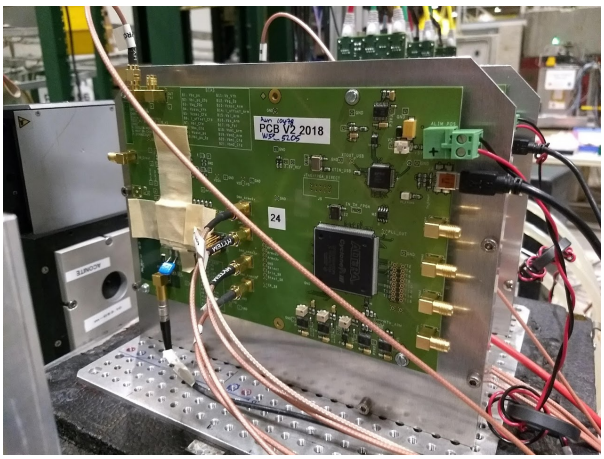

FIGURE 7.16: Picture of the ALTIROC0 DUTs mounted on the movable stage in the center of the telescope at the CERN north-area testbeam facility.

7.3.2 Results

For all the results presented hereafter, both modules were operated at a voltage of V_{bias} = - 120 V, to ensure the depletion of the sensor and a high gain. The leakage current was continuously monitored and was always found to be of the order of 10^{-2} µA for both sensors.

Pulse properties

The probe amplitude distribution of one channel of DUT A1 and A2 is shown in Figure 7.17a for the operating point of V_{bias} = -120 V. It can be seen that the two DUTs behave similarly with A2 showing slightly larger amplitude. The deposited charge in the sensor in testbeam is calculated from the integral of the preamplifier probe pulse. Calibration measurements with the picosecond pulse generator, in which the injected charge is known with a high accuracy, are used to determine the relation of the probe integral to the injected charge. This relation is then used to extract the equivalent deposited charge in the sensor in testbeam. The resulting distributions for a channel of DUT A1 and A2 are shown in Figure 7.17b. Both distributions are fitted with a Landau function convoluted with a Gaussian function, shown as a dashed line of the same colour, in order to extract the most probable value. It was found that, for V_{bias} = -120 V, the most probable deposited charge in testbeam was Q_{dep} = 18 fC for DUT A1 and Q_{dep} = 24 fC for DUT A2.[2]. With calibration signals, a difference in the response of the two ASICs is not observed, therefore it has been traced back to a different gain of the LGAD sensors. While, in both DUTs, the charge is higher than the planned benchmark point for the HGTD, it should be noted that the goal of the measurements presented here was the initial characterization of ALTIROC+LGAD un-irradiated modules. The study of the module performance at the lowest limit of the ALTIROC dynamic range is planned for future campaigns.

[2]These values correspond to a sensor gain of 35 and 47, respectively.

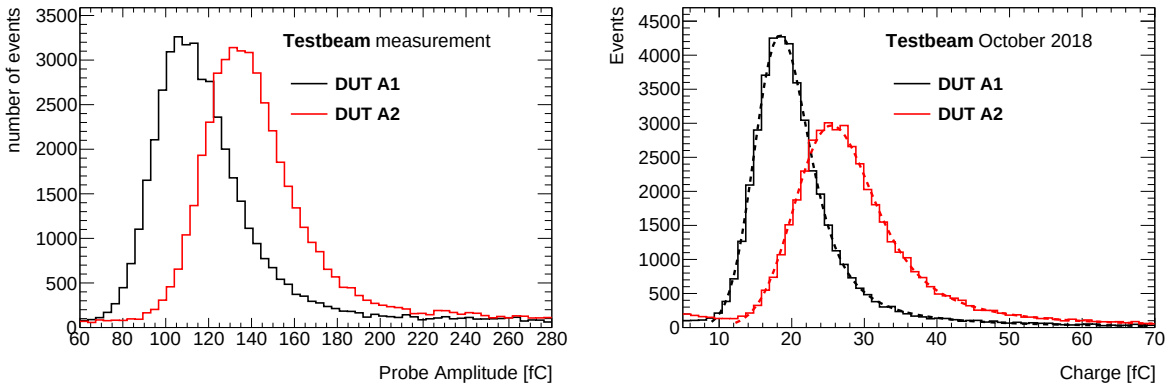

(a) (b)

FIGURE 7.17: Distribution of (a) the amplitude of the probe and (b) the deposited charge for the same ASIC channel of DUT A1 and A2 for a bias voltage of -120 V. A Landau function convoluted with a Gaussian function is fitted in each charge distribution to extract the most probable deposited charge. The functions are displayed as dashed lines of the same colour as the fitted distributions.

Time resolution

The time resolution of the DUT is estimated from the time difference between the time of arrival (TOA) of the DUT and the SIPM. The TOA is defined as the time at half of the maximal amplitude of the considered signal. The DUT resolution is the convolution of the jitter of the electronics, the Landau fluctuations of the sensor and the time walk effect. This last contribution can be corrected - the time walk of the SiPM has been measured to have a negligible effect and will be neglected in the following calculations. Due to the discrete behaviour of the discriminator falling edge that was discussed in section 7.2.3, the amplitude of the probe is used to correct for the time walk effect, as shown in Figure 7.18a. The correction is applied in a reduced range of 200 ps, as for larger charges, the probe was found to saturate. The impact of the probe activation to the jitter is negligible for Q_{inj} = 18 fC, as demonstrated in Figure 7.11.

After correction of the time walk effect, the time difference is also shown in Figure 7.18b where a Gaussian fit is applied. The expected time resolution of the SIPM has been measured in previous testbeam campaigns, using correlated signals with un-irradiated single-pad LGADs mounted on discrete electronics boards, similarly to the method described in 7.6.2. It's contribution was estimated to be 40 ps, and is quadratically subtracted from all following results. The overall time resolution is improved by a factor of 30% thanks to the time walk correction. The time resolution of each channel of the two DUTs after correction is summarised in Table 7.2. It should be noted that the DUT A2 provides systematically a better resolution. This can be explained by the larger most probable charge in A2 as shown in Figure 7.17b. With calibration signals, this difference is not observed therefore it has been traced back to a different gain of the LGAD sensors. The performance is better than 40 ps for all channels of the A2 DUT, with a best achieved time resolution of 34.7 ps after time walk correction.

This value was compared to a calibration run reproducing as close as possible the testbeam conditions; a jitter of 7 ps was found in this case for the testbeam-equivalent injected charge of Q_{inj} = 24 fC. Taking into account the Landau contribution of the sensor, which is known to be around 25 ps for un-irradiated LGADs [171, 172] , as well as the deterioration of the jitter (by a factor of 1.65) due to the longer duration of the LGAD signal compared to the calibration pulse, results in a performance of $\sim$ 27 ps. Finally, adding in quadrature the residual

of the time walk correction, already extracted from Figure 7.15b, results in an expected time resolution of ~ 30 ps, a value that is compatible with the best achieved testbeam performance.

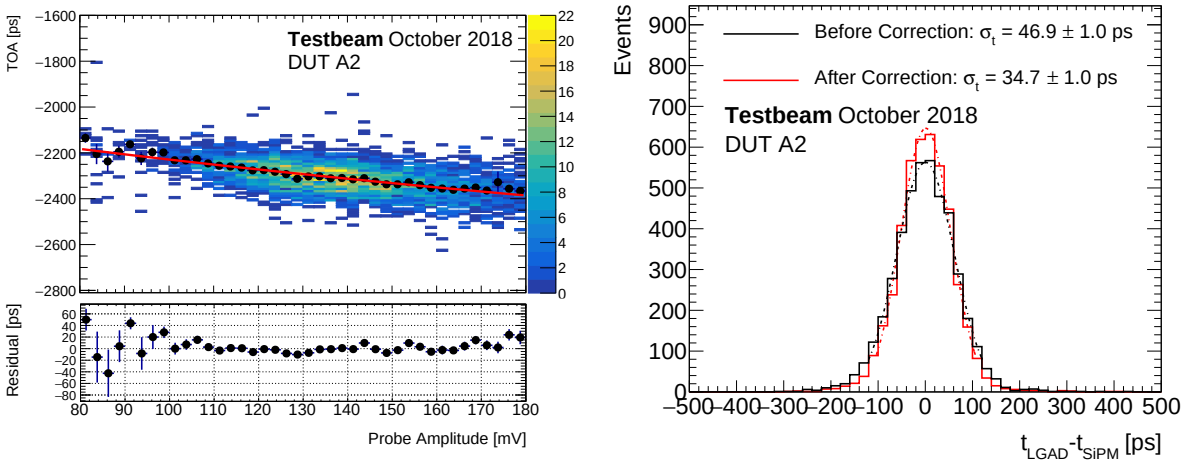

(a) (b)

FIGURE 7.18: (a) Time of arrival difference for a channel of an ALTIROC0-LGAD bare module as a function of the amplitude of the preamplifier probe. The profile of the 2D distribution (black points) and a polynomial fit (red line) are superimposed. The fit is used to correct for the time walk effect. (b) Distribution of the time of arrival difference for a channel ALTIROC0-LGAD bare module before and after time walk correction. A quartz+SiPM is used as a time reference and its contribution is subtracted from the quoted time resolution values.

TABLE 7.2: Time resolution and the statistical error (in ps) for the 4 channels of A1 and A2.

	Ch0	Ch1	Ch2	Ch3
A1	37.9 ± 1.1	40.6 ± 0.9	43.6 ± 1.1	45.6 ± 1.1
A2	36.6 ± 1.1	-	34.7 ± 1.0	38.0 ± 0.9

The time resolution was measured as a function of the discriminator threshold as shown in Figure 7.19a. The threshold was varied in from 153 to 173 mV, corresponding to a Q_{inj} ranging approximately from 2 to 7 fC; a small increase is observed for larger threshold. This behaviour is expected since the shape of the preamlifier output from an LGAD signal exhibits a smaller derivative close to the peak of the pulse. The deterioration of the performance with the threshold is reduced thanks to the time walk correction.

Figure 7.19b presents the time resolution as a function of the most probable deposited charge, Q_{dep}, for a channel of A1. The variation of Q_{dep} is obtained by changing the bias voltage between 60 and 120 V. It can be seen that, by lowering the bias voltage, or equivalently the charge, the jitter contribution increases due to the lower LGAD gain. After time walk correction, the time resolution reaches a plateau of 40 ps after 12 fC, while for lower charges, the performance deteriorates significantly. While this behaviour is sub-optimal for the desirable dynamic range of the final detector, it should be noted that MIP-equivalent (Q_{inj} = 10 fC) charge is reached for very low values of $V_{bias} \sim 60$ V, suggesting a high doping concentration of the sensor. A similar trend has been observed for highly doped single-pad LGAD sensors, as presented in [172], which could be due to the non-saturation of the carrier drift velocity. Studies are currently being performed to optimize the doping concentrations of the sensors.

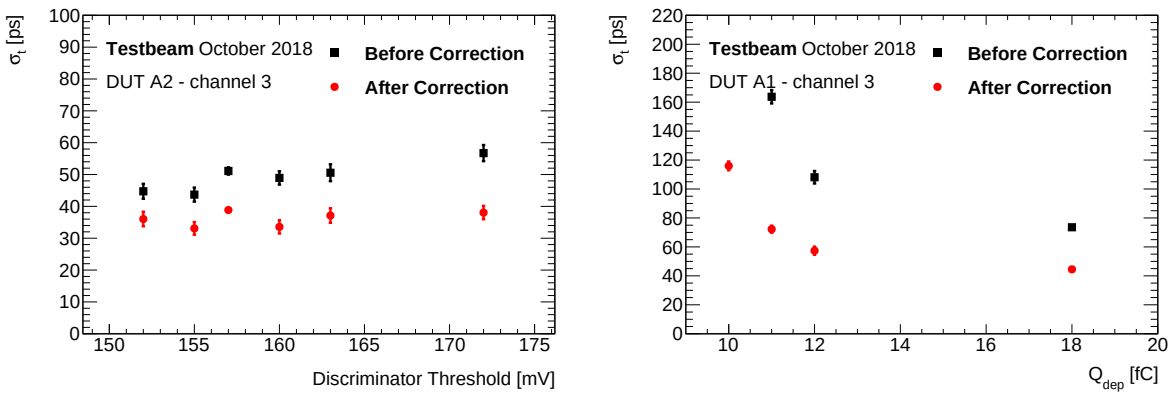

(a) (b)

FIGURE 7.19: Time resolution before and after time walk correction for a channel of an ALTIROC0-LGAD bare module as a function of (a) the discriminator threshold and (b) the most probable value of the deposited charge. A SiPM with a resolution of 40 ps is used as a time reference - it's contribution has been subtracted quadratically. The amplitude of the preamplifier probe is used to correct for the time walk.

Finally, the time resolution after time walk correction was extracted as a function of the position in the pad as shown in Figure 7.20. The bin size was chosen to ensure sufficient statistics for the computation of the time resolution. Within the statistical error, the time resolution is quite uniform.

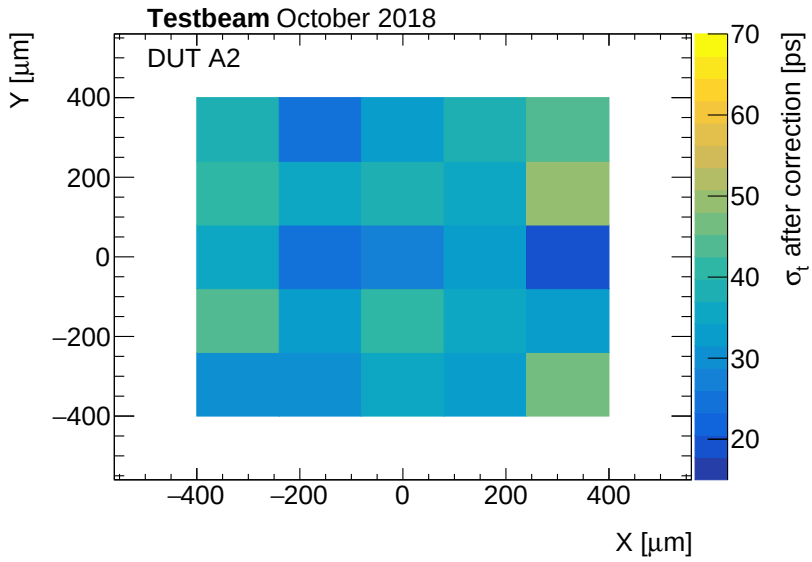

FIGURE 7.20: Time resolution for a channel of a ALTIROC0-LGAD bare module as a function of the position in the pad. The time resolution has been corrected for the time walk effect using the amplitude of the preamplifier probe and the resolution of the SiPM has been subtracted. There is a minimum of 200 events in each bin (of the size of $160\,\mu\text{m} \times 160\,\mu\text{m}$) so that the statistical error is about 4-5 ps.

Efficiency

The efficiency map of the bare module has also been measured. The efficiency is defined as the fraction of tracks that produce a discriminator response (above a given threshold) over the total number of tracks crossing the DUT at the same position. The track is required to have a signal in the SiPM to ensure synchronicity of the telescope and waveform data. The

2D distributions of the efficiency for the 4 channels of the A1 DUT are shown in Figure 7.21. The discriminator threshold applied for this measurement ranges between 1.5 and 3.2 fC for the different channels. Table 7.3 lists the average efficiency and it's statistical error for the 4 channels of A1 and A2. For the computation of the average efficiency, only the central 0.7 $\times$ 0.7 mm^2 bulk of the pad has been used. The bayesian approach with a beta function as a prior has been used for the calculation of the statistical error. All channels have an efficiency larger than 95% , quite similar to the performance of the testbeam measurements of LGAD sensors mounted to readout boards with discrete electronics [172] . Within a given channel, the efficiency is constant within 1% when varying the threshold from 1 to 9 fC.

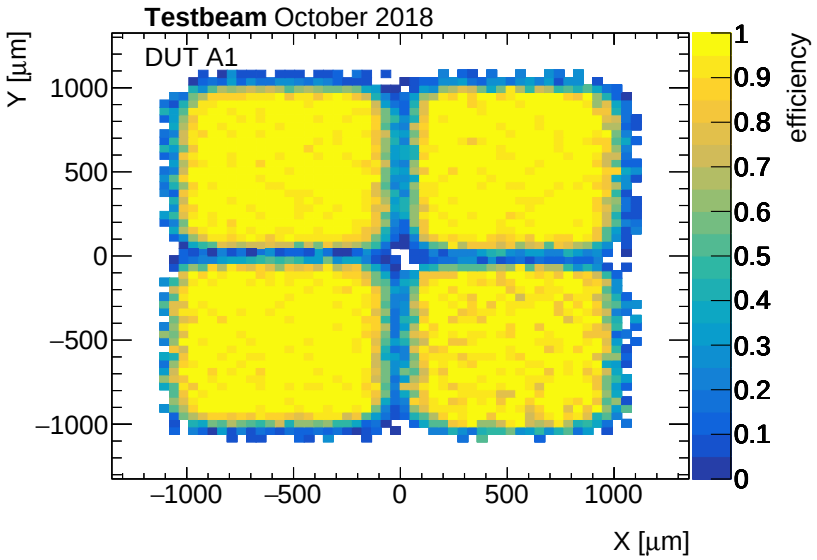

FIGURE 7.21: 2D distribution of the efficiency for the four channels of A1.

TABLE 7.3: Average efficiency (in %) and it's statistical error in the bulk of the pad for the 4 channels of A1 and A2.

	Ch0	Ch1	Ch2	Ch3
A1	97.7 $\pm$ 0.2	95.2 $\pm$ 0.4	97.6 $\pm$ 0.2	97.4 $\pm$ 0.2
A2	97.8 $\pm$ 0.2	-	97.7 $\pm$ 0.2	97.3 $\pm$ 0.2

7.4 ALTIROC1

A second iteration of the prototype, ALTIROC1, has been designed again by Omega in CMOS 130 nm in order to further test the analogue front-end performance. The final parts of the analogue front-end chain, the TDC units and channel buffers, have now been integrated in the single-channel design in addition to the preamplifier and discriminator stages. The chip has also been made larger to approach the final design and now consists of 25 channels organized in 5 columns. Three out of the five columns (15 channels) are equipped with voltage preamplifiers, while for the remaining two, pseudo-transimpedance ones have been used. The latter show similar trends in performance as in ALTIROC0 and will not be further discussed.

Most of the functionalities of the ALTIROC0 prototype (discussed in 7.1) have been retained for ALTIROC1. A 200 pF calibration capacitance is implemented for each channel and

selectable through slow control to allow for test-bench measurements. The internal calibration pulser, 5.5.5, is now integrated in each channel.

In the absence of an LGAD sensor, an additional capacitor can be added to the preamplifier input of the last channel in each column, to mimic the LGAD capacitance. In contrast to the previous version, the capacitor is now integrated inside the ASIC. It is connected to the preamplifier input through a programmable switch and can be modified in a range of 0 to 7 pF with 1 pF step through slow control. Both the input resistor R_2 and the current I_{d2} are tunable through slow control, in order to simultaneously adjust the total input impedance, the drain current I_d and the preamplifier fall time. For R_2 two possible values are available, 15 and 25 kOhm, while I_{d2} can be selected in a range from 15 to 850 µA. A pole capacitance is once again present in the preamplifier circuit, so as to be able to tune the preamplifier rise time.

The custom read-out board of ALTIROC1 is shown in Figure 7.22a. The ASIC is mounted in the dedicated central region of the board. An L-shaped HV pad is next to it, providing space for the HV wire bonds. The motivations for this particular shape have been already discussed in 7.2.3. In order to understand the performance of the ASIC prior to the digitization step, two analogue probes, one for the preamplifier and one for the discriminator output, are integrated. The board also contains various probes of the DC voltages that configure the delay values of the TDC cells.

For this prototype version, a separate board has been designed by SLAC to integrate the FPGA, powering units and a clock generator. The segmentation is motivated by the plan to perform irradiation measurements with the ASIC, in which case one would want to avoid including the FPGA in the high-fluence area. A photo of this board can be seen in the right side of Figure 7.22b. The FPGA is responsible for the transmission of clock and slow control to the ASIC as well as the digital data acquisition. It can also provide a square pulse directly to the ASIC TDC for the TDC calibration. This pulser should not be confused with the internal calibration circuit present in each channel of the ASIC, and is therefore referred to as "external pulser".

The interconnection of the two boards is ensured by a PCIe cable. The system can be operated either in self-trigger mode when the ASIC registers a hit, or as a "slave" by receiving an external trigger. It can also provide a trigger output, allowing for synchronization with other devices.

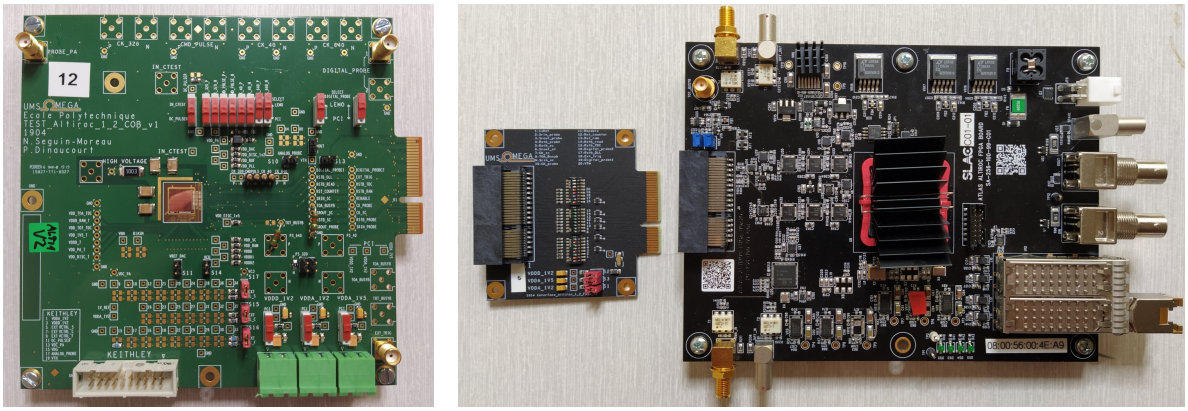

(a) (b)

FIGURE 7.22: Photograph of (a) an ALTIROC1 read-out board (b) an FPGA board (right) and a noise-filtering interface board (left). The ASIC board is connected first to the interface board and through a PCIe cable to the FPGA board.

In order to study and possibly reduce the noise contributions of various powering and digital signals to the ASIC, a small interface board, shown in the left side of Figure 7.22b, has been designed and integrated in the system. Ideally, this board is connected between the ASIC board and the PCIe cable end and allows to switch various signals and add RC filters through footprints on the back side. Two iterations of this noise filtering interface board have been produced; the second one is an improved version allowing for a further reduction of the jitter by 35%. However, as this version was produced in January 2020, it was not available for the measurements of this thesis - the initial version was used instead.

All of the following measurements have been performed with modules consisting of an ALTIROC1 ASIC bump-bonded to a 5×5 un-irradiated LGAD sensor with a pad size of 1.3 mm ×1.3 mm. Contrary to the previous prototype version, HPK sensors have been used, as they were found to perform better in irradiation tests with discrete electronics. The work of this thesis focuses mainly on the HPK 3.1 production, and the corresponding DUT is labelled as B1. An alternative DUT (B2), containing an ALTIROC1 ASIC bump-bonded to an HPK 3.2 sensor was also used in the testbeam campaign, in order to compare the two versions with beam particles. The main difference between the two sensor productions is the depth of the gain layer, which is $2.2\,\mu m$ for HPK 3.2 compared to $1.6\,\mu m$ for HPK 3.1. The deeper gain layer in HPK 3.2 results in a higher doping concentration, which is beneficial for the sensor performance after irradiation, as the acceptor removal is reduced. However, it was found that in un-irradiated HPK 3.2 sensors, the breakdown occurs before the saturation of the carriers' drift velocity is achieved. This is a limiting factor in the sensor timing performance, as will be seen in 7.6, and therefore, test-bench measurements focus on DUT B1 with an HPK 3.1 LGAD. The sensor R&D, particularly on the doping profile of the multiplication layer, is ongoing to reach a compromise between the performance before and after irradiation.

7.5 ALTIROC1 performance in testbench

This section presents, similarly to 7.2, results of the ALTIROC1 prototype performance acquired in testbench. All measurements are performed with DUT B1 (HPK 3.1). The sensor was always operated at V_{bias} = -100 V, in order to ensure the full depletion of the device.

7.5.1 Calibration setup

The calibration signal used for the timing performance studies of ALTIROC1 is provided from the internal pulser of each channel. The dynamic range of the pulser goes from 0 to 250 mV or equivalently from 0 fC up to $\sim$ 50 fC. The calibration of the TDC, described in 7.5.2, is performed by the external pulser, provided by the FPGA.

The FPGA board is connected through an ethernet cable to a PC. A Rogue [173] interface program configures the FPGA and provides functionalities for setting the slow control parameters, receiving and monitoring the digitized data. The preamplifier and discriminator probes, when active, are sampled with a Lecroy oscilloscope of 20 GSamples/s sampling rate and 2.5 GHz bandwidth. The acquisition is self-triggered.

7.5.2 TDC calibration

The accurate knowledge of the Least Significant Bit (LSB) value of the TDC (i.e. its bin size) is fundamental in order to obtain the real values of the TOA and TOT in time units. The LSB value can fluctuate from the design value for different ASICs or different channels and, therefore, a calibration of the TDC is fundamental in the characterization of the complete single-channel performance of ALTIROC1. The calibration procedure is as follows; a square

pulse from the external pulser is sent directly to the TDC input, bypassing the preamplifier and discriminator stages. This pulse can be delayed with 10 ps steps, and the measured TOA (or TOT) as a function of the delay value results in the LSB estimate. Figure 7.23a shows the measured TOA in raw units as a function of the delay value for a channel of DUT B1. A linear fit is applied on the data, the slope of which gives the LSB estimate. The bottom pad of the plot shows the average residual of the fit for each bin. A small differential non-linearity is observed, however it has been estimated that its impact on the TDC resolution is small. The calibration of the coarse TOT line has been performed in a similar manner, while the fine TOT TDC has not been used for any of the measurements, as it will be removed in future versions of the chip.

Figure 7.23b presents the ratio of the TOA and TOT LSB estimate to the average value for all the VPA channels of B1. The average digitization step of the TOA TDC is found to be 19.2 ps, close to the design value of 20 ps. For the TOT TDC (shown in red), the calibration has been performed on the coarse line, resulting in an average value of 164.8 ps, compared to the design value of 160 ps. The TOT calibration of channel 6 could not be performed, as the TOT TDC of the channel was found to be unresponsive. For both TOA and TOT measurements, a good uniformity is observed among different channels, with a standard deviation better than 5%. While these estimates are already fairly close to the nominals, they can be further improved using internal TDC slow control parameters to adjust these LSB values at the channel level. This possibility will be studied in the future.

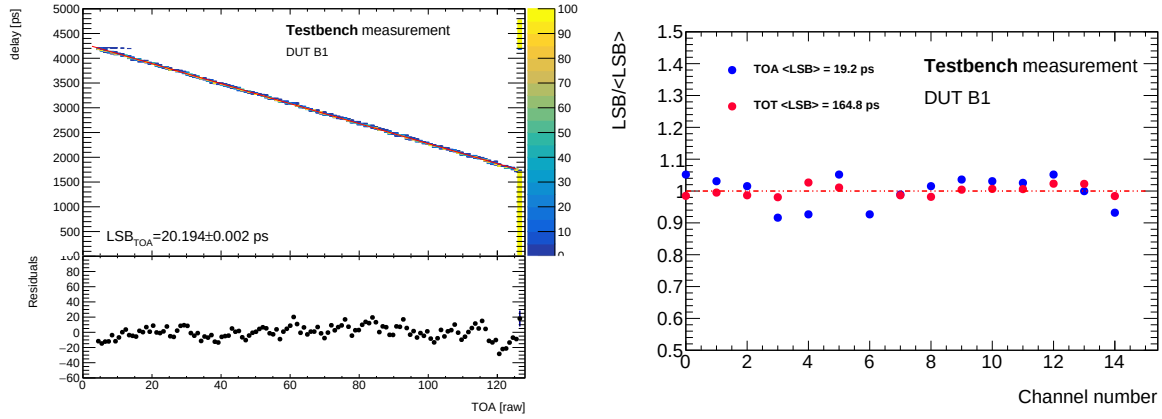

(a) (b)

FIGURE 7.23: (a) Programmable delay, as a function of the average Time Of Arrival raw measurement with the TDC. A linear fit is applied to extract the LSB value. The residual of the fit is displayed in the bottom pad of the figure. (b) Channel TOA and TOT LSB divided by the averaged LSB as function of the channel number for one ASIC. All measurements are performed with the external trigger.

7.5.3 Efficiency and timing performance

As already demonstrated in Figure 7.19a, low discriminator thresholds lead to an optimized timing performance, since the signal derivative of the preamplifier output is smaller close to the peak of the pulse, a behaviour that is predicted by simulation as has been shown in Figure 7.1b. Another reason for moving to lower thresholds is the reduction of the LGAD gain under irradiation. While, for the purposes of this thesis, only un-irradiated sensors were studied, the HGTD will have to operate up to a fluence of $2.5\times10^{15}\mathrm{N_{eq}/cm^2}$. At the highest fluence, the LGAD is expected to provide a charge of 4 fC, which the ASIC should be able to measure.

Figure 7.24a shows the efficiency, defined as the fraction of calibration pulses that give a valid TOA-TDC measurement over the total number of calibration pulses, as a function of the injected charge of the calibration pulse. The scan has been performed for various discriminator thresholds, shown in different colours. The charge-equivalent threshold is defined as the charge value for which the efficiency is 50%. It can be seen that for a threshold lower or equal to $\sim$ 3 fC, the efficiency plateaus to 100% before the target of 4 fC. However, there is a caveat when going to lower thresholds; in the case where the threshold is at the level of the noise, the discriminator will always be triggered. The reader should be reminded that the TOA TDC performs a measurement over a 2.5 ns window; when a pulse exceeds this window, the TDC registers an overflow, or saturated, measurement, which corresponds to its last bin. Therefore, in case the discriminator threshold is below the noise level, the TDC will always be saturated. This effect is illustrated in Figure 7.24b, where the fraction of pulses that cause a saturation is shown as a function of the injected charge. It is evident that the optimum threshold is the minimum one that does not cause a saturation of the TDC in the charge range of interest. A threshold of 3 fC satisfies this requirement for $Q_{inj} \geq 4$ fC, while, lower thresholds display some saturation. With this study, the ability of the ASIC to function properly within the HGTD at the highest expected fluence has been demonstrated.

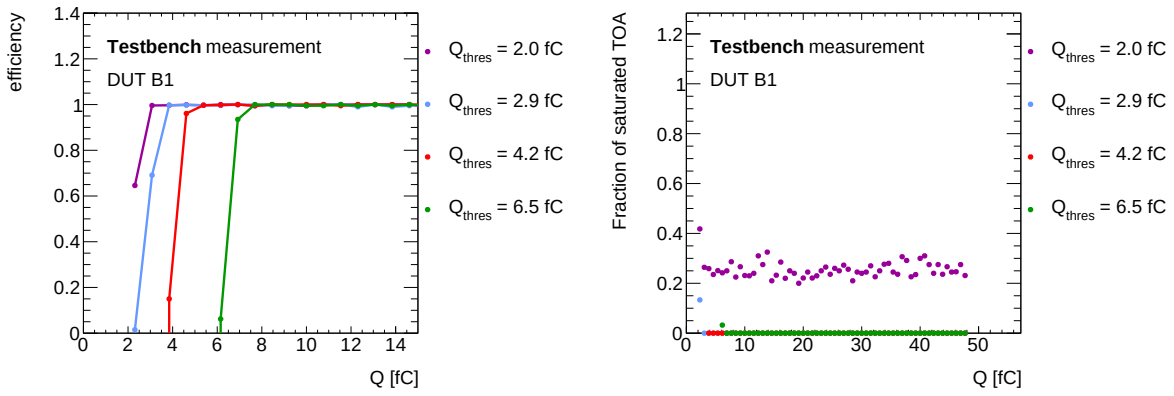

(a) (b)

FIGURE 7.24: (a) Efficiency and (b) fraction of saturated TOA events as a function of the injected charge for various discriminator thresholds. The measurements have been performed for an ASIC bump-bonded to a sensor with the calibration setup. The charge-equivalent threshold is calculated as the charge resulting in a 50% efficiency.

The TOA jitter is shown in Figure 7.25a, as a function of the injected charge for various thresholds. It is calculated as the Gaussian σ of the TDC TOA distribution, taking into account the LSB value. As expected, the performance is improved for lower thresholds, especially for low injected charge. For the optimum threshold of Q_{thres} = 2.9 fC, the jitter is found to be $\sim$ 40 ps for Q_{inj} = 4 fC, while for the nominal value of 10 fC, the performance is improved to 20 ps. A plateau of $\sim$ 15 ps is reached for higher values of the injected charge, which is largely due to the internal pulser resolution.

Figure 7.25b presents the average TOA value as a function of the average TOT, for various discriminator thresholds. The former is extracted from the TOA TDC, while the latter from the coarse line of the TOT TDC. Each point corresponds to a different injected charge, ranging from 4 to 50 fC. A time walk of $\sim$ 600 ps is observed in all the measurement sets. A step-like effect is seen for low threshold at TOT $\sim$ 6 ns, corresponding to a 5 fC injected charge. The same discontinuity is observed for higher thresholds, but displaced to higher charge values. This behaviour is compatible with the discreteness problem observed in ALTIROC0, indicating that the issue persists even after introducing the L-shaped HV board. After intensive

studies, the problem has been traced back to a coupling of the preamplifier falling edge to a digital signal that produces a trigger in case of a hit. This digital signal, called "TOA busy", is dedicated to testbeam, in order to trigger the SiPM time reference acquisition. In future R&D versions, the TOA busy will be outputed in a differential way in order to minimize the coupling, while it is not foreseen for the final version of the chip.

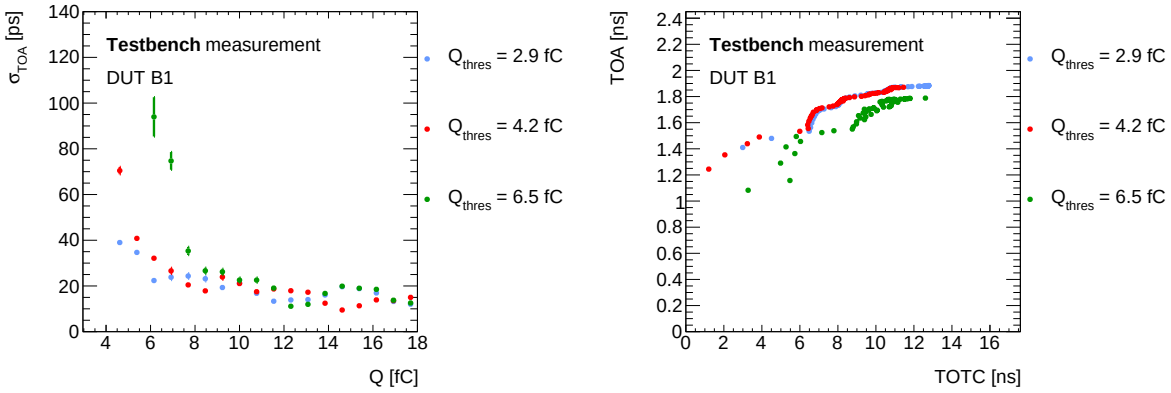

(a) (b)

FIGURE 7.25: (a) Jitter as a function of the injected charge and (b) average TOA as a function of the average coarse TOT for various discriminator thresholds. The measurements have been performed for an ASIC bump-bonded to a sensor with the calibration setup. The charge-equivalent threshold is calculated as the charge resulting in a 50% efficiency.

7.6 Testbeam results with ALTIROC1

Two unirradiated modules consisting of 5×5 LGADs bump-bonded to ALTIROC1 ASICs were exposed to a 5 GeV electron beam at DESY in November 2019. One of the ASICs was mounted to an HPK 3.1 sensor while the second one was bonded to an HPK 3.2. The used setup and obtained results are hereafter discussed.

7.6.1 Setup

Each module is mounted on a dedicated ASIC board and connected to a different FPGA board through a filtering interface board. The two FPGA boards receive a copy of the same 40 MHz clock, generated by a third FPGA, in order to ensure the synchronous operation of the two modules' TDCs. The timing reference is provided by a Cherenkov counter consisting of a 6×6 mm^2 quartz bar coupled to a 5×5 mm^2 SiPM. The digitized data of each module is transmitted through the FPGA to a control PC, while the full waveforms of the SiPM and analogue ASIC probes are sampled by a Lecroy oscilloscope of 20 GSamples/s sampling rate and 2.5 GHz bandwidth. Copies of the clocks of the two modules (in principle identical) are also sampled in order to be able to associate the digital information to the oscilloscope pulses.

One of the modules is always operated in self-trigger mode (master). A copy of the self-trigger is transmitted to the second module (slave) and the oscilloscope. While the digital data acquisition is done continuously, the oscilloscope buffers the data until its memory is full, at which point it needs to pause and transmit. Therefore, a busy logic has been implemented in the FPGA in order to stop the ASIC acquisition while the oscilloscope is being read-out.

The two modules and SiPM are mounted on a EUDET type telescope and operated at room temperature. A setup similar to the one described in 7.3.1, using an FEI4 plane, is used for the alignment of the two sensors to the beam and the SiPM. The alignment of the two DUTs was ensured at the per-channel level. However, due to the increasing complexity of the

synchronization of the different read-out chains and the low priority of position dependent measurements, the telescope was not further used in the main data acquisition. Figure 7.26 displays photos of the testbeam setup dedicated to ALTIROC1 measurements at DESY.

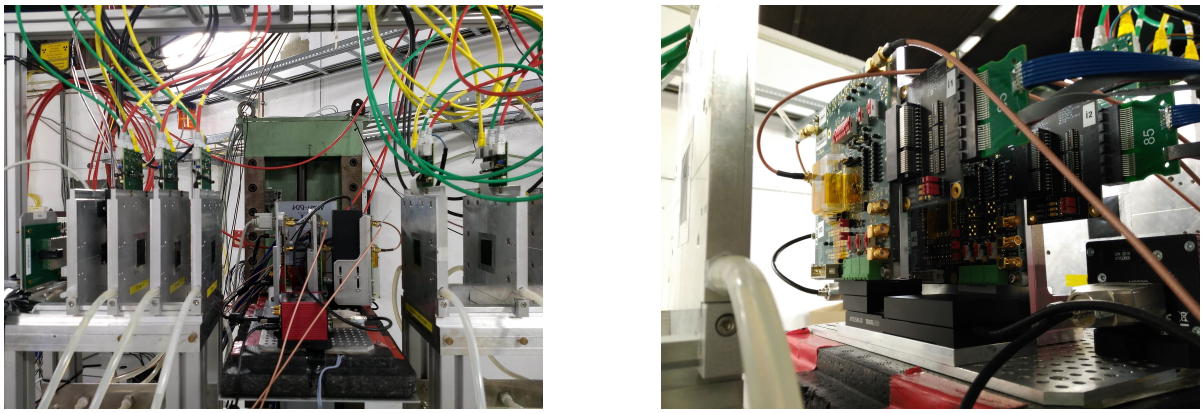

(a) (b)

FIGURE 7.26: Picture of (a) the ALTIROC1 DUTs mounted on the EUDET telescope at the DESY testbeam facility. (b) Close-up of the ALTIROC1 DUTs on the movable stage.

7.6.2 Results

Results from the November 2019 beam exposure of the two ALTIROC modules are presented below. The measurements were heavily focused on DUT B1, as it was found to be performing better in terms of timing resolution. The reason behind this discrepancy is further discussed hereafter.

Both devices were operated close to breakdown, at -230 V for B1 and -100 V for B2, to obtain the maximum gain. The leakage current was found to be around a few µA for B2 and below $0.1\,\mu A$ for B1. In general, a higher leakage current is expected with respect to ALTIROC0, as the current scales with the sensor size. The measured values are relatively small and the leakage current contribution to the time resolution is considered negligible in the following results. For most of the data-taking, only one channel was activated per DUT. This was done in order to avoid the increase of the jitter when multiple channels are active, an issue that is still under investigation.

Pulse properties

Figure 7.27a shows the average pulse of the preamplifier probe for one channel of DUT B1. The deformation of the fall time is due to a coupling of the preamplifier probe and the discriminator, which is activated during the measurement, but will not be present in the operation of the HGTD. The average most probable value (MPV) of the amplitude of all VPA channels of this DUT is 137 mV, corresponding to a charge of approximately 24 fC. The dispersion of the amplitude among different channels is found to be ~ 11 mV.

The noise was estimated from the preamplifier probe output in 40 ns intervals. The RMS noise distribution for two channels in different columns of DUT B1 is presented in Figure 7.27b. It is found to be around 1.7 mV, a value that is 10% higher than testbench measurements. Another confirmation that the noise in testbeam is larger compared to laboratory conditions is the fact that it was not possible to use the optimized thresholds, estimated from the method described in 7.5.3. For the next test beams campaigns, detailed investigations of the noise are planned to understand and mitigate this effect.

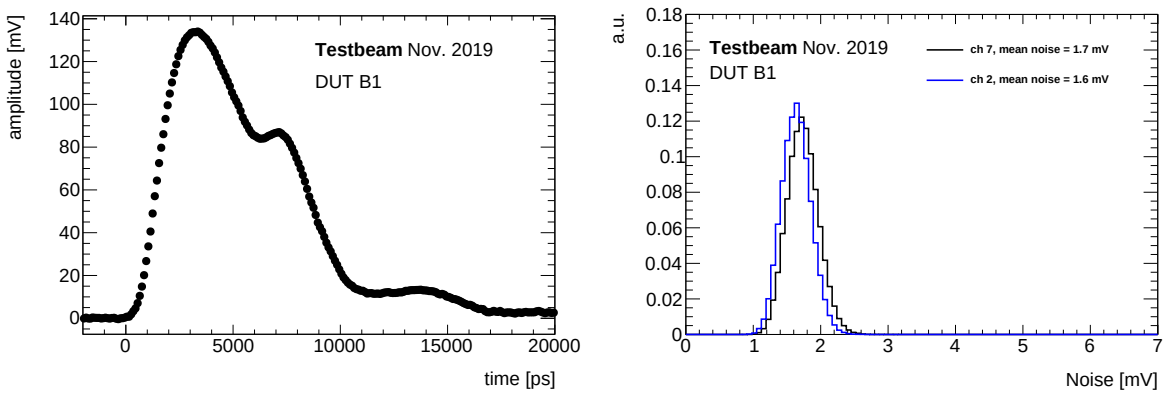

(a) (b)

FIGURE 7.27: (a) Average pulse of the preamplifier probe for a channel of DUT B1. The most probable value of this DUT is 137 mV (subject to channel variations) corresponding to $Q_{inj} \sim$ 20 fC. (b) Noise for 2 different channels of DUT B1.

TDC output

The distribution of the raw TOA values can be seen in Figure 7.28a for a channel of DUT B1. As a reminder, the TOA in time units can be obtained from the raw values multiplied by the TDC LSB. As expected, the raw values populate the entirety of the TDC range (127 bits - 2.5 ns). Some structures are observed and are due to a design flaw that makes the last TDC cell larger.[3] Since the TDC employs a cyclic structure with 4 cycles, this effect is seen 4 times at the values 32, 64, 96 and 128. Fluctuations originating from cell-by-cell delay variations can also affect the uniformity of the TDC. Within a TDC cycle, there are cases where large fluctuations are observed, suggesting non-uniform contributions to the TDC time. This effect could either be due to a design flaw of the TDC itself, or a time structure of the beam particles. The exact reason behind this behaviour is still under investigation.

The equivalent result for the coarse TOT is shown in Figure 7.28b. The range of this TDC in raw values is again 127 bits, but taking into account the much larger LSB size of 160 ps, brings the range to 20 ns. The deposited charge from beam particles follows a Landau and a similar trend would be expected from the TOT. However, a hole is observed in the middle of the distribution. TOT values lower than the hole are distributed in a reasonable way, however, after the gap, they appear to be highly degenerate and therefore cannot provide useful information on the signal amplitude. This characteristic shape is seen in all channels and for various thresholds, making the time walk correction with the TOT extremely challenging. Its origin is already discussed in 7.5.3.

The synchronicity of the data taking can be checked by the correlation of the TOA values between the DUTs, since a particle crosses both of them. The correlation of the LSB-weighted TOA between two aligned channels of B1 and B2 is shown in Figure 7.29a, where it can be seen that the two devices show a good correlation. The TOA values corresponding to the design flaws previously mentioned have been masked. In order to compare the absolute TOA value of the TDC to the SiPM time, a copy of the 40 MHz clock on which the TDC operates was sampled by the oscilloscope. The arrival time of the SiPM pulse t_{SiPM} in the TDC time frame is therefore given by the difference of the oscilloscope t^{osc}_{SiPM} and the leading edge of the clock. In the oscilloscope frame, the time of the SiPM is measured with a CFD algorithm using a 20% fraction parameter. The correlation between the TDC TOA of B1 and t_{SiPM} is shown in Figure

[3] This flaw has been corrected in the design of future versions of the chip.

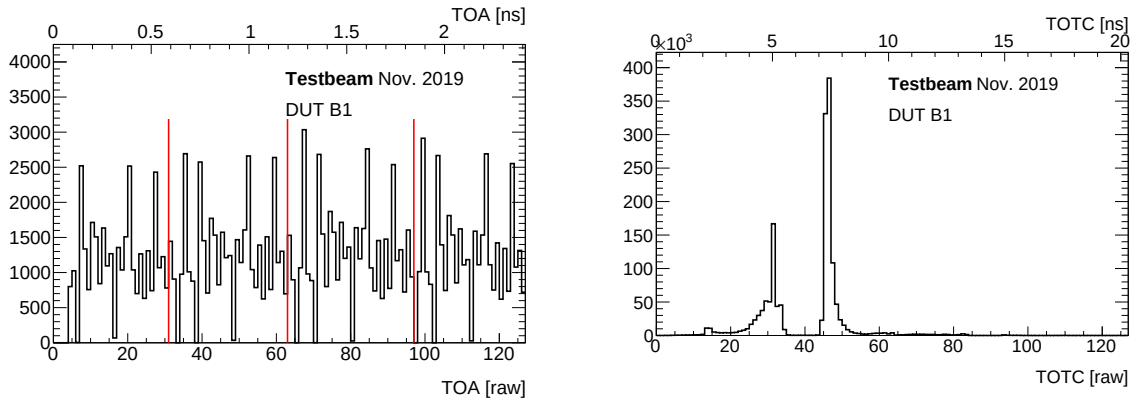

(a) (b)

FIGURE 7.28: (a) Values of the (a) TOA and (b) coarse TOT TDC in raw or time units. In Figure (a) the red lines correspond to the bins 32, 64 and 96, where the TDC structure is repeated.

7.29b. The synchronicity of the two devices is verified, and moreover, a better correlation is observed than when comparing B1 and B2. This is due to both the worse time resolution of B2, which will be further discussed in the following, and because of combined time walk effects of B1 and B2; for the SiPM, as was the case in ALTIROC0, the time walk is very small.

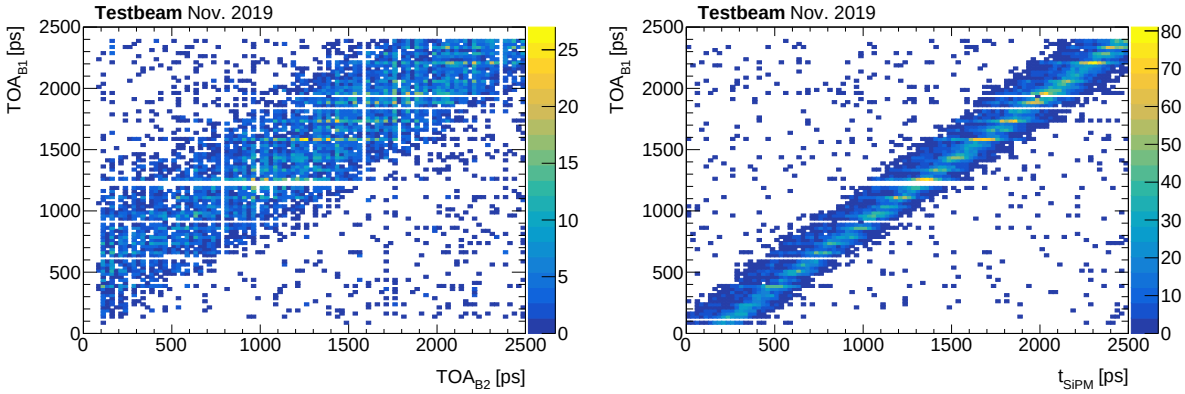

(a) (b)

FIGURE 7.29: (a) Correlation of the absolute TDC TOA (in ps) of B1 versus (a) the TDC TOA of B2 and (b) the SiPM time. In (a), the same channel has been used in both DUTs, after ensuring a channel-per-channel alignment. Certain TDC values have been masked to account for a known problem in the design. The arrival time of the SiPM pulse is measured with a CFD algorithm with a 20% fraction parameter. A copy of the 40 MHz clock on which the TDC runs is sampled by the oscilloscope, in order to relate the absolute TDC time to the oscilloscope time frame. The t_{SiPM} is then given by the time difference of the oscilloscope SiPM time and the leading edge of the clock.

Time resolution

As a first step, the time resolution of the new SiPM time reference needs to be established, since this was the first testbeam campaign in which it was used. To this end, special runs with the SiPM, the preamplifier probe of a DUT B1 channel and a single-pad unirradiated CNM LGAD (LGA35) with discrete electronics were taken. All three devices were aligned to each other and to the beam, in order to record coincidence events.

Figure 7.30 shows the time difference for the three possible combinations between the three

devices. For each DUT, the time is calculated with a CFD algorithm, using a 20% threshold. Only events that produce a signal above the noise in both DUTs of the combination are kept. This is done in order to ensure that the same particle has induced a correlated signal in the two devices. In each distribution, the Gaussian σ can be viewed as the quadratic sum of the resolution of the two DUTs. The three sets of possible DUT pairings yield three equations with the three DUT resolutions as unknowns; solving them gives a time resolution for the SiPM device of 28.9 $\pm$ 1.7 ps.

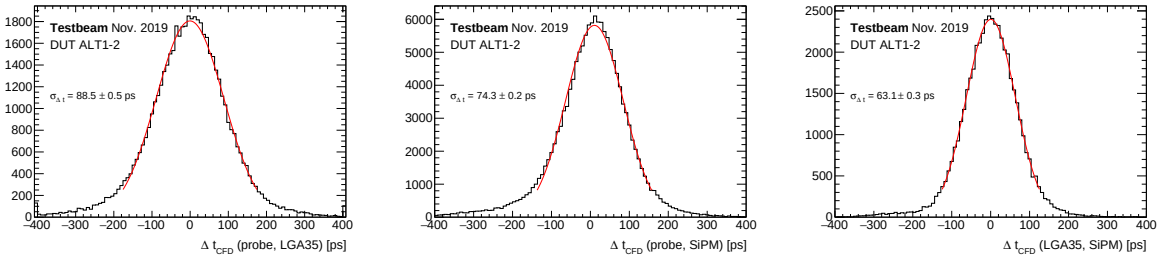

(a) (b) (c)

FIGURE 7.30: Distribution of the time difference between (a) the probe of DUT B1 and LGA35, (b) the probe of DUT B1 and the SiPM and (c) LGA35 and the SiPM. The time is computed with the CFD method, using a 20% fraction value. Only events that produce a signal above the noise in both DUTs are considered.

After the time resolution of the reference has been estimated, the time performance of the ALTIROC DUTs can be evaluated from the difference between the SiPM time (in the TDC time frame) and the TDC TOA, weighted by the channel LSB. The resulting distributions can be shown in Figure 7.31 for B1 (HPK 3.1) and B2 (HPK 3.2), before applying a time walk correction. The inclusive time resolution can be extracted by a Gaussian fit and is found to be 92.1 $\pm$ 0.4 ps for B1, while a significantly worse performance of 364.5 $\pm$ 2.6 ps is obtained for B2. This behaviour can be explained from the different sensors mounted on the different devices. Previous tests on HPK LGAD sensors have shown a consistently better performance of the HPK 3.1 version in comparison to the 3.2 before irradiation, due to the more moderate doping profile of the former. The situation is inverted with increasing irradiation, since the higher doping concentration of the HPK 3.2 sensors ensures that there is sufficient active dopants in the amplification layer to create some gain.

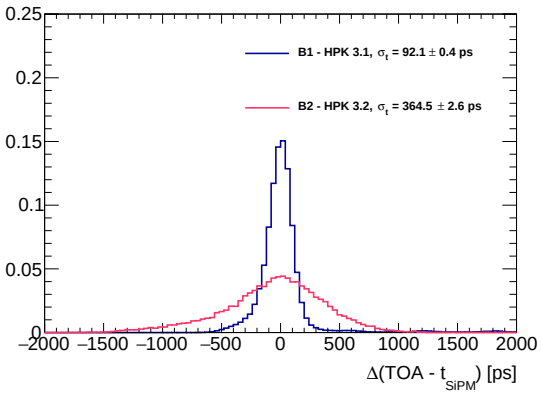

FIGURE 7.31: Distribution of the time of arrival difference between the TDC and the SiPM reference. The distribution is shown for a channel of DUT B1 (blue) and DUT B2 (pink). The inclusive time resolution (before time walk correction), extracted via a Gaussian fit, is quoted after subtracting quadratically the contribution of the reference.

The time difference between the TOA of one channel of B1 and the Quartz+SiPM system is presented in Figure 7.32a as a function of the TOT. Given the problematic "hole" behaviour of the TOT, a reduced range between 4 ns and 7 ns is displayed. In this range, a time walk of $\sim$ 200 ps is observed that can be corrected by the polynomial fit represented by the red line. The time difference distribution before and after time walk correction in the reduced TOT range shown in Figure 7.32b. The measured time resolution improves from 63.1 $\pm$ 1.6 ps to 52.2 $\pm$ 1.4 ps. Subtracting the Landau contribution (about 25 ps) results in a remaining resolution of 46 ps, consisting of the jitter, TDC and clock contributions. Assuming that the jitter is the dominant component suggests that a large improvement can be obtained with the new interface board version (35% reduction of jitter) in future campaigns.

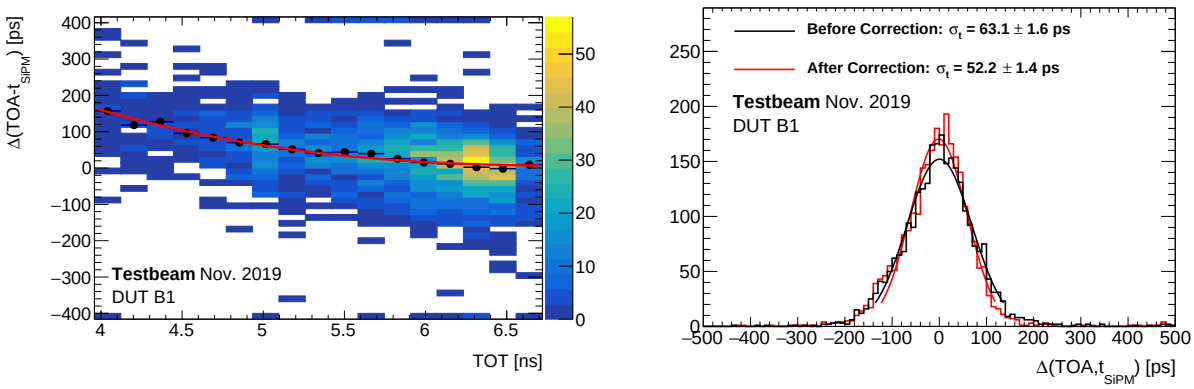

(a) (b)

FIGURE 7.32: (a) Distribution of the time difference between the LGAD+ALTIROC and the Quartz+SiPM systems as a function of the TOT. The dots correspond to the mean value of the TOA distribution for a given TOT bin extracted from a Gaussian. The red line is a polynomial fit of the average TOA as a function of the TOT. Distributions of the time difference between LGAD+ALTIROC and the Quartz+SiPM system before (red) and after (black) time walk correction together with Gaussian fits. The numbers are the fitted Gaussian widths where the time resolution of the Quartz+SiPM system has been subtracted quadratically.

For most channels of DUT B1, the time walk correction with the TOT measurement was not possible due to an extremely small range of usable TOT values. Instead, a time walk correction with the preamplifier probe was deployed, as in 7.3.2. A larger time walk of $\sim$ 400 ps was corrected with this method, resulting in a similar time resolution after correction of 53.15 $\pm$ 0.7 ps.

The performance of B1 was also studied for a lower gain, accomplished by reducing the bias voltage from 230 V to 200 V. Figure 7.33 shows the distribution of the time difference between one channel of the DUT and the SiPM time reference; the default voltage point, corresponding to an MPV charge value of 24 fC is demonstrated in blue, while the lower point, equivalent to 15 fC is shown in pink. The Q_{dep} values have been extracted by comparing the amplitude of the preamplifier probe to calibration measurements. The time resolution (before time walk correction) is quoted on the plot legend and is found to be 92.1 $\pm$ 0.4 ps for the high charge and 133.7 $\pm$ 0.8 ps for the low charge, i.e. 1.5 factor worse. For charges above 10 fC, a plateau is reached on the jitter for testbench measurements. This deterioration of the performance in testbeam could either indicate that the jitter in testbeam is higher than in testbench, or that there is an additional contribution to the time resolution that strongly depends on the charge. While the reason behind the strong dependence of the time resolution on the deposited charge is still not fully understood, a similar effect has also been observed in testbeam measurements for ALTIROC0, as shown in Figure 7.19b. The high doping profile of the

sensor could again be a possible explanation, as it leads to the carriers having a non-saturated drift velocity.

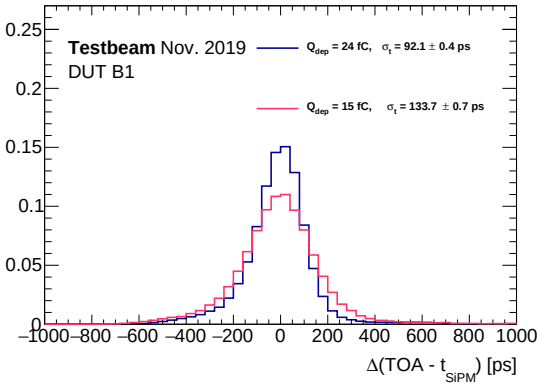

FIGURE 7.33: Distribution of the time of arrival difference between the TDC and the SiPM reference for a most probable value of Q_{dep} equal to 24 fC (blue) and 15 fC (pink). The inclusive time resolution (before time walk correction), extracted via a Gaussian fit, is quoted after subtracting quadratically the contribution of the reference. The most probable deposited charge is calculated from the preamplifier probe amplitude in comparison to calibration measurements.

7.7 Conclusions and prospects

An analogue front-end electronics prototype for picosecond precision time measurements with LGAD sensors has been designed to meet the challenging requirements of the HGTD. Two versions of the prototype, ALTIROC0 and ALTIROC1, have been extensively characterized with calibration signals and beam test particles during this thesis.

In calibration measurements with ALTIROC0, the various contributions to the time resolution, as well as the behaviour of the ASIC under different conditions, were studied. The jitter contribution to the time resolution, either with just the ASIC or with a module consisting of the ASIC and an LGAD sensor, was found to be better than 20 ps for a charge larger than 5 fC. A 6% improvement of the ASIC jitter for Q_{inj} = 10fC was achieved during measurements at T= $-30\,^{\circ}\mathrm{C}$, which will be around the default operating temperature for the HGTD. In tests with modules consisting of the ASIC bump-bonded to the sensor, the Time Over Threshold measurement was found to be discrete, which prevented the use of this variable for the time walk correction. The probe amplitude was used instead, while modified boards with an L-shaped HV pad were fabricated to investigate the origin of the problem. In all cases, the time walk could be corrected up to the required 10% level. Testbeam measurements with a pion beam at CERN were also undertaken to evaluate the performance of the ALTIROC0 module with LGAD pulses. The tested modules were operated at a bias voltage of -120 V, resulting in a most probable charge of $\sim$ 20 fC and a leakage current of O(10^{-2}) µA. A time resolution better than 40 ps was obtained for all channels after time walk correction, while the best-achieved performance was 34.7 $\pm$ 1 ps. This value was found to be compatible with the quadratic sum of the estimated jitter, residual of the time-walk correction and sensor contributions to the time resolution. The time resolution was distributed uniformly in the bulk of the sensor pads and the efficiency was found to be above 95% for all tested channels.

The next iteration of the ASIC, ALTIROC1, introduced the remaining parts of the analogue front-end readout, namely the TDC and single-channel memory blocks. It also integrated 25 channels, moving closer to the final pixel matrix size. As a first step, the calibration of the TDC was performed in order to estimate the Least Significant Bit value of each channel. The

average value was found to be 19.2 ps, close to the design value of 20 ps, while a good uniformity between channels was observed. In laboratory, the minimum achieved threshold was found to be 3 fC, with the efficiency plateau being reached before 4 fC. This proves the feasibility of a timing measurement at the highest irradiation point within the HGTD lifetime. Timing performance studies were repeated similarly to ALTIROC0. The jitter was found to be around 40 ps for 4 fC and rapidly decreasing to less than 20 ps for a $Q_{inj} \geq 10$ fC. A slight increase of the jitter is seen compared to ALTIROC0, which could be due to the TDC and clock contribution and the worse accuracy of the reference pulse provided by the internal pulser. In ALTIROC1, the L-shaped HV pad was the default option, however the discrete behaviour of the discriminator falling time was not fully mitigated. Testbeam results at DESY with 5 GeV electrons were also performed to evaluate the module performance with real particles. It was observed that the noise levels were higher in testbeam than in laboratory, leading to higher thresholds being used. The best-achieved timing performance was found to be 52.2 ± 1.4 ps after time walk correction with the TOT in a reduced charge range where the TOT is continuous. Assuming a Landau contribution of 25 ps, the remaining contribution is estimated to be around 46 ps. This component arises from the combined effect of the jitter, the TDC and the clock. A similar performance was obtained with the preamplifier probe.

One reason for the non-optimal performance of ALTIROC1 in test beam is due to larger noise coming from the FPGA board connected to the ASIC read-out board. An improved version of the interface board has been designed to reduce this noise and was made available in January 2020 (3 months after the testbeam and test bench measurements previously presented) to further reduce the noise. Thanks to the new interface board, the jitter was reduced by 35% compared to the old version in test bench conditions. If the same improvement factor is applied to the test beam results, the performance would reach about 30 ps instead of 46 ps. Testbeam campaigns are planned in the end of 2020 to confirm this prediction. Moreover, it was noticed that the noise was larger in test beam compared to test bench conditions since it was not possible to use the same thresholds. For the next test beams campaigns, detailed investigations of the noise are planned to mitigate this effect.

The non-continuous evolution of the TOT with the injected charge has been a long standing issue in the first two versions of the ALTIROC chip. A significant effort was put in this thesis to understand and mitigate this problem. While the discriminator behaviour improved with the introduction of an L-shaped HV pad that reduces inductance-induced couplings, with ALTIROC1 it became clear that an additional source of coupling was still present between the preamplifier and the discriminator stages. After detailed searches, the culprit was discovered to be a digital signal that provides a trigger for testbeam DAQ purposes. In particular, the coupling was caused by outputing this signal in a non-differential way. In ALTIROC0, while this trigger is not present, a similar effect is caused by the direct discriminator output, which is also non-differential.

An updated version of ALTIROC1 has been designed and submitted for fabrication in April 2020, in order to confirm the aforementioned theory. In this version, the trigger signal output is differential. Additionally, a design flaw which affects the last delay cell of the TDC will be corrected in the updated circuit. The new chips are expected to be delivered as this thesis is being finalized and will be extensively tested in the end of summer - autumn by the HGTD collaboration.

Finally, a single-channel version of the final front-end electronics, ALTIROC2, has been submitted and is expected to be received at approximately the same time. This prototype will integrate the complete common digital part along with existing single-channel analogue

and digital elements. Among some of the key measurements of this chip will be the characterization of the luminosity block performance, the validation of the hit storage and trigger-matching sequences as well as the data transfer through flex cables. Provided a good performance of the single-channel version, a complete chip with 225 channels will be submitted for production towards the end of 2020. This chip should demonstrate that the addition of a large amount of channels does not deteriorate the ability to provide accurate timing measurements and does not induce additional digital couplings.

8. Conclusions

The Run 2 of LHC was a major milestone in particle physics. The outstanding performance of the accelerator allowed the center of mass energy to be increased from 8 to 13 TeV, while the luminosity also augmented, allowing the experiments to collect a large amount of high quality data. Highlights of Run 2 achievements was the measurements of the Higgs boson properties, in particular its decays to new final states, the first observation of light-by-light scattering, as well as a plethora of searches for new physics. After a 3-year shutdown period, between 2019 and 2021, the LHC will be in operation again for the Run 3, where an even higher luminosity will be achieved, allowing the physicists to reach new limits of precision. The future of the accelerator and its experiments will be a high-luminosity phase, the HL-LHC, where novel technologies will allow for the luminosity to be pushed to even higher values, in the hope of discovering hints of physics Beyond the Standard Model, and ensuring the accurate measurement of SM parameters.

This thesis describes my work on these two crucial timelines of the LHC. Focusing on the present, I was heavily involved in the search of supersymmetry, expressed through the strong super-partners of quarks and gluons, the squarks and gluinos, utilizing the complete Run-2 dataset of the ATLAS experiment. The search was focused on final states with at least two highly energetic jets, no leptons and high missing transverse energy from the escape of the LSP. The collected luminosity of $139 fb^{-1}$, roughly four times more than in previous similar searches, allowed the enhancement of the search sensitivity, but also the deployment of more intricate analysis techniques. One such technique that I worked extensively on is the multi-bin fit, designed by statistically combining orthogonal regions created by segmenting the kinematic phase space in powerful discriminating variables. In this way, the signal over background separation is improved by taking into account the relative shape of the two components. As part of my work, I optimized the binning strategy and background normalization process for four separate multi-bin fits targeting different decay topologies of the hypothesized SUSY particles. The gain from using such a configuration, compared to the more traditional cut&count approach, was evaluated to be $\sim$ 40-70% in terms of expected upper limit on the excluded cross-section and 50-100 GeV in terms of the excluded masses of squarks and gluinos. Additionally, I participated in the evaluation of theory uncertainties related to the Top background and experimental uncertainties arising from the Jet Energy Scale, Jet Energy Resolution and resolution of the Missing Transverse Energy. Finally, I worked on the statistical treatment of the analysis, which can be broken down in three major steps. As a first step, I validated thoroughly the background estimation procedure in the so called background-only fit. After gaining confidence in the background normalization and extrapolation process, ensuring that no significant biases are observed, I moved on to the model-dependent interpretation, where the absence of inconsistencies with the SM prediction was confirmed and upper limits on generic BSM processes were derived. Finally, I performed the interpretation of the results in simplified supersymmetric models involving squarks and/or gluinos, along with a neutralino LSP. For a massless neutralino, the masses of 8-fold degenerate squarks and gluinos were excluded up to 1.85 TeV and 2.35 TeV, respectively, a result that significantly extends over previous rounds of the analysis. While this search is the legacy of the Run-2 searches for squarks and gluinos in fully hadronic final states with missing transverse energy, this is not the end of the story. The exclusion strength of the analysis makes it a particularly attractive candidate for re-interpretation campaigns, such as the scan of the 19-parameter pMSSM space or exotic models, such as leptoquarks. In the future, the higher luminosity and potentially energy acquired in Run 3 and the HL-LHC will allow to probe even higher squark and gluino

masses.

Shifting towards the future, I participated in the development of the High Granularity Timing Detector, a novel ATLAS upgrade project that exploits high precision timing and high granularity to aid in the mitigation of pile-up and the precise measurement of the luminosity. This upgrade will be a Si-based detector, utilizing the LGAD technology to achieve a resolution better than 50 ps per track. It will be installed before the HL-LHC startup in the forward region of ATLAS, enabling physicists to improve the object performance and enhance the sensitivity in various physics analyses. The CMS experiment is envisioning to also install a timing detector for the HL-LHC, consisting of an LGAD-based layer in the forward region and a crystal tile layer in the barrel. As more future experiments are opting to incorporate precise timing into their instruments, working on one of the first timing detectors with a O(10) picosecond precision for a large-scale experiment has definitely been an exciting experience. My contribution to this project can be broken down in two main subjects.

On one hand, I have participated in simulation studies to evaluate crucial detector parameters, such as the occupancy, the power dissipation and the bandwidth of the foreseen detector. In order to keep the occupancy below 10% throughout the active area, while maintaining a reasonable amount of channels, the sensor pad size was decided to be 1.3 mm $\times$ 1.3 mm. I have estimated the average total power consumption of the active components to be 17.7 kW during the nominal operation of HGTD, a value that is within the specifications of the cooling system. Additionally, I have used the calculated bandwidth of each ASIC to perform an optimization of the data transmission components, and particularly the lpGBTs and the optical links needed to serialise and transmit the data from the periphery of HGTD to the ATLAS DAQ system. An important result of this study was the conception of large peripheral board units that serve a large amount of modules, as this configuration was found to minimise the number of components, something that is beneficial not only in terms of cost, but also of available space. Finally, as the simulation of both ITk and HGTD continue to evolve, new requirements come to light, calling for re-optimisations of the read-out geometry. In order to facilitate the detector design under the continuously shifting conditions, I developed a simple framework that can help guide new layout designs by providing rough performance estimates. This framework has already been used to evaluate the impact of a layout re-organisation that has been conceived for the HGTD TDR. After confirming that a good performance can be maintained throughout the detector, the new layout is now being implemented in full simulation, so as to perform more detailed studies. At this phase of the detector development, where the constraints and requirements keep being updated, the simplified framework is an invaluable tool that can help quickly evaluate the potential impact in a change of the active area layout.

Finally, I worked on the characterisation of the prototype front-end electronics chip for precise time measurements within HGTD, ALTIROC. I tested two versions of the prototype, which integrated the analogue components of the read-out chain, both with calibration pulses and in test beam with highly energetic particles, either with the electronics alone, or coupled to non-irradiated LGAD sensors. The main purpose of this work was the evaluation of the timing performance of the analogue part of the readout chain, in particular the jitter, the time walk correction and the TDC. Additional studies included the estimation of the parasitic capacitance, the timing performance in cold temperature, efficiency and time uniformity. In all tested modules, the time resolution was found to be better than 55 ps, with a best-achieved performance of 34.7 $\pm$ 1 ps. One of the main challenges of the characterization campaign was the observed discreteness in the discriminator falling edge, which made the time walk correction a difficult endeavour. After intensive studies, the problem has been identified to originate

from digital couplings inside the ASIC, and will be fixed in future versions of the chip. Additionally, the noise was found to be larger in beam test measurements, which is sub-optimal for the minimum achievable threshold. This effect can have a significant impact for irradiated sensors, where the charge is lower, and will be further investigated in the future. The overall performance of the first two prototypes is extremely encouraging for the achievement of the requirements set by HGTD. Future campaigns will be focused on resolving the remaining issues and testing the front-end components with irradiated sensors. Additionally, new prototype productions are planned, to incorporate the final blocks of the front-end readout chain and increase the ASIC matrix to the scale envisioned by HGTD.

A. Appendix A

Multi-bin control region distributions for the 0-lepton analysis

This appendix contains CR distributions of the four multi-bin searches of the 0-lepton analysis, for the three binning variables, m_{eff}, $E_{\text{T}}^{\text{miss}}/\sqrt{H_{\text{T}}}$ and N_{j}. The MC background predictions arenormalised using cross-section times integrated luminosity, with the exception of multi-jet background which is normalised using data. The distributions are shown prior to the background-only fit.

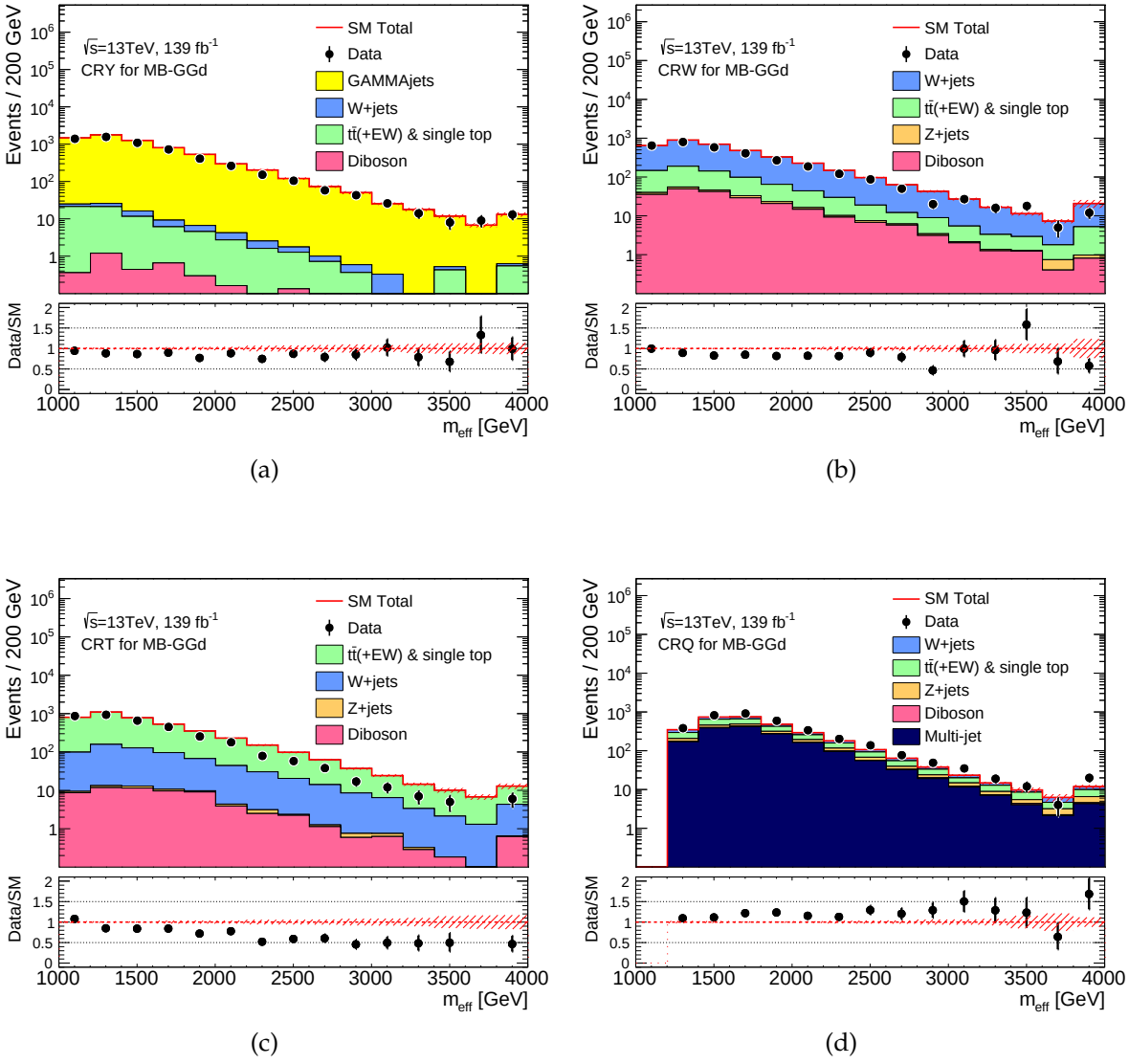

FIGURE A.1: Observed m_{eff} distributions in control regions (a) MB-CRY, (b) MB-CRW, (c) MB-CRT and (d) MB-CRQ after applying the MB-GGd control region criteria and after requiring that events pass any of the equivalent CR bin cuts. The histograms show the MC background predictions normalised using cross-section times integrated luminosity, with the exception of multi-jet background which is normalised using data. In the case of the γ+jets background, a κ factor described in the text is applied. The hatched (red) error bands indicate the combined MC statistical, experimental and theoretical uncertainties. The latter two are calculated using the coarser binning of the MB analysis rather than the fine binning of the histogram. The last bin includes overflow events.

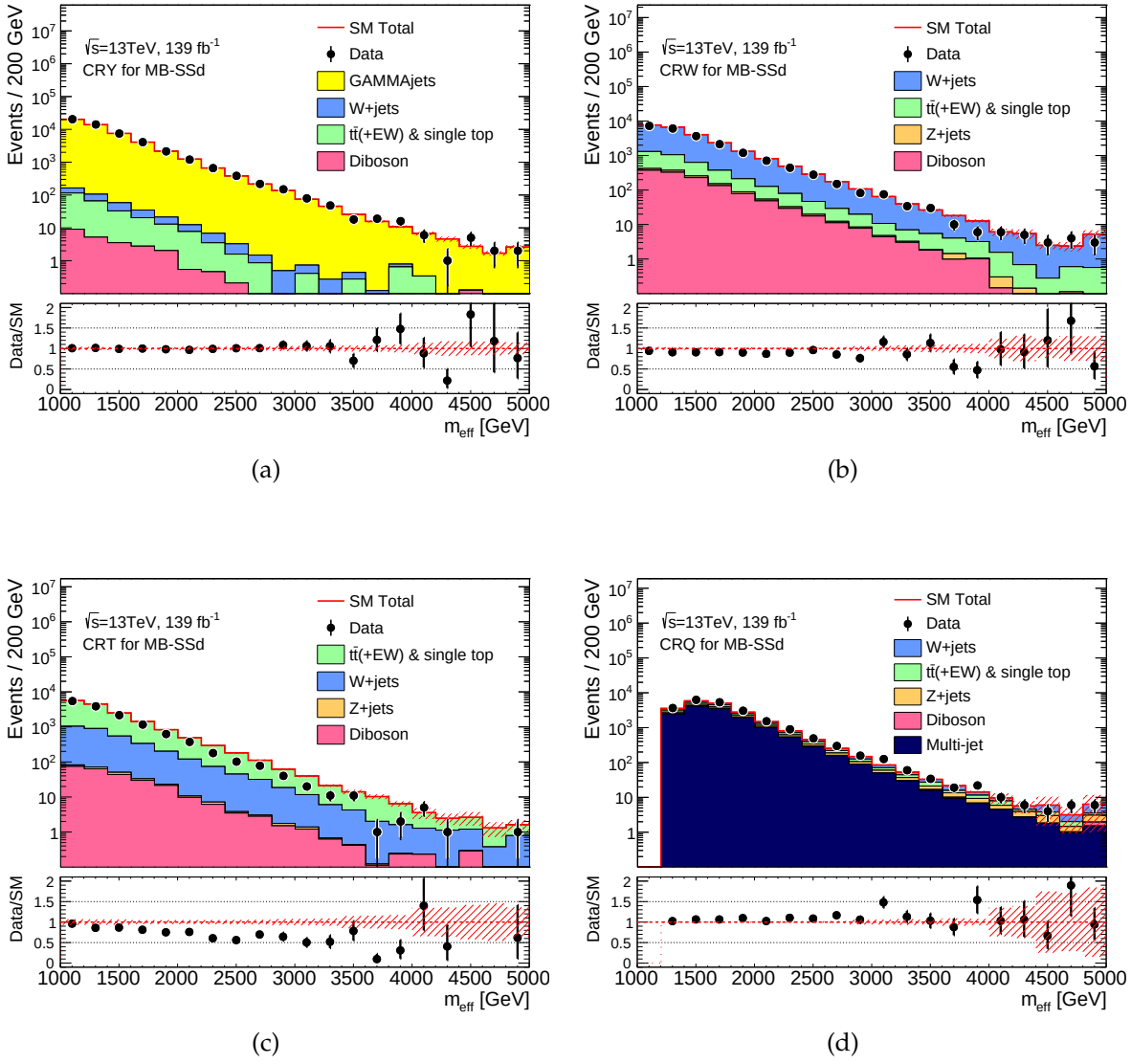

FIGURE A.2: Observed m_{eff} distributions in control regions (a) MB-CRY, (b) MB-CRW, (c) MB-CRT and (d) MB-CRQ after applying the MB-SSd control region criteria and after requiring that events pass any of the equivalent CR bin cuts. The histograms show the MC background predictions normalised using cross-section times integrated luminosity, with the exception of multi-jet background which is normalised using data. In the case of the γ+jets background, a κ factor described in the text is applied. The hatched (red) error bands indicate the combined MC statistical, experimental and theoretical uncertainties. The latter two are calculated using the coarser binning of the MB analysis rather than the fine binning of the histogram. The last bin includes overflow events.

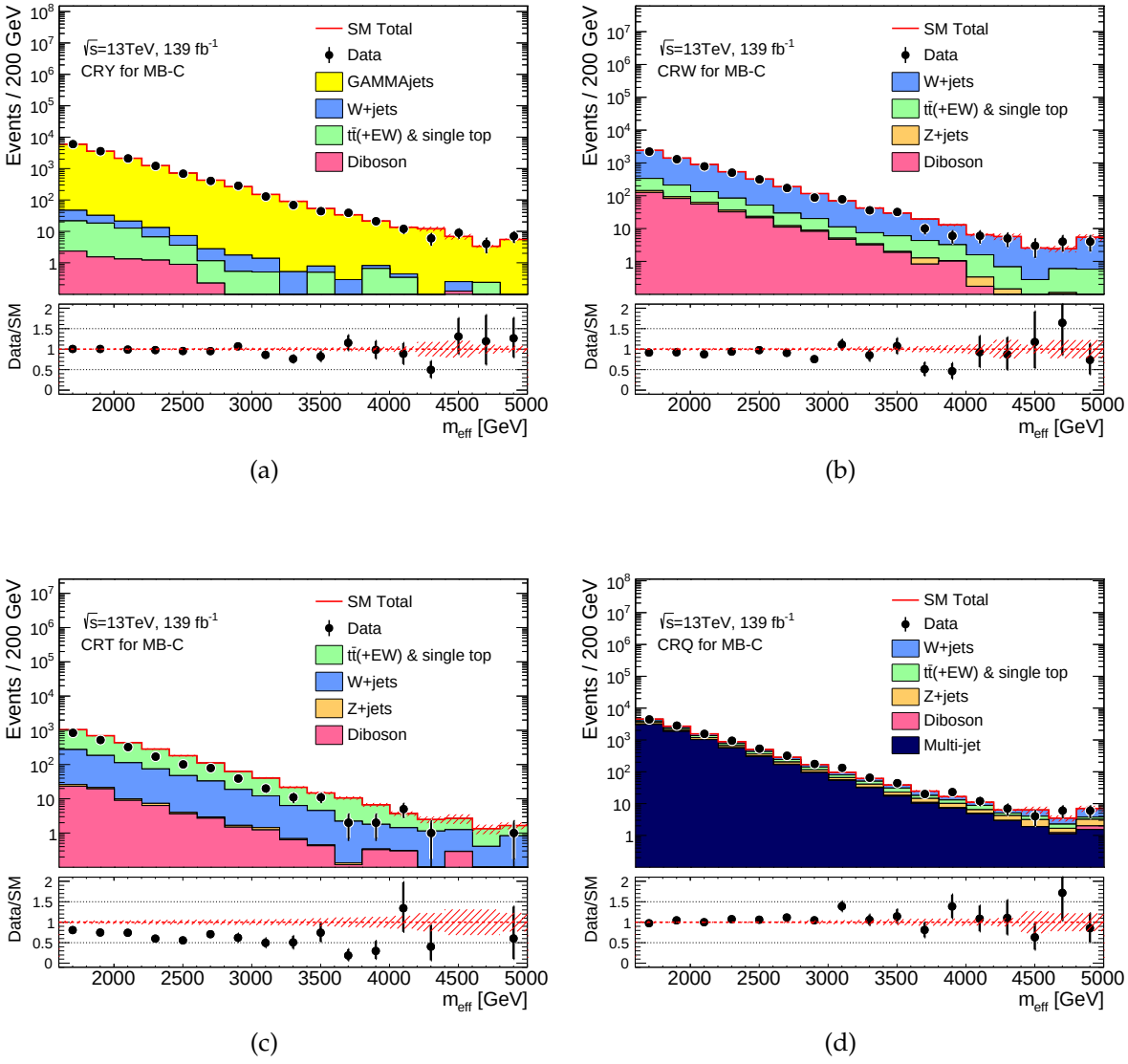

FIGURE A.3: Observed m_{eff} distributions in control regions (a) MB-CRY, (b) MB-CRW, (c) MB-CRT and (d) MB-CRQ after applying the MB-C control region criteria and after requiring that events pass any of the equivalent CR bin cuts. The histograms show the MC background predictions normalised using cross-section times integrated luminosity, with the exception of multi-jet background which is normalised using data. In the case of the γ+jets background, a κ factor described in the text is applied. The hatched (red) error bands indicate the combined MC statistical, experimental and theoretical uncertainties. The latter two are calculated using the coarser binning of the MB analysis rather than the fine binning of the histogram. The last bin includes overflow events.

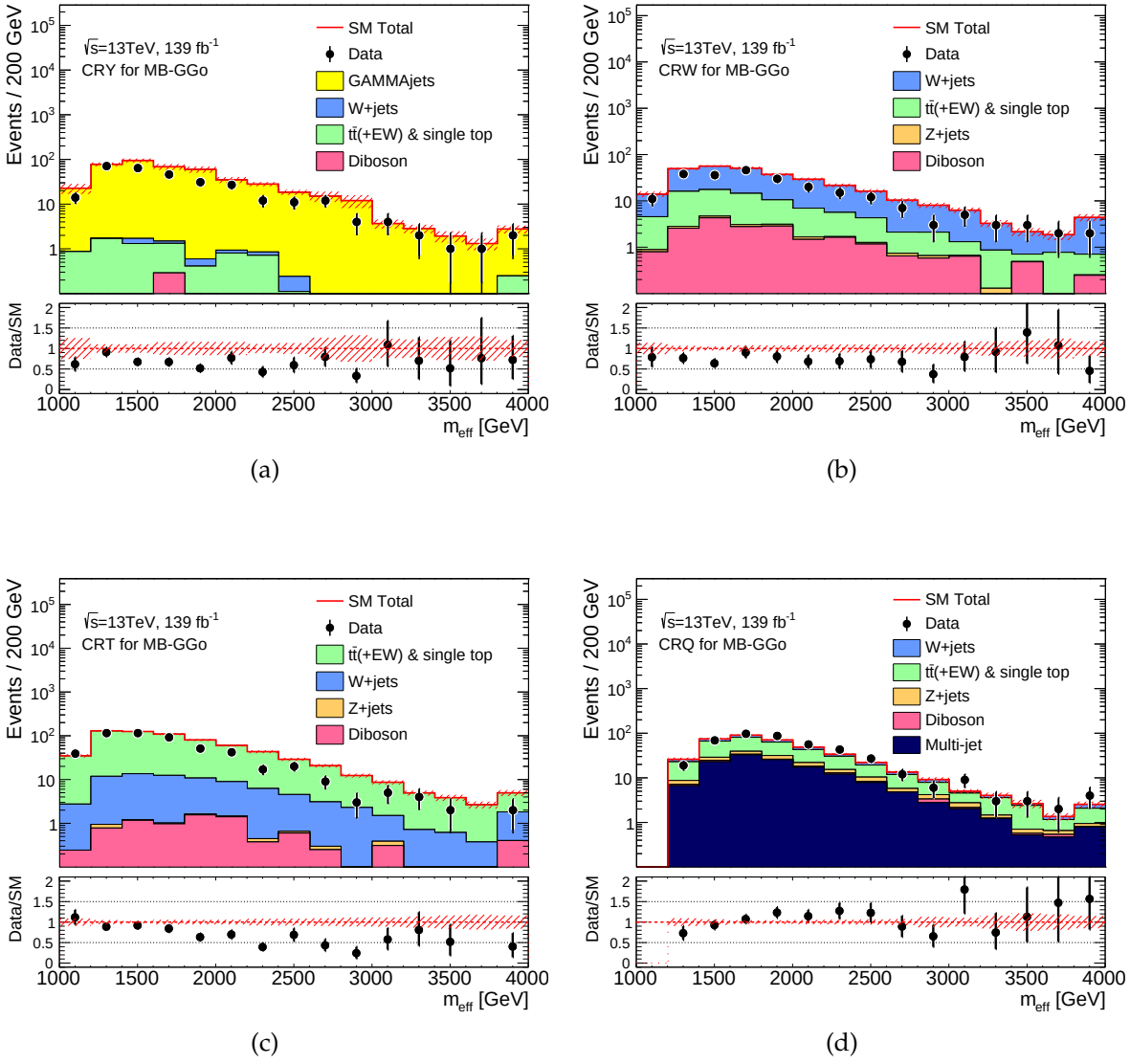

FIGURE A.4: Observed m_{eff} distributions in control regions (a) MB-CRY, (b) MB-CRW, (c) MB-CRT and (d) MB-CRQ after applying the MB-GGo control region criteria and after requiring that events pass any of the equivalent CR bin cuts. The histograms show the MC background predictions normalised using cross-section times integrated luminosity, with the exception of multi-jet background which is normalised using data. In the case of the γ+jets background, a κ factor described in the text is applied. The hatched (red) error bands indicate the combined MC statistical, experimental and theoretical uncertainties. The latter two are calculated using the coarser binning of the MB analysis rather than the fine binning of the histogram. The last bin includes overflow events.

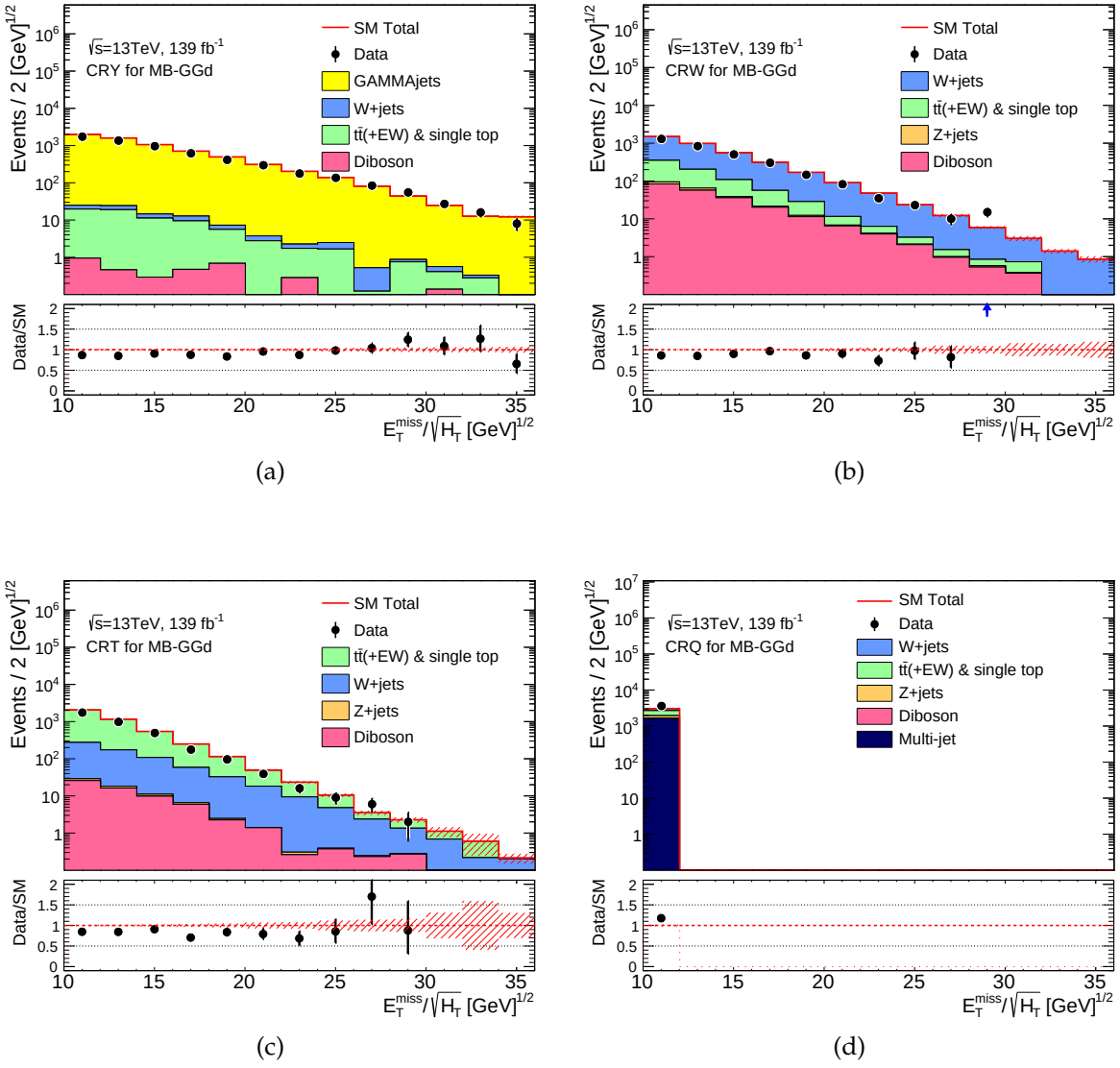

FIGURE A.5: Observed $E_{\mathrm{T}}^{\mathrm{miss}}/\sqrt{H_{\mathrm{T}}}$ distributions in control regions (a) MB-CRY, (b) MB-CRW, (c) MB-CRT and (d) MB-CRQ after applying the MB-GGd control region criteria and after requiring that events pass any of the equivalent CR bin cuts. The histograms show the MC background predictions normalised using cross-section times integrated luminosity, with the exception of multi-jet background which is normalised using data. In the case of the γ+jets background, a κ factor described in the text is applied. The hatched (red) error bands indicate the combined MC statistical, experimental and theoretical uncertainties. The latter two are calculated using the coarser binning of the MB analysis rather than the fine binning of the histogram. The last bin includes overflow events.

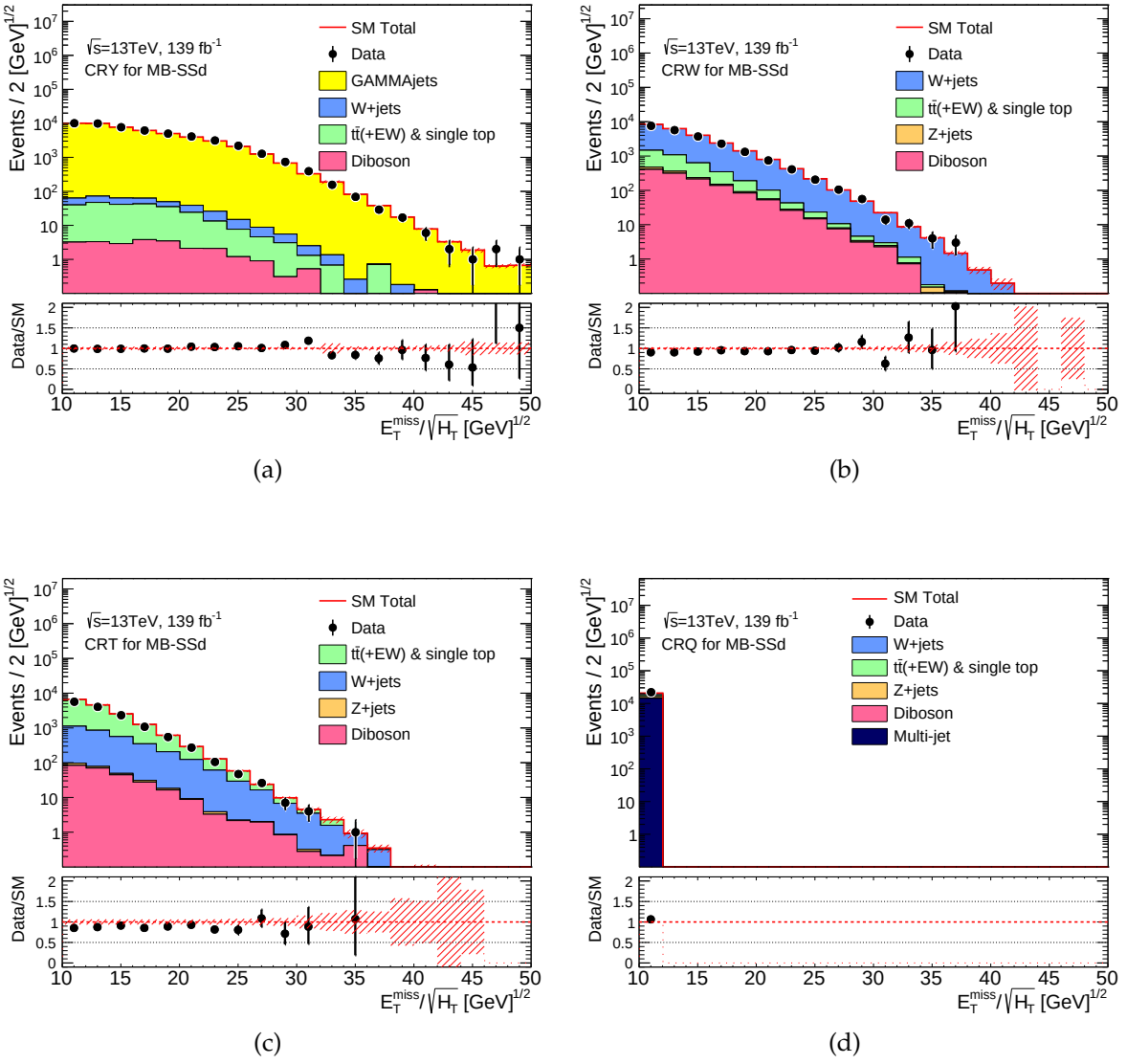

FIGURE A.6: Observed $E_{\mathrm{T}}^{\mathrm{miss}}/\sqrt{H_{\mathrm{T}}}$ distributions in control regions (a) MB-CRY, (b) MB-CRW, (c) MB-CRT and (d) MB-CRQ after applying the MB-SSd control region criteria and after requiring that events pass any of the equivalent CR bin cuts. The histograms show the MC background predictions normalised using cross-section times integrated luminosity, with the exception of multi-jet background which is normalised using data. In the case of the γ+jets background, a κ factor described in the text is applied. The hatched (red) error bands indicate the combined MC statistical, experimental and theoretical uncertainties. The latter two are calculated using the coarser binning of the MB analysis rather than the fine binning of the histogram. The last bin includes overflow events.

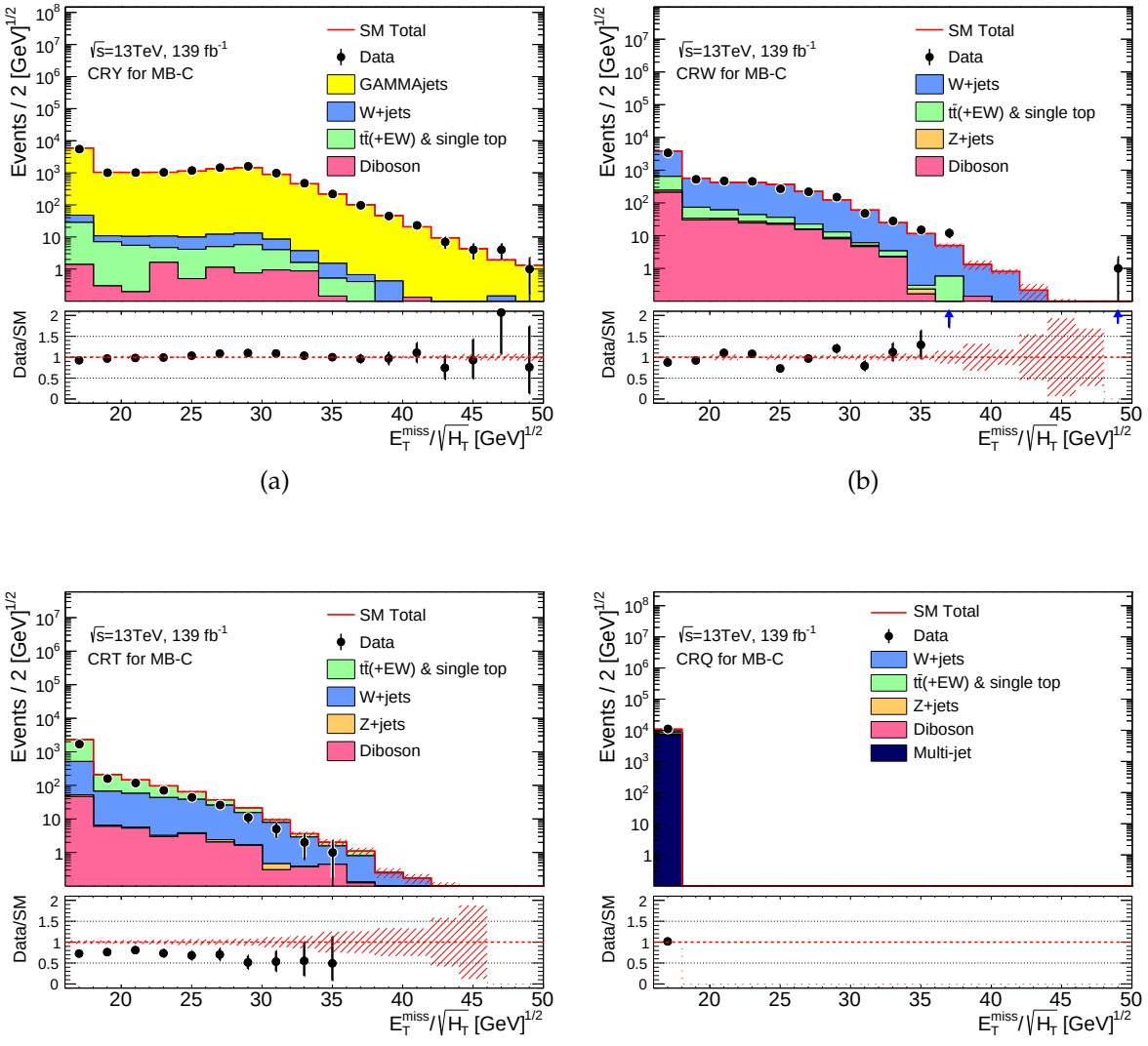

FIGURE A.7: Observed $E_{\mathrm{T}}^{\mathrm{miss}}/\sqrt{H_{\mathrm{T}}}$ distributions in control regions (a) MB-CRY, (b) MB-CRW, (c) MB-CRT and (d) MB-CRQ after applying the MB-C control region criteria and after requiring that events pass any of the equivalent CR bin cuts. The histograms show the MC background predictions normalised using cross-section times integrated luminosity, with the exception of multi-jet background which is normalised using data. In the case of the γ+jets background, a κ factor described in the text is applied. The hatched (red) error bands indicate the combined MC statistical, experimental and theoretical uncertainties. The latter two are calculated using the coarser binning of the MB analysis rather than the fine binning of the histogram. The last bin includes overflow events.

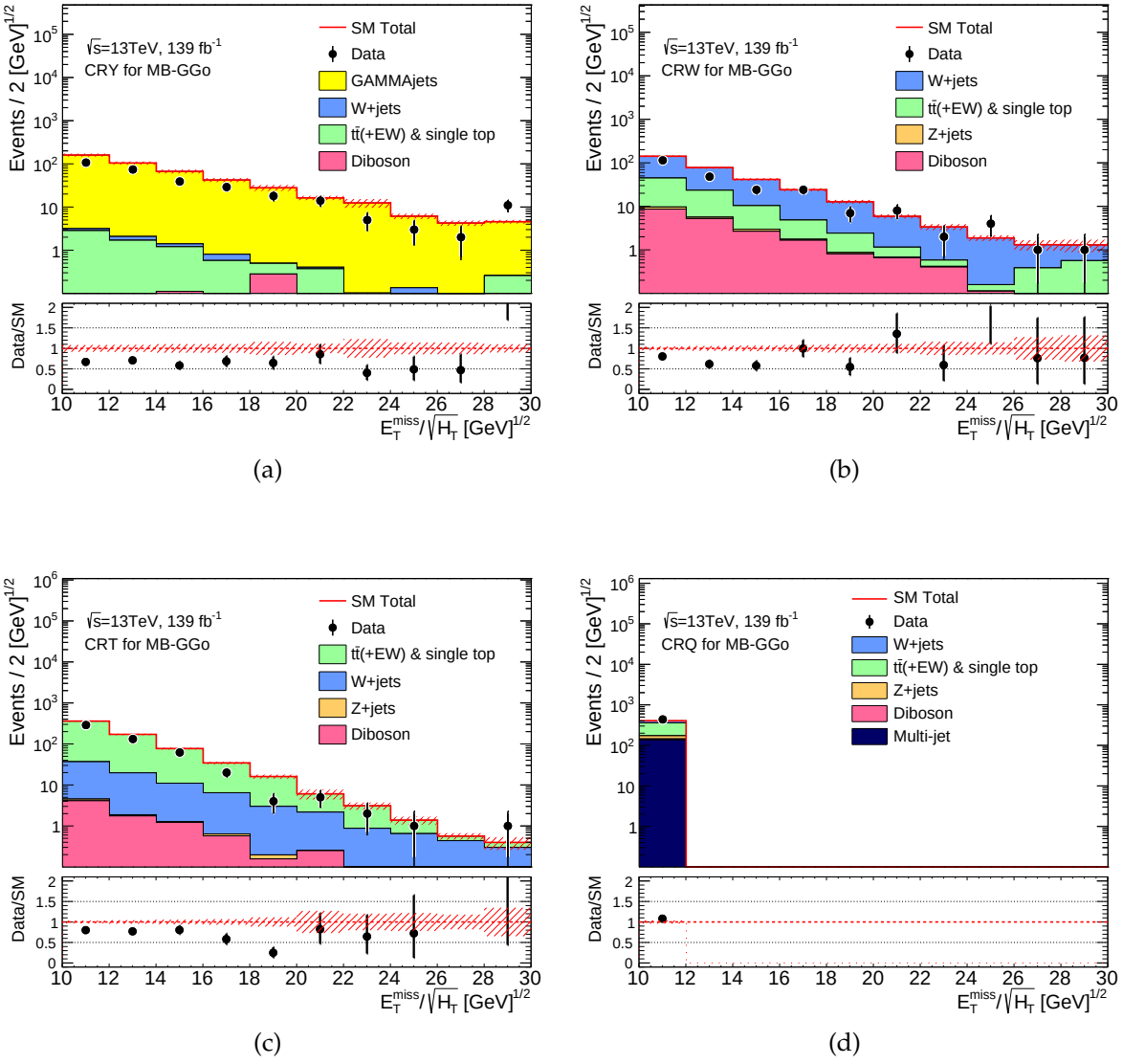

FIGURE A.8: Observed $E_{\mathrm{T}}^{\mathrm{miss}}/\sqrt{H_{\mathrm{T}}}$ distributions in control regions (a) MB-CRY, (b) MB-CRW, (c) MB-CRT and (d) MB-CRQ after applying the MB-GGo control region criteria and after requiring that events pass any of the equivalent CR bin cuts. The histograms show the MC background predictions normalised using cross-section times integrated luminosity, with the exception of multi-jet background which is normalised using data. In the case of the γ+jets background, a κ factor described in the text is applied. The hatched (red) error bands indicate the combined MC statistical, experimental and theoretical uncertainties. The latter two are calculated using the coarser binning of the MB analysis rather than the fine binning of the histogram. The last bin includes overflow events.

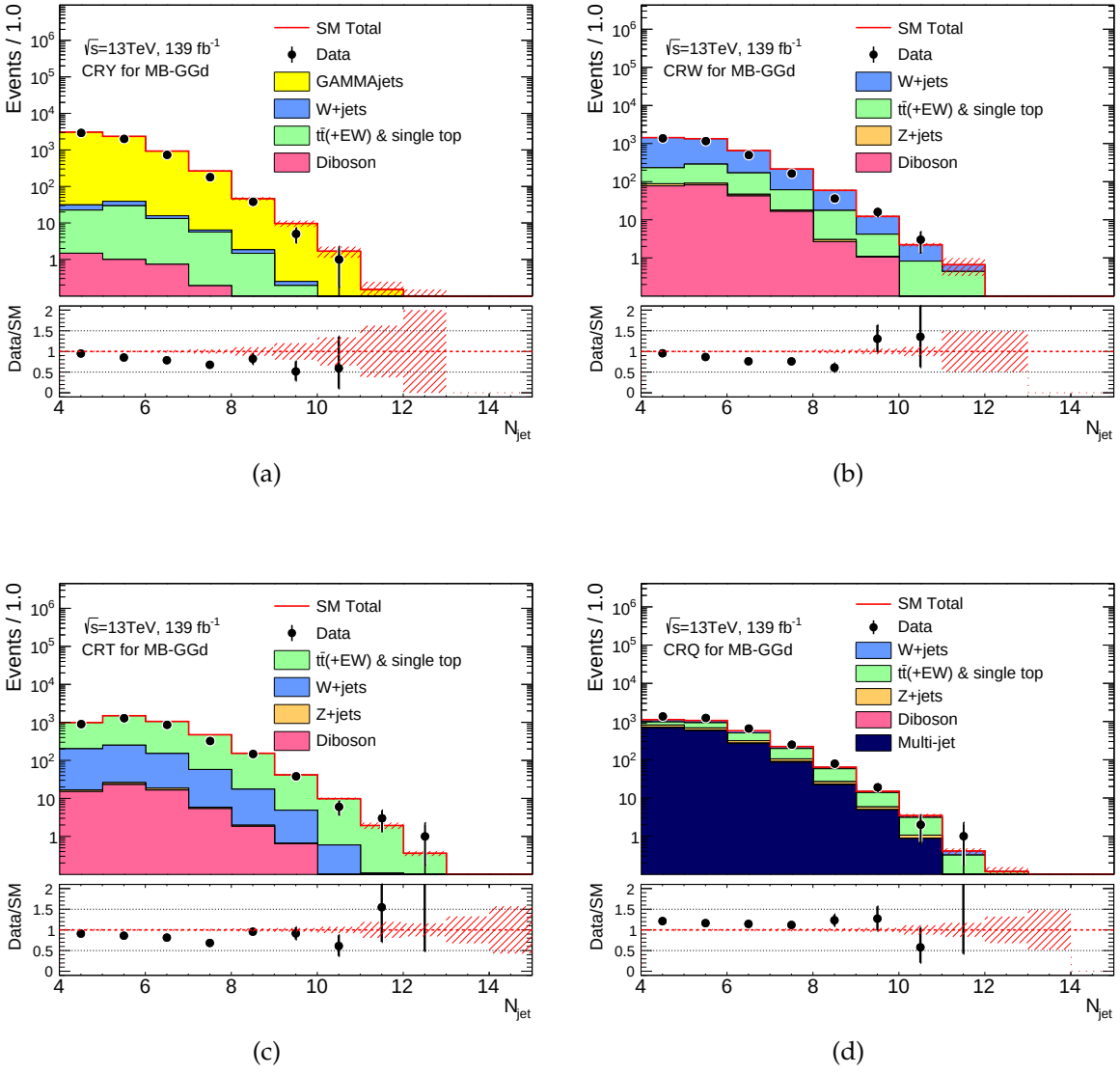

FIGURE A.9: Observed N_j distributions in control regions (a) MB-CRY, (b) MB-CRW, (c) MB-CRT and (d) MB-CRQ after applying the MB-GGd control region criteria and after requiring that events pass any of the equivalent CR bin cuts. The histograms show the MC background predictions normalised using cross-section times integrated luminosity, with the exception of multi-jet background which is normalised using data. In the case of the γ+jets background, a κ factor described in the text is applied. The hatched (red) error bands indicate the combined MC statistical, experimental and theoretical uncertainties. The latter two are calculated using the coarser binning of the MB analysis rather than the fine binning of the histogram. The last bin includes overflow events.

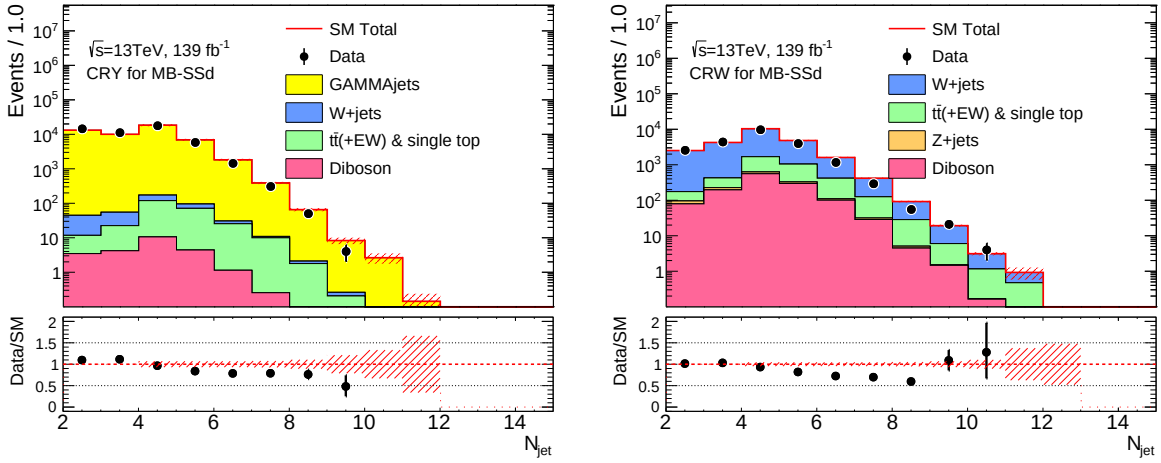

(a)

(b)

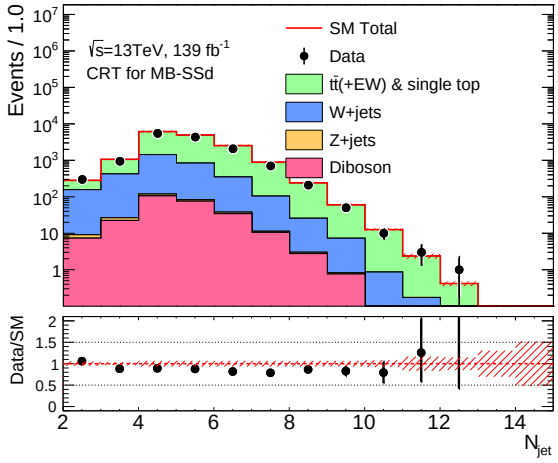

(c)

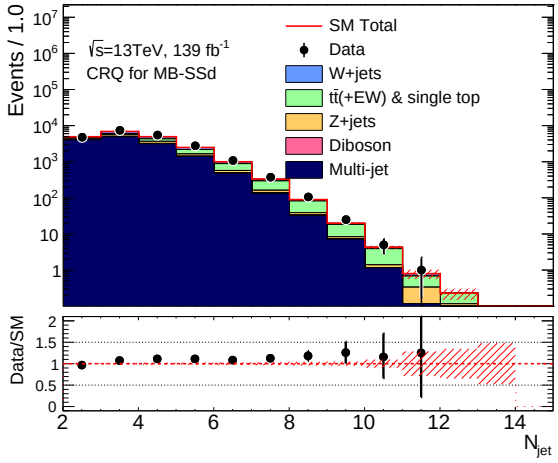

(d)

FIGURE A.10: Observed N_j distributions in control regions (a) MB-CRY, (b) MB-CRW, (c) MB-CRT and (d) MB-CRQ after applying the MB-SSd control region criteria and after requiring that events pass any of the equivalent CR bin cuts. The histograms show the MC background predictions normalised using cross-section times integrated luminosity, with the exception of multi-jet background which is normalised using data. In the case of the γ+jets background, a κ factor described in the text is applied. The hatched (red) error bands indicate the combined MC statistical, experimental and theoretical uncertainties. The latter two are calculated using the coarser binning of the MB analysis rather than the fine binning of the histogram. The last bin includes overflow events.

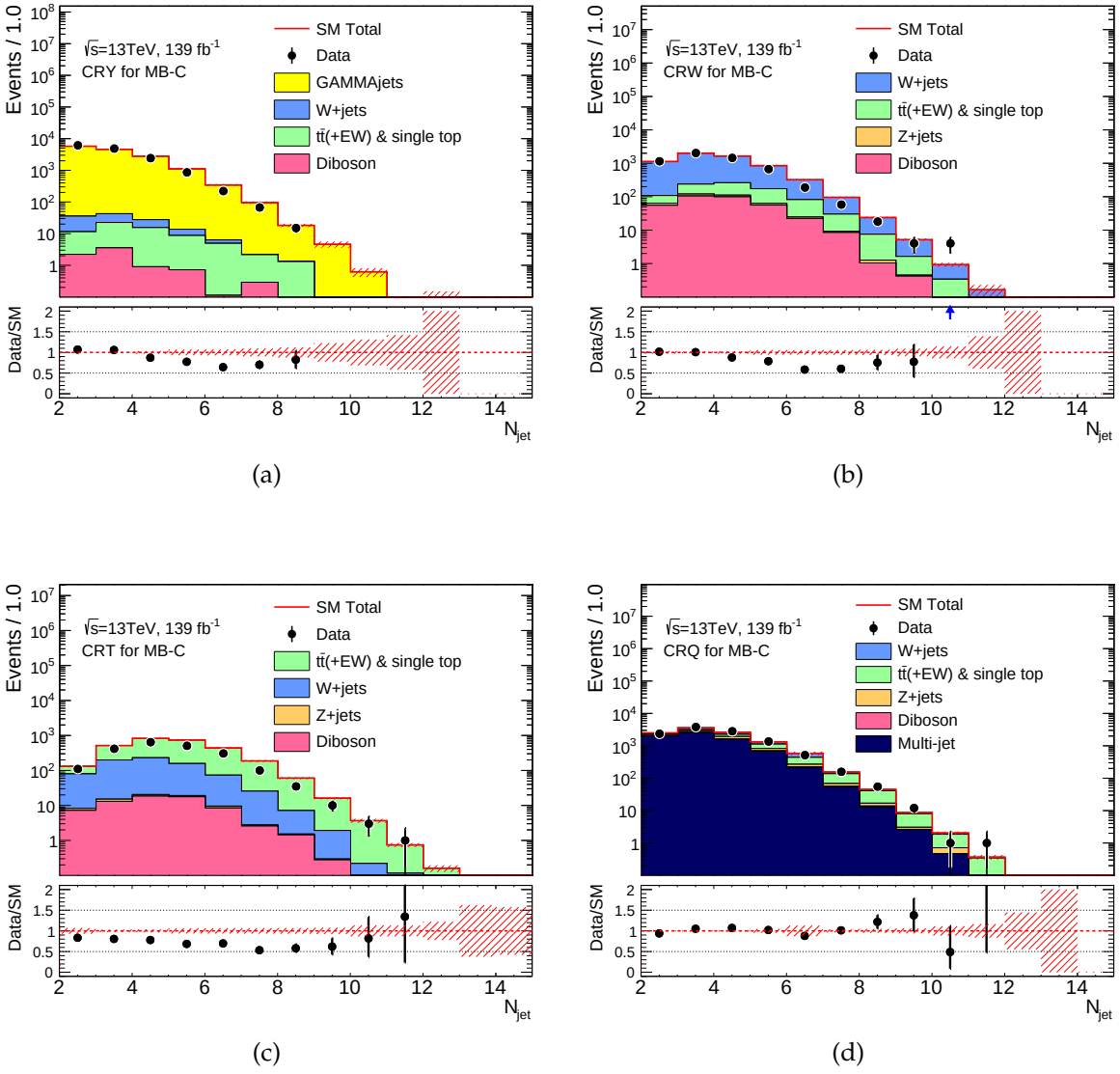

FIGURE A.11: Observed N_j distributions in control regions (a) MB-CRY, (b) MB-CRW, (c) MB-CRT and (d) MB-CRQ after applying the MB-C control region criteria and after requiring that events pass any of the equivalent CR bin cuts. The histograms show the MC background predictions normalised using cross-section times integrated luminosity, with the exception of multi-jet background which is normalised using data. In the case of the γ+jets background, a κ factor described in the text is applied. The hatched (red) error bands indicate the combined MC statistical, experimental and theoretical uncertainties. The latter two are calculated using the coarser binning of the MB analysis rather than the fine binning of the histogram. The last bin includes overflow events.

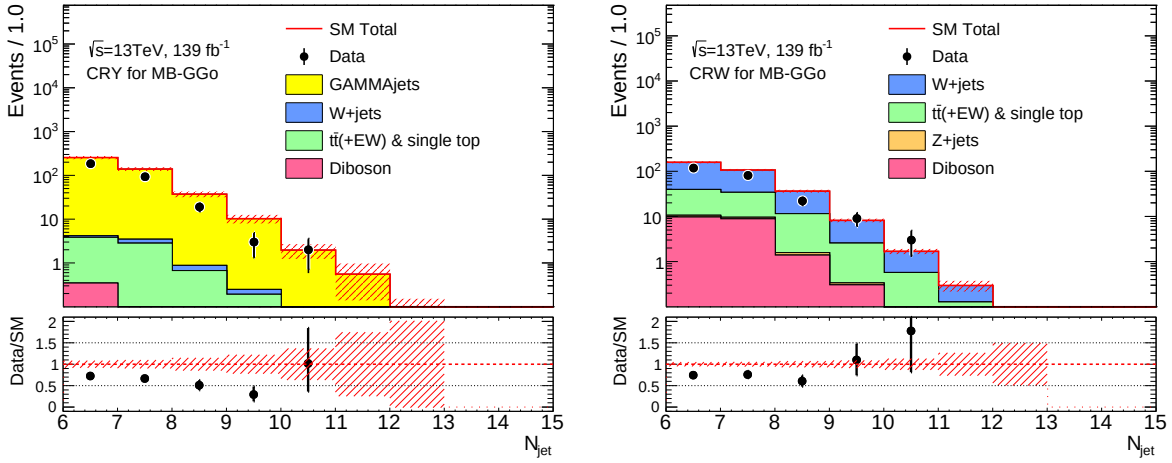

(a)

(b)

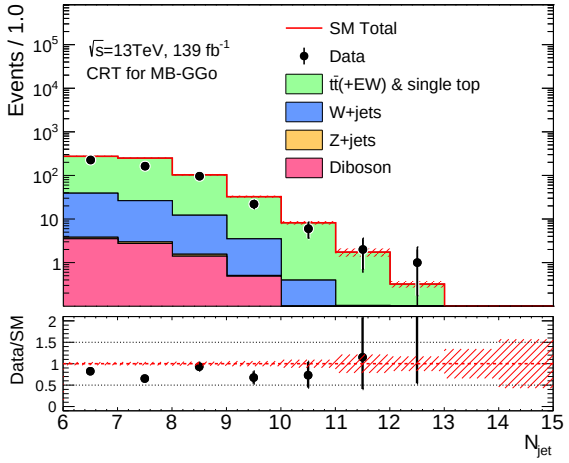

(c)

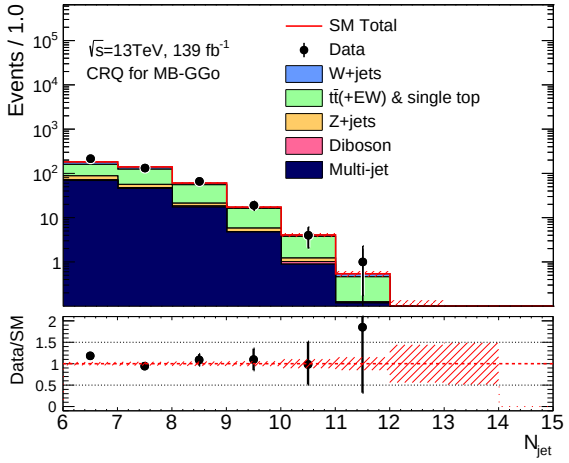

(d)

FIGURE A.12: Observed N_j distributions in control regions (a) MB-CRY, (b) MB-CRW, (c) MB-CRT and (d) MB-CRQ after applying the MB-GGo control region criteria and after requiring that events pass any of the equivalent CR bin cuts. The histograms show the MC background predictions normalised using cross-section times integrated luminosity, with the exception of multi-jet background which is normalised using data. In the case of the γ+jets background, a κ factor described in the text is applied. The hatched (red) error bands indicate the combined MC statistical, experimental and theoretical uncertainties. The latter two are calculated using the coarser binning of the MB analysis rather than the fine binning of the histogram. The last bin includes overflow events.

B. Appendix B

Best performing Signal Regions in the 0-lepton model-dependent interpretation

In this appendix, the best performing SRs (or multi-bin fits) for each mass point in the nine SUSY simplified models considered in the 0-lepton analysis, are presented. The results are presented, similarly to 4.10, in the form of exclusion limits in the 2-dimensional plane of the free mass parameters of each model. The expected limit at 95% CL is indicated by a grey dashed line, surrounded by a yellow band that shows the $\pm 1\sigma$ variations due to experimental and theoretical uncertainties. The bbserved limits are shown by dark maroon curves where the solid contour represents the nominal limit, and the dotted lines are obtained by varying the signal cross-section by the renormalization and factorization scale and PDF uncertainties. Results are compared with the observed limits obtained by the previous ATLAS searches with jets, missing transverse momentum, and no leptons [147], which are shown in light blue shade. The grey shaded text on the plots denotes the best performing signal region (or multi-bin fit) for each mass point.

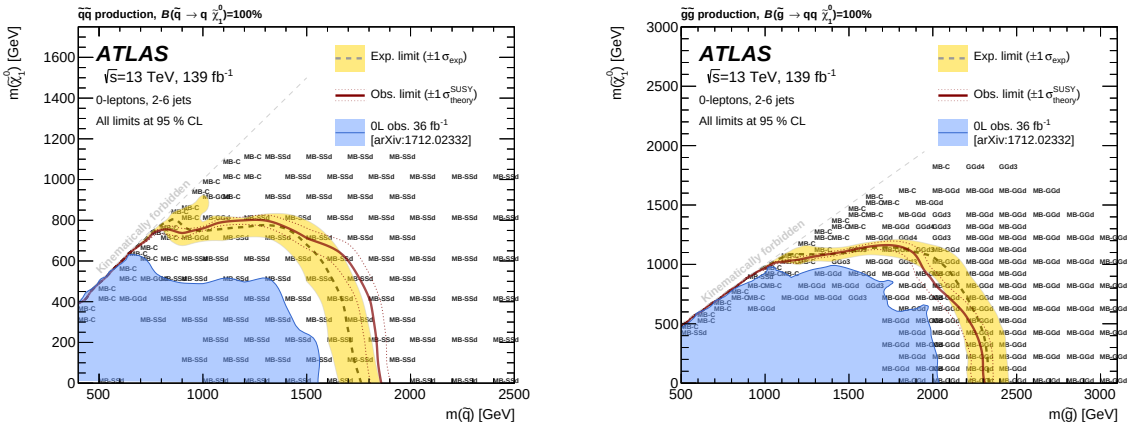

(a) (b)

FIGURE B.1: Exclusion limits in the mass plane of the lightest neutralino and (a) the first- and second-generation squarks assuming squark-pair production and direct decays $\tilde{q} \to q\tilde{\chi}_1^0$ and (b) the gluino, assuming gluino-pair production and direct decays $\tilde{g} \to qq\tilde{\chi}_1^0$. In Figure (a) models where squarks are considered as fully degenerate are considered. The gray text corresponds to the signal regions with the best expected sensitivity at each point, which is used to obtain the limits.

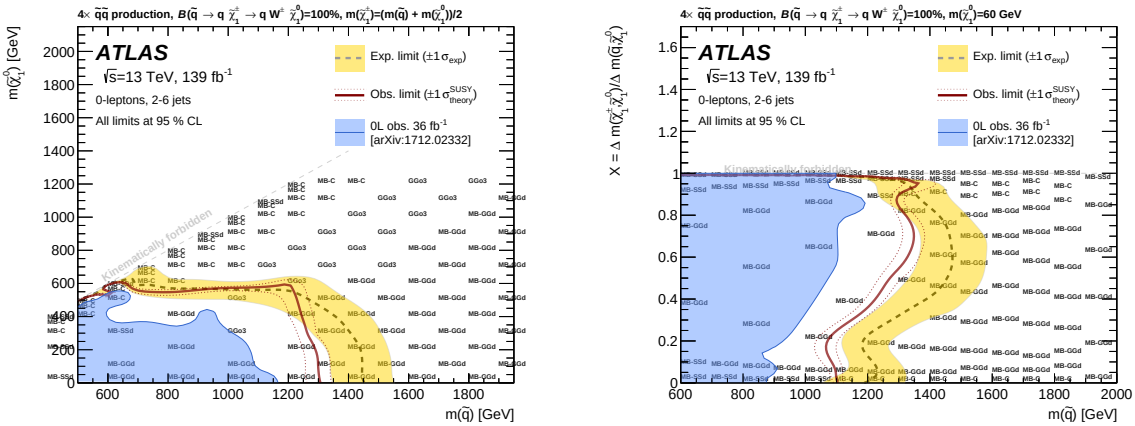

(a) (b)

FIGURE B.2: Exclusion limits for squark-pair production with a one-step decay via an intermediate chargino into $qW\tilde{\chi}_1^0$. Figure (a) shows the limits in the $(m(\tilde{q}), m(\tilde{\chi}_1^0))$ plane for a chargino mass fixed at $m(\tilde{\chi}_1^{\pm}) = (m(\tilde{q}) + m(\tilde{\chi}_1^0))/2$. Alternatively in Figure (b), the neutralino mass is fixed at 60 GeV and exclusion limits are given for $\chi = \Delta m(\tilde{\chi}_1^{\pm}, \tilde{\chi}_1^0)/\Delta m(\tilde{q}, \tilde{\chi}_1^0)$ as a function of the squark mass. The gray text corresponds to the signal regions with the best expected sensitivity at each point, which is used to obtain the limits.

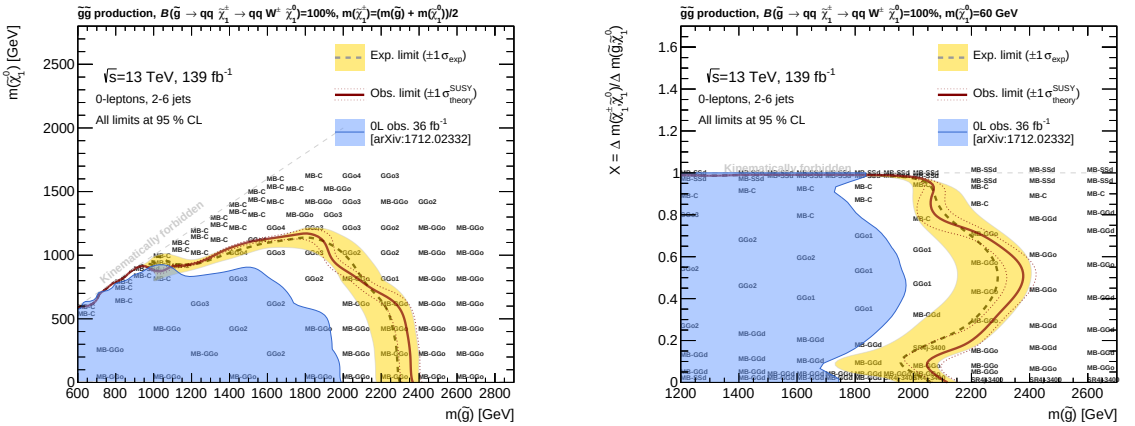

(a) (b)

FIGURE B.3: Exclusion limits for gluino-pair production with a one-step decay via an intermediate chargino into $qqW\tilde{\chi}_1^0$. Figure (a) shows the limits in the $(m(\tilde{g}), m(\tilde{\chi}_1^0))$ plane for a chargino mass fixed at $m(\tilde{\chi}_1^{\pm}) = (m(\tilde{g}) + m(\tilde{\chi}_1^0))/2$. Alternatively in Figure (b), the neutralino mass is fixed at 60 GeV and exclusion limits are given for $\chi = \Delta m(\tilde{\chi}_1^{\pm}, \tilde{\chi}_1^0)/\Delta m(\tilde{g}, \tilde{\chi}_1^0)$ as a function of the gluino mass. The gray text corresponds to the signal regions with the best expected sensitivity at each point, which is used to obtain the limits.

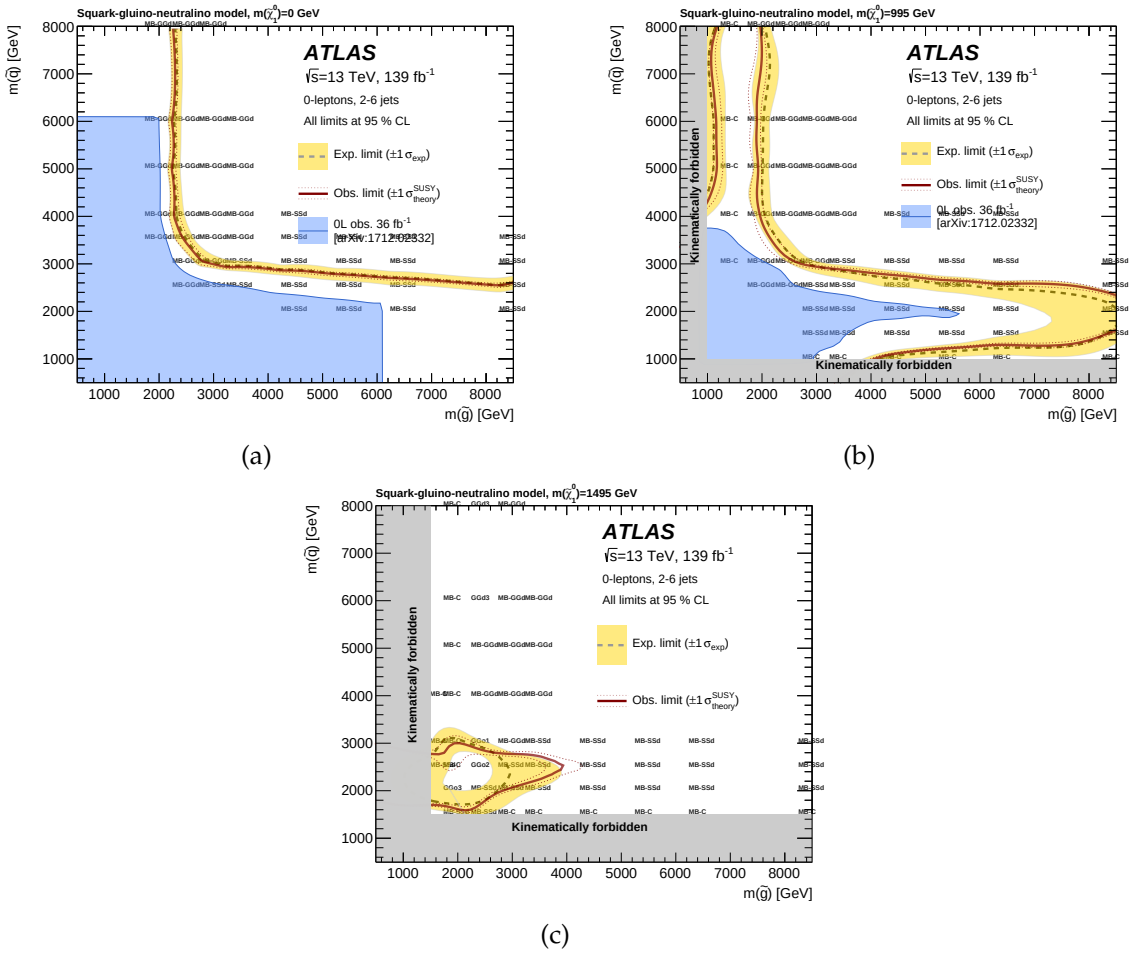

FIGURE B.4: Exclusion limits for the model with combined production of squark pairs, gluino pairs, and of squark-gluino pairs, for different assumptions on the neutralino mass: (a) $m(\tilde{\chi}_1^0) = 0$ GeV, (b) $m(\tilde{\chi}_1^0) = 995$ GeV and (c) $m(\tilde{\chi}_1^0) = 1495$ GeV varying values of $m(\tilde{g})$ and $m(\tilde{q})$ and assuming a purely bino $\tilde{\chi}_1^0$. The gray text corresponds to the signal regions with the best expected sensitivity at each point, which is used to obtain the limits.

C. Appendix C

Résumé

Le Modèle Standard MS de la physique des particules est une théorie quantique des champs qui décrit les particules élémentaires et leurs interactions. Ils existent deux types des particules; les fermions, qui ont un spin entier et qui constituent les briques de construction de la matière, et les bosons qui ont un spin entier. Ceux derniers sont responsables de la médiation des interactions fondamentales: l'interaction électromagnétique, médiatisée par le photon, l'interaction faible, médiatisée par les bosons W and Z et, finalement, l'interaction fort, transférée par le gluon. La dernière partie du MS et le mécanisme de Brout-Englert-Higgs, qui a été introduit pour expliquer les masses des particules et qui prédit un boson additionnel, le boson du Higgs. Ceci a été découvert par les expériences ATLAS et CMS en 2012.

Le MS et un modèle extrêmement réussi, avec plain des prédictions expérimentalement vérifiés. Malgré toutes ses réussites, ils existent des phénomènes qui ne peuvent pas être expliquées par le MS. Un exemple est le problème de hiérarchie de la masse boson du Higgs, qui n'est pas protégée contre corrections radiatives divergentes qui proviennent d'une théorie à haute échelle. Un autre défaut du MS est l'absence d'unification de trois forces à l'échelle Planck. Finalement, le MS ne dispose pas un candidat valable pour l'intégralité de la matière noire et ne permet pas d'expliquer l'asymétrie matière-antimatière dans l'univers.

Parmi les différentes théories au-delà du MS qui permettent de résoudre ces limitations, une est particulièrement attractive, il s'agit de la Supersymétrie (SUSY). En cette théorie, on suppose une symétrie supplémentaire entre les états fermioniques et bosoniques ce qui fait que chaque particule du MS a un partenaire supersymétrique. Les particules supersymétriques supplémentaires protègent la masse du boson du Higgs des corrections divergentes et modifient l'évolution de trois forces de façon que l'unification est possible a l'échelle Planck. Si on suppose une symétrie additionnelle, nommée R-parité, le particule supersymétrique le plus léger est stable et neutre, et donc peut donner un candidat pour la matière noire. Du fait de la supersymétrie, les particules et leurs partenaires supersymétriques devraient avoir la même masse, ce qui est en contradiction avec les observations expérimentales. Cette symétrie doit donc être brisée, ce qui amène les masses des particules supersymétriques à être plus élevées que celles de leurs partenaires du MS.

En partant du modèle standard on construit l'expression minimale d'une théorie encapsulant la supersymétrie, le MSSM (Minimal Supersymmetric Standard Model). Les particules du MS et leurs partenaires supersymétriques résident en "super-multiplets". Les quarks du MS s'associent avec des spin-0 s-quarks et les bosons gauge couplent avec des fermions supersymétriques, les gauginos. Il y a deux doublets complexes pour le champs du Higgs, donnant 5 bosons du Higgs. Les partenaires supersymétriques des ces bosons, les higgsinos, et les gauginos se mélangent pour créer quatre neutralinos: $\tilde{\chi}_1^0$, $\tilde{\chi}_2^0$, $\tilde{\chi}_3^0$ et $\tilde{\chi}_4^0$, et 2 charginos: $\tilde{\chi}_1^\pm$ et $\tilde{\chi}_2^\pm$. Les partenaires des quarks et du gluon, les squarks et le gluino, sont particulièrement

intéressantes pour les recherches à LHC, parce-que la section efficace attendue de leur production en collisions hadroniques est la plus grande pour une masse fixe.

Le Grand Collisionneur de Hadrons (LHC) est le plus grand accélérateur de particules. Dans son anneau de 27 km circonférence, des protons sont accélérés par des cavités de radiofréquence, tout en étant maintenus dans la trajectoire circulaire par des aimants dipôles superconducteurs. Dès qu'ils ont atteint l'énergie finale, les protons entrent en collision en quatre points d'interaction, où les quatre expériences principaux se situent: ATLAS, CMS, LHCb et ALICE. Depuis 2010 le LHC enregistre des données, passant par une énergie dans le centre de masse de $\sqrt{s}$ = 7 TeV en 2010 à $\sqrt{s}$ = 13 TeV pendant la période 2015-2018, ce qui constitue la Run 2.

ATLAS (A Toroidal LHC Apparatus) est une expérience généraliste, avec un programme de physique centré sur la mesure du boson du Higgs et ses propriétés, ainsi que la recherche de nouvelle physique. Il est un système hermétique, qui se compose de différents sous-détecteurs. Au cœur d'ATLAS, il se situe le Détecteur Interne (ID), qui reconstruit la trajectoire et l'impulsion des particules chargées qui le traversent. Pour déterminer la valeur de cette dernier, l'ID est immergé dans un champs magnétique. La deuxième fonction de ce détecteur est d'identifier les points d'interaction. Le deuxième système de détection sont les calorimètres, situes à l'extérieur de l'ID. Ils s'agitent d'une combinaison de matériaux actifs et passifs qui vont indure la création de gerbe au passage des particules, permettant la mesure de leur énergie. Il existe deux systèmes calorimétriques dans ATLAS, un calorimètre électromagnétique, placé en premier et qui mesure l'énergie des électrons et photons, et un calorimètre hadronique, placé après et qui est dédié à la mesure de l'énergie restante des hadrons. La partie finale d'ATLAS est le Spectromètre à Muons, un système de chambres à gaz, dédié à identifier et reconstruire la trajectoire et l'impulsion des muons qui traversent le sous-détecteurs précédents sans être absorbés.

C.1 Recherche de squarks et gluinos en états finaux avec des jets et de l'énergie transverse manquante

L'un des axes principaux du programme d'ATLAS sur la supersymétrie est la recherche des squarks et gluinos, les partenaires des particules quark et gluon. Ces particules supersymétriques devraient être instables et, en conséquence, se désintégreraient presque instantanément. Le sujet de l'analyse auquel je participe repose sur l'hypothèse selon laquelle l'R-parité est conservée. Les produits de la désintégration des particules squark et gluino seraient leurs partenaires du Modèle Standard ainsi que des particules supersymétriques, neutres et stables, qui n'interagissent pas avec les composants du détecteur ATLAS. La signature résultante d'une telle désintégration est, d'une part, la présence de nombreux jets de hadrons qui sont la signature expérimentale des quarks et gluons, et d'autre part, une grande valeur d'énergie transverse manquante due à la fuite des particules supersymétriques finales. Ces particules non détectées, qui on suppose être les neutralinos les plus légers, sont les candidates de la matière noire.

Afin d'améliorer la portée de l'exclusion de l'analyse, deux stratégies complémentaires et non-orthogonales sont utilisées: l'ajustement multi-dimensionnelle (Multi-bin ou MB) et la technique Boosted Decision Tree (BDT). Une troisième technique single-bin (SB) traditionnelle est aussi définie pour fournir une significance statistique indépendante des modèles dans l'espace de phase cinématique de l'ajustement MB. Les résultats sont interprétés avec l'aide des modèles supersymétriques simplifies, où le squarks ou le gluinos sont produits en paires et se désintègrent, directement ou en passant par un chargino intermédiaire, dans des particules du MS et des neutralinos. L'efficacité de l'analyse est limitée par des processus

du MS qui ressemble aux signaux. Les quatre contributions les plus significatives sont: les événements Z+jets et W+jets, les processus $t\bar{t}$ et single-t, les événements avec deux bosons vectoriels, et finalement le bruit du fond à cause des événements multijet.

Pour sélectionner les événements d'intérêt, un filtre sur l'énergie transverse manquante est appliqué. Afin d'augmenter la sensitivité de l'analyse au signaux supersymétriques, la variable "masse efficace", égal au somme scalaire de l'énergie transverse manquante et le somme scalaire de l'impulsion des jets reconstruites, est définie. Des variables additionnels, comme le nombre et l'impulsion des jets, la significance de l'énergie transverse manquante, $E_{\mathrm{T}}^{\mathrm{miss}}/\sqrt{H_T}$, et la séparation angulaire entre l'impulsion du jet et le vecteur de l'énergie transverse manquante, $\Delta\phi(j_i, \boldsymbol{p}_{\mathrm{T}}^{\mathrm{miss}})_{\,\mathrm{min}}$, sont utilises pour améliorer la séparation entre le signal et le bruit du fond. Dans la stratégie MB-fit, au lieu de couper sur ces variables pour définir une région du signal, on construit de régions orthogonales en tranchant l'espace de phase en trois dimensions: le nombre des jets, la masse efficace et la significance de l'énergie transverse manquante. Ces régions étant-elles orthogonales, elles peuvent être combinées à l'ajustement statistique pour augmenter la portée de l'exclusion des modèles supersymétriques. Grâce à cette configuration, le gain attendu en la section efficace exclue a été estimée à 40-70%, par opposition à l'approche traditionnelle "cut & count", en même temps que la masse exclue est attendu à être améliorée par 50 - 100 GeV.

Une estimation du bruit du fond dans les régions du signal doit être effectuée, afin de comparer le nombre des événements mesuré à celui attendu. Pour ce faire, on utilise la simulation Monte Carlo pour les processus Z+jets, W+jets, $t\bar{t}$ et single-t et diboson, sauf pour le composant multijet, où on utilise une méthode base sure les données. Afin d'améliorer notre estimation, on construit des régions du contrôle, qui sont orthogonales au régions du signal et sont enrichies en un des composants du bruit du fond. Les processus Z+jets sont estimés dans les régions du type CRY, qui sont construites en utilisant un sample γ+jets, le composants W+jets et Top sont approximés par des événements W($\rightarrow ll$) + jets, avec $l = e, \mu$, en demandant dans la première cas un b-veto (CRW) et dans l'autre un b-tag (CRT). Le bruit du fond au cause des événements multi-jet est estimé dans les régions CRQ, où les coupures de la région du signal sur les variables $E_{\mathrm{T}}^{\mathrm{miss}}/\sqrt{H_T}$ et $\Delta\phi(j_i, \boldsymbol{p}_{\mathrm{T}}^{\mathrm{miss}})_{\,\mathrm{min}}$ sont renversées. Finalement, le composant diboson est estimé purement de la simulation Monte Carlo. Afin d'augmenter le nombre des événements en cas de l'ajustement MB, les régions du contrôle sont tranchées juste en deux dimensions, le nombre des jets et la masse efficace. En chaque région du contrôle, on extrait un facteur de normalisation μ_{bkg}, en comparant le nombre des événements prévues par la simulation au nombre des données, qui est utilisé pour améliorer l'estimation du bruit du fond dans la région du signal. Afin de vérifier qu'il existe aucun biais dans l'extrapolation du bruit du fond de la région de contrôle à la région du signal, on définit des régions supplémentaires et intermédiaires, nommées régions de validation (VR). Pour ma partie, j'ai travaillé sur l'implémentation d'un groupe spéciale des régions de validation, les VRs 0-lepton ou VR0L. Ces régions sont construites dans le même espace de phase de la région du signal et la CRQ et valident simultanément tous les composants du bruit du fond. On valide l'extrapolation en deux dimensions, en rétablissant soit la coupe de la région du signal sur $E_{\mathrm{T}}^{\mathrm{miss}}/\sqrt{H_T}$ (régions VR0LmetSig) soit la coupe sur $\Delta\phi(j_i, \boldsymbol{p}_{\mathrm{T}}^{\mathrm{miss}})_{\,\mathrm{min}}$ (régions VR0LdPhi).

La puissance de l'analyse est limitée par des incertitudes en raison des limitations statistiques ou systématiques. Dans la deuxième catégorie, on inclue des incertitudes de la modélisation de la simulation Monte Carlo pour les bruits du fond ou le signal et des incertitudes expérimentales. Dans le cadre de mon travail, j'ai calculé le trois majeures contributions à l'incertitude expérimentale, c'est-à-dire l'incertitude à l'échelle et la résolution de l'énergie des jets et l'énergie transverse manquante (JES, JER et MET). J'ai trouvé que les incertitudes expérimentales s'élèvent

à moins de 30% dans la plupart des cas. J'ai aussi estimé les incertitudes théorétiques liés à la modélisation des processus du bruit du fond $t\bar{t}$ et single-t. Les incertitudes systématiques sont incorporées dans l'ajustement via paramètres de nuisance.

Avant la normalisation du bruit du fond, on a observé que la simulation Monte Carlo pour le composant $t\bar{t}$ et single-t surprend les données avec l'augmentation de la masse efficace en la région CRT. Cette mauvaise modélisation doit être prise en compte dans la stratégie de normalisation de la ajustement Multi-bin. Afin de choisir la meilleure stratégie de normalisation, j'ai testé des configurations différents, en passant d'un binning des facteurs de normalisation minimal, où j'utilise un facteur global pour tous les bins de chaque composant du bruit du fond, à un binning plus fine, où chaque bin de la région du contrôle est associé avec un différent facteur. Pour chaque cas, j'ai estimé la mauvaise modélisation résiduelle en regardant la désaccord entre données et simulation dans les régions de validation et la désaccord entre les valeurs des paramètres de nuisance avant et après l'ajustement. Naturellement, la dernière option couvre la mauvaise modélisation mais est plus conservative, car les facteurs de normalisation sont calculés avec moins de statistiques. J'ai trouvé le binning optimal afin de corriger la désaccord tout en gardant des statistiques aussi élevées que possible; les composants V+jets sont normalisés en utilisant un facteur par tranche de nombre des jets et pour les composants Top et multijet ont utilise le binning complet 2-dimensionnel des régions CRT et CRQ.

Aucun excès au-delà des prédictions du Modèle Standard n'a été trouvé, et, par conséquent, on extrait des limites sur les modèles supersymétriques simplifies. Les squarks et les gluinos possédant des masses allant respectivement jusqu'à 1.85 TeV et 2.35 TeV ont été exclus en modèles où ils sont produits en paires et désintègrent directement en neutralinos sans masse et jets. Des limites similaires sont observes pour les gluinos en cas la désintégration passe par un chargino intermédiaire, tandis que pour les squarks, ce limite est réduit à 1.3 TeV. Ces résultats portent une amélioration significative par rapport au cycle précédent de l'analyse, et sont l'une des contraintes les plus fortes sur les masses actuelles des squarks et des gluinos.

C.2 Participation au développement du Détecteur de temps fortement segmenté

Le Grand Collisionneur de Hadrons à Haute Luminosité (HL-LHC) est la seconde phase du programme du LHC, qui est prévu de commencer en 2026. Le principal objectif du HL-LHC est d'augmenter la luminosité instantanée par un facteur de 5, afin d'augmenter la statistique disponible pour les analyses de physique. En vue de cette transition, toutes les expériences du LHC, dont l'expérience ATLAS, doivent moderniser leurs systèmes de détection et acquisition pour s'adapter à ces nouvelles conditions. L'un des principaux challenges du HL-LHC est l'augmentation de l'empilement, qui sont les interactions secondaires autour de l'interaction principale d'intérêt rendant cette dernière difficile à mesurer. Afin de réduire l'impact des particules de l'empilement sur la performance du détecteur, l'expérience ATLAS envisage la remplacement de l'ID par un nouveau trajectoire Interne entièrement constitue de capteurs en silicium, le ITk, ainsi que l'installation d'un nouveau détecteur très granulaire avec une excellente résolution en temps pour la phase de prise de données HL-LHC.

Si la distance entre une interaction de signal et une interaction d'empilement est inférieure à la résolution du trajectographe, ces deux interactions seront indiscernables et les objets de signal risquent donc d'être contaminés par l'empilement. Ceci est particulièrement vrai vers l'avant du détecteur où la résolution du trajectographe est moins bonne. Pour remédier a ce problème, on peut utiliser une précise mesure du temps des différentes interactions, qui est décorrélée de la position, pour aider à la séparation des interactions et supprimer la

contamination des objets par l'empilement. L'expérience ATLAS réalisera ce concept avec l'introduction d'un nouveau détecteur, le Détecteur de temps fortement segmenté (HGTD).

Ce nouveau détecteur sera installe avant le début du HL-LHC, devant les bouchons de chaque coté d'ATLAS. Pour chaque bouchon deux couches seront installées, instrumentes par détecteurs au silicium sur les deux faces. L'objectif est d'atteindre une résolution en temps meilleure de 30 (50) ps pour les traces pendant la phase initiale (finale) du détecteur. Ce bout peut être atteint en utilisant des détecteurs à avalanche de faible gain (LGADs). Les LGADs sont des détecteurs au silicium optimisés pour des mesures temporelles de haute précision, grâce à leur système d'amplification interne et leur grande vitesse. Le système de lecture électronique initial doit profite de ces attributs des capteurs LGAD. Pour l'HGTD, un chip optimisé pour minimiser la contribution électronique sur la résolution en temps, l'ALTIROC, a été développé, et j'ai travaillé sur la caractérisation de deux premiers prototypes.

C.2.1 Études de l'occupation et optimisation de l'organisation de la région active

L'occupation du détecteur, c'est à dire la fraction des éléments de détection qui sont activés à chaque événement, est une paramètre très importante pour un détecteur. Pour l'HGTD, on voudrait une occupation modeste, afin d'être capable à associer les coups au traces provenant de l'ITk. Un valeur de 10% a été placé comme limite pour le design du détecteur. J'ai étudie l'occupation du HGTD en utilisant la simulation Monte Carlo avec des échantillons "minimum bias", où le nombre des interactions d'empilement est en moyenne 200, comme attendu au HL-LHC. En première étape, j'ai estimé l'occupation comme fonction du rayon des couches du HGTD et pour des tailles différentes des capteurs: $1\times$ 1, 1.3 $\times$ 1.3 ou $2\times$ 2 mm^2. L'occupation est fortement liée au rayon dans une couche, avec la plus grande valeur dans la partie interne du détecteur. L'option des grands capteurs ($2\times$ 2 mm^2) a été rejetée parceque l'occupation surpasse la limite de 10% pour des petites valeurs du rayon. Finalement, la taille de 1.3 $\times$ 1.3 mm^2 a été choisie, afin d'avoir de l'espace suffisant pour les composantes électroniques de lecture.

A partir de l'occupation, j'ai aussi calculé la bande passante nécessaire pour la lecture des données et la puissance consommée par les capteurs et les électroniques "front-end" du HGTD. Les données produites par les éléments de détection sont envoyées par des câbles-flexibles à l'extérieur du détecteur, où elles sont organisées et préparées pour transmission optique en cartes périphériques. A cause de l'espace limité, l'optimisation du nombre d'éléments de transportation et d'organisation des données est cruciale pour le HGTD. Pour minimiser le nombre des câbles-flexibles, j'ai fait correspondre la vitesse de transportation à la bande passante moyenne pour chaque ASIC; pour les ASICs avec R<220 mm, des câbles avec une vitesse de 1280 Mbps sont nécessaires, tandis que ce besoin est réduit a 640 Mbps pour ASICs entre 220 mm $< R <$ 405 mm et a 320 Mbps pour ASICs avec R> 405 mm. Les données qui arrivent sur les cartes périphériques sont regroupées et sérialisées dans les chips low power Gigabit Tranceivers (lpGBTs) - plusieurs câbles-flexibles peuvent être connectés dans un lpGBT, le nombre des entrées dépends de la vitesse de transmission. J'ai optimisé la regroupement des données dans les lpGBTs pour minimiser le nombre de ces derniers. J'ai montré que, en imaginant une configuration avec des grandes cartes périphériques qui lisent plusieurs files d'ASICs, le nombre des composants (lpGBTs et câbles optiques) est réduit de 20% par opposition à une approche où chaque fille est lu par une carte périphérique différente.

Pendant la déroulement de ma thèse, des nouveaux contraintes sur la dose de la irradiation maximale des capteurs et l'espace disponible sur les cartes périphériques ont été dévoilés, rendrant nécessaire une re-optimisation de la géométrie du HGTD. Les études précédentes ont été réalisées avec une simulation du détecteur GEANT4. Tandis que ce type de simulation est

très détaillé, son utilisation est un long processus. Afin de réduire le temps j'ai développé une simulation simplifiée, où seulement l'HGTD est implémenté, il n'y a pas de champs magnétique et l'interaction des particules avec la matière de détection n'est pas simulée en détail. Ce simulation simplifié surestime le nombre moyen de coups par trace par un facteur de 7%, qui est pris en compte pour les calculs suivants. Pour assurer que les capteurs LGAD survivent pendant la vie du HGTD avec la nouvelle tolérance à l'irradiation, on doit passer par une configuration de remplacement en deux anneaux en une configuration avec trois anneaux par couche. Pour compenser l'effet de la dose reçue qui est plus élevée a l'intérieur du détecteur, on veut obtenir 3 coups par trace à petit rayon et deux à rayon plus grande. Pour ce faire on utilise le fait que le détecteur est composé des couches double face avec des pixels à chaque coté. En utilisant la simulation simplifiée, j'ai optimisé la recouvrement des pixels entre les deux faces des couches; j'ai montré qu'une recouvrement de 74% pour R$<$ 230 mm, 54% pour 230 mm $< R <$ 470 mm et 20% pour l'anneau avec R$>$ 470 mm est optimale pour donner un nombre suffisant des coups par trace et maintenir une résolution temporelle par trace meilleure que 50 ps pour la vie du HGTD. J'ai aussi re-optimiser l'organisation des modules en filles, afin de distribuer plus uniformément les données à les cartes périphériques.

C.2.2 Caractérisation d'ALTIROC

Un prototype d'électronique front-end analogique pour des mesures de temps de précision en picoseconde avec des capteurs LGAD a été conçu pour répondre aux exigences élevées du HGTD. Deux versions du prototype, ALTIROC0 et ALTIROC1, ont été largement caractérisées avec des signaux d'étalonnage et des particules de faisceau au cours de cette thèse.

Grâce aux mesures d'étalonnage avec ALTIROC0, les différentes contributions à la résolution temporelle, ainsi que le comportement de l'ASIC dans différentes conditions, ont été étudiés. La contribution de la gigue à la résolution temporelle, soit uniquement avec l'ASIC, soit avec un module composé de l'ASIC et d'un capteur LGAD, est meilleure que 20 ps pour une charge supérieure à 5 fC. Une amélioration de 6% de la gigue de l'ASIC pour Q $_{inj}$ = 10fC a été obtenue lors des mesures à T = $-30\,^{\circ}\mathrm{C}$, qui sera autour de la température de fonctionnement pour le HGTD. Dans les tests avec des modules constitués de l'ASIC lié au capteur, il été observé que la mesure du temps de dépassement du seuil est discrète, ce qui a empêché l'utilisation de cette variable pour la correction de la marche temporelle. L'amplitude de la sonde du préamplificateur a été utilisée à la place, tandis que des cartes modifiées avec un bloc HV en forme de L ont été fabriquées pour investiguer l'origine du problème. Dans tous les cas, la marche temporelle peut être corrigée jusqu'au niveau requis de 10%. Des mesures de faisceaux avec un faisceau de pions au CERN ont également été entreprises pour évaluer les performances du module ALTIROC0 avec des impulsions LGAD. Les modules testés ont fonctionné à une haute tension de -120 V, résultant en une charge la plus probable de $\sim$ 20 fC et un courant de fuite de O(10 $^{-2}$) µA. Une résolution temporelle supérieure à 40 ps a été obtenue pour tous les canaux après correction de la marche temporelle, tandis que la meilleure performance obtenue était de 34.7 $\pm$ 1 ps. Cette valeur est compatible avec la somme quadratique de la gigue estimée, du résidu de la correction de la marche temporelle et des contributions du capteur à la résolution temporelle. La résolution temporelle a été répartie uniformément dans la majeure partie du capteur et l'efficacité s'est avérée supérieure à 95% pour tous les canaux testés.

La deuxième itération de l'ASIC, ALTIROC1, a introduit les parties restantes de la lecture frontale analogique, c'est a dire le TDC et les blocs de mémoire pour chaque canal. Elle a également intégré 25 canaux, se rapprochant de la taille finale de la matrice de pixels. Dans un premier temps, l'étalonnage du TDC a été effectué afin d'estimer la valeur de bit le moins significatif de chaque canal. La valeur moyenne a été estimée être de 19.2 ps, proche de la

valeur de conception de 20 ps, et une bonne uniformité entre les canaux a été observée. En laboratoire, le seuil minimal atteint était de 3 fC, le plateau d'efficacité étant atteint avant 4 fC. Cela prouve la faisabilité d'une mesure du temps au point d'irradiation le plus élevé pendant la durée de vie du HGTD. Les études de performance temporelle ont été répétées de la même manière que ALTIROC0. La gigue s'est avérée être d'environ 40 ps pour 4 fC et diminuant rapidement à moins de 20 ps pour un $Q_{inj} \geq 10$ fC. Une légère augmentation de la gigue est observée par rapport à ALTIROC0, ce qui pourrait être dû au TDC et à la contribution d'horloge et à la pire précision de l'impulsion de référence fournie par le pulser interne. Dans ALTIROC1, le bloc HV en forme de L était l'option par défaut, mais le comportement discret du temps de chute du discriminateur n'était pas entièrement atténué. Les résultats du faisceau de test à DESY avec des électrons de 5 GeV ont également été réalisés pour évaluer la performance du module avec des particules réelles. Il a été observé que le niveau de bruit était plus élevé avec le faisceau qu'en laboratoire, ce qui a conduit à l'utilisation de seuils plus élevés. La meilleure performance obtenue était de 52.2 $\pm$ 1.4 ps après correction de la marche temporelle avec le TOT dans un intervalle de charge réduit où le TOT est continu. En supposant une contribution Landau de 25 ps, la contribution restante est estimée à environ 46 ps. Ce composant résulte de l'effet combiné de la gigue, du TDC et de l'horloge. Une performance similaire a été obtenue avec la correction de la marche temporelle avec la sonde préamplificateur.

Bibliography

[1] M. Tanabashi *et al.* "Review of Particle Physics". In: *Phys. Rev.* D **98**, 030001 (2018). DOI: https://doi.org/10.1103/PhysRevD.98.030001.

[2] Michael E Peskin and Daniel V Schroeder. *An introduction to quantum field theory*. Boulder, CO: Westview, 1995. URL: https://cds.cern.ch/record/257493.

[3] ATLAS Collaboration. "Observation of a new particle in the search for the Standard Model Higgs boson with the ATLAS detector at the LHC". In: *Phys. Lett. B* 716 (2012), p. 1. DOI: 10.1016/j.physletb.2012.08.020. arXiv: 1207.7214 [hep-ex].

[4] CMS Collaboration. "Observation of a new boson at a mass of 125 GeV with the CMS experiment at the LHC". In: *Phys. Lett. B* 716 (2012), p. 30. DOI: 10.1016/j.physletb.2012.08.021. arXiv: 1207.7235 [hep-ex].

[5] Raymond Davis, Don S. Harmer, and Kenneth C. Hoffman. "Search for Neutrinos from the Sun". In: *Phys. Rev. Lett.* 20 (21 1968), pp. 1205–1209. DOI: 10.1103/PhysRevLett.20.1205. URL: https://link.aps.org/doi/10.1103/PhysRevLett.20.1205.

[6] Y. et al. (Super-Kamiokande Collaboration) Fukuda. "Evidence for Oscillation of Atmospheric Neutrinos". In: *Phys. Rev. Lett.* 81 (8 1998), pp. 1562–1567. DOI: 10.1103/PhysRevLett.81.1562. URL: https://link.aps.org/doi/10.1103/PhysRevLett.81.1562.

[7] Y. et al. (Double Chooz Collaboration) Abe. "Indication of Reactor $\overline{\nu}_e$ Disappearance in the Double Chooz Experiment". In: *Phys. Rev. Lett.* 108 (13 2012), p. 131801. DOI: 10.1103/PhysRevLett.108.131801. URL: https://link.aps.org/doi/10.1103/PhysRevLett.108.131801.

[8] Abdus Salam and John Clive Ward. "Weak and electromagnetic interactions". In: *Nuovo Cim. 11* 568-577 (1959). DOI: 10.1007/BF02726525.

[9] C. S. Wu et al. "Experimental Test of Parity Conservation in Beta Decay". In: *Phys. Rev.* 105 (4 1957), pp. 1413–1415. DOI: 10.1103/PhysRev.105.1413. URL: https://link.aps.org/doi/10.1103/PhysRev.105.1413.

[10] M. Banner et al. "Observation of single isolated electrons of high transverse momentum in events with missing transverse energy at the CERN pp collider". In: *Physics Letters B* 122.5 (1983), pp. 476 –485. ISSN: 0370-2693. DOI: https://doi.org/10.1016/0370-2693(83)91605-2. URL: http://www.sciencedirect.com/science/article/pii/0370269383916052.

[11] G. Arnison et al. "Experimental observation of lepton pairs of invariant mass around 95 GeV/c2 at the CERN SPS collider". In: *Physics Letters B* 126.5 (1983), pp. 398 –410. ISSN: 0370-2693. DOI: https://doi.org/10.1016/0370-2693(83)90188-0. URL: http://www.sciencedirect.com/science/article/pii/0370269383901880.

[12] F. Englert and R. Brout. "Broken symmetry and the mass of gauge vector mesons". In: *Phys. Rev. Lett.* 13 (1964), pp. 321–323. DOI: 10.1103/PhysRevLett.13.321.

[13] Peter W. Higgs. "Broken symmetries and the masses of gauge bosons". In: *Phys. Rev. Lett.* 13 (1964), pp. 508–509. DOI: 10.1103/PhysRevLett.13.508.

[14] Paul H Frampton et al. "Primordial black holes as all dark matter". In: *Journal of Cosmology and Astroparticle Physics* 2010.04 (2010), pp. 023–023. DOI: 10.1088/1475-7516/2010/04/023. URL: https://doi.org/10.1088%2F1475-7516%2F2010%2F04%2F023.

[15] Sebastien Clesse and Juan Garcia-Bellido. "Seven hints for primordial black hole dark matter". In: *Physics of the Dark Universe* 22 (2018), pp. 137 –146. ISSN: 2212-6864. DOI: https://doi.org/10.1016/j.dark.2018.08.004. URL: http://www.sciencedirect.com/science/article/pii/S2212686418301250.

[16] Andrei D Sakharov. "Violation of CP invariance, C asymmetry, and baryon asymmetry of the universe". In: *Soviet Physics Uspekhi* 34.5 (1991), pp. 392–393. DOI: 10.1070/pu1991v034n05abeh002497.

[17] Stephen P. Martin. "A Supersymmetry primer". In: *Adv. Ser. Direct. High Energy Phys.* 18 (1998), p. 1. DOI: 10.1142/9789812839657_0001,10.1142/9789814307505_0001. arXiv: hep-ph/9709356.

[18] Yu.A. Golfand and E.P. Likhtman. "Extension of the Algebra of Poincare Group Generators and Violation of p Invariance". In: *JETP Lett.* 13 (1971), pp. 323–326.

[19] J.-L. Gervais and B. Sakita. "Field theory interpretation of supergauges in dual models". In: *Nuclear Physics B* 34.2 (1971), pp. 632 –639. ISSN: 0550-3213. DOI: https://doi.org/10.1016/0550-3213(71)90351-8. URL: http://www.sciencedirect.com/science/article/pii/0550321371903518.

[20] D. V. Volkov and V. P. Akulov. "Is the Neutrino a Goldstone Particle?" In: *Phys. Lett. B* 46 (1973), p. 109. DOI: 10.1016/0370-2693(73)90490-5.

[21] Ian Aitchison. "Supersymmetry and the MSSM: An Elementary Introduction". In: (June 2005).

[22] H. Nishino et al. (Super-Kamiokande Collaboration). "Search for Proton Decay via $p \to e^+\pi^0$ and $p \to \mu^+\pi^0$ in a Large Water Cherenkov Detector". In: *Phys. Rev. Lett.* 102 (14 2009), p. 141801. DOI: 10.1103/PhysRevLett.102.141801. URL: https://link.aps.org/doi/10.1103/PhysRevLett.102.141801.

[23] Rabindra N. Mohapatra. "Supersymmetry and R-parity: an Overview". In: vol. 90. June 2015, p. 088004. DOI: 10.1088/0031-8949/90/8/088004. arXiv: 1503.06478 [hep-ph].

[24] Stephen P. Martin. "Some simple criteria for gauged R parity". In: *Phys. Rev. D* 46 (7 1992), R2769–R2772. DOI: 10.1103/PhysRevD.46.R2769. URL: https://link.aps.org/doi/10.1103/PhysRevD.46.R2769.

[25] Stephen P. Martin. "Implications of supersymmetric models with natural R-parity conservation". In: *Phys. Rev. D* 54 (3 1996), pp. 2340–2348. DOI: 10.1103/PhysRevD.54.2340. URL: https://link.aps.org/doi/10.1103/PhysRevD.54.2340.

[26] F. Gabbiani et al. "A complete analysis of FCNC and CP constraints in general SUSY extensions of the standard model". In: *Nuclear Physics B* 477.2 (1996), pp. 321 –352. ISSN: 0550-3213. DOI: https://doi.org/10.1016/0550-3213(96)00390-2. URL: http://www.sciencedirect.com/science/article/pii/0550321396003902.

[27] Ali H. Chamseddine, Richard L. Arnowitt, and Pran Nath. "Locally Supersymmetric Grand Unification". In: *Phys. Rev. Lett.* 49 (1982), p. 970. DOI: 10.1103/PhysRevLett.49.970.

[28] G.F. Giudice and R. Rattazzi. "Theories with gauge-mediated supersymmetry breaking". In: *Physics Reports* 322.6 (1999), pp. 419 –499. ISSN: 0370-1573. DOI: https://doi.org/10.1016/S0370-1573(99)00042-3. URL: http://www.sciencedirect.com/science/article/pii/S0370157399000423.

[29] ATLAS Collaboration. "Summary of the ATLAS experiment's sensitivity to supersymmetry after LHC Run 1 — interpreted in the phenomenological MSSM". In: *JHEP* 10 (2015), p. 134. DOI: 10.1007/JHEP10(2015)134. arXiv: 1508.06608 [hep-ex].

[30] Johan Alwall, Philip Schuster, and Natalia Toro. "Simplified Models for a First Characterization of New Physics at the LHC". In: *Phys. Rev. D* 79 (2009), p. 075020. DOI: 10.1103/PhysRevD.79.075020. arXiv: 0810.3921 [hep-ph].

[31] Daniele Alves et al. "Simplified Models for LHC New Physics Searches". In: *J. Phys. G* 39 (2012), p. 105005. DOI: 10.1088/0954-3899/39/10/105005. arXiv: 1105.2838 [hep-ph].

[32] W. Beenakker et al. "Squark and gluino production at hadron colliders". In: *Nucl. Phys. B* 492 (1997), p. 51. DOI: 10.1016/S0550-3213(97)00084-9. arXiv: hep-ph/9610490.

[33] W. Beenakker et al. "Stop production at hadron colliders". In: *Nucl. Phys. B* 515 (1998), p. 3. eprint: hep-ph/9710451.

[34] *Public Results - LHC SUSY Cross Section Working Group*. URL: https://twiki.cern.ch/twiki/bin/view/LHCPhysics/SUSYCrossSections.

[35] Christoph Borschensky et al. "Squark and gluino production cross sections in pp collisions at $\sqrt{s} = 13, 14, 33$ and 100 TeV". In: *Eur. Phys. J. C* 74 (2014), p. 3174. DOI: 10.1140/epjc/s10052-014-3174-y. arXiv: 1407.5066 [hep-ph].

[36] *LHC Higgs Cross Section Working Group*. URL: https://twiki.cern.ch/twiki/bin/view/LHCPhysics/LHCHXSWG.

[37] ATLAS Collaboration. "Search for squarks and gluinos in final states with jets and missing transverse momentum using 36 fb^{-1} of $\sqrt{s} = 13$ TeV pp collision data with the ATLAS detector". In: *Phys. Rev. D* 97 (2018), p. 112001. DOI: 10.1103/PhysRevD.97.112001. arXiv: 1712.02332 [hep-ex].

[38] Lyndon Evans and Philip Bryant. "LHC Machine". In: *JINST* 3 (2008), S08001. DOI: 10.1088/1748-0221/3/08/S08001.

[39] *The CERN accelerator complex - August 2018. Complexe des accélérateurs du CERN - Août 2018*. URL: https://cds.cern.ch/record/2636343.

[40] ATLAS Collaboration. "The ATLAS Experiment at the CERN Large Hadron Collider". In: *JINST* 3 (2008), S08003. DOI: 10.1088/1748-0221/3/08/S08003.

[41] CMS Collaboration. "The CMS experiment at the CERN LHC". In: *JINST* 3 (2008), S08004. DOI: 10.1088/1748-0221/3/08/S08004.

[42] K. Aamodt et al. "The ALICE experiment at the CERN LHC". In: *JINST* 3 (2008), S08002. DOI: 10.1088/1748-0221/3/08/S08002.

[43] Jr. Alves A.Augusto et al. "The LHCb Detector at the LHC". In: *JINST* 3 (2008), S08005. DOI: 10.1088/1748-0221/3/08/S08005.

[44] The ATLAS collaboration. "Luminosity determination in pp collisions at $\sqrt{s} = 13$ TeV using the ATLAS detector at the LHC". In: (2019).

[45] G. Avoni et al. "The new LUCID-2 detector for luminosity measurement and monitoring in ATLAS". In: *JINST* 13.07 (2018), P07017. DOI: 10.1088/1748-0221/13/07/P07017.

[46] V. Cindro et al. "The ATLAS beam conditions monitor". In: *JINST* 3 (2008), P02004. DOI: 10.1088/1748-0221/3/02/P02004.

[47] P. Grafstrom and W. Kozanecki. "Luminosity determination at proton colliders". In: *Prog. Part. Nucl. Phys.* 81 (2015), pp. 97–148. DOI: 10.1016/j.ppnp.2014.11.002.

[48] *ATLAS Luminosity Public Results Run2*. URL: https://twiki.cern.ch/twiki/bin/view/AtlasPublic/LuminosityPublicResultsRun2.

[49] ATLAS Collaboration. "The ATLAS Inner Detector commissioning and calibration". In: *Eur. Phys. J. C* 70 (2010), p. 787. DOI: 10.1140/epjc/s10052-010-1366-7. arXiv: 1004.5293 [hep-ex].

[50] ATLAS Collaboration. "Studies of the performance of the ATLAS detector using cosmic-ray muons". In: *Eur. Phys. J. C* 71 (2011), p. 1593. DOI: 10.1140/epjc/s10052-011-1593-6. arXiv: 1011.6665 [hep-ex].

[51] M. Capeans et al. "ATLAS Insertable B-Layer Technical Design Report". In: (Sept. 2010).

[52] Yosuke Takubo. "ATLAS IBL operational experience". In: *PoS* Vertex2016 (2017), p. 004. DOI: 10.22323/1.287.0004.

[53] ATLAS Collaboration. "ATLAS liquid argon calorimeter: Technical design report". In: (Dec. 1996).

[54] Morad Aaboud et al. "Electron and photon energy calibration with the ATLAS detector using 2015-2016 LHC proton-proton collision data". In: *JINST* 14.03 (2019), P03017. DOI: 10.1088/1748-0221/14/03/P03017. arXiv: 1812.03848 [hep-ex].

[55] ATLAS Collaboration. "ATLAS tile calorimeter: Technical design report". In: (Dec. 1996).

[56] P. Adragna et al. "Testbeam studies of production modules of the ATLAS tile calorimeter". In: *Nucl. Instrum. Meth. A* 606 (2009), pp. 362–394. DOI: 10.1016/j.nima.2009.04.009.

[57] A. Artamonov et al. "The ATLAS forward calorimeters". In: *JINST* 3 (2008), P02010. DOI: 10.1088/1748-0221/3/02/P02010.

[58] A.Ruiz Martinez. "The Run-2 ATLAS Trigger System". In: *J. Phys. Conf. Ser.* 762.1 (2016). Ed. by Luis Salinas and Claudio Torres, p. 012003. DOI: 10.1088/1742-6596/762/1/012003.

[59] ATLAS Collaboration. "Performance of the ATLAS track reconstruction algorithms in dense environments in LHC Run 2". In: *Eur. Phys. J. C* 77 (2017), p. 673. DOI: 10.1140/epjc/s10052-017-5225-7. arXiv: 1704.07983 [hep-ex].

[60] R. Fruhwirth. "Application of Kalman filtering to track and vertex fitting". In: *Nuclear Instruments and Methods in Physics Research Section A: Accelerators, Spectrometers, Detectors and Associated Equipment* 262.2 (1987), pp. 444 –450. ISSN: 0168-9002. DOI: https://doi.org/10.1016/0168-9002(87)90887-4. URL: http://www.sciencedirect.com/science/article/pii/0168900287908874.

[61] ATLAS Collaboration. "Reconstruction of primary vertices at the ATLAS experiment in Run 1 proton–proton collisions at the LHC". In: *Eur. Phys. J. C* 77 (2017), p. 332. DOI: 10.1140/epjc/s10052-017-4887-5. arXiv: 1611.10235 [hep-ex].

[62] Morad Aaboud et al. "Electron reconstruction and identification in the ATLAS experiment using the 2015 and 2016 LHC proton-proton collision data at $\sqrt{s}$ = 13 TeV". In: *Eur. Phys. J. C* 79.8 (2019), p. 639. DOI: 10.1140/epjc/s10052-019-7140-6. arXiv: 1902.04655 [physics.ins-det].

[63] Morad Aaboud et al. "Measurement of the photon identification efficiencies with the ATLAS detector using LHC Run 2 data collected in 2015 and 2016". In: *Eur. Phys. J. C* 79.3 (2019), p. 205. DOI: 10.1140/epjc/s10052-019-6650-6. arXiv: 1810.05087 [hep-ex].

[64] ATLAS Collaboration. "Muon reconstruction performance of the ATLAS detector in proton–proton collision data at $\sqrt{s} = 13$ TeV". In: *Eur. Phys. J. C* 76 (2016), p. 292. DOI: 10.1140/epjc/s10052-016-4120-y. arXiv: 1603.05598 [hep-ex].

[65] ATLAS Collaboration. "Topological cell clustering in the ATLAS calorimeters and its performance in LHC Run 1". In: *Eur. Phys. J. C* 77 (2017), p. 490. DOI: 10.1140/epjc/s10052-017-5004-5. arXiv: 1603.02934 [hep-ex].

[66] Matteo Cacciari, Gavin P. Salam, and Gregory Soyez. "The anti-k_t jet clustering algorithm". In: *JHEP* 04 (2008), p. 063. DOI: 10.1088/1126-6708/2008/04/063. arXiv: 0802.1189 [hep-ph].

[67] ATLAS Collaboration. "Measurements of b-jet tagging efficiency with the ATLAS detector using $t\bar{t}$ events at $\sqrt{s} = 13$ TeV". In: *JHEP* 08 (2018), p. 089. DOI: 10.1007/JHEP08(2018)089. arXiv: 1805.01845 [hep-ex].

[68] Andreas Hoecker et al. *TMVA - Toolkit for Multivariate Data Analysis*. 2007. arXiv: physics/0703039 [physics.data-an].

[69] ATLAS Collaboration. *Calibration of light-flavour b-jet mistagging rates using ATLAS proton–proton collision data at $\sqrt{s} = 13$ TeV*. ATLAS-CONF-2018-006. 2018. URL: https://cds.cern.ch/record/2314418.

[70] ATLAS Collaboration. "Jet energy scale measurements and their systematic uncertainties in proton–proton collisions at $\sqrt{s} = 13$ TeV with the ATLAS detector". In: *Phys. Rev. D* 96 (2017), p. 072002. DOI: 10.1103/PhysRevD.96.072002. arXiv: 1703.09665 [hep-ex].

[71] ATLAS Collaboration. "Jet reconstruction and performance using particle flow with the ATLAS Detector". In: *Eur. Phys. J. C* 77 (2017), p. 466. DOI: 10.1140/epjc/s10052-017-5031-2. arXiv: 1703.10485 [hep-ex].

[72] ATLAS Collaboration. "Performance of missing transverse momentum reconstruction with the ATLAS detector using proton–proton collisions at $\sqrt{s} = 13$ TeV". In: *Eur. Phys. J. C* 78 (2018), p. 903. DOI: 10.1140/epjc/s10052-018-6288-9. arXiv: 1802.08168 [hep-ex].

[73] "High-Luminosity Large Hadron Collider (HL-LHC): Technical Design Report V. 0.1". In: 4/2017 (Nov. 2017). Ed. by G. Apollinari et al. DOI: 10.23731/CYRM-2017-004.

[74] *The HL-LHC project*. URL: https://hilumilhc.web.cern.ch/content/hl-lhc-project.

[75] Andrea Dainese et al., eds. *Report on the Physics at the HL-LHC,and Perspectives for the HE-LHC*. Vol. 7/2019. CERN Yellow Reports: Monographs. Geneva, Switzerland: CERN, 2019. ISBN: 978-92-9083-549-3. DOI: 10.23731/CYRM-2019-007.

[76] ATLAS Collaboration. *Projections for measurements of Higgs boson cross sections, branching ratios, coupling parameters and mass with the ATLAS detector at the HL-LHC*. ATL-PHYS-PUB-2018-054. 2018. URL: https://cds.cern.ch/record/2652762.

[77] ATLAS Collaboration. *Measurement prospects of the pair production and self-coupling of the Higgs boson with the ATLAS experiment at the HL-LHC*. ATL-PHYS-PUB-2018-053. 2018. URL: https://cds.cern.ch/record/2652727.

[78] S. Schael et al. "Precision electroweak measurements on the Z resonance". In: *Phys. Rept.* 427 (2006), pp. 257–454. DOI: 10.1016/j.physrep.2005.12.006. arXiv: hep-ex/0509008.

[79] "A proposal for the measurement of the weak mixing angle at the HL-LHC". In: (Dec. 2017).

[80] ATLAS collaboration. "Evidence for $t\bar{t}t\bar{t}$ production in the multilepton final state in proton-proton collisions at $\sqrt{s} = 13$ TeV with the ATLAS detector". In: (June 2020).

[81] ATLAS Collaboration. *HL-LHC prospects for the measurement of the Standard Model four-top-quark production cross-section*. ATL-PHYS-PUB-2018-047. 2018. URL: https://cds.cern.ch/record/2651870.

[82] "Study of $W^{\pm}W^{\pm}$ production via vector boson scattering at the HL-LHC with the upgraded CMS detector". In: (Nov. 2018).

[83] ATLAS Collaboration. *Technical Design Report for the ATLAS Inner Tracker Pixel Detector*. Tech. rep. CERN-LHCC-2017-021. Geneva: CERN, 2018. URL: https://cds.cern.ch/record/2285585.

[84] ATLAS Collaboration. *Technical Design Report for the ATLAS Inner Tracker Strip Detector*. Tech. rep. CERN-LHCC-2017-005 ; ATLAS-TDR-025. CERN, 2017. URL: https://cds.cern.ch/record/2257755.

[85] ATLAS Collaboration. *Technical Proposal: A High-Granularity Timing Detector for the ATLAS Phase-II Upgrade*. Tech. rep. CERN-LHCC-2018-023. Geneva: CERN, 2018. URL: https://cds.cern.ch/record/2623663.

[86] M. Aleksa et al. "ATLAS Liquid Argon Calorimeter Phase-I Upgrade Technical Design Report". In: (Sept. 2013).

[87] ATLAS Collaboration. *Technical Design Report for the Phase-II Upgrade of the ATLAS LAr Calorimeter*. Tech. rep. CERN-LHCC-2017-018. ATLAS-TDR-027. Geneva: CERN, 2017. URL: https://cds.cern.ch/record/2285582.

[88] Benoit Lefebvre. "Muon Spectrometer Phase-I Upgrade for the ATLAS Experiment: the New Small Wheel project". In: *13th Conference on the Intersections of Particle and Nuclear Physics*. Oct. 2018. arXiv: 1810.01394 [physics.ins-det].

[89] ATLAS Collaboration. *Technical Design Report for the Phase-II Upgrade of the ATLAS Muon Spectrometer*. Tech. rep. CERN-LHCC-2017-017. ATLAS-TDR-026. Geneva: CERN, 2017. URL: https://cds.cern.ch/record/2285580.

[90] ATLAS Collaboration. *Technical Design Report for the Phase-II Upgrade of the ATLAS Trigger and Data Acquisition System*. Tech. rep. CERN-LHCC-2017-020 ; ATLAS-TDR-029. CERN, 2017. URL: http://cds.cern.ch/record/2285584.

[91] Miguel Escudero et al. "Toward (Finally!) Ruling Out Z and Higgs Mediated Dark Matter Models". In: *JCAP* 12 (2016), p. 029. DOI: 10.1088/1475-7516/2016/12/029. arXiv: 1609.09079 [hep-ph].

[92] ATLAS Collaboration. "Search for squarks and gluinos with the ATLAS detector in final states with jets and missing transverse momentum using $\sqrt{s} = 8$ TeV proton–proton collision data". In: *JHEP* 09 (2014), p. 176. DOI: 10.1007/JHEP09(2014)176. arXiv: 1405.7875 [hep-ex].

[93] ATLAS Collaboration. *Search for new phenomena in final states with large jet multiplicities and missing transverse momentum using $\sqrt{s} = 13$ TeV proton-proton collisions recorded by ATLAS in Run 2 of the LHC*. ATLAS-CONF-2020-002. 2020. URL: https://cds.cern.ch/record/2710420.

[94] D.R. Tovey. "Measuring the SUSY mass scale at the LHC". In: *Phys. Lett. B* 498 (2001), pp. 1–10. DOI: 10.1016/S0370-2693(00)01363-0. arXiv: hep-ph/0006276.

[95] ATLAS Collaboration. "ATLAS data quality operations and performance for 2015-2018 data-taking". In: *JINST* 15 (2020), P04003. DOI: 10.1088/1748-0221/15/04/p04003. arXiv: 1911.04632 [physics.ins-det].

[96] ATLAS Collaboration. *Luminosity determination in pp collisions at $\sqrt{s} = 13$ TeV using the ATLAS detector at the LHC*. ATLAS-CONF-2019-021. 2019. URL: https://cds.cern.ch/record/2677054.

[97] T. Gleisberg et al. "Event generation with SHERPA 1.1". In: *JHEP* 02 (2009), p. 007. DOI: 10.1088/1126-6708/2009/02/007. arXiv: 0811.4622 [hep-ph].

[98] R. Gavin, Y. Li, F. Petriello and S. Quackenbush. "FEWZ 2.0: A code for hadronic Z production at next-to-next-to-leading order". In: *Comput. Phys. Commun.* 182 (2011), pp. 2388–2403. DOI: 10.1016/j.cpc.2011.06.008. arXiv: 1011.3540 [hep-ph].

[99] Richard D. Ball et al. "Parton distributions for the LHC Run II". In: *JHEP* 04 (2015), p. 040. DOI: 10.1007/JHEP04(2015)040. arXiv: 1410.8849 [hep-ph].

[100] Stefan Höche et al. "QCD matrix elements and truncated showers". In: *JHEP* 05 (2009), p. 053. DOI: 10.1088/1126-6708/2009/05/053. arXiv: 0903.1219 [hep-ph].

[101] Simone Alioli et al. "A general framework for implementing NLO calculations in shower Monte Carlo programs: the POWHEG BOX". In: *JHEP* 06 (2010), p. 043. DOI: 10.1007/JHEP06(2010)043. arXiv: 1002.2581 [hep-ph].

[102] Michał Czakon, Paul Fiedler, and Alexander Mitov. "Total Top-Quark Pair-Production Cross Section at Hadron Colliders Through $O(\alpha_S^4)$". In: *Phys. Rev. Lett.* 110 (2013), p. 252004. DOI: 10.1103/PhysRevLett.110.252004. arXiv: 1303.6254 [hep-ph].

[103] M. Czakon and A. Mitov. "Top++: A Program for the Calculation of the Top-Pair Cross-Section at Hadron Colliders". In: *Comput. Phys. Commun.* 185 (2014), p. 2930. DOI: 10.1016/j.cpc.2014.06.021. arXiv: 1112.5675 [hep-ph].

[104] Richard D. Ball et al. "Parton distributions with LHC data". In: *Nucl. Phys. B* 867 (2013), p. 244. DOI: 10.1016/j.nuclphysb.2012.10.003. arXiv: 1207.1303 [hep-ph].

[105] Torbjörn Sjöstrand et al. "An Introduction to PYTHIA 8.2". In: *Comput. Phys. Commun.* 191 (2015), p. 159. DOI: 10.1016/j.cpc.2015.01.024. arXiv: 1410.3012 [hep-ph].

[106] ATLAS Collaboration. *ATLAS Pythia 8 tunes to 7 TeV data*. ATL-PHYS-PUB-2014-021. 2014. URL: https://cds.cern.ch/record/1966419.

[107] Nikolaos Kidonakis. "Two-loop soft anomalous dimensions for single top quark associated production with a W- or H-". In: *Phys. Rev. D* 82 (2010), p. 054018. DOI: 10.1103/PhysRevD.82.054018. arXiv: 1005.4451 [hep-ph].

[108] Nikolaos Kidonakis. "Next-to-next-to-leading-order collinear and soft gluon corrections for t-channel single top quark production". In: *Phys. Rev. D* 83 (2011), p. 091503. DOI: 10.1103/PhysRevD.83.091503. arXiv: 1103.2792 [hep-ph].

[109] M. Aliev et al. "HATHOR: HAdronic Top and Heavy quarks crOss section calculatoR". In: *Comput. Phys. Commun.* 182 (2011), pp. 1034–1046. DOI: 10.1016/j.cpc.2010.12.040. arXiv: 1007.1327 [hep-ph].

[110] P. Kant et al. "HatHor for single top-quark production: Updated predictions and uncertainty estimates for single top-quark production in hadronic collisions". In: *Comput. Phys. Commun.* 191 (2015), pp. 74–89. DOI: 10.1016/j.cpc.2015.02.001. arXiv: 1406.4403 [hep-ph].

[111] J. Alwall et al. "The automated computation of tree-level and next-to-leading order differential cross sections, and their matching to parton shower simulations". In: *JHEP* 07 (2014), p. 079. DOI: 10.1007/JHEP07(2014)079. arXiv: 1405.0301 [hep-ph].

[112] A. Lazopoulos, T. McElmurry, K. Melnikov and F. Petriello. "Next-to-leading order QCD corrections to $t\bar{t}Z$ production at the LHC". In: *Phys. Lett. B* 666 (2008), pp. 62–65. DOI: 10.1016/j.physletb.2008.06.073. arXiv: 0804.2220 [hep-ph].

[113] John M. Campbell and R. Keith Ellis. "$t\bar{t}W^{\pm}$ production and decay at NLO". In: *JHEP* 07 (2012), p. 052. DOI: 10.1007/JHEP07(2012)052. arXiv: 1204.5678 [hep-ph].

[114] ATLAS Collaboration. "Summary of ATLAS Pythia 8 tunes". In: *ATL-PHYS-PUB-2012-003* (2012). URL: https://cdsweb.cern.ch/record/1474107.

[115] Wim Beenakker et al. "NNLL-fast: predictions for coloured supersymmetric particle production at the LHC with threshold and Coulomb resummation". In: *JHEP* 12 (2016), p. 133. DOI: 10.1007/JHEP12(2016)133. arXiv: 1607.07741 [hep-ph].

[116] Wim Beenakker et al. "NNLL resummation for squark and gluino production at the LHC". In: *JHEP* 12 (2014), p. 023. DOI: 10.1007/JHEP12(2014)023. arXiv: 1404.3134 [hep-ph].

[117] Wim Beenakker et al. "Towards NNLL resummation: hard matching coefficients for squark and gluino hadroproduction". In: *JHEP* 10 (2013), p. 120. DOI: 10.1007/JHEP10(2013)120. arXiv: 1304.6354 [hep-ph].

[118] Wim Beenakker et al. "NNLL resummation for squark-antisquark pair production at the LHC". In: *JHEP* 01 (2012), p. 076. DOI: 10.1007/JHEP01(2012)076. arXiv: 1110.2446 [hep-ph].

[119] Wim Beenakker et al. "Soft-gluon resummation for squark and gluino hadroproduction". In: *JHEP* 12 (2009), p. 041. DOI: 10.1088/1126-6708/2009/12/041. arXiv: 0909.4418 [hep-ph].

[120] A. Kulesza and L. Motyka. "Soft gluon resummation for the production of gluino-gluino and squark-antisquark pairs at the LHC". In: *Phys. Rev. D* 80 (2009), p. 095004. DOI: 10.1103/PhysRevD.80.095004. arXiv: 0905.4749 [hep-ph].

[121] A. Kulesza and L. Motyka. "Threshold resummation for squark-antisquark and gluino-pair production at the LHC". In: *Phys. Rev. Lett.* 102 (2009), p. 111802. DOI: 10.1103/PhysRevLett.102.111802. arXiv: 0807.2405 [hep-ph].

[122] ATLAS Collaboration. "The ATLAS Simulation Infrastructure". In: *Eur. Phys. J. C* 70 (2010), p. 823. DOI: 10.1140/epjc/s10052-010-1429-9. arXiv: 1005.4568 [physics.ins-det].

[123] S. Agostinelli et al. "GEANT4: A Simulation toolkit". In: *Nucl. Instrum. Meth. A* 506 (2003), p. 250. DOI: 10.1016/S0168-9002(03)01368-8.

[124] ATLAS Collaboration. *The simulation principle and performance of the ATLAS fast calorimeter simulation FastCaloSim*. ATL-PHYS-PUB-2010-013. 2010. URL: https://cds.cern.ch/record/1300517.

[125] ATLAS Collaboration. *Optimisation of the ATLAS b-tagging performance for the 2016 LHC Run*. ATL-PHYS-PUB-2016-012. 2016. URL: https://cds.cern.ch/record/2160731.

[126] ATLAS Collaboration. "Performance of b-Jet Identification in the ATLAS Experiment". In: *JINST* 11.04 (2016), P04008. DOI: 10.1088/1748-0221/11/04/P04008. arXiv: 1512.01094 [hep-ex].

[127] ATLAS Collaboration. "Muon reconstruction performance of the ATLAS detector in proton–proton collision data at $\sqrt{s}$ =13 TeV". In: *Eur. Phys. J. C* 76.5 (2016), p. 292. DOI: 10.1140/epjc/s10052-016-4120-y. arXiv: 1603.05598 [hep-ex].

[128] ATLAS Collaboration. "Electron and photon performance measurements with the ATLAS detector using the 2015-2017 LHC proton-proton collision data". In: *JINST* 14 (2019), P12006. DOI: 10.1088/1748-0221/14/12/P12006. arXiv: 1908.00005 [hep-ex].

[129] ATLAS Collaboration. "Measurement of the photon identification efficiencies with the ATLAS detector using LHC Run-1 data". In: *Eur. Phys. J. C* 76 (2016), p. 666. DOI: 10.1140/epjc/s10052-016-4507-9. arXiv: 1606.01813 [hep-ex].

[130] ATLAS Collaboration. "Measurement of the photon identification efficiencies with the ATLAS detector using LHC Run 2 data collected in 2015 and 2016". In: *Eur. Phys. J.* (2018). arXiv: 1810.05087 [hep-ex].

[131] "Search for squarks and gluinos in final states with jets and missing transverse momentum using 139 fb^{-1} of $\sqrt{s}$ =13 TeV pp collision data with the ATLAS detector". In: (Aug. 2019).

[132] ATLAS Collaboration. *E_T^{miss} performance in the ATLAS detector using 2015–2016 LHC pp collisions*. ATLAS-CONF-2018-023. 2018. URL: https://cds.cern.ch/record/2625233.

[133] James D. Bjorken and Stanley J. Brodsky. "Statistical Model for Electron-Positron Annihilation into Hadrons". In: *Phys. Rev. D* 1 (5 1970), pp. 1416–1420. DOI: 10.1103/PhysRevD.1.1416. URL: https://link.aps.org/doi/10.1103/PhysRevD.1.1416.

[134] Magerl V. "Searches for squarks and gluinos in supersymmetric scenarios including prompt and displaced decays in pp collisions at $\sqrt{s} = 13$ TeV with the ATLAS detector". PhD thesis. Freiburg University, 2019. DOI: 10.6094/UNIFR/165570.

[135] Gareth Thomas Fletcher. "Multijet Background Estimation For SUSY Searches And Particle Flow Offline Reconstruction Using The ATLAS Detector At The LHC". PhD thesis. Sheffield U., Mar. 2015.

[136] ATLAS Collaboration. *Improvements in $t\bar{t}$ modelling using NLO+PS Monte Carlo generators for Run 2*. ATL-PHYS-PUB-2018-009. 2018. URL: https://cds.cern.ch/record/2630327.

[137] Jerzy Neyman and Egon Sharpe Pearson. "On the Problem of the Most Efficient Tests of Statistical Hypotheses". In: *Phil. Trans. Roy. Soc. Lond. A* 231.694-706 (1933), pp. 289–337. DOI: 10.1098/rsta.1933.0009.

[138] Glen Cowan. *Statistical data analysis*. Oxford science publications. Oxford : New York: Clarendon Press ; Oxford University Press, 1998. ISBN: 9780198501565 9780198501558.

[139] S. S. Wilks. "The Large-Sample Distribution of the Likelihood Ratio for Testing Composite Hypotheses". In: *Ann. Math. Statist.* 9.1 (Mar. 1938), pp. 60–62. DOI: 10.1214/aoms/1177732360. URL: https://doi.org/10.1214/aoms/1177732360.

[140] Abraham Wald. "Tests of statistical hypotheses concerning several parameters when the number of observations is large". en. In: *Transactions of the American Mathematical Society* 54.3 (Mar. 1943), pp. 426–426. ISSN: 0002-9947. DOI: 10.1090/S0002-9947-1943-0012401-3. URL: http://www.ams.org/jourcgi/jour-getitem?pii=S0002-9947-1943-0012401-3 (visited on 07/09/2020).

[141] Glen Cowan et al. "Asymptotic formulae for likelihood-based tests of new physics". In: *Eur. Phys. J. C* 71 (2011), p. 1554. DOI: 10.1140/epjc/s10052-011-1554-0. arXiv: 1007.1727 [physics.data-an]. Erratum: Eur. Phys. J. C **73** (2013) 2501.

[142] A. Read. "Presentation of search results: the CLs technique". In: *Journal of Physics G: Nucl. Part. Phys.* 28 (2002), pp. 2693–2704.

[143] M. Baak et al. "HistFitter software framework for statistical data analysis". In: *Eur. Phys. J. C* 75 (2015), p. 153. DOI: 10.1140/epjc/s10052-015-3327-7. arXiv: 1410.1280 [hep-ex].

[144] Johannes Bellm et al. "Herwig 7.0/Herwig++ 3.0 release note". In: *Eur. Phys. J. C* 76.4 (2016), p. 196. DOI: 10.1140/epjc/s10052-016-4018-8. arXiv: 1512.01178 [hep-ph].

[145] ATLAS Collaboration. *Jet calibration and systematic uncertainties for jets reconstructed in the ATLAS Detector at $\sqrt{s} = 13$ TeV*. ATL-PHYS-PUB-2015-015. 2015. URL: https://cds.cern.ch/record/2037613.

[146] William Buttinger and Michel Lefebvre. *Formulae for Estimating Significance*. Tech. rep. ATL-COM-GEN-2018-026. Geneva: CERN, 2018. URL: https://cds.cern.ch/record/2643488.

[147] ATLAS Collaboration. "Search for squarks and gluinos in final states with jets and missing transverse momentum using 36 fb^{-1} of $\sqrt{s} = 13$ TeV pp collision data with the ATLAS detector". In: *Phys. Rev. D* 97.11 (2018), p. 112001. DOI: 10.1103/PhysRevD.97.112001. arXiv: 1712.02332 [hep-ex].

[148] *SUSY May 2020 Summary Plot Update*. Tech. rep. ATL-PHYS-PUB-2020-013. Geneva: CERN, 2020. URL: http://cds.cern.ch/record/2718947.

[149] Albert M Sirunyan et al. "Search for supersymmetry in proton-proton collisions at 13 TeV in final states with jets and missing transverse momentum". In: *JHEP* 10 (2019), p. 244. DOI: 10.1007/JHEP10(2019)244. arXiv: 1908.04722 [hep-ex].

[150] Albert M Sirunyan et al. "Searches for physics beyond the standard model with the M_{T2} variable in hadronic final states with and without disappearing tracks in proton-proton collisions at $\sqrt{s} = 13$ TeV". In: *Eur. Phys. J. C* 80.1 (2020), p. 3. DOI: 10.1140/epjc/s10052-019-7493-x. arXiv: 1909.03460 [hep-ex].

[151] C.G. Lester and D.J. Summers. "Measuring masses of semiinvisibly decaying particles pair produced at hadron colliders". In: *Phys. Lett. B* 463 (1999), pp. 99–103. DOI: 10.1016/S0370-2693(99)00945-4. arXiv: hep-ph/9906349.

[152] Kyle Cranmer and Itay Yavin. "RECAST: Extending the Impact of Existing Analyses". In: *JHEP* 04 (2011), p. 038. DOI: 10.1007/JHEP04(2011)038. arXiv: 1010.2506 [hep-ex].

[153] ATLAS Collaboration. "RECAST framework reinterpretation of an ATLAS Dark Matter Search constraining a model of a dark Higgs boson decaying to two b-quarks". In: (2019).

[154] ATLAS Collaboration. *Technical Design Report: A High-Granularity Timing Detector for the ATLAS Phase-II Upgrade*. Tech. rep. CERN-LHCC-2020-007. Geneva: CERN, 2020. URL: https://cds.cern.ch/record/2719855.

[155] Hartmut Sadrozinski, Abraham Seiden, and Nicolo Cartiglia. "4-Dimensional Tracking with Ultra-Fast Silicon Detectors". In: *Reports on Progress in Physics* (2017). arXiv: 1704.08666. URL: http://iopscience.iop.org/10.1088/1361-6633/aa94d3.

[156] T.T. Bohlen et al. "The FLUKA Code: Developments and Challenges for High Energy and Medical Applications". In: *Nuclear Data Sheets* 120 (2014), pp. 211 –214. ISSN: 0090-3752. DOI: http://dx.doi.org/10.1016/j.nds.2014.07.049. URL: http://www.sciencedirect.com/science/article/pii/S0090375214005018.

[157] Alfredo Ferrari et al. "FLUKA: A multi-particle transport code (Program version 2005)". In: (2005).

[158] G. Kramberger et al. "Radiation hardness of thin Low Gain Avalanche Detectors". In: *Nucl. Instrum. Meth.* A891 (2018), pp. 68 –77. ISSN: 0168-9002. DOI: 10.1016/j.nima.2018.02.018. arXiv: 1711.06003. URL: http://www.sciencedirect.com/science/article/pii/S0168900218301682.

[159] J. Lange et al. "Charge collection studies of proton-irradiated n- and p-type epitaxial silicon detectors". In: *Nucl. Instrum. Meth. A* 624.2 (2010). Ed. by Laci Andricek et al., pp. 405–409. DOI: 10.1016/j.nima.2009.11.082.

[160] The lpGBT team. "The lpBT manual". In: (). URL: http://lpgbt.web.cern.ch/lpgbt.

[161] L Amaral et al. "The versatile link, a common project for super-LHC". In: *Journal of Instrumentation* 4.12 (2009), P12003.

[162] Paul Adrien Maurice Dirac. "Quantised singularities in the electromagnetic field," in: *Proc. Roy. Soc. Lond.* A133.821 (1931), pp. 60–72. DOI: 10.1098/rspa.1931.0130.

[163] Gerard 't Hooft. "Magnetic Monopoles in Unified Gauge Theories". In: *Nucl. Phys.* B79 (1974). [,291(1974)], pp. 276–284. DOI: 10.1016/0550-3213(74)90486-6.

[164] Y. M. Cho, Kyungtae Kimm, and J. H. Yoon. "Mass of the Electroweak Monopole". In: *Mod. Phys. Lett.* A31.09 (2016), p. 1650053. DOI: 10.1142/S021773231650053X. arXiv: 1212.3885 [hep-ph].

[165] Y. M. Cho and D. Maison. "Monopoles in Weinberg-Salam model". In: *Phys. Lett.* B391 (1997), pp. 360–365. DOI: 10.1016/S0370-2693(96)01492-X. arXiv: hep-th/9601028 [hep-th].

[166] ATLAS Collaboration. "Search for Massive Long-lived Highly Ionising Particles with the ATLAS Detector at the LHC". In: *Phys. Lett.* B698 (2011), pp. 353–370. DOI: 10.1016/j.physletb.2011.03.033. arXiv: 1102.0459 [hep-ex].

[167] ATLAS Collaboration. "Search for magnetic monopoles in $\sqrt{s} = 7$ TeV pp collisions with the ATLAS detector". In: *Phys. Rev. Lett.* 109 (2012), p. 261803. DOI: 10.1103/PhysRevLett.109.261803. arXiv: 1207.6411 [hep-ex].

[168] ATLAS Collaboration. "Search for magnetic monopoles and stable particles with high electric charges in 8 TeV pp collisions with the ATLAS detector". In: *Phys. Rev.* D93.5 (2016), p. 052009. DOI: 10.1103/PhysRevD.93.052009. URL: https://link.aps.org/doi/10.1103/PhysRevD.93.052009.

[169] H. Jansen et al. "Performance of the EUDET-type beam telescopes". In: *EPJ Techniques and Instrumentation* 3.1 (2016), p. 7. DOI: 10.1140/epjti/s40485-016-0033-2. arXiv: 1603.09669 [physics.ins-det].

[170] J. Albert et al. "Prototype ATLAS IBL Modules using the FE-I4A Front-End Readout Chip". In: *JINST* 7 (2012), P11010. DOI: 10.1088/1748-0221/7/11/P11010. arXiv: 1209.1906 [physics.ins-det].

[171] N. Cartiglia et al. "Beam test results of a 16 ps timing system based on ultra-fast silicon detectors". In: *Nucl. Instrum. Meth.* A850 (2017), pp. 83–88. DOI: 10.1016/j.nima.2017.01.021. arXiv: 1608.08681 [physics.ins-det].

[172] L. Masetti et al. "Beam test measurements of Low Gain Avalanche Detector single pads and arrays for the ATLAS High Granularity Timing Detector". In: *JINST* 13.06 (2018), P06017–P06017. DOI: 10.1088/1748-0221/13/06/p06017. arXiv: 1804.00622 [physics.ins-det].

[173] *SLAC Python Based Hardware Abstraction & Data Acquisition System*. URL: https://github.com/slaclab/rogue.

Titre: Recherche de la supersymétrie avec le détecteur ATLAS et développement du High Granularity Timing Detector

Mots clés: Détecteur de Temps, Supersymétrie, ATLAS

Résumé:
Le Modèle Standard de la physique des particules est un cadre théorique couronné d'un extrême succès, décrivant les particules élémentaires et leurs interactions. Avec la découverte du boson de Higgs par les expériences ATLAS et CMS en 2012, le Modèle Standard est désormais complet. Cependant, il demeure toujours des questions ouvertes, appelant un modèle théorique plus large qui englobe le Modèle Standard, tout en fournissant des mécanismes pour les phénomènes inexpliqués. La supersymétrie offre un tel cadre en introduisant une nouvelle symétrie entre bosons et fermions. Elle permet de résoudre le problème de la hiérarchie de la masse du boson de Higgs et offre également un candidat pour expliquer la matière noire de l'univers.
La première partie de cette thèse est la recherche de supersymétrie avec le détecteur ATLAS au LHC, en utilisant l'ensemble des données du Run 2, dont la luminosité intégrée s'élève à 139 fb^{-1}. Mon travail se focalise sur la recherche de squarks et de gluinos, les super-partenaires des quarks et des gluons, dans des modèles où la R-parité est conservée et dans les états finaux comprenant des jets et une grande énergie transverse manquante. Ma principale contribution à cette analyse fut le développement et l'optimisation d'une nouvelle technique, nommée ajustement "Multi-Bin", pour améliorer la séparation du signal par rapport au bruit et étendre la portée d'exclusion de la recherche. Le gain attendu en la section efficace exclue par l'utilisation d'une configuration d'ajustement Multi-Bin, par opposition à l'approche traditionnelle "cut& count", a été estimé à 40-70% dans les modèles étudiés. De plus, j'ai travaillé sur l'inférence statistique de la recherche, allant de l'évaluation des diverses systématiques à l'interprétation des résultats dans différents modèles supersymétriques simplifiés. Aucun excès au-delà des prédictions du Modèle Standard n'a été trouvé, et, par conséquent, les squarks et les gluinos possédant des masses allant respectivement jusqu'à 1.85 TeV et 2.34 TeV ont été exclus. Ce résultat est une amélioration significative par rapport au cycle précédent de l'analyse, et l'une des contraintes les plus fortes sur les masses actuelles des squarks et des gluinos.
La phase d'acquisition de données à haute luminosité (HL-LHC) verra le taux des collisions augmenter d'un facteur de 5 à 7. Afin d'atténuer l'augmentation de l'empilement, ATLAS installera un nouveau détecteur au silicium de haute granularité avec une très bonne résolution temporelle qui sera situé dans la région avant, le High Granularity Timing Detector (HGTD). L'objectif de ce détecteur est d'atteindre une résolution en temps meilleure que 50 ps par trace. La seconde partie de cette thèse porte sur deux aspects principaux du développement du HGTD. D'une part, j'ai effectué des études avec la simulation pour évaluer l'occupation et les besoins du système de lecture du détecteur avec diverses géométries. L'occupation du détecteur doit rester inférieure à 10 %, afin de pouvoir correctement attribuer les dépôts d'énergie des traces traversant le détecteur. Il a été constaté que cette limite était satisfaite avec une taille de capteur de 1.3 $\times$ 1.3 mm^2, qui est désormais la référence pour le futur détecteur. De plus, l'organisation du système de lecture a été optimisée afin de maximiser l'espace disponible et de minimiser les composants nécessaires. La performance de tout détecteur au silicium est fortement liée à la conception du circuit électronique front-end. Dans le cadre de mon travail à HGTD, j'ai également participé à la caractérisation de deux prototypes électroniques front-end, ALTIROC0 et ALTIROC1, à la fois en laboratoire avec un système d'étalonnage et en tests faisceaux avec des électrons et des protons de haute énergie. La résolution temporelle obtenue était inférieure à 55 ps dans tous les appareils testés, la meilleure performance obtenue étant de 34 ps.

Title: Research of Supersymmetry with the ATLAS detector and development of the High Granularity Timing Detector

Keywords: Timing Detector, Supersymmetry, ATLAS

Abstract:
The Standard Model of particle physics is an extremely successful theoretical framework, describing the elementary particles and their interactions. With the discovery of the Higgs boson by the ATLAS and CMS experiments in 2012, the Standard Model is now complete. However, open questions remain unanswered, calling for a larger theoretical model that encapsulates the Standard Model, while providing mechanisms for the unexplained phenomena. Supersymmetry offers such a framework by introducing a new symmetry between bosons and fermions. It provides potential solutions to the hierarchy problem for the Higgs boson mass and also offers a candidate to explain the dark matter of the universe.
The first part of this thesis is the search for supersymmetry with the ATLAS detector at LHC, using the full dataset of Run 2, amounting to an integrated luminosity of 139 fb^{-1}. The focus is on the search for squarks and gluinos, the "super-partners" of quarks and gluons, in models where R-parity is conserved and in final states with jets and large missing transverse momentum. My main contribution to this analysis was the development and optimization of a novel technique named Multi-Bin fit to enhance the signal to background separation and extend the exclusion reach of the search. The expected gain in the excluded cross section from using a Multi-Bin fit configuration, opposed to the traditional "cut&count" approach, was estimated to be 40 - 70 % in the studied models. In addition, I worked on the statistical inference of the search, ranging from the evaluation of various systematics to the interpretation of the results in various simplified supersymmetric models. No excess above the Standard Model prediction was found and therefore squarks and gluinos with masses up to 1.85 TeV and 2.34 TeV were excluded, respectively. This result is a significant improvement over the previous round of the analysis and one of the strongest constraints on squark and gluino masses today.
The high-luminosity data acquisition phase (HL-LHC) will see an increase of the collision rate by a factor of 5 to 7. In order to mitigate the increase of pile-up, ATLAS will install a new highly granular silicon detector with a very good time resolution that would be located at the forward region, the High Granularity Timing Detector (HGTD). The goal of this detector is to provide a time resolution better than 50 ps per track. The second part of this thesis focuses on two main aspects in the development of HGTD. On one hand, I performed simulation studies to evaluate the occupancy and read-out requirements of the detector under various geometries. The occupancy of the detector must remain below 10%, in order to correctly assign energy deposits to tracks crossing the detector. It was found that this requirement was met with a sensor size of 1.3 $\times$ 1.3 mm^2, which is now the baseline for the future detector. Additionally, the organization of the on-detector read-out system was optimised, in order to maximise the available space and minimise the necessary components. The performance of any silicon detector is strongly linked to the design of the front-end electronic circuit. As part of my work in HGTD, I also participated in the characterization of two front-end electronic prototypes, ALTIROC0 and ALTIROC1, both in laboratory with a calibration system and in testbeam with highly energetic electrons and protons. The temporal resolution was found to be better than 55 ps in all tested devices, with a best achieved performance of 34 ps.

Université Paris-Saclay

Espace Technologique / Immeuble Discovery

Route de l'Orme aux Merisiers RD 128 / 91190 Saint-Aubin, France